

THE MEASUREMENT OF PEROXY  
RADICALS IN REMOTE  
ATMOSPHERE:  
THE PERCA TECHNIQUE

Thesis submitted for the degree  
Of Doctor of Philosophy  
at the University of Leicester

by

Arunasalam Karunaharan (MSc)  
Department of Chemistry  
University of Leicester

September 2011

The work in this thesis was conducted at the Department of Chemistry of the University of Leicester in the Atmospheric Chemistry group between June 2006 and September 2011. The work is that of the author unless acknowledged in the thesis.

The thesis may be made available for consultation within the library of the University of Leicester.

Arunasalam Karunaharan

Leicester

07<sup>th</sup> September 2011

# The measurement of peroxy radicals in remote atmosphere: the PERCA technique

Thesis abstract

Submitted by Arunasalam Karunaharan

September 2011

Peroxy radicals act as chain carriers in trace gas oxidation reactions. Total peroxy radicals are  $\text{HO}_2 + \text{RO}_2$ .  $\text{HO}_2$  is the hydro peroxy radical and  $\text{RO}_2$  is the family of alkyl peroxy radicals, where R is an alkyl group. The oxidation chemistry driven by peroxy radicals is vital for controlling tropospheric ozone production/loss rates. The thesis details the University of Leicester PEroxy Radical Chemical Amplifier (PERCA (Version 3.5)) instrument. Peroxy radical measurements using a single- and dual-channel PERCA instrument were taken in two relatively clean sites: the tropical rainforest boundary layer in Borneo for two campaigns in 2008 and the tropical marine boundary layer at Cape Verde for three campaigns in 2009.

In the tropical rainforest boundary layer in Borneo, the diurnal cycle of peroxy radicals' concentrations showed an asymmetric shape that was considerably shifted towards the afternoon owing to the high  $[\text{HO}_2 + \text{RO}_2]$  measured for midday, these can persist during the afternoon under low  $\text{NO}_x$  conditions. Night-time  $[\text{HO}_2 + \text{RO}_2]$  were measured up to 29 pptv (parts per trillion by volume). The calculation of production and loss terms in the ozone budget indicated that there was net ozone production in the rainforest. Ozone production rates were greatest when  $[\text{NO}_x]$  were high, while increasing  $[\text{isoprene}]$  decreased ozone production.

The peroxy radical measurements for the Seasonal Oxidant Study (SOS) campaigns at Cape Verde show a diurnal cycle that reaches a maximum at midday and a minimum during the night. Net ozone production was negative (i.e. an ozone loss) and was maximised for summer months. An analysis of the Cape Verde ozone loss rate calculated with and without including halogen species is presented, and concludes that whilst ozone production was mainly  $\text{NO}_x$  controlled, halogen chemistry could have a major contribution to the ozone loss.

# Acknowledgements

I would like to thank my supervisor Prof Paul Monks for encouragement, his fresh ideas, insights, and suggestions and help in moving my analyses forward and modern data analysis techniques and writing-up that has gone into producing this thesis and he offered nice foreign travel opportunities over the course of my Ph.D., and for being confident even when my face wasn't good. I express my deep and sincere gratitude to my supervisor for his patience and encouragement that carried me on through difficult times such as in field site (Borneo jungle and Cape Verde), stressful incidents, and his valuable feedback contributed greatly to this thesis. I can't forget him in my life to be honest.

The resubmitted thesis was examined (the viva took place on 15<sup>th</sup> December 2011) by Dr Claire Reeves (Environmental Sciences, University of East Anglia) and Dr Stephen Ball (Department of Chemistry, University of Leicester). Special thanks go to them individually, both of examiners provided very valuable and constructive comments, with consistent quality ideas throughout this thesis and great thanks again, keep up the good work. The Examiners comments were to help me write the resubmitted thesis as well.

A huge thank you to the PSM groups for always being there for fun or to talk to - Dan, Alex and Kevin for welcoming me and starting me off, Bob for the pleasure of your jokes, special thanks to Dan for teaching me how to run PERCA and for sharing the laboratory with me, Virginia for an experience through hard times in jungle, Roland for stress relief at the CVAO (Cape Verde Atmospheric Observatory) field campaign in

and out, Zoe helped towards the end of the CVAO campaign, and Chris, Kerry, Rebecca, Timo, Matt, Mindy, Gary, Jonny, Andy, Steve, Karen, Becca, Erica, Ian, Mark and Corey, for Department cricket match and many others work and Leicester somewhere I wanted to be. All the friends I have made on OP3, SOS and other field campaigns, thank you for making this an interesting period of my life.

I wish to express my warm and sincere thanks to Chris Goddard for organising everything through the Department and University with standard and quick response.

Phil Acton, Julie Spence, Justine Shepard, Anne Crane, Keith Wilkinson, John Wheald, Carl Schieferstein, Roy Batchen, Si Choudhury and, thank you for never complaining no matter what the request and at how short notice - I still can't quite believe how much you put yourselves out to support our work.

Finally and most importantly my family, especially Mum and Dad, Father in Law and Mother in Law for never ending and unconditional support and My Wife for tireless encouragement, useful comments and supporting financial wise and My Sister's and their families and Brother in Laws. Without you all I would never have done it.



1.5.4.4. Variability of peroxy radical concentration with NO <sub>x</sub>	37
1.5.4.5. Non-zero peroxy radical concentration at night time	38
1.6 Research in this thesis: What do we want to achieve?	39
1.7 Summary	40
<b>Chapter 2 - Peroxy Radical Measurement</b>	<b>42</b>
2.1 The PERCA technique	43
2.1.1 PEroxy Radical Chemical Amplification – Laser Induced Fluorescence (PERCA-LIF)	46
2.2 Matrix Isolation Electron Spin Resonance (MI-ESR)	47
2.3 Fluorescence Assay by Gas Expansion (FAGE)	48
2.4 Peroxy radical Chemical Ionisation Mass Spectrometry (PerCIMS)	50
2.5 The University of Leicester dual-channel PERCA (V3.5) instrument	53
2.5.1 Deployment in the field	57
2.5.1.1 The inlet system	59
2.5.1.2 Detector systems	63
2.5.1.3 Linearisation unit	65
2.5.1.4 Data-capture and computer system	66
2.5.1.5 Scrubbing system	67
2.5.1.6 Reagent gases	67
2.5.1.7 The pumping system	69
2.5.2 The calibration system	69

2.5.2.1	NO <sub>2</sub> sensitivity calibration of the luminol detectors	69
2.5.2.2	Chain length calibration	73
2.5.2.3	Measurement of $j(\text{CH}_3\text{I})$	88
2.5.2.4	Water vapour interference correction	92
2.6	Error analysis	95
2.6.1	Dual-channel PERCA (V3.5 and V4) instrument	98
2.7	Data work-up	100
2.8	Summary	104
<b>Chapter 3</b>	<b>Peroxy radical measurements in South East Asian</b>	<b>105</b>
	<b>Tropical rainforest boundary layer (OP3)</b>	
3.1	Introduction to the Malaysian rainforest campaigns	105
3.1.1	Campaign meteorology	108
3.1.2	Overview of the measurements made in OP3	112
3.1.3	Data averaging process for the OP3 (1) and OP3 (3) campaigns	115
3.2	Results	119
3.2.1	Time series of chemical profile	119
3.2.2	Chemical Observations at OP3 (1) and OP3 (3)	121
3.2.3	Peroxy radicals in the OP3 campaigns	124
3.2.3.1	Time series of peroxy radicals and $j(\text{O}^1\text{D})$	124
3.2.3.2	Average diurnal cycles of peroxy radicals and $j(\text{O}^1\text{D})$	126
3.2.3.3	NO <sub>x</sub> and peroxy radicals during daytime	132
3.2.3.4	Night time radicals	135
3.2.3.5	Overall photochemistry	140
3.2.3.6	Peroxy radicals and isoprene	153



## SOS (3) campaigns from the BADC website

4.4 Results	205
4.4.1 Campaign meteorology	205
4.4.2 Peroxy radicals and wind direction	207
4.4.3 Steady state analysis for SOSs	209
4.4.3.1 Time series of peroxy radical in SOS (1), SOS (2) and SOS (3) campaigns	213
4.4.3.2 Mean diurnal cycles of peroxy radicals, $j(\text{O}^1\text{D})$ and $\sqrt{j(\text{O}^1\text{D})}$	217
4.4.3.3 Linear correlation between peroxy radicals, $j(\text{O}^1\text{D})$ and $\sqrt{j(\text{O}^1\text{D})}$	220
4.4.3.4 Mean linear correlation between peroxy radicals, OH and $\sqrt{\text{OH}}$ for SOS (1), SOS (2) and SOS (3)	223
4.4.3.5 Mean diurnal cycles of peroxy radicals, OH for SOS (1), SOS (2) and SOS (3)	226
4.4.3.6 Peroxy radical and NO <sub>x</sub> relationships during daytime	227
4.4.3.7 HO <sub>2</sub> : (HO <sub>2</sub> +RO <sub>2</sub> ) ratio	229
4.4.3.8 Night-time chemistry	232
4.5 Photochemical ozone production	237
4.5.1 Halogen compounds possible contribution to ozone loss to ozone loss	247
4.5.2 The ozone production rate $P(\text{O}_3)$ , peroxy radicals and NO relationships	256
4.5.3 Ozone compensation point	260

4.6 Peroxy radical production and loss	265
4.6.1 Sensitivity analysis of radical budget with halogen Chemistry	270
4.6.2. Effect of averaging period on data analysis for SOS (1), SOS (2) and SOS (3) campaigns	280
4.7 Conclusions from the SOS campaigns	280
<b>Chapter 5 A comparison of boundary layer photochemistry             in both tropical rainforest and tropical marine air</b>	<b>283</b>
5.1 Introduction	283
5.1.1 Role of rainforest and marine in the atmosphere	283
5.1.2 Characteristics of Borneo rainforest GAW station, and Cape Verde Atmospheric Observatory	285
5.2 Results	286
5.2.1 A comparison of chemical species between rainforest and marine campaigns	286
5.2.1.1 Peroxy radical diurnal cycles	286
5.2.1.2 Peroxy radical correlation with other chemical species	289
5.2.1.3 The effect of NO <sub>x</sub> on peroxy radical concentrations	290
5.2.1.4 Night time radicals	291
5.2.2 Photochemical ozone formation	294
5.2.2.1 Comparisons of daily ozone production between campaigns	294
5.2.2.2 Comparisons of daily ozone lose between	296

SOS (3) campaigns	
5.2.2.3 <i>N</i> (O <sub>3</sub> ) variations through the campaigns	299
5.2.2.4 Ozone photochemistry variations	301
5.3 Conclusion	304
<b>Chapter 6 Conclusions and future work</b>	<b>305</b>
6.1 Peroxy radical measurements	309
6.2 Global picture of ozone photochemistry in both the rainforest and marine sites	312
6.3 Summary of peroxy radical levels and trends in this thesis	314
<b>Appendix A - Postgraduate Record</b>	<b>316</b>
A.1 Induction/Training Sessions Attended	316
A.2 Academic Courses	317
A.3 Departmental Seminars	317
A.4 Summer school attended	318
A.5 Conferences and meetings	318
A.5.1 Conferences	318
A.5.2 Meetings	319
A.6 Presentations	320
A.7 Field campaigns	320
A.8 Publications	321
A.9 References	322

# Glossary and Definitions

<b>AMS</b>	<b>Aerosol Mass Spectrometry</b>
<b>BOC</b>	<b>British Oxygen Company Ltd.</b>
<b>BADC</b>	<b>British Atmospheric Data Centre</b>
<b>CCN</b>	<b>Cloud Condensation Nucleus</b>
<b>CL</b>	<b>Chain Length</b>
<b>DOAS</b>	<b>Differential Optical Absorption Spectroscopy</b>
<b>DPC</b>	<b>Data Personal Computer</b>
<b>FAGE</b>	<b>Fluorescence Assay by Gas Expansion</b>
<b>FT</b>	<b>Free Troposphere</b>
<b>GC</b>	<b>Gas Chromatography</b>
<b>GPS</b>	<b>Global Positioning System</b>
<b>IGAC</b>	<b>International Global Atmospheric Chemistry</b>
<b>LIF</b>	<b>Laser Induced Fluorescence</b>
<b>MCM</b>	<b>Master Chemical Mechanism</b>
<b>MFC</b>	<b>Mass Flow Controller</b>
<b>MFM</b>	<b>Mass Flow Meter</b>
<b>MIESR</b>	<b>Matrix Isolation Electron-Spin Resonance</b>
<b>NERC</b>	<b>Natural Environment Research Council</b>
<b>NMHC</b>	<b>Non Methane Hydrocarbon</b>
<b>OP3</b>	<b>Oxidant Particle (3 campaigns)</b>
<b>OVOC</b>	<b>Oxygenated Volatile Organic Compound</b>
<b>PAN</b>	<b>Peroxyacetyl nitrate</b>
<b>PBL</b>	<b>Planetary Boundary Layer</b>

<b>PC</b>	<b>P</b> ersonal <b>C</b> omputer
<b>PERCA</b>	<b>P</b> Eroxy <b>R</b> adical <b>C</b> hemical <b>A</b> mplifier
<b>PerCIMS</b>	<b>P</b> eroxy <b>R</b> adical <b>C</b> hemical <b>I</b> onisation <b>M</b> ass <b>S</b> pectrometry
<b>PMT</b>	<b>P</b> hoto <b>M</b> ultiplier <b>T</b> ube
<b>ppbv</b>	<b>p</b> arts <b>p</b> er <b>b</b> illion by <b>v</b> olume ( $10^{-9}$ )
<b>ppmv</b>	<b>p</b> arts <b>p</b> er <b>m</b> illion by <b>v</b> olume ( $10^{-6}$ )
<b>pptv</b>	<b>p</b> arts <b>p</b> er <b>t</b> rillion by <b>v</b> olume ( $10^{-12}$ )
<b>PTR-MS</b>	<b>P</b> roton <b>T</b> ransfer <b>R</b> eaction – <b>M</b> ass <b>S</b> pectrometry
<b>ROXMAS</b>	<b>R</b> Ox <b>M</b> ass <b>S</b> pectrometry
<b>sccm</b>	standard cubic centimetres per <b>m</b> inute
<b>slpm</b>	standard litres <b>p</b> er <b>m</b> inute
<b>SOS</b>	<b>S</b> easonal <b>O</b> xidant <b>S</b> tudy
<b>UK SOLAS</b>	<b>U</b> nited <b>K</b> ingdom <b>S</b> urface <b>O</b> cean <b>L</b> ower <b>A</b> tmosphere <b>S</b> tudy
<b>UL</b>	<b>U</b> niversity of <b>L</b> eicester
<b>UPS</b>	<b>U</b> ninterruptible <b>P</b> ower <b>S</b> upply
<b>VOC</b>	<b>V</b> olatile <b>O</b> rganic <b>C</b> ompound
<b>VUV</b>	<b>V</b> acuum <b>U</b> ltra <b>V</b> iolet

# Chapter 1

## Introduction

Photolysis of tropospheric molecules and the subsequent reaction of the photoproducts drive much of the oxidation photochemistry in the atmosphere. The work contained within this thesis is primarily concerned with the role of peroxy radicals in the photochemistry of a tropical Borneo rainforest and the tropical marine boundary layer. Total peroxy radicals are  $\text{HO}_2 + \text{RO}_2$ .  $\text{HO}_2$  is the hydro peroxy radical and  $\text{RO}_2$  is the family of alkyl peroxy radicals, where R is an alkyl group. This chapter provides an introduction to the atmosphere and relevant atmospheric chemistry.

### 1.1 The Earth's atmosphere

The Earth's atmosphere is a thin blanket of gas which stretches above the surface of the planet out to a distance of approximately 100 km. The atmosphere's mass is estimated to be  $5.2 \times 10^{18}$  kg, approximately 90% of which is contained by the troposphere according to Wayne *et al.*, (2000). As far as its composition is concerned, it has been established that it has a dry mixture of 78% nitrogen, 21% oxygen, and 1% argon, and it is an important to emphasize that the percentages mentioned are essentially constant until close to an altitude of 80-90 km. The atmosphere is vital for our existence.

However, it is not only these bulk components that are liable to be encountered within the Earth's atmosphere, as there are traces of plenty of other species, such as gases or aerosols, e.g. ash from volcanoes. Although these trace species amount to less than 1%

of the atmosphere's composition, they still play an essential role in its chemistry and physics. The sources of these trace gases result from various biogenic, anthropogenic, chemical or geological processes occurring mainly at the Earth's surface. Among the trace species present in the atmosphere, there are carbon species such as CO, CO<sub>2</sub>, CH<sub>4</sub> and other volatile organic compounds (VOCs), nitrogen containing species such as NO, NO<sub>2</sub>, NO<sub>3</sub>, N<sub>2</sub>O, peroxyacetylnitrate (PAN) and NH<sub>3</sub>, sulphur species such as SO<sub>2</sub>, dimethylsulphide (DMS) and H<sub>2</sub>S, and halogenated compounds such as chloroflorocarbons (CFCs), hydrochloroflorocarbons (HCFCs), HCl, HF, CH<sub>3</sub>Cl, CH<sub>3</sub>Br and CH<sub>3</sub>I. Other trace gases such as ozone, water and various radical species are also formed photo chemically.

### 1.1.1 The structure of the atmosphere

The change of temperature with altitude is the key factor in separating the atmosphere into four different regions. Figure 1.1 shows the vertical temperature profile:

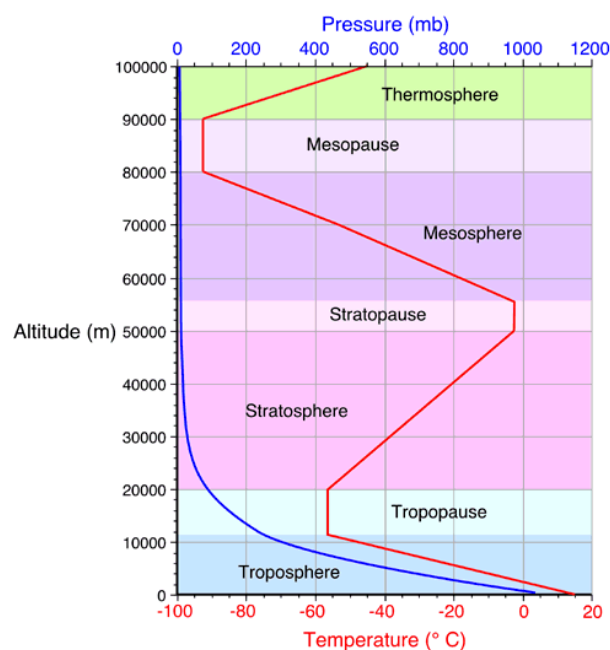


Figure 1.1 - Vertical temperature profile, pressure through the Earth's atmosphere, from (<http://www.chem.duke.edu/~bonk/Chem8304/read2207.html>)

As can be seen in Figure 1.1, the troposphere is the closest region to the Earth's surface, its maximum altitude reaching about 15 km and its temperature decreasing as the altitude increases. Its name originating from the Greek *tropos* = turning and *sphaira* = ball, (Finlayson-Pitts *and* Pitts (2000)), the troposphere is the region that allows relatively rapid mixing of chemical species; mixing can be completed in a matter of days from the Earth's surface to the very top of the troposphere depending on weather conditions, e.g. deep convection in weather system.

Within the troposphere, there is another key division: the planetary boundary layer (PBL), which has a variation in extension from a few hundred metres during night time, reaching approximately 0.5-2 km during day time at mid latitudes, above which lies the free troposphere (FT). The PBL is characterised owing to the intensive heating from the Earth's surface, as well as the contact of air masses with the ground, the layer closer to the ground. PBL is continuously influenced by the processes taking place at the surface level. The PBL acts to "trap" emissions at the surface.

The next region within the atmosphere is the stratosphere, which extends from 15 to 50 km above the planetary surface, and in contrast to the troposphere is characterized by very little mixing (its name from the Latin *stratum* = layer). Wayne *et al.*, (2000) pointed out that the slow process of mixing is the main reason for the rise of temperature through the stratosphere due to the absorption of solar radiation by the ozone. The slow mixing therefore makes it more difficult for species to be transported through the stratosphere, which can take years.

The next region above the stratosphere is called the mesosphere and is characterized by a decrease of temperature as the altitude increases, the coldest part of this region being encountered at the border between the mesosphere and the thermosphere, i.e. mesopause, at an altitude of about 85 km. The mesosphere contains only 0.1% of the atmospheric mass. Decrease in temperature stops at the level of the mesopause, where due to the absorption of short wavelength solar radiation by molecular nitrogen and oxygen, the temperature starts rising again.

## 1.2 Ozone in the Atmosphere

Also bearing the name of the ‘ozone layer’, the stratosphere is the atmospheric region where the highest concentration of ozone can be found. Figure 1.2 shows that the maximum occurs at the altitude of 20-30 km above the Earth’s surface.

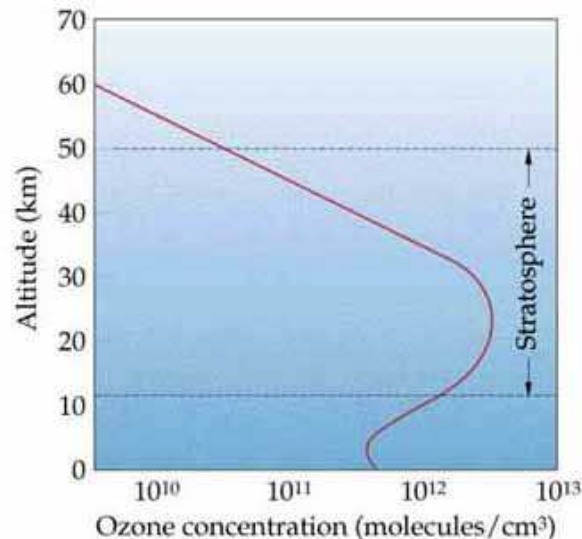


Figure 1.2 - Variation in ozone concentration in the atmosphere, as a function of altitude from (<http://wps.prenhall.com/wps/media/objects/3312/3392285/blb1803.html>)

The critical role of the ozone layer is to protect life on the Earth by a way of absorbing damaging UV solar radiation.

The reactions that take place within the ozone layer and which lead to a steady-state concentration of ozone (Chapman scheme) are:



where M, in reaction 1.2, is a third body (usually nitrogen or oxygen in the atmosphere). This is a simplification of ozone chemistry in stratosphere. This inter-conversion process converts UV radiation into thermal energy, heating the stratosphere.

However, Farman *et al.*, (1985) brought attention to the destructive nature of mankind's actions via the continuous release of chlorofluorocarbons, whose photolysis and subsequent chemistry lead to a reduction of the ozone layer over Antarctica. The mechanism was further elaborated by Molina and Rowland (1974) who stressed that the radical species released into the stratosphere (e.g. chlorine and bromine atoms) from the photolysis of CFCs act as a reactive halogen source under the conditions present in the winter /spring time Antarctic stratosphere. Halogen species are the main cause for the destruction of the ozone layer via catalytic cycles.



This is a simplification as mechanism of ClO chemistry in stratosphere.

## 1.2.1 Tropospheric ozone

As much as the benefits of the ozone layer are apparent, the presence of ozone in the troposphere can cause harm. Tropospheric ozone formed by photochemical smog can degrade health in humans, animals or plant life. Lippman *et al.*, (1993) noted that excess of ozone can cause irritation to the respiratory system, an increase in respiratory infection and the effects of asthma, as well as degrade lung function. Regarding plant life, Fiore *et al.*, (1998) explored the range of damage that excessive ozone can cause to crops. Concrete examples of the harmful effects have been emphasized by Stedman *et al.*, (2004), where between 423 and 769 excess deaths (21-38% of excess deaths) occurring in Europe during the heat wave of August 2003 were as a result of increasing ozone and PM<sub>10</sub> (particulate matter with a diameter of 10µm or less) concentrations in the UK .

Simmonds *et al.*, (2004) has shown an increase in the ozone concentration in remote areas such as Mace Head, Ireland (53° 19' N, -9° 54' W), between 1987 and 2003. Liu *et al.*, (1987) observed that ozone exists in the troposphere (living for several months) can be formed as a result of trace gases being processed photochemically and thus forming ozone close to the surface, as will be detailed in sections 1.3 and 1.4.1. This process can take place far from the emissions, owing to the fact that air pollutants can travel away from their sources on surface, for a distance of 400-500 km per day depending on wind speed. Mickley *et al.*, (2004) emphasized that changes in tropospheric ozone and its precursors (NO<sub>x</sub>, CO and VOCs) are coupled to the Earth's climate system. Ozone precursors influence the amount of other greenhouse gases in the atmosphere. Cutting back emissions of methane and O<sub>3</sub> precursors is as important as reducing CO<sub>2</sub> emissions (Hansen *et al.*, (2000)). CO<sub>2</sub> is being more effective global

warmer than tropospheric ozone on a global scale. However, increases in tropospheric ozone concentrations have climate importance. The distribution of ozone means that any ozone formation may occur away from precursor emission regions. The processes and consequences of ozone production in the tropical Borneo rainforest are covered in section 1.5.

### 1.3 Tropospheric photochemistry

The vital factor responsible for the chemical processes initiated in the atmosphere, as well as for the loss of stable molecules within it, is photochemistry. Tropospheric photochemistry can only occur in the case of wavelengths longer than 290 nm due to the absorption of light both by the ozone in the stratosphere and by oxygen. The ozone absorbs wavelengths between 210-290 nm, while the oxygen absorbs the wavelengths shorter than 230 nm; therefore 290 nm is the “atmospheric cut-off”. There is a variation in the intensity of solar radiation reaching the Earth’s surface, this variation being influenced by the species that constitute the atmosphere. The photochemical reactions in Figure 1.3 (Kraus and Hofzumahaus (1998)) are important factors for the lifetime of various compounds and for producing radicals. Figure 1.3 shows some of the species photodissociated by solar flux in the troposphere and the corresponding wavelengths at which they photolyse.

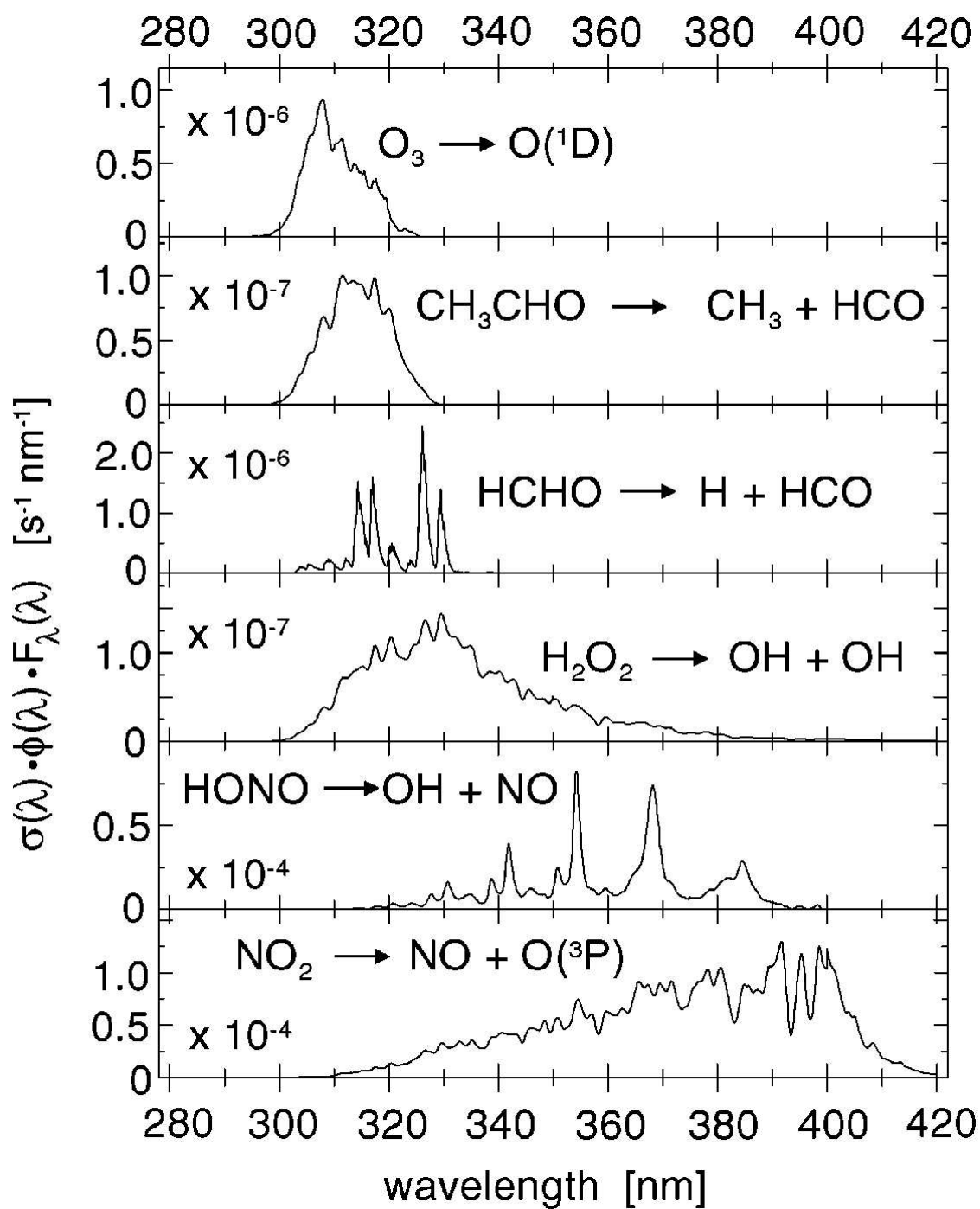


Figure 1.3 - Action spectrum showing photodissociation wavelengths for  $O_3$ ,  $CH_3CHO$ ,  $HCHO$ ,  $H_2O_2$ ,  $HONO$  and  $NO_2$  from Kraus and Hofzumahaus *et al.*, (1998)

### 1.3.1 Photolysis rates

This section attempts to underline the importance of the rate at which photochemistry is taking place within the atmosphere. If a molecule absorbs light of sufficient energy that a molecule could be photodissociated. Photodissociation can be represented in the first order chemical reaction:



The rate constant of this photodissociation, symbolized by  $j_{(AB)}$ , depends on the solar actinic flux experienced by the molecule,  $F(\lambda)$ , the photodissociation quantum yield of the molecule,  $\phi$ , and the absorption cross-section of the molecule,  $\sigma$ .

$$j_{(AB)} = \int_{\lambda_{\min}}^{\lambda_{\max}} F(\lambda) \phi(\lambda, T) \sigma(\lambda, T) d\lambda \quad (1.10)$$

The actinic flux,  $F(\lambda)$ , is the spherical flux density, incident over all angles. The actinic flux is capable of producing photodissociation in photo-actively labile molecules through the atmosphere. The unit of the actinic flux is photons  $\text{cm}^{-2} \text{s}^{-1} \text{nm}^{-1}$ . The quantum yield,  $\phi$ , is the number of molecules dissociated per photon of light absorbed. The absorption cross-section,  $\sigma$  ( $\text{cm}^2 \text{molecule}^{-1}$ ) is efficiency with which a molecule can absorb light. All the quantities actinic flux, absorption cross section and quantum yield depend on wavelength.

Through equation (1.10), the photolysis rate of the molecule can be established, provided that  $F(\lambda)$ , the actinic flux, is measured over the wavelengths that can be absorbed by that particular molecule and supposing that the absorption cross-section and quantum yield for that specific molecule are known. In practice, it is only the

wavelengths from 290 nm to a molecule specific upper wavelength that are to be considered for the process of photodissociation and owing to the atmospheric cut-off. The upper wavelength depends on the specific molecule, e.g. 340 nm and 420 nm are upper wavelengths for ozone and NO<sub>2</sub> molecules, respectively. One of the main processes important for the atmospheric chemistry is the photolysis of ozone to form electronically excited oxygen atoms O(<sup>1</sup>D), for which it is necessary to have a wavelength of less than 340 nm, an aspect which shall be discussed in section 1.3.2. For the photolysis of NO<sub>2</sub> it is required to have 320-420 nm wavelengths.

### 1.3.2 The OH radical

Among the reactions taking place in the atmosphere, the oxidation of the trace gas species is vital, and many of these processes occur due to hydroxyl radical (OH) chemistry which has been called a “cleanser” of the troposphere (Heard and Pilling (2003)). Two other oxidants ozone and the NO<sub>3</sub> radical (during night time) also contribute to the atmosphere’s oxidising capacity. Owing to the fact that OH can only act as a cleanser during day time because it is produced photochemically and only survives in the atmosphere for the order of seconds. Much of night time chemistry is initiated by a complementary species, the NO<sub>3</sub> radical, which only survives during night time because it is photolysed rapidly during day time. There is a greater concentration of NO<sub>3</sub> in the atmosphere, of the order of 10<sup>9</sup> molecule cm<sup>-3</sup>, compared to the 10<sup>6</sup> molecules cm<sup>-3</sup> of OH. Wayne *et al.*, (2000) noted that the OH is more reactive than NO<sub>3</sub> within the atmosphere. The reaction rates depend on the product of rate coefficient and concentration. Atkinson and Arey (2003) explained that the kinetic database for the OH radical reactions is significantly larger than that for the NO<sub>3</sub> radical reactions. For example, Atkinson and Arey (2003) showed that the rate constant

for the reactions of OH with propene ( $2.63 \times 10^{-11} \text{ cm}^3 \text{ molecule}^{-1} \text{ s}^{-1}$  at 298 K, 1bar) is greater than that for the reaction between  $\text{NO}_3$  and propene ( $9.49 \times 10^{-15} \text{ cm}^3 \text{ molecule}^{-1} \text{ s}^{-1}$  at 298 K, 1bar).

The chemical reaction of ozone photolysis needs to be considered, the result of which is an electronically excited O ( $^1\text{D}$ ) atom, which is then involved in the reaction with water vapour to form two OH radicals (Levy *et al.*, (1971)):



A large fraction of O( $^1\text{D}$ ) molecules is quenched by collisions with a molecule of the atmosphere's bulk gases M to return the oxygen atom to the ground state O ( $^3\text{P}$ ). The ground state oxygen atoms then recombine with oxygen molecules to reform ozone. Thus,



Although ozone photolysis is the primary method of OH production, there are also secondary methods of producing OH: the photodissociation of acetone, formaldehyde, HONO and  $\text{H}_2\text{O}_2$ . Monks *et al.*, (2005) reviewed that this contribution is important in polluted air. The compounds mentioned above are an integral part of the process of OH initiated oxidation.



HONO builds up overnight in the presence of  $\text{NO}_2$ . HONO is rapidly photolysed in the early morning. OH is formed in the early morning is a result of the photolysis of HONO. At the moment when the sun is lower in the sky, there are consequently more ozone molecules to absorb the solar radiation as it passes through the atmosphere. Therefore,  $j(\text{O}^1\text{D})$  is more influenced than  $j(\text{HONO})$  by the moments when there are faced with high solar zenith angles (i.e. the low position of the sun in the sky) as HONO has a longer wavelength of photolysis than the ozone. Therefore, early morning photolysis of HONO can produce more OH than ozone photolysis and early morning photolysis of HONO can be an important source for the early morning peroxy radical production compared to the ozone photolysis as well (see section 3.3.1.4 in Chapter 3).

## 1.4 Peroxy radicals in the troposphere

Monks *et al.*, (2003a) reviewed photochemistry in the troposphere, especially the reactions of peroxy radicals that are to be considered the intermediates between the hydroxyl (OH) radical and ozone formation/destruction.  $\text{HO}_2$ , the major peroxy radical has a lifetime on the order of a minute in clean air and much less than a minute in polluted air (Monks *et al.*, (2005)). The lifetime of OH in clean atmosphere is short (typically 1s), and the cycling process of the peroxy radical ( $\text{HO}_2$ ) back to OH takes about 100-150 seconds under typical atmospheric conditions (Carslaw *et al.*, (1999)).

### 1.4.1 Peroxy radicals and tropospheric ozone production

The processes of oxidation of CO,  $\text{CH}_4$  and other organic compounds in the presence of OH, result ultimately in the products of  $\text{CO}_2$  and  $\text{H}_2\text{O}$ , but en route reaction cycles

involving peroxy radicals HO<sub>2</sub> and sum of RO<sub>2</sub> occur (where R is an alkyl group, RO<sub>2</sub> is the family of alkyl peroxy radicals):



Here CH<sub>3</sub>O<sub>2</sub>, the methyl peroxy radical, is the simplest member of the family of alkyl peroxy radicals denoted RO<sub>2</sub> where R is an alkyl group.

In an environment where there is a much reduced quantity of NO<sub>x</sub>, like the marine background troposphere, RO<sub>2</sub> is essentially all in the form of CH<sub>3</sub>O<sub>2</sub>, as the product of OH molecules reacting with CH<sub>4</sub>. In this type of environment, there is typically ozone destruction owing to peroxy radical reactions, thus:

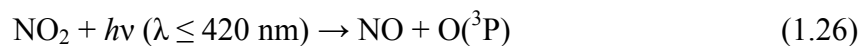


Zanis *et al.*, (1999) demonstrated the way to contrast ozone destruction or production by analyzing the relationship between peroxy radicals and the rate coefficient for ozone photolysis to the oxygen atom (O<sup>1</sup>D). Penkett *et al.*, (1997) showed that in relatively clean air (low [NO<sub>x</sub>]) the peroxy radical concentration shows a square root dependence on *j*(O<sup>1</sup>D).

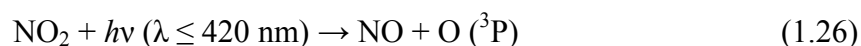
On the other hand, in environments where there is certain amount of NO, and in the presence of peroxy radicals, there is the process of oxidation of NO into NO<sub>2</sub>, as well as at the recycling of HO<sub>2</sub> to OH without consuming ozone ( reaction 1.23)



As a result of a chemical reaction, the only way of producing tropospheric ozone is through NO<sub>2</sub> photolysis:



The main source of NO<sub>2</sub> is from fossil fuel burning, but it can also be produced chemically as a result of the reaction between NO and ozone, but in this case there is no production of ozone, as it involves destruction of ozone.



Penkett *et al.*, (1997) found a linear relationship between [HO<sub>2</sub> + RO<sub>2</sub>] and (*j*(O<sup>1</sup>D)) in more polluted air ([NO] > 50 pptv), where peroxy radical contributes to ozone production exceeds destruction via reactions (1.23), (1.26) and (1.14).

Peroxy radicals can promote the oxidation of NO to NO<sub>2</sub> without consuming ozone, and they also act as net ozone production. It is important to underline the key role

peroxy radical have as intermediates and chain carriers in the photochemical production of ozone and also chain carriers of ozone loss chemistry in the clean atmosphere.

Apart from the simple reactions of the oxidation of CO and CH<sub>4</sub>, there are very many complex reactions containing intermediates, for example, the oxidation of organic hydrocarbons. In this case, relatively stable alkyl nitrates, RONO<sub>2</sub> and peroxy nitrates, RO<sub>2</sub>NO<sub>2</sub>, are formed as a result of higher alkyl peroxy radicals (resulting from the oxidation of large organic hydrocarbons) combining with NO and NO<sub>2</sub>. The higher the carbon number in nitrates compounds, the more stable they are, an example of very stable compound being secondary alkylperoxy radicals. Paulson *et al.*, (1992a, 1992b and 1992c) and Jenkin *et al.*, (1997) reported that acetyl peroxy radicals formed from the photolysis of methyl vinyl ketone (CH<sub>2</sub>CHC(O)CH<sub>3</sub>, MVK), methacrolein (CH<sub>2</sub>C(CH<sub>3</sub>)CHO, MACR) and methyl glyoxal (CH<sub>3</sub>C(O)CHO). Peroxy acetyl nitrate (PAN), can be formed through the reaction of acetyl peroxy radicals with NO<sub>x</sub>. PAN is being a phototoxic compound; the formation of PAN is one of the major harmful compounds in photochemical smog (Carter *et al.*, (1981); Schrimpf *et al.*, (1995)).

A simplified peroxy radical chain cycle showing ozone production is in Figure 1.4

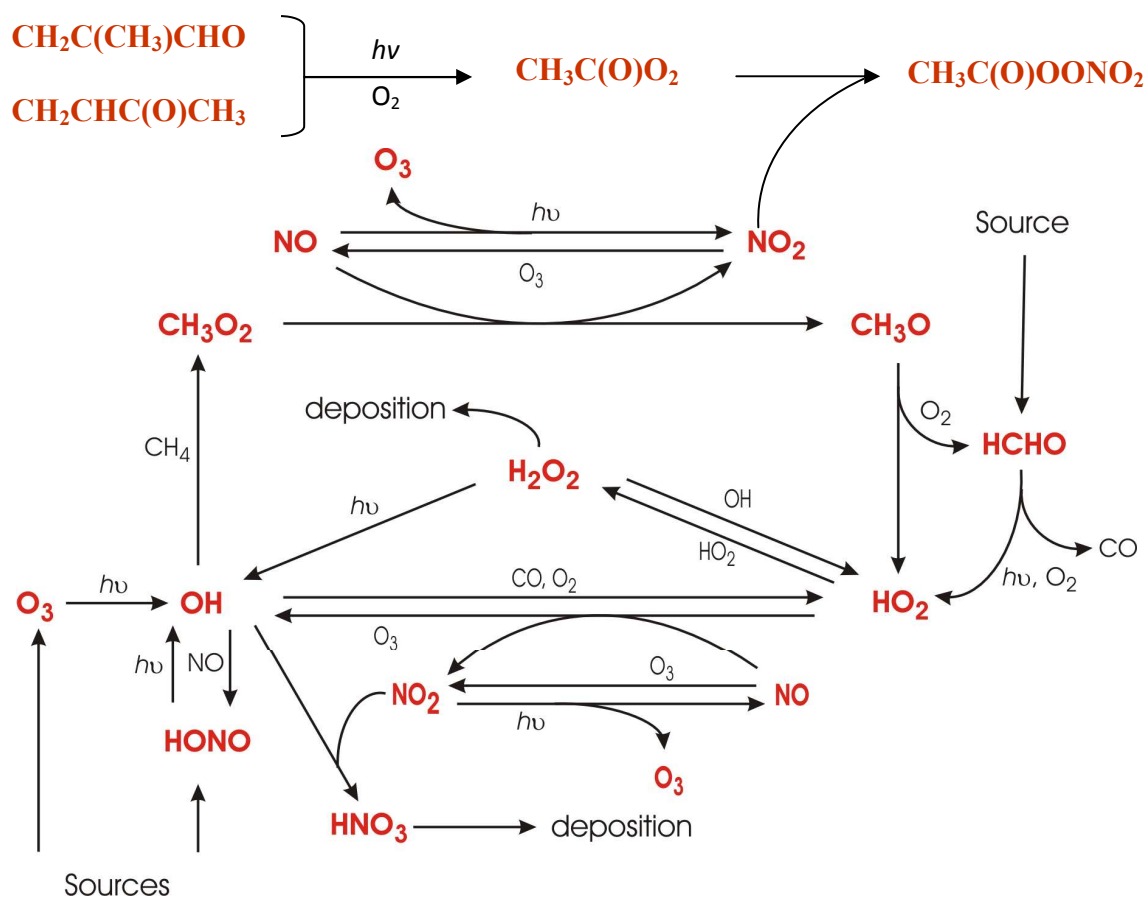


Figure 1.4 - Simplified HOx and ROx cycle showing ozone production from Parker (2007)

### 1.4.2 Additional peroxy radical sources

The methods of producing  $\text{HO}_2$  and  $\text{CH}_3\text{O}_2$  through the reaction of  $\text{OH}$  with  $\text{CO}$  and  $\text{CH}_4$  were been overviewed in section 1.4.1. In this section the focus is on other methods of producing peroxy radicals, especially the oxidation of organic compounds like alkenes and aldehydes. Wayne *et al.*, (1991) explained that the oxidation of these VOCs can also be started through a reaction with  $\text{NO}_3$  at night time. It was Monks, (2005) who remarked that  $\text{NO}_3$  reactions occur at night time as  $\text{NO}_3$  is rapidly photolysed and therefore its lifetime during day time is only about 5 seconds. Although having such a short lifetime, the action of  $\text{NO}_3$  is an essential element within heavily

polluted atmospheres, e.g., Geyer *et al.*, (2003). For less polluted atmosphere, Fleming *et al.*, (2006b) and Salisbury *et al.*, (2001) show that there is active peroxy radical chemistry established in Ireland, at Mace Head during the night time via this route.

NO<sub>3</sub> is formed by the oxidation of NO<sub>2</sub> by O<sub>3</sub>,



and from the decomposition of N<sub>2</sub>O<sub>5</sub>, which is itself formed from the reaction of NO<sub>2</sub> and NO<sub>3</sub>:



Fleming *et al.*, (2006b), Heard *et al.*, (2004) and Salisbury *et al.*, (2002) have demonstrated another route for a larger fraction of peroxy radical production, through ozone-alkenes reaction during the night time. There is an addition reaction of ozone across the carbon-carbon double bond of an alkene: there is a primary formation of ozonide, the decomposition of which results into carbonyl compounds and Criegee intermediates. The night time generation of peroxy radicals are observed at the Cape Verde marine boundary layer from the reactions of O<sub>3</sub> with alkenes, specifically propene. Data analysis of ozonolysis of propene will be detailed in section 4.4.3.8 in Chapter 4.

Monks *et al.*, (2005), Rickard *et al.*, (1999) and Salisbury *et al.*, (2001) have shown that these Criegee intermediates can quickly be deactivated and dissociated as they turn into OH, HO<sub>2</sub> and RO<sub>2</sub> radicals as shown in Figure 1.5 .

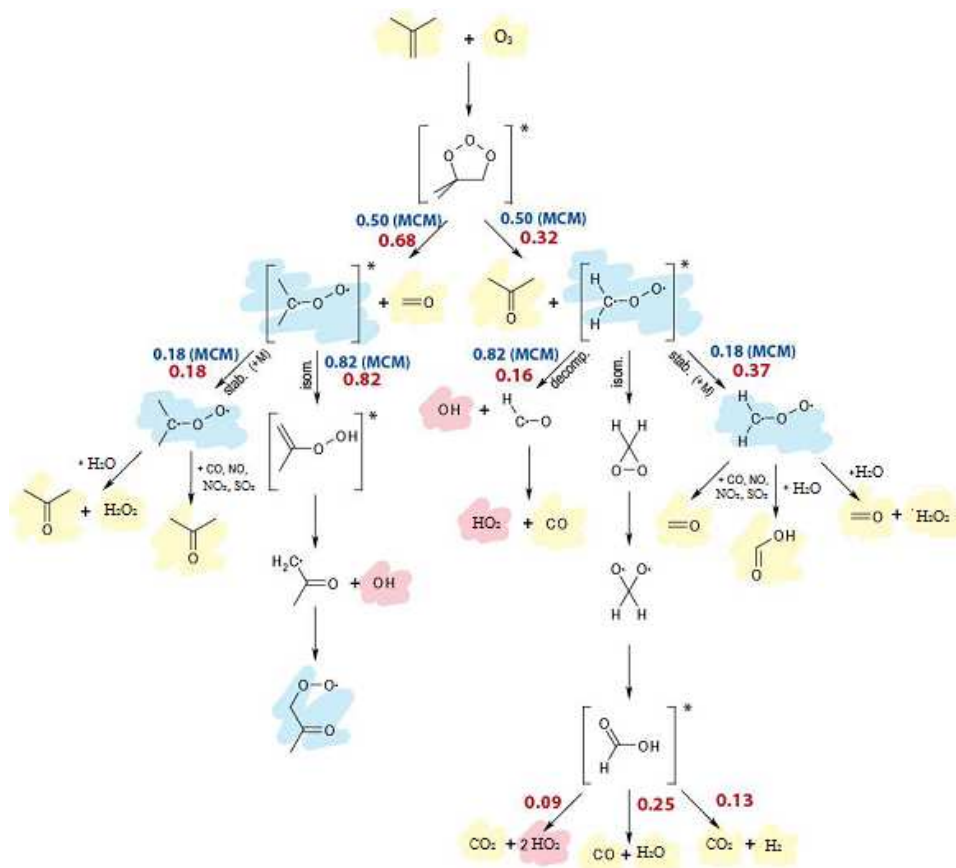
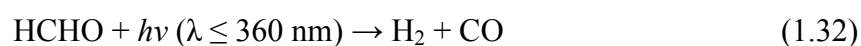
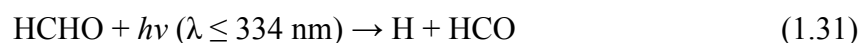


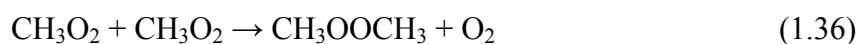
Figure 1.5 - Pathway for the ozonolysis of a generic alkene from Jenkin *et al.*, (2003), Saunders *et al.*, (2003), Johnson *et al.*, (2008), Atkinson *et al.*, (1997), Calvert *et al.*, (2000) and Rickard *et al.*, (1999).

The other important route of peroxy radical production is through the photolysis of formaldehyde; this chemical reaction leads at the same time to the production of 2 molecules of HO<sub>2</sub> per molecule of HCHO, *via* one of its two photolysis channels (1.31, 1.18 and 1.33)

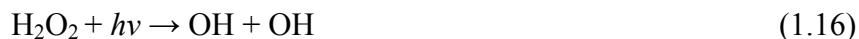


### 1.4.3 Peroxy radical loss pathways

This section introduces peroxy radical loss processes, which can take place either through self-reaction (reactions (1.34), (1.36)) or cross-reaction (reaction (1.35)). The resulting products are being hydrogen peroxides ( $\text{H}_2\text{O}_2$ ), Methyl hydroperoxide ( $\text{CH}_3\text{OOH}$ ) and dimethyl peroxide ( $\text{CH}_3\text{OOCH}_3$ ),



These peroxides can be lost by deposition. Alternatively, the photolysis of peroxides (products of the above self-/cross-reactions) can also reform the HOx radicals, *viz*



Furthermore, in polluted regions the most important sink for HOx ( $\text{OH} + \text{HO}_2$ ) and NOx ( $\text{NO} + \text{NO}_2$ ) is often the reaction between OH with  $\text{NO}_2$  to form  $\text{HNO}_3$ ,



Under some circumstances halogens can have the loss pathway for peroxy radicals. Usually halogens are present in coastal marine sites, halogen can have effect  $\text{HO}_2$  and OH concentrations through the reaction of XO ( $\text{X} = \text{Br}, \text{I}$ ) with  $\text{HO}_2$  and also altering the  $\text{HO}_2/\text{OH}$  partitioning.





Where HOX= hypohalous acids,

Bloss *et al.*, (2005b) showed the existence of a HO<sub>2</sub> loss via reaction 1.40 of about 40% and also production of total midday OH by the reaction 1.41 up to 15% in Ireland, at Mace Head coastal marine site. It has been established that the reaction of IO with HO<sub>2</sub> was important.

#### 1.4.4 Control of tropospheric ozone production

With respect to ozone production, it has been shown in section 1.4.1 the importance of NO<sub>x</sub> (NO+NO<sub>2</sub>) and Volatile Organic Compounds (VOCs) for this process to take place and the relative importance of NO<sub>x</sub> and non-methane hydrocarbons (NMHC) concentrations in the atmosphere in order to have ozone production or destruction.

Figure 1.6 shows the rate of the ozone production depending on the concentration of NO<sub>x</sub> and VOCs:

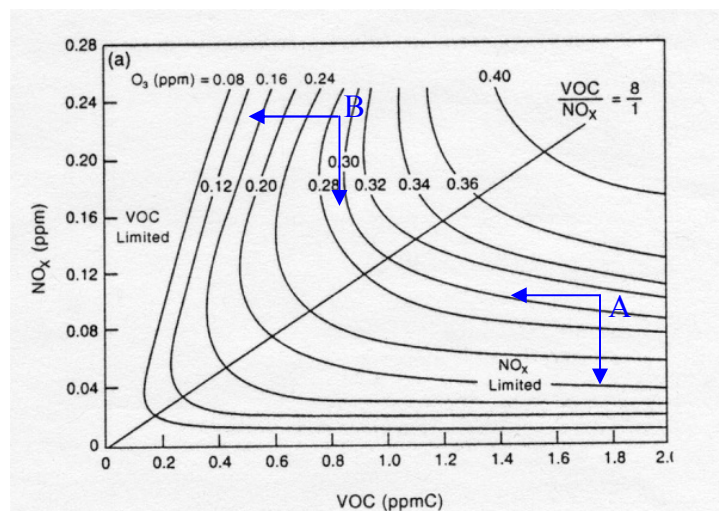


Figure 1.6 - Typical ozone isopleth from Finlayson-Pitts and Pitts (1993). A, represents the NO<sub>x</sub> limited regime where as B represents the VOCs limited regime, see text for the description.

An analysis of Figure 1.6 can easily lead to the conclusion that in the process of ozone production, it is the NO<sub>x</sub> concentration which plays a more important role than VOC concentration owing to the fact that a reduction in NO<sub>x</sub> concentration can easily lead to a reduction in ozone production, a thing that does not happen on the same scale for a reduction in VOC concentration. The ozone production environment at point A is thus said to be NO<sub>x</sub> limited. However, the situation at point B is the opposite – reducing the VOC mixing ratios will rapidly reduce ozone production, whilst reducing NO<sub>x</sub> is ineffective and is therefore a VOC limited ozone production regime. In this case B, when there is a VOC limited regime, there can even be modest increase in the ozone production accompanying NO<sub>x</sub> reduction, provided that there is a high enough concentration of NO<sub>x</sub>. As a result of its reaction with NO, ozone should start to decrease owing to removal by the following reaction:



Though removed now, ozone can be recycled and reformed again: NO<sub>2</sub> obtained in the reaction (1.27) is photolysed thus producing NO and O(<sup>3</sup>P) (reaction 1.26); it is the latter, in combination with O<sub>2</sub>, which will finally reform the ozone (reaction 1.14). NO<sub>2</sub> is not always photolysed, sometimes it reacts with OH in order to form nitric acid, HNO<sub>3</sub>. This usually occurs when there are high concentrations of NO<sub>2</sub> and in this chemical reaction; there is always a competition between NO<sub>2</sub> and VOCs for the reaction with OH. In this situation, there is a slow rate of ozone production owing to the elimination of NO<sub>2</sub> within the process, as well as a break in the process of oxidation of VOCs, owing to the removal of OH. As NO<sub>x</sub> is initially lowered, this radical chain termination effects become less important and thus more ozone is produced. On the other hand, in the case where the NO<sub>x</sub> concentration is further decreasing, this can

affect the lower ozone production as a result of the smaller quantity of NO<sub>2</sub> that is to be photolysed for ozone production. Finlayson-Pitts and Pitts (1993) identified that the approximate point VOC/NO<sub>x</sub> = 8 is the point within the process of ozone production where there is a transition between the two regimes: NO<sub>x</sub> limited regime to a VOC limited regime and the other way around, although this point can easily change. This shift between the two regimes when they are relevant to a specific region of the atmosphere becomes vital in the process of ozone production in terms of formally establishing a system for pollution control (the controls will differ in a VOC limited regime from a NO<sub>x</sub> limited regime).

## 1.5 Tropical rainforest chemistry

Pollution is a global issue. Guenther *et al.*, (1995, 2006) noted that the half of the source of reactive volatile organic compound (VOC) emissions is in the tropical and equatorial forests. Hewitt *et al.*, (2010) state that tropical forests produce 500 Tg C/year out of the 1150 Tg C/year global total (where Tg C= teragrams of carbon). Little has been investigated regarding the roles of tropical VOC compounds in respect to chemical budgets locally, regionally or globally, although their importance as mediators in the chemical reactions occurring in the atmosphere has been recognised (Lelieveld *et al.*, (2008)). Chamber studies also indicate that biogenic VOCs, such as monoterpenes (Hoffmann *et al.*, (1997)), and possibly isoprene (Kroll *et al.*, (2005); Limbeck *et al.*, (2003)), have high aerosol formation yields and so are also thought to be an important source of SOA. Furthermore, Barth *et al.*, (2005) remarked that these biological primary and secondary organic aerosol particles may even influence precipitation within the regions covered by forests owing to the fact that they are essential in forming cloud condensation nuclei (CCN).

### 1.5.1 Tropical rainforest chemical processes

Moreover, according to Fuentes *et al.*, (2000), it is the planetary boundary layer (PBL) and the lower troposphere that are the areas most influenced by BVOCs (biogenic volatile organic compounds) owing to the fact that their lifetime is shorter compared to that of anthropogenic VOCs.

In order to confirm this, the measurements performed over the tropical Borneo rainforest using satellite retrieval of HCHO and NO<sub>2</sub> were generally low, with their column amounts typically towards their background values of  $5 \times 10^{15}$  and  $5 \times 10^{14}$  molecules cm<sup>-2</sup> respectively. Hewitt *et al.*, (2010) indicate that it has not been notably influenced by anthropogenic pollution. Therefore, according to Hewitt *et al.*, (2010), it is BVOCs and soil emissions of reactive nitrogen oxides that drive the chemistry of the tropical Borneo rainforest. In addition, a modelling study by Poisson *et al.*, (2000) expanded the analysis of BVOCs and remarked that BVOCs could affect the composition of the entire troposphere due to the formation of longer-lived intermediates (e.g. CO), which lead to significant rise of concentrations of O<sub>3</sub> and a decrease of OH concentration. In order to reinforce the importance of BVOCs, Poisson *et al.*, (2000) and Tan *et al.*, (2001a) underlined the way BVOCs oxidation products are essential in HOx production within the upper atmosphere through their convection and subsequent photolysis, although long-lived oxides of nitrogen such as PAN can influence remote tropospheric NOx, and thus, ozone chemistry. Liu *et al.*, (1987) mentioned that ozone can be transported to greater distance because it has a relatively long lifetime in the troposphere, of about several months. In addition to this idea of rapid movement of chemical species emitted in the vicinity of the ground level in the free troposphere, according to Andreae *et al.*, (2001) there is a quite a lot of dynamic

convective uplift, especially in the tropics due to the large amounts of solar radiation. An immediate consequence of this aspect is the fact that chemical reactions involving these trace gas emissions above the tropics automatically can take place at higher altitudes of the atmosphere. Furthermore, it has already been explained in sections 1.4.1 and 1.4.4 how the ozone precursor species (such as nitrogen oxides and organic compounds) produce ozone *in situ* at sites removed from the original sources due to the fact that these ozone precursor species are transported within masses of air with long-range transport (LRT). As a result of the continuous movement of the air masses, there is clearly a movement of pollution and precursors, so it is not sufficient to apply regional control of pollution; it has to be applied at the global scale.

## 1.5.2 Tropical marine chemical processes

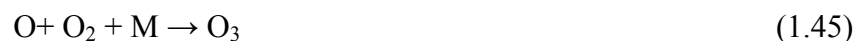
Among the short lived species always influencing the composition of the atmosphere, tropospheric ozone is essential within the atmospheric chemical reactions by virtue of its photolysis which starts free radical chemistry thus integral to the balance of trace gases in the troposphere. According to Monks *et al.*, (1998), the reaction of ozone photolysis and the relation between free radical sources and sinks can be best studied in the remote marine boundary layer. More specifically, Ayers *et al.*, (1992, 1996) demonstrated the destruction of ozone through photolysis leading to production of peroxides, the data being collected from measurements at Cape Grim Baseline Air Pollution station (40° 40' 60" S, 144° 40' 60" E) on north western Tasmania, Australia during the summer of 1995.

There is definitely a summer minimum and a winter maximum in terms of ozone records indicated in the measurements completed at various coastal background sites.

For example, the measurements from the Cape Grim in NW Tasmania show how the coastal background ozone concentration during winter time actually is double that during summer time (Monks *et al.*, (2000b)). Therefore, ozone has a greater lifetime during winter conditions.

In the tropics, there is a rapid production rate of OH from the reaction of O(<sup>1</sup>D) atoms with water vapour (the O(<sup>1</sup>D) coming from near-UV photolysis of ozone) owing to the presence of high solar radiation intensity and high humidities, e.g. Bloss *et al.*, (2005a). Furthermore, the tropics have a beneficial environment for the rapid rate of methane oxidation with OH and therefore about 75% of methane oxidation happens between 30° S and 30° N discussed by Lawrence *et al.*, (2001) and Bloss *et al.*, (2005a). Among the other climate gases whose activity is influenced by the tropics, it is worth mentioning the production and loss of tropospheric ozone happening through photolysis.

Monks *et al.*, (2005) described that during the daylight hours halogen atoms can be recycled in a steady-state null cycle, thus



During the daylight hours, iodine monoxide, IO, exists in a fast photochemical equilibrium with I atoms, via reaction (1.44) (I is one of the member of the halogen denoted X). However, another role of halogen monoxide does contribute to the removal HO<sub>2</sub>. The basis for halogen monoxide chemistry is discussed below. The reaction between HO<sub>2</sub> and XO generates HOX (reaction 1.40). If HOX is photolysed, X is

regenerated (see Section 1.4.3, reaction 1.41) and null cycle (reactions 1.43, 1.44 and 1.45) takes place. If HOX is lost by aerosol via reaction 1.42, there is a chance to have a sink for radical species and ozone.

Halogen concentrations can stimulate a further ozone loss and this process has been demonstrated by the box model calculations of halogen oxide observed at a background marine site (Cape Verde) mentioned in the work of Read *et al.*, (2008). She further concluded that ozone loss in the tropical Atlantic Ocean boundary layer is greatly controlled by halogen chemistry. Read *et al.*, (2008) reported that 8 months of spectroscopic measurements took place continuously in 2007 at the Cape Verde Observatory indicating both of bromine monoxide and iodine monoxide presence in the tropical marine boundary layer. Low-level of aircraft measurements with supporting other surface trace gas measurements showed that the averaged daily ozone loss observed was nearly 50% greater than a one without halogens photochemistry model. Further information is described in Chapter 4.

### 1.5.3. Previous studies of peroxy radical measurements

Table 1.1 lists previous field campaigns of peroxy radical measurements. There are plenty of environments which have been used for these measurements: the marine boundary layer, remote locations, rural, urban, forest, Antarctica and the upper troposphere.

Acronym and date	Location	Technique (s)	Midday max [HO <sub>2</sub> + sum of RO <sub>2</sub> ] / pptv	Reference (s)
1990	Schauninsland	MIESR	40	Mihelcic <i>et al.</i> , (1993)
ROSE 1 1990	Alabama	PERCA	150	Frost <i>et al.</i> , (1998) Cantrell <i>et al.</i> , (1992,1993a,1995)
MLOPEX 2 1991-2	Mauna Loa, Hawai	PERCA	25	Cantrell <i>et al.</i> , (1996a, 1997a)
FIELDVOC 1993	Brittany, France	PERCA	60	Cantrell <i>et al.</i> , (1996c)
TOHPE 1993	Idaho Hill, Colorado	PERCA FAGE	60	Cantrell <i>et al.</i> , (1995, 1997b), Stevens <i>et al.</i> , (1997)
WAO-TIGER 1994, 1995	Weybourne	PERCA	12	Clemmitshaw <i>et al.</i> , (1997), Carslaw <i>et al.</i> , (1997), Carpenter <i>et al.</i> , (1998), Allan <i>et al.</i> , (1999), Penkett <i>et al.</i> , (1999)
SOAPEX 1995, 1998	Cape Grim, Tasmania	PERCA FAGE	11, 20	Monks <i>et al.</i> , (1996, 1998, 2000b), Carpenter <i>et al.</i> , (1997), Penkett <i>et al.</i> , (1997), Salisbury <i>et al.</i> , (2001)
ATAPEX 1995	Mace Head	PERCA	5	Carpenter <i>et al.</i> , (1997)
ACSOE-EASE 1996, 1997	Mace Head	PERCA, FAGE	25	Creasey <i>et al.</i> , (1997) Carslaw <i>et al.</i> , (1999,

				2000),Salisbury <i>et al.</i> , (2001, 2002)
FREETEX 1996, 1998, 2001	Junfraujoch, Switzerland		20	Zanis <i>et al.</i> , (1999, 2000a, 2003)
BERLIOZ 1998	Berlin, Germany	FAGE, MIESR, PERCA	30	Geyer <i>et al.</i> , (2003), Holland <i>et al.</i> , (2003), Mihelcic <i>et al.</i> ,(2003), Volz-Thomas <i>et al.</i> , (2003)
PROPHET 1997, 1998	Michigan	PERCA	65,70	Mihele and Hastie (2003), Tan <i>et al.</i> , (2001b)
Southern oxidants study 1999	Nashville, Tennessee	LIF	N/A	Thornton <i>et al.</i> , (2002)
ALBATROSS 1996	Atlantic Ocean	PERCA	80	Burkert <i>et al.</i> , (2001)
AEROSOLS99	Atlantic and Southern Indian Oceans	PERCA	N/A	Andres-Hernandez <i>et al.</i> , (2001)
INDOEX	Indian ocean	PERCA	N/A	Burkert <i>et al.</i> , (2003)
TOPSE 2000	Colorado to Canada (aircraft)	CIMS	N/A	Cantrell <i>et al.</i> , (2003a,b), Stroud <i>et al.</i> , (2004)
TRACE-P 2001	Pacific (aircraft)	CIMS		Cantrell <i>et al.</i> , (2003c)
	Britain (aircraft)	PERCA		Green <i>et al.</i> , (2002)
HOPE 2000	Hohenpeissenberg, Germany	PERCA	70	Handisides <i>et al.</i> , (2003)
2002	Pennsylvania	LIF perCIMS	45	Ren <i>et al.</i> , (2003)
WAOWEX winter 2002	Weybourne	PERCA	25	Fleming <i>et al.</i> , (2006a)
NAMBLEX 2002	Mace Head	PERCA FAGE	40	Bloss <i>et al.</i> , (2005b) Smith <i>et al.</i> , (2006) Fleming <i>et al.</i> , (2006b)
INSPECTRO 2002	Weybourne	PERCA	12	Fleming <i>et al.</i> , (2006a)

TORCH 2003, TORCH 2004	1. Writtle college, Essex 2. Weybourne	PERCA,FAGE	120	Emmerson <i>et al.</i> , (2007), Lee <i>et al.</i> , (2006) Not yet published
ITOP 2004	Azores	FAGE, PERCA	44	Parker <i>et al.</i> , (2009)
CHABLIS 2004-2005	Halley, Antarctica	FAGE, PERCA	N/A	Bloss <i>et al.</i> , (2007)
TEXAQS 2006	Gulf of Mexico	PERCA	110	Sommariva <i>et al.</i> , (2011)
OOMPH 2007	Punta Arenas- Africa (Atlantic)	PERCA	150	Hosaynali Beygi <i>et al.</i> , (2011)
AMMA 2006	Africa (land- flights)	FAGE, PERCA	35	Brookes <i>et al.</i> , (2010) Andrés-Hernández <i>et al.</i> , (2010)
OP3 2008	<b>Borneo</b> Land and flight	FAGE, PERCA		This thesis
SOLAS (SOS) 2009	<b>Cape Verde</b>	FAGE, PERCA		This thesis

Table 1.1 - Summary of previous field campaigns of peroxy radical measurements.

#### 1.5.4. Synthesis of previous measurement campaign

This section describes to address the key aspects of understanding of peroxy radical chemistry from previous measurement campaigns (see Table 1.1). The key aspects can be considered in the following topics: peroxy radicals are important for photochemical ozone production (see section 1.5.4.1), peroxy radical vs ozone photolysis depends on [NO<sub>x</sub>] (see section 1.5.4.2). Aspects of asymmetric diurnal profiles of peroxy radical (see section 1.5.4.3); variability of [HO<sub>2</sub>+RO<sub>2</sub>] with [NO<sub>x</sub>] during day and night time (see section 1.5.4.4) and non-zero [HO<sub>2</sub>+RO<sub>2</sub>] at night time (see section 1.5.4.5).

##### 1.5.4.1. Peroxy radicals are species for photochemical production of ozone

Peroxy radicals are key species for photochemical production of ozone, with higher concentration at midday when photochemistry is at a maximum (e.g. Monks *et al.*,

(2000b). Maximum of peroxy radical concentrations reached at midday.

The main source of peroxy radicals is ozone photolysis, clearly indicated in the experiment performed in north western Tasmania, Australia during the summer of 1995 at Cape Grim Baseline Air Pollution station, during SOAPEX 1 (The Southern Ocean Atmospheric Photochemistry Experiment). Monks *et al.*, (1996, 1998, 2000b) noted that the highest measured concentration of peroxy radicals was almost 11 pptv at midday, while this chemistry results in the destruction of ozone.

The Tropospheric Ozone Production about the Spring Equinox (TOPSE) campaign aimed to prove the change of peroxy radical concentrations taking place together with a move northwards from latitude of 40° to 85°N and altitudes from the surface to 7.5 km over the North American continent. Cantrell *et al.*, (2003a, b) explained that NCAR/NSF C-130 aircraft used for TOPSE experiment during February and March 2000. The Chemical Ionisation Mass Spectrometer (CIMS) instrument helped in the measurements that indicate the fact that a longer sunlit day as well as the maximum solar elevation contribute to an increase of peroxy radicals. There have been defined a middle-latitude band (MLB) and a high-latitude band (HLB), and the measurements showed that (HO<sub>2</sub> + RO<sub>2</sub>) concentrations oscillate between 11.5 pptv in MLB and 7.8 pptv in HLB.

The Jungfraujoch Atmospheric Observatory in the Swiss Alps was the location used for the FREETEX experiments (The FREE Tropospheric Experiment) performed in April-May 1996, March-April 1998, respectively February-March 2001 (Zanis *et al.*, 1999, 2000a, 2000b, 2003, Carpenter *et al.*, 2000). PERCA employed to measure the peroxy

radical concentration during FREETEX experiments and aiming to demonstrate the seasonal behaviour of peroxy radicals. There is clear seasonal behaviour of peroxy radicals with a gradual increase in concentrations at midday from around 12 pptv in February to around 20 pptv in May (Zanis *et al.*, (2003)).

A strong correlation between peroxy radical production and reactions of OH and VOCs, as well as reactions of ozone with alkenes, was established at a rural site, more specifically Rock Spring, Pennsylvania during the campaign taking place at a research farm during the summer of 2002. Ren *et al.*, (2003) deployed that the instruments used were laser induced fluorescence (LIF) and chemical ionization mass spectrometry (CIMS) that contributed to the measurements showing a maximum of peroxy radicals of 45 pptv at midday. The measurements were also used in determining an exact value of 86% as the proportion in which peroxy radicals production occurs due to OH and VOCs reactions, while the rest is a result of O<sub>3</sub> and alkenes reactions.

Parker *et al.*, (2009) demonstrated air-masses, more precisely long-range transport air-masses, can determine the increase of peroxy radicals, as shown by the measurements during the ITOP (Intercontinental Transport of Ozone and Precursors) campaign in July-August 2004 taking place over the mid-Atlantic, onboard the UK Meteorological Office/Natural Environment Research Council British Aerospace 146-300 atmospheric research aircraft based at Horta Airport, Faial, Azores. Ozone photolysis is the primary source of peroxy radicals. The increase of peroxy radicals from 28pptv at 0-0.5 km to 44 pptv at 5-5.5 km above the Atlantic, when compared to the measurements of peroxy radicals existent in other air-masses of marine origin (which showed no evident altitude profile of the peroxy radicals), is a clear proof of the fact that long-range transport

occurring above the Atlantic is affecting the photochemical activity through a broadening of peroxy radicals as the altitude rises.

The BERLIner OZone experiment (BERLIOZ) shows the time of the day when peroxy radical concentration were maximum and the sources influencing this concentration. This experiment was performed near Berlin, during the summer of 1998 and the instruments employed within this experiment for measuring HO<sub>2</sub> and peroxy radicals were LIF by Geyer *et al.*, (2003), MIESR by Holland *et al.*, (2003) and PERCA by Mihelcic *et al.*, (2003) and Volz-Thomas *et al.*, (2003). The main source of peroxy radicals is ozone photolysis and the maximum of peroxy radical concentrations almost reached 30 pptv at midday, while HO<sub>2</sub>/RO<sub>2</sub> ratios of 1 were registered. In addition, the maximum ozone production rate was calculated 8 ppbv ozone hour<sup>-1</sup>.

#### 1.5.4.2. Peroxy radical vs ozone photolysis depends on [NO<sub>x</sub>]

The relationship of peroxy radical vs ozone photolysis depends on NO<sub>x</sub> concentrations. Penkett *et al.*, (1997) found a linear relationship between [HO<sub>2</sub> + RO<sub>2</sub>] and  $j(\text{O}^1\text{D})$  in more polluted air ([NO] > 50 pptv) while the peroxy radical concentration shows a square root dependence on  $j(\text{O}^1\text{D})$  in relatively clean air (low [NO<sub>x</sub>]). The following experiments are good examples to study the behaviour of the peroxy radical against ozone photolysis for the different NO<sub>x</sub> environments.

Monks *et al.*, (2000b) found that, there is a good linear relationship between peroxy radical concentrations and square-root of  $j(\text{O}1\text{D})$  during SOAPEX 1 experiment (explained in section 1.5.4.1) for low NO<sub>x</sub> environment (hourly average [NO] varied from 1 to 6 pptv at Cape Grim). In contrast, Carpenter *et al.*, (1997) found at the

ATlantic AtmosPheric EXperiment (ATAPEX 1) in May 1995 at Mace Head that the relationship between peroxy radical concentrations and  $j(\text{O}1\text{D})$  switched from a square-root dependence in clean oceanic air to a first-order dependence in more polluted air (Hourly average daytime  $[\text{NO}]$  were about 30 pptv at Mace head). Net ozone destruction calculated from SOAPEX1 experiment whereas net ozone production derived from (ATAPEX 1) experiment in the afternoon.

#### 1.5.4.3. Asymmetric diurnal profile

Secondary products of photochemical oxidation in the late afternoon can be important sources for peroxy radical production. Several processes lead to increased radical concentrations peaking later into the day. Higher concentration of peroxy radicals were observed during the afternoon from several previous measurement campaigns. This behaviour was observed in the following experiments. The most important factors leading to these high concentrations in the afternoon was the photolysis of formaldehyde and methylglyoxal.

A higher concentration of peroxy radicals was observed during the afternoon, the measurements reaching up to 40 pptv, during the experiment called NAMBLEX (The North Atlantic Marine Boundary Layer Experiment). Fleming *et al.*, (2006b) demonstrated that this experiment taking place at Mace Head during the summer of 2002 used PERCA to measure the concentration of peroxy radicals, while the most important factor leading to these high concentrations in the afternoon was the photolysis of formaldehyde. A good correlation found between  $j(\text{HCHO}) \cdot [\text{HCHO}]$  and HCHO was found to be an important source of peroxy radicals in the remote atmosphere, especially in the afternoon.

Another experiment that reached the conclusion that the photolysis of formaldehyde is an essential source of peroxy radicals was ALBATROSS (The Air chemistry and Lidar studies of TROpospheric and Stratospheric Species). The measurements of this experiment took place in 1996 on the Polarstern research vessel during a voyage from Germany to Argentina across the Atlantic Ocean. Burkert *et al.*, (2001) pointed out maximum peroxy radical concentrations measured up to 80 pptv at midday. The diurnal cycle of the measured peroxy radical was observed to be significantly broader and this behaviour indicates that more peroxy radical is present in the early morning and late afternoon compared to midday.

Formaldehyde photolysis is proved once more to be a very important source of peroxy radicals through the campaign done in a rural site, i.e. at ground level between June and July 1990 at Kinterbish Wildlife Management Area and aircraft between 13<sup>th</sup> and 28<sup>th</sup> of June 1990 over an area comprising Alabama and Mississippi. The campaign called ROSE (The Rural Oxidants in the Southern Environment), being performed both at the Earth's surface and on a aircraft, provided a vertical influents, as well as a regional one of the measured species. Frost *et al.*, (1998) mentioned the usage of PERCA within the campaign assisted in the measurements displaying a maximum of 150 pptv of [HO<sub>2</sub>+RO<sub>2</sub>] at midday (particularly broader diurnal cycle), moment at which the measured [HCHO] reached a maximum of 7 ppbv. These measurements are therefore more than representative for the fact that formaldehyde photolysis is an essential source of peroxy radicals in this rural site. Another significant radical source was the photolysis of non-HCHO carbonyl compounds such as methylglyoxal (MGLY).

Production of peroxy radicals is particularly driven by NMHCs (Non Methane Hydro

Carbons) oxidation during the afternoon (i.e. asymmetric diurnal profile). Emissions of biogenic VOC's, e.g. isoprene, monoterpenes and PAN (Peroxy Acetyl Nitrates) influence peroxy radicals in the afternoon from the following experiments.

According to Handisides *et al.*, (2003) a very high concentration of peroxy radicals, of 70 pptv was observed in the early afternoon, during June 2000. The exact location of HOPE is the Meteorological Observatory Hohenpeissenberg (MOHp), in the Alps, at an altitude of 980m. The HOPE experiment (Hohenpeissenberg Photochemical Experiment) showed significant oxidation of isoprene and the monoterpenes. This experiment having been performed in a rural agricultural and forested area indicating that the production of peroxy radicals in these regions is particularly driven by NMHCs oxidation.

It is the same molecule isoprene that has been observed to drive peroxy radical production during an experiment in a forested site in northern Michigan. The experiment was called PROPHET (The Program for Research on Oxidants: PHotochemistry Emissions and Transport) and was performed during the summer of 1997 (Mihele and Hastie (2003)). Measurements of peroxy radicals oscillated between 20 and 65 pptv after midday and are mainly the result of isoprene chemistry. This experiment proves that it is essentially isoprene chemistry, and not only ozone photolysis, that influences radical production in forested sites. There was a significant correlation found between the  $[\text{HO}_2+\text{RO}_2]$  and that of [isoprene] ( $R^2 = 0.8$ ).

Andres-Hernandez *et al.*, (2010) explored the role of fast photochemical processing during the European Project AMMA (African Monsoon Multidisciplinary Analysis)

West African Monsoon (WAM) period in summer 2006. The AMMA aim was to improve the knowledge about the WAM influence on global atmospheric composition. Trace gases were measured using 5 different aircrafts (Reeves *et al.*, (2010)). Andres-Hernandez *et al.*, (2010) explained that on 16<sup>th</sup> August 2006, peroxy radicals were measured by two similar instruments deployed on two scientific aircraft during the AMMA campaign: the German DLR-Falcon aircraft carrying DUALER (DUAL channel Airborne peroxy radical chemical amplifier) and the British FAAM-BAe-146 aircraft carrying PERCA flew for approximately 30 min over Burkina Faso, first in a straight and level westward run at 697 hPa (PERCA's  $[\text{HO}_2+\text{RO}_2]$  are varied from 15 to 35 pptv). At the second pressure level (485 hPa), DUALER's  $[\text{HO}_2+\text{RO}_2]$  oscillates between 15 and 45 pptv (no PERCA measurement observed at 485 hPa level). Ozone photolysis is an important source of peroxy radicals during the day time and  $[\text{HO}_2+\text{RO}_2]$  diurnal cycle is asymmetrical towards afternoon due, high concentrations persisting at night (night time peroxy radical will be detailed in section 1.5.4.5). Several processes lead to increased radical concentrations peaking later into the day. Emissions of biogenic VOC's, e.g. isoprene and monoterpenes, influence peroxy radicals in the afternoon.

Lee *et al.*, (2006) observed very high concentrations of 120 pptv of peroxy radical measured during the TORCH (The Tropospheric ORganic Chemistry) experiment. The sources of the peroxy radicals are, in this case, ozone, PAN and peroxides, i.e. secondary products of photochemical oxidation. This campaign was carried out in Writtle, Essex, and 25 miles northeast of London during July and August 2003, employing PERCA as the instrument to measure  $\text{HO}_2+\text{RO}_2$ . Measurements performed in the atmosphere during mid afternoon show a 120 pptv concentration of peroxy

radicals, while the maximum of ozone is registered at the same moment of the time. During the daytime, acetyl peroxy radical formation was dominated by PAN thermolysis, whose afternoon lifetime averaged only 18.3 min, but which was sustained at a concentration greater than 750 pptV. A strong correlation between isoprene and PAN production rate suggest that PAN and isoprene species may have contributed to the later afternoon increases seen in surface O<sub>3</sub>.

#### 1.5.4.4. Variability of peroxy radical concentration with NO<sub>x</sub>

Fleming *et al.*, (2006a) demonstrated that during (WAOWEX -Weyborne Atmospheric Observatory Winter Experiment and INSPECTRO- Influence of clouds on the spectral actinic flux in the lower troposphere) of two experiments at Weyborne Atmospheric Observatory, one during winter time (January-February 2002) and the other during the summer of 2002. The aim of these two experiments performed at the same site in two different seasons was to draw a comparison between the peroxy radical concentrations during winter time and summer time: Typically 12 pptv of peroxy radical was measured at midday during summer time and, on the other hand, typically 30 pptv at night during winter (night time peroxy radical will be detailed in section 1.5.4.5). The experiment demonstrated that the correlation between NO<sub>x</sub> and peroxy radicals is the key factor in determining the fluctuation of peroxy radical concentrations.

Production of peroxy radicals left aside; there can be a total absence of peroxy radicals, the responsible factor for this being the high concentration of NO contained by air-masses. According to Sommariva *et al.*, (2011), this suppression has been observed during two experiments (TexAQS II - The Texas Air Quality Study and GoMACCS - Gulf of Mexico Atmospheric Composition and Climate Study). These two experiments

took place between July and September 2006 along the Texas coast and inside Galveston Bay and Houston port. These areas are impacted by the highly polluted air masses coming from Southern Texas. Therefore, the high quantities of NO (maximum NO<sub>x</sub> measured up to 15 ppbv) are affecting the [HO<sub>2</sub>+RO<sub>2</sub>] during day time. Typically, there was a variation for the hourly averaged [HO<sub>2</sub>+RO<sub>2</sub>] during day time from 20 pptv to 40 pptv, while during night time the values vary between 10 pptv and 20 pptv. See the section 1.5.4.5 for night time peroxy radical sources during TexAQS II and GoMACCS experiments. The fluctuation of day and night time is a result of peroxy radical's suppression towards day time because of high quantities of NO.

#### 1.5.4.5. Non-zero peroxy radical concentration at night time

Nighttime oxidation chemistry is thought to be initiated either by nitrate radicals, NO<sub>3</sub>, or through ozone + alkene reactions which are active throughout the day (Wayne, 2000).

The maximum of peroxy radical concentration measured up to 20 pptv during night time for BERLIner OZone experiment (BERLIOZ) (explained in section 1.5.4.1). This concentration is influenced by NO<sub>3</sub>, (concentrations of NO<sub>3</sub> varied from 10 to 70 pptv during night time) (Geyer *et al.*, (2003)).

High concentrations of peroxy radical are persisting at night during AMMA experiment (explained in section 1.5.4.3) median values of the order 30 pptv represent significant night-time concentrations, Andres-Hernandez *et al.*, (2010) and Brookes, (2010). The enhanced radical concentrations associated with biomass burning plume at night, Brookes (2010). There was a chance to have the oxidation of isoprene within the

monsoon flow and the enhanced measurement of RO<sub>x</sub> could be mixed with the air flow at night time. The proposed recycling of OH from isoprene oxidation study provides a potential explanation of the existences of RO<sub>2</sub>, HO<sub>2</sub> and potentially OH at night, e.g. Lelieveld *et al.* (2008), Peeters *et al.* (2009), and Silva *et al.* (2010).

WAOWEX experiment (explained in section 1.5.4.4) is another example for non-zero peroxy radical, 30 pptv of peroxy radical measured at night during winter Fleming *et al.*, (2006a) suggested that enhanced measurement of peroxy radical from NO<sub>3</sub> chemistry because [NO<sub>x</sub>] measured more than 1ppbv during winter at night-time.

Maximum peroxy radical reached up to 134 ppt during night time from TexAQS II and GoMACCS experiment (explained in section 1.5.4.4). This high concentration of peroxy radical related to night time oxidation reaction (O<sub>3</sub> or NO<sub>3</sub>) of highly reactive VOC. During this experiment, the GC-MS detected a plume, possibly emitted from one of the nearby petrochemical plants. Largely composed of C<sub>2</sub>-C<sub>5</sub> alkenes with a combined mixing ratio of 190 ppb were detected from plume sample (Gilman *et al.*, (2009)). Sommariva *et al.*, (2011) suggested that an ozone reaction with alkenes was responsible for the formation of such high [HO<sub>2</sub>+RO<sub>2</sub>].

## 1.6 Research in this thesis: What do we want to achieve?

Sections 1.4.1 and 1.4.4 showed that peroxy radicals are essential in determining the tropospheric oxidation capacity of the atmosphere and control the removed of primary pollutants (NO<sub>x</sub> and VOCs). Peroxy radicals also play an important role in the production of secondary pollutants such as ozone. This comprehensive role that peroxy radicals have in the atmosphere can be understood through the relationship between

peroxy radical concentrations in the atmosphere and ozone, NO<sub>x</sub>, VOC, OH and solar flux measurements. High time resolution measurements are important owing to the short life-times of peroxy radicals. Long term measurements reveal how average concentrations vary from site to site and season to season.

In this thesis, peroxy radical measurements from both of the tropical Borneo rainforest and the tropical marine Cape Verde have been collected. These data are analysed to compare peroxy radical behaviour between marine and rainforest boundary layer sites and between seasons. Model results are included to illustrate how our knowledge of peroxy radical reactions compares with real measurements in the atmosphere. The role of peroxy radicals in understanding tropospheric ozone formation and destruction is of key interest in this thesis.

## 1.7 Summary

Chapter 1 has provided an introduction to the study of tropospheric photochemistry and the role of peroxy radicals in ozone photochemistry. Quite an important aspect of this chapter is represented by the summary of previous measurement campaigns which has been detailed as an insight into the meteorological and geographical conditions which create a substantial peroxy radical database.

Chapter 2 is intended to encompass the experimental aspects of peroxy radical measurements, but the main focus is on the PERCA (PEroxy Radical Chemical Amplification) method, which has been used in order to carry out all the peroxy radical measurements presented along this thesis. PERCA instrument calibrations carried out during these campaigns are also detailed in this chapter.

Chapter 3 consists of a discussion related to the performance of the PERCA instrument in the field campaigns. Furthermore, it provides in depth study of peroxy radicals and ozone production in the tropical Borneo rainforest during the Oxidant and Particle Photochemical Processes (OP3 (1) and OP3 (3)) campaigns and briefly debates seasonal fluctuations between the two campaigns and the fundamental budgets from both campaigns.

Chapter 4 details a peroxy radical seasonal comparison carried out at the Cape Verde Atmospheric Observatory during 2009 when three major experiments were undertaken to investigate the fundamentals of ozone photochemistry in the remote marine boundary layer. A close study of these experiments illustrates the fluctuation of peroxy radical diurnal cycles in different seasons. Net ozone production rates from peroxy radicals are calculated and compared for the 3 different seasons, together with the net ozone production compensation points.

Chapter 5 aims to draw together the findings from Chapters 3 and 4 in order to provide a contrast between peroxy radical measurements at the tropical Borneo rainforest and tropical marine Cape Verde sites. The chapter offers an in depth study of the ozone production loss chemistry which has been modelled using these  $[HO_2+RO_2]$  and thus it can present the reasons which lay at the basis of ozone formation and destruction at the various sites.

Finally, Chapter 6 concludes the thesis, with a summary of the key findings in the previous chapters and makes suggestions for areas of further research.

# Chapter 2

## Peroxy Radical Measurement

This chapter focuses on the various methods available for measuring peroxy radicals in the atmosphere. The University of Leicester's Peroxy Radical Chemical Amplifier (PERCA (V3.5)) is detailed; as this has been used to perform peroxy radical measurements in the Borneo rainforest and at Cape Verde to be described in this thesis.

A summary of the major atmospheric peroxy radical measurement techniques is given in Table 2.1. A more detailed presentation of Table 2.1 is explained in Sections 2.1-2.4.

Technique	Errors	Detection Limit	Sampling Time	Pros	Cons
PERCA (all versions) HO <sub>2</sub> + sum of RO <sub>2</sub>	~ ± 40%	1 pptv	1 minute	Relatively low cost, sensitivity portable, reliable, reasonable.	Indirect, HO <sub>2</sub> + sum of RO <sub>2</sub> measured, dangerous reagents
FAGE (OH, HO <sub>2</sub> )	~ ± 30%	0.006 pptv (OH) and 0.004 – 0.04 pptv (HO <sub>2</sub> )	30 seconds	Separate OH and HO <sub>2</sub> measurements, Highly sensitivity	Requires calibration no RO <sub>2</sub> (yet), more complicated expensive
PerCIMS (HO <sub>2</sub> , sum of RO <sub>2</sub> )	~ ± 40%	< 0.4 pptv	15 seconds	Separated HO <sub>2</sub> and RO <sub>2</sub> , good sensitivity	Indirect
MIESR (HO <sub>2</sub> , CH <sub>3</sub> C(O)O <sub>2</sub> , sum of RO <sub>2</sub> )	~ ± 5%	20 pptv	20 – 30 minutes	Small errors, allows some speciation, direct technique,	Long sampling time, low sensitivity, lab analysis required

				calibration standard	
PERCA (V4) – LIF (HO <sub>2</sub> + sum of RO <sub>2</sub> )	~ ± 10%	3 pptv	1 minute	Highly sensitive LIF detection, Sensitive to HOx and RO <sub>2</sub> ,	Indirect, dangerous reagents, more complicated detection method interferences, varying sensitivity by radical.

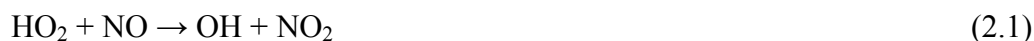
Table 2.1 - Comparison of major atmospheric peroxy radical measurement techniques. Where HO<sub>2</sub> is hydro peroxy radicals and R is an alkyl group, RO<sub>2</sub> is the family of alkyl peroxy radicals.

Table 2.1 provides a qualitative summary of the strengths and weaknesses of each technique. Section 2.1 will provide an overview of various techniques for the measurement of peroxy radicals.

## 2.1 PERCA technique

It was in the early 1980's that the Chemical Amplification technique was first employed for peroxy radical measurements by Cantrell (Cantrell and Stedman *et al.*, 1982; Cantrell *et al.*, 1984) since and it has been widely applied for measuring peroxy radicals in various locations (Cantrell *et al.*, 1993a; Green *et al.*, 2006; Mihele and Hastie 2003; Monks *et al.*, 1998; Zanis *et al.*, 2000a). Peroxy radicals are HO<sub>2</sub> and sum of RO<sub>2</sub>, where HO<sub>2</sub> is the hydro peroxy radical and, RO<sub>2</sub> is the family of alkyl peroxy radicals where R is an alkyl group. Table 1.1 in Chapter 1 summarizes previous measurement campaigns during which peroxy radical measurements have been performed as well as presenting measurements performed using the PERCA technique.

The basis of the PERCA technique relies on using the HO<sub>2</sub> radical to catalyse the conversion of NO and CO into NO<sub>2</sub> and CO<sub>2</sub> respectively. The HO<sub>2</sub> concentration is then obtained from the amount of NO<sub>2</sub> formed from the PERCA instrument's inlet chemistry, (see Section 2.5). NO (3 ppmv) and CO (6% v/v) are added to ambient air containing the radicals in the PERCA instrument's inlet region.



As well as the HO<sub>2</sub> radical, PERCA will also detect organic peroxy radicals (RO<sub>2</sub>) as they are a source of HO<sub>2</sub> through the conversion



The efficiency of the conversion of RO<sub>2</sub> into HO<sub>2</sub> is dependent on the size and the structure of the organic group, (Ashbourn *et al.*, 1998; Clemitshaw *et al.*, 1997). As shown in reactions 2.7 and 2.8, there are competing reactions of RO<sub>2</sub> and RO in the process that form organic nitrates 2.7 and nitrites 2.8. An organic nitrates and nitrites do not yield a conversion of NO to NO<sub>2</sub> under the inlet conditions present under the normal operating mode of the University of Leicester PERCA instrument. All these reactions take place together with the chain propagating reactions 2.5 and 2.6.



However, it has been observed by Clemitshaw *et al.*, (1997) that the conversion of RO<sub>2</sub> to HO<sub>2</sub> efficiency rates are high, i.e. 0.85 for CH<sub>3</sub>O<sub>2</sub>, when this conversion occurs in the case of simple organic groups. The result of the inlet chemistry is an amount of NO<sub>2</sub> and CO<sub>2</sub> produced is equal to

$$CL * [HO_2 + \text{sum of } RO_2 + OH]$$

where CL is the chain length. The chain length is defined as the number of HO<sub>2</sub>/OH conversion cycles which are produced before termination. It has been noted by Mather *et al.*, (1997) that the factor influencing the amounts of NO<sub>2</sub> and CO<sub>2</sub> within these reactions is actually

$$CL * [HO_2 + \text{sum of } RO_2]$$

The above equation is a good approximation owing to the fact that in the lower troposphere the concentration of OH is significantly lower than that of HO<sub>2</sub> and RO<sub>2</sub>. PERCA does not measure HO<sub>2</sub> and RO<sub>2</sub> directly. The conversion of NO<sub>2</sub> from NO by HO<sub>2</sub> is part of a radical chain reaction. A single HO<sub>2</sub> molecule makes many NO<sub>2</sub> from NO, by recycling of the OH product (reactions 2.1 to 2.3). NO<sub>2</sub> produced by the chemical amplification radical chain can be identified through chemiluminescence reactions typically using liquid luminol II (5-amino-2, 3-dihydro-1, 4-phthalazinedione) chemiluminescence at  $\lambda = 424 \text{ nm}$  (Green *et al.*, (2006)). Consequently, the concentration of peroxy radicals is determined measuring the amount of NO<sub>2</sub> produced from the HO<sub>2</sub> (and RO<sub>2</sub>) catalysed oxidation of NO, divided by the chain length of the amplification process.

$$[HO_2 + \text{sum of } RO_2] = \Delta NO_2 / CL \quad (2.9)$$

PERCA has a much greater sensitivity than it would do for stoichiometric conversion of NO<sub>2</sub> from NO by HO<sub>2</sub>. Atmospheric samples already contain some NO and NO<sub>2</sub> and therefore the PERCA measurement has to distinguish between the ΔNO<sub>2</sub> signal from HO<sub>2</sub> chemistry and existing NO<sub>x</sub>. Therefore a measured background signal is subtracted.

All the peroxy radical measurements that have been included and described within this thesis have been performed through the use of the PERCA technique, and Section 2.5 will provide a more detailed presentation of the University of Leicester PERCA (V3.5) instrument and performance.

### 2.1.1 Peroxy Radical Chemical Amplification - Laser Induced Fluorescence (PERCA-LIF)

Sadanaga *et al.*, (2004) have described another variant of the PERCA technique. This variant has at its basis the same principle as the PERCA technique, the main variation consisting in a slightly different NO<sub>2</sub> detection method. Therefore, the PERCA's luminol chemiluminescence for NO<sub>2</sub> detection has been replaced by laser induced fluorescence (LIF) detection of NO<sub>2</sub>, the advantage of which is to offer an increased sensitivity than the 'traditional' PERCA technique. Sadanaga *et al.*, (2004) have achieved a detection limit of 3 pptv, which improves precision, but, on the other hand, this technique comes with the price disadvantage, compared with the 'traditional' PERCA method.

## 2.2 Matrix Isolation Electron Spin Resonance (MI-ESR)

Matrix Isolation Electron Spin Resonance (MI-ESR) was introduced by Mihelcic *et al.*, (1978). HO<sub>2</sub>, CH<sub>3</sub>C(O)O<sub>2</sub> and sum of alkyl peroxy radicals are measured independently through the isolation of an air sample in a D<sub>2</sub>O matrix at 77 K. A series of electron spin resonance scans are performed within this matrix, followed by establishing an average of these scans in order to refine the signal-to-noise ratio. Mihelcic *et al.*, (1985) reported collection efficiency for MI-ERS of (90 ± 10) %, while the detection limit during the measurements reached 20 pptv, MI-ERS has the ability to identify all the radicals within the matrix. Apart from this advantage, Mihelcic *et al.*, (1993) observed that through this technique there is the possibility to have a simultaneous measurement also of NO<sub>2</sub> and NO<sub>3</sub>.

MI-ESR also presents some disadvantages: the impossibility of using MI-ESR in aircraft measurements or in regimes where [HO<sub>2</sub> + sum of RO<sub>2</sub>] concentrations are changing rapidly, owing to the fact that this technique needs a long time for the measurement (20-30 minutes). The measurements are undertaken at 77 K and there is need for large quantities of liquid N<sub>2</sub> to be present. Another difficulty is encountered regarding the conditions for transporting the measured matrix to be the laboratory: the matrix has to be kept at 77 K as well as under vacuum. Platt *et al.*, (2002) showed that a comprehensive set of simultaneous radical measurements performed by MI-ESR (Holland *et al.*, (2003)), PERCA (Mihelcic *et al.*, (2003); Volz-Thomas *et al.*, (2003)) and Laser Induced Fluorescence (LIF) (Geyer *et al.*, (2003)) during the BERLIner OZone experiment (BERLIOZ) (see Section 1.5.3, Chapter 1) campaign. The measured values of the each of free radical are useful to have inter comparison at a rural, semi-

polluted site in the continental boundary layer and inter comparison provides a good agreement.

## 2.3 Fluorescence Assay by Gas Expansion (FAGE)

The Fluorescence Assay by Gas Expansion (FAGE) technique does not have the ability to measure all the peroxy radicals; it can measure OH and HO<sub>2</sub>, but not RO<sub>2</sub> directly. It was first reported by Hard and O'Brien in the 1980s (Hard *et al.*, 1984). The process of detecting OH is via Laser Induced Fluorescence (LIF). The surrounding air is expanding through a pinhole into a chamber by laser excitation at 308 nm at low-pressure (1 mbar). The OH undergoes a transition from the ground electronic state, X<sup>2</sup>Π, to the first excited electronic state, A<sup>2</sup>Σ. The need of a low-pressure expansion is explained by the fact that the fluorescence lifetime of OH is increased to approximately 100-200 ns so that it becomes possible to detect the very small OH fluorescence signal. In similar conditions of low-pressure expansion, the process of HO<sub>2</sub> measurement takes place. The expanded air reacts with the excess of NO and the products are OH and NO<sub>2</sub> via reaction (2.1). The OH produced is subsequently measured as before. The conversion of RO<sub>2</sub> into HO<sub>2</sub> can be obtained through reaction with NO and then with O<sub>2</sub>, but the difference between this method and the method employed by PERCA is that the reaction of RO with O<sub>2</sub> in order to form HO<sub>2</sub> is not actually taking place owing to the pressures present in the chamber. It has been reported by Heard and Pilling (2003) for a 30s integration time that HO<sub>2</sub> measurements have an accuracy of about 30%, and typical detection limit 0.004-0.04 pptv and 0.006 pptv for OH.

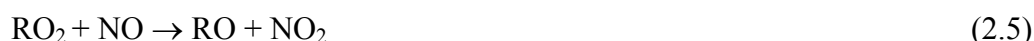
The FAGE technique is undergoing further development in order to enable it to detect RO<sub>2</sub>, in addition to HO<sub>2</sub>. The reaction of RO with oxygen actually takes place and thus

forms HO<sub>2</sub>. A higher pressure in the chamber is required as at low pressure the reaction is too slow. There is a disadvantage in increasing the pressure in the chamber, i.e. large OH amounts are lost, which makes the measuring process difficult. Fuchs *et al.*, (2006) reported that the process of conversion of RO<sub>2</sub> into HO<sub>2</sub> is taking place through a two-phase process in two chambers. A pre-reaction chamber is used for conversion of RO<sub>2</sub> into HO<sub>2</sub> and a second chamber is employed for further expansion at lower-pressure. The results of deploying this two-phase technique are a detection limit increased between 0.1 to 0.3 pptv for an integration time of 30 s and a signal-to-noise ratio of 2.

The deployment of the FAGE technique has been reported during various field campaigns, for measurements taking place both at ground level and on airborne platforms (Brune *et al.*, 1998; Brune *et al.*, 1999; Faloona *et al.*, 2000; Holland *et al.*, 2003; Ravetta *et al.*, 2001; Smith *et al.*, 2006; Tan *et al.*, 2001a). See also Table 1.1.

## 2.4 Peroxy Radical Chemical Ionisation Mass Spectrometry (PerCIMS)

Peroxy Radical Chemical Ionisation Mass Spectrometry (PerCIMS) is an Ion Molecule Reaction-Mass Spectrometry (IMR-MS) (Hanke *et al.*, (2002), Reiner *et al.*, (1997)). PerCIMS uses a detection technique based on the amplified chemical conversion of ambient peroxy radicals into a bisulfate ion ( $\text{HSO}_4^-$ ), which is quantified by mass spectrometry. The perCIMS instrument consists of a pinhole inlet, a reaction tube, an ion drift tube, a mass spectrometer chamber, injection valves, pressure pumps, lenses, and mass flow controllers. Ambient air enters into the instrument through the inlet pin hole, which approximately 100 micro meters in diameter. The pin hole leads into a teflon reaction tube where inlet chemistry occurs at low pressure (typically 200 hPa). The addition of NO and  $\text{SO}_2$  to the sampled air chemically converts the peroxy radicals into  $\text{H}_2\text{SO}_4$  in the inlet.



As shown in reaction (2.12)  $\text{HSO}_3$  rapidly reacts with the oxygen under atmospheric conditions:



The resulting HO<sub>2</sub> helps for the continuation of the cycle. The SO<sub>3</sub> co-product reacts with water and forms H<sub>2</sub>SO<sub>4</sub> as shown in reaction (2.13):



Behind the reaction tube is an ion source radioactive metal, Americium (<sup>241</sup>Am). There is an ion drift tube located between the radioactive metal and the mass spectrometer, which is the region where ion chemistry occurs after the chemical amplification reaction chemistry has occurred. In this ionizing region, the Americium metal ionizes HNO<sub>3</sub> gas injected into the system to form NO<sub>3</sub><sup>-</sup> ions (reaction 2.14), which subsequently reacts with the H<sub>2</sub>SO<sub>4</sub> gas to form HNO<sub>3</sub> and HSO<sub>4</sub><sup>-</sup> ions (as an acid base of reaction 2.15).



The PerCIMS measurement experiments were carried out in two modes. These are signal mode and background mode. In this single mode operation, inlet chemistry allows the conversions of peroxy radicals to H<sub>2</sub>SO<sub>4</sub> gas, which is converted by ion chemistry to HSO<sub>4</sub><sup>-</sup> as shown in reactions 2.1, 2.10, 2.5, 2.6, 2.12, 2.13, 2.14 and 2.15. NO and SO<sub>2</sub> are injected into the inlet through the front injection valve which allows the reactions 2.1, 2.10, 2.5, 2.6, 2.12 and 2.13 to occur while reactions 2.14 and 2.15 occur in the ion drift tube. Ion counts from the single mode correspond to the sum of counts from peroxy radical, noise and ambient HSO<sub>4</sub><sup>-</sup> ions.

In the background mode of measurement, NO is injected through the front injection valve and SO<sub>2</sub> in the rear injection valve of the inlet. NO gas reacts with HO<sub>2</sub> to form

OH and NO<sub>2</sub>. OH is a very reactive radical that rapidly react with NO to form HONO and RONO in RO<sub>2</sub> case before it gets to the SO<sub>2</sub> region. Both HONO and RONO are cannot be broken down within the instrument. The formation of these compounds causes the loss of peroxy radicals within the instrument therefore, reactions 2.1, 2.5 and 2.6 occurs insignificantly. However, reactions 2.14 and 2.15 occur as normally. Ion counts from this mode are the sum of ambient HSO<sub>4</sub><sup>-</sup> and noise. In order to obtain the actual count rate, it is necessary to subtract background from the signal mode.

Measurements can be carried out within the perCIMS instrument in two sub-modes under the signal and background modes. First is the HO<sub>2</sub> only mode in which counts detected are from conversion of HO<sub>2</sub> radicals to HSO<sub>4</sub><sup>-</sup> ions. Edwards *et al.*, (2003) and Hanke *et al.*, (2002) have reported that speciation of HO<sub>2</sub> and RO<sub>2</sub> by varying the concentration of NO. In the HO<sub>2</sub> mode only, high concentrations of NO and SO<sub>2</sub> gases were used to inhibit the conversion of RO<sub>2</sub> to HO<sub>2</sub>. NO concentrations are key factor in this mode because it converts RO<sub>2</sub> radicals to RONO (by leading to the reactions 2.5 and 2.8) in order to detect prevent RO<sub>2</sub> detection. As a consequence of the NO concentration increase, the efficiency of measuring RO<sub>2</sub> becomes lower, being reported at about 10% by Edwards *et al.*, (2003), compared to the efficiency of HO<sub>2</sub> measurement and thus, CIMS is more efficient with HO<sub>2</sub> measurements only. Second is the HOxROx in which diluted NO and SO<sub>2</sub> gases are used to measure the concentration of HO<sub>2</sub> and RO<sub>2</sub> radicals. Using diluted NO reduces the formations of RONO in the inlet. Initially, RO<sub>2</sub> radicals are converted to HO<sub>2</sub> (by leading to the reactions of 2.5 and 2.6) and afterward converted to HSO<sub>4</sub><sup>-</sup> ions. Therefore, the count detected in this mode is a sum of HO<sub>2</sub> and RO<sub>2</sub> concentrations. Clemitshaw *et al.*, (2004) and Eisele and Tanner (1993) noticed that in the absence of NO, CIMS has the ability to measure

OH through the same technique detailed above. In this case, CIMS detection limit is lower than 0.4 pptv while its accuracy is between 35 – 41%, and its precision is estimated at 10%.

## 2.5 The University of Leicester dual-channel PERCA (V3.5) instrument

The operating principles are absolutely identical for all versions of the PERCA instruments, i.e. based on the chemical amplification technique, see Section 2.1. The generations of PERCA V (1), PERCA V (2) and PERCA V (3) were deployed by the University of East Anglia (UEA), Norwich, England, U. K. PERCA V (3.5) and PERCA V (4) are recently developed jointly by the University of East Anglia and the University of Leicester, Leicester, England, U. K. There were a number of improvements which have been made over the period 1993 to 2003. PERCA V (1) and PERCA V (2) are made for ground level measurement and both are single channel. The PERCA V (2) is a modified version of the PERCA (1) instrument described in detail by Clemitshaw *et al.* (1997), with a heated inlet system to control the inlet temperature. PERCA V (3) (e.g. Green *et al.* , (2003)) and PERCA V (4) (e.g. Parker *et al.*, 2009) are developed for aircraft measurements and PERCA (V3.5) is developed for ground level measurement and all these three generations are performed for dual channel feature. The setup of the PERCA V (3.5) system is shown in Figure 2.2, 2.3 and 2.5 and the significance of PERCA V (3.5) can be summarised: Two inlets are installed into the inlet box which is away from the instrument rack (see Figure 2.2), having better power supplies via electrical loom between the instrument rack and the inlet system (see Section 2.5.1.1). Two individual LMA-3 Scintrex NO<sub>2</sub> detectors and

features of adjustable luminol flow by needle valves (see Section 2.5.1.2). The linearisation NO<sub>2</sub> flows (see Section 2.5.1.3), data logging, computer system, main control unit and flow controllers (see Section 2.5.1.4). The scrubbing system (see Section 2.5.1.5), gases are supplied from cylinders stored separately (see Section 2.5.1.6 and Figure 2.4). The pumping system (see Section 2.5.1.7) and a separate radical calibration source unit (see Section 2.5.2.2 and Figure 2.12).

Following equation (2.9) to achieve a measurement of  $\Delta[\text{NO}_2]$  the University of Leicester PERCA (V3.5) instruments employ a dual channel system (two inlets and two detectors) to measure both the amplification chemistry produced NO<sub>2</sub> (NO<sub>2</sub>, amp) and the background NO<sub>2</sub> (NO<sub>2</sub>, back) concentrations simultaneously. The amplified NO<sub>2</sub> concentration is derived by background subtraction ( $\Delta[\text{NO}_2] = ([\text{NO}_2]_{\text{amp}} - [\text{NO}_2]_{\text{back}})$ ). The total NO<sub>2</sub> measured by the detector is therefore due to peroxy radical conversion, background NO<sub>2</sub> present in the ambient atmosphere and NO<sub>2</sub> from the oxidation of NO by ozone within the PERCA (V3.5) inlet itself due to the additional NO added into the PERCA (V3.5)'s inlet. The dual system employed involves the periodic switching of the measurement mode (“chain amplification mode” to “background measurement mode” and vice versa) between the measurement channels, such that the chain chemistry is always active in one channel whilst radical termination in the other channel allows the background measurement. The switching process between the two operations modes are explained in Sections 2.5.1.1, 2.6.1 and 2.7. There is a continuous interchange between the periods of amplification of peroxy radical signal and the periods when the radical signal is allowed to terminate in the inlets and only ambient NO<sub>2</sub> and NO<sub>2</sub> formed due to ozone chemistry of the added NO reagent are measured.

The difference between amplification mode and termination or background mode can be explained in the following way. In amplification mode, the NO and CO reagent gases are injected together into the inlet exactly where the ambient air is sampled. In background or termination mode, the NO is first injected in the inlet, followed by CO injection. In termination mode, OH produced through reaction 2.1 and the conversion of OH cannot be recycled into HO<sub>2</sub> (through reactions 2.2 and 2.3 and see top right panel in Figure 2.1). Reaction of ambient CO is too slow to recycle OH into HO<sub>2</sub>. An amount of the OH reacting with NO in a chain termination step 2.11 determines the loss of HO<sub>2</sub>, which reacts with NO<sub>2</sub>.



The amplification and background cycles are summarised in the top panels of Figure 2.1.

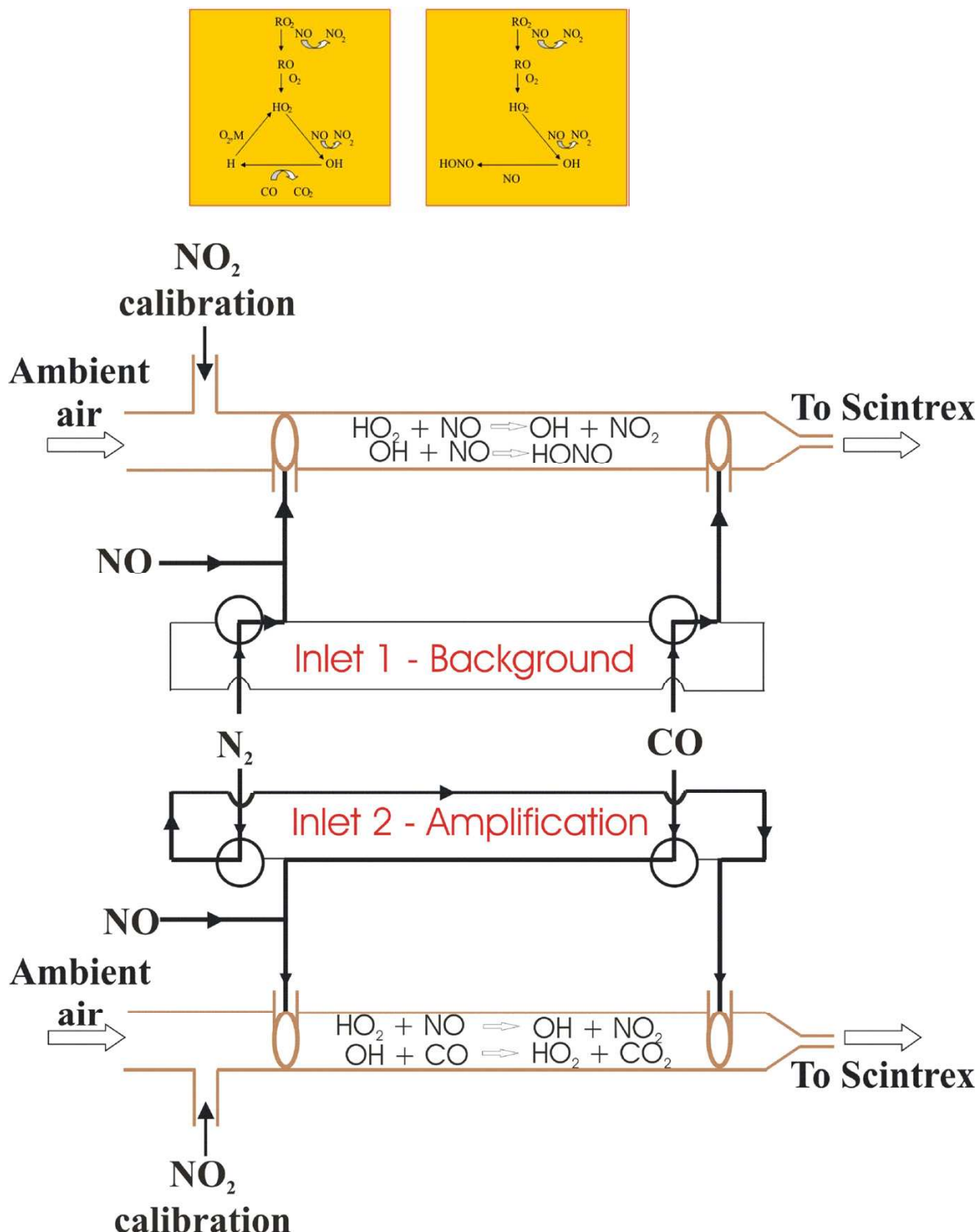


Figure 2.1- Left and right top panel represent amplification and backgrounds cycles, respectively. Bottom panel shows the injection of reagent gases into inlets in amplification and background modes, (Jacob, 2006).

## 2.5.1 Deployment in the field

This section focuses on presenting in more detail the role of each sub-system of the PERCA instrument. Figure 2.2 shows the outside view of the PERCA (V3.5) instrument with an inlet box fixed on post 2 metres above the field platform sea

con

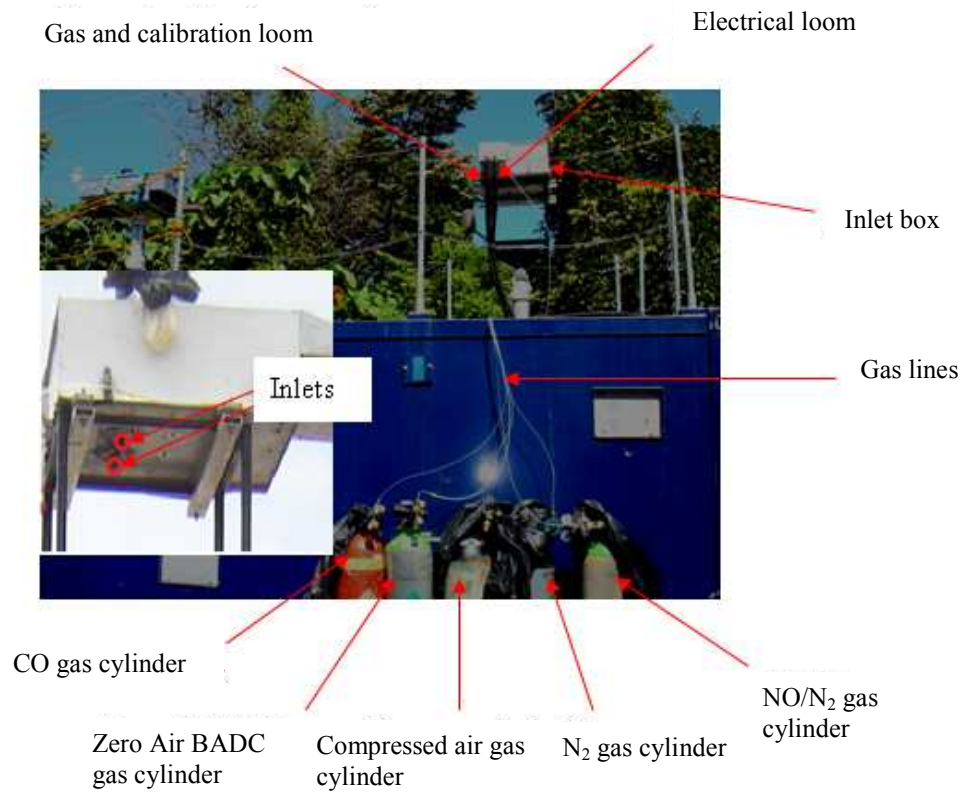


Figure 2.2 - PERCA (V3.5) inlet unit collecting sample air mid-rainforest in Borneo ~ 6m inlet height from ground.

The inlet box is connected to the mobile laboratory through the system of control and detection leads. Although connected to the mains electricity of the laboratory, the unit can run off an Uninterrupted Power Supply (UPS) provided by the Leicester sea container, which is helpful in case of short power-cuts. The assemblies constituting the instrument are: the main rack and the inlet system. Both systems will be described in detail below.

The PERCA (V3.5) instrument is mounted in a 19" rack unit containing the control and processing systems and this unit is called the Main Rack. A vacuum pump can also be found inside the Leicester sea container to draw ambient air and reagent gases through the instrument. The gas cylinders are placed outside the container. The main rack is shown in both Figures 2.3 and 2.5 and the gas rack is shown in Figure 2.4.



Figure 2.3 - The main rack inside the Leicester sea container at the Cape Verde campaign



Figure 2.4 - Gas cylinders secured with sea container (left panel) and gas cylinders left between two campaigns in mid jungle (right panel).

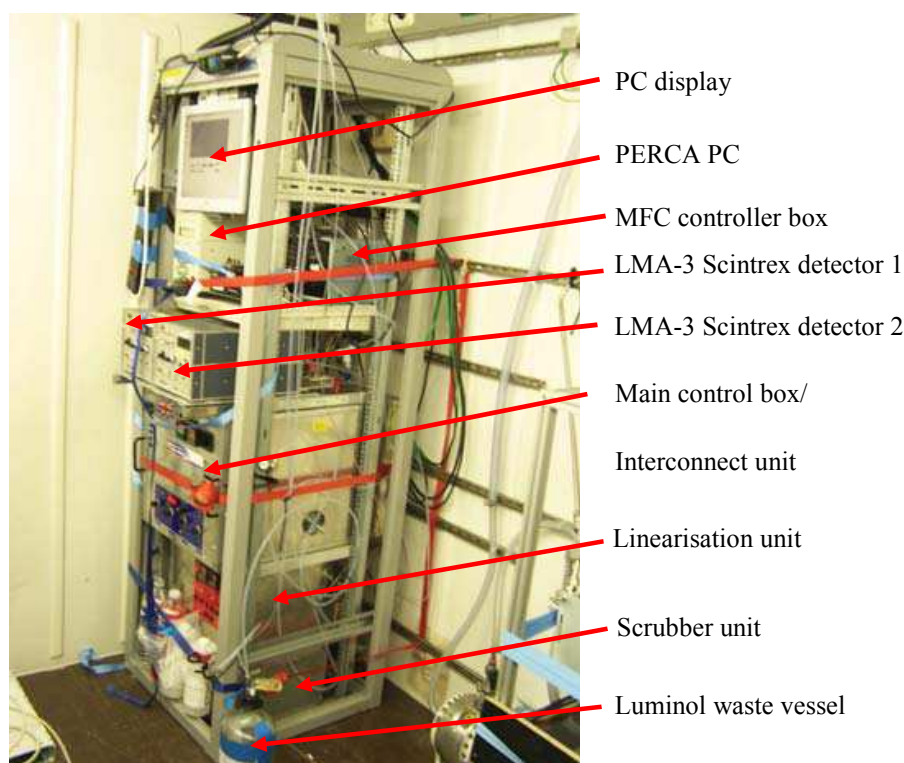


Figure 2.5 - PERCA (V3.5) main rack and its sub devices (Brookes, 2010)

### 2.5.1.1 The inlet system

It is in the Pyrex inlets, which are placed in the inlet box together with the gas handling equipment, where the process of peroxy radical amplification takes place. The function of the Pyrex inlets, which extend 10 cm below the box, is to draw the air (at a flow of  $2 \text{ l min}^{-1}$ ) roughly perpendicularly to the ambient airflow (Green *et al.*, (2002)) as shown in Figure 2.2. The inlets are kept at a constant temperature of  $30 \text{ }^\circ\text{C}$ . The inlets have a length of about 180 mm and a 25 mm diameter and the reagent gases are introduced via three side-arms. The side-arms serve for the following purposes: the closest arm to the ambient end of the inlet is used for introducing  $\text{NO}_2$  /zero-air mixture for calibration, while the other two arms are used for introducing NO, respectively CO and  $\text{N}_2$  to the inlet as shown in Figure 2.1. The combinations of reagent gases are explained in Section 2.5. During the amplification phase CO and NO are added at the same time to

the sample flow into the inlet (see Figure 2.1 for inlet 2), while they are added at different places during the termination phase (see Figure 2.1 for Inlet 1). The reason for adding the N<sub>2</sub> flow is to confer stability to the dynamics of gas flow in both of the operation modes, as well to offer the possibility of having a rapid settlement of the flow post-switch between the amplification and the background modes and elimination of pressure pulsing and assures the stability of the sample gas flow when the modes of operation switch.

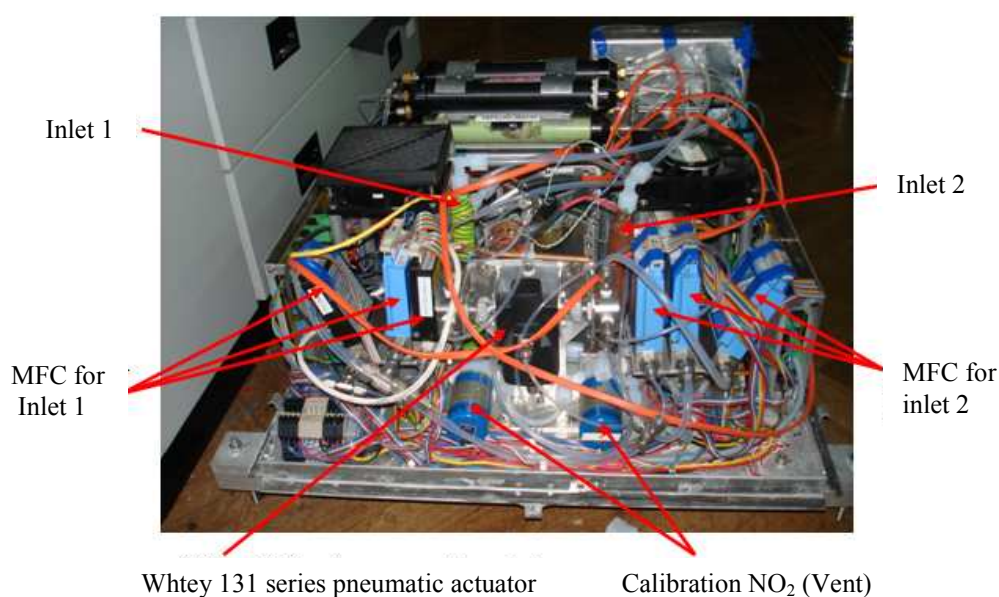


Figure 2.6 - PERCA (V3.5) inlet box and its electronics system

A Swagelok series 40 ball valve (SS-43YF2), is switched via a Whitey 131 series pneumatic actuator (MS-131-31DA) (see Figure 2.6), fired by nitrogen (BOC, O<sub>2</sub> free), this switches between the two operation modes at 100 psi (psi- Pounds per Square Inch) and the process is controlled by a Mac PME-501CAA solenoid. The constancy and the measurements of the flows of CO, NO and N<sub>2</sub> to the inlet are assured by six mass-flow controllers (shown in Figure 2.6). Gas flows are controlled with Mykrolis FC-260 mass flow controllers (MFCs) and typically provide 10 sccm (standard cm<sup>3</sup>

minute<sup>-1</sup>) NO diluted in N<sub>2</sub> (600 ppmv NO in N<sub>2</sub>, Messer, certified ± 2%), 100 sccm CO (Messer, 99.9%) and 100 sccm N<sub>2</sub> (BOC, zero grade). Thus, 3 ppmv NO and 6% v/v CO are injected into the inlet region.

Calibrated sources of methyl iodide (CH<sub>3</sub>I) (see Section 2.5.2.2 used for calibration) and NO<sub>2</sub> (see Section 2.5.2.1 used for calibration) are required for PERCA (V3.5) chain length calibrations and determination of the LMA-3 Scintrex detector's NO<sub>2</sub> sensitivity. The field and laboratory work along this project were facilitated by the use of several permeation tubes which were bought uncalibrated from VICI Metronics Inc.; the permeation rates of each uncalibrated permeation tube are identified (within ± 25 %) and a particular tube is selected depending on the concentration of calibration mixture covering an appropriate range easily obtained by staged dilution. Summary of the permeation rates are shown in Table 2.2.

Compound	Part number	Nominal perm. rate	Calibrated perm. rate (± 3σ)
CH <sub>3</sub> I	100-007-4600-U40	350 ng min <sup>-1</sup>	408.97 ± 29.6 ng min <sup>-1</sup>
NO <sub>2</sub>	140-633-0081-U40	460 ng min <sup>-1</sup>	530.2 ± 9.1 ng min <sup>-1</sup>
NO <sub>2</sub>	140-633-0081-U50	230 ng min <sup>-1</sup>	224.04 ± 16.0 ng min <sup>-1</sup>

Table 2.2 - Measured and nominal permeation rates of calibration permeation tubes for PERCA (V3.5) (Brookes, 2010).

The low permeation rates (hundreds of nanograms per minute) required the use of precise weighing scales (Mettler Toledo, AG245) to establish the loss of mass down to 10<sup>-5</sup>g, and measurements were carried out over extended periods in time (approximately every 2 weeks for a 12 week period). The introduction of CH<sub>3</sub>I and NO<sub>2</sub> permeation tubes kept at a constant temperature of 40 °C in a permeation oven within the inlet box is necessary for assuring a constant release of these compounds at

fixed rates. By weighing the tubes prior and post-experiments, show the mass loss of the tubes which is used to calculate the permeation rate. These tubes are kept under a constant flow of  $N_2$ , which has a measured rate of 50 sccm, while  $CH_3I$  or  $NO_2$  concentrations are modified during calibrations owing to the presence of two mass-flow controllers which have the role of diluting zero-air. Through a calibration tube, permeation flows of  $CH_3I$  (see Section 2.5.2.2 for  $CH_3O_2$  calibration flow) in air (BOC, BTCA 178 grade) and  $NO_2$  (see Section 2.5.2.1 for  $NO_2$  calibration flow) in air (BOC, BTCA 178 grade) can be added to the inlets. Metron technology 203-3414 series three-way valves and Parker series 9 three-way valves have the role of changing the calibration flows between the inlets and vent shown in Figure 2.6.

There is a good protection against weather conditions or any sort of impact that the inlet might suffer from through wrapping the gas and electrical lines connecting the inlet to the instrument in the laboratory in a 20 metre PVC umbilical tube. The inlet is placed on a 5-10 meter tower, on a black metal platform fixed firmly to a pneumatic lifting mast. The mast can be raised to a distance of ten meters and be easily pulled down for calibration or for modification to the inlet box.

### 2.5.1.2 Detector systems

PERCA (V3.5) has two separate identical LMA-3 units (Unisearch Scintrex which work on the principle of the chemiluminescence) detectors as shown in Figure 2.5. NO<sub>2</sub> concentrations are measured in the two sample lines. Each sample air flow is directed to a detector cell (and measurement channel) where it comes into contact with the luminol flow.

Luminol is an organic compound. Kelly *et al.*, (1990) reported that NO<sub>2</sub> initiates the process of luminol chemiluminescence, which happens at  $\lambda = 424$  nm. The reaction with luminol occurs in the presence of two NO<sub>2</sub> molecules, and the reaction rate is consequently quadratic at low NO<sub>2</sub> concentrations. There is a linear reaction occurring at higher concentration of NO<sub>2</sub> (above 2-3 ppbv), the rate limiting step of this reaction modifies the solvation of second NO<sub>2</sub> molecule and also 3-aminophthalate ion produced in an excited state. The electrons in the atom absorb energy from the chemical reaction, causing them to go to an excited state as shown in Figure 2.7a.

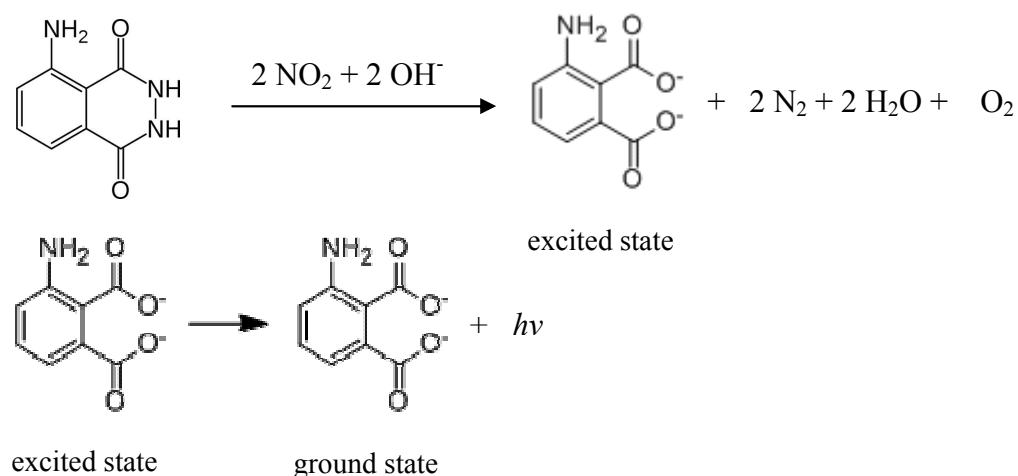


Figure 2.7a - Reaction of luminol with NO<sub>2</sub> (Cantrell *et al.*, 1993b)

The electrons return to the ground state since the excited state is unstable, releasing a photon of light by the second reaction shown in Figure 2.7a. The chemiluminescence

light signal is measured through the use of a photomultiplier tube, as shown in Figure 2.7b also present in the Scintrex LMA-3 detector, opposite a wick, while the measurement process occurs through producing a signal which is measured in volts. The detector box houses the couple of needle valves (Swagelok SS-SS2-A) which have the function of adjusting the liquid flow. One is control the supply prior to detector cell and another is control the luminol flow to the waste reservoir after the detector cell. There is also an acetal cell present in the detectors and its role is that of housing a wick, down which luminol solution is run, and control electronics.

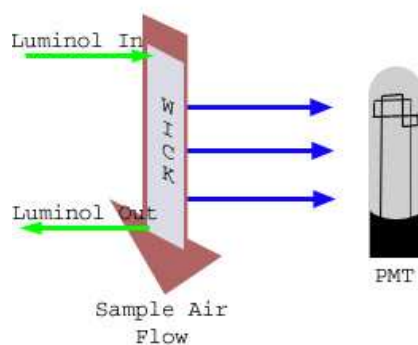


Figure 2.7b - Schematic diagram of Scintrex LMA-3 detector (Green *et al.*, 2003)

Luminol is stored in a 2 litre glass bottle which is kept in a refrigerator at 5°C and was pressurised by a N<sub>2</sub> flow. The luminol flow is 0.5 ml per minute for each detector. It is quite important to keep the wick moist and this aspect is achieved through making sure that pull more air than liquid out. Hence, the luminol is not deposited on the wick and there is a more rapid outflow than inflow. The used luminol solution is kept in the waste reservoir in the fridge.

### 2.5.1.3. Linearisation unit

The linearisation unit is shown in Figure 2.5. The linearization unit oven, contain two Dynacal 50F3, NO<sub>2</sub> permeation devices (for both Scintrex LMA-3 detectors), with an approximate output of 224 ng min<sup>-1</sup>. These permeation devices have the ability of releasing a constant flow if a temperature of 40 °C is permanently ensured. These are required because as noted in Section 2.5.1.2, the order of the NO<sub>2</sub> with luminol reaction changes with [NO<sub>2</sub>] and, thus the Scintrex LMA-3 detector's response to [NO<sub>2</sub>] is linear above [NO<sub>2</sub>] of about 20 parts per billion by volume (ppbv). Clemitshaw *et al.*, (1997) noted that in a situation of a reduced concentration of the sampled NO<sub>2</sub> concentration below 20 ppbv, a supplementary flow of 20 ppbv is required, provided by the linearisation system. The extra NO<sub>2</sub> flow of 50 cm<sup>3</sup> minute<sup>-1</sup> (sccm) N<sub>2</sub> is introduced within the detector before the introduction of the ambient air sample entering the detector. Linearisation NO<sub>2</sub> flows are controlled using mass flow controllers (Mykrolis FC-260). In polluted air containing high concentrations of ozone, the ozone is titrated out to form NO<sub>2</sub> by reaction with the NO added to the inlet as the gas flow is carried from the inlet to the detector. If the [NO<sub>2</sub>] is more than 20 ppbv then the linearization NO<sub>2</sub> flow is not needed. The essential experiment when the linearization flow is best employed is in calibration of the chain lengths (because there is no introduction of ambient air or background ozone into the detector), as well as of the remote backgrounds, e.g. Cape Verde, where the studies occur in clean conditions.

#### 2.5.1.4. Data-capture and computer system

In house software is used to collect the data during the experiment. Separate files are generated for each day. They include the flow rates of the reagent and the zero-air gas, all the PMT raw voltage signals, as well as the measured temperature by thermocouples which are installed in the inlet box, and the valve's switching states. All data collection is collected at 1 Hz. There is a special PC designed for instrument control and data acquisition containing this "house keeping" program, which is written in Microsoft Visual Basic 4.0. This 1.2 GHz Pentium IV PC has a single board (Rocky-3702EV, Wordsworth) which is held within the 19" rack (shown in Figure 2.5) industrial PC case (Rack 360, Wordsworth) and has a CD-RW drive to allow data to be transferred. The data acquisition is performed through special analogue-to-digital boards which are held within the main control unit (shown in Figure 2.5) and the way these boards (PCI-DAS6402/16, CIO-DAC16/16 and PCI-DAS-TC) interface with the Visual Basic software is through the use of the Computer Boards universal Library. The control software houses stepper motors (RS components) which have the role of controlling the commercial mass-flow meters (FC-360, Mykrolis), which, in their turn, control the sample flow rates within the PERCA (V3.5) instrument. Thus, through employing the stepper motor system, it is possible to maintain a sample flow rate of 2 slpm through each detector. In order to conduct the data work, the raw file from each day has to be transformed into the Wavemetrics software package, called IGOR.

### 2.5.1.5. Scrubbing system

The role of the scrubbing unit is to take the PERCA (V3.5) waste gases and harmful emissions, e.g. CO is hazardous to human health. CO and NO emissions from the PERCA (V 3.5) instrument can alter the ambient measurements of other species during field campaigns. Converting the CO and NO to less harmful species are important for health and safety and scientific importance as well. This process of reducing CO and NO emissions occurs through the use of three separate wide-bore glass traps. The first trap contains zeolite molecular sieves ( $\text{Na}_2\text{O} \cdot \text{Al}_2\text{O}_3 \cdot (2.8 \pm 0.2) \text{SiO}_2 \cdot (6\sim7) \text{H}_2\text{O}$  and ratio of  $\text{SiO}_2: \text{Al}_2\text{O}_3 \approx 2.6\text{-}3.0$ ) which have the role of removing moisture which can degrade the performance of the second trap. It is in the second trap where the oxidation of CO and NO occurs; this trap contains Hopcalite ( $\text{CuMn}_2\text{O}_4$  and a mixture of 50% MnO, 30% CuO, 15%  $\text{Co}_2\text{O}_3$ , and 5%  $\text{Ag}_2\text{O}$ ) which oxidises the 6% CO to  $\text{CO}_2$  in the exhaust flow and the 3 ppmv NO in to  $\text{NO}_2$ . Within the third trap, the  $\text{NO}_2$  from the flow is removed by Sofnofil ( $\text{Al}_2\text{O}_3 > 80\%$  and  $\text{KMnO}_4 < 6\%$  of % W/W). These trap materials were purchased from Molecular Products Limited and used in the field and laboratory work carried out during this project. Afterwards, all the scrubbed exhaust gases are vented 100 metres downwind of the experiment location via a long waste line.

### 2.5.1.6. Reagent gases

During the field campaigns, for safety reasons, all the gas cylinders are kept outside the lab (shown in Figure 2.2). Transportation of these gases into the lab and then into the umbilical that connects the lab to the mast of the inlet box, is accomplished through the use of Teflon tubes. In order for the inlet reactions to take place, it is necessary to use: BOC Zero grade nitrogen (99.998 % pure), carbon monoxide (99.9 % pure) and a BOC

Special Gases (Beta-volumetric standard) mixture of 600 ppmv NO in N<sub>2</sub>. The other gas is used for powering the valve which controls the phase switch oxygen-free N<sub>2</sub> (at high pressure ~ 100 psi (~ 7 bar, where psi- Pounds per Square Inch), while BTCA 178 zero-air (< 0.1 ppm hydrocarbons, < 1 ppm CO, 300 ppm CO<sub>2</sub> and 0.1 ppm NO) is used as a calibration dilution gas. Figure 2.8 shows the gas flows through four 200 cm<sup>3</sup> traps for pre-inlet gas scrubbing.

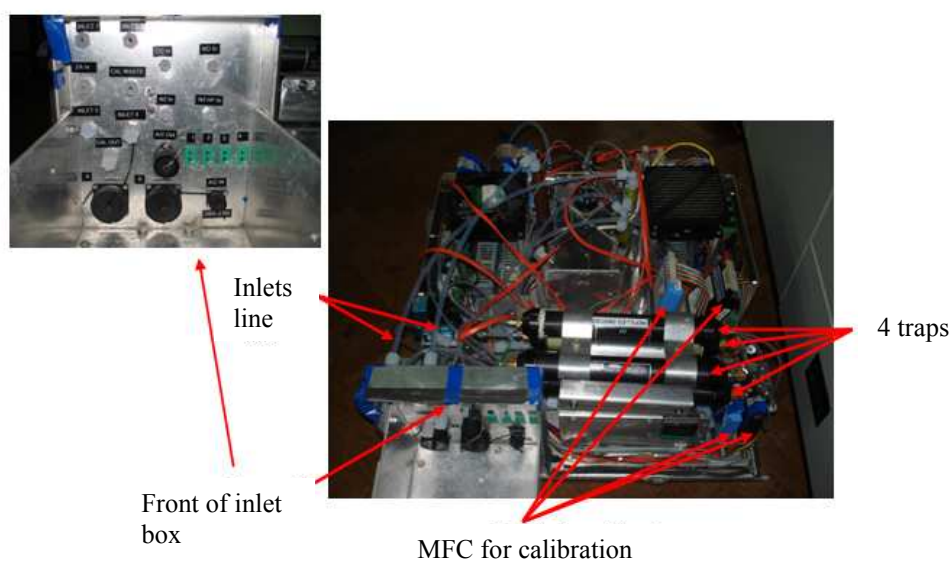


Figure 2.8 – Left panel represents the front view of the inlet box. Right panel represents the inside the view of inlet box in which contains electronic devices (e.g. temperature, mass flow controllers, fan, etc); the ambient air is entering into the inlets.

First and second traps containing an iodinated charcoal, first trap removes metal-carbonyl species (Ni(CO)<sub>4</sub>, Fe(CO)<sub>6</sub>) from the CO gas where as second traps removes hydrocarbons and NO<sub>2</sub> from the N<sub>2</sub> gas. The third trap contains FeSO<sub>4</sub>, which eliminates trace amounts of NO<sub>2</sub> from the NO-N<sub>2</sub> mixture. The Sofnofil and the activated charcoal contained within the fourth trap help absorb the NO<sub>2</sub>, as well as the hydrocarbons from the calibration flow (BTCA 178 zero-air).

### 2.5.1.7. The pumping system

The pump used is a Leybold Sogevac SV16 rotary vane vacuum pump, which is filled with oil and delivers a base of pressure 1.5 mbar, as well as a pumping rate which can reach up to  $14.5 \text{ m}^3 \text{ h}^{-1}$ . The presence of an oil return line within the pump ensures that no oil is lost through the exhaust line. The role of the pump is that of extracting the sample flows from the detectors, the regulators and the scrubber, and, by lowering the pressure of the luminol waste chamber, to eliminate waste luminol from the detectors.

## 2.5.2 The calibration system

### 2.5.2.1 $\text{NO}_2$ sensitivity calibration of the luminol detectors

As previously discussed in Sections 2.5.1.2 and 2.5.1.3, the order of the  $\text{NO}_2$  and luminol reaction varies with  $[\text{NO}_2]$ , so additional  $\text{NO}_2$  is supplied by a linearization unit to ensure that response of the luminol detector system to  $\text{NO}_2$  is essentially linear (as long as  $> 20$  ppbv). The purpose of calibrating every day is to observe the efficiency of the detection system, as well as to characterise the gradient of the chemiluminescence vs.  $[\text{NO}_2]$  response of the luminol detectors. In order to provide various concentrations of  $\text{NO}_2$ , it is necessary to perform a combination of zero-air (BTCA 178 grade, BOC) at five different flow rates (2, 2.5, 3, 3.5, 4 and  $5 \text{ lmin}^{-1}$ ) with a stream of  $\text{NO}_2$  in 50 sccm of  $\text{N}_2$ . A flow of  $\text{NO}_2$  from a permeation device (approximate output of  $530 \text{ ng min}^{-1}$ ) is diluted by the varying zero-air flows, giving a concentration of  $\text{NO}_2$  between 55 and 140 ppbv.

In order to have  $[\text{NO}_2]$  values which are typical for the normal operating range of the detectors, it is necessary to introduce the following airflows: zero-air (BTCA 178

grade, BOC) to zero the detector, as well as calibrant gas stream, which is injected through the calibration side arm. The transformation from the voltage output of the PMT Scintrex detector into ppbv of NO<sub>2</sub> is thus calibrated through the calibration procedure. The permeation rate, as well as the quantity of zero-air which dilutes the NO<sub>2</sub> flows allows a quantification of the NO<sub>2</sub> concentrations for each calibration point.

The sensitivities of each channel are determined for each inlet by plotting the measured PMT signal in volts versus the calculated NO<sub>2</sub> concentration in ppbv from the NO<sub>2</sub> calibration flows. Thus, the sensitivity is actually the gradient of this plot. For ambient air samples, the raw signal from the detectors (in volts) can then be divided by each inlet's sensitivity to give [NO<sub>2</sub>] for each channel in ppbv. Single channel PERCA (V3.5) instrument was deployed in the tropical rainforest in Borneo because of the failure of a LMA-3 detector and dual channel PERCA (V3.5) instrument deployed in the marine boundary layer at Cape Verde.

Figure 2.9 shows a typical sensitivity plot obtained whilst on field work in the tropical rainforest in Borneo (top group) and in the marine boundary layer at Cape Verde (bottom graph).

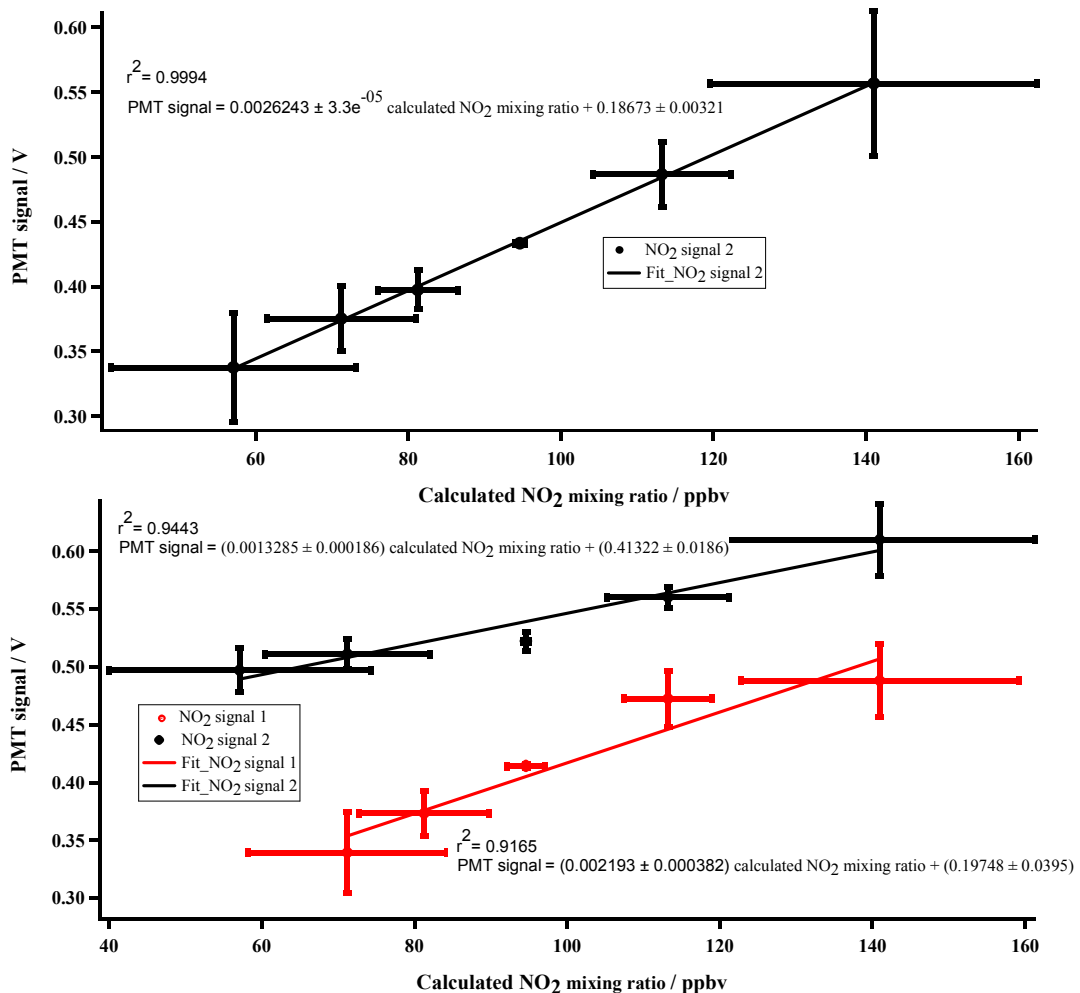


Figure 2.9 - Typical NO<sub>2</sub> sensitivity calibration: Top graph for the tropical rainforest campaign on 4<sup>th</sup> of May 2008 and bottom graph for the tropical marine campaign on 4<sup>th</sup> of March 2009. Error bars represent 1 $\sigma$ .

Different NO<sub>2</sub> sensitivity values (gradient) and the uncertainties of NO<sub>2</sub> sensitivity calibrations were obtained from the linear regression line of the PMT (Photomultiplier tubes) signal (V) vs. calculated NO<sub>2</sub> (ppbv) in the OP3 (1) and SOS (1) campaign as shown in Figure 2.9. These uncertainties of NO<sub>2</sub> detection were 1 % for inlet 2 on 4<sup>th</sup> of May 2008 from OP3 (1) campaign as shown in Figure 2.9 top graph. LMA-3 detector 1 had a technical problems in OP3 (1) and OP3 (3) campaigns, therefore no NO<sub>2</sub>

sensitivity calibration calculated for inlet 1. From the NO<sub>2</sub> sensitivity calibration on 4<sup>th</sup> of March 2009 during SOS (1) campaign, the uncertainties of NO<sub>2</sub> detection were 14% for inlet 1 and 17% for inlet 2 as shown in Figure 2.9 bottom graph. The basis for this is discussed below.

The luminol flow is controlled only by a combination of needle valves at the detector box, see Section 2.5.1.2. Hence, the sensitivity of NO<sub>2</sub> LMA 3 Syntrex detector could be variable (by variability of PMT signal, see Figure 2.9) throughout the field campaign, because the same flow rate of luminol does not run at exactly via the detector, see Section 2.5.1.2 for luminol chemiluminescence reaction. PMT signal is depends on the luminol flow rate. The very slow-flowing luminol slowly vaporises within the tubing, developing a solid residue settle in the detector wick area. It causes: slow down the flow and changing the efficiency of detective system. Therefore, there is bigger variability of the PMT signal (noticeable as error bar along the y axis) in case of larger (5 l/m) and smaller (2 l/m) calibration flow rates owing to the luminol flow instability as shown in Figure 2.9.

Clemmitshaw *et al.*, (1997) report that with use of the proprietary luminol II solution (as used in this work) good linearity was observed in the range 5-120 ppbv, with correlation coefficient at least 0.99. There is a small error bar obtained when the NO<sub>2</sub> mixing ratio is approximate 100 ppbv, in contrast the bigger error bar derived in the case of NO<sub>2</sub> mixing ratio with a smaller value (~ 60 ppbv) and larger (~ 140 ppbv) with respect to 100 ppbv for tropical rainforest and tropical marine boundary layer as shown in Figure 2.9. A low rate of dilution flow (2 slpm) generates a high concentration of NO<sub>2</sub> mixing ratio (~ 140 ppbv) whilst a high rate of dilution flow (5 slpm) produces a

low concentration of NO<sub>2</sub> mixing ratio (~ 60 ppbv) into the dilution flow mixed with constant NO<sub>2</sub>, (see Section 2.5.2.1 for constant NO<sub>2</sub> flow from a permeation device). It can be concluded that the low (2 slpm) and high (5 slpm) rates of dilution flows might affect the response of the LMA-3 detector and also cause bigger uncertainties during calibration.

Deionised water is used for washing out the detector system, and these procedures are carried out every four days during the measurement campaign. Daily calibrations were carried out throughout the measurement campaign and these calibrations were applied to each day's data processing calculations. Errors from drifting sensitivities throughout the day, as well as applying only one sensitivity to each day's data suggests that more frequent calibrations are to be required, but this causes gaps in the measurements. The peristaltic pump was removed in the University of Leicester PERCA systems (Green *et al.*, 2006). Typically a peristaltic pump (can be work independently) and internal luminol reservoirs would be necessary to stabilise the luminol flow throughout the measurement campaign.

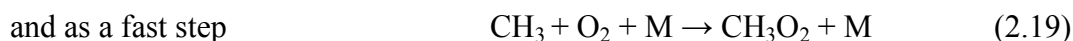
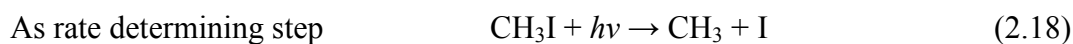
### 2.5.2.2 Chain length calibration

Chain lengths are likely to change from week to week in field campaigns, it is necessary to perform multipoint chain calibration every week during the field campaigns. During each field campaign chain length calibration experiments were carried out on each inlet during the measurement periods at each field site on a weekly basis and serve the purpose of checking changes that can occur in the HO<sub>2</sub> chemistry in the inlet. This is essential because the inlets can be affected in terms of wall-loss qualities by particles, e.g. sea salt in marine sites, that can build up on the inlet in time.

As pointed out by (Salisbury *et al.*, 2001) and (Brookes, 2010) the chain length reduction in the presence of water was not a result of wall losses of  $\text{CH}_3\text{O}_2$ , but a result of a change in  $\text{HO}_2$  chemistry in the inlet.

A TUV low-pressure mercury atomic emission lamp and a quartz cell are accommodated within a thermally insulated photolysis box made out of aluminium (Figure 2.17 set up). The link between the outlet of the calibration cell and the glass inlet is a Teflon tube with a length of approximately 6 cm, broadened at the end in order to make sure that there is a continuous and uniform flow entering the inlet, while the part of the tube that is inside the inlet only measures about 5 to 10 mm as shown in Figure 2.12. In order to have a suitable connection between the outlet of the calibration cell and the glass inlet it is necessary to have wooden blocks supporting the calibration cell as shown in Figure 2.12.

Clemmitshaw *et al.*, 1997 described the calibration source by showing how the chain length of the radical amplification chemistry occurring inside the all versions of PERCA (V3.5) inlet can be calibrated by known amounts of  $\text{CH}_3\text{O}_2$  generated by the calibration unit. The inlet box also houses a  $\text{CH}_3\text{I}$  wafer permeation device (Dynacal 4600, approximate output  $409 \text{ ng min}^{-1}$ , VICI Metronics). The devices are kept at a constant temperature of  $40 \text{ }^\circ\text{C}$  with a constant flow of 50 sccm of  $\text{N}_2$  (zero grade, BOC) passing over it. A combination of  $\text{CH}_3\text{I}/\text{N}_2$  and varying amounts of zero air (BTCA 178 grade, BOC) are used through a flow tube, which has a mercury lamp (TUV 15W UV, Koninklijke Philips N.V) next to it. The  $\text{CH}_3\text{I}$  is photolysed at  $\lambda = 253.7 \text{ nm}$  by the mercury lamp to produce the methyl radicals that then combination with oxygen to form methyl peroxy radical, thus:



The concentration of the peroxy radical,  $\text{CH}_3\text{O}_2$  is modified by introducing various flows of zero air, which can vary between 2, 3, 4 and 5 slpm to each of the PERCA (V3.5) inlets. In the presence of unknown species capable of producing peroxy radicals, it is necessary to have a varying flow rate of zero air, and inevitably, varying periods of calibration that correspond to each flow rate of zero air, as well as an absence of  $\text{CH}_3\text{I}$  in order to take out this 'artefact'. Some modification of the trace can occur as the conditions of a background signal changes significantly compared to the depth of the modulation, often simultaneously with a switch of the calibration flow. These modifications are caused by errors that might appear in the case of the subtraction in the single-channel measurement (errors that might occur for the chain length calibration as well), due to the fact that the calculation of the background during the amplification cycle is obtained through an average of the surrounding background measurement cycles. PERCA (V3.5) shows a good precision to a given concentration of peroxy radicals and this is indicated by the  $\Delta [\text{NO}_2]$  line shown in Figure 2.10.

The concentration of  $\text{CH}_3\text{O}_2$  is given by the following equation:

$$[\text{CH}_3\text{O}_2] = j_{(\text{CH}_3\text{I})} \cdot t_{\text{res}} \cdot [\text{CH}_3\text{I}] \quad (2.20)$$

where  $j(\text{CH}_3\text{I})$  is the photolysis rate of  $\text{CH}_3\text{I}$  (see Section 2.5.2.3) and  $t_{\text{res}}$  is the residence time of the  $\text{CH}_3\text{I}$ /air mix in the photolysis flow tube

$$t_{\text{res}} = \frac{\text{volume of flow tube (103 cm}^3\text{)}}{\text{zero air flow (2,2.5,....4.5,5 x (1000/60) cm}^3\text{/sec) x (T/T}_{\text{std}}\text{) x (P/P}_{\text{std}}\text{)}} \quad (2.21)$$

[CH<sub>3</sub>I] is calculated in ppbv from the flow rate through the permeation tube:

$$[\text{CH}_3\text{I}]_{\text{perm tube}} = \frac{\text{permeationrate} \times 10^{-9}}{\text{Mw}_{\text{CH}_3\text{I}} \times (22400/\text{gasflow rate})} \quad (2.22)$$

where the CH<sub>3</sub>I permeation tube permeation rate is 409 ng min<sup>-1</sup>, Mw is the molecular weight of CH<sub>3</sub>I, which is 142 g mol<sup>-1</sup>, 22,400 cm<sup>3</sup> is the volume occupied by 1 mole of gas at STP. The concentration of CH<sub>3</sub>I in the photolysis cell is calculated from the known dilution of the CH<sub>3</sub>I permeation tube concentration where the flow rate of the N<sub>2</sub> running through the CH<sub>3</sub>I permeation tube is 50 sccm and the zero air diluted flow varies between 2000 and 5000 sccm.

$$[\text{CH}_3\text{I}]_{\text{photolysis cell}} = \frac{[\text{CH}_3\text{I}]_{\text{perm tube}} \times 50}{(\text{zero - air flow (2000 - 5000sccm)} + 50)} \quad (2.23)$$

The chain length is obtained by subtracting the NO<sub>2</sub> created from zero air with added CH<sub>3</sub>I, the change in NO<sub>2</sub> that was produced from zero air alone and then measured by the detector at each flow rate, and then dividing the ΔNO<sub>2</sub> obtained by the known concentration of CH<sub>3</sub>O<sub>2</sub>.

$$\text{CL} = \frac{\Delta[\text{NO}_2]_{\text{CH}_3\text{I} + \text{artefact}} - \Delta[\text{NO}_2]_{\text{artefact}}}{\text{CH}_3\text{O}_2} \quad (2.24)$$

The entire process of calibration takes about 2-2.5 hours for each inlet. Approximately five to nine signal modulations are needed at each zero air flow during the typical chain length calibrations with and without of the CH<sub>3</sub>I flow as shown in Figure 2.10

Figures 2.10 and 2.11 show examples of raw signal during a  $\text{CH}_3\text{O}_2$  chain length calibration whilst on field work in the tropical rainforest in Borneo for inlet 2 (see Section 2.5.2.1) and in the marine boundary layer at Cape Verde for inlet 1 and inlet 2.

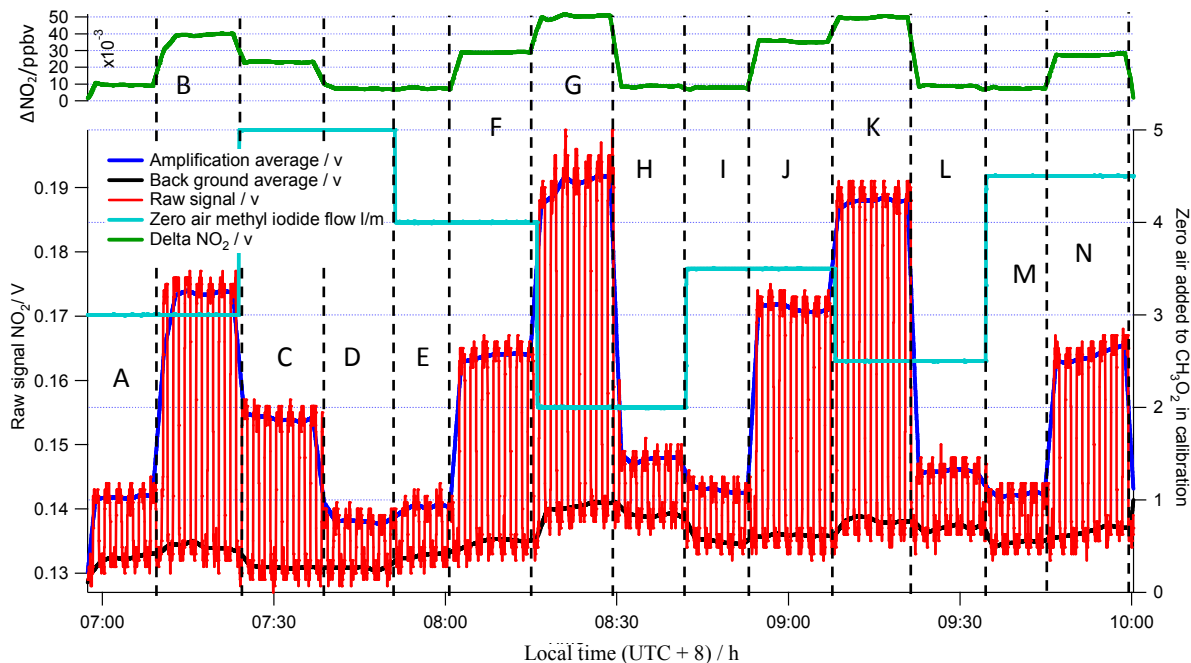


Figure 2.10 - Example of the raw signal during a  $\text{CH}_3\text{O}_2$  chain length calibration in tropical rainforest in Borneo on 4<sup>th</sup> of May 2008 for single inlet.

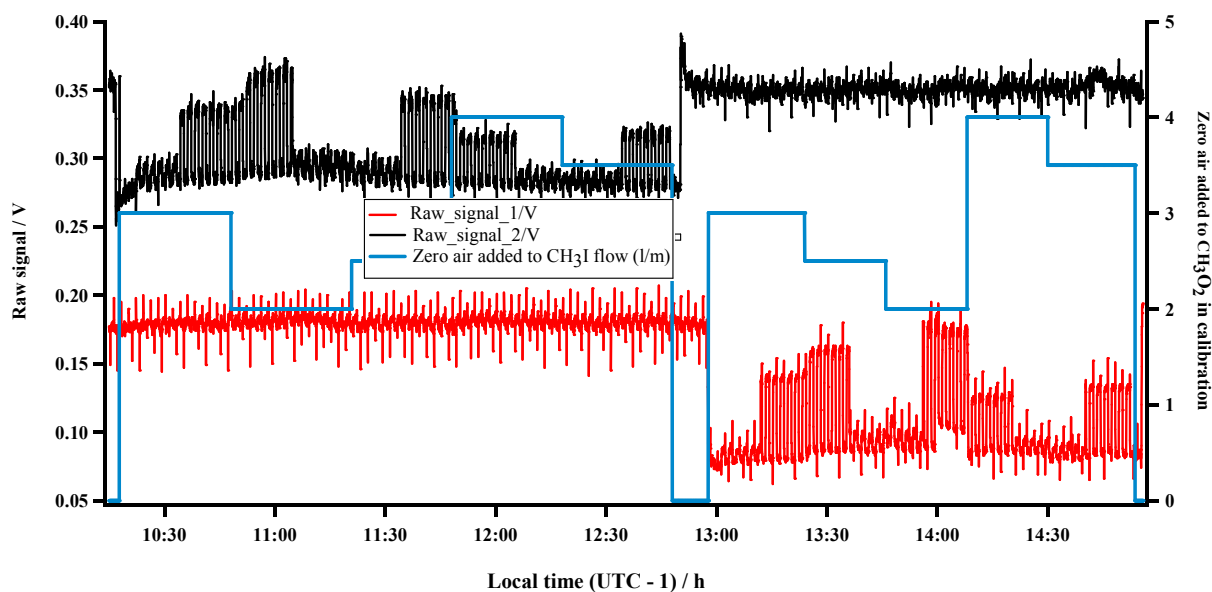


Figure 2.11 - Example of the raw signal during a  $\text{CH}_3\text{O}_2$  chain length calibration in the tropical marine boundary layer at Cape Verde on 15<sup>th</sup> of March 2009 for inlet 1 and inlet 2.

Table 2.3 explains the different modes in Figure 2.10 that is the insertion of various zero air flows to the CH<sub>3</sub>O<sub>2</sub> brings about several changes during the chain length calibration. The different dilution flow mixed with CH<sub>3</sub>O<sub>2</sub> and there are different depth of modulation occurred with CH<sub>3</sub>I present (Artefact + CH<sub>3</sub>O<sub>2</sub>) and ambient CH<sub>3</sub>I (Artefact). The upper plot in the Figure 2.10 shows the artefact and (Artefact + CH<sub>3</sub>O<sub>2</sub>) signal zones represented by the lower and the upper green line, respectively.

Raw signal zone	Zero air flow rate / SLPM	Modulation	CH <sub>3</sub> I switch
A	3	Artefact	CH <sub>3</sub> I off
B	3	Artefact + CH <sub>3</sub> O <sub>2</sub>	CH <sub>3</sub> I on
C	5	Artefact + CH <sub>3</sub> O <sub>2</sub>	CH <sub>3</sub> I on
D	5	Artefact	CH <sub>3</sub> I off
E	4	Artefact	CH <sub>3</sub> I off
F	4	Artefact + CH <sub>3</sub> O <sub>2</sub>	CH <sub>3</sub> I on
G	2	Artefact + CH <sub>3</sub> O <sub>2</sub>	CH <sub>3</sub> I on
H	2	Artefact	CH <sub>3</sub> I off
I	3.5	Artefact	CH <sub>3</sub> I off
J	3.5	Artefact + CH <sub>3</sub> O <sub>2</sub>	CH <sub>3</sub> I on
K	2.5	Artefact + CH <sub>3</sub> O <sub>2</sub>	CH <sub>3</sub> I on
L	2.5	Artefact	CH <sub>3</sub> I off
M	4.5	Artefact	CH <sub>3</sub> I off
N	4.5	Artefact + CH <sub>3</sub> O <sub>2</sub>	CH <sub>3</sub> I on

Table 2.3 - Characteristics of a chain length calibration

Figure 2.10 shows the following features: At each [CH<sub>3</sub>O<sub>2</sub>] (set according to amount of zero air mixed with CH<sub>3</sub>O<sub>2</sub> produced by the CH<sub>3</sub> I photolysis source, shown as 3, 5, 4,

2, 3.5, 2.5 and 4.5  $\text{lmin}^{-1}$  by light blue colour on right-hand axis), an  $\text{NO}_2$  signal (by red line) with  $[\text{CH}_3\text{O}_2]$  signal was measured, as well as an artefact signal by passing the same amount of zero air through the photolysis source that had previously passed through the  $\text{CH}_3\text{I}$  source. Black and dark blue lines are obtained from calculating a running average of background and amplification mode at each dilution flow.  $\Delta [\text{NO}_2]$  is stepped up and down by varying the dilution air as indicated by the green line trace in the upper plot of the Figure 2.10.  $\Delta [\text{NO}_2]$  is determined from the difference between the running average of dark blue line (amplification mode) and black line (background mode).  $\text{CH}_3\text{O}_2$  concentration is obtained by taking away from the average of a period  $\text{CH}_3\text{O}_2$  measurement, the average of a period of artefact measurement at the same flow. A gradient for graph of  $\Delta [\text{NO}_2]$  vs. calculated  $\text{CH}_3\text{O}_2$  gives the chain length.

Figure 2.12 (top panel) shows the chain length calibration with calibration unit in the tropical rainforest in Borneo. Furthermore, Figure 2.12 (bottom panel) shows a different viewpoint from the normal operation of the inlet box as shown in Figure 2.2 and explained in Section 2.5.1.

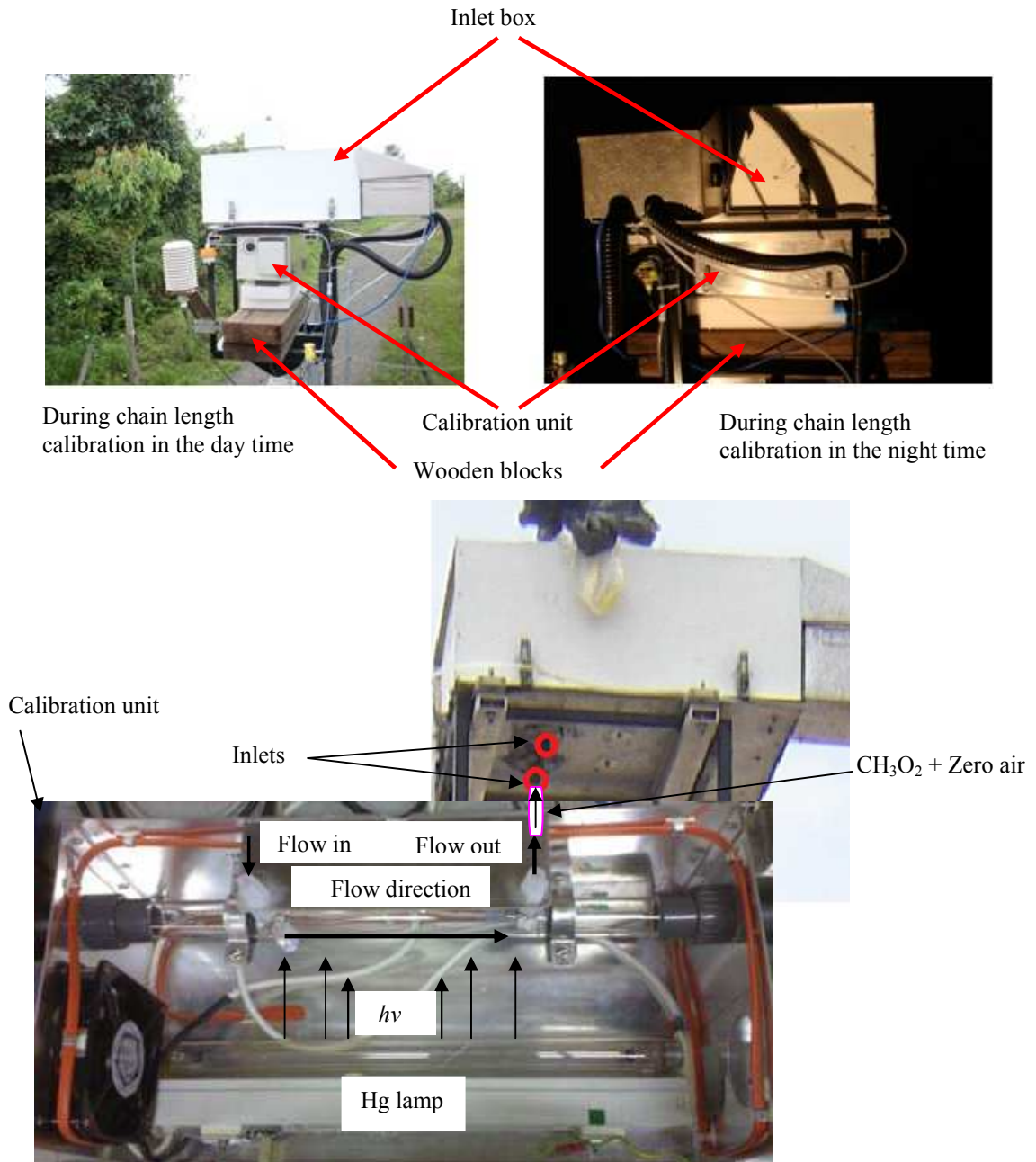


Figure 2.12 - Chain length calibration with calibration unit in tropical rainforest in Borneo. Bottom panel shows the arrangement of the calibration unit and delivery of the calibration flow to inlet during the calibration process.

During the OP3 (1) campaign, two chain length calibrations were carried out in the late afternoon of the 29<sup>th</sup> April 2008 and in the morning of 4<sup>th</sup> May 2008, while the chain lengths that were obtained for these calibrations were 61 and 60, as shown in Figures 2.13 and 2.14. Along the entire the OP3 (1) campaign, average the two of chain lengths together was 60 and has been used for the all data processing calculations.

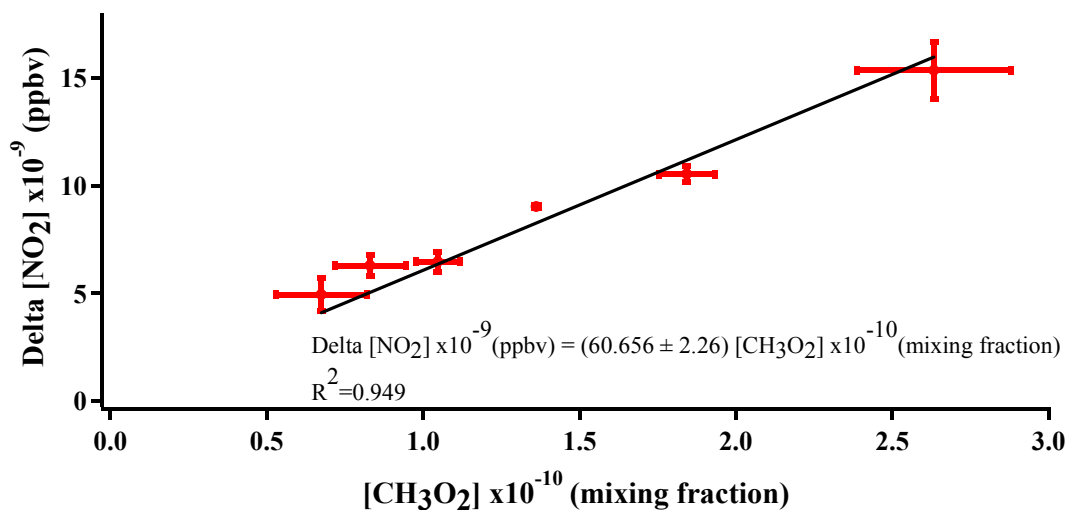


Figure 2.13 - OP3 (1) chain length calibration graph for 29<sup>th</sup> April 2008 in tropical rain forest in Borneo. Error bars represent 1 $\sigma$ .

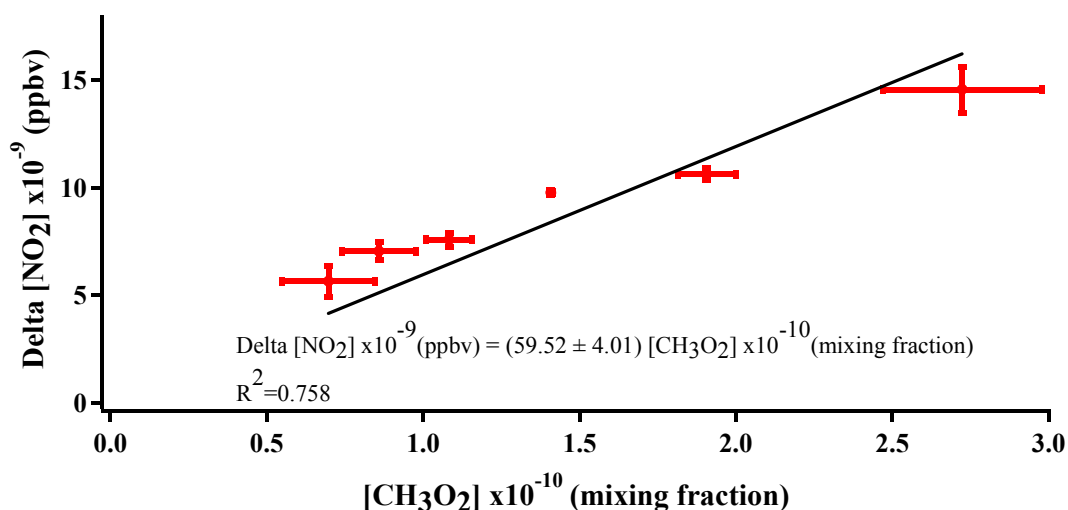


Figure 2.14 - OP3 (1) chain length calibration graph for 4<sup>th</sup> May 2008 in tropical rain forest in Borneo. Error bars represent 1 $\sigma$ .

For the chain length calibrations during the OP3 (1) campaign, six different concentrations of CH<sub>3</sub>O<sub>2</sub> have been obtained by using six different corresponding

quantities of zero air in order to alter the constant flow of permeated  $\text{CH}_3\text{I}$ , which has been previously photolysed and oxidised into  $\text{CH}_3\text{O}_2$ .

Figures 2.13 and 2.14 correspond to the calibration graphs for the chain length derivations in the case of inlet number 2 (single channel PERCA (V3.5) deployed in the tropical rainforest in Borneo as explained in Section 2.5.2.1), in which case, the linear fit between the six varying  $\text{CH}_3\text{O}_2$  calibrant concentrations appears to be satisfactory. In the case of inlet number 2, the variation of the coefficient  $R^2$  for the linear correlation is between 0.949 as showed in Figure 2.13 and 0.758 as showed in Figure 2.14.

During the OP3 (3) campaign, more precisely on the morning of 4<sup>th</sup> of July and in the late afternoon of 12<sup>th</sup> of July, two calibrations have been carried out. As shown in Figures 2.15 and 2.16, five and six CH<sub>3</sub>O<sub>2</sub> concentrations have been obtained through the use of five and six different corresponding quantities of zero air in order to alter the constant flow of permeated CH<sub>3</sub>I, respectively, which has been previously photolysed and oxidised to CH<sub>3</sub>O<sub>2</sub>.

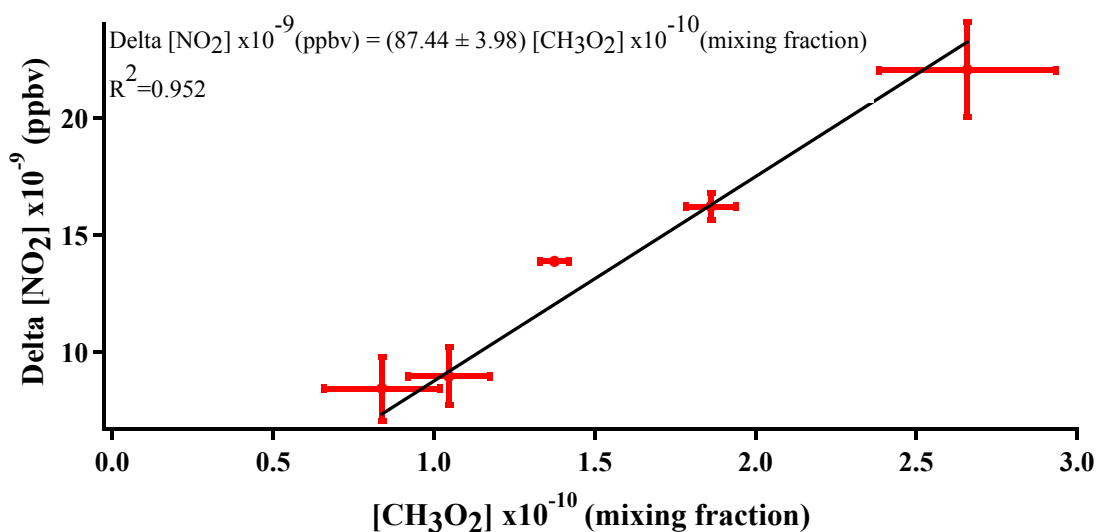


Figure 2.15 - OP3 (3) chain length calibration graph for 4<sup>th</sup> July 2008 in tropical rain forest in Borneo. Error bars represent 1 $\sigma$ .

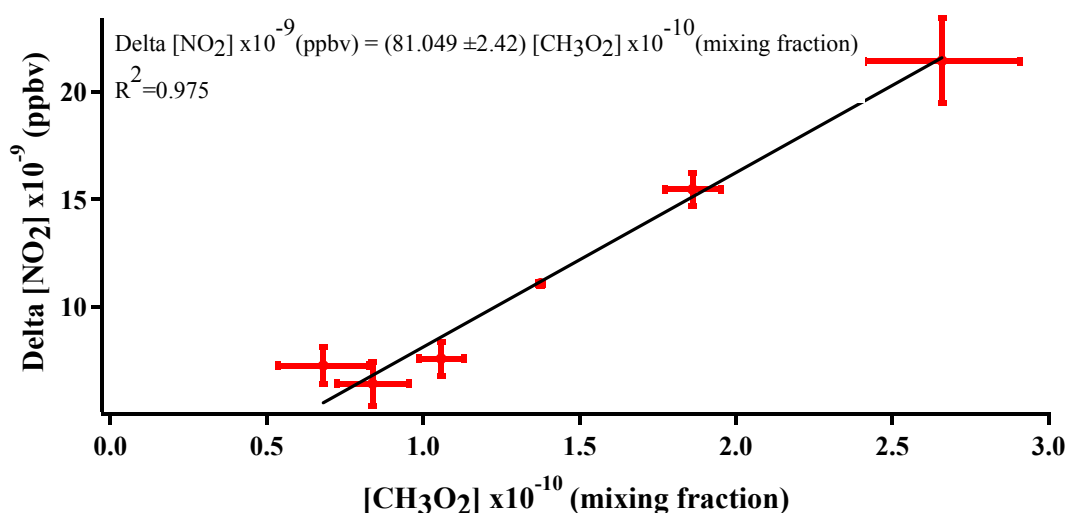


Figure 2.16 - OP3 (3) chain length calibration graph for 12<sup>th</sup> July 2008 in tropical rain forest in Borneo. Error bars represent 1 $\sigma$ .

Figures 2.15 and 2.16 correspond to the calibration graphs that have been employed for all the chain lengths calibrations for inlet number 2. Inlet 2 showed a better linear fit in Figure 2.15 for 5 different  $[\text{CH}_3\text{O}_2]$ , in Figure 2.16 for 6 different  $[\text{CH}_3\text{O}_2]$ , respectively. In the case of inlet 2, there is variation of the linear correlation coefficient  $R^2$  between 0.952, as shown in Figure 2.15 and 0.975, as shown in Figure 2.16. The chain lengths for these calibrations have been obtained at 87 and 81 for inlet 2. In OP3 (3) campaign, average the two of chain lengths together was  $84 (\pm 3)$  and has been used for the all data processing calculations. The uncertainty for these two various chain lengths are obtained and listed in the Table 2.6. LMA-3 Detector 1 had a technical problems in OP3 (1) and OP3 (3) campaigns, therefore no chain length calibration performed for inlet 1 and not listed in the Table 2.4 (see Section 2.5.2.1). Table 2.4 shows the list of PERCA (V3.5) chain lengths for the two rainforest and three marine campaigns.

Campaign	Julian day	Chain length	
		Inlet 1	Inlet 2
OP3 (1)	J119	N/A	$60.7 \pm 2.3$
OP3 (1)	J124	N/A	$59.5 \pm 4.0$
OP3 (3)	J185	N/A	$87.4 \pm 4.0$
OP3 (3)	J193	N/A	$81.0 \pm 2.4$
SOS (1)	J74	$88.1 \pm 3.5$	$92.0 \pm 3.0$
SOS (2)	J144	$70.3 \pm 1.3$	$58.1 \pm 4.3$
SOS (3)	J258	$58.0 \pm 5.3$	$55.3 \pm 6.1$

Table 2.4 - PERCA (V3.5) chain lengths for the OP3 campaigns in the tropical rainforest in Borneo and the SOS campaigns in the tropical marine boundary layer at Cape Verde.

Owing to the fact that the inlet conditions during the two OP3 campaigns vary, then the wall loss rate is therefore different as well during the campaigns. There is a 40 day gap between these two campaigns, while the inlet box has been left on the roof of the Leicester sea container, being covered with polythene (as shown in Figure 2.4); on the other hand, during the first campaign, the inlet box had been secured inside the container during the shipping. Therefore the inlet conditions between these two campaigns are different.

On the other hand, during the three of SOS campaigns, the inlet box has been stored back in the container after finishing each campaign, but there is still a change in the inlet wall conditions during the measuring time due to the influence of the sea salt which covers the box and inlets inhaling air permanently for day and night, as well as due to the contact of the box with the sea air caused by the wind direction (see Section 4.3.1, Chapter 4). It is worth noting that the chain length values were decreased during the SOS campaigns, but chain length values were improved during OP3 (1) and OP3 (3) campaigns (see Table 2.4).

The way that the chain length varies has been observed in past field campaigns, e.g. NAMBLEX (see Section 1.5.4.3 in Chapter 1) as reported by Fleming, (2006) and TexAQS (see Section 1.5.4.4 in Chapter 1) as reported by Sommariva *et al.*, (2011). PERCA V (4) and PERCA V (3.5) were deployed during NAMBLEX and TexAQS measurement campaigns, respectively. It is worth comparing the PERCA 3.5 chain length values from the OP3 and SOS campaigns with the TeXAQS campaign.

Chain length values are listed in Table 2.5 for the NAMBLEX and TeXAQS campaigns.

Campaign	Julian day	Chain length	
		Inlet 1	Inlet 2
NAMBLEX	J217	129	110
NAMBLEX	J223	150	133
NAMBLEX	J231	155	175
NAMBLEX	J238	174	116
NAMBLEX	J245	267	184
TeXAQS	J209	87	40
TeXAQS	J214	110	18
TeXAQS	J218	235	44
TeXAQS	J220	104	41
TeXAQS	J224	72	40
TeXAQS	J229	244	40
TeXAQS	J235	157	38
TeXAQS	J238	160	34
TeXAQS	J242	142	40
TeXAQS	J246	131	35
TeXAQS	J251	127	45
TeXAQS	J253	137	40

Table 2.5- Chain length for the NABLEX campaign in the in North Atlantic Marine Boundary Layer air, at Mace Head in Ireland, (Fleming, personal communication, (2012)) and TeXAQS campaign at the Gulf of Mexico, (Sommariva, personal communication, (2012)).

Chain lengths were more variable in the inlet 1 than the inlet 2 during the TeXAQS campaign as shown in Table 2.5. Throughout the TeXAQS, no real trend of chain lengths was observed for inlet 1 (see Table 2.5). It could be conclude that less variability of chain length values obtained for inlet 2 throughout the TeXAQS campaign (see Table 2.5), similar to that observed during the OP3 (1) and OP3 (3) campaigns for this work (see Table 2.4). The values of chain length obtained for inlet 1 were higher in TeXAQS compared to the OP3 and SOS campaigns (see Table 2.4 and 2.5). On the other hand, the chain length values of inlet 2 were lower in TeXAQS than in the OP3 and SOS campaigns as listed in Table 2.4 and 2.5. Inlet 1 in TeXAQS campaign presents a higher variability between chain lengths calibrations than in OP3 and SOS campaigns. In contrast, for inlet 2 the variability was lower between chain length calibrations in TeXAQS campaign than in the OP3 and SOS campaigns (see Table 2.4 and 2.5).

NAMBLEX, presents higher values of chain length and its variability between calibrations for inlet 1 and inlet 2 compared to the OP3 and SOS campaigns as listed in Table 2.4 and 2.5. In Table 2.5, no trend of chain lengths was observed for inlet 2 along the NAMBLEX campaign. For inlet 1, there appears to be an overall increase in chain length throughout the NAMBLEX campaign (see Table 2.5). This increase is the opposite of what Salisbury (2001) found in the EASE 97 and SOAPEX 2 campaigns and also decreases in chain length observed for the SOS (1), SOS (2) and SOS (3) campaigns (see Table 2.4).

### 2.5.2.3. Measurement of $j_{\text{CH}_3\text{I}}$

A measurement of  $j_{\text{CH}_3\text{I}}$  for the specific conditions employed in the calibration source was an essential factor for calculating the concentrations of methyl peroxy radicals generated by the calibration unit (see Section 2.5.2.2). As shown in Figure 2.17, the apparatus was assembled using the method described by Carpenter (1996). In order to produce varying  $\text{CH}_3\text{I}$  vapour pressures in the cell during each experiment, it is essential to use a diffusion tube diluted in zero air to provide  $\text{CH}_3\text{I}$  vapour. As it is shown in Figure 2.17 the resultant mixture is introduced through the two Teflon taps ( $\otimes$ ), which are used to seal the photolysis cell, while the two lamps are switched on: first the reference lamp (Model L2196 deuterium lamp, Hamamatsu Photonics K.K.) and then, the photolysis lamp.

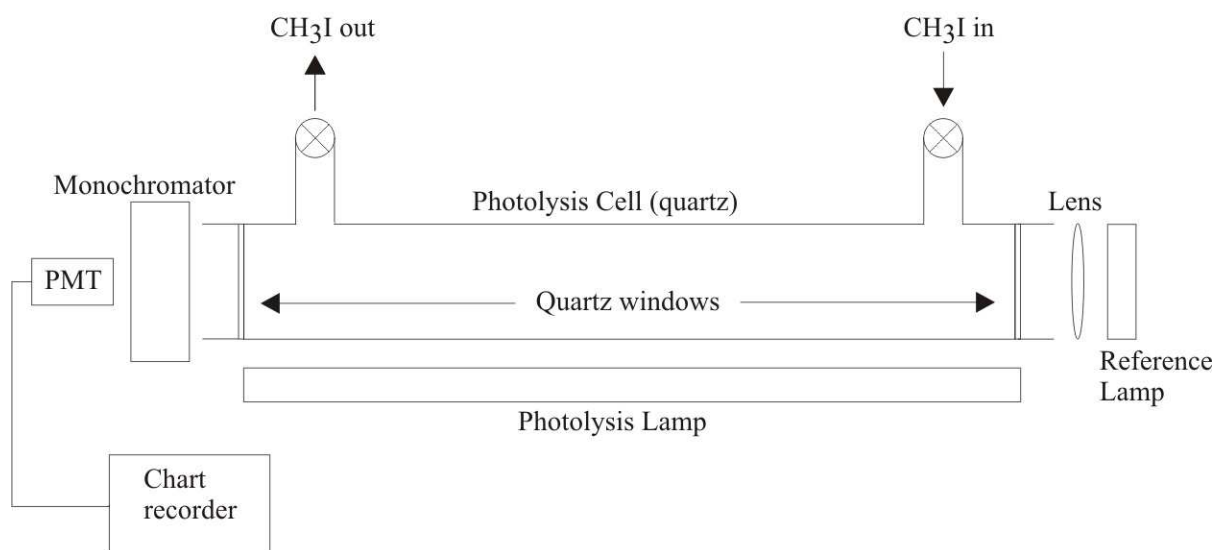


Figure 2.17 - Apparatus for measuring the photolysis of  $\text{CH}_3\text{I}$ ,  $j_{\text{CH}_3\text{I}}$  diagram from Parker, 2009).

Owing to the importance of focusing the light coming from the reference lamp through the cell, the apparatus contains a lens of focal length 60 cm (PLCX-25.4-257.5-UV,

Elliot Scientific) positioned between the reference lamp and the photolysis cell. CH<sub>3</sub>I vapour absorbs at  $\lambda = 265$  nm, measured with a Cornerstone ¼-m path-length monochromator (Oriel Instruments Ltd.) connected to a photomultiplier tube (PMT) (Model R4315, Hamamatsu Photonics K.K.), which is, in turn, linked to a chart recorder. The reference lamp is not able to photolyse the CH<sub>3</sub>I.

In order to calculate the initial concentration of CH<sub>3</sub>I that is first present in the cell, the Beer-Lambert law (equation (2.25)) can be employed and thus,  $I_0$  stands for the incident intensity of the reference lamp in the absence of CH<sub>3</sub>I present,  $I$  represents the intensity of the reference lamp in the presence of CH<sub>3</sub>I in the cell,  $c$  symbolizes the concentration of CH<sub>3</sub>I,  $l$  is the path length of the reference lamp light through the photolysis cell, while  $\sigma$  is the absorption cross section for CH<sub>3</sub>I at 265 nm.

$$I = I_0 \exp(-\sigma[c]l) \quad (2.25)$$

Hence the concentration of the absorber is given by:

$$[C] = \frac{1}{l\sigma} \ln\left(\frac{I_0}{I}\right) \quad (2.26)$$

The photolysis of methyl iodide can be represented as a first order process hence:

$$\frac{d[C]}{dt} = -j_{CH_3I}[C] \quad (2.27)$$

Rearranging and integrating both side

$$\int_{[C]_0}^{[C]_t} \frac{d[C]}{[C]} = -j_{CH_3I} \int_0^t dt \quad (2.28)$$

$$\ln[C]_t - \ln[C]_0 = -j_{CH_3I}(t - 0) \quad (2.29)$$

Taking the natural logarithm of both sides of the equation (2.26) gives,

$$\ln [C] = \ln \left\{ \frac{1}{l\sigma} \ln \left[ \frac{I_0}{I} \right] \right\} \quad (2.30)$$

Substitution of  $\ln[c]$  from equation 2.29, and since the initial condition state that  $[c] \rightarrow [c]_0$  at  $t=0$ , and also  $\text{CH}_3\text{I}$  is being photolysed over the time,  $t$  while  $[c] \rightarrow [c]_t$ ,

Equation (2.29) becomes,

$$\ln \left\{ \frac{1}{l\sigma} \ln \left[ \frac{I_0}{I_{[C] \rightarrow [C]_t}} \right] \right\} = -j_{\text{CH}_3\text{I}}t + \ln \left\{ \frac{1}{l\sigma} \ln \left[ \frac{I_0}{I_{[C] \rightarrow [C]_0}} \right] \right\} \quad (2.31)$$

$$\ln \left\{ \ln \left[ \frac{I_0}{I_{[C] \rightarrow [C]_t}} \right] \right\} = -j_{\text{CH}_3\text{I}}t + \ln \left\{ \ln \left[ \frac{I_0}{I_{[C] \rightarrow [C]_0}} \right] \right\} \quad (2.32)$$

The photolysis rate can be determined by monitoring the throughput intensity,  $I$ , as a function of time during photolysis (and therefore concentration) and by measurement of the intensity without the absorber present,  $I_0$ . A subsequent gradient of  $-j_{\text{CH}_3\text{I}}$  can be obtained through a plot of the natural log of the natural log of the ratio of the light intensity without methyl iodide present ( $I_0$ ) to when it is being photolysed  $I_{[C] \rightarrow [C]_t}$  against time.

Figure 2.18 illustrates such a plot.

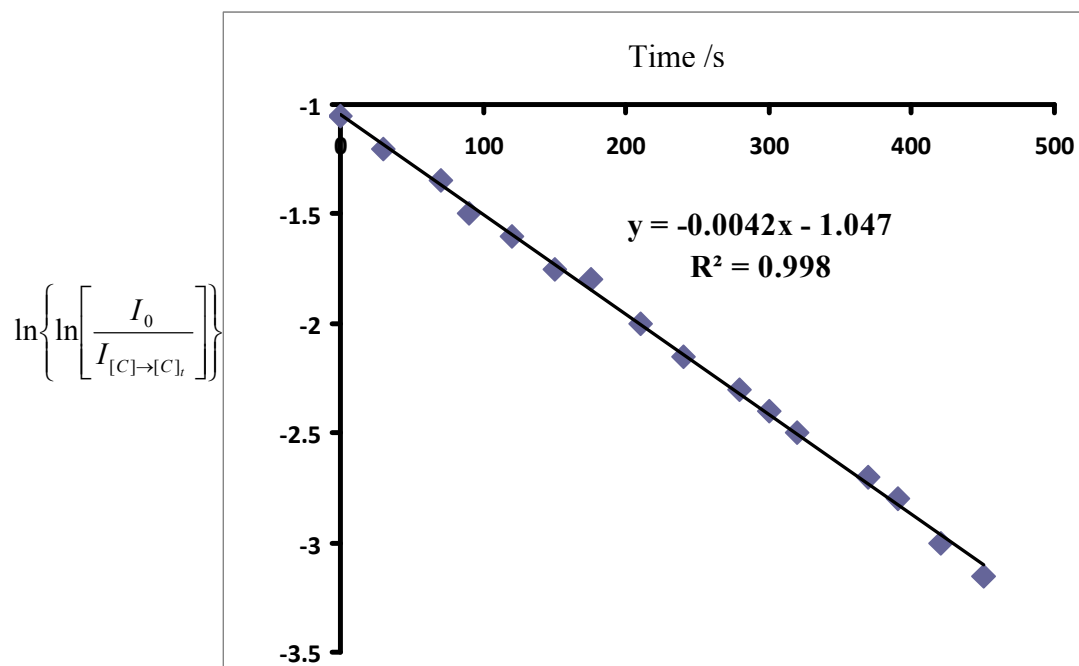


Figure 2.18 - Example of a  $j_{\text{CH}_3\text{I}}$  measurement obtained whilst during lab work in the first year of PhD.

This experiment was performed several times in the lab to get the average of  $j_{\text{CH}_3\text{I}}$ , results summarised in Table 2.6. All the data in the campaigns in this thesis have been obtained by applying the same  $j_{\text{CH}_3\text{I}}$  ( $5.5 \times 10^{-3} \text{s}^{-1}$ ) for using the particular cell.

$j(\text{CH}_3\text{I})$ measurements/ $\times 10^{-3} \text{s}^{-1}$	Mean(standard deviation)
6 5.8 5.3 4.7 4.5 5.7 4.3 5.5 6.3 6.4 6.4	5.5 (0.76)

Table 2.6 - Results of  $j_{\text{CH}_3\text{I}}$  measurements obtained whilst on lab work during first year of PhD.

#### 2.5.2.4. Water vapour interference correction

PERCA (V3.5) chain lengths were calibrated twice per OP3 and once per SOS campaign. The chain length is the sum of OH/HO<sub>2</sub> inter-conversion cycles occurring for each peroxy radical before the radical chain is terminated by reactions (2.1), (2.2) or (2.3).

It has been previously noted that chain length calibrations are conducted in dry air, and not the humid conditions of measurement (Mihele and Hastie (1998), Mihele *et al.*, (1999)). Previous work has shown the PERCA (V4) chain length depend on both ambient humidity and temperature (Salisbury *et al.*, 2002; Reichert *et al.*, 2003). Therefore, the chain length is usually determined in dry air and then corrected using a correction factor. Taking this correction into account for chain length calibrations, the Leicester PERCA (V3.5) employs dry gas for the process of calibration, while compressed gas is drawn into the inlets from cylinders. The inlet is kept at a constant temperature of 30 °C (at Cape Verde field campaign external heaters have been employed in order to keep this temperature, it was controlled by inlet's thermocouple in the rainforest); not only does this constant temperature seem to show a decrease in the wall-loss reactions, but it also stabilises the chain length during field conditions.

Brookes, (2010) derived a functional form of the humidity correction to be

$$CF_{CL} = \exp\left(\frac{RH}{\tau_{cl}}\right) \quad (2.33)$$

$$\tau_{CL} = 48.92 \pm 0.96 (1\sigma) \quad (2.34)$$

where  $\tau_{CL}$  is the decay constant and RH is relative humidity. This equation is generally suitable for both the aircraft and ground inlets.

The correction for the humidity brings a change in the  $[\text{HO}_2+\text{RO}_2]$ . Thus, the humidity correction once employed for the peroxy radical data set for the tropical rainforest in Borneo, as well as for the tropical marine boundary layer at Cape Verde campaign, makes the hourly average peroxy radical concentration 3.5 to 6.2 and from 4.3 to 6.4 times bigger when compared to the uncorrected versions respectively. Application of the analysis would lead to unrealistically high concentration of peroxy radicals (~ few hundreds of pptv). Therefore the peroxy radical data set from both the rainforest and the marine campaigns in this thesis were not corrected for relative humidity. The basis for this is discussed below.

Pugh *et al.*, (2010) reported that CiTTyCAT atmospheric chemistry model had better fits with the uncorrected PERCA (V3.5) data. The model was driven with auxiliary measurements to get accurate representatives of the chemical species in terms of physical processes over the tropical rainforest in Borneo (see Sections 3.4 and 3.4.1, Chapter 3 for further explanation). It was not suitable to use the humidity correction for the PERCA data set and therefore uncorrected data was used to draw the comparison.

Brooks (2010) observed that when the PERCA (V4) was deployed for aircraft measurements, applying the correction for humidity produced a factor of 4.4 increase in  $[\text{HO}_2+\text{RO}_2]$ , on average, producing several hundreds of pptv of peroxy radicals during the AMMA campaign (African Monsoon Multidisciplinary Analysis campaign in summer 2006, see Section 1.5.3, Chapter 1). The AMMA campaign has conditions similar to the tropical rainforest in Borneo, i.e. active biogenic species and the fast photochemical processing during the West African Monsoon (WAM) period. Owing to the fact that concentrations of peroxy radicals this high have not been reported in the

tropical atmosphere, this increase in the concentration produced by applying the humidity correction is again regarded as unrealistic. Brookes, (2010) showed that the uncorrected data was evaluated for any systematic bias with humidity by drawing a comparison between the uncorrected PERCA (V4) data to and the data obtained through the DSMACC (Dynamically Simple Model of Atmospheric Chemical Complexity) (Emmerson and Evans *et al.*, 2009; Stone *et al.*, 2010). Andres-Hernandez *et al.*, (2010) explored that peroxy radicals measured by the DUALER (DUAL channel airborne peroxy radical chemical amplifier) and PERCA V (4) at the two pressure levels during the AMMA campaign. Inter comparison of the DUALER and PERCA (V4) peroxy radical measurements are in good agreement within the instrumental errors, provided that relative humidity correction was not applied to the PERCA V (4) measurements.

This also occurred in the case of the PERCA (V3.5) instrument during the TexAQS 2006 campaign which has conditions similar to the tropical marine boundary layer at Cape Verde marine boundary layer, i.e. clean conditions of the air masses brought from the Gulf of Mexico and the Atlantic Ocean (discussed in Section 1.5.3, Chapter 1), while Sommariva *et al.*, (2011) reported that the relative humidity of the raw data has not been corrected. Sommariva *et al.*, (2011) agreed that there was a good agreement between the uncorrected HO<sub>2</sub> + sum of RO<sub>2</sub> data under the overall accuracy of the PERCA measurements and the results produced by the box – model.

So PERCA (V3.5) data recorded during each field campaign reported in this thesis have been corrected using one or more chain length calibration performed *in situ*, rather than using typical chain length values determined in the laboratory or on

previous field sites under potentially different conditions. Hence, no water correction has been carried out in the case of all peroxy radical data that has been reported within this thesis.

## 2.6 Error analysis

The factors that influence the calculation of the chain length are the following: the measurement of  $j(\text{CH}_3\text{I})$  for the calibration source, the precision of mass flow controller (MFCs), calculating the volume of the photolysis cell, and the permeation ratio of the  $\text{CH}_3\text{I}$  and miscellaneous errors (different chain length, e.g. OP3 (3) campaign). Moreover, having luminol stability from a thermal viewpoint ensures reproductively of  $\text{NO}_2$  detection. Overall error  $\sigma$  has been calculated from:

$$\sigma = \sqrt{(\sigma_{\text{MFC}})^2 + (\sigma_{\text{cell volume}})^2 + (\sigma_{\text{permeation rate}})^2 + (\sigma_{\text{humidity}})^2 + (\sigma_{\text{different CL}})^2 + (\sigma_{\text{NO}_2 \text{ detection}})^2 + (\sigma_{j(\text{CH}_3\text{I})})^2} \quad (2.35)$$

Table 2.7 present an overview of the sum of elements, which have been individually analyzed, for uncertainty.

Affected component	Source	Estimated uncertainty /%
Chain length	$j(\text{CH}_3\text{I})$ measurement	14
	MFC accuracy ( $\text{CH}_3\text{I}$ and zero air)	5
	Photolysis cell volume	5
	$\text{CH}_3\text{I}$ permeation rate	7
	miscellaneous	4
$\text{NO}_2$ detection	Background variability	31
	+	
	luminol thermal stability	
Humidity		unknown
Overall		36%

Table 2.7 - Contributions to PERCA (V3.5) measurement error

The calculation above leads to the conclusion that for a single-channel PERCA (V3.5), the overall uncertainty is 36% and this value ignores any uncertainty contribution from humidity effects on chain length. The standard errors in the  $j(\text{CH}_3\text{I})$  values in Table 2.6 are the basis for the calculations of the errors appearing in the measurement of  $j(\text{CH}_3\text{I})$ . Some distortions of the error might have been included in Table 2.7 owing to the instrument used for calibrations of MFC flow ratios, which is a primary flow calibrator (Gillian Gilibrator 2, Sensidyne Inc.) which can determine the flow ratios to be highly reproducible. More difficult to estimate  $\text{NO}_2$  detection error, Carpenter's, (1996) approximation of this uncertainty is considered for this work. The calculated uncertainty in the estimation of  $\text{NO}_2$  detection is 31% from the  $\text{NO}_2$  calibration in

Section 2.5.2.1 and is included in Table 2.7. This value is derived by adding the NO<sub>2</sub> sensitivity (dV/dNO<sub>2</sub>) of 1% (gradients' uncertainty in Figure 2.9 (top)) and calculated uncertainty of 30 % from the error bars of calculated [NO<sub>2</sub>] and detected PMT signal together.

Reducing the errors of the calculation of the permeation rate can be accomplished through the process of weighing the permeation tubes, a procedure imposed by the mass loss of the permeation tubes at a rate of about 409 ng min<sup>-1</sup> and carried out by using a high precision balance. PERCA (V3.5) was deployed at several different locations in 2008 and in 2009 and there was not the chance to provide a constant N<sub>2</sub> flow through the permeation tubes. Measured and nominal permeation rates of calibration permeation tubes for PERCA (V3.5) are represented in Table 2.2. Highest error calculated for the CH<sub>3</sub>I permeation rate are listed in the Table 2.7.

The typical standard deviation of CH<sub>3</sub>I calibrations represents the basis for calculating the accuracy of PERCA (V3.5); thus, during a calibration, the calculation of the signal deviation is connected with the CH<sub>3</sub>O<sub>2</sub> quantity added to the inlet. An accuracy of about 5% is usually provided by a standard calibration. Green *et al.*, (2006) reported that the determined accuracy provided by PERCA (V4) is 25% and its precision is 1 pptv (on a minute-averaged timescale). This accuracy percentage has increased to 35% for a non-humidity corrected single channel measurement, according to the error calculations performed by Salisbury (2001), while Clemitshaw *et al.*, (1997) reported an accuracy of 30% of the PERCA (V1) for the originally quoted non-humidity corrected single-channel instrument.

## 2.6.1 Dual-channel PERCA instrument

A measurement of the background and of the ambient signal should be performed at the same time (Cantrell *et al.*, (1996b)). The difference between the single-channel and the dual-channel instruments is enhanced by the possibility of measuring the background signal and the amplified signal at the same time through the dual-channel instrument owing to the presence of two inlet and detection systems that are run out in anti-phase, while the inlet in the single-channel the measurement of the background and the ambient signal cannot be performed at the same time. The improvements brought by the dual-channel instrument through the simultaneous measurement of the background and ambient signal, mainly consist a decrease in the noise from the atmospheric instability, as well as of the inaccuracies that might appear with measurements due to the unstable NO<sub>2</sub> concentrations as well as unstable background ozone. Moreover, another advantage of the dual-channel is the possibility of a quicker response, compared to the single-channel. The measurements through a dual-channel set-up can be performed in as little as one second. There is, still, one disadvantage of the dual-channel instrument, i.e. the fact that there is an increase in the error percentage from NO<sub>2</sub> detection, of up to 47%, to obtain the signal from the difference of two measurements each subject to a 31 % error, see Section 2.6 and Table 2.7. Some errors, such as luminol stability apply equally to both of the channels and do not have to be included twice, but the fact that they can be added can bring an overestimation to the NO<sub>2</sub> detection errors. The maximum NO<sub>2</sub> detection error limit can reach 47% because of the complicated process of separating the factors that should or should not be included when an estimation of the NO<sub>2</sub> detection errors is performed. Thus, there is an increase in the error level through the dual-channel instrument owing to the fact that both channels bring their own errors into the total calculation. On the other hand, the

advantage of the dual-channel is the capacity of performing measurements under instable background conditions and it also presents a decrease in the uncertainty for NO<sub>2</sub> background instability.

Figure 2.19 represents a comparison between the dual and the single channel and it can be noticed that many noise spikes have been removed, while there is also decrease in the overall instability.

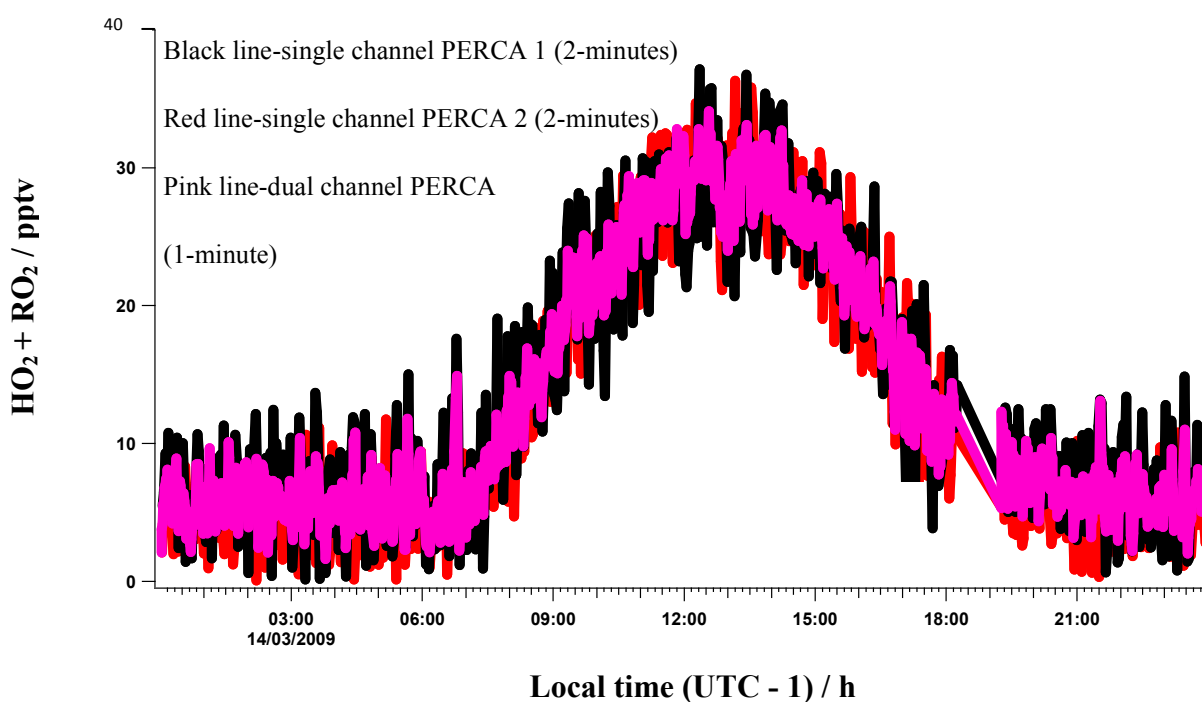


Figure 2.19 - A typical dual-channel peroxy radicals compared to single-channel measurement and plot obtained whilst on field work in the marine boundary layer at Cape Verde on 14<sup>th</sup> of March 2009 during the SOS (1) campaign.

## 2.7 Data work-up

The peroxy radical concentrations from PERCA (V3.5) are obtained through the measurements of  $\Delta\text{NO}_2$ . The process of getting radical concentration in the case of the single-channel instrument is quite simple. In a single-channel instrument, the inlet is switch between amplification and background mode every 30 seconds. It is necessary to calculate an average of the amplification phase, as well as of the two background phases surrounding it and subtract the average of the background phases from the amplification period.

On the other hand, the process for the dual-channel becomes more complex: in the conditions of the inlets being run out of phase and having regular measurements performed for both the amplified and the background signal, the peroxy radical concentration is therefore obtained by taking away the background channel from the amplification channel.

The one second-averaged  $\text{NO}_2$  signals for each detector are registered in volts, but the PERCA (V3.5) also has the ability of registering a signal for the phase of the instrument, this signal being a ‘modmode’. Thus, the instrument can show when the inlets are in amplification mode or background mode. When the ‘modmode’ is showing 1, inlet 1 is in amplification phase and inlet 2 is in background phase, while when ‘modmode’ is pointing to 0, there is a switch of phase for the inlets, background for inlet 1 and amplification for inlet 2, respectively. A change in the inlet gas flows so they can switch from amplification to background phase have a six second waiting period for the flows to become steady again. This six second’s waiting time recorded after the swap in the ‘modmode’ is excluded from data workup.

Figure 2.20 shows the midpoint between the amplification and the background mode, which is obtained for each channel by interpolating between one minute-averaged amplification and background phases.

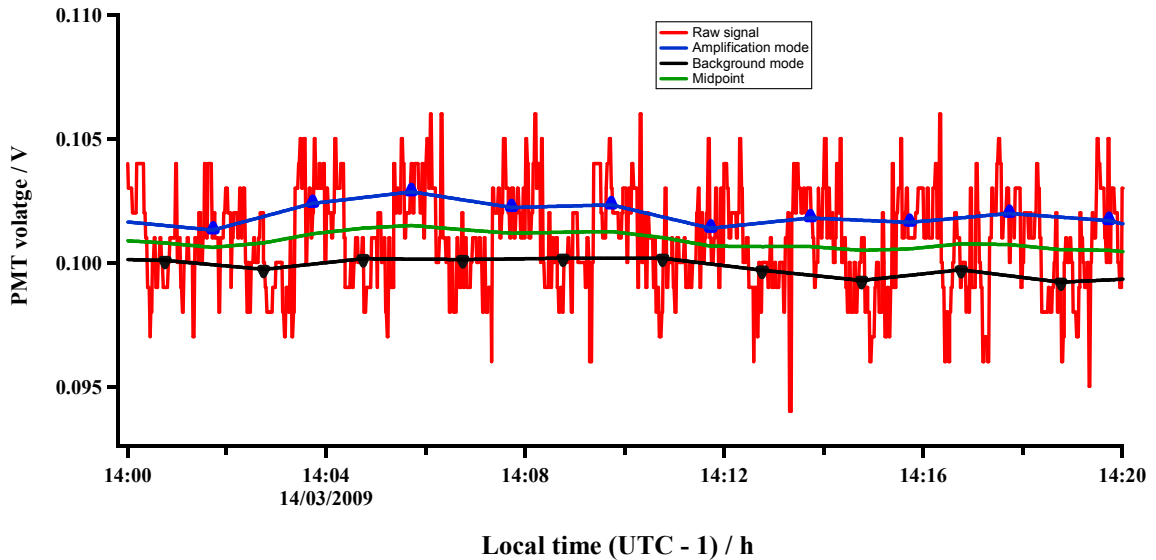


Figure 2.20 - Interpolated one minute averages for background and amplification phases and obtained midpoint for an inlet and the midpoint between the amplification and background lines is then obtained (green) and plot. Obtained whilst on field work in the marine boundary layer at Cape Verde on 14<sup>th</sup> of March 2009 during the SOS (1) campaign.

By taking away the interpolated midpoint from the raw signal results gives a positive signal in amplification phase and a negative one in background phase is observed. In the background phase there is an inversion of the negative value to positive data happening before the next procedure, i.e. calculation of NO<sub>2</sub> mixing ratio in ppbv (see Figure (2.22)). Both channels are involved in calculating the background and the amplification signals at all times. The result of this subtraction is the positive signal in volts which is then turned into a NO<sub>2</sub> mixing ratio in ppbv. It is also necessary to obtain one minute positive average figures for both of the modes, amplification and background modes. A  $\Delta\text{NO}_2$  from peroxy radical amplification is then obtained by taking away the background minute average from one channel from the amplification minute average for the corresponding time for the other channel. The  $\Delta\text{NO}_2$  divided by

the chain length of the inlet, which was in amplification when the  $\Delta\text{NO}_2$  was measured, results in a peroxy radical mixing ratio.

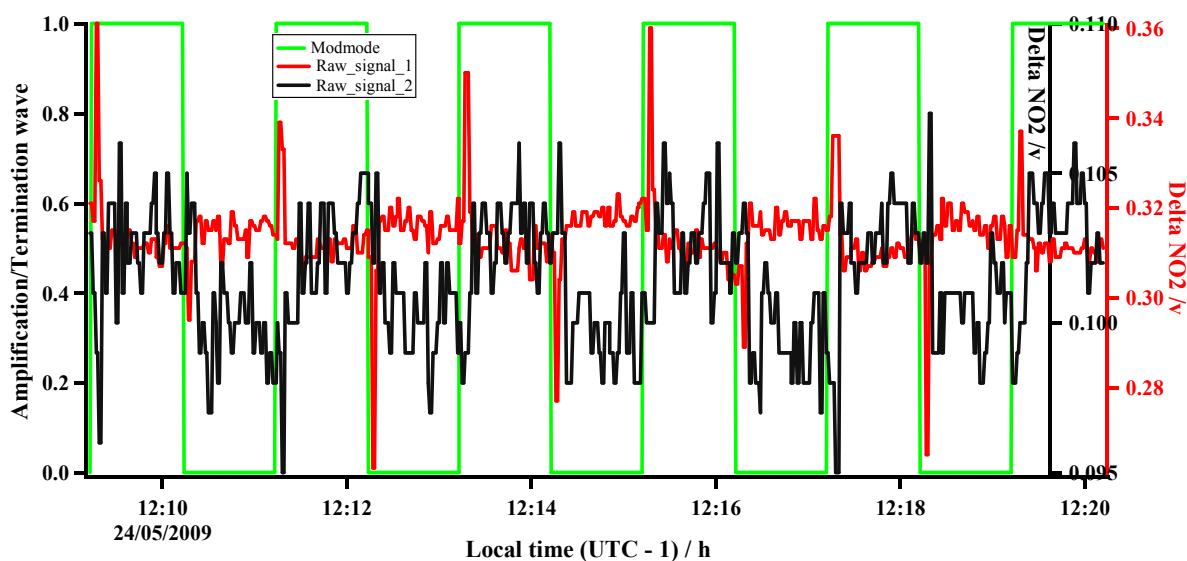


Figure 2.21 -  $\text{NO}_2$  signal from amplification chemistry alone for both channels and plot obtained whilst on field work in the marine boundary layer at Cape Verde on 24<sup>th</sup> of May 2009 during the SOS (2) campaign. The green line represents the amplification phase as 1 and the background phase as zero for the 1 minute switching.

The  $\text{NO}_2$  produced from peroxy radical amplification is the result of the subtraction performed at the level of the two channels: the subtraction of the background minute averages performed for one channel from the corresponding amplification minutes performed for the other channel.

Figure 2.22 represents through a diagram the steps that are performed in the data work-up

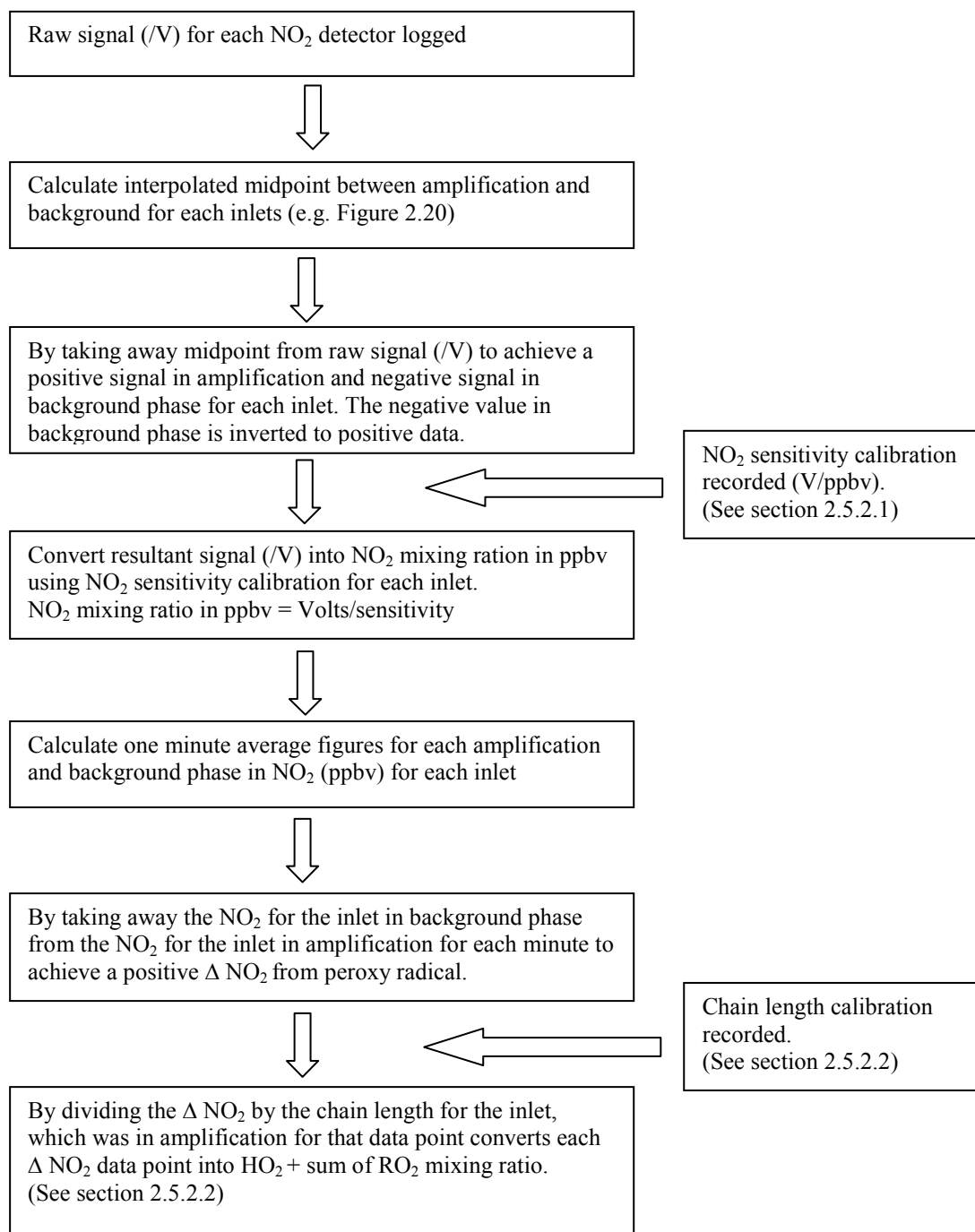


Figure 2.22 - Flow diagram showing main data work-up steps for converting raw signals in volts into HO<sub>2</sub> + sum of RO<sub>2</sub> in pptv

## 2.8 Summary

This chapter provides a detailed description of techniques for measuring peroxy radicals, special attention being dedicated to the instrument employed for peroxy radical measurements that are discussed in this thesis; this instrument being PERCA (V3.5). Apart from a description of the instrument that has been used for the measurements, the chapter also includes a presentation of the experiments that have been carried out for an optimization of the instrument performance, as well as a presentation of the calibration method. The chapter also comprises of a discussion regarding the advantages of the dual-channel PERCA (V3.5) as compared to the single-channel PERCA (V3.5) instrument. The chapter includes an explanation of the technique used for data work-up from the raw signals into peroxy radical concentrations, as well as the error analysis which has been carried out.

# Chapter 3

## Peroxy radical measurements in South East Asian Tropical rainforest boundary layer

### (OP3)

#### 3.1 Introduction to the Malaysian rainforest campaigns

This chapter aims to develop a more detailed analysis of the two ground level peroxy radical measurement campaigns. There were 3 phases for the OP3 (“Oxidant and particle photochemical processes above a south-east Asian tropical rain forest”) Danum 08 field campaign: (i) OP3 (1) was carried out during April-May 2008 with ground based measurements only, (ii) in OP3 (2) flux measurement were conducted in a oil palm estate during May-June 2008, and (iii) OP3 (3) was carried out during June-July 2008 comprised of both ground and aircraft measurements (Hewitt *et al.*, (2010)).

Bukit Atur Global Atmospheric Watch station (4° 58' 59" N, 117° 50' 39" E) was the main location for the ground based measurements of atmospheric composition. Hewitt *et al.*, (2010) has given a detailed description of the site and measurements. The reference height for most of the measurements was ~5 m above the surface, but this goes up to 30 m for PAN measurements and up to 75 m for VOCs, which were also measured at 5 m above the ground. The Bukit Atur GAW station has regular measurements for CO<sub>2</sub> and O<sub>3</sub>, and a range of aerosol parameters. The station is located

in a forest and above a hill and comprises of four air-conditioned laboratories within a main building placed at the base of a tower of 100 m height, the whole surface of the station being of  $\sim 150 \times 50$  m. Compared to the 100 m height of the tower, the forest surrounding the tower only reaches a height of  $\sim 10$  m above the base of the tower. In order to accommodate extra instruments, it was necessary to have extra lab space, i.e. four mobile sea-container laboratories. At a 2 km distance east of the station, there were generators which provided the electrical power. In the process of data analysis, pollution phenomena are removed by identifying of high concentrations of oxides of nitrogen, as well as wind direction analysis.

Table 3.1 presents a summary of the measurements made at Bukit Atur and the critical measurements covered the following aspects:

- Eddy covariance and gradient flux measurements of trace gases and particles
- Speciated concentration measurements of the trace gases and particles
- Measurements of the aerosol size-dependent hygroscopicity and critical supersaturations for cloud growth
- Concentration measurements of OH, HO<sub>2</sub>, as well as the sum of hydroperoxy and organic peroxy radicals
- OH reactivity measurements (the rate at which OH is removed from the atmosphere)
- Characteristics of boundary layer turbulence and mixing

The Natural Environment Research Council/UK Meteorological Office's BAe 146-301 Facility for Airborne Atmospheric Measurements (FAAM) aircraft was used for airborne measurements (Lewis *et al.*, (2007)). Kota Kinabalu airport was used as a base

location less than 30 min flight from Bukit Atur. A repeatable flight plan was deployed for each flight, with one profile up and one down, and it is characterized by straight and level runs at altitudes of 100-250, 1500, 3000 and 6000 m above the rain forest (centred on Bukit Atur). Other flights were made above an extensive and homogeneous agro-industrial oil palm landscape, which comprises of the Sabahmas oil palm plantation estate. Two flights were undertaken over the ocean up-and down-wind of Sabah during morning and during afternoon in order to obtaining an overview of the concentrations of trace gases and particles during day time.

By undertaking flights right above the Bukit Atur station more than ten times, at the same height as the base of GAW tower and then at an altitude of 750 m above sea-level, it was possible to connect the ground-based and airborne measurements.

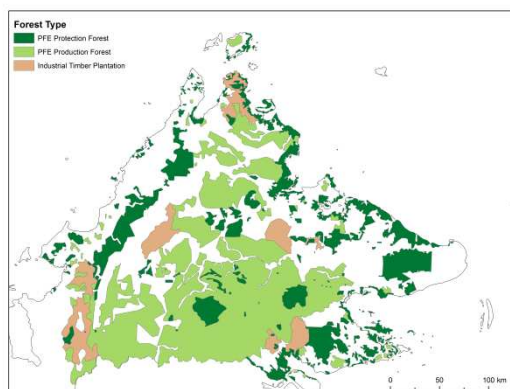


Figure 3.1 - Land-cover map of Sabah from Hewitt *et al.*, (2010).

The targets of the OP3 project included (a) understanding how emissions of reactive trace gases from a tropical rainforest mediate the regional scale production and processing of oxidants and particles, and (b) better understanding the impacts of these processes on local, regional and global scale atmospheric composition, chemistry and climate. By connecting the ground-based and airborne measurements of surface fluxes

and atmospheric composition of reactive trace gases and particles, the chemical processes can be studied in models.

The project tackled the following questions as taken directly from Hewitt *et al.*, (2010):

- a. What are the rates of transfer of organic compounds emitted from the tropical forest?
- b. How are these organic compounds chemically processed immediately after release?
- c. To what extent do the regional organic emissions contribute to the atmospheric aerosol in the region, and what are the effects of the aerosol? What is the composition of the organic fraction of the aerosol?
- d. What are the effects of these biogenic emissions on global chemistry and climate?

### 3.1.1 Campaign meteorology

The period during which the OP3 measurements were carried out, between April to July 2008, was characterized by plenty of rainfall, approximately 1045 mm. On a long-term basis, the month of April was established to be the driest. The mean temperature is being 27.1°C during the April–July 2008. The influence of convective events on rainfall occurrence also brings about a localisation of the rainfall area and it has been proved by Bidin and Chappel (2003) that within the 5 km<sup>2</sup> area comprising the summit of Bukit Atur, the inter-gauge correlation in yearly rainfall total amounts decreased to 0.90 over distances of just 1.1 km, which is a short scale even for a convective weather system.

The rainfalls seem to follow a distinctive pattern during day time, even in the limits of the records established within the short OP3 campaign period of April-July (Figure 3.2).

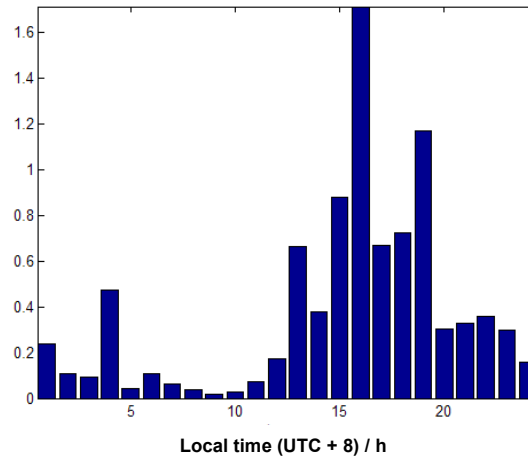


Figure 3.2 - Observations of the mean rainfall from Hewitt *et al.*, (2010) for both of OP3 (1) and OP3 (3) campaigns at Bukit Atur in the tropical rainforest in Borneo during April-July 2008.

By using aspirated thermocouples, it was possible to measure the temperatures at different heights at Bukit Atur during both the OP3 (1) and OP3 (3) campaigns, and these median temperatures and presented in Figure 3.3.

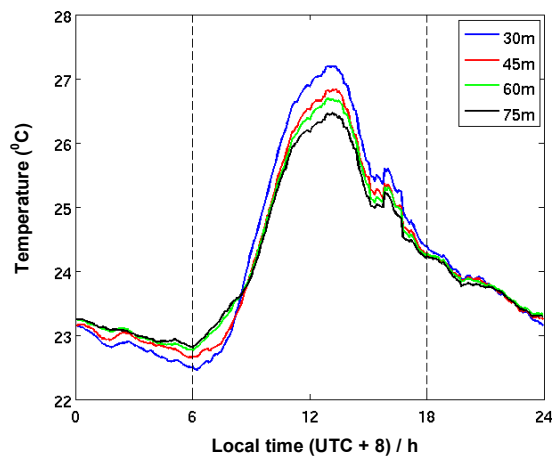


Figure 3.3 - Median temperature from Hewitt *et al.*, (2010) for both of OP3 (1) and OP3 (3) campaigns at different heights the Bukit Atur GAW tower in the tropical rainforest in Borneo during April-July 2008.

At a 30 m altitude the median registered temperature was  $25.1 \pm 1.6$  °C. This measured temperature coincides with the surface temperature from long-term measurements at the site. An analysis of the atmospheric stability during night time determines a stable aspect, while there is a characteristic instability during the middle of the day, which is typical for a convective area with low wind speeds.

Figure 3.4 presents the diurnal cycle in photosynthetically active radiation (PAR) (is the amount of light available for photosynthesis, which is light in the 400 to 700 nm wavelength range), measured at canopy-top height. Overall, the campaign period was bright, characterized by a median close to the climatologically 95<sup>th</sup> percentile.

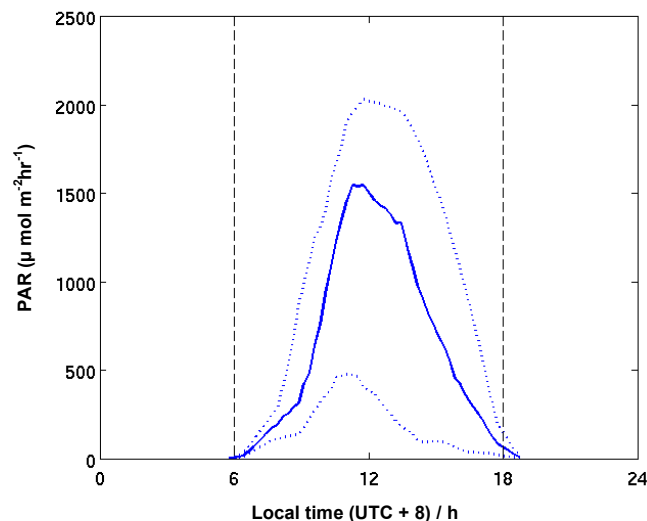


Figure 3.4 - Observation of the median canopy-top Photosynthetically Active Radiation (PAR), from Hewitt *et al.*, (2010) for both of OP3 (1) and OP3 (3) campaigns at Bukit Atur in the tropical rainforest in Borneo during April-July 2008.

The sunrise and sunset are represented by dashed lines within the temperature and PAR graphs, while the 5<sup>th</sup>, respectively the 95<sup>th</sup> percentiles are illustrated through dotted lines (See Figure 3.4).

During the measurement campaigns at Bukit Atur, backwards air mass trajectories were analysed in order to characterise the origins of measured longer lived chemical species. By employing the European Centre for Medium-Range Weather Forecasts (ECMWF) wind fields, it was possible for the British Atmospheric Data Centre (BADC) Web Trajectory Service to calculate the trajectory along which the air parcel is thought to have travelled. During OP3 (1) and OP3 (3) campaigns the trajectories were obtained every hour. It is necessary to calculate the back trajectories 24 hours before the arrival at the station with a 30-minute time resolution, as well as a pressure altitude of 950 hPa, while back trajectories touching the ground were removed. Figure 3.5 illustrates the air mass residency time on a  $0.1^\circ \times 0.1^\circ$  grid for all back trajectories, starting from the first OP3 (1) campaign on the left and second campaign OP3 (3), on the right side.

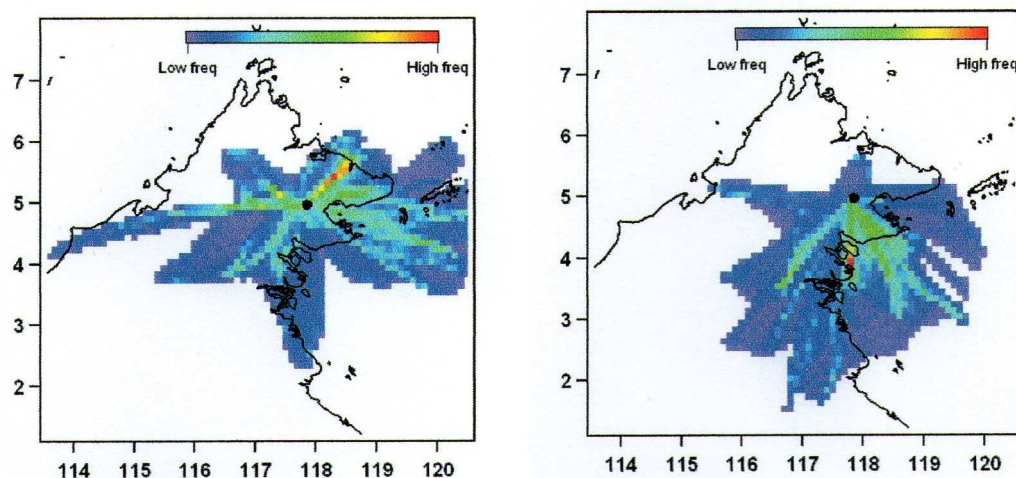


Figure 3.5 - Shows the air mass residency times reaching Bukit Atur (black circle) from Hewitt *et al.*, (2010) for campaigns OP3 (1) (left graph) and OP3 (3) (right graph) at Bukit Atur in the tropical rainforest in Borneo during April-May and June-July 2008. No air masses passing over the area in the last 24 hours is represented by non-colour.

Compared to the first campaign period, OP3 (1) where the influence came from air masses from most directions, the influences during OP3 (3) were represented

predominantly by air masses from the south. The air during the OP3 (3) originates from two areas: the SE air coming from the sea and the SW air over land.

### 3.1.2 Overview of the measurements made in OP3.

A selection of ground level measurements used in reaction to HO<sub>2</sub>+RO<sub>2</sub> chemistry are summarised in Table 3.1. The instrument type, detection limit and accuracy are also listed in Table 3.1.

Species	Technique	Sampling period or Frequency	Detection Limit	Measurement Uncertainty	Reference
NMHC, including isoprene and oxygenates	Disjunct eddy covariance flux measurement with continuous flow and analysis by PTR-MS	Fluxes: 30 min Mixing ratios: ~ 7s	Fluxes: < 0.05 mg m <sup>-2</sup> h <sup>-1</sup> Mixing ratios: 10 – 100 pptv	Fluxes: Precision = ~ ±30% Mixing ratios ~ ± 10%	(Langford <i>et al.</i> , 2009)
NMHC, including isoprene, monoterpenes and oxygenates	Dual Channel Gas Chromatograph with Flame ionisation detectors (DC-GC-FID)	1 hour ground variable air	1 pptv	variable, typically around 10 %	(Lewis <i>et al.</i> , 2007; Lewis <i>et al.</i> , 2005)
Terpenoids, alcohols, aldehydes	GC-PID, portable mass spectrometer				
CO <sub>2</sub> /H <sub>2</sub> O flux	Eddy-covariance flux using infrared gas analyser Li-Cor 7000/7500	30 min fluxes			(Aubinet <i>et al.</i> , 2000)
NO <sub>2</sub> flux	Eddy covariance using laser induced fluorescence	30 min fluxes			(Farmer <i>et al.</i> , 2006)

OH, HO <sub>2</sub>	FAGE (Fluorescence Assay by Gas Expansion) laser-induced fluorescence	10 s	(OH) 2.4 x 10 <sup>5</sup> molecule cm <sup>-3</sup> (3 min av.)  (HO <sub>2</sub> ) 3.8 x 10 <sup>6</sup> molecule cm <sup>-3</sup> (3 min av.)	44 % (OH) 50 % (HO <sub>2</sub> ) (2 σ)	(Whalley <i>et al.</i> , 2010)
OH Reactivity	FAGE	1 min		22 % (2 σ)	(Ingham <i>et al.</i> , 2009)
Sum of RO <sub>2</sub> + HO <sub>2</sub>	PERCA(V4) (PEroxy Radical Chemical Amplifier), dual inlet	1 min	0.4 pptv (10min)	38% (1 σ)	(Fleming <i>et al.</i> , 2006)
NO <sub>3</sub> , CH <sub>2</sub> O, NO <sub>2</sub> , HONO, O <sub>3</sub> , CHOCHO	Differential Optical Absorption Spectroscopy	10min	2 ppt, 480 ppt, 80 ppt, 150 ppt, 4.6 ppb, 150 ppt	1.5 ppt, 500 ppt, 60 ppt, 130 ppt, 4 ppb, 130 ppt	(Plane and Saiz-Lopez, 2006)
Photolysis frequencies (incl. <i>j</i> (O <sup>1</sup> D), <i>j</i> (NO <sub>2</sub> ))	Calibrated filter (2π and 4π sr) radiometers and spectral-radiometer	1 s	n/a	14% and 13% 0- 90° SZA	(Bohn <i>et al.</i> , 2008; Edwards and Monks, 2003; Volz-Thomas, <i>et al.</i> , 1996)
O <sub>3</sub>	UV absorption	1 s	0.6 ppbv	10%±3.4 ppbv (±1σ)	(Heard <i>et al.</i> , 2006)
O <sub>3</sub> flux eddy correlation	Dry chemiluminescence	30 min fluxes from 0.05s	0.1 ppbv		(Gusten <i>et al.</i> , 1990; Gusten and Heinrich, 1996)
O <sub>3</sub> /NO/NO <sub>2</sub> gradient	Chemiluminescence (O <sub>3</sub> ), thermal converter	15 min			
NO NO <sub>2</sub> ΣNO <sub>y</sub> , ΣNO <sub>y</sub> -HNO <sub>3</sub>	NO/O <sub>3</sub> chemiluminescence detectors Photochemical converter + above  Gold tube/CO converter + above Gold tube converter and denuder	10 min	3 pptv for NO,  7 pptv for NO <sub>2</sub>	15% for NO and 20% for NO <sub>2</sub> at 50 pptv	(Pike <i>et al.</i> , 2010)
NO <sub>2</sub>	Laser-induced fluorescence (LIF)	1 Hz	3.6 pptv/60 s	20%	(Dari-Salisburgo <i>et al.</i> , 2009)
H <sub>2</sub> O vapour	Dew point hygrometer				
H <sub>2</sub> O flux	Eddy-covariance using UV Absorption	30 min fluxes 100 Hz		8% (q-dependent)	(Coe <i>et al.</i> , 1995)

CH <sub>2</sub> O	Fluorometric detection (Hantzsh reaction)	1 min	100pptv	17% (2σ)	(Still <i>et al.</i> , 2006)
CO	Chemiluminescence				(Gerbig <i>et al.</i> , 1999)
PAN	GC/ECD (electron capture detection)	10 min	PAN:15pptv, PPAN, MPAN : 25 pptv	20% (2σ)	(Harrison <i>et al.</i> , 2006)
Meteorological parameters (Wind speed & direction, solar radiation, PAR, precipitatin, wetness, pressure, temperature, RH, turbulence, sensible heat flux)	Standard meteorological sensors (aspirated thermocouples, Vaisala WXT)	30 min temperature gradients			
Boundary Layer Height	LIDAR	1 s	20-60 m		(Pearson <i>et al.</i> , 2009)

Table 3.1 - Some of the instruments, their measurement techniques, detection limits and accuracy from Hewitt *et al.*, (2010) for campaigns OP3 (1) and OP3 (3) at Bukit Atur in the tropical rainforest in Borneo during April-May and June-July 2008.

### 3.1.3 Data averaging process for the OP3 (1) and OP3 (3) campaigns

The following measurements were directly used to calculate the hourly average data and hourly average diurnal profile of each species in this work for OP3 (1) and OP3 (3) campaign. The instrument type, institute, time resolution of data and data coverage on BADC are also listed in the Table 3.2.

Species	Instrument (Institute)	Original time resolution of instrument (if known)	Time resolution of data available on BADC	Data coverage on BADC	
				OP3 (1)	OP3 (3)
HO <sub>2</sub> +RO <sub>2</sub>	PERCA University of Leicester	2 min Single channel	10 min	Data starts: 14/04/2008 Data ends: 02/05/2008 Fully missing: 17/04, 18/04. Partly missing: 14/04, 19/04, 23/04, 24/04, 28/04.	Data starts: 23/06/2008 Data ends: 22/07/2008 Fully missing: 03/07. Partly missing: 23/06, 29/06.
NO	NOxy Chemiluminescence University of York	1 min	10 min	Data starts: 14/04/2008 Data ends: 02/05/2008 Fully missing: not fully missing Partly missing: 14/04, 16/04, 18/04, 19/04, 20/04, 25/04, 26/04, 28/04, 30/04, 01/05.	Data starts: 08/07/2008 Data ends: 23/07/2008 Fully missing: not fully missing Partly missing: 10/07, 14/07, 15/07, 19/07, 22/07, 23/07.
NO <sub>2</sub>	Photolysis + chemiluminescence University of York	1min	10 min	Data starts: 14/04/2008 Data ends: 02/05/2008 Fully missing: not fully missing Partly missing: 14/04, 18/04, 19/04, 20/04, 23/04, 25/04, 26/04, 28/04, 30/04, 01/05, 02/05.	Data starts: 08/07/2008 Data ends: 23/07/2008 Fully missing: not fully missing Partly missing: 10/07, 14/07, 15/07, 19/07, 22/07, 23/07.

O <sub>3</sub>	Thermo Electron Instrument (TEI) Model 49i UV Analyser University of York	20sec	1 min	Data starts: 08/04/2008 Data ends: 02/05/2008 Fully missing: not fully missing Partly missing: 08/04, 10/04, 19/04.	Data starts: 08/07/2008 Data ends: 23/07/2008 Fully missing: not fully missing Partly missing: 24/06, 23/07.
isoprene	PTR-MS University of Lancaster	30 min	30 min	Data starts: 20/04/2008 Data ends: 02/05/2008 Fully missing: not fully missing Partly missing: 20/04, 25/04, 26/04, 28/04.	Data starts: 22/06/2008 Data ends: 22/07/2008 Fully missing: not fully missing Partly missing: 22/06, 23/06, 24/06, 25/06, 27/06, 29/06, 01/07, 11/07, 16/07, 17/07, 21/07, 22/07.
<i>j</i> (O <sup>1</sup> D)	Filter radiometer University of Leicester	1 min	1 min	Data starts: 14/04/2008 Data ends: 02/05/2008 Fully missing: not fully missing Partly missing: 15/04, 17/04, 19/04, 20/04, 21/04, 22/04, 24/04, 28/04, 29/04.	Data starts: 23/06/2008 Data ends: 21/07/2008 Fully missing: 05/07. Partly missing: 26/06, 27/06, 28/06, 29/06, 30/06, 01/07, 02/07, 04/07, 06/07, 08/07, 21/07.
<i>j</i> (HONO)	Spec rad University of Leicester	1 min	1 min	Not measured	Data starts: 12/07/2008 Data ends: 24/07/2008 Fully missing: 13/07. Partly missing: 12/07, 24/07.
<i>j</i> (HCHO)	Spec rad University of Leicester	1 min	1 min	Not measured	Data starts: 12/07/2008 Data ends: 24/07/2008 Fully missing: 13/07. Partly missing: 12/07, 24/07.
OH	FAGE University of Leeds	10 sec	3 min, 10 min, 30 min and 1 hour	Data starts: 14/04/2008 Data ends: 02/05/2008 Fully missing: not available Partly missing: 14/04, 15/04, 16/04, 17/04, 19/04, 20/04, 21/04, 22/04, 24/04, 25/04, 28/04, 29/04, 30/04, 02/05.	Data starts: 06/07/2008 Data ends: 22/07/2008 Fully missing: not available Partly missing: 06/07, 07/07, 08/07, 13/07, 17/07, 18/07, 19/07, 20/07, 21/07, 22/07.

HO <sub>2</sub>	FAGE University of Leeds	10 sec	10 min, 30 min, 1 hour	Not measured	Data starts: 06/07/2008 Data ends: 18/07/2008 Fully missing: not available Partly missing: 06/07, 07/07, 08/07, 13/07, 17/07, 18/07.
HCHO	aerolaser Hantzsch fluorescent method University of East Anglia	1 min	1 min	Not measured	Data starts: 10/07/2008 Data ends: 16/07/2008 Fully missing: not available Partly missing: 10/07, 12/07, 16/07.
HONO				Not measured	Not measured
Methacrolein ethane, propane, acetylene, acetaldehyde, acetone, $\gamma$ -terpinene, limonene, camphene	Dual Channel Gas Chromatograph with Flame ionisation detectors (DC- GC-FID) University of York	1 hour	1 hour	Data starts: 08/04/2008 Data ends: 02/05/2008 Fully missing: 11/4, 12/4, 13/4, 14/4. Partly missing: 19/04, 25/04.	Data starts: 25/06/2008 Data ends: 21/07/2008 Fully missing: 27/6, 03/7, 13/7, 19/7. Partly missing: 20/07.
Temperature	Vaisala probe University of Manchester		30 min	Data starts: 14/04/2008 Data ends: 02/05/2008 Fully missing: complete data set Partly missing: not available	Data starts: 22/06/2008 Data ends: 23/07/2008 Fully missing: complete data set Partly missing: not available
Relative Humidity	Vaisala probe University of Manchester		30 min	Data starts: 14/04/2008 Data ends: 02/05/2008 Fully missing: complete data set Partly missing: not available	Data starts: 22/06/2008 Data ends: 23/07/2008 Fully missing: complete data set Partly missing: not available
Photosynthetically Active Radiation (PAR)	Skye Instruments PAR Quantum sensor (model SKP 215)		15 min	Data starts: 14/04/2008 Data ends: 02/05/2008 Fully missing: complete data set Partly missing: not available	Data starts: 22/06/2008 Data ends: 23/07/2008 Fully missing: complete data set Partly missing: not available

Table 3.2 - Some of the instruments, their measurement technique from Hewitt *et al.*, (2010) for campaigns OP3 (1) and OP3 (3) at Bukit Atur in the tropical rainforest in Borneo during April-May and June-July 2008, respectively. The names of the institutes, the time resolution of the data and the data coverage are available on the BADC, while the data has been taken for this work from the OP3 archive on the BADC website.

High time resolution measurements are important owing to the short lifetime of peroxy radical measurements (see Section 1.4 in Chapter 1, e.g. the lifetime of HO<sub>2</sub> approx 60 s). Unfortunately, a high time resolution averaging (i.e. 1 min or 100 s) for the analysis could not be carried out in this work because some of the important measurements data were available in hourly basis in the OP3 data archive at the BADC after removing the reduced-quality data, data from below the detection limit, as well as invalid or missing data, e.g. isoprene, NO<sub>x</sub>, OH and HO<sub>2</sub>. Various analyses of different types of hourly averaged have been performed throughout the thesis and the basis of these analyses is to be discussed below.

Hourly averaged data is generated by the taking data from the OP3 archive at BADC with consecutive 60 minute data, i.e. 00:00-00:59, 01:00-01:59....etc for the listed species in the Table 3.2 for the OP3 (1) and OP3 (3) campaigns. Hourly averaged time series of the listed species generated from the hourly averaged data are generated for the OP3 (1) and OP3 (3) campaigns. Hourly averaged diurnal profiles of the listed species for the whole campaign have been constructed from the averaged time series data or subsets (e.g. day, night) for the corresponding time. Figure 3.6 shows the data averaging steps for the OP3 (1) and OP3 (3) campaigns.

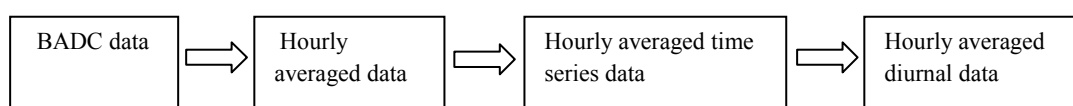


Figure 3.6 – Different type of data averaging method

## 3.2 Results

### 3.2.1 Time series of chemical profile

NO and NO<sub>2</sub> were measured by the University of York NO<sub>x</sub>y, whilst isoprene measured by the University of Lancaster PTRMS. O<sub>3</sub> was measured by the University of York UV absorption detector (Thermo Environmental Instruments, Model 49i) (see Table 3.2). NO, NO<sub>2</sub> and isoprene data taken from the OP3 data archive at BADC and hourly averaged obtained by the author in this work for OP3 (1) and OP3 (3) campaigns (see Section 3.1.3 for data averaging process). Figure 3.7 shows the hourly averaged time series of O<sub>3</sub>, isoprene, NO and NO<sub>2</sub> for OP3 (1) campaign.

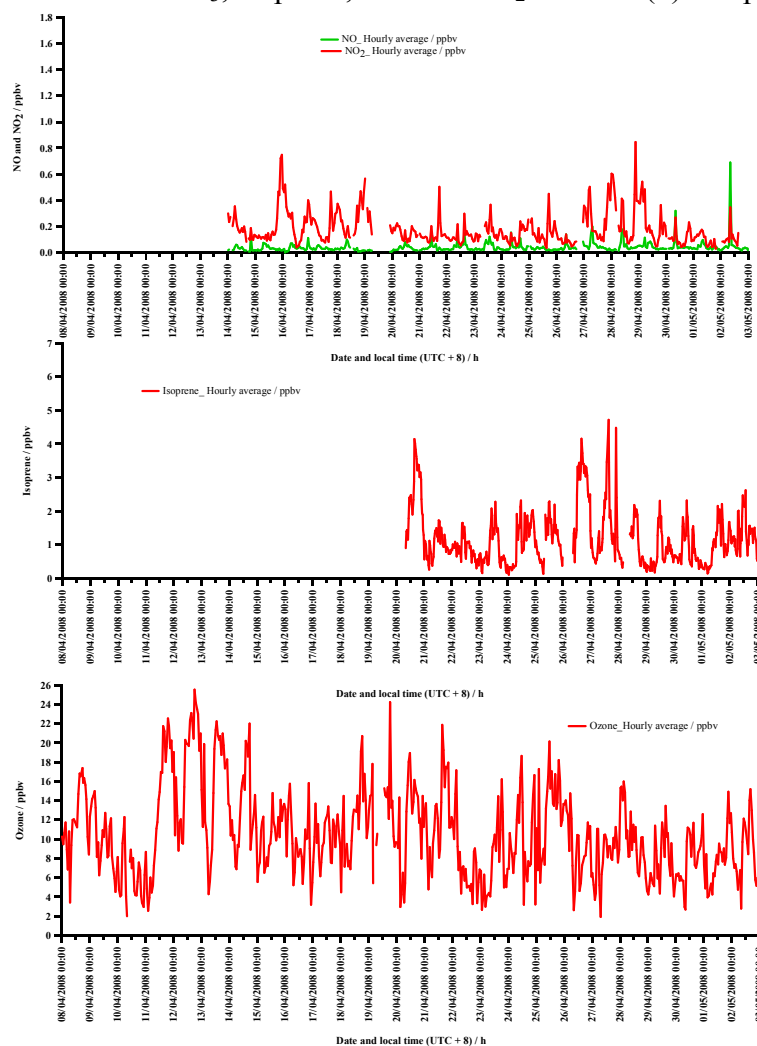


Figure 3.7 - Hourly averaged time series of O<sub>3</sub>, isoprene, NO and NO<sub>2</sub> from OP3 (1) campaign at Bukit Atur in the tropical rainforest in Borneo during April-May 2008.

Figure 3.8 shows hourly averaged time series of O<sub>3</sub>, isoprene, NO and NO<sub>2</sub> from OP3 (3) campaign.

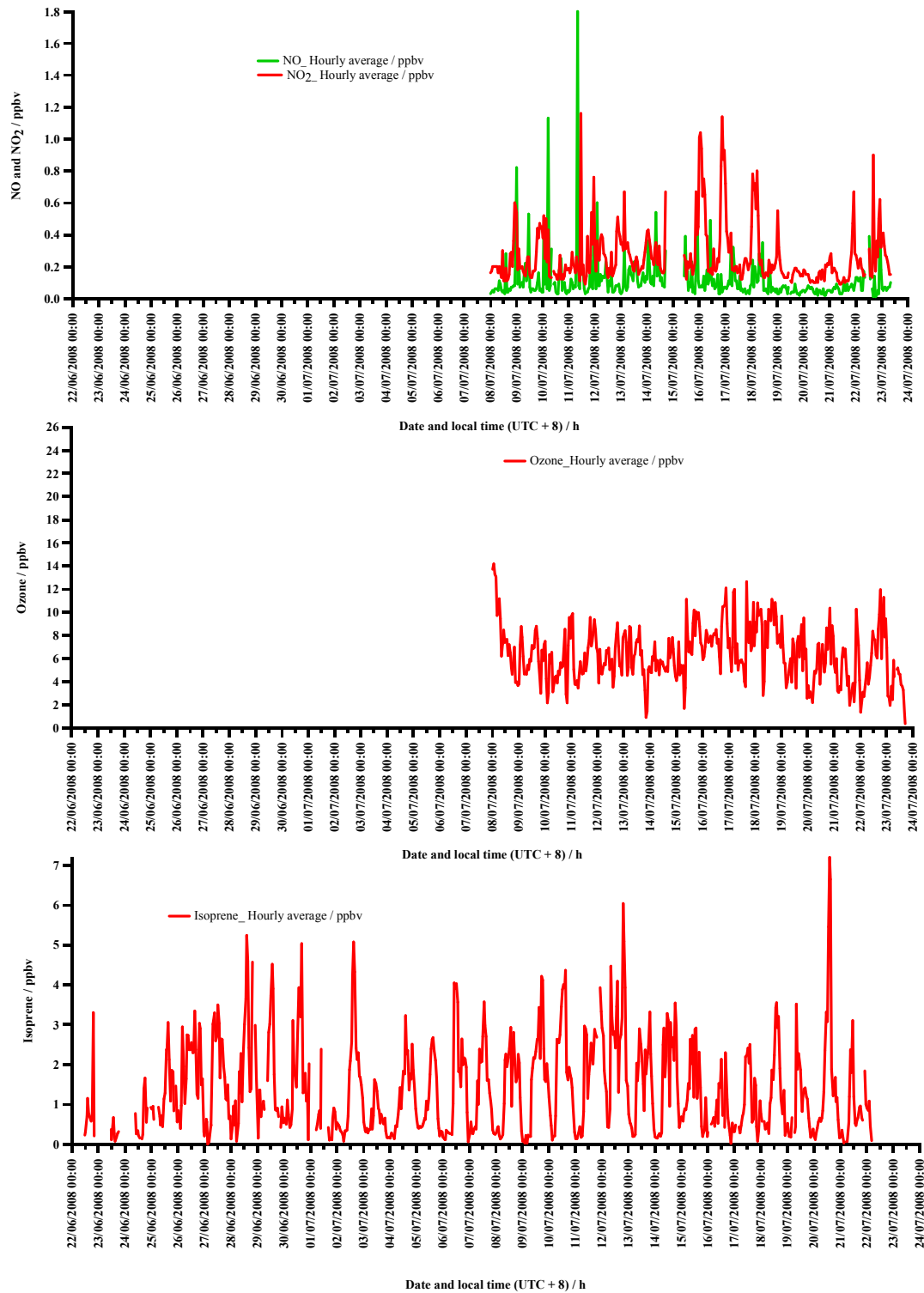


Figure 3.8 - Hourly averaged time series of O<sub>3</sub>, isoprene, NO and NO<sub>2</sub> from OP3 (3) campaign at Bukit Atur in the tropical rainforest in Borneo during June-July 2008.

Hourly averaged for time series of O<sub>3</sub>, isoprene, NO and NO<sub>2</sub> highlight the differences between the two seasons, as illustrated in Figures 3.7 and 3.8. Higher concentrations of isoprene, NO, NO<sub>2</sub> were detected in second campaign than in first campaign. There was no significant difference in ozone concentration found between seasons, although O<sub>3</sub> concentrations were more variable in the first campaign than the second campaign.

### 3.2.2. Chemical observations at OP3 (1) and OP3 (3)

HO<sub>2</sub>+RO<sub>2</sub> were measured by the University of Leicester using a PERCA, whilst OH measured using a FAGE by the University of Leeds.  $j(\text{O}^1\text{D})$  was measured using a filter radiometer by the University of Leeds. Methacrolein, ethane, propane, acetylene, acetaldehyde, acetone,  $\gamma$ -terpinene, limonene and camphene were measured by the dual Channel Gas Chromatograph with Flame ionisation detectors (DC-GC-FID) system by the University of York (see Table 3.2). All the data sets were obtained from the OP3 archive on BADC (see Table 3.2) at the instruments' original time resolution as shown in Table 3.1. The mean, median and standard deviation were obtained in this work by the author to the campaign of these species for during whole time (LT) from the OP3 (1) and OP3 (3) campaigns.

Table 3.3 shows the mean, median and standard deviation of campaign of trace composition species for during whole time (LT) from the campaigns OP3 (1) and OP3 (3).

Data #	Mean		Median		Standard deviation ( $\sigma$ )	
	OP3 (1)	OP3 (3)	OP3 (1)	OP3 (3)	OP3 (1)	OP3 (3)
NO /ppbv	0.041	0.098	0.029	0.059	0.061	0.305
NO <sub>2</sub> /ppbv	0.184	0.253	0.143	0.182	0.134	0.216
O <sub>3</sub> /ppbv	10.5	7.02	9.91	6.75	3.03	1.27
HO <sub>2</sub> +RO <sub>2</sub> /pptv	16.2	19.0	14.6	15.9	8.1	8.3
isoprene /ppbv	1.20	1.40	1.03	1.06	0.80	1.20
OH /molecule cm <sup>-3</sup>	1.17x10 <sup>6</sup>	1.79x10 <sup>6</sup>	8.09x10 <sup>5</sup>	1.07x10 <sup>6</sup>	1.10x10 <sup>6</sup>	2.00x10 <sup>6</sup>
<i>j</i> (O <sup>1</sup> D) /s <sup>-1</sup>	1.12x10 <sup>-5</sup>	1.27 x10 <sup>-5</sup>	5.90x10 <sup>-6</sup>	2.92x10 <sup>-7</sup>	1.24x10 <sup>-5</sup>	1.14x10 <sup>-5</sup>
methacrolein /pptv	65.7	103	55.9	85.3	35.8	58.7
ethane /pptv	723	380	684	361	218	122
propane /pptv	148	144	123	94.4	126	187
acetylene /pptv	228	140	190	131	173	46.6
acetaldehyde /pptv	-	72.1	-	65.3	-	27.2
Acetone /pptv	-	360	-	322	-	154
$\gamma$ -terpinene /pptv	69.7	109	62.1	91.1	28.0	66.6
limonene /pptv	85.0	52.1	65.7	38.7	54.7	32.5
camphene /pptv	36.7	46.3	28.8	27.2	28.7	40.2

Table 3.3 - Mean, median and standard deviation of campaign of trace composition species for during whole time (LT) from the OP3 (1) and OP3 (3) campaigns at Bukit Atur in the tropical rainforest in Borneo during April-May and June-July 2008.

There were higher measured mean concentrations of ethane, acetylene and limonene in OP3 (1) than OP3 (3), and the data in OP3 (1) had more variability than the OP3 (3) campaign. On the other hand, there were higher mean concentrations of methacrolein, camphene and  $\gamma$ -terpinene detected in OP3 (3) compared to OP3 (1). Similar mean concentration of propane was measured in both of the campaigns.

It can be seen that in both of the campaigns the measurements indicate a higher concentration of isoprene observed, but very small concentrations of other biogenic VOCs detected, including acetone and acetaldehyde (see also Hewitt *et al.*, (2010)). The reason for the intense photochemical processing of isoprene is the fact that there is an increase in the concentrations of its oxidation products, methyl vinyl ketone and methacrolein, which were measured at slightly higher concentrations.

### 3.2.3 Peroxy radicals in the OP3 campaigns

#### 3.2.3.1 Time series of peroxy radicals and $j(\text{O}^1\text{D})$

$\text{HO}_2+\text{RO}_2$  was measured via University of Leicester PERCA, whilst  $j(\text{O}^1\text{D})$  measured by the University of Leeds filter radiometer (See Table 3.2 and see Section 3.1.3 for data averaging process). Figure 3.9 shows the hourly averaged time series of peroxy radicals and  $j(\text{O}^1\text{D})$  from OP3 (1) (left graph) and OP3 (3) (right graph) campaigns.

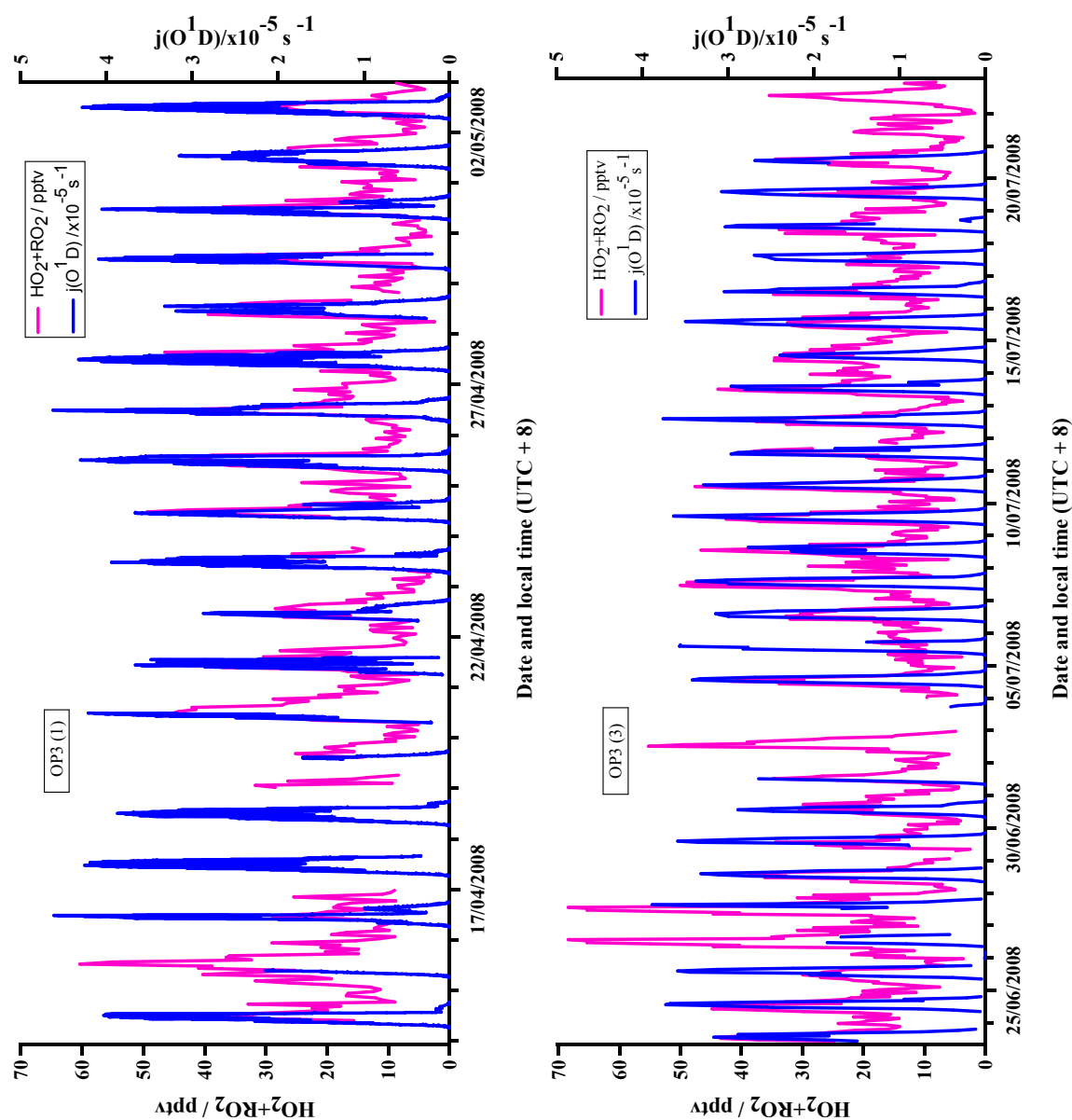


Figure 3.9 - Hourly averaged time series of peroxy radicals and  $j(\text{O}^1\text{D})$  from campaigns OP3 (1) during April-May (left graph) and OP3 (3) during June-July 2008 (right graph) at Bukit Atur in the tropical rainforest in Borneo.

The maximum  $j(\text{O}^1\text{D})$  reached was  $4.4 \times 10^{-5} \text{s}^{-1}$  at 11:30 on 16<sup>th</sup> and 26<sup>th</sup> April during OP3 (1) and  $3.9 \times 10^{-5} \text{s}^{-1}$  at 15:30 on 27<sup>th</sup> June and OP3 (3), respectively. During these campaigns, the detection limit of the PERCA instrument for peroxy radicals concentrations was about 1 pptv. The maximum value for the peroxy radical concentration was observed at 68 pptv at 13:30 on 26<sup>th</sup> and 27<sup>th</sup> July in day time during OP3 (3) campaign, while the night time concentrations reached a maximum 29 pptv at 22:30 on 15<sup>th</sup> April during OP3 (1) campaign (see Figure 3.9). There is a variation for the day time peroxy radical concentrations in OP3 (1) campaign from 2 pptv at 06:30 on 28<sup>th</sup> April to 62 pptv at 12:30 on 15<sup>th</sup> April, while during OP3 (3) campaign, the values vary between 4 pptv at 06:30 on 21<sup>st</sup> July to 68 pptv at 13:30 on 26<sup>th</sup> and 27<sup>th</sup> July as shown in Figure 3.9. It should be noted that the values for the day and night time averaged peroxy radical concentrations are 20 pptv and 11 pptv during OP3 (1), while they observed 24 and 13 pptv, respectively, during OP3 (3) (see also Table 5.2, section 5.2.1.4 in Chapter 5). Hence, during both of the campaigns, the average peroxy radical concentration in the hours of daylight were 1.8 times higher than at night time during OP3 (1) and 1.9 times higher during OP3 (3). From the smaller number of these ratios, it can be concluded that significant night time peroxy radical chemistry was observed in the tropical rainforest in Borneo. Night time peroxy radicals will be detailed in sections 3.2.3.4.

### 3.2.3.2 Averaged diurnal cycles of peroxy radicals and $j(\text{O}^1\text{D})$

The hourly averaged diurnal cycles of peroxy radical and  $j(\text{O}^1\text{D})$  for whole campaign have constructed from the averaging time series of peroxy radical and  $j(\text{O}^1\text{D})$  data for corresponding time as shown in Figure 3.9 (see Section 3.1.3 for data averaging process). Figure 3.10 shows hourly averaged diurnal cycles for the peroxy radical concentrations and for  $j(\text{O}^1\text{D})$ , for OP3 (1) (top graph) and OP3 (3) (bottom graph) campaigns, respectively.

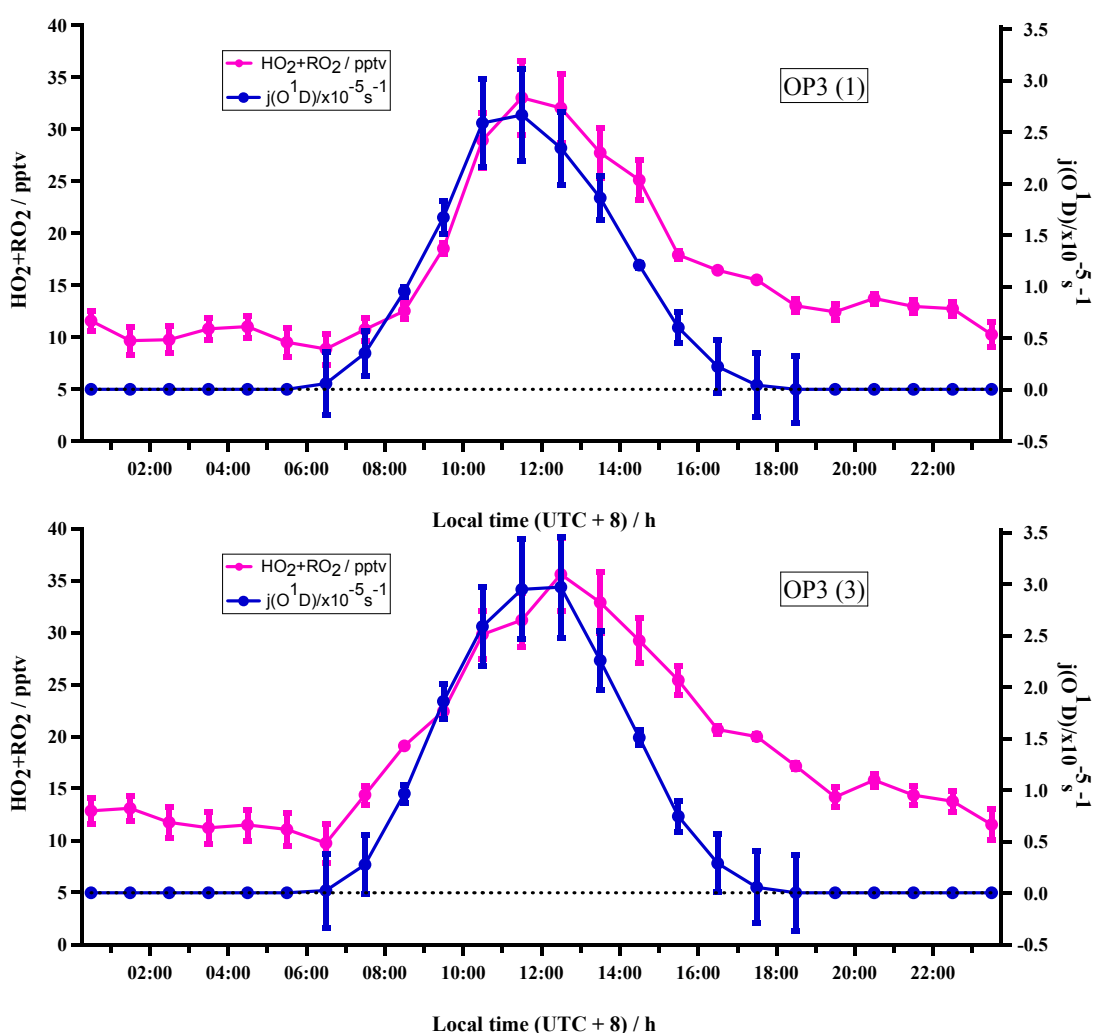


Figure 3.10 - Hourly averaged diurnal cycles for  $[\text{HO}_2 + \text{RO}_2]$  and photolysis rate coefficients of  $j(\text{O}^1\text{D})$  from campaigns OP3 (1) during April-May (top graph) and OP3 (3) during June-July 2008 (bottom graph) at Bukit Atur in the tropical rainforest in Borneo. Figure 3.10 generated from the time series of peroxy radical and  $j(\text{O}^1\text{D})$  show previously in Figure 3.9. Error bars show  $\pm 1\sigma$  of hourly averaged diurnal values.

During the OP3 (1) campaign, the midday average  $[\text{HO}_2+\text{RO}_2]$  were  $33.0 \pm 3.5$  ( $1\sigma$ ) pptv, while in OP3 (3) they were obtained at a value of  $35.6 \pm 3.5$  ( $1\sigma$ ) pptv as shown in Figure 3.10. The midday averages of  $j(\text{O}^1\text{D})$  were  $2.7 \times 10^{-5} \pm 0.5 \times 10^{-5}$  ( $1\sigma$ )  $\text{s}^{-1}$  in OP3 (1) and  $3.0 \times 10^{-5} \pm 0.5 \times 10^{-5}$  ( $1\sigma$ )  $\text{s}^{-1}$  in OP3 (3) campaigns (see also Figure 3.10).

Peroxy radicals and photolysis rate coefficients of  $j(\text{O}^1\text{D})$  were measured by PERCA (V3.5) and filter radiometer respectively for the campaigns OP3 (1) (top graph) and OP3 (3) (bottom graph) at Bukit Atur in the tropical rainforest in Borneo during April-May and June-July 2008. Regarding the concentrations of peroxy radicals and  $j(\text{O}^1\text{D})$ : owing to the fast photochemistry producing OH and the  $\text{HO}_2$  from ozone photolysis,  $j(\text{O}^1\text{D})$  and peroxy radicals concentration are at a maximum during day time compared to night time, which are the lowest. Owing to the high peroxy radical concentrations measured for midday, these can persist during the afternoon under low  $\text{NO}_x$  conditions, which gives an asymmetry in the diurnal cycle of the peroxy radical concentrations during daytime. An emission of isoprene is an important source of the peroxy radicals in the afternoon, i.e. asymmetric diurnal profile (this basis for this is discussed in the next paragraph) (see Section 3.3.1, e.g. Figures 3.30 and 3.34). The asymmetry in the diurnal cycle has been encountered in previous campaigns as well, in low- $\text{NO}_x$  environments by Fleming *et al.*, (2006a) at Mace Head in 2006, Brookes, (2010) and Andres-Hernandez *et al.*, (2010) during AMMA field measurement (see Section 1.5.4.3 in Chapter 1 for the details of the experiments and influences for the asymmetric diurnal profile).

After sunrise, there is an increase in concentration for peroxy radicals together with  $j(\text{O}^1\text{D})$ , while during the afternoon, the  $j(\text{O}^1\text{D})$  hourly averaged values decline more

rapidly causing a deviation in the peroxy radical concentrations curve from the  $j(\text{O}^1\text{D})$  curve after approximately 13:00 LT. Hewitt *et al.*, (2010) demonstrated evidence for the active photochemical processing of isoprene provided by the increase in concentrations of its oxidation products, i.e. methyl vinyl ketone and methacrolein observed in the afternoons. The isoprene oxidation products methyl glyoxal (MGLY), methylvinyl ketone (MVK), and methacrolein (MACR) are effective sources of the peroxy acetyl radical, e.g. Liu *et al.*, (2010) (see Section 3.2.3.6). Peroxy acetyl radical is one of the most abundant and important organic peroxy radicals in the atmosphere. Fast peroxy acetyl self-reaction results in the generation of methyl peroxy radical, peroxy acetyl radical is a one of the important intermediate in atmospheric chemistry (Roehl *et al.*, (1995). The subsequent fate of the peroxy acetyl radicals is primarily guided by self reaction and reaction with other peroxy radicals (see Table 3.4). Low concentration of NO ( $\sim 20$  pptv) observed during afternoon (Hewitt *et al.*, (2010)) therefore self and cross reactions of peroxy acetyl radicals are important than the reactions of peroxy acetyl radicals with NO.

Reaction	Rate coefficient/ $\text{cm}^3 \text{ molecule}^{-1} \text{ s}^{-1}$	Reference
$\text{HO}_2 + \text{HO}_2$	$2.6 \times 10^{-12}$	Atkinson <i>et al.</i> , (2006)
$\text{HO}_2 + \text{CH}_3\text{O}_2$	$5.2 \times 10^{-12}$	Atkinson <i>et al.</i> , (2006)
$\text{CH}_3\text{O}_2 + \text{CH}_3\text{O}_2$	$3.5 \times 10^{-13}$	Atkinson <i>et al.</i> , (2006)
$\text{HO}_2 + \text{CH}_3\text{C}(\text{O})\text{O}_2$	$1.4 \times 10^{-11}$	Atkinson <i>et al.</i> , (2006)
$\text{CH}_3\text{O}_2 + \text{CH}_3\text{C}(\text{O})\text{O}_2$	$1.1 \times 10^{-11}$	Atkinson <i>et al.</i> , (2006)
$\text{CH}_3\text{C}(\text{O})\text{O}_2 + \text{CH}_3\text{C}(\text{O})\text{O}_2$	$1.6 \times 10^{-11}$	Atkinson <i>et al.</i> , (2006)

Table 3.4 – Rate coefficients of the peroxy radical self and cross reaction at 298K and 1 atmosphere.

It can be seen from Table 3.4 that peroxy acetyl is a fast-reacting peroxy radical compared to methyl peroxy and hydroperoxy. Peroxy acetyl radicals self react quickly

according to reaction 3.1. The resulting  $\text{CH}_3\text{C}(\text{O})\text{O}$  radicals then undergo rapid thermal decomposition to yield methyl radicals (reaction 3.2), which add  $\text{O}_2$  to produce  $\text{CH}_3\text{O}_2$  (reaction 3.3), (Finlayson-Pitts & Pitts, 2000):



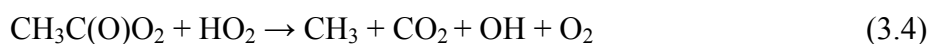
Hence, build up of  $\text{CH}_3\text{O}_2$  precursor (peroxy acetyl radicals) during the afternoon which gives an extra  $\text{CH}_3\text{O}_2$  during afternoon. It might be suggested that role of peroxy acetyl radicals is an important for the asymmetric diurnal profile of the peroxy radical (see Figure 3.10).

There is an increasing deviation during the late afternoon due to the fact that  $\text{HO}_2 + \text{RO}_2$  losses dominate over production. The route through  $\text{CH}_3\text{O}_2$  involved not only reaction of OH with  $\text{CH}_4$ , but also NMHCs in the rainforest region, e.g. isoprene and its oxidation products (see Section 3.2.3.6 for oxidation of isoprene mechanism).  $\text{HO}_2$  can react with  $\text{O}_3$  whilst  $\text{CH}_3\text{O}_2$  cannot react with  $\text{O}_3$  leading to a different loss. Monks *et al.*, (1996, 2000b) observed that  $\text{CH}_3\text{O}_2$  is the main peroxy radical during the late afternoon, i.e. organic peroxy radicals are dominant over  $\text{HO}_2$ . The main peroxy radical present during the afternoon has been concluded to be  $\text{CH}_3\text{O}_2$  ( $\text{CH}_3\text{O}_2 : \text{HO}_2$  2.7:1) by Monks *et al.*, (1996) during SOAPEX experiment (see Section 1.5.4.1 Chapter 1 for the experiment details). During the OP3 (3) campaign, the established proportions for  $\text{CH}_3\text{O}_2 : \text{HO}_2$  reached 7:1 during the afternoon compared with  $\text{CH}_3\text{O}_2 : \text{HO}_2$  of 5.8:1 during day time, while a dramatic growth has been observed for this proportion during the night, when FAGE and PERCA (V3.5) measurement have been employed for

providing these proportions (see Section 3.2.3.5). The process of organic peroxy radicals being transformed into HO<sub>x</sub> radicals is most efficiently achieved by reaction with NO. Hewitt *et al.*, (2010) observed a reduced NO concentration (~20 pptv) during the late afternoon and evening for the tropical rainforest in Borneo. Therefore, at low NO concentrations and high isoprene concentrations could produce a decrease in the HO<sub>2</sub>:CH<sub>3</sub>O<sub>2</sub> ratio. Furthermore, the loss of radicals occurs immediately after sunset through chain termination reactions such as HO<sub>2</sub>+HO<sub>2</sub> and HO<sub>2</sub>+CH<sub>3</sub>O<sub>2</sub> involving the HO<sub>2</sub> radicals, as the rate coefficients for these reactions are much higher than those for pairs of methyl peroxy radicals (CH<sub>3</sub>O<sub>2</sub>+CH<sub>3</sub>O<sub>2</sub>) (see Table 3.4). The method for loss of the remaining methyl peroxy radicals through self-reactions (of the type, CH<sub>3</sub>O<sub>2</sub>+CH<sub>3</sub>O<sub>2</sub>) is much slower. The CH<sub>3</sub>O<sub>2</sub>+CH<sub>3</sub>O<sub>2</sub> self-reactions have much smaller rate coefficients than HO<sub>2</sub>+HO<sub>2</sub> as shown in Table 3.4. The half-life of the CH<sub>3</sub>O<sub>2</sub>+CH<sub>3</sub>O<sub>2</sub> reactions is a few hours owing to the very low mixing ratio (the range of 10 to 15 pptv as shown in Figure 3.10), and owing to this aspect, there is a decrease in HO<sub>2</sub>+CH<sub>3</sub>O<sub>2</sub> during evening time as it can be seen in Figure 3.10. Monks *et al.*, (1996) noticed that there is a “tailing” of the peroxy radical concentration values towards night time, when the  $j(\text{O}^1\text{D})$  decrease towards zero during SOAPEX experiment (see Section 1.5.4.1 in Chapter 1 for the experiment details). Peroxy radical concentrations persist into the night-time, which shows that oxidation chemistry does occur at night time in OP3 (1) and OP3 (3) campaigns (will be discussed in section 3.2.3.4 for night time chemistry).

During the late afternoon, another factor that influences the production of peroxy radicals is the photolysis of HCHO. HCHO photolysis occurs at longer wavelengths and still occurs near sunrise and sunset (i.e. a wider diurnal profile than ozone photolysis), thus leading to the formation of a shoulder in Fig 3.8. Yang *et al.*, (2002)

observed in data from Summit, Greenland (38.5° W, 2.6° N) that HCHO photolysis was a significant factor for peroxy radical production during the afternoon. Solberg *et al.*, (2001) found that during summer time HCHO photolysis was important at various stations: Mace Head, Ireland and at two stations in Germany and Norway. Photolysis of other photo-labile compounds (e.g. HCHO and HONO) can produce a broader peroxy radical diurnal cycle than that expected from ozone photolysis alone (see Section 3.3.1.4). Section 3.3.1.4 explains that, photolysis of HONO is an important source of peroxy radical during early morning, also in the case of rainforest atmosphere; HCHO photolysis can lead to efficient production of peroxy radicals, i.e. HOx. In addition, HCHO mostly originates from isoprene oxidation in forested region, Sumner *et al.*, (2001). According to Hewitt *et al.*, (2010), HCHO was closely correlated with isoprene (should be major source in this environment, also see Section 3.2.3.6 for the oxidation of isoprene mechanism), and peaked in the early afternoon (mixing ratio ~ 4.5 ppbv). Owing to the fact that the lifetime of HCHO is ~ 3 hours and that HCHO is present throughout the late afternoon, HCHO could produce HO<sub>2</sub> for a longer time. Thornton *et al.*, (2002) found that reactions of HO<sub>2</sub> with peroxy acetyl radicals may not be as efficient HOx sinks, but they may have rather function, i.e. recycling OH. Laboratory studies showed that the reaction of peroxy radical (particularly those derived from isoprene, e.g. peroxy acetyl radicals) with HO<sub>2</sub> can regenerate OH by reaction 3.4, (Dillon and Crowley, 2008; Hasson *et al.*, (2004); Jenkin *et al.*, (2007)):



It should be noted that self ( $\text{CH}_3\text{C}(\text{O})\text{O}_2 + \text{CH}_3\text{C}(\text{O})\text{O}_2$ ) and cross ( $\text{CH}_3\text{C}(\text{O})\text{O}_2 + \text{HO}_2$ ) reactions of peroxy acetyl radicals are important source of CH<sub>3</sub>O<sub>2</sub> during the afternoon.

The asymmetry in the  $[\text{HO}_2+\text{RO}_2]$  diurnal profile relied on the measured  $[\text{HO}_2+\text{RO}_2]$  being the longer-lived  $\text{RO}_2$ . Consequently, isoprene oxidation products could influence the process of the observed tail in the peroxy radical profile.

### 3.2.3.3 $\text{NO}_x$ and peroxy radicals during daytime

$\text{HO}_2+\text{RO}_2$  was measured by PERCA, whilst  $\text{NO}_x$  measured by  $\text{NO}_x$ y (see Table 3.2). During the OP3 (1) and OP3 (3) campaigns, hourly averaged time series of  $\text{HO}_2+\text{RO}_2$  and  $\text{NO}_x$  concentrations were generated between 06:00-19:00 LT (UTC+8) from BADC (see Section 3.1.3 for data averaging process). Peroxy radical concentrations do not correlate with  $\text{NO}_x$  concentrations between 06:00-19:00 LT during the OP3 (1) and OP3 (3) campaigns (see Figure 3.11a). Vehicles arriving in early morning and leaving in late afternoon at the measurement site, therefore the site has artificially polluted traffic air.

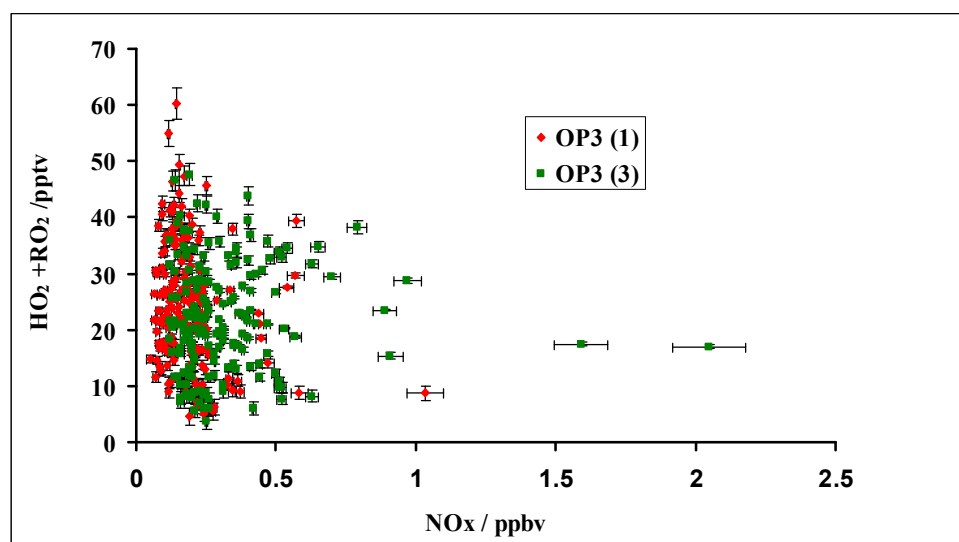


Figure 3.11a - Hourly averaged peroxy radical concentration vs. hourly averaged  $\text{NO}_x$  concentration between 06:00-19:00 LT from the OP3 (1) and OP3 (3) campaigns during April-May 2008 at Bukit Atur in the tropical rainforest in Borneo. Error bars show  $\pm 1\sigma$  of hourly averaged values.

It is worth noting that, during the OP3 (1) campaign, hourly averaged time series of  $\text{HO}_2+\text{RO}_2$  and  $\text{NO}_x$  concentrations were generated between 10:00-16:00 LT to

understand how the  $[\text{HO}_2+\text{RO}_2]$  correlates with the changing concentration of  $\text{NO}_x$ . The hourly averaged peroxy radical data were divided into two regimes according to their associated  $\text{NO}_x$  values. The data with  $[\text{NO}_x] < 570$  pptv (maximum  $[\text{NO}_x]$  reached 570 pptv during OP3 (1) campaign) and  $[\text{NO}_x] < 175$  pptv ( $[\text{HO}_2 + \text{RO}_2]$  remain approximately constant whilst  $[\text{NO}_x] > 175$ ) are used in this section for investigating the effect of  $\text{NO}_x$  on peroxy radicals concentrations during daytime.

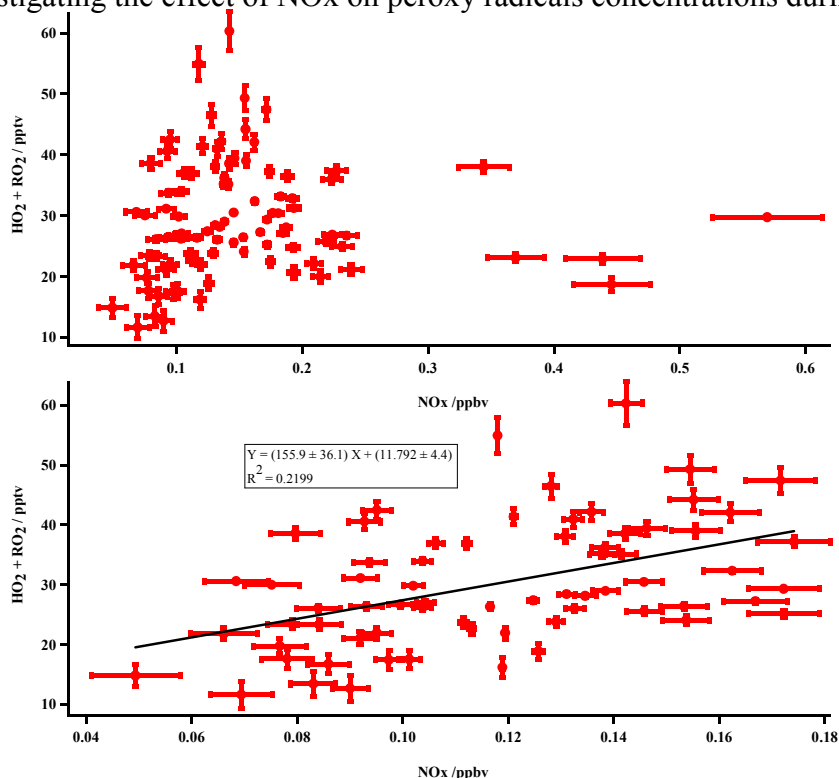


Figure 3.11b - Hourly averaged  $[\text{HO}_2+\text{RO}_2]$  vs. hourly averaged  $[\text{NO}_x]$  ( $< 570$  pptv) (top graph) and hourly averaged  $[\text{HO}_2+\text{RO}_2]$  vs. hourly averaged  $[\text{NO}_x]$  ( $< 175$  pptv) (bottom graph) between 10:00-16:00 LT from the OP3 (1) campaign during April-May 2008 at Bukit Atur in the tropical rainforest in Borneo. Error bars show  $\pm 1\sigma$  of hourly averaged values.

Figure 3.11b (bottom) shows that as  $\text{NO}_x$  increases, peroxy radical concentration increases with a poor correlation ( $R^2 = 0.22$ ). In contrast Figure 3.11b (top) shows that at the higher  $\text{NO}_x$  concentrations from ca.175-570 pptv, the peroxy radical concentration values remain approximately constant with increasing  $\text{NO}_x$ .

Liu *et al.*, (1980) and Logan *et al.*, (1981) showed that at low to intermediate NO<sub>x</sub> concentration, RO<sub>2</sub> could increase with increasing NO<sub>x</sub> because its precursors may correlate with NO<sub>x</sub> (< 175 pptv), e.g. HCHO. In the presence of NO<sub>x</sub>, the reaction of NO with CH<sub>3</sub>O<sub>2</sub> leads to the formation of HO<sub>2</sub> and HCHO. HCHO is an important source of peroxy radicals (see Sections 3.2.3.2 and 3.3.1.4). Peroxy acetyl radical can originate from isoprene oxidation (see Sections 3.2.3.2 and 3.2.3.6). In the presence of NO<sub>x</sub>, the reaction of NO with CH<sub>3</sub>C(O)OO leads to the formation of CH<sub>3</sub>C(O)O rather than the reaction of NO<sub>2</sub> with CH<sub>3</sub>C(O)OO to form PAN.



The relative rates of reactions 3.5 and 3.6, as well as the relative concentrations of NO<sub>2</sub> and NO influence the reformation of PAN versus the formation of extra peroxy radicals. A rate constant ratio for the reactions of the CH<sub>3</sub>C(O)OO radical with NO<sub>2</sub> ( $k_{3.5}$ ) and NO ( $k_{3.6}$ ) of  $k_{3.6}/k_{3.5} = (1.95 \pm 0.28)$  independent of temperature over the range 283-313 K (Tuazon *et al.*, (1991)). Moreover, the relative concentrations of NO<sub>2</sub> and NO also contribute to the radical yield. During OP3 (1), the median of the relative concentrations of NO<sub>2</sub> and NO is 1.90 for low NO<sub>x</sub> (< 175 pptv) regime between 10:00-16:00 LT. Hence, relative rates and concentrations of NO<sub>2</sub> and NO values, it might be suggested that the reaction of CH<sub>3</sub>C(O)OO with NO is marginally important than the reaction of CH<sub>3</sub>C(O)OO with NO<sub>2</sub>. CH<sub>3</sub>C(O)O radical rapidly decomposes to CH<sub>3</sub>+CO<sub>2</sub> and the CH<sub>3</sub> radical is converted promptly to CH<sub>3</sub>O<sub>2</sub> in the presence of O<sub>2</sub>

(see Section 3.2.3.2) and (Finlayson-Pitts & Pitts, 2000). It can be seen in the average of all days during OP3 (1) campaign as shown in Figure 3.11b (bottom).

As NO<sub>x</sub> concentrations increase, NO converts peroxy radicals to OH more efficiently, then OH reacts with NO<sub>2</sub> to form HNO<sub>3</sub>, reducing the rate of peroxy radical regeneration via OH oxidation of CO and hydrocarbons. Thus, peroxy radical concentrations should start to decrease at high NO<sub>x</sub> owing to their removal by radical-NO<sub>x</sub> reactions. For the OP3 (1) campaign, taking the time series as a whole during daytime, the loss of peroxy radical is dominated almost exclusively by the peroxy radical self-reactions rather than the reaction of OH with NO<sub>2</sub> (explained in section 3.3 using parameters  $\alpha$ ,  $\beta$  and  $\gamma$ ). Therefore no negative correlation is observed between peroxy radical and NO<sub>x</sub> at higher NO<sub>x</sub> values 175-570 pptv as seen in Figure 3.11b (top). It is worth noting that, peroxy radical concentrations do not correlate with NO<sub>x</sub> concentrations between 10:00-16:00 LT during the OP3 (3) campaign.

Carpenter *et al.*, (1998) found a negative correlation between PSS (photochemical steady state)-derived peroxy radical concentrations and NO<sub>x</sub> at Weybourne in winter 1994. Holland *et al.*, (2003) established during the BERLIOZ campaign, outside Berlin (Germany), that for [NO<sub>x</sub>] > 1 ppbv, HO<sub>2</sub> decreased as NO<sub>x</sub> increased and that in the conditions of [NO<sub>x</sub>] being < 1 ppbv, HO<sub>2</sub> increased with increasing NO<sub>x</sub>.

#### 3.2.3.4 Night time radicals

Apart from photochemistry, there are other methods of producing peroxy radicals, which can occur during night time. NO<sub>3</sub>, the nitrate radical, (Carslaw *et al.*, 1997; Allen *et al.*, 1999; Penkett *et al.*, 1999; Salisbury *et al.*, 2001; Geyer *et al.*, 2003;

Fleming *et al.*, 2006b) and ozone both react with alkenes (Hu and Stedman, 1995; Rickard *et al.*, 1999; Kanaya *et al.*, 1999, 2000, 2002 Salisbury *et al.*, 2001; Fleming *et al.*, 2006b) and are established to be two methods of peroxy radical production in the marine influenced atmosphere at night.

Figure 3.12 shows hourly averaged diurnal cycles together for  $[HO_2+RO_2]$  from the OP3 (1) and OP3 (3) campaigns (see Section 3.1.3 for data averaging process and also explained in Section 3.2.3.2).

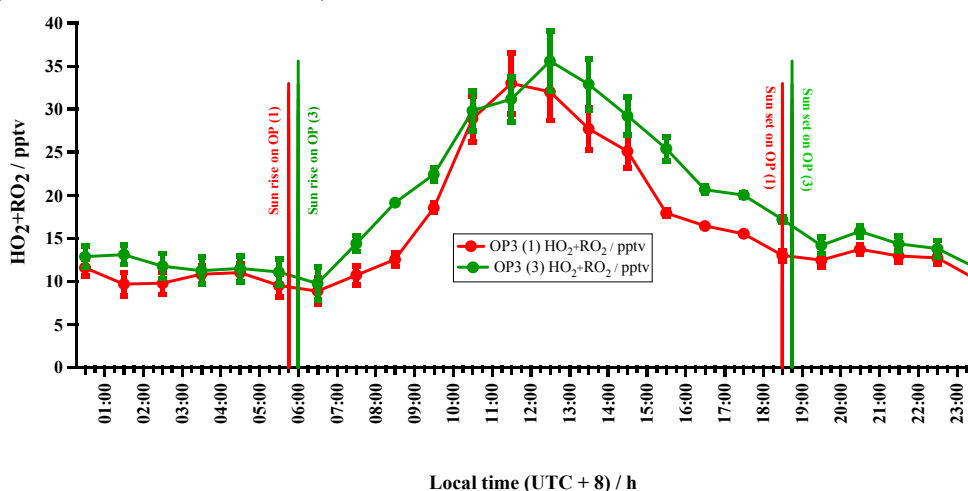


Figure 3.12 – Hourly averaged diurnal cycles together for  $[HO_2+RO_2]$  from campaigns OP3 (1) during April-May and OP3 (3) during June-July 2008 at Bukit Atur in the tropical rainforest in Borneo. Figure 3.12 generated from the time series of peroxy radical shown previously in Figure 3.9. Figure 3.12 shows the same data as plotted previously in Figure 3.10. The sunrise and sunset times were obtained from measured photosynthetically active radiation (PAR) when the values as above zero for OP3 (1) and OP3 (3) campaigns. Error bars show  $\pm 1\sigma$  of hourly averaged diurnal values.

In the case of Southeast Asian tropical rainforest, the measurements indicate a maximum night time peroxy radical concentration value of 29 pptv at 22:30 on 15<sup>th</sup> April during OP3 (1) campaign as shown in Figure 3.9 (left). Non-zero  $[OH]$  ( $0.4 \times 10^6$  molecule  $cm^{-3}$ ) and [isoprene] ( $\sim 40$  pptv) were observed during the night time, e.g. Hewitt *et al.*, (2010) and Whalley *et al.*, (2011). According to Lelievre *et al.*, (2008), Peeters *et al.*, (2009) and Silva *et al.*, (2010) it has been proposed that recycling of OH

from isoprene oxidation chemistry, also could offer a potential explanation of the persistence of RO<sub>2</sub>, HO<sub>2</sub> and potentially OH. These concentrations are indicative of the active peroxy radical chemistry during night time and therefore, of substantial oxidant levels persisting at night. The peroxy radical concentration tended to be variable throughout the night as shown in Figure 3.12. Night time peroxy radicals will be discussed with NO<sub>x</sub> chemistry in the next paragraph.

### NO<sub>x</sub> influences

During the OP3 (1) and OP3 (3) campaigns, hourly averaged time series of HO<sub>2</sub>+RO<sub>2</sub> (see left graph on Figure 3.9 for OP3 (1) and right graph on Figure 3.9 for OP3 (3)) and NO<sub>x</sub> concentrations (see top graph on Figures 3.7 for OP3 (1) and top graph on Figure 3.8 for OP3 (3)) were generated between 19:00-06:00 LT (UTC+8) from instruments of PERCA and NO<sub>x</sub>y, respectively (see Table 3.2 and Section 3.1.3 for data averaging process). Figure 3.13 shows hourly averaged time series of peroxy radical and NO<sub>x</sub> concentrations between 19:00-06:00 LT during the OP3 (1) and OP3 (3) campaigns.

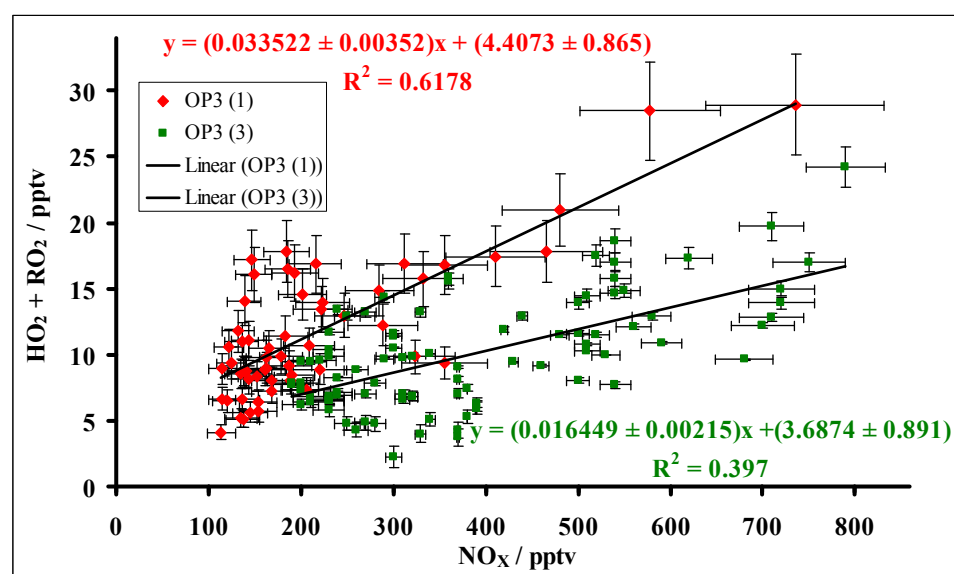


Figure 3.13 – Hourly averaged time series of peroxy radical and NO<sub>x</sub> concentrations between 19:00-06:00 LT from campaigns OP3 (1) during April-May and OP3 (3) during June-July 2008 at Bukit Atur in the tropical rainforest in Borneo. Error bars show  $\pm 1\sigma$  of hourly averaged values.

OP3 (1) and OP3 (3) campaigns shown in Figure 3.13 have a positive trend of peroxy radicals with NO<sub>x</sub> between 19:00-06:00 LT, with a slightly greater dependence on NO<sub>x</sub> for the first campaign: that campaign has a gradient of just 0.03, compared to 0.016 in the second campaign. Moderately stronger linear correlation of NO<sub>x</sub> vs. peroxy radical concentration was observed of 0.62 during the OP3 (1) campaign, compared to the value of the OP3 (3) campaign, of 0.4. Figure 3.13 also shows the variations observed for OP3 (1) and OP3 (3) in the NO<sub>x</sub> mixing ratio and peroxy radical concentrations: while in OP3 (1) NO<sub>x</sub> mixing ratio fluctuates between 100 to 720 pptv, in OP3 (3) these values are between 180 and 790 pptv; as for peroxy radical concentrations, in OP3 (1), they rose from 3 to 29 pptv, compared to the OP3 (3), when the values range between 3 to 24 pptv.

Owing to the remote nature of the OP3 measurement location, soil NO<sub>x</sub> has a more substantial contribution to the NO<sub>x</sub> budget than anthropogenic contributions, Pugh *et al.*, (2010). The soils typically associated with the occurrence of Borneo forest formation in tropical Asia are the Ultisol group, i.e. red and yellow acidic soil of warm, humid areas (Baillie, 1996 and Chappell *et al.*, 2007). Emission of NO from forest soils is primarily a result of microbial activity, with NO thought to be an intermediate in microbial nitrification and denitrification processes (e.g. Ludwig *et al.* 2001; Zechmeister-Boltenstern *et al.* 2002). Nitrification is the oxidation of soil NH<sub>4</sub><sup>+</sup> to NO<sub>3</sub><sup>-</sup> and denitrification is the anaerobic reduction of soil NO<sub>3</sub><sup>-</sup> to N<sub>2</sub>O and N<sub>2</sub> (Fowler *et al.*, (2009)). Emission of NO from soil is controlled by a wide variety of variables including forest type, soil nutrient content, temperature, soil moisture and moisture history (Dorsey *et al.* ., (2004)). The non-zero night-time concentrations, suggests a local NO source (mainly from soil) that was diluted throughout the boundary layer.

[NO] values remain approx constant throughout the night  $\sim 20$  pptv (Hewitt *et al.*, (2010)). At night NO is irreversibly oxidized to NO<sub>2</sub> by O<sub>3</sub> (NO<sub>3</sub> formed followed by the reaction of NO<sub>2</sub> with O<sub>3</sub>). Therefore, the region of coexistence for NO<sub>3</sub> and NO is often shallow, while its vertical movement is influenced by the emission strength and vertical stability of NO (Geyer and Stutz, 2004).

With increasing NO<sub>x</sub>, radical cycling from RO<sub>2</sub> to HO<sub>2</sub> and HO<sub>2</sub> to OH becomes more significant, e.g. Bloss *et al.*, (2007). The reactions between NO<sub>3</sub> and RO<sub>2</sub> will play an important role in determining the oxidizing capacity of the night-time troposphere. Kinetic studies of reactions of the nitrate radical (NO<sub>3</sub>) with peroxy radicals (RO<sub>2</sub>) show it can be an indirect source of OH at night (Vaughan *et al.*, (2006)). Additionally, the presence of NO<sub>3</sub>, it can react with organic peroxy radicals to form HO<sub>2</sub> and potentially OH ([NO]  $\sim 20$  pptv). During night, approximately 10 pptv of peroxy radical concentration and  $0.4 \times 10^6$  molecule cm<sup>-3</sup> of OH concentration were measured by PERCA and FAGE, respectively. This suggests that nitrate radical chemistry may be present. It might be suggested that in the case of the tropical rainforest boundary level, NO<sub>3</sub> chemistry is unavoidable.

### 3.2.3.5 Overall photochemistry

Through measuring peroxy radical concentrations, it is possible to determine the net photochemical ozone production or loss within air mass. The instantaneous in-situ ozone production or loss rate,

$$N(O_3) = P(O_3) - L(O_3)$$

is defined from Kleinman *et al.*, (1995) and net ozone rate as

$$N(O_3) = k_c [HO_2 + RO_2][NO] - \{ff(O^1D) + k_{3.7}[OH] + k_{3.8}[HO_2]\}[O_3] \quad (A)$$

$$\text{where ozone production rate, } P(O_3) = k_c [HO_2 + RO_2][NO] \quad (B)$$

$$\text{where ozone loss rate, } L(O_3) = \{ff(O^1D) + k_{3.7}[OH] + k_{3.8}[HO_2]\}[O_3] \quad (C)$$

where  $k_c$  represents the combined rate constant for oxidation of NO to NO<sub>2</sub> by

$\sum_i R_i O_2$  and HO<sub>2</sub>, and  $k_{3.7}$  and  $k_{3.8}$  represent the reaction rate coefficients for reactions

3.7 and 3.8, respectively.



Tropospheric ozone is mainly produced and destroyed in the photostationary state between ozone, NO and NO<sub>2</sub> (see section 1.4.1).



This represents a null cycle. In the troposphere, the only known route for tropospheric ozone formation is through the photolysis of NO<sub>2</sub>. NO<sub>2</sub> is formed through the reaction of NO with ozone as part of the photostationary state between ozone and NO<sub>x</sub>, but this

represents a null cycle, i.e. no ozone production or loss has been remake. The photolysis of  $\text{NO}_2$  and the reaction of the photoproduct  $\text{O}(^3\text{P})$  are part of the photostationary state so have no net effect. The method of ozone production is the first term represented in the Equation A, which additional conversion of  $\text{NO}$  to  $\text{NO}_2$  occurs over the photostationary steady state between  $\text{NO}_x$  and ozone without the loss of an ozone molecule (in contrast to 3.11) through the reaction with peroxy radicals. The result of the oxidation of  $\text{NO}$  by peroxy radicals, i.e.,  $\text{NO}_2$ , is then photolysed to produce oxygen atoms that then forms ozone (via reaction 3.9).

The other terms represented in equation (A) the loss processes of ozone in the troposphere. There are firstly the photolysis of ozone to form excited oxygen atoms multiplied by  $f$  ( $f$  will defined in Section 3.3, on page 163 in equation D), the proportion of  $\text{O}(^1\text{D})$  that reacts with water vapour rather than being quenched to  $\text{O}(^3\text{P})$  which then reform ozone; secondly the reaction of ozone with  $\text{OH}$  (reaction 3.7); and thirdly the reaction of ozone with  $\text{HO}_2$  (reaction 3.8). It must be mentioned that in the process of calculating the net ozone production or loss rates from equation (A), certain ozone sinks have not been taken into account: cloud processes, dry deposition of ozone, and reactions of ozone with alkenes and halogens. Nevertheless, equation (A) remains a good approximation for the troposphere. For example, Atkinson and Arey (2003) showed that the rate constant for the reactions of  $\text{OH}$  with ozone ( $1.3 \times 10^{-14} \text{cm}^3 \text{molecule}^{-1} \text{s}^{-1}$  at 298 K, 1bar) and  $\text{HO}_2$  with ozone ( $7.3 \times 10^{-14} \text{cm}^3 \text{molecule}^{-1} \text{s}^{-1}$  at 298 K, 1bar) are greater than that for the reaction between isoprene and ozone ( $1.27 \times 10^{-17} \text{cm}^3 \text{molecule}^{-1} \text{s}^{-1}$  at 298 K, 1bar).

The hourly averaged of  $P(O_3)$ ,  $L(O_3)$  and  $N(O_3)$  were calculated using the equation of (B), (C) and (A) between 06:00-19:00 LT, respectively for the OP3 (1) and OP3 (3) campaigns. The following measurements are available to calculate  $P(O_3)$ ,  $L(O_3)$  and  $N(O_3)$  for the OP3 (1) and OP3 (3) campaigns: PERCA measurements of  $[HO_2+RO_2]$  (see left graph on Figure 3.9 for OP3 (1) and right graph on Figure 3.9 for OP3 (3)); NO<sub>x</sub> measurements of NO (see top graph on Figure 3.7 for OP3 (1) and top graph on Figure 3.8 for OP3 (3)); filter radiometer measurement of  $j(O^1D)$  (see left graph on Figure 3.9 for OP3(1) and right graph on Figure 3.9 for OP3 (3)); FAGE measurements of  $[OH]$  and  $[HO_2]$  ( $[HO_2]$  was available for OP3 (3) campaign,  $[HO_2]$  was not available for OP3 (1) but the assumption was made for OP3 (1) (see in the next paragraph)); UV absorption detector (Thermo Environmental Instruments, Model 49i) measurement of ozone (bottom graph on Figure 3.7 for OP3 (1) and bottom graph on Figure 3.8 for OP3 (3)) (see also Table 3.2 and section 3.1.3 for data averaging process).

There was no  $HO_2$  data available for OP3 (1) campaign. The assumption was made for the  $[HO_2]$  in the basis for this is discussed follow. Hourly averaged of  $\alpha$ ,

$$\alpha = \frac{[HO_2]}{[HO_2 + RO_2]}$$

was generated between 06:00-19:00 LT using from the measured

$HO_2$  by FAGE (see Table 3.2) and  $HO_2+RO_2$  by PERCA (see right graph on Figure 3.9) during the OP3 (3) campaign (see Section 3.13 for the data averaging process), respectively. Hourly averaged diurnal values of  $\alpha$  was obtained for OP3 (3) campaign from the generated hourly averaged values of  $\alpha$  from the OP3 (3) campaign (see Section 3.1.3 for the data averaging process). Hourly averaged time series of  $[HO_2]$  generated for OP3 (1) campaign by the multiplication of hourly averaged diurnal values of  $\alpha$  (obtained from the OP3 (3) campaign) and hourly averaged time series of

[HO<sub>2</sub>+RO<sub>2</sub>] for the OP3 (1) campaign (see left graph on Figure 3.9). The hourly averaged rates for photolysis of ozone, the reaction of ozone with OH and the reaction of ozone with HO<sub>2</sub> were obtained between 06:00-19:00 LT for the OP3 (1) and OP3 (3) campaigns. The hourly averaged time series of rates of photolysis of ozone, the reaction of ozone with OH and the reaction of ozone with HO<sub>2</sub> were obtained between 06:00-19:00 LT for the OP3 (1) and OP3 (3) campaigns. The hourly averaged diurnal data of rates for photolysis of ozone, the reaction of ozone with OH and the reaction of ozone with HO<sub>2</sub> for whole campaigns between 06:00-19:00 LT have been constructed from the averaging of time series of rates for photolysis of ozone, the reaction of ozone with OH and the reaction of ozone with HO<sub>2</sub> data for corresponding time (see section 3.1.3 for data averaging process). Figure 3.14 shows hourly averaged diurnal relative contribution of ozone loss terms,  $L(O_3)$  to total  $L(O_3)$  between 06:00-19:00 LT during the OP3 (1) campaign.

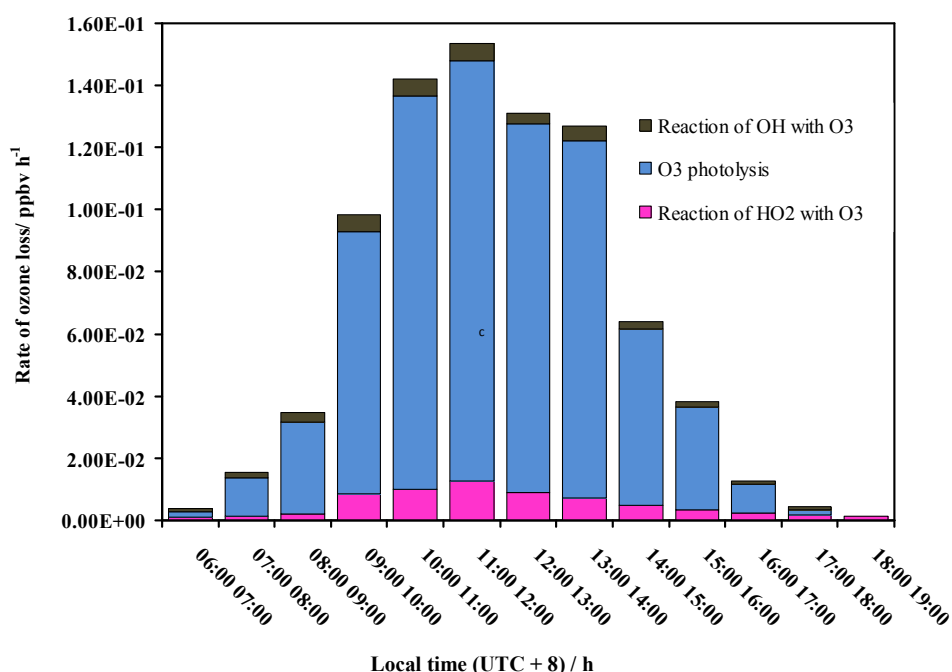


Figure 3.14 - Hourly averaged diurnal relative contributions of ozone loss terms,  $L(O_3)$  to total  $L(O_3)$  between 06:00-19:00 LT from the campaign OP3 (1) during April-May 2008 at Bukit Atur in the tropical rainforest in Borneo.

Figure 3.14 shows that photolysis has a largest contribution to the ozone loss. It can also be seen from Figure 3.14 that the  $\text{OH}+\text{O}_3$  reaction contributes little to  $L(\text{O}_3)$  which is consequently relatively insensitive to OH concentration.

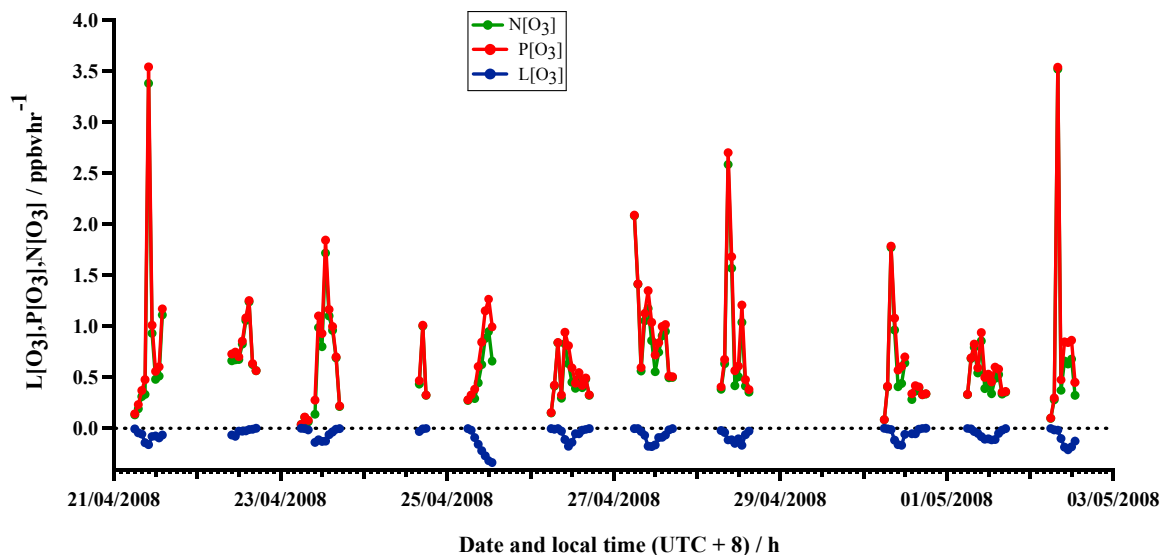


Figure 3.15 - Hourly averaged time series of ozone production rate,  $P(\text{O}_3)$  ozone loss rate,  $L(\text{O}_3)$  and net ozone rate,  $N(\text{O}_3)$  between 06:00-19:00 LT from the campaign OP3 (1) during April-May 2008 at Bukit Atur in the tropical rainforest in Borneo.

Figure 3.15 shows hourly averaged time series of ozone production rate,  $P(\text{O}_3)$  ozone loss rate,  $L(\text{O}_3)$  and net ozone rate,  $N(\text{O}_3)$  between 06:00-19:00 LT during the OP3 (1) campaign. There is a net positive value for ozone production for the air-masses encountered, with a median  $N(\text{O}_3)$  of  $0.51 \text{ ppbv hr}^{-1}$  and a mean  $N(\text{O}_3)$  of  $0.68 \text{ ppbv hr}^{-1}$  for hourly averages during daytime (06:00-19:00 LT) for the entire time series during OP3 (1) campaign. The maximum and minimum net ozone production rate calculated during daytime for OP3 (1)  $3.52 \text{ ppbv hr}^{-1}$  at 08:30 on 02<sup>nd</sup> of May and  $0.04 \text{ ppbv hr}^{-1}$  at 06:30 on 23<sup>rd</sup> April, respectively, as shown in Figure 3.15. Lowest net ozone production rate calculated  $0.04 \text{ ppbv hr}^{-1}$ , it is worth noting that, OP3 (1) was always in ozone production regime.

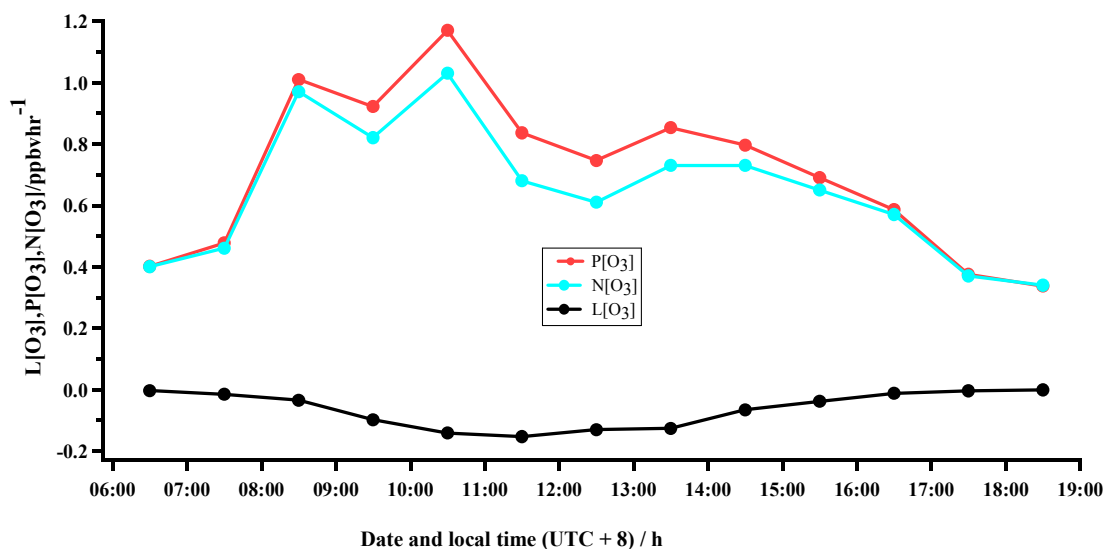


Figure 3.16 - Hourly averaged diurnal data for  $N(O_3)$ ,  $P(O_3)$ , and  $L(O_3)$  between 06:00-19:00 LT from the campaign OP3 (1) during April-May 2008 at Bukit Atur in the tropical rainforest in Borneo. Figure 3.16 generated from the hourly averaged time series of ozone production rate,  $P(O_3)$  ozone loss rate,  $L(O_3)$  and net ozone rate,  $N(O_3)$  show previously in Figure 3.15.

The hourly averaged diurnal data of  $N(O_3)$ ,  $P(O_3)$  and  $L(O_3)$  for whole campaign between 06:00-19:00 LT have been constructed from averaging the time series of  $N(O_3)$ ,  $P(O_3)$ , and  $L(O_3)$  data for the corresponding time as shown in Figure 3.15 (see Section 3.1.3 for data averaging process). Figure 3.16 shows hourly averaged diurnal data for  $N(O_3)$ ,  $P(O_3)$ , and  $L(O_3)$  between 06:00-19:00 LT during the OP3 (1) campaign. The diurnal averaged value for  $P(O_3)$  and  $N(O_3)$  varied throughout the day time, with the maximum reached at 10:30 LT during OP3 (1) campaign as shown in Figure 3.16.  $N(O_3)$  tends to follow  $P(O_3)$  fairly closely between 06:00-19:00 LT because  $P(O_3)$  is rather larger than  $L(O_3)$  at all times.  $L(O_3)$  has its maximum at midday when photochemistry was at its maximum, and  $L(O_3)$  is lower during early morning and afternoon.

The same form of data analysis was repeated for the OP3 (3) campaign. Figure 3.17 shows hourly averaged diurnal relative contributions of ozone loss terms to total  $L(O_3)$  on daily basis for daytime (06:00-19:00 LT) from the OP3 (3) campaign.

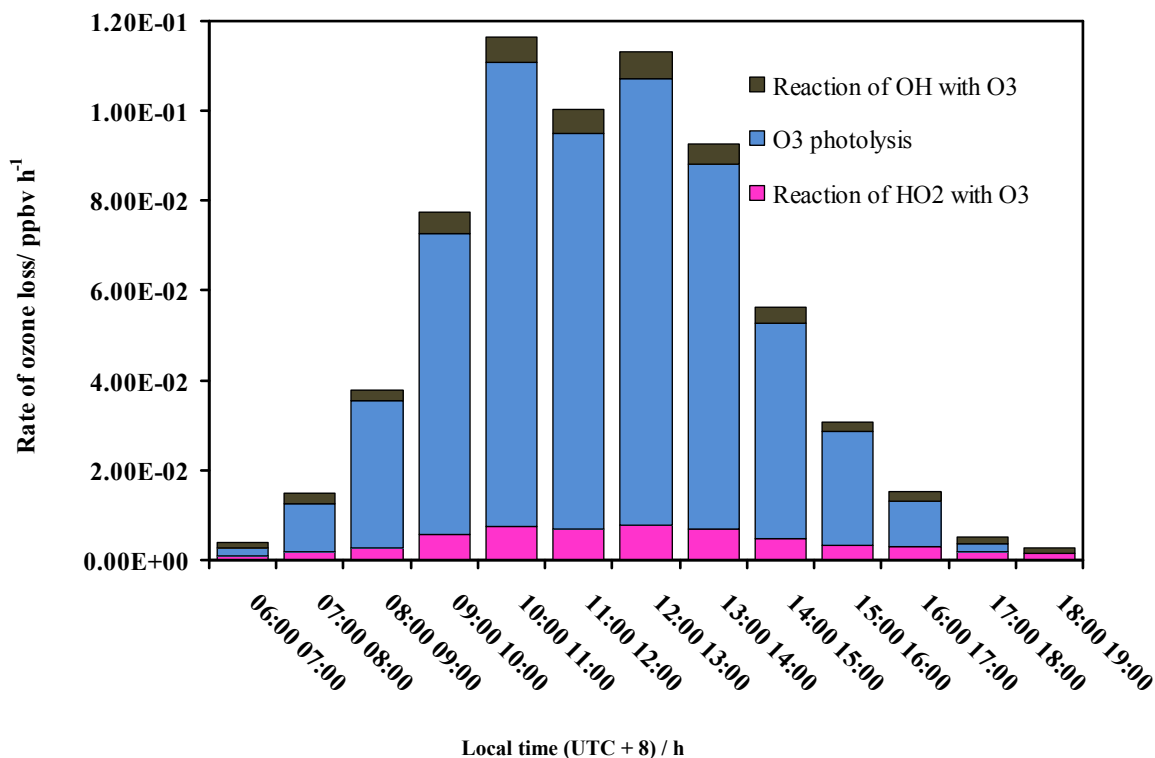


Figure 3.17 – Hourly averaged diurnal relative contributions of ozone loss terms to total  $L(O_3)$  between 06:00-19:00 LT from the campaign OP3 (3) during June-July 2008 at Bukit Atur in the tropical rainforest in Borneo.

Figure 3.17 shows that ozone photolysis is a dominant loss process to the ozone loss. Figure 3.17 shows that the ratio of the  $OH+O_3$  and  $HO_2+O_3$  reactions to  $L(O_3)$  are still small during OP3 (3) for daytime. All three loss processes have photochemical origin and these three loss processes are largest around middle of the day. Figures 3.14 and 3.17 represent a comparison between calculated during OP3 (1) and OP3 (3) photochemical ozone loss and the contribution of the individual terms between 06:00-19:00 LT,  $L(O_3)$  which has similar fraction to OH concentration for during OP3 (1) and OP3 (3).

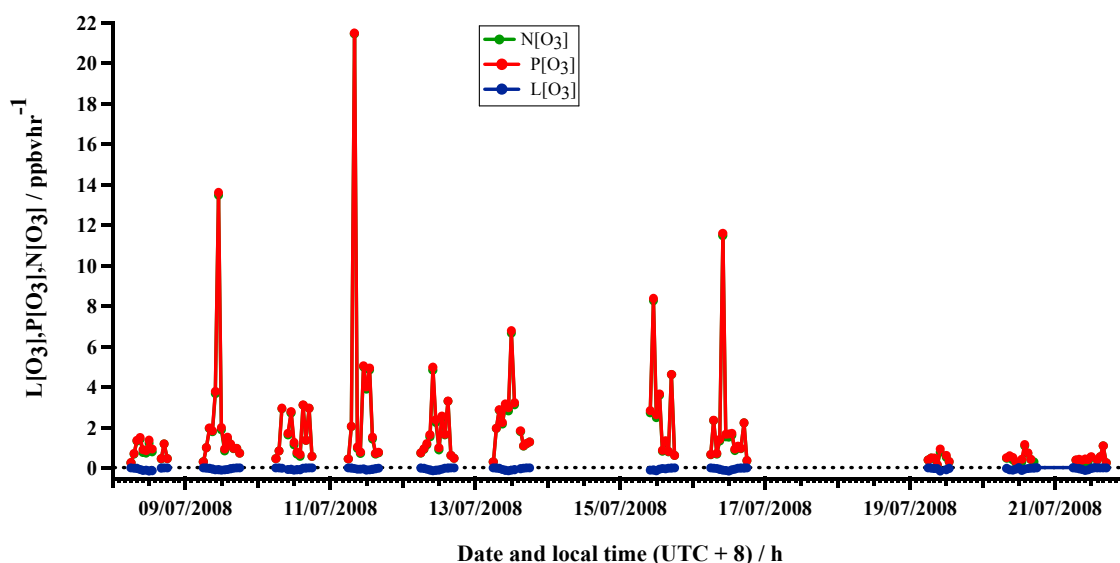


Figure 3.18 – Hourly averaged time series of ozone production rate,  $P(O_3)$  ozone loss rate,  $L(O_3)$  and net ozone rate,  $N(O_3)$  between 06:00-19:00 LT from the campaign OP3 (3) during June-July 2008 at Bukit Atur in the tropical rainforest in Borneo.

Figure 3.18 shows hourly averaged time series of  $P(O_3)$ ,  $L(O_3)$  and  $N(O_3)$  between 06:00-19:00 LT during the OP3 (3) campaign. The ozone production values are still net positive during OP3 (3) and indeed the median and mean  $N(O_3)$  values for the entire time series are higher than for OP3 (1) campaign. The median  $N(O_3)$  value for the OP3 (3) time series is  $0.98 \text{ ppbv hr}^{-1}$  and compared to  $0.51 \text{ ppbv hr}^{-1}$  for OP3 (1). The mean  $N(O_3)$  value for the OP3 (3) time series is  $1.80 \text{ ppbv hr}^{-1}$  and compared to  $0.68 \text{ ppbv hr}^{-1}$  for OP3 (1). Substantial day time value of  $N(O_3)$  were calculated up to  $21 \text{ ppbv hr}^{-1}$  at 08:30 on 11<sup>th</sup> July during OP3 (3) campaign as shown in Figure 3.18. Figure 3.7 and 3.18 show, the large spike of NO determines large values for  $N(O_3)$ , calculated at  $\sim 21 \text{ ppbv hr}^{-1}$  (See Section 3.3.2 for further discussion on the limitation of data analysis based on hourly average, especially sunrise and sunset).

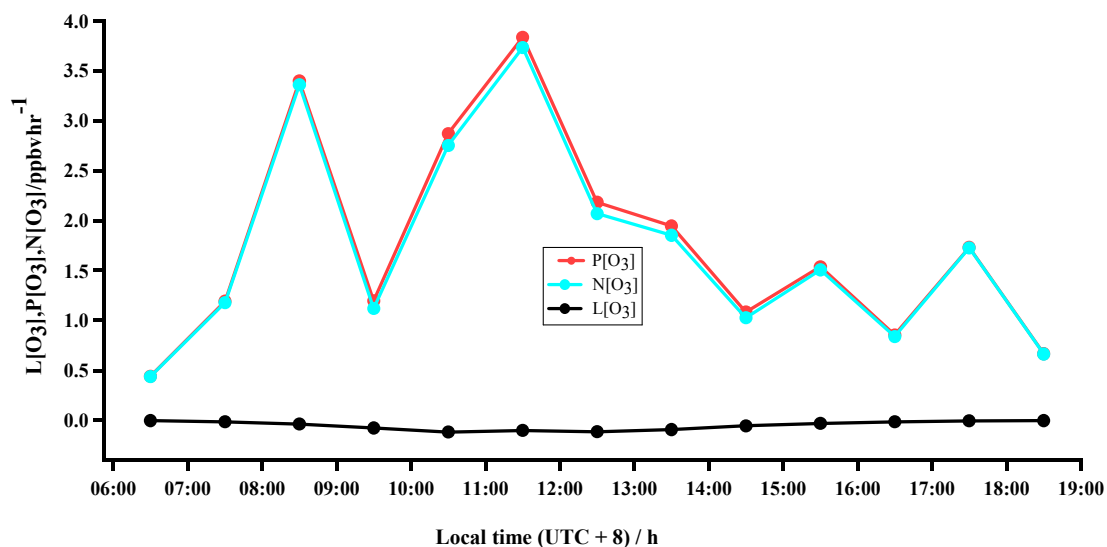


Figure 3.19 - Hourly averaged diurnal data for  $N(O_3)$ ,  $P(O_3)$ , and  $L(O_3)$  between 06:00-19:00 LT from the campaign OP3 (3) during June-July 2008 at Bukit Atur in the tropical rainforest in Borneo. Figure 3.19 generated from the hourly averaged time series of ozone production rate,  $P(O_3)$  ozone loss rate,  $L(O_3)$  and net ozone rate,  $N(O_3)$  show previously in Figure 3.18.

The hourly averaged diurnal data of  $N(O_3)$ ,  $P(O_3)$ , and  $L(O_3)$  for whole campaign between 06:00-19:00 LT have been constructed from averaging the time series of  $N(O_3)$ ,  $P(O_3)$ , and  $L(O_3)$  data for the corresponding time as shown in Figure 3.18 (see Section 3.1.3 for data averaging process). Figure 3.19 shows hourly averaged diurnal data for  $N(O_3)$ ,  $P(O_3)$ , and  $L(O_3)$  between 06:00-19:00 LT during the OP3 (3) campaign. The  $P(O_3)$  diurnal profile has two different peaks as shown in Figure 3.19.  $P(O_3)$  appears to closely follow both NO and peroxy radicals in terms of their peaks between 06:00-19:00 LT. The NO peak time was observed during early morning (between 08:00-09:00 LT), e.g. Pike *et al.*, (2010) and Pugh *et al.*, (2010)), while peroxy radicals exhibit a diurnal cycle with a midday peak as showed in Figures 3.10 and 3.12. It might be suggested that the early morning and midday peaks are associated with NO and peroxy radicals, respectively. The highest  $P(O_3)$  and  $N(O_3)$  values during daytime peaked at 11:30 h LT and there is a tendency for the values to vary during day

time during OP3 (3) shown in Figure 3.19. It can be noticed in Figures 3.16 and 3.19 the way the mean diurnal cycles differs from one season to the other. Furthermore, the explanation for the increase and the decrease in ozone production for the two periods, June-July and April-May days, is considered to be the difference that arises from  $P(O_3)$  compared to  $L(O_3)$  between the two seasons,  $P(O_3)$  has a 62 % difference, while the values for  $L(O_3)$  are almost equal.

The hourly averaged of rates for photolysis of ozone, the reaction of ozone with OH and the reaction of ozone with  $HO_2$  were obtained between 06:00-19:00 LT for the OP3 (1) and OP3 (3) campaigns (see Section 3.1.3 and beginning of this Section 3.2.3.5 for data averaging process). A comparison between OP3 (1) and OP3 (3) campaigns during April-May and June-July 2008 in terms of the photochemical total loss rates  $L(O_3)$  and their percentage contribution to the overall loss rate between 06:00-19:00 LT are shown in the Table 3.5.

<b>Ozone removal, <math>L(O_3)</math> / ppbv day<sup>-1</sup></b>				
<b>Experiment</b>	<b>Photolysis</b>	<b><math>HO_2+O_3</math></b>	<b><math>OH+O_3</math></b>	<b>Total</b>
<b>OP3 (1) (April-May)</b>	$0.73 \pm 0.05$ (87)	$0.07 \pm 0.01$ (8)	$0.04 \pm 0.01$ (5)	$0.84 \pm 0.07$
<b>OP3 (3) (June-July)</b>	$0.57 \pm 0.04$ (86)	$0.05 \pm 0.01$ (8)	$0.04 \pm 0.01$ (6)	$0.66 \pm 0.06$

Table 3.5 - A comparison between the campaigns OP3 (1) during April-May and OP3 (3) during June-July 2008 at Bukit Atur in the tropical rainforest in Borneo in terms of the hourly averaged time series of photochemical total loss rates  $L(O_3)$  and their percentage contribution in brackets to the overall loss rates between 06:00-19:00 LT.

The percentage contribution for the ozone photolysis during OP3 (1) and OP3 (3) campaigns, respectively are 87 and 86 between 06:00-19:00 LT. Thus in the case of

tropical rainforest in Borneo, the photochemical loss process for ozone is shown to be mainly obtained through photolysis in both seasons. The lowest percentage contribution to the ozone loss is via the reaction of OH with ozone.

The hourly averaged values of  $N(O_3)$  were also calculated between 06:00-19:00 LT for the OP3 (1) and OP3 (3) campaigns (see Section 3.1.3 and beginning of this Section 3.2.3.5 for data averaging process). Table 3.6 provides details of  $N(O_3)$  in terms of the median, mean, standard deviation and 10<sup>th</sup> and 90<sup>th</sup> percentiles between 06:00-19:00 LT values.

<b>Ozone tendencies <math>N(O_3)</math> /ppbv hr<sup>-1</sup></b>		
	<b>OP3 (1)</b>	<b>OP3 (3)</b>
<b>Median</b>	0.51	0.98
<b>Mean</b>	0.68	1.80
<b>Standard deviation</b>	0.57	2.68
<b>10th percentile</b>	0.27	0.37
<b>90th percentile</b>	1.10	3.38

Table 3.6 –Hourly averaged time series of  $N(O_3)$ , Median, mean, standard deviation and 10<sup>th</sup> and 90<sup>th</sup> percentiles between 06:00-19:00 LT from the campaigns OP3 (1) during April-May and OP3 (3) during June-July 2008 at Bukit Atur in the tropical rainforest in Borneo.

The calculated net ozone production rate during April-May and June-July periods are not same, while the fact that between 06:00-19:00 LT mean net ozone production rate during June-July period is ~ 2.6 times bigger compared to April-May. There were higher median and standard deviation values of net ozone production rate calculated in OP3 (3) compared to OP3 (1). These calculations are mainly caused by the seasonal

variations of NO and peroxy radical. The basis for ozone production rate is further discussed in the next paragraph and section 3.2.3.7. Higher concentration of NO measured in the OP3 (3) campaign compared to OP3 (1) campaign as shown in Figure 3.8 and 3.7, the concentration of peroxy radicals were slightly lower in the OP3 (1) than in the OP3 (3) campaign as shown in Figures 3.10 and 3.12.

Hourly averaged of  $N(O_3)$ ,  $P(O_3)$ , and  $L(O_3)$  were calculated between 06:00-19:00 LT for OP3 (1) and OP3 (3) campaigns. Table 3.7 shows hourly averaged time series of  $N(O_3)$ ,  $P(O_3)$  and  $L(O_3)$  between 06:00-19:00 LT during OP3 (1) and OP3 (3) campaigns (see Section 3.1.3 and beginning of this Section 3.2.3.5 for data averaging process).

Rate / ppbv hr <sup>-1</sup>	OP3 (1)	OP3 (3)
$P(O_3)$	0.74	1.85
$L(O_3)$	0.06	0.05
$N(O_3)$	0.68	1.80

Table 3.7 - Hourly averaged time series of  $N(O_3)$ ,  $P(O_3)$  and  $L(O_3)$  between 06:00-19:00 LT from the campaigns OP3 (1) during April-May and OP3 (3) during June-July 2008 at Bukit Atur in the tropical rainforest in Borneo.

It can be observed in Table 3.7 that  $L(O_3)$  is similar for both campaigns, but  $P(O_3)$  is much bigger in OP3 (3), while  $N(O_3)$  is positive for both OP3 campaigns. The rate of ozone production is depending on the concentration of NO<sub>x</sub> and VOCs (see Section 1.4.4 in Chapter 1). There were higher concentration of NO<sub>x</sub> and isoprene measured in OP3 (3) than in OP3 (1) as shown in Figures 3.7 and 3.8. Concentration of HO<sub>2</sub>+RO<sub>2</sub> was slightly higher in OP3 (3) than in OP3 (1) as shown in Figures 3.10 and 3.12. Hewitt *et al.*, (2010) observed that isoprene was the most abundant biogenic compound

and the concentrations of other biogenic VOCs, including acetone and acetaldehyde were smaller (see also Table 3.3 for their mixing ratio). Increasing NO<sub>x</sub> concentration will lead to increase of the rate of ozone production whilst enhancing isoprene concentrations will reduce the rate of ozone production (will explained in Section 3.2.3.7). Section 3.2.3.7 will also explain that the photochemical ozone production limited by NO<sub>x</sub> and not limited by isoprene or peroxy radicals. It might be concluded that the magnitude of photochemical ozone production influenced by the availability of NO<sub>x</sub> during the period between June-July than April-May for the in-situ ozone production through photochemistry.

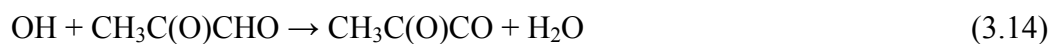
### 3.2.3.6 Peroxy radicals and isoprene

An important sources for peroxy radical production can be biogenic hydrocarbons such as isoprene, owing to their fast reaction with primary atmospheric oxidants such as OH and NO<sub>3</sub>, and also owing to the fact that large quantities of isoprene emitted from the rainforest.

From data from an EASE 96 (Eastern Atlantic Summer Experiment) field campaign at Mace Head in Ireland, it was found that biogenic species such as isoprene can be essential for the production of peroxy radicals. Figure 3.20 shows a schematic view of the chemical mechanism for the OH-initiated oxidation of isoprene. The initial OH reaction leads to the formation of two (major) products: methyl vinyl ketone (CH<sub>2</sub>CHC(O)CH<sub>3</sub>, MVK) which is the major product (ca. 50% of the total product formation) and methacrolein (CH<sub>2</sub>C(CH<sub>3</sub>)CHO, MACR) which is the minor product (ca. 25% of the total product formation) (Paulson *et al.*, 1992a, 1992b and 1992c). The rest of 25% of the total product formation is to other products. Jenkin *et al.*, (1997) showed that peroxy acetyl radicals can be formed through MVK and MACR photolysis, viz



Another method leading to peroxy acetyl production is through MVK and MACR oxidation (reaction with OH) leading to the formation of methyl glyoxal (CH<sub>3</sub>C(O)CHO). Peroxy acetyl radical has two routes of formation from MVK and MACR: loss of methyl glyoxal from MVK and MACR either through oxidation with OH (by leading the reactions of 3.14 and 3.15) or photolysis (by the reaction of 3.16).



where PA is peroxy acetyl radical

High concentrations of peroxy acetyl radical can be obtained through isoprene oxidation. Further, as per scheme 3.20 there are a wide range of peroxy radicals produced by the OH initiated oxidation of isoprene, as well as potentially via O<sub>3</sub> and NO<sub>3</sub>.

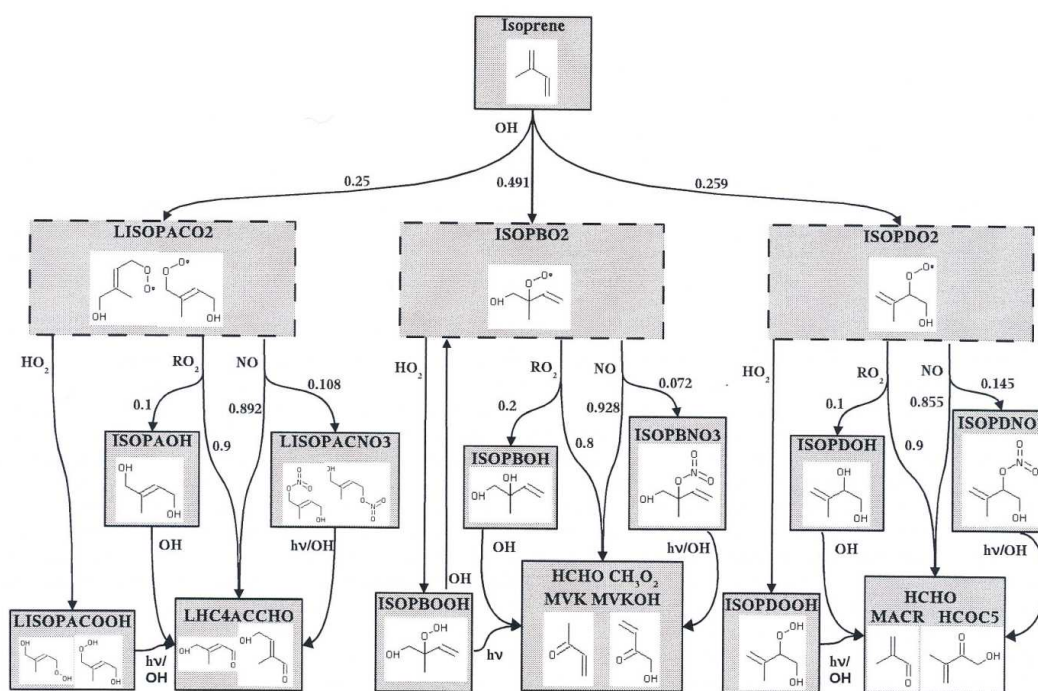


Figure 3.20 - The oxidation of isoprene mechanism (Taraborrelli *et al.*, 2009).

HO<sub>2</sub>+RO<sub>2</sub> was measured by PERCA, whilst isoprene measured by PTRMS (see Table 3.2). The hourly averaged diurnal cycles of peroxy radical (see Figures 3.10 and 3.12)

and isoprene for whole campaign have constructed from the averaging time series of peroxy radical (see left graph on Figure 3.9 for OP3 (1) and right graph on Figure 3.9 for OP3 (3) campaigns) and isoprene (middle graph on Figures 3.7 for OP3 (1) and middle graph on Figures 3.8 for OP3 (3) campaigns) data for corresponding time (see section 3.1.3 for data averaging process). Taking the natural logarithms of hourly-averaged diurnal cycle data of isoprene and peroxy radical concentrations and plotting logarithm [isoprene] vs. logarithm [peroxy radical] yielded scatter plot with good linear correlations. The gradients of the plots,  $d\ln(\text{peroxy radical})/d\ln(\text{isoprene})$ , provides a measure of the sensitivity of peroxy radical to isoprene. Graphs for both the campaigns are shown together in Figure 3.21 for day time between 06:00-19:00 LT, in Figure 3.22 for before midday between 06:00-13:00 LT as the top graph and for after midday between 12:00-19:00 LT as the bottom graph, in respectively.

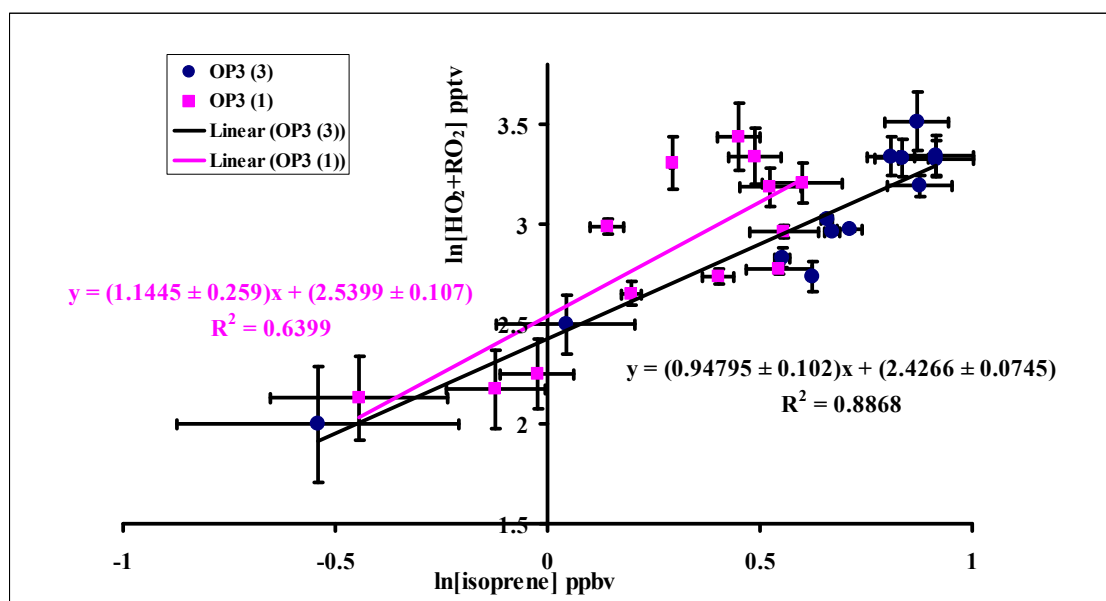


Figure 3.21 – Natural logarithms of hourly-averaged diurnal cycle data of isoprene and peroxy radical concentrations between 06:00-19:00 LT from the campaigns OP3 (1) during April-May and OP3 (3) June-July 2008 together at Bukit Atur in the tropical rainforest in Borneo. Error bars show  $\pm 1\sigma$  of hourly averaged diurnal values.

Both campaigns shown in Figure 3.21 have a fairly similar trend of peroxy radicals with isoprene between 06:00-19:00 LT, with a slightly greater dependence on isoprene

for the first campaign: that campaign has a gradient of just 1.14, compared to 0.95 in the second campaign.

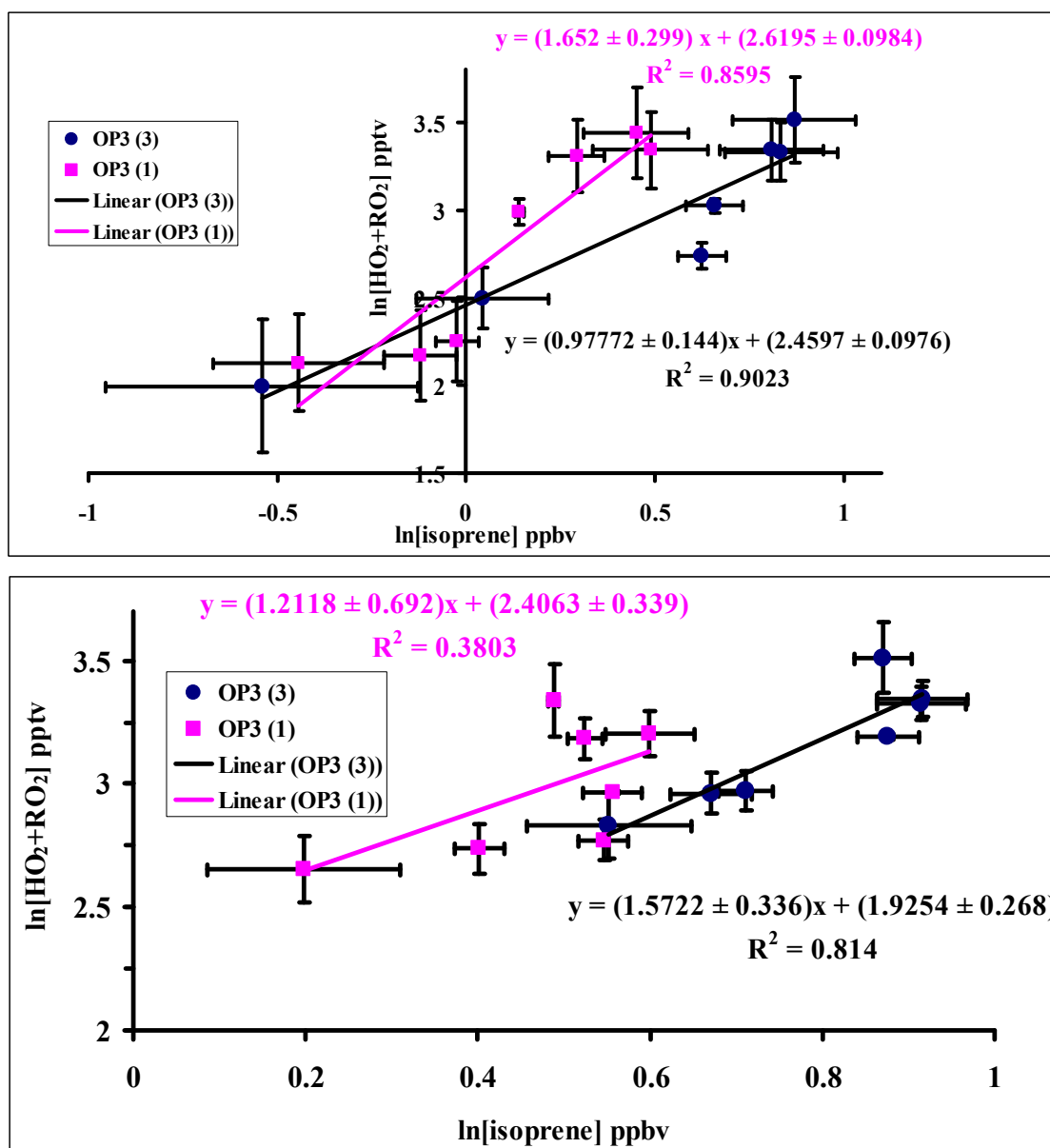


Figure 3.22 - Natural logarithms of hourly-averaged diurnal cycle data of isoprene and peroxy radical concentrations between 06:00-13:00 LT as top graph and between 12:00-19:00 LT as bottom graph from the campaigns OP3 (1) during April-May and OP3 (3) during June-July 2008 together at Bukit Atur in the tropical rainforest in Borneo. Error bars show  $\pm 1\sigma$  of hourly averaged diurnal values.

The gradients and correlation coefficients are listed in Table 3.8 for before midday between 06:00-13:00 LT, after midday between 12:00-19:00 LT and between 06:00-19:00 LT for both campaigns.

ln[peroxyradical] vs. ln[isoprene]	OP3 (1)		OP3 (3)	
	Gradient	Correlation	Gradient	Correlation
Before midday	1.65	0.86	0.98	0.90
After midday	1.21	0.38	1.57	0.81
Day time	1.14	0.64	0.95	0.89

Table 3.8 - Gradient and correlation coefficients of natural logarithms of hourly-averaged diurnal cycle data of isoprene and peroxy radical concentrations between 06:00-13:00 LT, between 12:00-19:00 LT and between 06:00-19:00 LT from the campaigns OP3 (1) during April-May and OP3 (3) during June-July 2008 at Bukit Atur in the tropical rainforest in Borneo. These values have been taken from the correlation plots in Figure 3.21 and 3.22.

From Figures 3.21 and 3.22 it can be observed that during the OP3 (1) campaign, peroxy radical formation is more sensitive to isoprene concentrations in the morning time and less sensitive to the whole day time to the isoprene relative to afternoon time: morning time has a gradient is 1.65 and the correlation is 0.86; day time has a gradient is 1.14 and correlation is 0.64 compared to 1.21 and 0.38 in afternoon time; on the other hand, it has been concluded for the OP3 (3) campaign, peroxy radical formation is less sensitive in the morning time and greater sensitive to afternoon time to the isoprene compare to the whole day time: morning time has a gradient is 0.98 and correlation is 0.90 where as afternoon time has a gradient is 1.57 and 0.81 compared to 0.95 and 0.89 in day time. It is interesting to note that the daytime gradient does not lie in between morning and afternoon. South East Asian rainforest peroxy radical

production was more sensitive to isoprene during the morning in April-May and afternoon in the June-July. Mihele and Hastie (2003) found a highly significant positive correlation between the peroxy radical concentration and that of isoprene ( $R^2 = 0.8$ ) for a campaign at PROPHET 97 near Pellston, Michigan (see Section 1.5.4.3 in Chapter 1 for experiment details).

### 3.2.3.7. The ozone production rate $P(O_3)$ , peroxy radicals, isoprene and NO relationships

Correlations plots were generated to understand how the rate of ozone production correlates with the changing concentration of  $HO_2+RO_2$ , NO and isoprene. This analysis carried out between 10:00-16:00 LT because Hewitt *et al.*, (2009) demonstrated the similar analysis between 10:00-16:00 LT. These plots were constructed from the following averaged diurnal cycle data:  $P(O_3)$  (see Figure 3.16 for OP3 (1) and Figure 3.19 for OP3 (3));  $HO_2+RO_2$  (see Figures 3.10 and 3.12 for OP3 (1) and OP3 (3)); NO (generated from the top graph on Figure 3.7 for OP3 (1) and from the top graph on Figure 3.8 for OP3 (3)); and isoprene (generated from the middle graph on Figure 3.7 for OP3 (1) and from the middle graph on Figure 3.8 for OP3 (3)) (see Table 3.2 and see Section 3.1.3 for data averaging process). Plots of  $\ln P(O_3)$  vs.  $\ln(HO_2+RO_2)$ ,  $\ln P(O_3)$  vs.  $\ln(NO)$  and  $\ln P(O_3)$  vs.  $\ln(\text{isoprene})$  were generated for both campaigns. Figure 3.23 shows  $\ln P(O_3)$  vs.  $\ln(HO_2+RO_2)$ , Figure 3.24 show  $\ln P(O_3)$  vs.  $\ln(NO)$  (bottom graph) and  $\ln P(O_3)$  vs.  $\ln(\text{isoprene})$  (top graph) respectively between 10:00-16:00 LT for both campaigns together.

Figure 3.23 shows that, the natural logarithms of  $P(O_3)$  with the natural logarithms of  $HO_2+RO_2$  concentration exhibits a poor correlation ( $R^2 = 0.20$ ) and ( $R^2 = 0.02$ ) in OP3 (1) and OP3 (3) respectively.

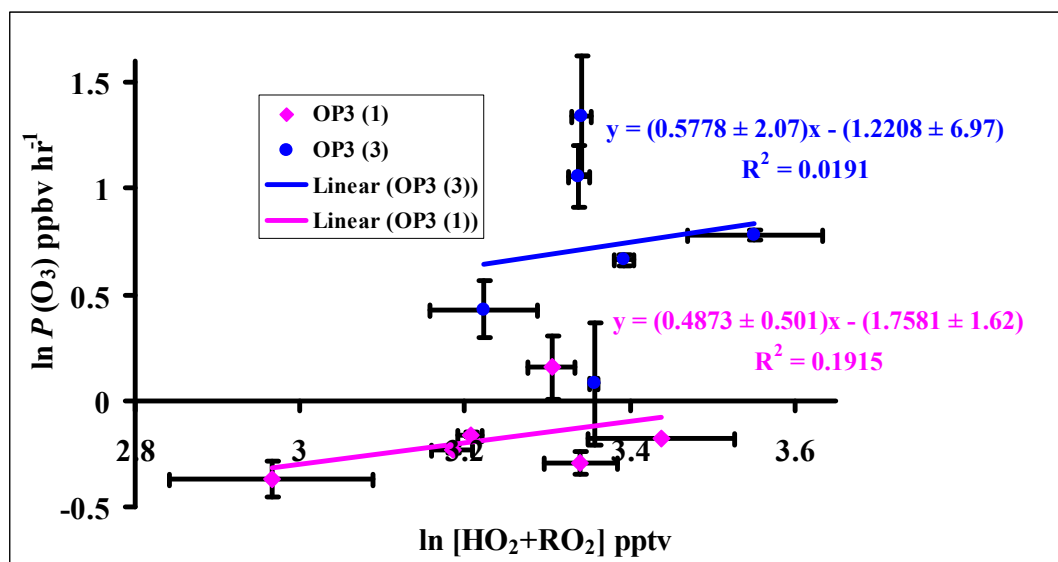


Figure 3.23 - Natural logarithms of hourly-averaged diurnal cycle data of  $P(O_3)$  and peroxy radical concentrations between 10:00-16:00 LT from the campaigns OP3 (1) during April-May and OP3 (3) during June-July 2008 at Bukit Atur in the tropical rainforest in Borneo. Error bars show  $\pm 1\sigma$  of hourly averaged diurnal values.

For the OP3 (1) and OP3 (3) campaigns, the absence of any correlation would appear to suggest that  $P(O_3)$ , is not limited by peroxy radical. Higher concentrations of NO and isoprene were measured in OP3 (3) than in OP3 (1), and there is also a higher rate of ozone production calculated from measured species in OP3 (3) than in OP3 (1).

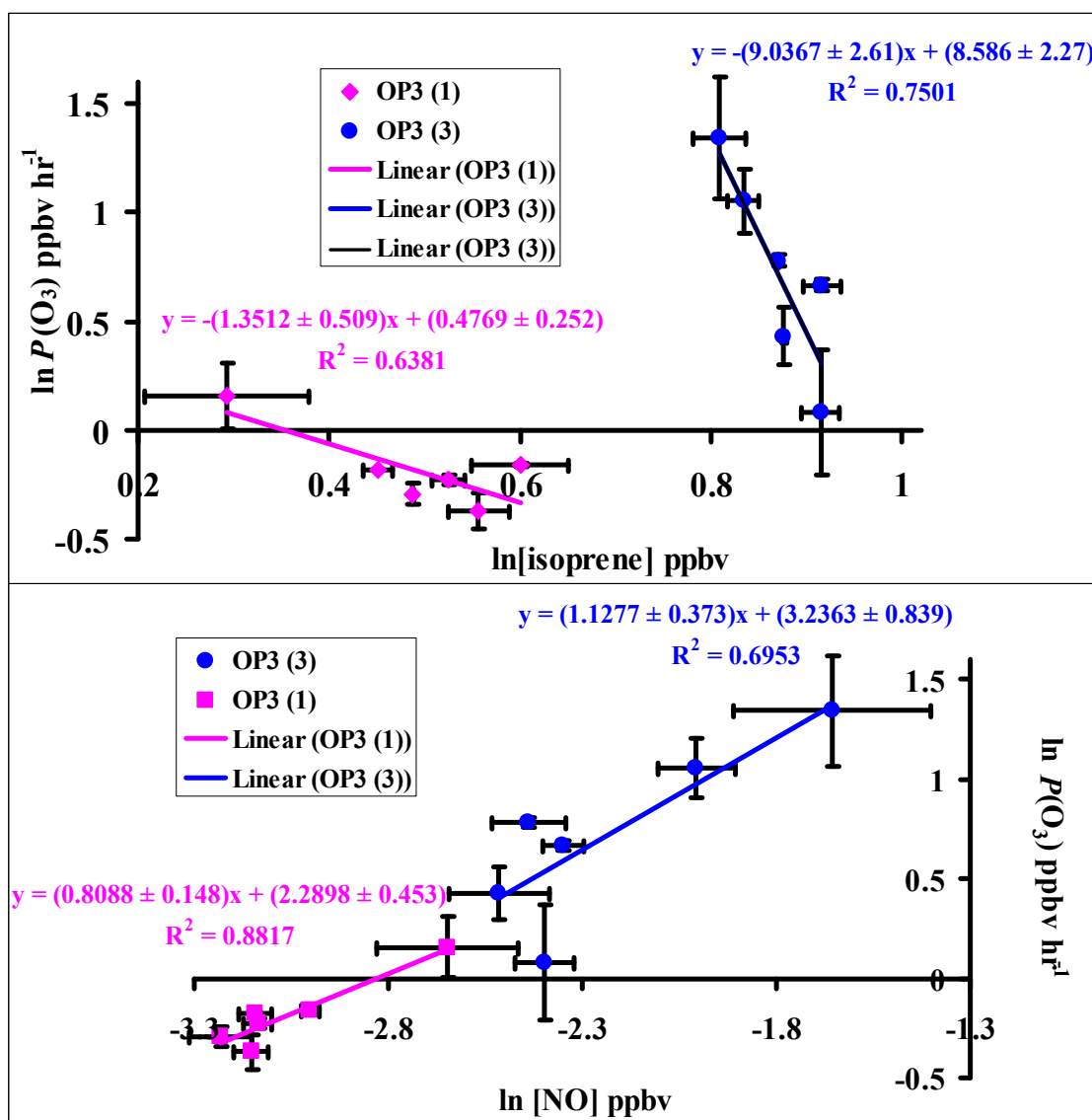


Figure 3.24 - Natural logarithms of hourly-averaged diurnal cycle data of  $P(O_3)$  and isoprene concentrations (top graph) and natural logarithms of hourly-averaged diurnal cycle data of  $P(O_3)$  and NO concentrations (bottom graph) between 10:00-16:00 LT from the campaigns OP3 (1) during April-May and OP3 (3) during June-July 2008 together at Bukit Atur in the tropical rainforest in Borneo. Error bars show  $\pm 1\sigma$  of hourly averaged diurnal values.

The time period between 10:00-16:00 LT during the OP3 (1) and OP3 (3) campaigns, the hourly averaged diurnal concentrations of NO increased to 113 pptv in OP3 (3) from 48 pptv in OP3 (1) whilst hourly averaged diurnal concentrations of isoprene increased to 2.45 pptv in OP3 (3) from 1.63 pptv in OP3 (1). Figure 3.24 (bottom graph) shows the  $\ln P(O_3)$  vs. NO positive gradient increased to 1.13 from 0.81 whereas

Figure 3.24 (top graph) shows the  $\ln P(\text{O}_3)$  vs. isoprene negative gradient increased to 5.75 from 1.35: these results prove that ozone production rate has a positive and negative correlation with NO and isoprene respectively and also  $P(\text{O}_3)$  itself limited by NO.

Table 3.9 shows the gradients and correlation coefficients of  $\ln P(\text{O}_3)$  vs.  $\ln(\text{HO}_2+\text{RO}_2)$ ,  $\ln P(\text{O}_3)$  vs.  $\ln(\text{NO})$  and  $\ln P(\text{O}_3)$  vs.  $\ln(\text{isoprene})$  for both campaigns, respectively.

Ln[peroxyradical] vs. ln[isoprene]	OP3 (1)		OP3 (3)	
	Gradient	Correlation	Gradient	Correlation
$\ln P(\text{O}_3)$ vs. $\ln[\text{isoprene}]$	-1.35	0.64	-5.75	0.48
$\ln P(\text{O}_3)$ vs. $\ln[\text{HO}_2+\text{RO}_2]$	0.49	0.20	0.58	0.02
$\ln P(\text{O}_3)$ vs. $\ln[\text{NO}]$	0.81	0.88	1.13	0.70

Table 3.9 - Gradient and correlation coefficients for natural logarithms of hourly-averaged diurnal cycle data of  $P(\text{O}_3)$  vs. isoprene,  $P(\text{O}_3)$  vs.  $\text{HO}_2+\text{RO}_2$  and  $P(\text{O}_3)$  vs. NO between 10:00-16:00 LT from the campaigns OP3 (1) during April-May and OP3 (3) during June-July 2008 at Bukit Atur in the tropical rainforest in Borneo.

Increasing  $\text{NO}_x$  concentrations will lead to increase of the rate of ozone production, and enhancing isoprene concentrations will reduce the rate of ozone production. Hewitt *et al.*, (2009) noticed how increase of  $\text{NO}_x$  concentration rapidly determines an increase of the rate of ozone production, unlike the case of isoprene.

For example, during the OP3 (1) campaign: hourly averaged calculated of  $P(\text{O}_3)$  (see Figure 3.16); hourly averaged measured concentrations of  $\text{HO}_2+\text{RO}_2$  (see left graph on Figure 3.9); NO (see top graph on Figure 3.7) and isoprene (see middle graph on

Figure 3.7) were performed between 06:00-18:00 (LT). Figure 3.25 shows examples of the strong correlation between NO and  $P(O_3)$  during day time.

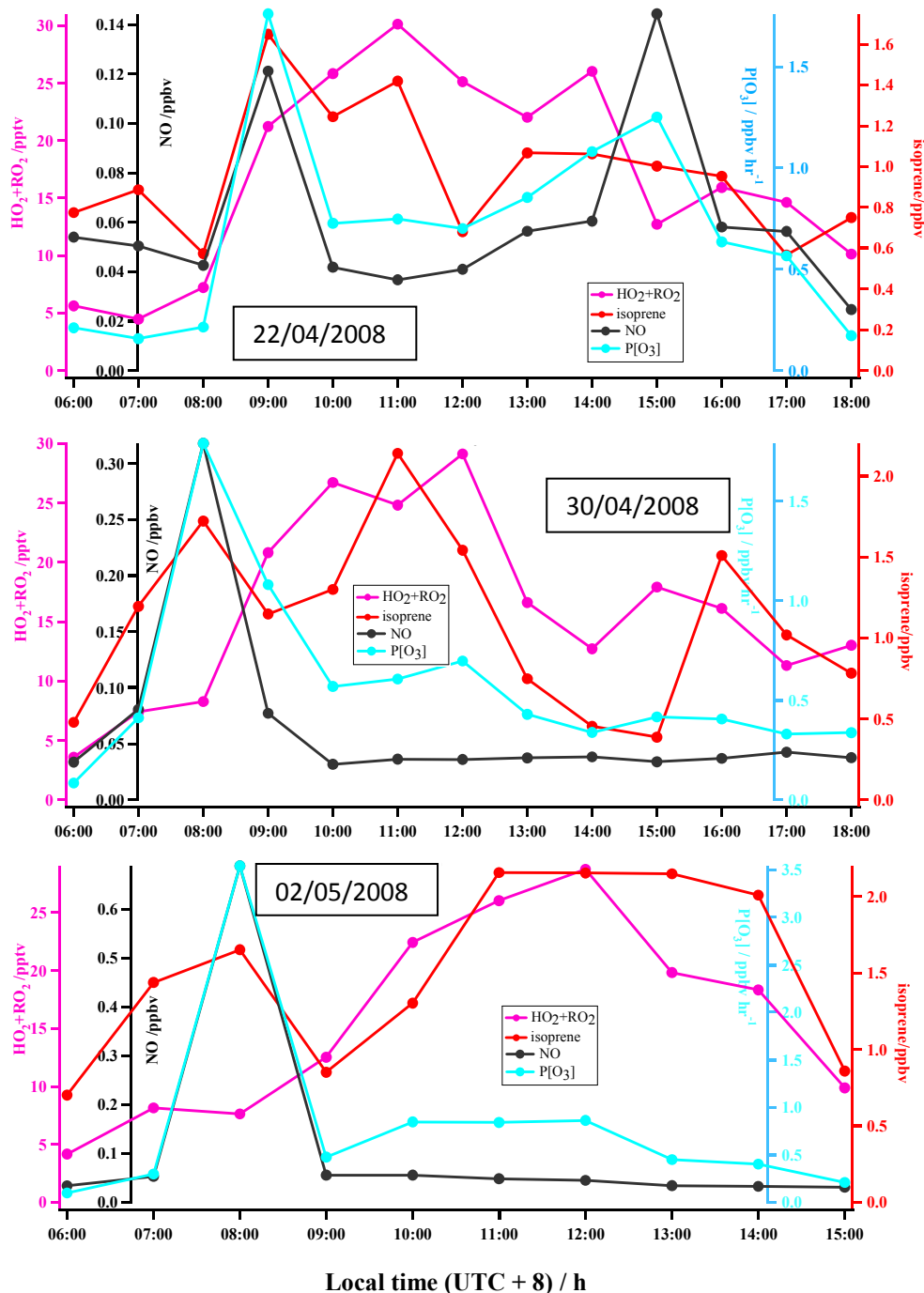


Figure 3.25 - Hourly average of peroxy radicals, isoprene, NO concentration, as well as the calculated  $P(O_3)$ , between 06:00-18:00 LT from the campaign OP3 (1) during April-May 2008 at Bukit Atur in the tropical rainforest in Borneo.

### 3.3 Radical budget

A steady state analysis of the production and loss of peroxy radicals during two of OP3 campaigns has been carried out based on the method described by Mihele and Hastie (2003). In this analysis, it is assumed that peroxy radicals are in steady state, thus

$$\frac{d[\text{HO}_2 + \text{RO}_2]}{dt} = P_{\text{HO}_2 + \text{RO}_2} - L_{\text{SR}} - L_{\text{NO}_2} = 0 \quad (\text{B})$$

where  $P_{\text{HO}_2 + \text{RO}_2}$  is the rate of production of peroxy radicals,  $L_{\text{SR}}$  is the rate of loss of peroxy radicals owing to self-reaction, and  $L_{\text{NO}_2}$  is the rate of loss of peroxy radicals owing to reaction of OH with  $\text{NO}_2$ . The reaction of OH with  $\text{NO}_2$  acts as a HOx sink, and not the direct reaction of peroxy radical with  $\text{NO}_2$ , where  $\text{HOx} = \text{OH} + \text{HO}_2 + \text{RO}_2$ . Assuming the major radical source is ozone photolysis,  $\gamma$  was introduced by Mihele and Hastie (2003) to represent the fraction of additional radical production from routes such as the photolysis of carbonyl compounds, PAN decomposition and alkene ozonolysis. A zero value of  $\gamma$  of zero indicates no excess production, whilst a  $\gamma$  of less than zero indicates that higher concentration of peroxy radical is obtained from ozone photolysis than is actually observed. Including the  $\gamma$  term, the radical production term becomes:

$$P_{\text{HO}_2 + \text{RO}_2} = 2 f * j(\text{O}^1\text{D})[\text{O}_3](1 + \gamma) \quad (\text{C})$$

where  $f$  is a measure of the proportion of  $\text{O}^1\text{D}$  produced that consequently reacts with water vapour to produce OH radicals and is given by equation D,

$$f = \frac{k_{3.11}[\text{H}_2\text{O}]}{k_{3.17}[\text{H}_2\text{O}] + k_{3.18}[\text{M}]} \quad (\text{D})$$

where  $k_{3.17}$  and  $k_{3.18}$  are the reaction rate coefficients for reaction 3.17 and reaction 3.18 respectively.



It may appear that there is an assumption in equation (C) that all OH, formed by the photolysis of ozone to form  $\text{O}(^1\text{D})$  and subsequent reaction of this  $\text{O}(^1\text{D})$  with water vapour, will then react with VOCs to form peroxy radicals, and that the potential loss of OH by reaction with  $\text{NO}_2$  has been ignored. However, OH loss by reaction with  $\text{NO}_2$  is accounted for in the peroxy radical loss due to reaction with  $\text{NO}_2$  term ( $L_{\text{NO}_2}$ ) in equation (B) (see later for equation (L)). Mihele and Hastie (2003) found that the self-reaction rates of  $\text{HO}_2$  and  $\sum_i R_i\text{O}_2$  are combined into a representative rate constant  $k_{\text{self}}$ , giving

$$\beta = \frac{L_{\text{NO}_2}}{L_{\text{SR}}}, \quad (\text{E})$$

and  $\beta$  is a measure of the dominant loss process for peroxy radicals. If  $\beta$  is less than one, then the dominant loss process is radical self-reaction,  $L_{\text{SR}}$ , rather than loss through reaction of OH with  $\text{NO}_2$ . Otherwise if  $\beta$  is greater than 1, the dominant loss process for peroxy radicals is by through the reaction of OH with  $\text{NO}_2$  ( $L_{\text{NO}_2}$ ). To describe the dominant loss mechanism and introducing parameter  $\alpha$  to describe the partitioning between  $\text{HO}_2$  and  $\text{RO}_2$ , thus

$$\alpha = \frac{[\text{HO}_2]}{[\text{HO}_2 + \text{RO}_2]} \quad (\text{F})$$

gives the radical loss terms as:

$$L_{HO_2+RO_2} = L_{SR} + L_{NO_2} \quad (G)$$

From equation (E),  $L_{NO_2} = \beta L_{SR}$  obtained, substituting  $L_{NO_2} = \beta L_{SR}$  into equation (G)

and taking out the factor,  $L_{SR}$

$$L_{HO_2+RO_2} = (1 + \beta)L_{SR} \quad (H)$$

where the loss owing to self-reaction is given by the following equations, (see Section 1.4.3 in Chapter 1)



$$L_{SR} = 2k_{3.19}[HO_2][HO_2] + 2k_{3.20}[HO_2][RO_2] + 2k_{3.21}[RO_2][RO_2] \quad (I)$$

The rate constants are  $k_{3.19} = 2.6 \times 10^{-12} \text{ cm}^3 \text{ molecule}^{-1} \text{ s}^{-1}$  (Atkinson *et al.*, 2006),  $k_{3.20} = 5.2 \times 10^{-12} \text{ cm}^3 \text{ molecule}^{-1} \text{ s}^{-1}$  (Atkinson *et al.*, 2006) and  $k_{3.21} = 3.5 \times 10^{-13} \text{ cm}^3 \text{ molecule}^{-1} \text{ s}^{-1}$  (Atkinson *et al.*, 2006) at 1 atmosphere pressure and 298 K (see Table 3.4). Hence, given their rate constants, assuming that  $k_{3.19} \approx k_{3.20}$ , and that  $k_{3.21}$  is slow ( $\ll k_{3.19} \approx k_{3.20}$ ) enough that reaction (3.21) can be discarded, Equation (I) reduces to that found in Mihele and Hastie (2003):

$$L_{SR} = 2k_{SR} \{ [HO_2]^2 + [HO_2][RO_2] \}$$

$$L_{SR} = 2k_{SR}[HO_2] \{ [HO_2] + [RO_2] \} \quad (J)$$

Substituting  $\alpha = \frac{[HO_2]}{[HO_2 + RO_2]}$  into equation (J)

$$\text{Equation (J) becomes } L_{SR} = 2k_{SR}\alpha[HO_2 + RO_2]^2 \quad (K)$$

$$\text{But } L_{NO_2} = k[OH][NO_2] \quad (L)$$

Substituting  $L_{SR}$  and  $L_{NO_2}$  into equation (E)

$$\beta = \frac{k[\text{OH}][\text{NO}_2]}{2\alpha k_{SR}[\text{HO}_2 + \text{RO}_2]^2} \quad (\text{M})$$

Substituting  $L_{SR}$  into equation (H)

$$L_{\text{HO}_2+\text{RO}_2} = 2k_{SR}\alpha(1+\beta)[\text{HO}_2 + \text{RO}_2]^2 \quad (\text{N})$$

However, the assumption in the derivation of the self-reaction loss rate that  $k_{3.19} \approx k_{3.20}$  only holds if  $\text{RO}_2$  is solely in the form of  $\text{CH}_3\text{O}_2$ , neglecting the contribution of other  $\text{RO}_2$  species, Parker, (2007), Parker *et al.*, (2009) and Brookes, (2010). Organic peroxy radicals are mainly in the form of  $\text{CH}_3\text{O}_2$  (see Section 3.2.3.2). Fast peroxy acetyl self-reaction results in the generation of methyl peroxy radical, (Roehl *et al.*, (1995); Pieterse *et al.*, (2009)). Thornton *et al.*, (2002) found that reactions of  $\text{HO}_2$  with peroxy acetyl radicals may not be as efficient HOx sinks, and may instead act to recycle OH. The reaction of peroxy radical (particularly those derived from isoprene, e.g. peroxy acetyl radicals) with  $\text{HO}_2$  regenerate OH, (Dillon and Crowley, 2008; Hasson *et al.*, (2004); Jenkin *et al.*, (2007)). The implication of this recycling is that both OH and as a result peroxy radicals may be sustained under low NOx conditions. Assuming that all  $\text{RO}_2$  is in the form of  $\text{CH}_3\text{O}_2$ , the peroxy radical steady state can thus be re-written as

$$\frac{d[\text{HO}_2 + \text{RO}_2]}{dt} = 2ff(\text{O}^1\text{D})[\text{O}_3](1+\gamma) - 2k_{SR}\alpha(1+\beta)[\text{HO}_2 + \text{RO}_2]^2 = 0 \quad (\text{O})$$

Under the assumption that  $[\text{HO}_2+\text{RO}_2]$  really is in steady state, equation (O) can be rearranged to give the following expression for peroxy radical concentrations,

$$[\text{HO}_2 + \text{RO}_2] = \sqrt{\frac{2ff(\text{O}^1\text{D})[\text{O}_3](1+\gamma)}{2k_{SR}\alpha(1+\beta)}}$$

$$[\text{HO}_2 + \text{RO}_2] = \sqrt{\frac{fj(\text{O}^1\text{D})[\text{O}_3]}{k_{SR}}} \sqrt{\frac{1}{\alpha}} \sqrt{\frac{1}{1+\beta}} \sqrt{1+\gamma} \quad (\text{P})$$

Alternatively the steady state equation (O) can be rearranged to give an expression for  $\gamma$ .

$$\gamma = \frac{[\text{HO}_2 + \text{RO}_2]^2 \alpha (1 + \beta) k_{SR}}{fj(\text{O}^1\text{D})[\text{O}_3]} - 1 \quad (\text{Q})$$

The hourly averaged time series of  $\beta$  was calculated using the equation of (M) between 06:00-19:00 LT during the OP3 (1) and OP3 (3) campaigns using the University of Leicester PERCA measurements of  $[\text{HO}_2 + \text{RO}_2]$  (see left graph on Figure 3.9 for OP3 (1) campaign, see right graph on Figure 3.9 for OP3 (3) campaign), University of Leeds FAGE measurements of  $[\text{OH}]$  (see Section 3.2.3.5 and Table 3.2) and  $[\text{HO}_2]$  ( $[\text{HO}_2]$  available for OP3 (3) (see Table 3.2 and see Section 3.2.3.5 for OP3 (1)). The University of York NOxy measurements of  $\text{NO}_2$  (see top graph on Figures 3.7 for OP3 (1) and see top graph on Figure 3.8 for OP3 (3)) also taken to calculate to  $\beta$  (see Table 3.2 and section 3.1.3 for data averaging process).

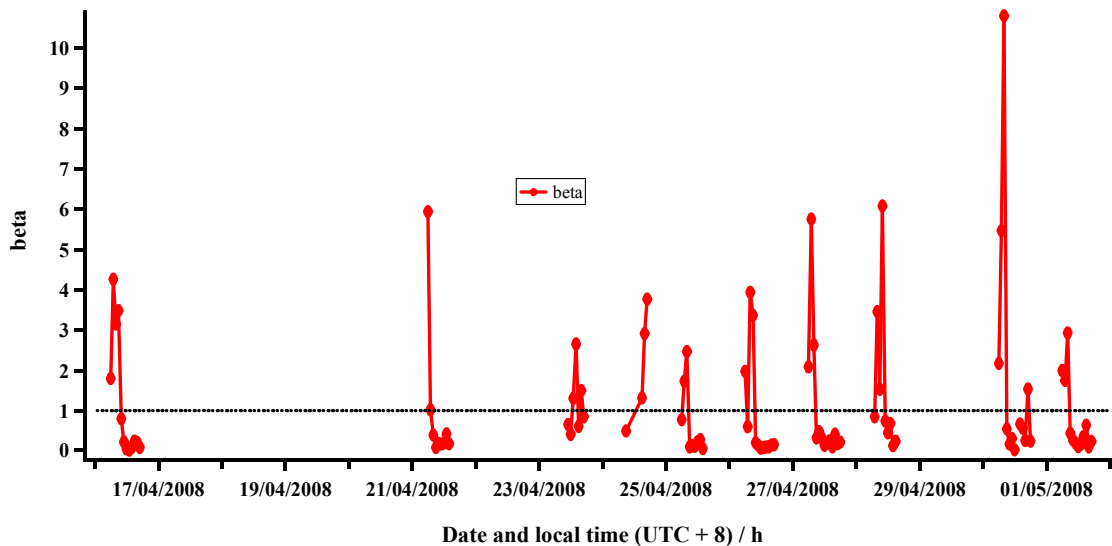


Figure 3.26 - Hourly averaged time series of  $\beta$  between 06:00-19:00 LT from the campaign OP3 (1) during April-May 2008 at Bukit Atur in the tropical rainforest in Borneo.

Figure 3.26 shows hourly averaged time series of  $\beta$  between 06:00-19:00 LT from the OP3 (1) campaign. It can be observed that,  $\beta$  is mostly less than 1; the median of beta is 0.41. The mostly  $\beta$  less than 1 values indicate that the loss of peroxy radical is dominated by the peroxy radical self-reaction, rather than the reaction of OH with  $\text{NO}_2$ . Large values of  $\beta$  ( $>1$ ) are calculated during early morning (06:00-19:00 LT) and late afternoon (18:00-19:00 LT) as shown in Figure 3.26. Considering the  $\beta$  values, this indicates that the loss of peroxy radical is controlled by the reaction of OH with  $\text{NO}_2$  rather than the peroxy radical self reaction during early morning and late afternoon. It could be implied that the concentration of  $\text{NO}_2$  is exceeded in early morning and late afternoon (early morning mixing ratio  $\sim 200$  pptv and late afternoon mixing ratio  $\sim 180$  pptv) than in the midday (mixing ratio  $\sim 90$  pptv), e.g. Pike *et al.*, (2010).

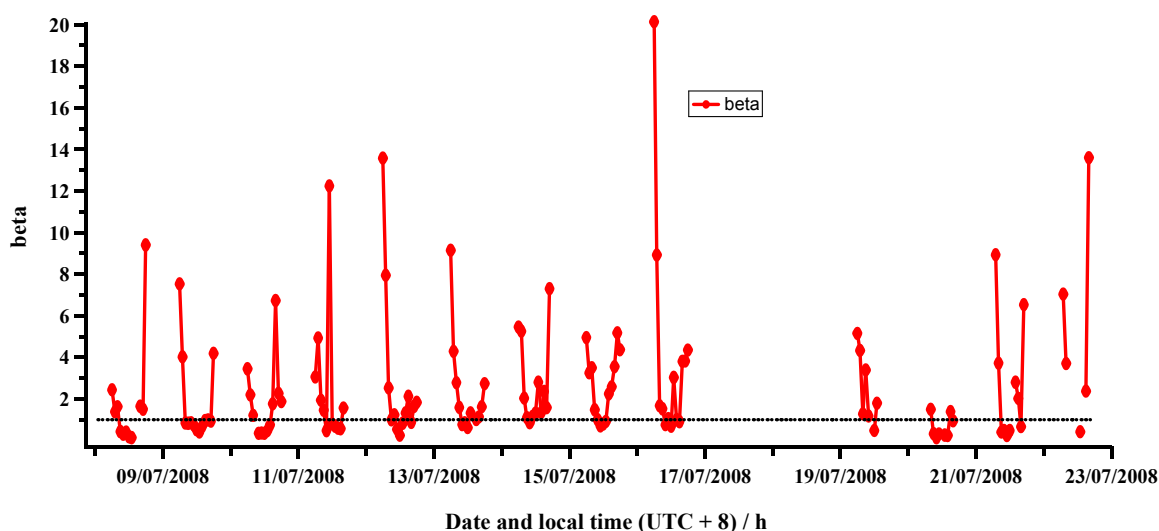


Figure 3.27 - Hourly averaged time series of  $\beta$  between 06:00-19:00 LT from the campaign OP3 (3) during June-July 2008 at Bukit Atur in the tropical rainforest in Borneo.

Figure 3.27 shows hourly averaged time series of  $\beta$  between 06:00-19:00 LT during the OP3 (3) campaign. In contrast to OP3 (1) (and Figure 3.26), the conclusion from Figure 3.27 is that the loss of peroxy radical in OP3 (3) is mainly determined by the reaction of OH with  $\text{NO}_2$  rather than the peroxy radical self- reactions because  $\beta$  is

mostly greater than 1, while the median of beta is 1.10. The median of  $\beta$  higher in OP3 (3) compared to OP3 (1) due to a larger quantity of  $\text{NO}_2$  available in OP3 (3). Therefore there is a greater loss of peroxy radicals through reaction of OH with  $\text{NO}_2$  when high concentrations of  $\text{NO}_2$  are available. The reaction of OH with  $\text{NO}_2$  has become the dominant loss process for peroxy radical in OP3 (3) and  $\beta$  changes from being less than 1 in OP3 (1) to being greater than 1 in OP3 (3).

Lower values of  $\beta$  ( $<1$ ) are calculated during midday as shown in Figure 3.26. Considering the  $\beta$  values, this indicates that the loss of peroxy radical is controlled by the peroxy radical self-reaction, rather than the reaction of OH with  $\text{NO}_2$  during midday. It can be implemented by the combination of alpha,  $k_{SR}$  and  $[\text{HO}_2+\text{RO}_2]$ ,  $[\text{NO}_2]$ . Peroxy radicals are maximised during midday ( $\sim 33$  pptv) than rest of the day, (see Figures 3.10 and 3.12). Concentrations of peroxy radicals are key factor to drive the self reactions during the midday. It might be suggested that the Equation (M) shows that  $\beta$  is inversely proportional to square of the peroxy radicals.

The hourly averaged time series of  $\gamma$  was calculated using the equation of (Q) between 06:00-19:00 LT from the measured atmospheric species during the OP3 (1) and OP3 (3) campaigns: University of Leicester PERCA measurements of  $[\text{HO}_2+\text{RO}_2]$  (see left graph on Figure 3.9 for OP3 (1) campaign, see right graph on Figure 3.9 for OP3 (3) campaign); University of Leeds FAGE measurements of  $[\text{OH}]$  (see Section 3.2.3.5 and Table 3.2) and  $[\text{HO}_2]$ , ( $[\text{HO}_2]$  is available for OP3 (3) (see Table 3.2), see Section 3.2.3.5 for OP3 (1)); University of Leeds filter radiometer measurement of  $j(\text{O}^1\text{D})$  (see Figure 3.9); University of York thermo Electron Instrument (TEI) Model 49i UV Analyser measurement of ozone (see bottom graph on Figure 3.7 for OP3 (1) and see

bottom graph on Figure 3.8 for OP3 (3)); and University of York NO<sub>x</sub> measurement of NO<sub>2</sub> (see top graph on Figures 3.7 for OP3 (1) and see top graph on Figure 3.8 for OP3 (3)) (see Table 3.2 and section 3.1.3 for the data averaging process). Figure 3.28 shows hourly averaged time series of  $\gamma$  between 06:00-19:00 LT during the OP3 (1) campaign. Gamma is mostly less than 0, except early mornings and late afternoons for every day, while the median of gamma is -0.76.

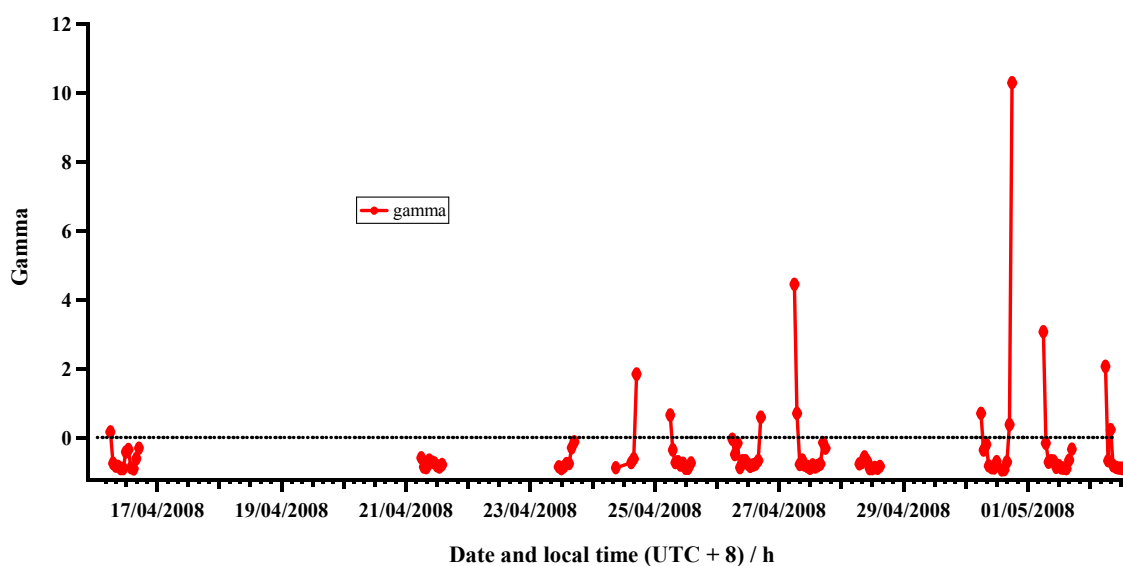


Figure 3.28 - Hourly averaged time series of  $\gamma$  between 06:00-19:00 LT from the campaign OP3 (1) during April-May 2008 at Bukit Atur in the tropical rainforest in Borneo.

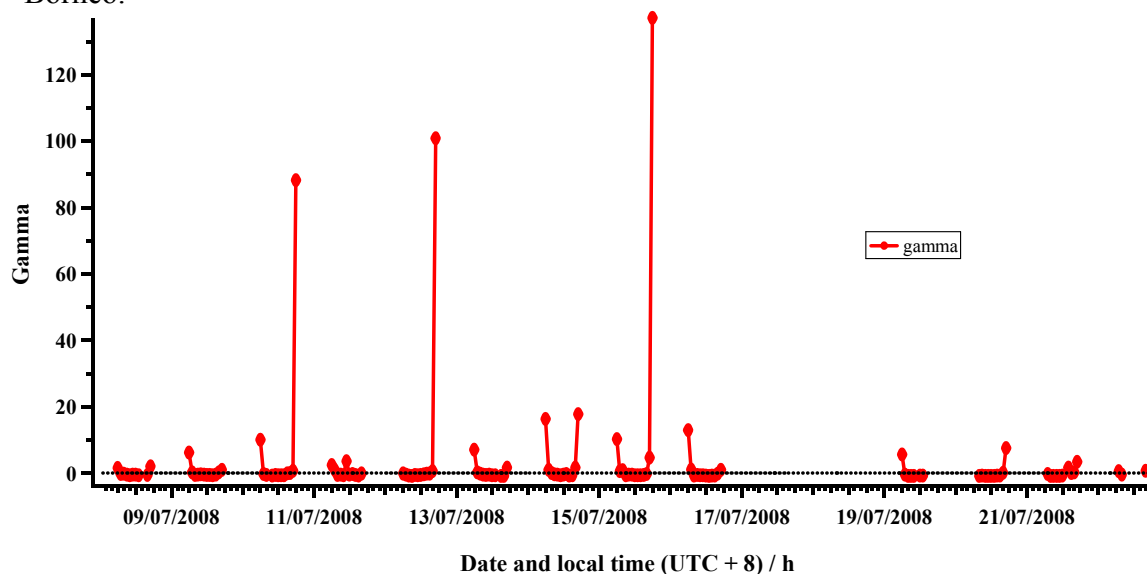


Figure 3.29 - Hourly averaged time series of  $\gamma$  between 06:00-19:00 LT from the campaign OP3 (3) during June-July 2008 at Bukit Atur in the tropical rainforest in Borneo.

The same observations of  $\gamma$  that have been made for OP3 (1) also apply to the OP3 (3) campaign, with  $\gamma$  is mostly less than 0 except early mornings and late afternoons for every day. The median of gamma was -0.46, slightly larger than for OP3 (1).

The very high  $\gamma$  values calculated particularly during late afternoon (18:00-19:00 LT) when the measured ozone photolysis rate is very slow ( $\times 10^{-9} \text{s}^{-1}$ ) illustrate that the  $[\text{HO}_2 + \text{RO}_2]$  sources in late afternoon may be from reactions other than ozone photolysis.  $j(\text{O}^1\text{D})$  will be a small number with large associated error around sunset, hence expect gamma values to be highly uncertain. Higher values of  $\gamma$  calculated in OP3 (3) than in OP3 (1) are possibly the result of the greater value of  $\beta$  calculated in OP3 (3) than in OP3 (1); the relationship between  $\beta$  and  $\gamma$  are represented in the equation (Q).

The different median of gamma values for OP3 (1) and OP3 (3), -0.76 and -0.46, might be an indicator that either the peroxy radical production from ozone photochemistry has been overestimated (could be missing OH sources than ozone photolysis) or the peroxy radical losses have been underestimated (could be missing peroxy radical sinks). It could be suggested that OH sources are considered as ozone photolysis within this analysis identified by the negative  $\gamma$  values. It could be implemented by considering the isoprene chemistry in the tropical rainforest in the Borneo, OH reformation is an important except OH from the ozone photolysis (see Section 3.2.3.6). The reaction of peroxy acetyl radical (e.g. from isoprene) with  $\text{HO}_2$  regenerate OH, (Dillon and Crowley, 2008; Hasson *et al.*, (2004); Jenkin *et al.*, (2007)) (see Section 3.2.3.2). Archibald *et al.*, (2011) found that the inclusion of uni-molecular isomerisations of the isoprene hydroxyl-peroxy radicals leads to enhanced production of HOx radicals. The underestimation of peroxy radical losses is possible in the current

analysis which has neglected peroxy self-reactions ( $\text{CH}_3\text{O}_2+\text{CH}_3\text{O}_2$ ), i.e.  $k_{3.15} = 0$  and that all  $\text{RO}_2$  are present in the form of  $\text{CH}_3\text{O}_2$ , i.e. that  $k_{3.13}$  has been set equal to  $k_{3.14}$ . The proportions for  $\text{CH}_3\text{O}_2:\text{HO}_2$  reached 7:1 for afternoon compare with  $\text{CH}_3\text{O}_2:\text{HO}_2$  5.8:1 for day light hours (see Section 3.2.3.2). Therefore,  $\text{CH}_3\text{O}_2$  comprises the vast majority of peroxy radicals.  $\text{CH}_3\text{O}_2$  is being a key species of the asymmetry in the peroxy radical diurnal profile (see Section 3.2.3.2). The reaction 3.15 has been neglected from the  $\alpha$ ,  $\beta$  and  $\gamma$  analysis. It might be suggested that the  $\text{CH}_3\text{O}_2+\text{CH}_3\text{O}_2$  reaction should be a vital part of the  $\alpha$ ,  $\beta$  and  $\gamma$  analysis. Pugh *et al.*, (2010) and Whalley *et al.*, (2011) concluded that peroxy radicals which contain a carbonyl group have been found to regenerate OH upon reaction with  $\text{HO}_2$  radicals, i.e. some  $\text{HO}_2+\text{RO}_2$  cross reactions are not a perfect sink for  $\text{RO}_2$ . Whalley *et al.*, (2011) also found that models may be missing both an OH source mechanism (OH regeneration during isoprene oxidation, e.g. Peeters *et al.*, 2009) and a separate  $\text{HO}_2$  loss mechanism.

### 3.3.1 Case studies

$\text{HO}_2+\text{RO}_2$  was measured by the University of Leicester PERCA, whilst isoprene measured by the University of Lancaster PTRMS (see Table 3.2). Hourly averages of isoprene (see middle graph on Figures 3.7 for OP3 (1) and see middle graph on Figure 3.8 for OP3 (3)) and  $\text{HO}_2+\text{RO}_2$  (see left graph on Figure 3.9 for OP3 (1) and see right graph on Figure 3.9 for OP3 (3)) measurements and gamma (as explained in Section 3.3, Figures 3.28 for OP3 (1) and Figure 3.29 for OP3 (3)) have been calculated between 06:00-19:00 LT on 27<sup>th</sup> April for OP3 (1) and on 10<sup>th</sup> and 20<sup>th</sup> July for OP3 (3) campaigns. These three days were chosen for case studies because the weather was warm and high concentration of isoprene was encountered (see Figures 3.7 and 3.8).

Higher concentrations of isoprene and peroxy radicals also were observed during the afternoon as shown in Figures 3.29, 3.31 and 3.33 on these three days. Secondary products of photochemical oxidation in the late afternoon are important sources of peroxy radical production. Temperature maximised during midday as shown in Figure 3.3. Particularly, temperature peaked at mid afternoon on 27<sup>th</sup> April for OP3 (1) and on 10<sup>th</sup> and 20<sup>th</sup> July for OP3 (3) campaigns. It is necessary to use the hourly averaged data of isoprene and HO<sub>2</sub>+RO<sub>2</sub> between 06:00-19:00 LT on 27<sup>th</sup> April, in order to compare them with the hourly averaged diurnal data of isoprene and HO<sub>2</sub>+RO<sub>2</sub> between 06:00-19:00 LT for the OP3 (1) campaign (see Section 3.3.1.1). Similar analysis repeated for 10<sup>th</sup> July (see Section 3.3.1.2) with the OP3 (3) campaign and 20<sup>th</sup> July (see Section 3.3.1.3) with the OP3 (3) campaign, respectively.

#### 3.3.1.1 Case study 1

Data from the 27<sup>th</sup> April 2008 during the OP3 (1) are shown in Figure 3.30. Particularly large positive  $\gamma$  values are calculated during the early morning indicating large amounts of excess radical production over that from ozone photolysis alone. There is no OH and  $j(\text{O}^1\text{D})$  data available during late afternoon time to calculate  $\gamma$ .

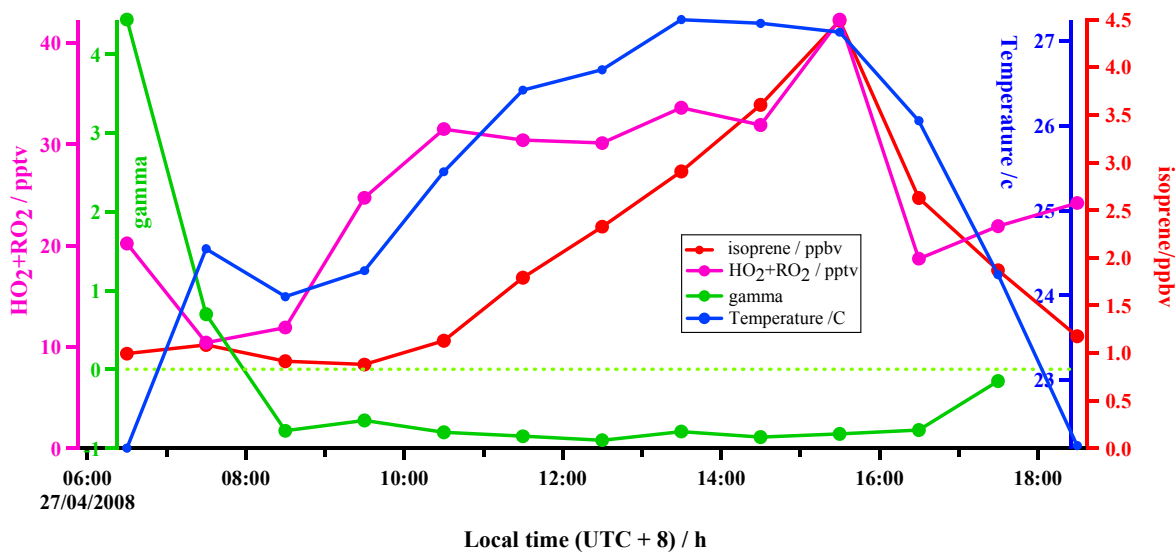


Figure 3.30 - Hourly average of measured peroxy radicals and isoprene concentration, as well as the calculated gamma on 27<sup>th</sup> April 2008 between 06:00-19:00 LT from the campaign OP3 (1) during April-May 2008 at Bukit Atur in the tropical rainforest in Borneo.

The mean and median of isoprene concentration were observed to be 1.98 ppbv and 1.80 ppbv on 27<sup>th</sup> April 2008, compared to the overall values for the OP3 (1) campaign of 1.38 ppbv and 1.50 ppbv between 06:00-19:00 LT. Values of 26 pptv and 25 pptv are found for the mean and median peroxy radical concentrations on 27<sup>th</sup> April 2008, and these values are higher than the overall values of OP3 (1), observed at 19 pptv and 19 pptv, respectively.

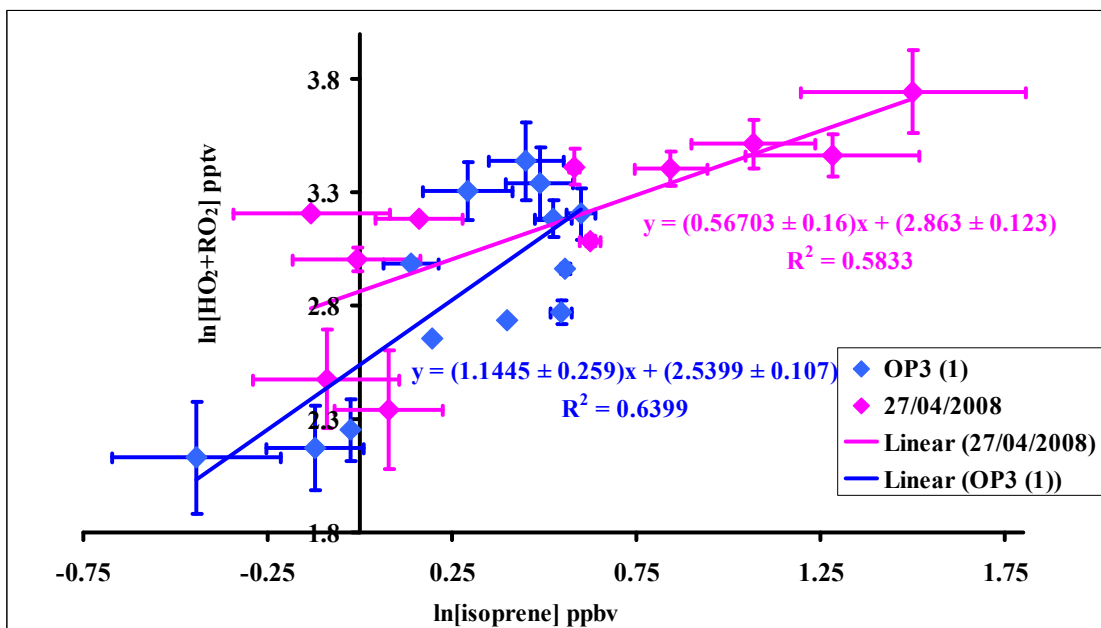


Figure 3.31 - Natural logarithms of hourly average of peroxy radical and isoprene concentration on 27<sup>th</sup> April 2008 compare with hourly-averaged diurnal cycle data of isoprene and peroxy radical concentrations between 06:00-19:00 LT from the campaign OP3 (1) during April-May at Bukit Atur in the tropical rainforest in Borneo. The blue data points for the whole OP3 (1) campaign are the same data as plotted previously on Figure 3.21. Pink error bars show  $\pm 1\sigma$  of hourly averaged values. Blue error bars show  $\pm 1\sigma$  of hourly averaged diurnal values.

Figure 3.31 shows a log-log plot of hourly averaged peroxy radical and isoprene concentrations on 27<sup>th</sup> April 2008. The values obtained for the day time gradient and linear correlation of isoprene vs. peroxy radical concentrations were 0.57 and 0.58 on 27<sup>th</sup> of April 2008, compared to 1.14 and 0.63, respectively, which are the overall values of the campaign for OP3 (1). It can be concluded that photochemical oxidation of isoprene in the late afternoon is an important source for peroxy radical production (see Section 3.2.3.6). The behaviour of the Figure 3.30 shows the asymmetric diurnal profile of peroxy radical in the tropical rainforest in Borneo.

### 3.3.1.2 Case study 2

Figure 3.32 contains the data from the 10<sup>th</sup> July 2008 during the OP3 (3) campaign and it can be noticed that particularly large positive  $\gamma$  values have been calculated during the early morning and late afternoon, which proves that large amounts of excess radical production over that obtained from ozone photolysis.

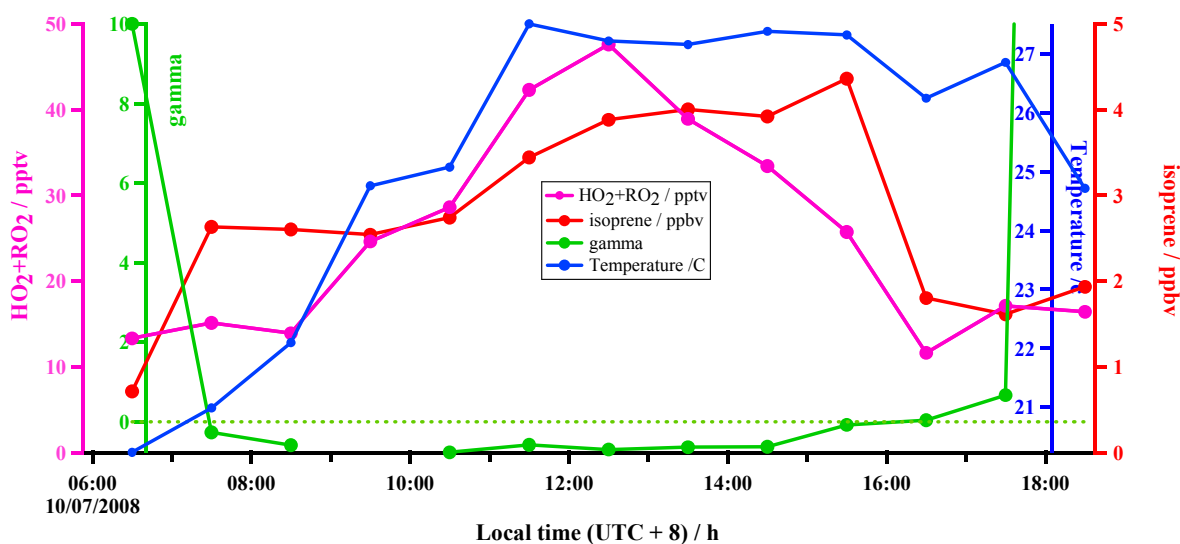


Figure 3.32 - Hourly average of measured peroxy radicals and isoprene concentration, as well as the calculated gamma on 10<sup>th</sup> July 2008 between 06:00-19:00 LT from the campaign OP3 (3) during June-July 2008 at Bukit Atur in the tropical rainforest in Borneo.

The values of 2.78 ppbv and 2.63 ppbv correspond between 06:00-19:00 LT mean and median of isoprene concentrations on 10<sup>th</sup> of July 2008, and they are higher than the overall values of the campaign during the OP3 (3), which have been observed at a value of 1.96 ppbv and 2.03 ppbv. The values of 25 pptv and 24 pptv have been observed for mean and median of peroxy radical concentration during daytime on 10<sup>th</sup> of July 2008, compared to the overall values of the OP3 (3) campaign, of 22 pptv and 21 pptv .

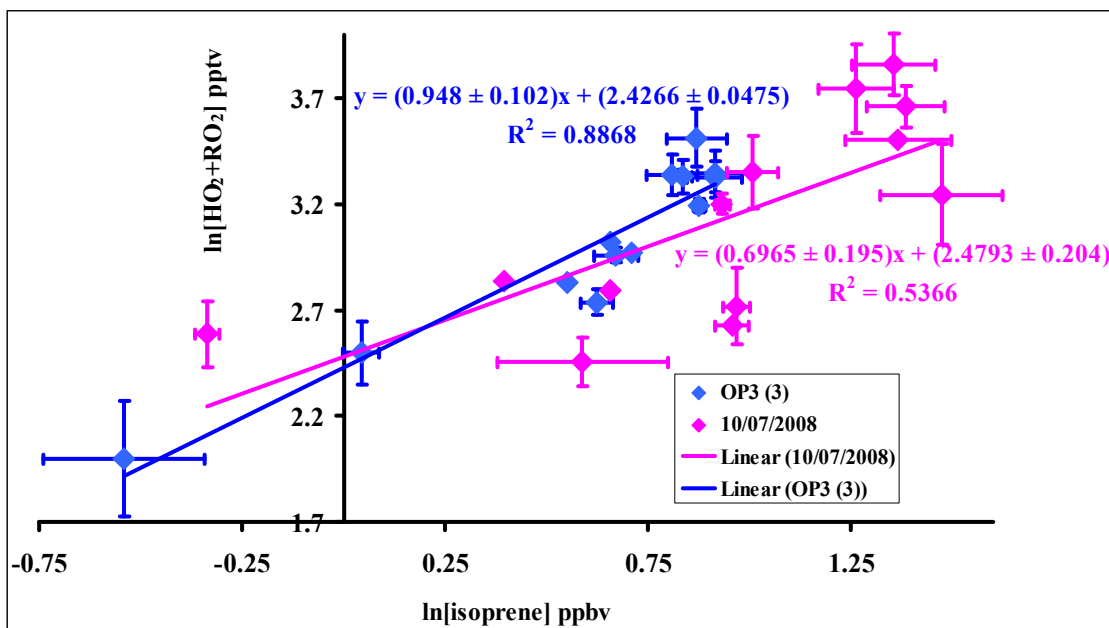


Figure 3.33 - Natural logarithms of hourly average of peroxy radical and isoprene concentration on 10<sup>th</sup> July 2008 compare with hourly-averaged diurnal cycle data of isoprene and peroxy radical concentrations between 06:00-19:00 LT from the campaign OP3 (3) during June-July 2008 at Bukit Atur in the tropical rainforest in Borneo. The blue data points for the whole OP3 (3) campaign are the same data as plotted previously on Figure 3.21. Pink error bars show  $\pm 1\sigma$  of hourly averaged values. Blue error bars show  $\pm 1\sigma$  of hourly averaged diurnal values.

Figure 3.33 shows a log-log plot of hourly averaged of peroxy radical and isoprene concentrations on 10<sup>th</sup> July 2008. The values of 0.70 and 0.54 correspond to the day time gradient and linear correlation of isoprene vs. peroxy radical concentrations on 10<sup>th</sup> of July 2008, and the gradient is better linked to the overall value of the campaign, which have been obtained at a value of 0.94 and linear correlation is 0.89, respectively. It can be concluded that photochemical oxidation of isoprene in the late afternoon is important source for peroxy radical production (see Section 3.2.3.6). The diurnal cycle of the measured peroxy radical was observed to be significantly broader and this behaviour indicates that more peroxy radical is present in the early morning and late afternoon.

### 3.3.1.3 Case study 3

Data from the 20<sup>th</sup> July 2008 during the OP3 (3) are shown in Figure 3.34. There is a lack of OH data available during morning time for calculating  $\gamma$ .

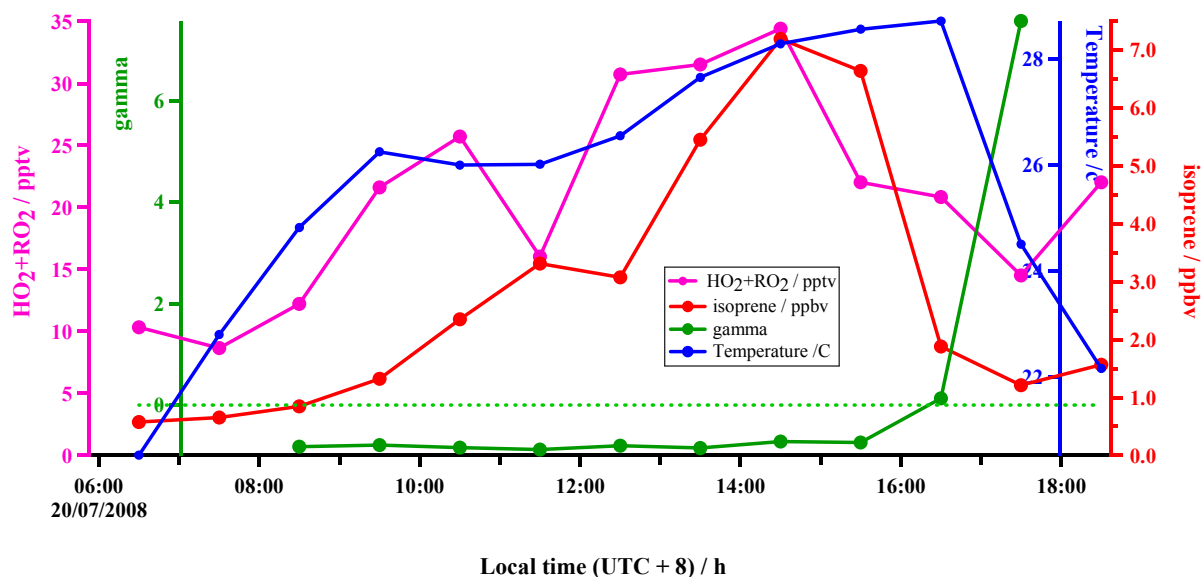


Figure 3.34 - Hourly average of measured peroxy radicals and isoprene concentration, as well as the calculated gamma on 20<sup>th</sup> July 2008 between 06:00-19:00 LT from the campaign OP3 (3) during June-July 2008 at Bukit Atur in the tropical rainforest in Borneo.

Particularly large positive  $\gamma$  values are calculated for the mid afternoon, proving that at this moment of the day, there are large amounts of excess radical production than determined by ozone photolysis alone. The values observed for the day time mean and median of isoprene concentrations were 2.80 ppbv and 1.90 ppbv on 20<sup>th</sup> of July 2008, compared to 1.96 ppbv and 2.03 ppbv, respectively, which are the overall values of the campaign for OP3 (3) campaign. The mean and median of peroxy radical concentrations were observed 21 pptv and 22 pptv on 20<sup>th</sup> July 2008, compared to the overall values of the OP3 (3) campaign, of 22 pptv and 21 pptv between 06:00-19:00 LT.

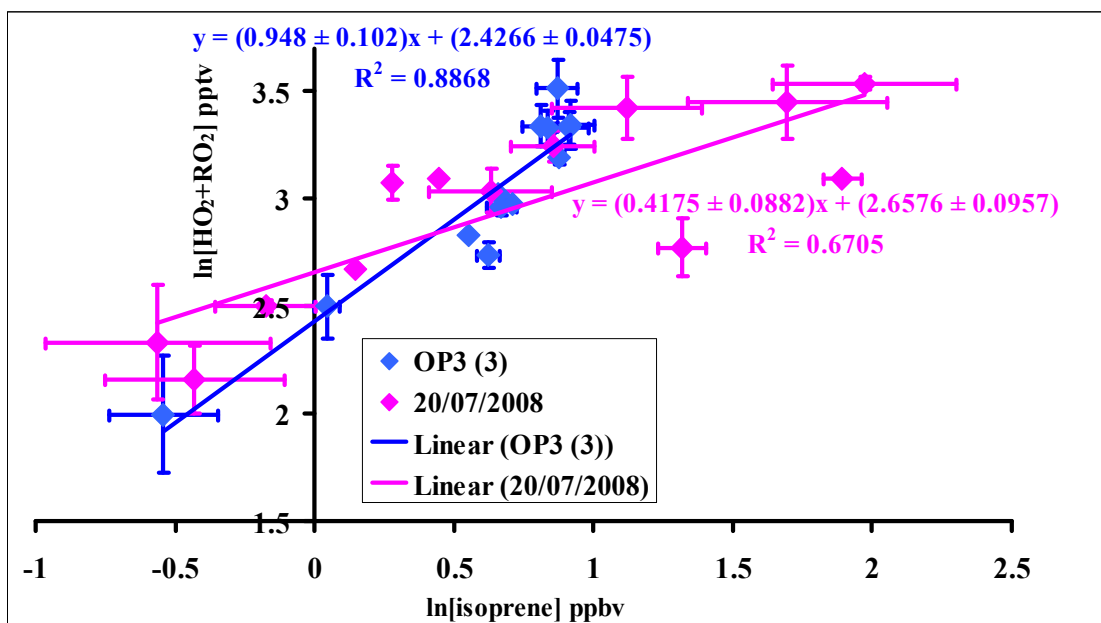


Figure 3.35 - Natural logarithms of hourly average of peroxy radical and isoprene concentration on 20<sup>th</sup> July 2008 compare with hourly-averaged diurnal cycle data of isoprene and peroxy radical concentrations between 06:00-19:00 LT from the campaign OP3 (3) during June-July 2008 at Bukit Atur in the tropical rainforest in Borneo. The blue data points for the whole OP3 (3) campaign are the same data as plotted previously on Figure 3.21. Pink error bars show  $\pm 1\sigma$  of hourly averaged values. Blue error bars show  $\pm 1\sigma$  of hourly averaged diurnal values.

Figure 3.35 shows a log-log plot of hourly averaged peroxy radical and isoprene concentrations on 20<sup>th</sup> July 2008. The gradient and linear correlation of isoprene vs. peroxy radical concentrations were 0.42 and 0.67 on 20<sup>th</sup> July 2008, compared to the overall values of the OP3 (3) campaign between 06:00-19:00 LT, of 0.95 and 0.89, respectively. It can be suggested that photochemical oxidation of isoprene in the late afternoon is important source of peroxy radical production (see Section 3.2.3.6). The behaviour of the Figure 3.34 shows the asymmetric diurnal profile of peroxy radical in the tropical rainforest in Borneo.

The emission of biogenic hydrocarbons, of which isoprene is a known contributor [Hurst *et al.*, 2001; Barket *et al.*, 2001; Westberg *et al.*, 2001], are driven largely by

temperature and so their concentrations typically rise through the afternoon. This behaviour is apparent in the timing of the isoprene maximum concentration in Figures 3.30, 3.32 and 3.34 because peroxy radical production also has other sources than ozone photolysis, the presence of the biogenic species isoprene has an impact on peroxy radical concentrations through impacts on both radical production and loss rate in the tropical rainforest in Borneo campaigns. The oxidation of isoprene mechanism and the conclusion achieved in the Section 3.2.3.6 suggest that peroxy radical production was more sensitive to isoprene in the tropical rainforest in Borneo.

#### 3.3.1.4 Additional peroxy radical production sources

It was noted in the previous section 3.3 that the hourly averaged  $\gamma$  values are greater than zero for the late afternoons and early mornings for every day during both of the campaigns (see Figures 3.28 and 3.29). This corresponds to an additional radical production route other than via ozone photolysis. The photolysis of species such as HCHO and HONO is considered in this section as a possible candidate for the additional peroxy radical production sources using a case study of data on 14<sup>th</sup> and 15<sup>th</sup> of July for the OP3 (3) campaign. There was no HCHO measurement made during the OP3 (1) campaign. Only HCHO data was available at the BADC between 10<sup>th</sup> and 16<sup>th</sup> July for the OP3 (3) campaign (see Table 3.2). Higher concentration of peroxy radical measured (see Figures 3.9 and 3.36) and large  $\gamma$  values are calculated during early morning and late afternoon on 14<sup>th</sup> and 15<sup>th</sup> as shown in Figures 3.29 and 3.36. HCHO data was not available to do the similar analysis on 12<sup>th</sup> July (see Table 3.2). University of Leicester Spectral radiometer was arrived to the measurement site in the later part of the OP3 (3) campaign owing to the unexpected late transport (see Table 3.2). Therefore no spectral radiometers' data is available to use for the OP3 (1) campaign.

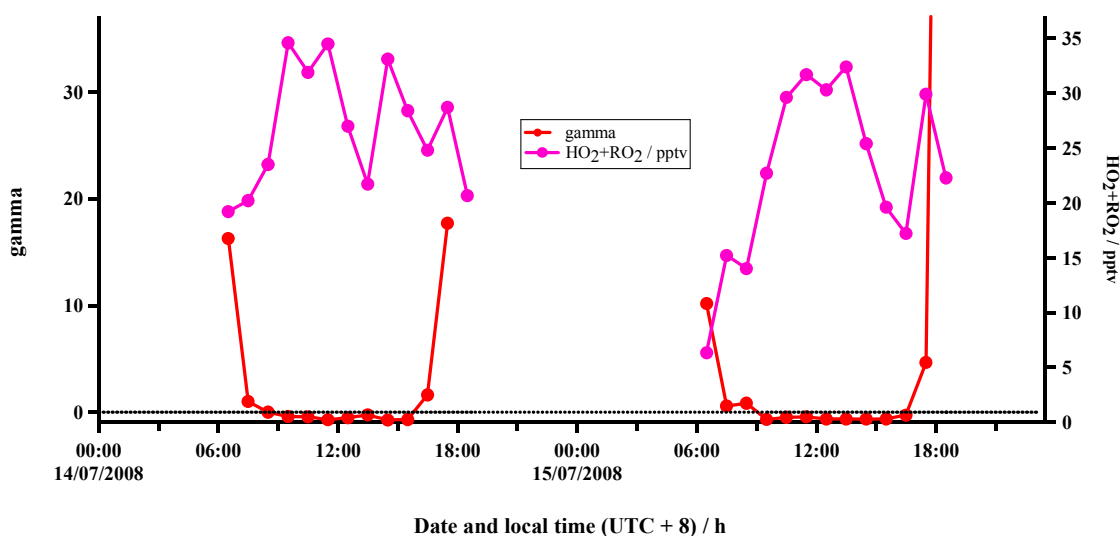


Figure 3.36 - Hourly average of peroxy radicals and gamma on 14<sup>th</sup> and 15<sup>th</sup> July 2008 between 06:00-19:00 LT from the campaign OP3 (3) during June-July 2008 at Bukit Atur in the tropical rainforest in Borneo.

An aspect of isoprene degradation following its reaction with OH is the potential for significant production of formaldehyde (HCHO) (see section 3.2.3.6). Formaldehyde, in a similar way to methyl glyoxal, can react with OH or be photolysed and give rise to peroxy radicals (see section 3.2.3.6). After the absorption of a photon of wavelength  $\lambda > 334$  nm, photolysis of one molecule of HCHO can lead to the production of two molecules of HO<sub>2</sub> (see section 1.4.2 in Chapter 1). Significant features of HCHO chemistry have already been explained in section 3.2.3.2.

HCHO was measured via the University of East Anglia Aero Laser, whilst ozone measured by the University of York Thermo Electron Instrument (TEI) Model 49i UV Analyser (see Table 3.2). HCHO and ozone data taken from the OP3 data archive at BADC and hourly averaged obtained in this work (see Section 3.1.3 for data averaging process). Hourly averaged photolysis rate (ppbv hour<sup>-1</sup>) of the HCHO and O<sub>3</sub> have been obtained between 17:00-19:00 LT on 14<sup>th</sup> and 15<sup>th</sup> of July during the OP3 (3) campaign

by multiplying the measured HCHO (see Table 3.2) and ozone concentrations (ppbv) (see bottom graph on Figure 3.8 for the OP3 (3)) with the photolysis rate ( $s^{-1}$ ). Photolysis rates of ozone (see right graph on Figure 3.9 for the OP3 (3)) and HCHO (see Table 3.2) were measured by the University of Leeds filter radiometer and University of Leicester spectral radiometer, respectively. Comparison of the  $j(O^1D)$  measurements made using the filter radiometer and a spectral radiometer (later part of the OP3 (3)) were in excellent agreement, Whalley *et al.*, (2011).

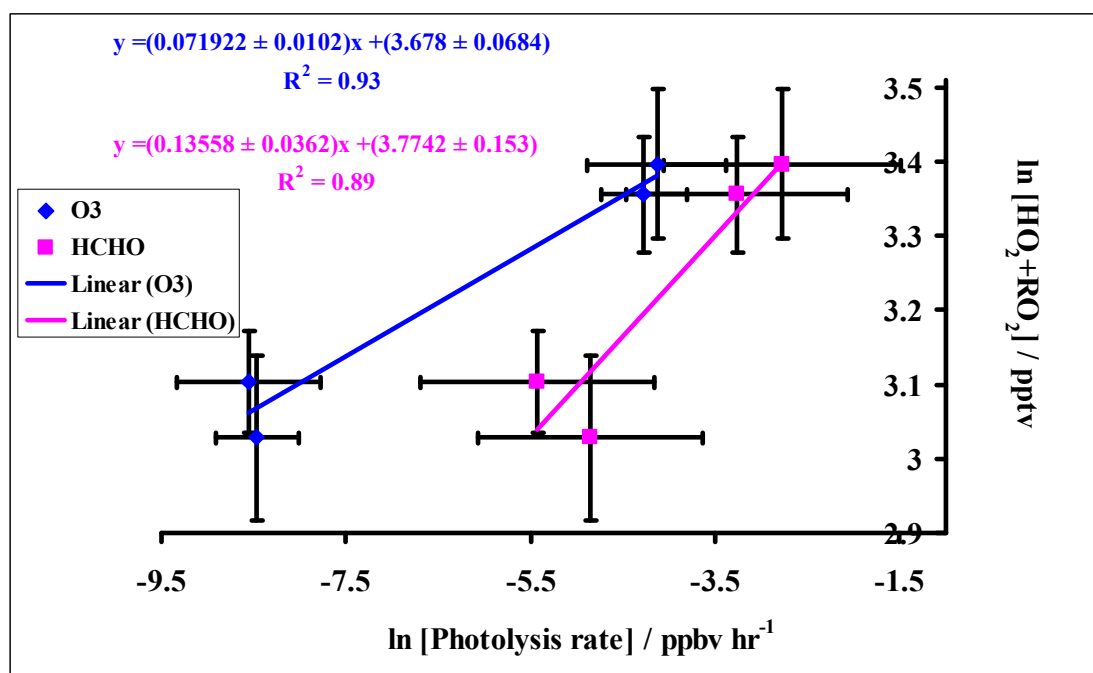


Figure 3.37 - Hourly averaged peroxy radical concentration and photolysis rate (ppbv hour<sup>-1</sup>) of the HCHO and O<sub>3</sub> between 17:00-19:00 LT on 14<sup>th</sup> and 15<sup>th</sup> from the campaign OP3 (3) during June-July 2008 at Bukit Atur in the tropical rainforest in Borneo. Four data points from both days suggest one value for each hour between 17:00-19:00 LT. Error bars show  $\pm 1\sigma$  of hourly averaged values.

Hewitt *et al.*, (2010) noted that a peak value of  $\sim 100$  pptv was often observed for NO between 07:00-08:00 LT, and that this corresponds to the beginning of HONO photolysis (i.e. the peak value of NO is registered at a time to when  $j(\text{HONO})$  is beginning to increase), and could be explained by an overnight accumulation of HONO which is then photolysed to provide the abundance of NO. Pugh *et al.*, (2010) and Pike

*et al.*, (2010) explained that other sources for NO were considered to be the spikes from vehicles or the spikes in soil emissions (sunlight and rain shower). OH is directly produced through HONO photolysis in the wavelength range of 300-400 nm. The OH generated from HONO then starts the oxidation of CO, CH<sub>4</sub> and other organic compounds leads to peroxy radical production, other than from ozone photolysis. Unfortunately, measured HONO data are not available for this analysis, and therefore HONO concentrations have been estimated by using the typical percentage of HONO being 2% of the concentration of NO<sub>2</sub>. NO<sub>2</sub> was measured by the University of York NO<sub>x</sub> (see top graph on Figure 3.8). HCHO was measured by the University of East Anglia Aero Laser, whilst ozone measured by the University of York Thermo Electron Instrument (TEI) Model 49i UV Analyser (see Table 3.2). There was no NO<sub>2</sub> data available on 15<sup>th</sup> July between 06:00-09:00 LT to estimate [HONO] for this work (see Table 3.2). On 14<sup>th</sup> of July, during the OP3 (3) campaign, the hourly averaged photolysis rate (ppbv hour<sup>-1</sup>) of HCHO, O<sub>3</sub> and HONO for the early morning between 06:00-09:00 LT has been obtained through multiplication of the measured HCHO and O<sub>3</sub> concentration (ppbv) and estimated [HONO] (ppbv) with the photolysis rate (s<sup>-1</sup>) of HCHO, O<sub>3</sub> and HONO. Photolysis rates of ozone (see right graph on Figure 3.9) was measured by the University of Leeds filter radiometer whilst HCHO and HONO were measured by the University of Leicester spectral radiometer, respectively (see Table 3.2).

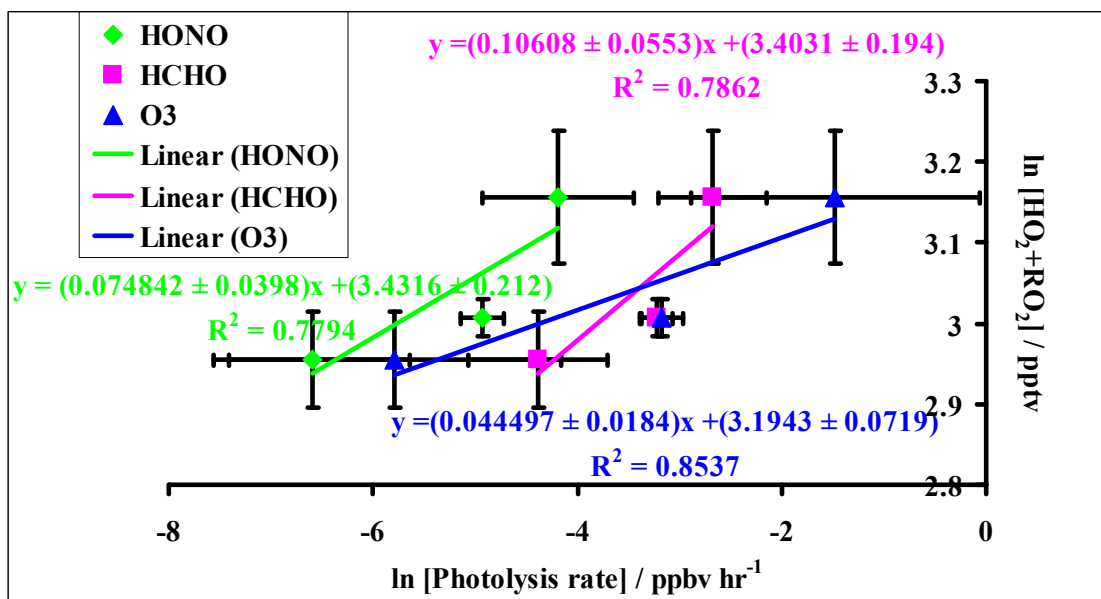


Figure 3.38 - Hourly averaged peroxy radical concentration and photolysis rate (ppbv hour<sup>-1</sup>) of the HCHO, HONO and O<sub>3</sub> between 06:00-09:00 LT on 14<sup>th</sup> July from the campaign OP3 (3) during June-July 2008 at Bukit Atur in the tropical rainforest in Borneo. Three data points on 14<sup>th</sup> July suggest one value for each hour between 06:00-09:00 LT. Error bars show  $\pm 1\sigma$  of hourly averaged values.

Figure 3.37 and 3.38 show that the photolysis rate of the HCHO has a greater gradient than that of O<sub>3</sub> with peroxy radicals during the early morning and late afternoon, whereas the photolysis rate of the HONO has a greater gradient than that of O<sub>3</sub> with peroxy radical during the early morning. During early morning, peroxy radicals are more sensitive to the photolysis of HONO than to the photolysis of ozone. During early morning and late afternoon, peroxy radicals appear to present a more increased sensitivity to the photolysis of HCHO than to the photolysis of ozone. It is during early morning and late afternoon that the largest increase in peroxy radicals has been observed, when the photolysis rates of HCHO increase, as compared to the photolysis rates of ozone. It is still during early morning, when the photolysis rates of HONO increase, compared to the photolysis rates of ozone, that the largest increase in peroxy radicals is observed. This suggests that photolysis of HONO and HCHO are dominant sources of peroxy radicals during early morning and late afternoon, respectively. Fried

*et al.*, (1997) concluded that a potential essential source for HO<sub>2</sub> production during the late afternoon is considered to be formaldehyde photolysis.

To conclude, it has been shown that the observed chemistry during the two OP3 campaigns is greatly influenced by isoprene. Isoprene provides a fast process for peroxy radical production, which is mainly caused by the OH addition to isoprene double bond. Especially during the late afternoon, there is an additional route of HO<sub>2</sub> production via to the formation and photolysis of photo-labile products such as formaldehyde, acetaldehyde and glyoxal. These OVOCs being intermediate products in isoprene oxidation (see section 3.2.3.6). Photolysis of HONO could also be an important source of peroxy radical during early morning potentially more important than ozone photolysis.

### 3.3.2. Caveat: effects on data averages of using hourly averaged data series

Average measurement data into hourly averages commonly used method for interpreting field data. A short but very large spike of NO will substantially perturb the radical chemistry; but this perturbation will only last a few minutes. However, when averaging a large NO spike into a one-hour measurement, this will result in the production of an hour of artificially high values for NO, but it will determine the calculation of artificially high ozone production rates for that hour as well. The process of establishing how the rapid variability in the real atmosphere influences the results determined by time-averaged atmospheric data can be quite challenging, e.g. the large spike of NO determines large values for  $N(O_3)$ , calculated at  $\sim 21$  ppbv hr<sup>-1</sup> (see Figure 3.7). Photolysis rate of  $j(O^1D)$  and  $j(HCHO)$  changes by a factor of 10 inside a 1 hour

time step around sunrise and sunset. Hourly average  $j(\text{O}^1\text{D})$  and  $j(\text{HCHO})$  photolysis rates will therefore be a small number with large associated error around sunrise and sunset (see Figures 3.37 and 3.38) and using these data to calculate ozone production/loss will also yield calculated hour averaged values subject to large errors as well.

### 3.4 Model Description and parameterisation

The CiTTyCAT model (Wild *et al.*, 1996, Evans *et al.*, 2000, Emmerson *et al.*, 2004 and Donovan *et al.*, 2005) has been used in a stationary box mode by Pugh *et al.*, (2010) to model the chemistry at ground level at the Bukit Atur GAW location. To investigate radical chemistry, the following details are shown from the Pugh *et al.*, (2010) results.

All model species are permitted to develop freely and are not limited to observations. In order to attain a steady diurnal cycle that can enable the carrying out of comparisons for all data employing the last date output, it was necessary to have model runs for 8 day periods. For repeating and obtaining the field concentrations, a summary of the cost function was undertaken for the model output to determine the best emission fluxes, cost function described by a number and a small number indicates a better fit by model). The median values of OH, NO, NO<sub>2</sub>, O<sub>3</sub>, isoprene, monoterpenes and HO<sub>2</sub>+RO<sub>2</sub> obtained during the OP3 (1) campaign for each hour during a 24 hour cycle have been employed for the cost function. Only 10:00-18:00 LT concentrations were considered, as LIDAR measurements provide confidence that the flux tower is completely covered by the PBL between 10:00-18:00 LT, hence the well-mixed assumptions of the model are valid.

Pearson *et al.*, (2010) explained that at day time, the box height corresponds to the height of the well-mixed PBL and thus, vertical velocity variance measurements from a pulsed Doppler LIDAR (light detection and ranging) indicate a PBL height of 800 m between 10:00-18:00 LT. These vertical velocity variance measurements indicate a direct measurement of the turbulent mixing process and therefore, Tucker *et al.*, (2009) showed that they are essential for the approximation of mixing height during convective conditions. This approximation of mixing height agrees closely with that derived from aerosol backscatter. The mixing height may be considered an indicator of the vertical stage of mixing.

There are two distinct layers within the box at 18:00 LT, when the well-mixed boundary layer falls apart: the nocturnal boundary layer (NBL), which is inversion-capped and has a lower position, and the upper one constituting the residual layer. There is no transport between the two layers at night time and thus, they are incorporated individually. Pearson *et al.*, (2010) noticed that between 08:00-10:00 LT the next morning, LIDAR measurements indicate that the vigorous mixing re-starts: this process is modelled by the residual layer concentrations being integrated step by step into the lower box as the mixing height grows, until the residual layer is absorbed by the lower box.

### 3.4.1 Best fit model concentration compare with measurements

Figure 3.39 represents a comparison between the output produced by operating the model with emissions and the in situ measurements carried out at Bukit Atur during OP3 (1). There should not exist a direct comparison between the 5m level measurements and the concentrations produced in the night-time residual layer (dashed

blue line), which are shown for context. There is no representation for the concentrations between 08:00-10:00 LT as they depend on the height of the observer in the boundary layer. The grey dots signify the upper and lower extremes for the measurements, while measurement height is shown as the subscript on the y-axis labels. The well mixed daytime box is indicated by the thick blue line, whilst the nighttime residual layer concentrations are represented by a dashed line. There is a mixing of the layers between 08:00-10:00 LT and thus, there is a discontinuity for these times.

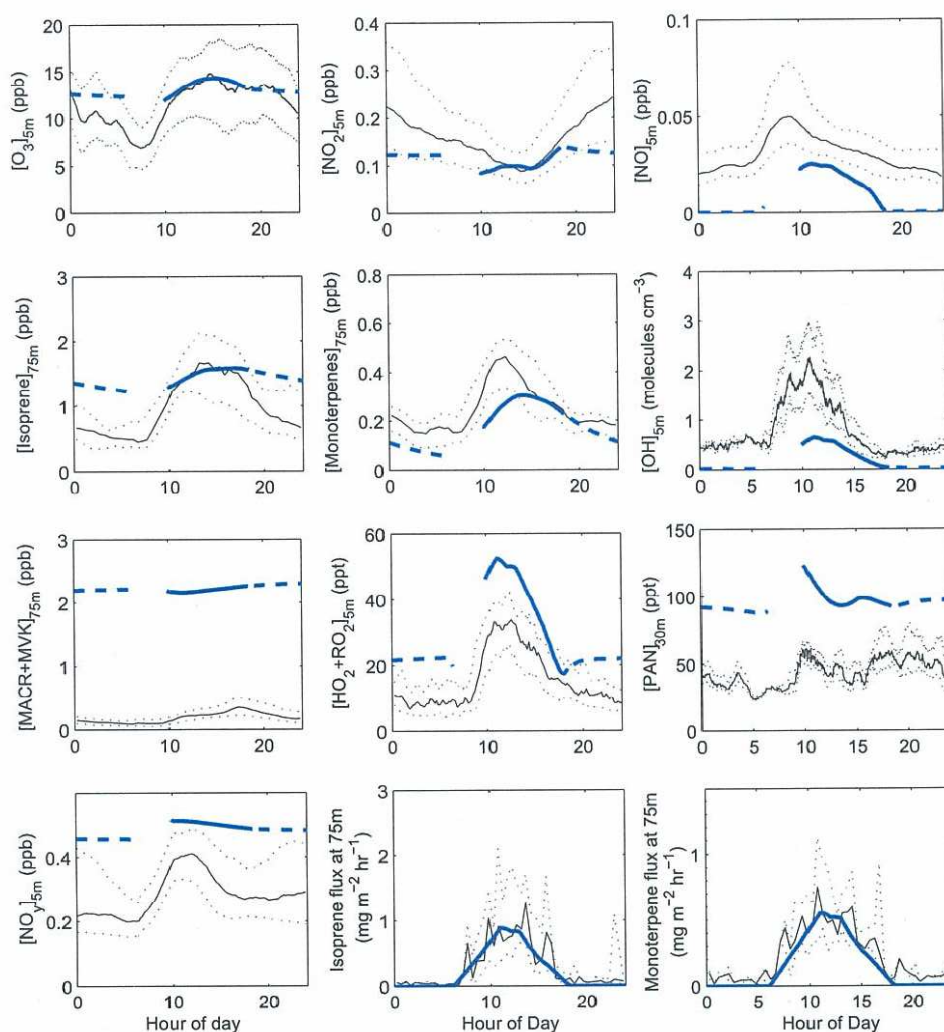


Figure 3.39 - Comparison of model best fits (blue line) against the OP3 (1) average Figures taken from Pugh *et al.*, (2010) at Bukit Atur (black line) in the tropical rainforest in Borneo during April-May 2008.

Pugh *et al.*, (2010) showed that the optimised model fit validates the secondary species such as HO<sub>2</sub>+RO<sub>2</sub>, PAN and NO<sub>y</sub> also show improved appropriate fits to the measurements, further demonstrating the importance of the physical processes are believed to make the accurate simulations of the chemistry.

### 3.5 Conclusion from the OP3 campaigns

The sum of peroxy radicals was measured with the peroxy radical chemical amplification (PERCA (V3.5)) technique during April-May 2008 (from 14<sup>th</sup> April to 2<sup>nd</sup> May 2008) and June-July 2008 (from 23<sup>rd</sup> June to 22<sup>nd</sup> July 2008), inclusive along with a range of photolysis rates and supporting measurements.

These data analyses were performed on hourly averaged data. As noted in Section 3.3.2, this approach has some draw-back for analysing photochemistry. However within the caveats of this approach, this chapter's main conclusions are:

The calculation of net ozone production rates points out that the Borneo rainforest cause tropospheric ozone production. The ozone production rate is strongly dependent on [NO] having an approximately linear sensitivity ( $d\ln(P(O_3))/d\ln(NO)$ ) is 0.81 in OP3 (1) and is 1.13 in OP3 (3). The results imply that the  $P(O_3)$  will be strongly sensitive in the rainforest boundary layer to changes in [NO], therefore ozone production rate is itself limited by NO<sub>x</sub> .

The sources and sinks of peroxy radical can be determined through a  $\beta$  and  $\gamma$  analysis (Mihele and Hastie (2003)). Calculated the hourly averaged  $\beta$  during day time is mostly less than 1 and the median of  $\beta$  is 0.41 in OP3 (1); on the other hand, in OP3 (3), it is mostly greater than 1 and the median is 1.10. It can be concluded from these  $\beta$

values that loss of peroxy radical is dominated by the peroxy radical self-reaction in OP3 (1) and by the reaction of OH with NO<sub>2</sub> in OP3 (3). The different median gamma values for OP3 (1) and OP3 (3), -0.76 and -0.46, might be an indicator that either the peroxy radical production from ozone photochemistry has been overestimated or the peroxy radical losses have been underestimated. The key point is that  $\gamma$  is negative for both campaigns, additional sources of OH are discussed in Section 3.3.

Early morning and late afternoon gamma calculated for both OP3 (1) and OP3 (3) campaigns has been determined to be positive for every day, and this clearly illustrates a significant radical production source other than ozone photolysis. Further case studies in Section 3.3.1.4 indicate the extra peroxy radical source is likely to be HCHO photolysis.

# CHAPTER 4

## Peroxy Radical Measurements in North East Atlantic Marine Boundary Layer Air Seasonal Oxidant Study (SOS)

In this chapter, measurement of peroxy radicals at Sao Vicente, Cape Verde made with the PERCA (V3.5) technique are put into the context of tropical marine boundary layer chemistry. A suite of other chemical parameters (NO, NO<sub>2</sub>, CO, O<sub>3</sub>, OVOCs, OH), photolysis frequencies and meteorological measurements are used to present a detailed analysis of the ratios of peroxy radicals in tropospheric oxidation cycles during three intensive experiments that took place at the Cape Verde Atmospheric Observatory in February-March, May-June and September 2009. The aims of these campaigns were to investigate the seasonal changes in atmospheric oxidants in the tropical marine boundary layer.

### 4.1 Introduction

#### 4.1.1 Geography and Environment

The characteristic features for Cape Verde islands, except for Boa Vista, Maio and Sal are the following: volcanic origin, rocky high altitudes with steep valleys. The coastal plains consist of sandy beaches, while at high altitudes thin forests are present. ([http://en.wikipedia.org/wiki/Geography\\_of\\_Cape\\_Verde](http://en.wikipedia.org/wiki/Geography_of_Cape_Verde)).



Figure 4.1 – Left panel represents the map of the Cape Verde islands from (<http://geography.about.com/library/cia/blccapeverde.htm>) and right panel represents the Cape Verde's position relative to the Africa from ([http://www.worldatlas.com/header\\_final/search.html?q=cape%20verde](http://www.worldatlas.com/header_final/search.html?q=cape%20verde)).

#### 4.1.2. Climate

A two season tropical climate characterizes Cape Verde. From December to June there is a cool dry season, while between July and November there is a warm season, with reduced rain falls usually occurring during August and September (less than 250 mm (9.8 inch) of annual rainfall from ([http://en.wikipedia.org/wiki/Cape\\_Verde](http://en.wikipedia.org/wiki/Cape_Verde)). Carpenter *et al.*, (2010) observed the weather during the three SOS campaigns in 2009, the February-March period featured cloudy days mixed with short periods of light rain, while the average temperature is  $\sim 294$  K. Measurements pointed out that the driest month was June, with an average temperature of  $\sim 296$  K. The most varied weather conditions were for September, through torrential rainfall (for example, 14-15<sup>th</sup>) alternating with strong sunlight and higher than average temperatures ( $\sim 303$  K). The dominating weather conditions for all year are the tropical heat and high humidity unless spared by the northeast sea breezes.

## 4.2 Scientific Objectives of work

The following information was obtained from the proposal for a UK SOLAS observatory ([http://ncasweb.leeds.ac.uk/capeverde/index.php?option=com\\_content&view=article&id=47&Itemid=54](http://ncasweb.leeds.ac.uk/capeverde/index.php?option=com_content&view=article&id=47&Itemid=54)) at Cape Verde. The primary objectives of work at Cape Verde are the following:

1) To provide a regional focal point and long-term data context for relatively short-term UK SOLAS campaigns, experiments and process studies. Since atmosphere-ocean feedbacks are the main topic of interest for the programme, such studies - and the observatory - need to be in an area subject to natural seasonal atmospheric and/or oceanic variability.

2) To initiate long-term studies of inter-annual variability and trends in marine troposphere composition and associated meteorological, geophysical and oceanographic factors at an open-ocean site that is representative of a region likely to be sensitive to future climate change, and is minimally influenced by local effects and intermittent continental pollution. The collection of such data (hopefully to be continued beyond the lifetime of the SOLAS programme) and their integration with satellite-based work will permit evaluation and improvement of regional and global ocean atmosphere models.

The scientific goals for the Cape Verde include:

The lifetime of certain greenhouse gases might be influenced within the tropics (see section 1.5.2 in Chapter 1). Lawrence *et al.*, (2001) and Bloss *et al.*, (2005a) noted that

among the gases whose lifetime is mediated by their chemistry, e.g. methane, while ozone has been identified by Horowitz *et al.*, (2003).

Bridgeman *et al.*, (2000) pointed out that the movement of species into the stratosphere usually happens within the tropics. The stratospheric ozone chemistry can be altered through the tropics. The influence of dust on the marine ecosystem can be identified at Cape Verde because there is a rare opportunity to have a heavy dust transfers from land to ocean. The Cape Verde Observatory is down wind of the Mauritanian upwelling region off northwest Africa. Hence, Cape Verde Observatory can provide the information of the connections between the upwelling and atmospheric composition.

#### 4.2.1 Summary of previous results at Cape Verde Atmospheric Observatory

There are various universities atmospheric study programs performed at Cape Verde, such as first HO<sub>x</sub> measurement in May 2006. In secondly, the reactive halogens in the Marine Boundary Layer (RHAMBLE) field measurement made in May and June 2007. The following results for Cape Verde Atmospheric Observatory are taken from ([http://www.ncas.ac.uk/composition/index.php?option=com\\_content&task=view&id=43&Itemid=58](http://www.ncas.ac.uk/composition/index.php?option=com_content&task=view&id=43&Itemid=58)). The back trajectories at the site show that it is influenced by air from Saharan Africa, coastal Africa or the North Atlantic. Noontime NO concentrations do not often exceed 10 pptv, while the noontime median is ~5 pptv. Concentration of NO<sub>2</sub> varies between 5-100 pptv, and the median is ~25 pptv. NO<sub>2</sub> spikes are affected by shipping traffic. A 2 ppb day<sup>-1</sup> of average ozone destruction is observed at the site owing to the

reduced NO<sub>x</sub> concentrations, while 8 ppb day<sup>-1</sup> of ozone destruction also observed during the cleanest day.

NERC ARSF 228 aircraft was used to explore vertical profiles of ozone surrounding the observatory in May 2007 for “Chemical and Physical Structure of the Lower Atmosphere of the Tropical Eastern North Atlantic” experiment. Read *et al.*, (2008) showed that the vertical profile of ozone loss observed entire the boundary layer by the aircraft measurements. Measurement of IO and BrO were carried out at the site using a long path DOAS instrument between Nov 2006 and June 2007 for eight month period (Mahajan *et al.*, (2010) and Read *et al.*, (2008)). Noontime concentrations of IO and BrO are 1.5 and 2.5 pptv, respectively. The box-model experiment excludes halogen chemistry and measurements of iodine and bromine oxide for this site, i.e. a classical photochemistry scheme. Mahajan *et al.*, (2010) pointed out that the ozone destruction appears to be ~50% greater than the one produced by a box model experiment. When included the measured halogen oxides to the box model, the results from the box model calculations indicate that the observed halogen concentrations appear to generate the additional ozone loss needed for the models to correspond to the observations. These results indicate that significant influence of halogen chemistry on photochemical ozone loss in the tropical Atlantic Ocean boundary layer.

Ozone in the lower atmosphere is a greenhouse gas, e.g. Read *et al.*, (2008). Ozone chemistry determines the reduction of the third most abundant greenhouse gas, methane. Ozone photolysis induces OH production that, in turn, determines the greenhouse gas methane rate of destruction. The amount of ozone destroyed above the ocean for this region is actually induced by the existence of the bromine oxide and

iodine oxide, e.g. Mahajan *et al.*, (2010). Sources of bromine oxide are long lifetime of inorganic bromine (~ 10 days) from sea-salt aerosols in the gas phase in the tropics (Von Glasow *et al.*, (2004) and Mahajan *et al.*, (2010)). Sources of iodine oxide are biologically active (e.g. Mahajan *et al.*, (2010), Read *et al.*, (2008), Fallowski *et al.*, 1997) and photolysis for emissions of iodocarbon (Martino *et al.* (2009).

VOCs have a meaningful function in establishing the concentrations of methane, ozone, and organic aerosols. Subsequently, VOCs have essential influences in the atmospheric oxidative and climate systems. Significant emission and deposition fluxes of organic compounds into the oceans are important. Organic compounds will influence considerably the cycling of oxidants in the marine environment. Zhou & Mopper *et al.*, (1997) presented evidence for formaldehyde, ethanal and propanal being produced photochemically in the sea-surface microlayer or photic zone, while Carpenter *et al.*, (2004) observed a net methanol also released into the North Atlantic Ocean. Singh *et al.*, (2003) established as a result of field campaigns carried out over the Pacific Ocean that certain OVOCs (notably aldehydes) concentrations have a considerably larger values compared to those determined by conventional chemistry. The larger values of these concentrations affect the HO<sub>x</sub> concentration. The speciation of NO<sub>y</sub> also identified over these regions and also affects the proportion of ozone production.

### 4.3 Overview of the SOS campaign

A number of ground-based measurements were carried out at the Cape Verde Atmospheric Observatory station at a height of ~5m above the ground level.

Concentrations of NO<sub>2</sub>, NO, CO<sub>2</sub> and O<sub>3</sub>, as well as different aerosol parameters are measured on a regular basis.

The intensive measurement campaigns consisted of three separate seasonal periods. The three different periods investigating the seasonal influences on HO<sub>2</sub>+RO<sub>2</sub> chemistry: SOS (1) during February-March, in May-June during SOS (2), and SOS (3) in September in 2009 (see section 4.1.2).

The long-term measurements were started in October 2006 at the Observatory. A first aerosol measurement was made in November 2006. Flask sampling of greenhouse gases deployed in May 2007. Halocarbon and aerosol measurements were made in June 2008 and October 2008, respectively. Greenhouse gases measurements were introduced by on-line in October 2008. The three SOS campaigns carried out at Cape Verde are the most detailed studies of the marine boundary layer for this area.



Figure 4.2 - Cape Verde Atmospheric Watch station from ([http://www.ncas.ac.uk/index.php?option=com\\_content&task=view&id=566&Itemid=299](http://www.ncas.ac.uk/index.php?option=com_content&task=view&id=566&Itemid=299))

The aim of the work was to

- Use the surface measurements carried out at the Observatory to detect the seasonal cycle of OH, RO<sub>2</sub> and HO<sub>2</sub> in the tropical Atlantic boundary layer.

Compare the initial analysis of the budgets of OH, HO<sub>2</sub> to those out coming from supporting trace gas data, and other modelling studies contained by the SOLAS programme.

- Use analysed correlations and comparisons of measured and model-predicted behaviour to estimate the rapid photochemical budget of the oxidative chemistry within the tropical marine boundary layer.
- Determine the role of oxygenated species in photochemistry and the radical budget within the remote marine atmosphere.
- To assess the controlling features of tropical MBL reactive sink (and source) conditions for ozone, methane, and OVOCs.

### 4.3.1 Site and instruments deployed

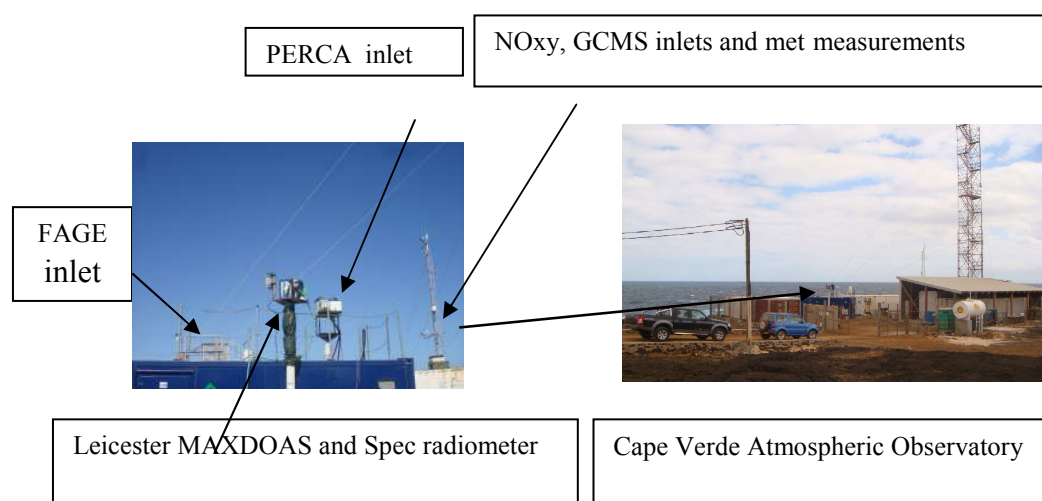


Figure 4.3 - Instruments deployed for SOS campaigns

The station contains a 30-meter tower (see right panel on Figure 4.3). The base of the tower is surrounded by four mobile sea-container laboratories for deploying additional instruments for the Seasonal Oxidant Study (see right panel on Figure 4.3). The Cape

Verde Atmospheric Observatory is located at Calhau, NW direction and opposite the sandy beach in Sao Vicente (16° 51' 49" N, 24° 52' 02" W) (CVAO). The Cape Verde Atmospheric Observatory is situated at 500 km off the West coast of Africa and alongside the ocean, it is under the direct influence of the dominant trade winds blowing off the ocean.

There are no significant coastal characteristics like extensive shallows or thick seaweed beds present. This makes good conditions for ground-based studies of marine air, without having a coastal macrophyte background. On the other hand, Mace Head, Ireland presents powerful coastal influences, especially on halogenated gases. McFiggans *et al.*, (2010) and Lee *et al.*, (2010) observed that the Cape Verde Atmospheric Observatory is being situated on a beach without having any considerable coastal factors. These factors could influence boundary layer chemistry. The Cape Verde Atmospheric Observatory experienced with low concentrations of pollution from local activities.

### 4.3.2 Overview of the measurements made in SOS (1), SOS (2) and SOS (3)

Table 1 gives details of the instrumentation and their performance.

Species	Method / Analytical Technique	Temporal Resolution	Detection Limit	Measurement Uncertainty	Reference
C <sub>2</sub> -C <sub>8</sub> NMHC and lightweight o-VOC and oxygenates	Dual Channel Gas Chromatograph with Flame ionisation detectors (DC-GC-FID)	1 hour ground variable air	1 pptv	variable, typically around 10 %	(Lewis <i>et al.</i> , 2007; Lewis <i>et al.</i> , 2005)
OH, HO <sub>2</sub>	FAGE (Fluorescence Assay by Gas Expansion) laser-induced fluorescence	60 s	(OH) 2.3x10 <sup>6</sup> molecule cm <sup>-3</sup> (1 min av.) (HO <sub>2</sub> ) 2.0x10 <sup>6</sup> molecule cm <sup>-3</sup> (1min av.)	28 % (OH & HO <sub>2</sub> ) (2 σ)	(Ingham <i>et al.</i> , 2009)
ΣRO <sub>2</sub> +HO <sub>2</sub> , HO <sub>2</sub>	PERCA (PEroxy Radical Chemical Amplifier), dual inlet	1 min	0.4 pptv (10 min)	38% (1 σ)	(Fleming <i>et al.</i> , 2006)
IO, BrO	CMAX-DOAS (UOLeicester)		(IO) 3×10 <sup>13</sup> molecule cm <sup>3</sup> (BrO) 9×10 <sup>13</sup> molecule cm <sup>3</sup>		Leigh <i>et al.</i> , (2006); Kramer <i>et al.</i> , (2008)
Photolysis frequencies (incl. <i>j</i> (O <sup>1</sup> D), <i>j</i> (NO <sub>2</sub> ))	spectral-radiometer	1s	n/a	14% and 13% 0-90° SZA	(Bohn <i>et al.</i> , 2008; Edwards, Monks, 2003)
O <sub>3</sub>	Thermo Electron Instrument (TEI) Model 49i Photometric Analyser	20 s	1.0 ppbv	variable, typically around 1 %	(Heard <i>et al.</i> , 2006)

NO/NO <sub>x</sub> / NO <sub>y</sub>	Air Quality Design Inc	NO 140s NO <sub>2</sub> 140s NO <sub>y</sub> 60s	NO 1.5 pptv NO <sub>2</sub> 4.1 pptv NO <sub>y</sub> 3.4 pptv		(Pike <i>et al.</i> , 2010)
Wind speed, wind direction, atmospheric pressure, temperature and relative humidity, radiation	cv-met-cambell and cv-met- webdaq	1 min			
CO	ultraviolet fluorescence CO analyser (Aerolaser 5001)	30 s	< 1 ppbv		(Gerbig <i>et al.</i> , 1999)
IO, BrO, NO <sub>3</sub> and various other species	Long-path Differential Optical Absorption Spectrometer (UOLeeds) (LP- DOAS)	20 min	BrO ~ 0.5 pptv IO ~ 0.9 pptv		Mahajan <i>et al.</i> , (2010)
BrO/ IO/ O <sub>3</sub> / NO <sub>2</sub> / I <sub>2</sub> / OIO/ HONO/ HCHO/ ClO/ NO <sub>3</sub> / Glyoxal	Long-path Differential Optical Absorption Spectrometer (UOHeidelberg) (LP-DOAS)	25 min	BrO ~ 0.8 pptv IO ~ 0.6 pptv		(Merten <i>et al.</i> , 2011)

Table 4.1 - Overview of the measurements made in SOS (1), SOS (2) and SOS (3). These instruments, their detection limits and accuracy are listed in Table 4.1 from Carpenter *et al.*, (2010) and [http://ncasweb.leeds.ac.uk/capeverde/index.php?option=com\\_content&view=article&id=51&Itemid=58](http://ncasweb.leeds.ac.uk/capeverde/index.php?option=com_content&view=article&id=51&Itemid=58).

The University of York fixed meteorological station recorded ambient air temperature, relative humidity, and wind speed and direction, was employed for obtaining meteorological data. Supporting measurements, e.g. NO, NO<sub>2</sub>, CO, O<sub>3</sub>, OVOCs are important to HO<sub>2</sub>+RO<sub>2</sub> chemistry and peroxy radical. These measurements are used in this work to assess the variation with season of the in-situ ozone production/loss rates, ozone compensation point and the sensitivity of the ozone photochemistry to NO<sub>x</sub>.

### 4.3.3 Data averaging process for the SOS (1), SOS (2) and SOS (3) campaigns from the BADC website

The following measurements were directly used to calculate the hourly average data and hourly average diurnal profile of each species in this work for SOS (1), SOS (2) and SOS (3) campaign (data averaging process discussed in section 3.1.3 in Chapter 3).

The instrument type, institute, time resolution of data and data coverage on BADC are also listed in the Table 4.2.

Species	Instrument	Original time resolution of instrument (if known)	Time resolution of data available on BADC	Data coverage on BADC		
				SOS (1)	SOS(2)	SOS(3)
HO <sub>2</sub> +RO <sub>2</sub>	PERCA University of Leicester	1 min Dual channel	10 min	Data starts 27/02/2009 Data ends 14/03/2009 Fully missing: not available Partly missing: 01/03, 07/03, 08/03	Data starts 20/05/2009 Data ends 02/06/2009 Fully missing: 27/05 Partly missing: 24/05, 28/05, 29/05, 30/05, 31/05, 01/06, 02/06.	Data starts 30/08/2009 Data ends 13/09/2009 Fully missing: 31/08, 05/09. Partly missing: 30/08, 01/09, 02/09, 08/09, 09/09, 13/09.
NO	NOxy Chemiluminescence University of York	140 sec	10 min	Data starts 25/02/2009 Data ends 14/03/2009 Fully missing: 05/03 Partly missing: 25/02, 26/02, 03/03, 04/03, 06/03, 07/03, 08/03, 09/03, 10/03, 11/03, 12/03, 14/03.	Data starts 15/05/2009 Data ends 28/05/2009 Fully missing: Partly missing: 16/05, 17/05, 19/05, 20/05, 21/05, 23/05, 24/05, 26/05, 27/05, 28/05	Data starts 02/09/2007 Data ends 12/09/2007 Fully missing: 11/09 Partly missing: 10/09, 12/09.

NO <sub>2</sub>	Photolysis + chemiluminescence University of York	140 sec	10 min	Data starts 27/02/2009 Data ends 14/03/2009 Fully missing: 05/03, 06/03, 07/03, 08/03, 09/03, 10/03 Partly missing: 28/02, 01/03, 12/03, 13/03	Data starts 20/05/2009 Data ends 28/05/2009 Fully missing: 22/05, 27/05 Partly missing: 20/05, 21/05, 26/05, 28/05.	Non-SOS (3) campaign Data starts 03/09/2007 Data ends 12/09/2007 Fully missing: 05/09 Partly missing: 10/09
O <sub>3</sub>	Thermo Electron Instrument (TEI) Model 49i UV Analyser University of York	20 sec	1 min	Data starts 25/02/2009 Data ends 14/03/2009 Fully missing: not available Partly missing: 01/03, 03/03	Data starts 15/05/2009 Data ends 05/06/2009 Fully missing: not available Partly missing: 19/05, 21/05, 22/05	Data starts 25/08/2009 Data ends 15/09/2009 Fully missing: not available Partly missing: 01/09, 02/09, 13/09, 14/09, 15/09/
Propene and isoprene	Dual Channel Gas Chromatograph with Flame ionisation detectors (DC-GC-FID) University of York	1 hour	1 hour	Not measured	Not measured	Data starts: 04/09 Data ends: 12/09 Fully missing: 05/09, Partly missing: 04/09, 06/09, 07/09, 08/09, 09/09, 10/09, 11/09, 12/09
<i>j</i> (O <sup>1</sup> D)	Spec rad University of Leicester	1 min	1 min	Data starts 27/02/2009 Data ends 13/03/2009 Fully missing: not available Partly missing: 20/02, 08/03, 13/03	Data starts 20/05/2009 Data ends 02/06/2009 Fully missing: not available Partly missing: 20/05, 21/05, 23/05, 25/05, 26/05, 27/05, 28/05, 29/05, 31/05	Data starts 01/09/2009 Data ends 13/09/2009 Fully missing: not available Partly missing: 01/09
CO	ultraviolet fluorescence CO analyser (Aerolaser 5001) University of York	30 sec	1 min	Data starts 25/02/2009 Data ends 14/03/2009 Fully missing: not available Partly missing: not available	Data starts 20/05/2009 Data ends 5/06/2009 Fully missing: not available Partly missing: not available	Not measured
HO <sub>2</sub>	FAGE (Aircraft) University of Leeds	60 sec	4 min	Data starts 27/02/2009 Data ends 08/03/2009 Fully missing: not available Partly missing: 27/02, 28/02, 01/03, 03/03, 05/03, 06/03, 07/03, 08/03	Data starts 07/06/2009 Data ends 11/06/2009 Fully missing: not available Partly missing: 06/06, 07/06, 08/06, 09/06, 10/06, 11/06	Data starts 31/08/2009 Data ends 14/09/2009 Fully missing: 04/09, 08/09, 11/09, 12/09, 13/09, Partly missing: 31/08, 01/09, 02/09, 03/09, 05/09, 06/09, 07/09, 08/09, 09/09, 10/09, 14/09.

IO	Longpath DOAS University of Leeds	20 min	30 min 1 hour	Not measured	Non-SOS (2) campaign Data starts 20/05/2007 Data ends 01/06/2007 Fully missing: 22/05, 23/05, 27/05, Partly missing: 20/05, 21/05, 24/05, 26/05, 28/05, 29/05, 30/05, 31/05, 01/06.	Not measured
BrO	Longpath DOAS University of Heidelberg)	25 min		Not measured	Non-SOS (2) campaign Data obtained from Carpenter <i>et al.</i> , (2010)	Not measured
Temperature	cv-met-campbell University of York	1 min	1min	Data starts 25/02/2009 Data ends 14/03/2009 Fully missing: Complete data set Partly missing: not available	Data starts 15/05/2009 Data ends 05/06/2009 Fully missing: Complete data set Partly missing: not available	Data starts 25/08/2009 Data ends 15/09/2009 Fully missing: Complete data set Partly missing: not available
Relative Humidity	cv-met-campbell University of York	1 min	1 min	Data starts 25/02/2009 Data ends 14/03/2009 Fully missing: Complete data set Partly missing: not available	Data starts 15/05/2009 Data ends 05/06/2009 Fully missing: Complete data set Partly missing: not available	Data starts 25/08/2009 Data ends 15/09/2009 Fully missing: Complete data set Partly missing: not available

Table 4.2 - Some of the instruments, their measurement technique from Carpenter *et al.*, (2010) for campaigns SOS (1), SOS (2) and SOS (3) at Cape Verde Atmospheric Observatory in the tropical marine boundary layer during February-March, May-June and September 2009, respectively. The names of the institutes, the time resolution of the data and the data coverage are available on the BADC, while the data has been taken for this work from the Cape Verde archive on the BADC website.

The data was processed in this Chapter by the same methods as did in Chapter 3 (see Section 3.1.3 for data averaging process).

## 4.4 Results

### 4.4.1 Campaign meteorology

For each of the SOS (1), SOS (2) and SOS (3) campaigns at Cape Verde, the observed temperature, relative humidity, and wind speed, CO, NO and O<sub>3</sub> has been archived on BADC and the hourly averages have been obtained by the author in this work (see Table 4.2 for data coverage and see Section 3.13 in Chapter 3 for data averaging process). Figure 4.4 shows the hourly averaged diurnal cycle for temperature (top graph) and relative humidity (bottom graph) from the SOS (1), SOS (2) and SOS (3) campaigns at Cape Verde Atmospheric Observatory in the tropical marine boundary layer during February-March, May-June and September respectively 2009.

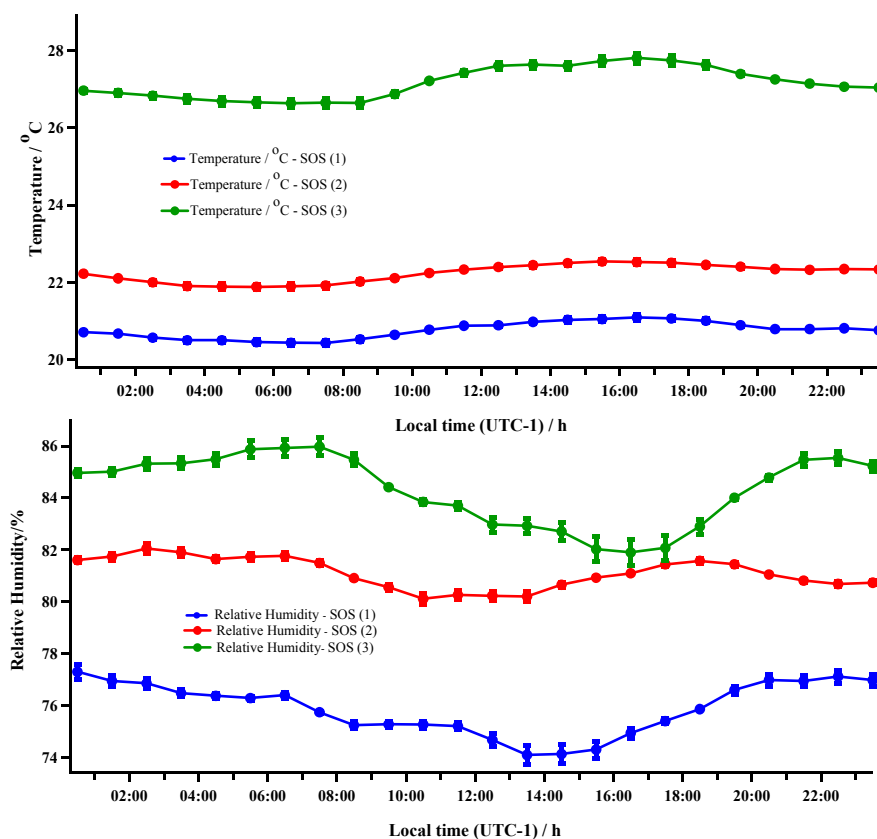


Figure 4.4 - Hourly averaged diurnal cycle data of temperature (top graph) and relative humidity (bottom graph) from the campaigns SOS (1) during February-March, SOS (2) during May-June and SOS (3) during September 2009 at Cape Verde Atmospheric Observatory in the tropical marine boundary layer. Error bars show  $\pm 1\sigma$  of hourly averaged diurnal values.

A higher temperature and relative humidity are observed in SOS (3) over that in SOS (1) and SOS (2), and lower temperature and relative humidity measured in SOS (1) over that in SOS (2) and SOS (3). Figure 4.5 shows the hourly averaged diurnal cycle for CO (top graph), NO (middle graph) and O<sub>3</sub> (bottom graph) from SOS (1), SOS (2) and SOS (3) campaigns.

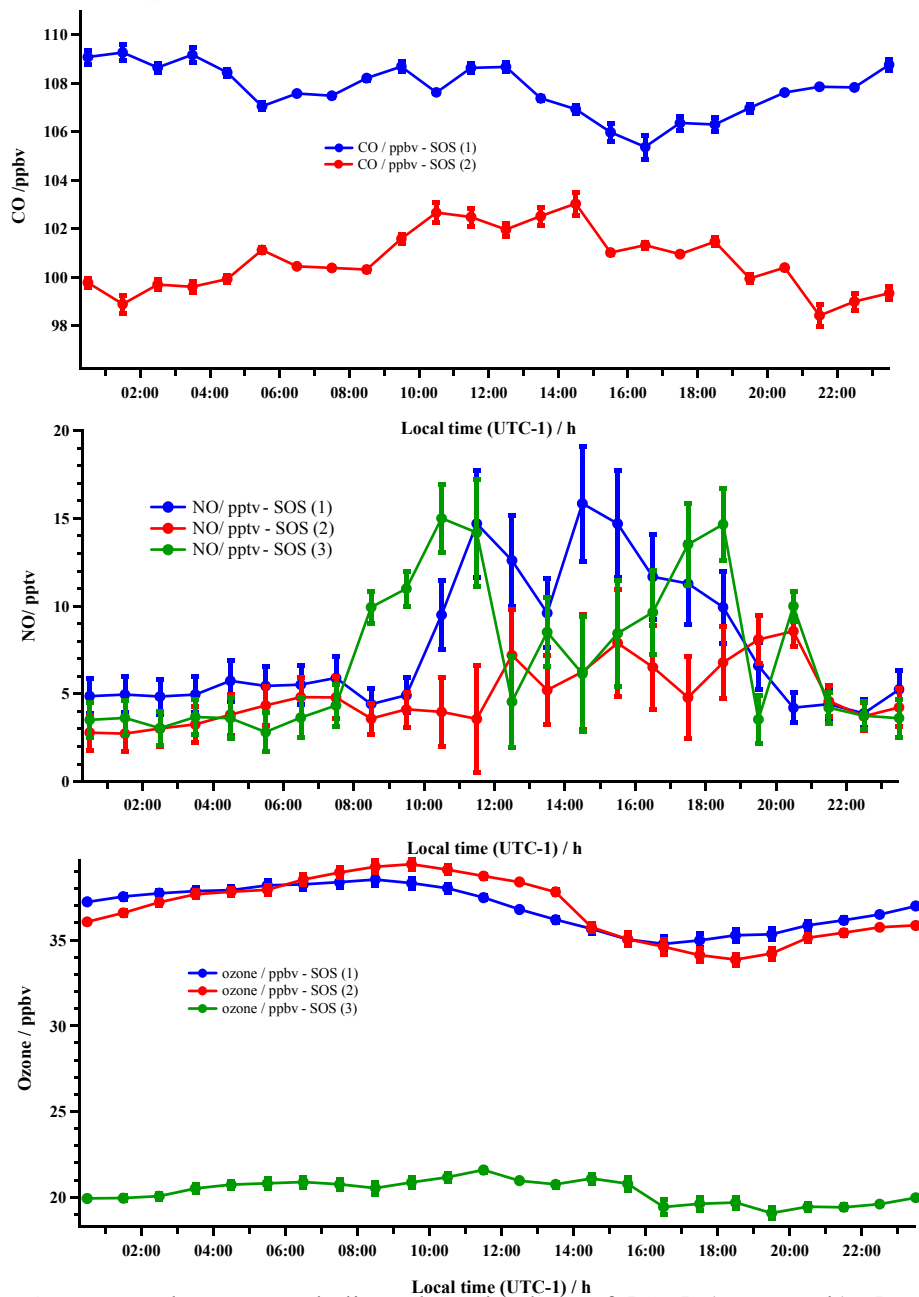


Figure 4.5 - Hourly averaged diurnal cycle data of [CO] (top graph), [NO] (middle graph) and [O<sub>3</sub>] (bottom graph) from the campaigns SOS (1) during February-March, SOS (2) during May-June and SOS (3) during September 2009 at Cape Verde Atmospheric Observatory in the tropical marine boundary layer. Error bars show  $\pm 1\sigma$  of hourly averaged diurnal values.

Higher concentrations of ozone were observed in SOS (1) and SOS (2) than SOS (3), and ozone concentrations in SOS (1) and SOS (2) were not significantly different. CO data is not available for SOS (3) campaign. Very low concentrations of NO were measured in all campaigns, particularly SOS (2). The three SOS campaigns have variation in the NO concentration measured during the day time, as opposed to night time, when the concentration is lower (see middle graph on Figure 4.5). Carpenter *et al.*, (2010) noted that NO<sub>x</sub> air masses were associated with African soil emissions. The NO originating from the soil has effect during day and night. The NO concentration is likely to be low during the night time owing to the inability of recycle NO without photochemistry.

Typically clean ocean in air has low concentration of NO during the night time, e.g. Cape Grim Baseline Air Pollution station (40° 40' 60" S, 144° 40' 60" E) (Monks *et al.*, 2000b) and Pico ( 38° 28' 0" N, 28° 20' 0" S ) (Kleissl *et al.*, 2007), i.e. no oceanic sources. Monks *et al.*, (2000b) observed that hourly averaged NO mixing ratio at Cape Grim varied between 1-6 pptv, whereas at Pico Mountain, its fluctuation was between 0 and 6 pptv (Martin *et al.*, (2008)).

#### 4.4.2 Peroxy radicals and wind direction

Peroxy radicals were measured by PERCA (V3.5) with wind direction that has been taken from BADC for the Cape Verde archive. HO<sub>2</sub>+RO<sub>2</sub> concentration and wind direction averages were obtained for each hour of the every day for whole time for SOS (1) and SOS (2) campaigns.

The polar plots (see Figure 4.7) show peroxy radical mixing ratio against wind direction from SOS (1) (top plot) and SOS (2) (bottom plot) campaigns.

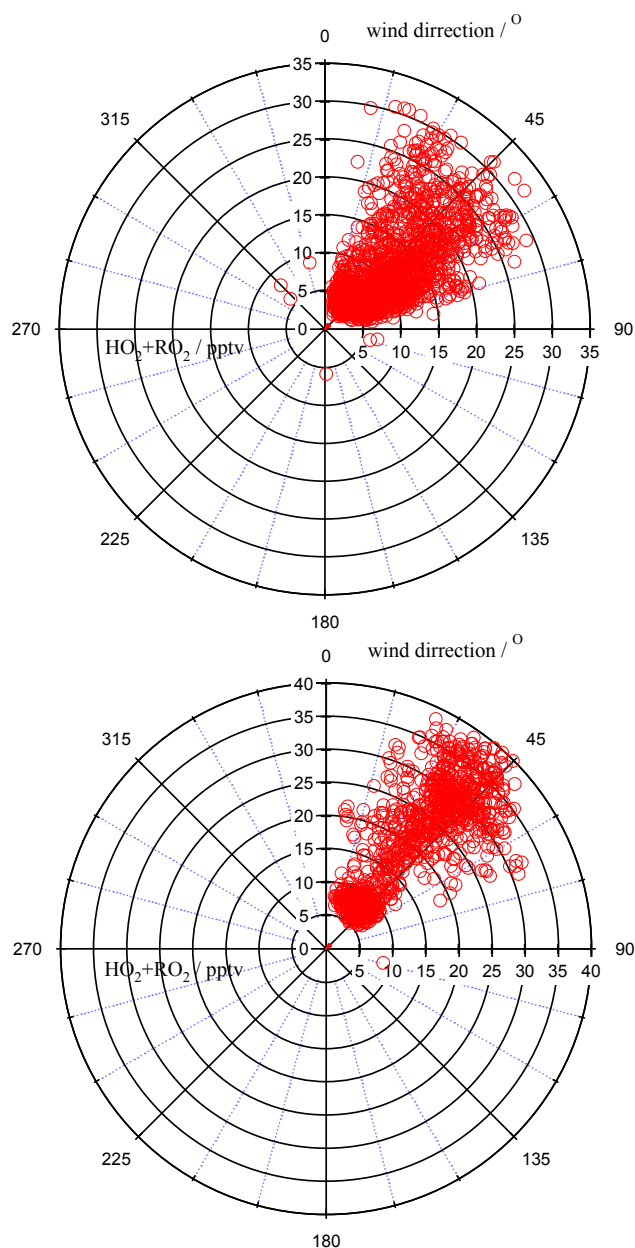


Figure 4.7 - Polar plot showing  $[\text{HO}_2 + \text{RO}_2]$  against wind direction from SOS (1) (top plot) and SOS (2) (bottom plot) campaigns at Cape Verde Atmospheric Observatory in the tropical marine boundary layer during February-March and May -June 2009.

Cape Verde Atmospheric Observatory shows the influence of the strong NE trade winds during SOS (1) and SOS (2); CVAO was sited to receive air masses well processed within the marine troposphere, with very little pollution from local activities.

Unfortunately, owing to technical problems with the data logging the wind data from SOS (3) campaign were unusable.

#### 4.4.3 Steady state analysis for SOSs

As described in section 1.4.1 in Chapter 1, in clean air where [NO<sub>x</sub>] is low, steady-state analysis can be applied to OH, HO<sub>2</sub> and RO<sub>2</sub> to give the following expressions (Penkett *et al.*, (1997))

$$\frac{d[\text{OH}]}{dt} = 2f\dot{f}(\text{O}^1\text{D})[\text{O}_3] + k_{\text{HO}_2+\text{O}_3}[\text{HO}_2][\text{O}_3] - k_{\text{OH}+\text{CO}}[\text{OH}][\text{CO}] - k_{\text{OH}+\text{CH}_4}[\text{OH}][\text{CH}_4] \approx 0 \quad (\text{A})$$

$$\frac{d[\text{HO}_2]}{dt} = k_{\text{OH}+\text{CO}}[\text{OH}][\text{CO}] - k_{\text{HO}_2+\text{O}_3}[\text{HO}_2][\text{O}_3] - 2k_{\text{HO}_2+\text{HO}_2}[\text{HO}_2]^2 - k_{\text{HO}_2+\text{CH}_3\text{O}_2}[\text{HO}_2][\text{CH}_3\text{O}_2] \approx 0 \quad (\text{B})$$

$$\frac{d[\text{CH}_3\text{O}_2]}{dt} = k_{\text{OH}+\text{CH}_4}[\text{OH}][\text{CH}_4] - k_{\text{HO}_2+\text{CH}_3\text{O}_2}[\text{HO}_2][\text{CH}_3\text{O}_2] \approx 0 \quad (\text{C})$$

In Equation (A),  $f$  is the fraction of O(<sup>1</sup>D) that reacts with water vapour to form OH,  $f$  is described in section 3.3 in Chapter 3. The net change in the free radical concentration (i.e., OH + HO<sub>2</sub> + CH<sub>3</sub>O<sub>2</sub>) is given by the sum of Equations (A) → (C):

$$\frac{d[\text{OH} + \text{HO}_2 + \text{CH}_3\text{O}_2]}{dt} = 2f\dot{f}(\text{O}^1\text{D})[\text{O}_3] - 2k_{\text{HO}_2+\text{HO}_2}[\text{HO}_2]^2 - k_{\text{HO}_2+\text{CH}_3\text{O}_2}[\text{HO}_2][\text{CH}_3\text{O}_2] \quad (\text{D})$$

Under steady-state conditions, the net change is 0. Setting the right hand site of Equation (D) to zero

$$2f\dot{f}(\text{O}^1\text{D})[\text{O}_3] - 2k_{\text{HO}_2+\text{HO}_2}[\text{HO}_2]^2 - k_{\text{HO}_2+\text{CH}_3\text{O}_2}[\text{HO}_2][\text{CH}_3\text{O}_2] = 0$$

$$f\dot{f}(\text{O}^1\text{D})[\text{O}_3] = [\text{HO}_2](k_{\text{HO}_2+\text{HO}_2}[\text{HO}_2] + k_{\text{HO}_2+\text{CH}_3\text{O}_2}[\text{CH}_3\text{O}_2]) \quad (\text{E})$$

If the  $\frac{[\text{HO}_2]}{[\text{HO}_2]+[\text{CH}_3\text{O}_2]}$  ratio, denoted here  $\alpha$ , is known then the sum of peroxy

radicals  $\text{RO}_2 = \text{HO}_2 + \text{CH}_3\text{O}_2$ ,  $\alpha = \frac{[\text{HO}_2]}{[\text{HO}_2]+[\text{CH}_3\text{O}_2]}$  and,  $\alpha[\text{CH}_3\text{O}_2] = (1-\alpha)[\text{HO}_2]$

also  $[\text{HO}_2] = \alpha ([\text{HO}_2]+[\text{CH}_3\text{O}_2])$

substitute  $[\text{HO}_2] = \alpha ([\text{HO}_2]+[\text{CH}_3\text{O}_2])$  into Equation (E),

$$fj(\text{O}^1\text{D})[\text{O}_3] = \alpha ([\text{HO}_2] + [\text{CH}_3\text{O}_2]) (k_{\text{HO}_2+\text{HO}_2}[\text{HO}_2] + k_{\text{HO}_2+\text{CH}_3\text{O}_2}[\text{CH}_3\text{O}_2])$$

$$j(\text{O}^1\text{D})[\text{O}_3] = ([\text{HO}_2] + [\text{CH}_3\text{O}_2]) (\alpha k_{\text{HO}_2+\text{HO}_2}[\text{HO}_2] + \alpha k_{\text{HO}_2+\text{CH}_3\text{O}_2}[\text{CH}_3\text{O}_2]) \quad (\text{F})$$

Introducing factor Y into equation (F)

$$j(\text{O}^1\text{D})[\text{O}_3] = ([\text{HO}_2] + [\text{CH}_3\text{O}_2]) (Y) \quad (\text{G})$$

$$\text{where } Y = (\alpha k_{\text{HO}_2+\text{HO}_2}[\text{HO}_2] + \alpha k_{\text{HO}_2+\text{CH}_3\text{O}_2}[\text{CH}_3\text{O}_2]) \quad (\text{H})$$

Substitute  $\alpha[\text{CH}_3\text{O}_2] = (1-\alpha)[\text{HO}_2]$  into equation (H)

$$\text{Equation (H) becomes, } Y = \alpha k_{\text{HO}_2+\text{HO}_2}[\text{HO}_2] + (1-\alpha)k_{\text{HO}_2+\text{CH}_3\text{O}_2}[\text{HO}_2]$$

$$\text{Extend the brackets } Y = \alpha k_{\text{HO}_2+\text{HO}_2}[\text{HO}_2] + k_{\text{HO}_2+\text{CH}_3\text{O}_2}[\text{HO}_2] - \alpha k_{\text{HO}_2+\text{CH}_3\text{O}_2}[\text{HO}_2] \quad (\text{I})$$

Substitute  $[\text{HO}_2] = \alpha([\text{HO}_2]+[\text{CH}_3\text{O}_2])$  into equation (I)

$$Y = \alpha k_{\text{HO}_2+\text{HO}_2} (\alpha([\text{HO}_2]+[\text{CH}_3\text{O}_2])) + k_{\text{HO}_2+\text{CH}_3\text{O}_2} (\alpha([\text{HO}_2]+[\text{CH}_3\text{O}_2])) - \alpha k_{\text{HO}_2+\text{CH}_3\text{O}_2} (\alpha([\text{HO}_2]+[\text{CH}_3\text{O}_2])) \quad (\text{J})$$

Equation (J) becomes

$$Y = k_{\text{HO}_2+\text{HO}_2} \alpha^2 [\text{HO}_2] + k_{\text{HO}_2+\text{HO}_2} \alpha^2 [\text{CH}_3\text{O}_2] + k_{\text{HO}_2+\text{CH}_3\text{O}_2} \alpha [\text{HO}_2] + k_{\text{HO}_2+\text{CH}_3\text{O}_2} \alpha [\text{CH}_3\text{O}_2] - k_{\text{HO}_2+\text{CH}_3\text{O}_2} \alpha^2 [\text{HO}_2] - k_{\text{HO}_2+\text{CH}_3\text{O}_2} \alpha^2 [\text{CH}_3\text{O}_2]$$

Taking the  $k_{\text{HO}_2+\text{HO}_2}$  and  $k_{\text{HO}_2+\text{CH}_3\text{O}_2}$  as common factors

Y=

$$k_{\text{HO}_2+\text{HO}_2} \alpha^2 ([\text{HO}_2] + [\text{CH}_3\text{O}_2]) + k_{\text{HO}_2+\text{CH}_3\text{O}_2} \alpha ([\text{HO}_2] + [\text{CH}_3\text{O}_2]) - k_{\text{HO}_2+\text{CH}_3\text{O}_2} \alpha^2 ([\text{HO}_2] + [\text{CH}_3\text{O}_2])$$

Taking  $([\text{HO}_2] + [\text{RO}_2])$  out of the set of these brackets,

$$Y = ([\text{HO}_2] + [\text{CH}_3\text{O}_2]) (k_{\text{HO}_2+\text{HO}_2} \alpha^2 + k_{\text{HO}_2+\text{CH}_3\text{O}_2} \alpha - k_{\text{HO}_2+\text{CH}_3\text{O}_2} \alpha^2)$$

Rearranging inside the brackets, becomes,

$$Y = ([\text{HO}_2] + [\text{CH}_3\text{O}_2]) (\alpha^2 \cdot (k_{\text{HO}_2+\text{HO}_2} - k_{\text{HO}_2+\text{CH}_3\text{O}_2}) + \alpha \cdot k_{\text{HO}_2+\text{CH}_3\text{O}_2})$$

Substitute  $Y = ([\text{HO}_2] + [\text{CH}_3\text{O}_2]) (\alpha^2 \cdot (k_{\text{HO}_2+\text{HO}_2} - k_{\text{HO}_2+\text{CH}_3\text{O}_2}) + \alpha \cdot k_{\text{HO}_2+\text{CH}_3\text{O}_2})$  into

equation (G) becomes,

$$j(\text{O}^1\text{D})[\text{O}_3] = ([\text{HO}_2] + [\text{CH}_3\text{O}_2]) \{ ([\text{HO}_2] + [\text{CH}_3\text{O}_2]) (\alpha^2 \cdot (k_{\text{HO}_2+\text{HO}_2} - k_{\text{HO}_2+\text{CH}_3\text{O}_2}) + \alpha \cdot k_{\text{HO}_2+\text{CH}_3\text{O}_2}) \}$$

$$j(\text{O}^1\text{D})[\text{O}_3] = ([\text{HO}_2] + [\text{CH}_3\text{O}_2])^2 \cdot k_{\text{sum}} \quad (\text{K})$$

$$[\text{HO}_2] + [\text{CH}_3\text{O}_2] = \sqrt{\frac{j(\text{O}^1\text{D})[\text{O}_3]}{k_{\text{sum}}}} \quad (4.1)$$

where  $k_{\text{sum}} = \alpha^2 \cdot (k_{\text{HO}_2+\text{HO}_2} - k_{\text{HO}_2+\text{CH}_3\text{O}_2}) + \alpha \cdot k_{\text{HO}_2+\text{CH}_3\text{O}_2}$



$k_{\text{sum}}$  is a composite rate constant made up of the individual rate constants for the peroxy radical self- and cross-reactions (1.34 and 1.35) (see Sections 1.4.3 in Chapter 1, Sections 3.2.3.2 and 3.3 in Chapter 3). The peroxy radical concentrations in the absence of NO should vary with the square root of  $j(\text{O}^1\text{D})$  under relatively constant ozone concentrations (see Equation 4.1). See section 4.4.3.3 for the application of Equation 4.1.

Furthermore, the peroxy radical concentration can be linked with [OH] (Penkett *et al.*, (1997)). Mauldin *et al.*, (1998) demonstrated the secondary sources of OH, both interconversion from HO<sub>2</sub> *via* reaction with NO or ozone. Other sources of HO<sub>2</sub> and OH such as HCHO or H<sub>2</sub>O<sub>2</sub> are relatively small in the clean marine boundary layer. Assume all OH reacts with CO and CH<sub>4</sub>, via the following reactions,



Hence, the reaction of HO<sub>2</sub> with O<sub>3</sub> can be discarded; a steady-state analysis can be applied to OH to give the following expressions (Penkett *et al.*, (1997))

$$\frac{d[\text{OH}]}{dt} = 2\dot{f}(\text{O}^1\text{D})[\text{O}_3] - k_{\text{OH}+\text{CO}}[\text{OH}][\text{CO}] - k_{\text{OH}+\text{CH}_4}[\text{OH}][\text{CH}_4] \approx 0$$

Under steady-state conditions, the net change is 0. Therefore Equation (D) becomes,

$$2\dot{f}(\text{O}^1\text{D})[\text{O}_3] = k_{\text{OH}+\text{CO}}[\text{OH}][\text{CO}] + k_{\text{OH}+\text{CH}_4}[\text{OH}][\text{CH}_4] \quad (\text{M})$$

$$\dot{f}(\text{O}^1\text{D})[\text{O}_3] = ([\text{HO}_2] + [\text{CH}_3\text{O}_2])^2 \cdot k_{\text{sum}} \quad (\text{K})$$

Equations (K) and (M),

$$2([\text{HO}_2] + [\text{CH}_3\text{O}_2])^2 k_{\text{sum}} = k_{\text{OH}+\text{CO}}[\text{OH}][\text{CO}] + k_{\text{OH}+\text{CH}_4}[\text{OH}][\text{CH}_4]$$

$$[\text{HO}_2] + [\text{CH}_3\text{O}_2] = \sqrt{\frac{(k_{\text{OH}+\text{CO}}[\text{CO}] + k_{\text{OH}+\text{CH}_4}[\text{CH}_4])[\text{OH}]}{2k_{\text{sum}}}} \quad (4.7)$$

See Section 4.4.3.4 for the application of Equation 4.7.

#### 4.4.3.1 Time series of peroxy radical in SOS (1), SOS (2) and SOS (3) campaigns

$[\text{HO}_2+\text{RO}_2]$  was measured by University of Leicester PERCA. A spectral radiometer (University of Leicester) was deployed next to the PERCA (V3.5) inlet as shown in Figure 4.3 and measured the photolysis rate coefficient for  $j(\text{O}^1\text{D})$ .  $j(\text{O}^1\text{D})$  has been used for data analysis from the three of SOS campaigns (See Table 4.2 and see Section 3.1.3 for data averaging process). The Figures 4.8, 4.9 and 4.10 below and on the following pages show hourly averaged time series of peroxy radicals concentrations and  $j(\text{O}^1\text{D})$  in SOS (1), SOS (2) and SOS (3) campaigns respectively.

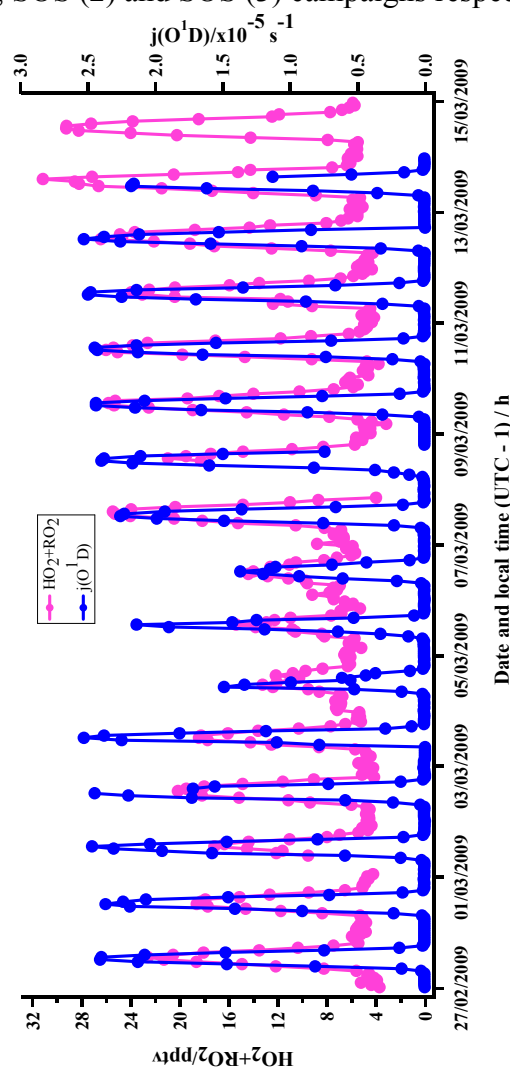


Figure 4.8 - Hourly averaged time series of  $[\text{HO}_2+\text{RO}_2]$  and photolysis rate coefficients of  $j(\text{O}^1\text{D})$  from the campaign SOS (1) during February-March 2009 at Cape Verde Atmospheric Observatory in the tropical marine boundary layer.

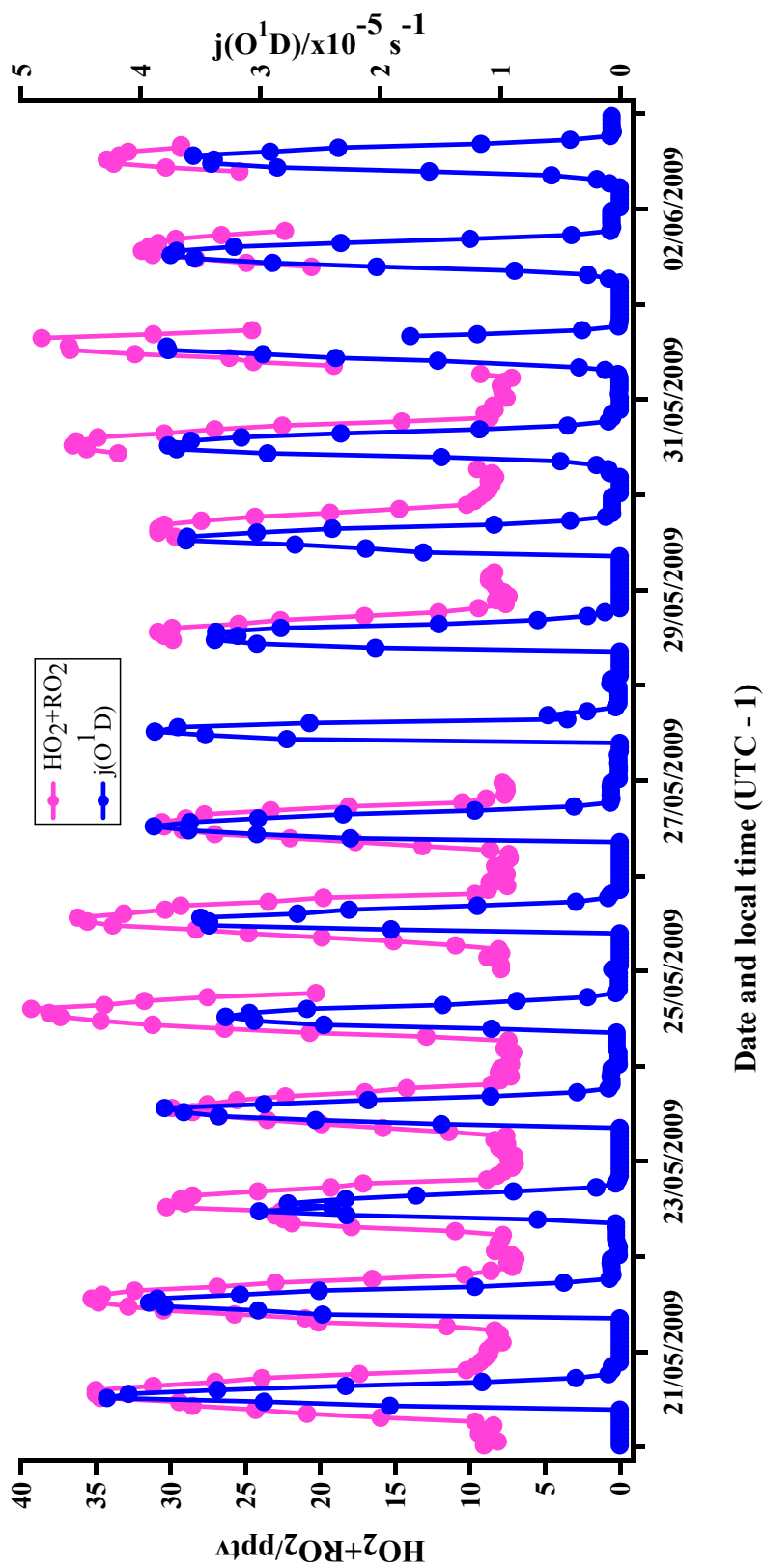


Figure 4.9 - Hourly averaged time series of  $[\text{HO}_2+\text{RO}_2]$  and photolysis rate coefficients of  $j(\text{O}^1\text{D})$  from the campaign SOS (2) during May-June 2009 at Cape Verde Atmospheric Observatory in the tropical marine boundary layer.

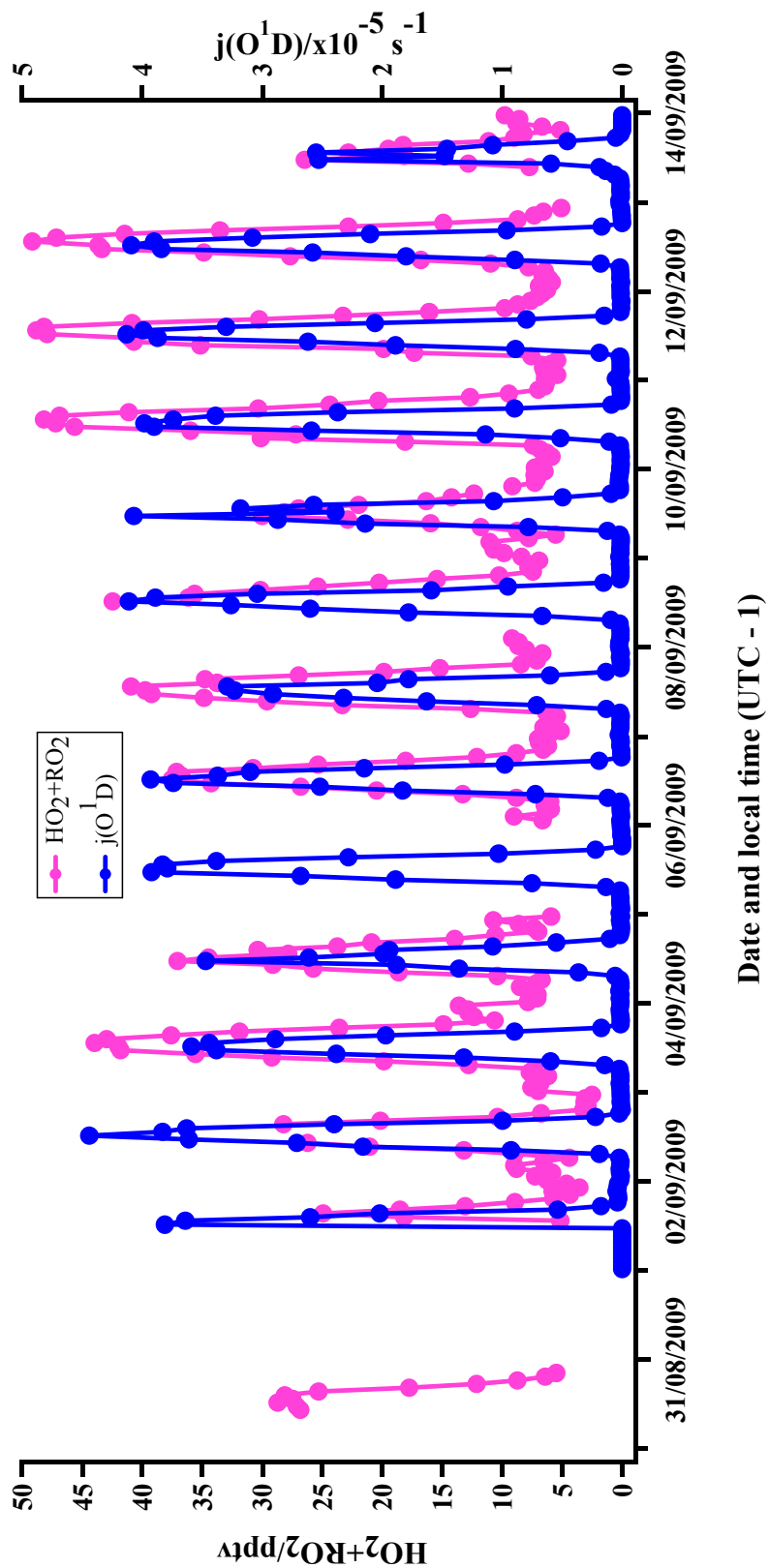


Figure 4.10 - Hourly averaged time series of  $[\text{HO}_2 + \text{RO}_2]$  and photolysis rate coefficients of  $j(\text{O}^1\text{D})$  from the campaign SOS (3) during September 2009 at Cape Verde Atmospheric Observatory in the tropical marine boundary layer.

The lowest value for the hourly averaged peroxy radical concentration measured by the instrument at night time during these campaigns was approximately 2.5 pptv and rarely exceeded the value of 8 pptv as shown in Figures 4.7-4.10. Maximum night time peroxy radical concentrations were measured up to 13 pptv at 23:30 on 3<sup>rd</sup> September during SOS (3) campaign (see Figure 4.10). The highest and lowest peroxy radical measured for SOS (1) campaign 32 pptv at 14:30 on 13<sup>th</sup> March and 3pptv at 04:30 on 9<sup>th</sup> March as shown in Figure 4.11. There is a fluctuation for the peroxy radical concentrations in SOS (2) campaign from 2 pptv at 23:30 on 21<sup>st</sup> May to 39 pptv at 2:30 on 24<sup>th</sup> May, while during SOS (3) campaign, the values vary between 3 pptv at 23:30 on 2<sup>nd</sup> September to 48 pptv at 13:30 on 12<sup>th</sup> September (see Figures 4.12-4.13). The hourly averaged peroxy radical concentrations generated during the hours of day and night for the three SOSs campaigns. The values for the day time averaged peroxy radical concentrations are 15, 24 and 26 pptv during SOS (1), SOS (2) and SOS (3), respectively (see also Table 5.2, section 5.2.1.4 in Chapter 5). The night time averaged peroxy radical concentrations are 5, 8 and 7 pptv during SOS (1), SOS (2) and SOS (3), respectively (see also Table 5.2, section 5.2.1.4 in Chapter 5). It can be concluded that, the concentration values during day time were 3, 3 and 3.5 higher than at night time during SOS (1), SOS (2) and SOS (3) respectively.

#### 4.4.3.2 Mean diurnal cycles of peroxy radicals, $j(O^1D)$ and $\sqrt{j(O^1D)}$

Figure 4.11 shows hourly averaged diurnal cycles for peroxy radicals between,  $j(O^1D)$  and  $\sqrt{j(O^1D)}$  from the SOS (1) (top graph), SOS (2) (middle graph) and SOS (3) (bottom graph).

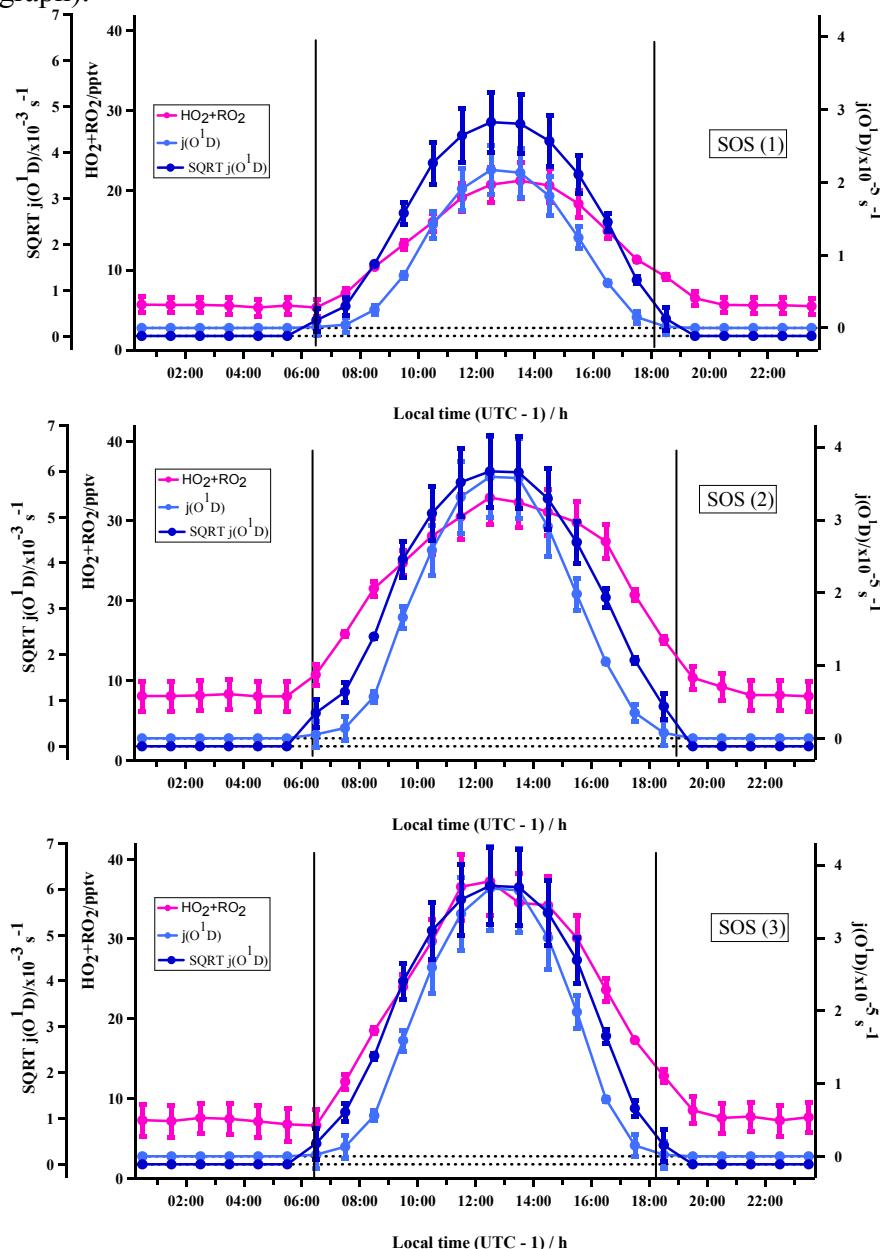


Figure 4.11 - Shows hourly averaged diurnal cycles data for  $[HO_2+RO_2]$ , between photolysis rate coefficients of  $j(O^1D)$  and square root of photolysis rate coefficients of  $j(O^1D)$ , from the campaigns SOS (1) during April-May (top graph), SOS (2) during June-July 2008 (bottom graph) and SOS (3) during September 2009 (bottom graph) Cape Verde Atmospheric Observatory site during in the tropical marine boundary layer. Figure 4.11 generated from the time series of peroxy radical and  $j(O^1D)$  show previously in Figures 4.8, 4.9 and 4.10. Error bars show  $\pm 1\sigma$  of hourly averaged diurnal values.

The peroxy radical concentration follows  $j(\text{O}^1\text{D})$  fairly closely, with higher concentrations at midday when photochemistry is at a maximum with lower concentrations at night. The increased midday concentrations persist throughout the afternoon to give an asymmetry to the diurnal cycle (less asymmetry than OP (3) campaigns, e.g. Figure 3.10 in Chapter 3). This form of asymmetrical diurnal cycle has been noted before in low-NO<sub>x</sub> environments by Monks *et al.*, (1996) at Cape Grim; Fleming *et al.*, (2006) at Mace Head in 2006 (see Sections 1.5.4.1 and 1.5.4.3 in Chapter 1 for the details of the experiments and influences for the asymmetric diurnal profile).

The midday averages concentration of the peroxy radicals are  $22.2 \pm 2.3$  ( $1\sigma$ ) in SOS (1),  $32.3 \pm 3.2$  ( $1\sigma$ ) in SOS (2) and  $37.2 \pm 3.3$  ( $1\sigma$ ) (all in the units of pptv) in SOS (3) (see Figure 4.10). The midday averages of the  $j(\text{O}^1\text{D})$  are  $2.2 \times 10^{-5} \pm 0.3 \times 10^{-5}$  ( $1\sigma$ ) in SOS (1),  $3.6 \times 10^{-5} \pm 0.6 \times 10^{-5}$  ( $1\sigma$ ) in SOS (2) and  $3.7 \times 10^{-5} \pm 0.6 \times 10^{-5}$  ( $1\sigma$ )  $\text{s}^{-1}$  in the SOS (3) as shown in Figure 4.10 where as SOS (1), night time radicals are lowest and SOS (2) peroxy radicals are highest.

The measured radical concentrations during September and May-June periods are approximately similar, while the fact that the day time means peroxy radical concentration during these two periods is  $\sim 1.6$  times bigger compared to February-March period is mainly caused by the seasonal variation of the photolysis rate of ozone. Figure 4.11 shows that there is a growing deviation during the late afternoon for all three of the measurement periods which indicates the fact that loss dominates over-production. The main peroxy radical present during the afternoon has been concluded to be  $\text{CH}_3\text{O}_2$  ( $\text{CH}_3\text{O}_2:\text{HO}_2$ , 2.7:1) by Monks *et al.*, (1996) during SOAPEX experiment

(see Section 1.5.4.1 Chapter 1 for the experiment details). This growth at night time probably happens because of the dominant presence of organic peroxy radicals (Monks *et al.*, 2000b). Within this work, the proportions for  $\text{CH}_3\text{O}_2:\text{HO}_2$  reached 2.5:1 in spring, 3.3:1 in summer and 5:1 in autumn during the afternoon and there has been noted a dramatic growth of this proportion at the beginning of the night time for all three measurement periods, when FAGE and PERCA (V3.5) measurement have been employed for establishing these proportions (see section 4.4.3.7).

The initial hydroxyl radical attack on a hydrocarbon produces an organic peroxy radical ( $\text{RO}_2$ ). Lee *et al.*, (2009) who analysed 2007  $\text{O}_3$  and  $\text{NO}_x$  data that the Cape Verde has observed a much reduced  $\text{NO}$  concentration during evening time (See middle graph on Figure 4.5 for SOS campaigns). Low  $\text{NO}$  concentrations could also decrease the  $\text{HO}_2:\text{RO}_2$  ratio because the conversion of organic peroxy radicals to  $\text{HO}_x$  radicals begins with the reduction of the radical, which is most efficiently done by  $\text{NO}$  and  $\text{XO}$  (especially in marine site, see section 4.6.1, e.g. Bloss *et al.*, (2007); Bloss *et al.*, (2010)). The loss of radicals starts to proceed after sunset through the chain termination reactions such as  $\text{HO}_2+\text{HO}_2$  and  $\text{HO}_2+\text{RO}_2$  involving the  $\text{HO}_2$  radical, and this happens due to the rate coefficients for  $\text{HO}_2+\text{HO}_2$  and  $\text{HO}_2+\text{RO}_2$  reactions exceeding those for pairs of organic peroxy radicals ( $\text{RO}_2$ ) (see Sections 3.2.3.2 and 3.3 in Chapter 3). The  $\text{HO}_2$  radicals thus reduced faster than  $\text{RO}_2$ , the exclusive loss process for the left organic peroxy radicals is through the self-reactions (of the type,  $\text{RO}_2+\text{RO}_2$ ) which have more reduced rate coefficients than  $\text{HO}_2+\text{HO}_2$ . At mixing ratio of a few pptv (5-10 pptv), the half-life for  $\text{RO}_2+\text{RO}_2$  processes are in the order of a few hours. It must be mentioned that peroxy radical concentrations ( $\sim$  5-10 pptv) remains flat after 21:00 through the sunrise at 06:00 next day (see Figure 4.11).

#### 4.4.3.3 Linear correlation between peroxy radicals, $j(\text{O}^1\text{D})$ and $\sqrt{j(\text{O}^1\text{D})}$

Hourly measured concentrations have been obtained for  $\text{HO}_2+\text{RO}_2$ , photolysis rate coefficients of  $j(\text{O}^1\text{D})$  and  $\sqrt{j(\text{O}^1\text{D})}$  each day during the three SOS campaigns. To understand how the formation of peroxy radical correlates with the concentration of  $\sqrt{j(\text{O}^1\text{D})}$  and  $j(\text{O}^1\text{D})$ , it is necessary to use the obtained averaged diurnal cycle data of  $[\text{HO}_2+\text{RO}_2]$ ,  $j(\text{O}^1\text{D})$  and  $\sqrt{j(\text{O}^1\text{D})}$  to plot  $[\text{HO}_2+\text{RO}_2]$  vs.  $j(\text{O}^1\text{D})$  and  $[\text{HO}_2+\text{RO}_2]$  vs.  $(\sqrt{j(\text{O}^1\text{D})})$  for the three of campaigns. Figure 4.8 shows  $[\text{HO}_2+\text{RO}_2]$  vs.  $j(\text{O}^1\text{D})$  and Figure 4.9 shows  $[\text{HO}_2+\text{RO}_2]$  vs.  $(\sqrt{j(\text{O}^1\text{D})})$  between 06:00-19:00 LT, for the three campaigns together.

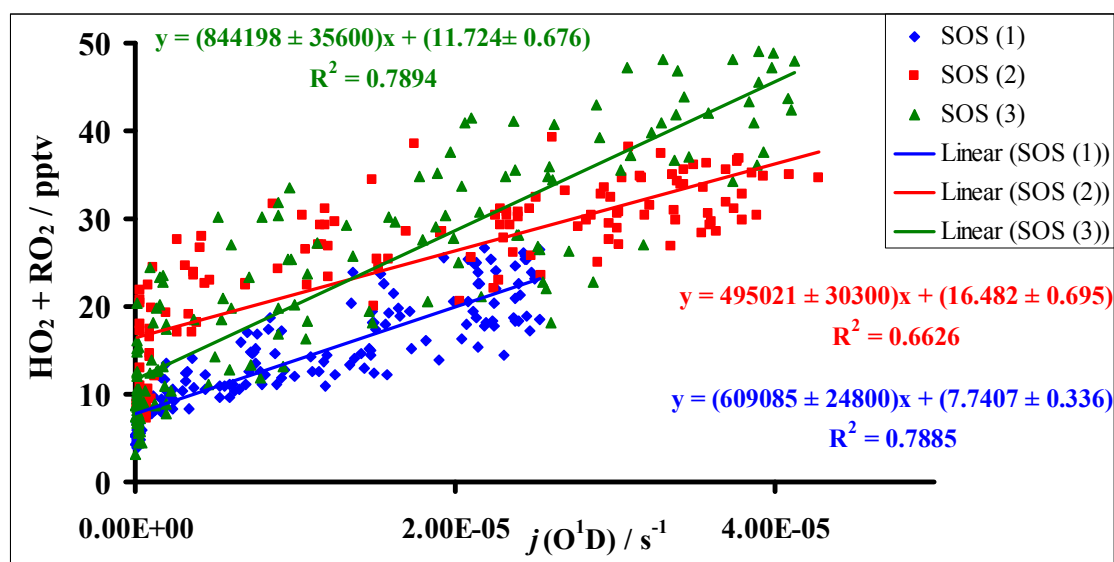


Figure 4.12 – Hourly averaged time series of  $[\text{HO}_2+\text{RO}_2]$  and photolysis rate coefficients of  $j(\text{O}^1\text{D})$  between 06:00-19:00 LT from the campaigns SOS (1) during February-March, SOS (2) during May-June and SOS (3) during September 2009 at Cape Verde Atmospheric Observatory in the tropical marine boundary layer.

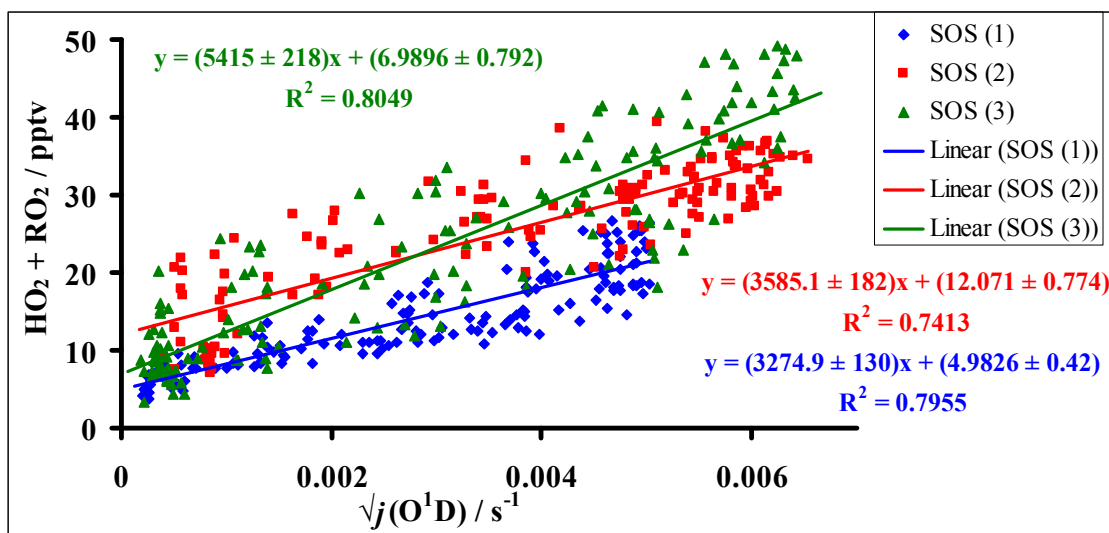


Figure 4.13 - Hourly-averaged time series of  $[\text{HO}_2 + \text{RO}_2]$  and square root of photolysis rate coefficients of  $j(\text{O}^1\text{D})$  between 06:00-19:00 LT from the campaigns SOS (1) during February-March, SOS (2) during May-June and SOS (3) during September 2009 at Cape Verde Atmospheric Observatory in the tropical marine boundary layer.

Penkett *et al.*, (1997) proved that the photochemical ozone production and destruction can be identified through the connection between the total amount of peroxy radicals and the ozone photolysis rate coefficient (to the singlet oxygen atom),  $j(\text{O}^1\text{D})$ . Penkett *et al.*, (1997), Monks *et al.*, (1998), Zanis *et al.*, (1999) and Creasey *et al.*, (2003) concluded that  $\text{HO}_2 + \text{RO}_2$  is proportionate with  $j(\text{O}^1\text{D})$  when  $\text{NO}_x$  amounts are high, while it is proportionate with  $\sqrt{j(\text{O}^1\text{D})}$  in clean conditions, through there remains some uncertainty in the mid- $\text{NO}_x$  regime.

Figure 4.12 and Figure 4.13 illustrates the linear correspondence between  $\sqrt{j(\text{O}^1\text{D})}$  and peroxy radical concentration is marginally improved compared to the one between  $j(\text{O}^1\text{D})$  and peroxy radicals during SOS (1), SOS (2) and SOS (3) campaigns (see Table 4.3). Net photochemical destruction of ozone can only be achieved through the linear interaction between  $\sqrt{j(\text{O}^1\text{D})}$  and  $[\text{HO}_2 + \text{RO}_2]$  and ozone destruction described more in sections 4.5 and 4.5.1.

Table 4.3 shows a comparison of the linear trend and correlation coefficient for  $[\text{HO}_2+\text{RO}_2]$  vs.  $j(\text{O}^1\text{D})$  and  $[\text{HO}_2+\text{RO}_2]$  vs.  $\sqrt{j(\text{O}^1\text{D})}$  between 06:00-19:00 LT from the SOS (1), SOS (2) and SOS (3) campaigns.

Campaign	$[\text{HO}_2+\text{RO}_2]$ (pptv) vs. $j(\text{O}^1\text{D})$ ( $\text{s}^{-1}$ )		$[\text{HO}_2+\text{RO}_2]$ (pptv) vs. $\sqrt{j(\text{O}^1\text{D})}$ ( $\text{s}^{-1}$ )	
	Gradient	Correlation	Gradient	Correlation
SOS (1)	$609085 \pm 24800$	0.79	$3274.9 \pm 237$	0.80
SOS (2)	$495021 \pm 30300$	0.66	$3585.1 \pm 182$	0.74
SOS (3)	$844198 \pm 35600$	0.79	$5415.1 \pm 218$	0.80

Table 4.3 - Gradient and correlation coefficients of hourly-averaged time series of  $[\text{HO}_2+\text{RO}_2]$  vs. photolysis rate coefficients of  $j(\text{O}^1\text{D})$  and  $[\text{HO}_2+\text{RO}_2]$  vs. square root of photolysis rate coefficients of  $j(\text{O}^1\text{D})$  between 06:00-19:00 LT from the campaigns SOS (1) during February-March, SOS (2) during May-June and SOS (3) during September 2009 at Cape Verde Atmospheric Observatory in the tropical marine boundary layer.

Table 4.3 presents the data sets and the correlation coefficient for the three campaigns for the hourly averaged time series of  $[\text{HO}_2+\text{RO}_2]$  vs.  $j(\text{O}^1\text{D})$  and  $[\text{HO}_2+\text{RO}_2]$  vs.  $\sqrt{j(\text{O}^1\text{D})}$ . Monks *et al.*, (2000b) found that at Cape Grim correlation coefficient between  $[\text{HO}_2+\text{RO}_2]$  vs.  $j(\text{O}^1\text{D})$  and  $\sqrt{j(\text{O}^1\text{D})}$  are 0.884 and 0.959 respectively and this was taken to be clear evidence for the control of radical process by ozone photolysis and radical self-and cross- reactions, similar to that observed during the three SOS campaigns for this work.

#### 4.4.3.4 Mean linear correlation between peroxy radicals, OH and $\sqrt{\text{OH}}$ for SOS (1), SOS (2) and SOS (3)

[OH] and [HO<sub>2</sub>] were measured by University of Leeds FAGE (see Table 4.2). Both of PERCA (V3.5) and FAGE instruments were deployed together on the SOS (1), SOS (2) and SOS (3) field campaigns in Cape Verde and both inlets are fixed at quite similar heights and 6 m horizontal separation between of PERCA (V3.5) and FAGE inlets. HO<sub>2</sub> measurements of FAGE will be detailed in Section 4.4.3.7. [OH] and  $\sqrt{[\text{OH}]}$  were obtained between 06:00-19:00 LT from BADC for SOS (1), SOS (2) and SOS (3) campaigns. It needs to be noted that PERCA and FAGE instruments did not work simultaneously for many days during SOS (2) campaign because of technical problem with the FAGE set-up. To understand how the formation of peroxy radical correlates with the [OH] and  $\sqrt{[\text{OH}]}$ , it is necessary to apply the obtained average diurnal cycle data of [HO<sub>2</sub>+RO<sub>2</sub>], [OH] and  $\sqrt{[\text{OH}]}$  to plot [HO<sub>2</sub>+RO<sub>2</sub>] vs. [OH] and [HO<sub>2</sub>+RO<sub>2</sub>] vs.  $\sqrt{[\text{OH}]}$  for the three SOS campaigns. Figure 4.14 shows [HO<sub>2</sub>+RO<sub>2</sub>] vs. [OH] as top graph, [HO<sub>2</sub>+RO<sub>2</sub>] vs.  $\sqrt{[\text{OH}]}$  as bottom graph between 06:00 -19:00 LT for the three campaigns together.

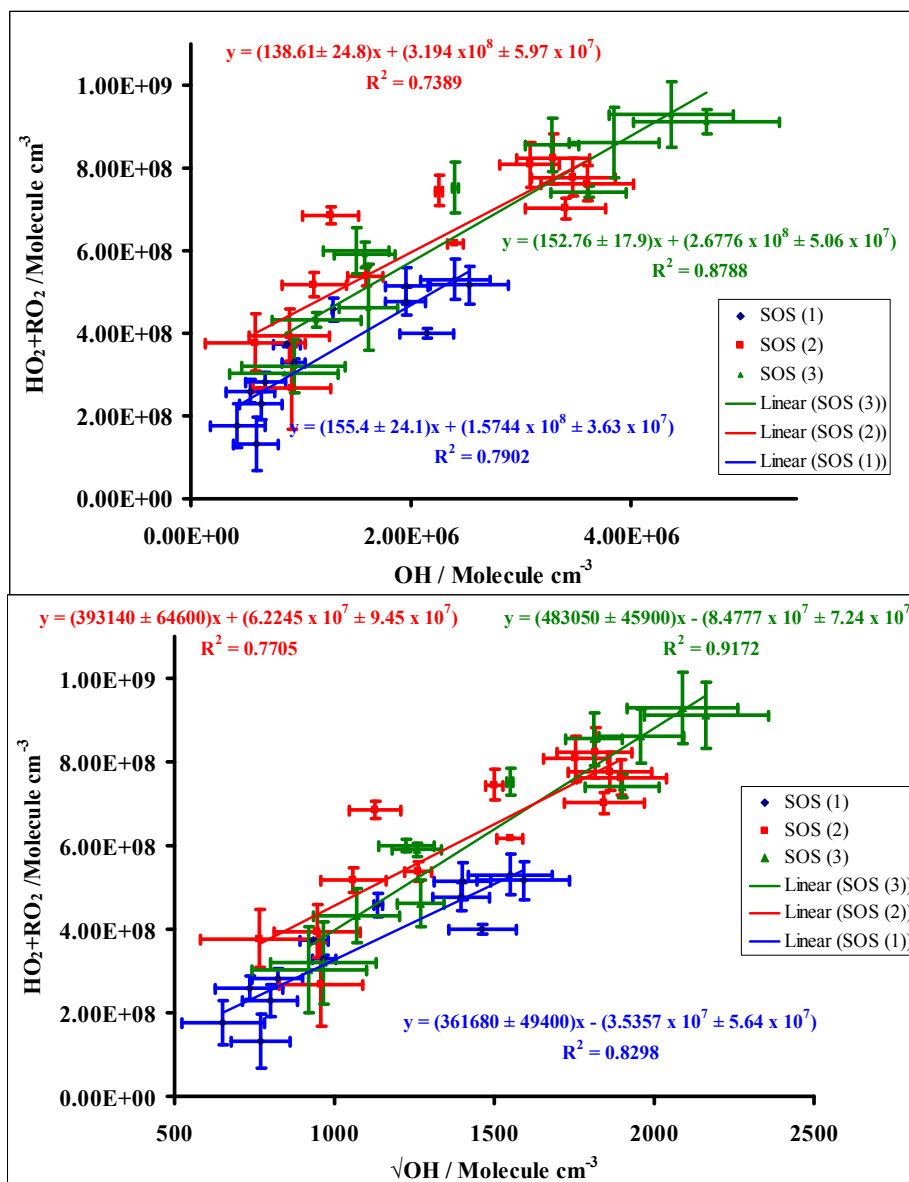


Figure 4.14 - Hourly-averaged diurnal cycle data of  $[\text{HO}_2+\text{RO}_2]$  vs.  $[\text{OH}]$  and  $[\text{HO}_2+\text{RO}_2]$  vs.  $\sqrt{[\text{OH}]}$  between 06:00-19:00 LT from the campaigns SOS (1) during February-March, SOS (2) during May-June and SOS (3) during September 2009 at Cape Verde Atmospheric Observatory in the tropical marine boundary layer. Error bars show  $\pm 1\sigma$  of hourly averaged diurnal values.

Equation 4.7 gives the linear inter relation between  $[\text{HO}_2+\text{RO}_2]$  and  $\sqrt{\text{OH}}$  as demonstrated by Penkett *et al.*, (1997) indicating that a site is characterized by reduced  $\text{NO}_x$  concentration as well as clean air. In order to get a linear relationship between  $[\text{HO}_2+\text{RO}_2]$  and  $\sqrt{\text{OH}}$  in equation 4.7, the measurement site has to be reduced  $\text{NO}_x$

concentration, under relatively constant ozone (Penkett *et al.*, (1997)). Furthermore, photolysis of ozone is the main source of OH whilst the reactions of OH with CO and CH<sub>4</sub> are the major sink for the OH (i.e. assume all OH reacts with CO and CH<sub>4</sub>, see Section 4.4.3 and reactions 4.5 and 4.6). The HO<sub>2</sub>+RO<sub>2</sub> with √OH trend appears to be the similar during the three of SOS campaigns. Table 4.4 shows a comparison of the linear trend and correlation coefficient for [HO<sub>2</sub>+RO<sub>2</sub>] vs. [OH] and [HO<sub>2</sub>+RO<sub>2</sub>] vs. √OH for day time (06:00-19:00 LT) from SOS (1), SOS (2) and SOS (3) campaigns at the Cape Verde Atmospheric Observatory.

Campaign	[HO <sub>2</sub> +RO <sub>2</sub> ] (molecule cm <sup>-3</sup> ) vs. [OH] (molecule cm <sup>-3</sup> )		[HO <sub>2</sub> +RO <sub>2</sub> ] (molecule cm <sup>-3</sup> ) vs. √[OH] (molecule cm <sup>-3</sup> )	
	Gradient	Correlation	Gradient	Correlation
SOS (1)	155.4 ± 24.1	0.79	361680 ± 49400	0.83
SOS (2)	138.61 ± 24.8	0.74	393140 ± 64600	0.77
SOS (3)	152.76 ± 17.9	0.88	483050 ± 45900	0.92

Table 4.4 - Gradient and correlation coefficients of hourly-averaged diurnal cycle data of [HO<sub>2</sub>+RO<sub>2</sub>] vs. [OH] and [HO<sub>2</sub>+RO<sub>2</sub>] vs. √[OH] between 06:00-19:00 LT from the campaigns SOS (1) during February-March, SOS (2) during May-June and SOS (3) during September 2009 at Cape Verde Atmospheric Observatory in the tropical marine boundary layer.

All three SOS campaigns show a significant linear relationship between 06:00-19:00 LT in the [HO<sub>2</sub>+RO<sub>2</sub>] vs. square root [OH] marginally better than the relationship with [OH]. This result is indicative of low NO<sub>x</sub> conditions with the three of SOS campaigns. Zanis *et al.*, (1999) pointed out that equation 4.7 is not applicable for semi-polluted conditions, i.e. when [NO] is over 50 pptv, as under these conditions the dominant reaction becomes the recycling of HO<sub>2</sub> to OH by NO; by using of the result at Cape Verde, it might be suggested that under low NO<sub>x</sub> conditions encountered, the

possible OH loss through reaction with  $\text{NO}_2$  is small (see section 4.6), while the recycling of  $\text{HO}_2$  to OH by NO is not a major process (see Section 4.6.1).

#### 4.4.3.5 Mean diurnal cycles of peroxy radicals, OH for SOS (1), SOS (2) and SOS (3)

Figure 4.15 (top graph) shows hourly averaged diurnal cycles together for [OH] between 06:00-21:00 LT whereas Figure 4.15 (top graph) shows hourly averaged diurnal cycles together for [ $\text{HO}_2+\text{RO}_2$ ] from the SOS (1), SOS (2) and SOS (3) campaigns (see Table 4.2 and Section 3.1.3 in Chapter 3 for data averaging process).

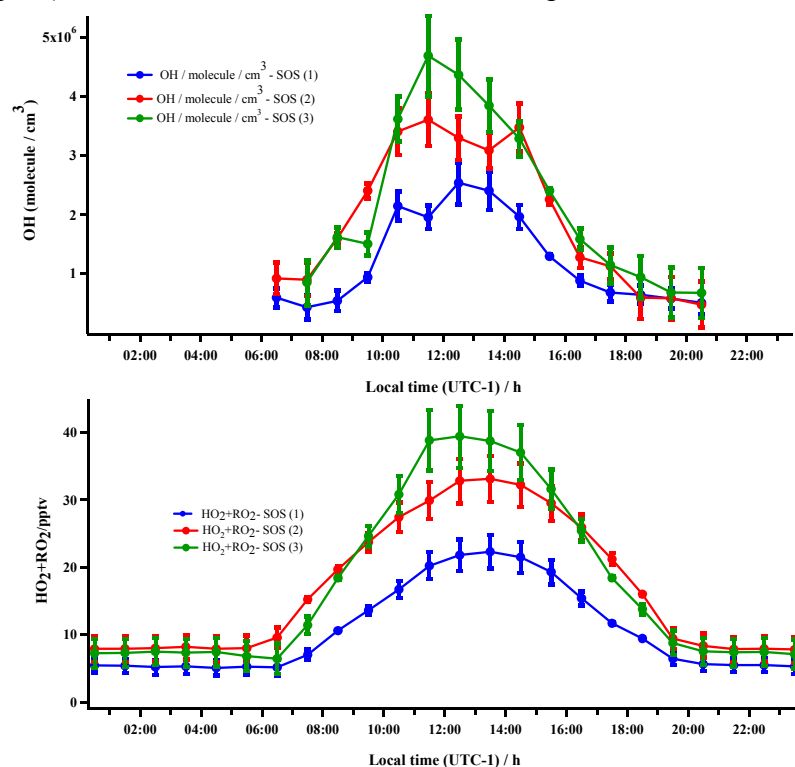


Figure 4.15 - Hourly averaged diurnal cycles together of [OH] (top graph) between 06:00-21:00 LT and hourly averaged diurnal cycles together of [ $\text{HO}_2+\text{RO}_2$ ] (bottom graph) from the campaigns SOS (1) during February-March, SOS (2) during May-June and SOS (3) during September 2009 at Cape Verde Atmospheric Observatory in the tropical marine boundary layer. Figure 4.15 (bottom) has generated from the time series of peroxy radical shown previously in Figures 3.8-3.10. Figure 4.15 shows the same data as plotted previously in Figure 4.11. Error bars show  $\pm 1\sigma$  of hourly averaged diurnal values. OH data was only available between 06:00-21:00 for SOS (1), SOS (2) and SOS (3) campaigns.

Peroxy radicals are formed *via* the oxidation (mainly by OH) of anthropogenic and biogenic species in the atmosphere such as CO, CH<sub>4</sub> and other organic compounds. The peak values of  $j(\text{O}^1\text{D})$  followed the trend SOS (1) < SOS (2) ~ SOS (3) as shown in Figure 4.11 and Figures 4.8-4.10. Figures 4.15 (top graph) and 4.15 (bottom graph) show similar qualitative trends were observed for the [HO<sub>2</sub>+RO<sub>2</sub>] and [OH] to each other. (It needs to be noted that the PERCA and FAGE instruments did not run simultaneously during SOS (2) (see Section 4.4.3.4). High photochemical activity is evident at this tropical location. It is clear that the maxima in radical concentration scales with season.

#### 4.4.3.6 Peroxy radical and NO<sub>x</sub> relationships during daytime

HO<sub>2</sub>+RO<sub>2</sub> was measured by PERCA, whilst NO<sub>x</sub> measured by NO<sub>x</sub>y (see Table 4.2). During the SOS (1) and SOS (2) campaigns, hourly averaged time series of HO<sub>2</sub>+RO<sub>2</sub> and NO<sub>x</sub> concentrations were generated between 06:00-19:00 LT (UTC-1) from BADC (see Section 3.1.3 in Chapter 3 for data averaging process). NO<sub>2</sub> data is not available for SOS (3) campaign (see Table 4.2). To explore the formation of peroxy radical correlates with the concentration of NO<sub>x</sub> during day time, it is necessary to use the obtained hourly averaged diurnal cycle data of [HO<sub>2</sub>+RO<sub>2</sub>] and [NO<sub>x</sub>] to plot [HO<sub>2</sub>+RO<sub>2</sub>] vs. [NO<sub>x</sub>] for SOS (1) and SOS (1) campaigns. The form of Figure 4.16 shows, there is a positive and moderately strong correlation ( $R^2=0.58$  for SOS (1) and  $R^2=0.77$ ) between [HO<sub>2</sub>+RO<sub>2</sub>] and [NO<sub>x</sub>] for SOS (1) and SOS (3) campaigns.

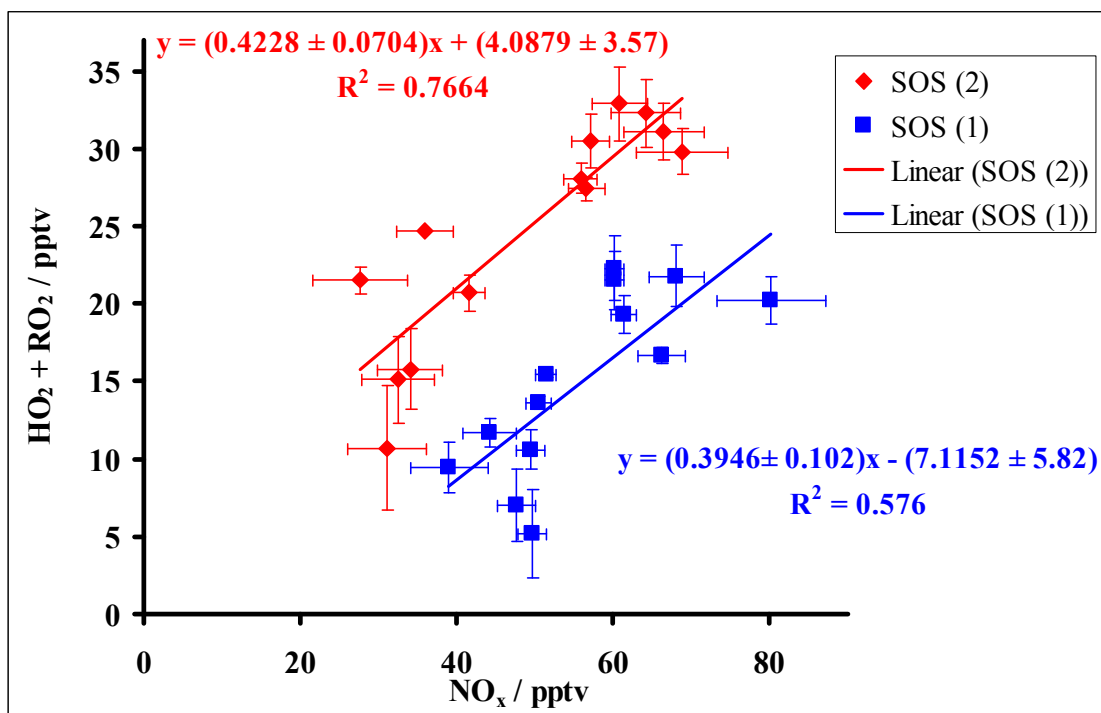


Figure 4.16 - Hourly averaged diurnal cycle data of [HO<sub>2</sub>+RO<sub>2</sub>] and [NO<sub>x</sub>] between 06:00-19:00 LT from the campaigns SOS (1) during February-March and SOS (2) during May-June 2009 at Cape Verde Atmospheric Observatory in the tropical marine boundary layer. Error bars show  $\pm 1\sigma$  of hourly averaged diurnal values.

Liu *et al.*, (1980) and Logan *et al.*, (1981) showed that at low to intermediate NO<sub>x</sub> concentrations, RO<sub>2</sub> could increase with increasing NO<sub>x</sub> because its precursors may correlate with NO<sub>x</sub>. This could correspond to NO<sub>x</sub> concentrations where peroxy radicals show an increase for SOS (1) and SOS (2) campaigns as shown in Figure 4.16. Holland *et al.*, (2003) found at the BERLIOZ campaign, outside Berlin (Germany), that for [NO<sub>x</sub>] >1 ppbv, HO<sub>2</sub> decreased as NO<sub>x</sub> increased and that for [NO<sub>x</sub>] <1 ppbv, HO<sub>2</sub> increased with increasing NO<sub>x</sub>. During the TOPSE campaign (in N. America), Stroud *et al.*, (2004) found that peroxy radical concentration appears to decrease with NO<sub>x</sub> in the winter (when radicals are lower) and increase in the spring (when peroxy radicals are higher).

Liu *et al.*, (1980) and Logan *et al.*, (1981) explained further that, at high NO<sub>x</sub> concentrations peroxy radicals should decrease owing to removal by radical-NO<sub>x</sub> reactions: this is not applicable for Cape Verde site because low concentration of NO<sub>x</sub> were measured during SOS (1) and SOS (2) campaigns. During the SOS (2) and SOS (2) campaigns, the loss of peroxy radical is basically controlled by the peroxy radical self-reaction, rather than the reaction of OH with NO<sub>2</sub>. The process of peroxy radical loss estimated to be owing to reaction of OH with NO<sub>2</sub> appears to be less favourable as seen in Figure 4.16 (explained in section 4.6 using parameters  $\alpha$ ,  $\beta$  and  $\gamma$ ).

#### 4.4.3.7 HO<sub>2</sub>: (HO<sub>2</sub>+RO<sub>2</sub>) ratio

The photochemical oxidation of organic species in the atmosphere, as well as the ozone loss and production, is mediated by peroxy radicals (Monks *et al.*, 2003a) (see section 1.4, Chapter 1). An estimate amount of the radical budgets can be determined by having information about the HO<sub>2</sub> to RO<sub>2</sub> proportions, as well as concentrations of other gaseous species and photolysis frequencies and temperature and this offers a connection between O<sub>3</sub> precursor VOCs and *in situ* O<sub>3</sub> production.

The complexity of organic peroxy radicals (RO<sub>2</sub>) is increased by an increase in the chemical complexity of non-methane VOCs. Monks *et al.*, (2005) pointed out that many RO<sub>2</sub> end up by being transformed into HO<sub>2</sub>; therefore, a growth of the RO<sub>2</sub> mixing ratio does not necessarily lead to a growth in the RO<sub>2</sub>:HO<sub>2</sub> proportions.

PERCA (V3.5) necessarily measures the sum of HO<sub>2</sub>+RO<sub>2</sub> where as HO<sub>2</sub> measurements taken by FAGE provide the HO<sub>2</sub> mixing ratio directly. Generally, the interference by RO<sub>2</sub> radicals would be small in clean remote environments, when short

chain alkanes influence the OH reactivity, but it increases in polluted environments. Fuchs *et al.* (2011) have recently reported interference in HO<sub>2</sub> measurements using a similar FAGE instrument. The interference caused by the partial chemical conversion of certain RO<sub>2</sub> species to OH on addition of NO in the FAGE detection cell. The interference has the potential to cause a systematic positive bias in HO<sub>2</sub> measurements. Therefore, HO<sub>2</sub> observations reported using the FAGE technique may be higher than the true ambient HO<sub>2</sub> concentrations. Under the operating conditions employed during the OP3 and SOS campaigns, the University of Leeds FAGE instrument was relatively insensitive to detection of RO<sub>2</sub> species (Whalley *et al.*, (2011)). Recent laboratory tests have showed a 12% yield of HO<sub>2</sub> owing to the decomposition of ethene-derived RO<sub>2</sub> in the presence of NO. Ethene-derived RO<sub>2</sub> species provided the largest HO<sub>2</sub> yield compared with other RO<sub>2</sub> species, e.g. derived from isoprene (yield of 10 %) and higher alkanes. This small interference falls within the uncertainty of the HO<sub>2</sub> (50 %) observations and should have very little impact on the OP3 and SOS results. For FAGE, HO<sub>2</sub> data is used between 06:00-19:00 LT and obtained hourly averaged are used to produce diurnal averages for three campaigns SOS (1), SOS (2) and SOS (3) in order to compare with PERCA (V3.5) HO<sub>2</sub>+RO<sub>2</sub> (see Table 4.2 and see Section 3.13 in Chapter 3 for data averaging process)

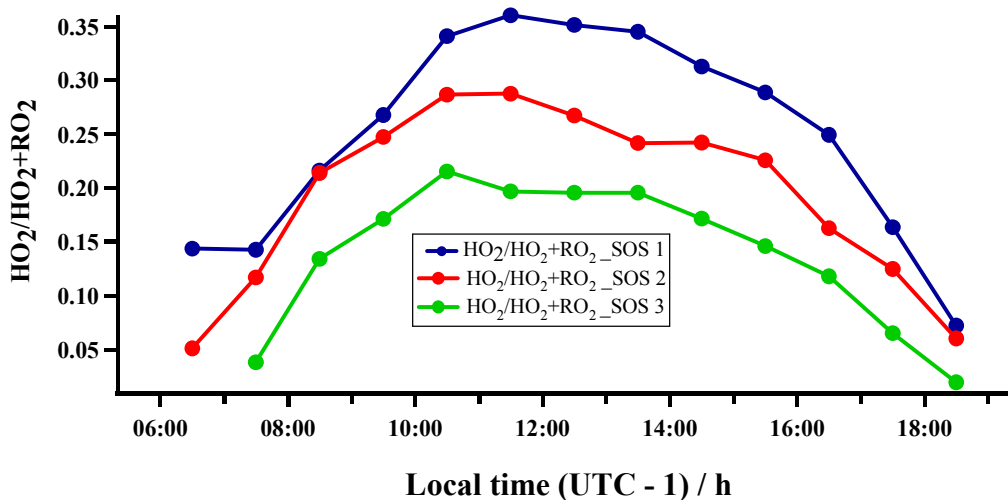


Figure 4.17 - The measured hourly-averaged diurnal cycle data of  $[\text{HO}_2]/[\text{HO}_2+\text{RO}_2]$  ratios between 06:00-19:00 LT using FAGE and PERCA (V3.5) instruments from the campaigns SOS (1) during February-March, SOS (2) during May-June and SOS (3) during September 2009 at Cape Verde Atmospheric Observatory in the tropical marine boundary layer.

The hourly averaged diurnal values of  $[\text{HO}_2]/[\text{HO}_2+\text{RO}_2]$  ratios tended to be variable between 06:00-19:00 during the SOS (1), SOS (2) and SOS (3) campaigns as shown in Figure 3.17. Hourly averaged diurnal values of  $[\text{HO}_2]/[\text{HO}_2+\text{RO}_2]$  ratios were largest around middle of the day than in the morning and afternoon during the SOS (1), SOS (2) and SOS (3) campaigns as shown in Figure 4.17. Further,  $[\text{HO}_2]/[\text{HO}_2+\text{RO}_2]$  ratios were greater in SOS (1) than in SOS (2) and SOS (3) between 06:00-19:00 as shown in Figure 4.17. Whalley *et al* (2010) found that  $[\text{HO}_2]$  sources are dominated by the reaction of OH with CO during May-June 2007 at the Cape Verde Atmospheric Observatory. Carpenter *et al.*, (2010) observed that a decrease in daily peak  $[\text{HO}_2]$  with a decrease in  $[\text{CO}]$ . The  $[\text{HO}_2]$  might be determined by the  $[\text{CO}]$ . Hourly averaged diurnal mixing ratios of CO were higher in SOS (1) than in SOS (2) (see top graph on Figure 4.5) for this analysis. The hourly averaged diurnal values of  $[\text{HO}_2]/[\text{HO}_2+\text{RO}_2]$  was higher in SOS (1) than in SOS (2) (see Figure 4.17).  $[\text{CO}]$  was taken to be evidence for the presence of  $[\text{HO}_2]$ , similar to that observed during the SOS (1), SOS (2) and SOS (3) campaigns for this work. Unfortunately, there was no measured  $[\text{CO}]$

data available for SOS (3) campaign to test the similar hypothesis (see Table 4.2 and Figure top graph on Figure 4.5). Furthermore,  $\text{CH}_3\text{O}_2$  are predominantly in the form of peroxy radical between 06:00-19:00 during SOS (1), SOS (2) and SOS (3) campaigns (see Figure 4.5). See Section 4.4.3.8 for ratio of  $[\text{HO}_2] / [\text{HO}_2 + \text{RO}_2]$  during night time. See the sections 4.5, 4.5.1, 4.6 and 4.6.1 for the applications of  $[\text{HO}_2] / [\text{HO}_2 + \text{RO}_2]$  ratio.

#### 4.4.3.8 Night-time chemistry

In the absence of photochemistry, there is a series of night-time peroxy radical-producing channels.  $\text{NO}_3$  (nitrate) radical (Carslaw *et al.*, 1997; Allen *et al.*, 1999; Penkett *et al.*, 1999; Salisbury *et al.*, 2001; Geyer *et al.*, 2003; Fleming *et al.*, 2006) and ozone reactions with alkenes (Hu and Stedman, 1995; Rickard *et al.*, 1999; Kanaya *et al.*, 1999, 2000, 2002; Salisbury *et al.*, 2001; Fleming *et al.*, 2006) have been found to be active in the marine influenced atmosphere.

The value for  $[\text{HO}_2 + \text{RO}_2]$  tended to be identical throughout the night time during the SOS (1), SOS (2) and SOS (3) campaigns (see bottom graph on Figure 4.15). Night time  $[\text{HO}_2 + \text{RO}_2]$  were measured up to 8, 10 and 13 pptv during SOS (1), SOS (2) and SOS (3) campaigns, respectively (see Figures 4.8-4.10).

#### NO<sub>x</sub> influences

During the SOS (1) and SOS (2) campaigns, hourly averaged time series of  $\text{HO}_2 + \text{RO}_2$  (see Figure 4.8 for SOS (1) and Figure 4.9 for SOS (2)) and  $\text{NO}_x$  concentrations (see Table 4.2 for SOS (1) and SOS (2)) were generated between 19:00-06:00 LT (UTC-1) from BADC (see Section 3.1.3 in Chapter 3 for data averaging process). Figure 4.19

shows hourly averaged time series of  $[\text{HO}_2+\text{RO}_2]$  and  $[\text{NO}_x]$  between 19:00-06:00 LT from the campaigns SOS (1) and SOS (2).  $\text{NO}_2$  data is not available for SOS (3) campaign (see Table 4.2).

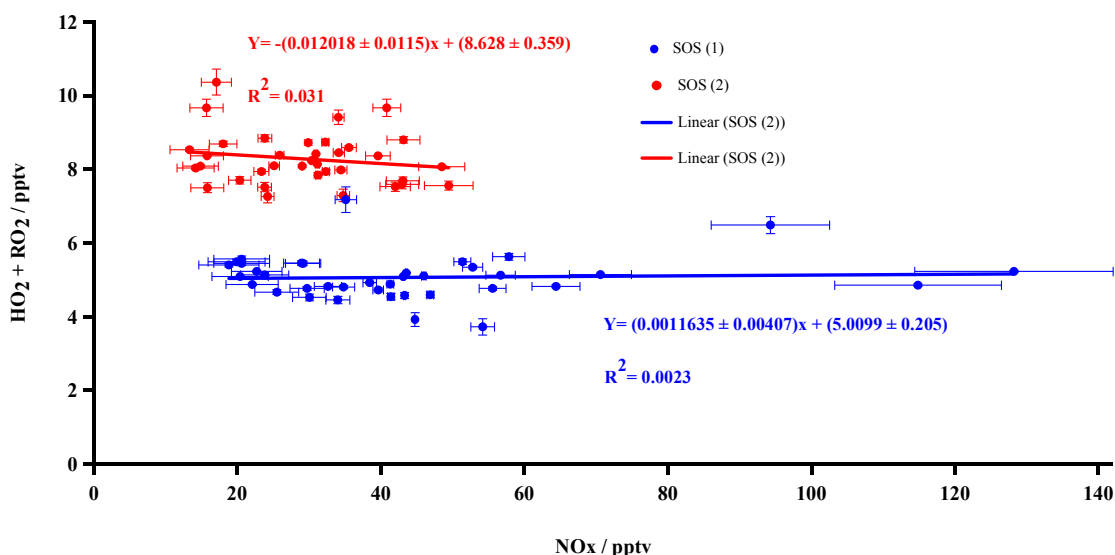


Figure 4.18 - Hourly averaged time series of  $[\text{HO}_2+\text{RO}_2]$  and  $[\text{NO}_x]$  between 19:00-06:00 LT from campaigns SOS (1) during February-March and SOS (2) during May-June 2009 at Cape Verde Atmospheric Observatory in the tropical marine boundary layer. Error bars show  $\pm 1\sigma$  of hourly averaged values.

At night, peroxy radical's trend is pretty flat and  $[\text{HO}_2+\text{RO}_2]$  is not correlated with  $[\text{NO}_x]$  from the SOS (1) and SOS (2) campaigns (see Figure 4.19). The  $\text{NO}_x$  mixing ratio was very low and did not exceed 50 pptv during the SOS (2) campaign whereas  $\text{NO}_x$  mixing ratio varied between 18 and 128 pptv during the SOS (1) campaign as shown in Figure 4.18.  $[\text{HO}_2+\text{RO}_2]$  tended to be similar throughout the night with the maximum concentration at the start of the night (see Figure 4.11 and see bottom graph on Figure 4.15).

Under the relatively low  $[\text{NO}_2]$  (night time average mixing ratio 39 pptv for SOS (1), 24 pptv for SOS (2)) conditions at Cape Verde,  $\text{NO}_3$  and  $\text{N}_2\text{O}_5$  rapidly equilibrate and any loss of  $\text{N}_2\text{O}_5$  resulted in the removal of  $\text{NO}_3$  from the system.  $\text{N}_2\text{O}_5$  can be

removed by reaction with H<sub>2</sub>O and by uptake on aerosol. Removal of N<sub>2</sub>O<sub>5</sub> can be a major loss pathway for NO<sub>3</sub> (Allan *et al.*, 1999, 2000b). An important issue in night-time chemistry is the concentration of nitric oxide. NO<sub>3</sub> radical night time chemistry could be unimportant at the Cape Verde in the tropical marine boundary layer because there is no correlation seen in Figure 4.18. [NO<sub>3</sub>] data is not available to do the further analysis for SOS (1), SOS (2) and SOS (3) campaigns. Without supporting [NO<sub>3</sub>] data it is impossible to know the role of NO<sub>3</sub> chemistry at Cape Verde in the tropical marine boundary layer. Whalley *et al.*, (2010) observed that the reaction of NO<sub>3</sub> with alkenes is not a significant source of HO<sub>2</sub> at Cape Verde, unlike Mace Head (Salisbury *et al.*, 2001).

To explore the night time radicals at the Cape Verde in the tropical marine boundary layer, ozone-alkene reactions could be important (e.g. Salisbury *et al.*, (2001)) (see Section 1.4.2 in Chapter 1). Night time averaged mixing ratio of ozone were measured 37, 36 and 20 ppbv during SOS (1), SOS (2) and SOS (3) campaigns, respectively (see bottom graph on Figures 4.5). Rate coefficients for the reactions of ozone with propene and isoprene were used to calculate the rate of the ozone reactions with propene and isoprene, respectively. Hourly averaged rate of the ozone reaction with propene has been generated between 19:00-06:00 during the SOS (3) campaign by multiplying the measured [O<sub>3</sub>] (see Table 4.2 and see Section 3.13 in Chapter 3 for data averaging process) with rate coefficients for the reaction of ozone with propene (see Table 4.5). Similar analysis carried out for the hourly averaged rate of the ozone reaction with isoprene using measured [isoprene] (see Table 4.2) and the rate coefficients for the reaction of ozone with isoprene (see Table 4.5).

Reaction	Rate coefficient/ $\text{cm}^3 \text{ molecule}^{-1} \text{ s}^{-1}$	Reference
$\text{O}_3 + \text{isoprene}$	$1.03 \times 10^{-14} \exp^{(-1995/T)}$	(IUPAC, 2006))
$\text{O}_3 + \text{propene}$	$5.5 \times 10^{-15} \exp^{(-1880/T)}$	(IUPAC, 2006))

Table 4.5 – Rate coefficients for the reactions of ozone with isoprene and propene are at 298 K and 1 atmosphere.

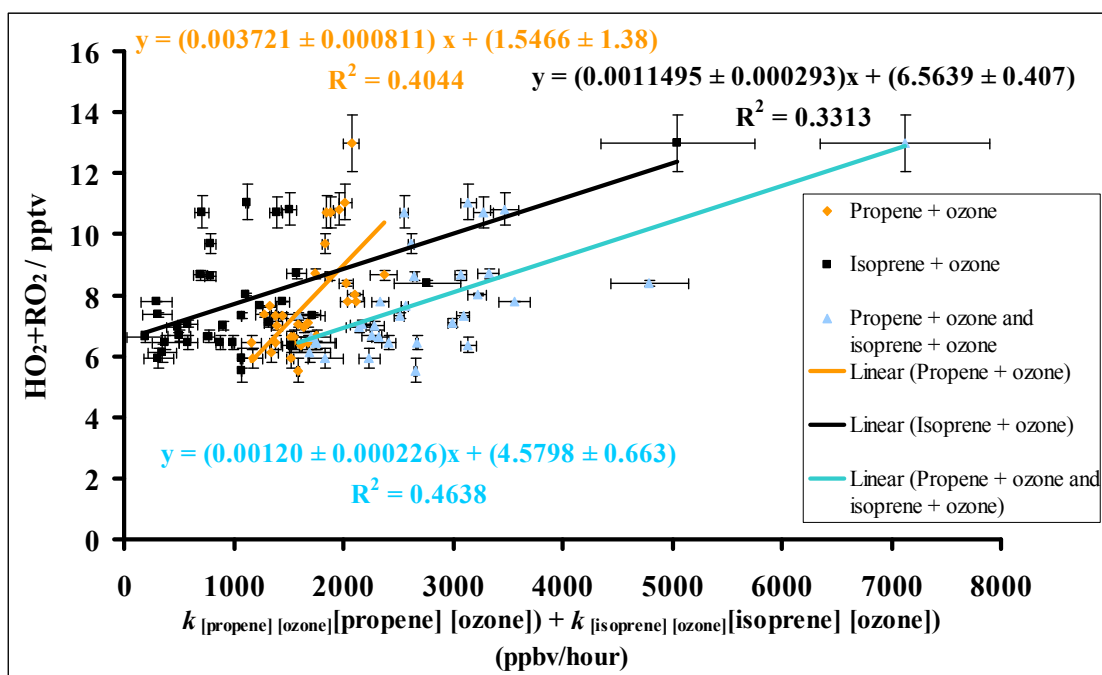


Figure 4.19 – Hourly averaged time series of  $[\text{HO}_2 + \text{RO}_2]$  and the rate of the ozone reactions with propene and isoprene between 19:00-06:00 LT from the campaign SOS (3) during May-June 2009 at Cape Verde Atmospheric Observatory in the tropical marine boundary layer. Error bars show  $\pm 1\sigma$  of hourly averaged values.

$[\text{HO}_2 + \text{RO}_2]$  measured up to 13 pptv during the night time for SOS (3) campaign (see Figures 4.13-4.14). Carpenter *et al.*, (2010) explained that it was only during SOS (3), for one night, that the FAGE system measured. For that night, it has been observed that  $[\text{HO}_2]$  were reduced ( $< 1$  pptv) and this led to the conclusion that  $[\text{HO}_2]$  supplied less than 10% of the night time peroxy radical budget.  $\text{CH}_3\text{O}_2$  is the main peroxy radical during the night time. Organic peroxy radicals are dominant over  $\text{HO}_2$  in the clean

marine boundary layer (see section 4.4.3.2 and 4.4.3.7 for  $\text{CH}_3\text{O}_2:\text{HO}_2$ ). Non zero  $[\text{OH}]$  ( $\sim 0.75 \times 10^6$  molecule  $\text{cm}^{-3}$ ) was measured between 19:00-21:00 during SOS (3) campaign (see top graph on Figure (4.15)). Unfortunately,  $[\text{OH}]$  data is not available between 21:00-06:00 during the SOS (3) campaign.

Phytoplankton in oceans is known to produce a large suite of VOCs (Moore *et al.*, 1994; Shaw *et al.*, 2003). The oceans around Cape Verde are biologically active (Whalley *et al.*, (2010), Read *et al.*, (2008)). During the night time,  $[\text{HO}_2+\text{RO}_2]$  appear to present a slightly more increased sensitivity to the reaction of ozone with propene than to the reaction of ozone with isoprene (see Figure 4.19 in terms of their gradient). The largest increase in  $[\text{HO}_2+\text{RO}_2]$  has been observed, when the rate of the reaction of ozone with propene increase, as compared to the rate of the reaction of ozone with isoprene during the night time (see Figure 4.19). Whalley *et al.*, (2010) observed that low concentrations (0.6 pptv) of  $\text{HO}_2$  were measured by FAGE on two nights during May-June 2007 at the Cape Verde Atmospheric Observatory. No night time OH measurements were made during May-June 2007. Whalley *et al.*, (2010) found that the reactions of  $\text{O}_3$  with alkenes, specifically propene and isoprene and its oxidation products become the source for the night time generation of  $[\text{OH}]$  and  $[\text{HO}_2]$  in the MCM box model. The OH produced through the reactions of ozone with alkenes. OH reacts with acetaldehyde and methane and leads to the formation of peroxy radicals. Peroxy radicals generate  $\text{HO}_2$  through self-reaction or reaction with NO. Alternatively,  $\text{HO}_2$  can also be generated through the direct reaction of OH with CO. The OH and  $\text{HO}_2$  radicals are strongly coupled at night.

An alternative source for a night time peroxy radicals: The entrainment of peroxyacetyl nitrate (PAN) may also act as a night time source of radicals (Carpenter *et al.*, 2010 and Whalley *et al.*, 2010)).  $\text{CH}_3\text{C}(\text{O})\text{O}$  radical rapidly decomposes to  $\text{CH}_3$  and  $\text{CO}_2$  and the  $\text{CH}_3$  radical is converted promptly to  $\text{CH}_3\text{O}_2$  in the presence of  $\text{O}_2$  (see Section 3.2.3.3 in Chapter 3). Night-time observations can be considered by air masses with high concentrations of peroxyacetyl nitrate (PAN) of  $\sim 100$  ppt. There is a lack of seasonal PAN measurements made at the CVAO, therefore this conclusion remains untested. Jacobi *et al.*, (1999) observed that [PAN] was observed as high as 120 pptv during a cruise off the west coast of Africa in the north of  $10^\circ\text{N}$ . No modelling results are available at this moment for SOS (1), SOS (2) and SOS (3) campaigns.

#### 4.5 Photochemical ozone production

In order to construct an ozone budget, the essential factors that control the ozone concentration in the marine boundary layer during the day or night over a seasonal cycle have to be determined. As described in section 3.2.3.5 in Chapter 3 it is possible to calculate the instantaneous *in-situ* net ozone production or loss. This has been done for the period of measurements in this Chapter. FAGE was the instrument employed in all three of SOS campaigns for  $[\text{HO}_2]$  and  $[\text{OH}]$  measurements and an hourly  $\alpha$  ( $=[\text{HO}_2]/[\text{HO}_2 + \text{RO}_2]$ ) was obtained every day during day time on the basis of  $[\text{HO}_2]$  and  $[\text{RO}_2]$  as shown in Figure 4.17. There are independent measurements for  $[\text{OH}]$  and  $[\text{HO}_2]$ , but owing to their concurrence with other measurements for some days, their ratio was obtained as an hourly averaged diurnal data for each campaign. Equation (A) has been employed for calculating the net ozone production or loss rates,

$$N(\text{O}_3) = k_c[\text{HO}_2 + \text{RO}_2][\text{NO}] - \{ff(\text{O}^1\text{D}) + k_{3,7}[\text{OH}] + k_{3,8}[\text{HO}_2]\} [\text{O}_3] \quad (\text{A})$$

Certain ozone sinks calculations have not been considered in equation (A) (see Section 3.2.3.5 for the discussion). Nevertheless, equation (A) remains a good approximation for the troposphere.  $k_c, f, k_{3.7}$  and  $k_{3.8}$  are described in section 3.3 in Chapter 3.

The hourly averaged of  $P(O_3)$ ,  $L(O_3)$  and  $N(O_3)$  were calculated between 06:00-19:00 LT, for the SOS (1), SOS (2) and SOS (3) campaigns (see Section 3.2.3.5). The hourly averaged of rates for photolysis of ozone, the reaction of ozone with OH and the reaction of ozone with HO<sub>2</sub> were obtained between 06:00-19:00 LT for the SOS (1), SOS (2) and SOS (3) campaigns (see Section 3.2.3.5 for data averaging process). The following measurements were taken to calculate  $P(O_3)$ ,  $L(O_3)$  and  $N(O_3)$  for the SOS (1), SOS (2) and SOS (3) campaigns: PERCA measurements of [HO<sub>2</sub>+RO<sub>2</sub>] (see Figure 4.8 for SOS (1), Figure 4.9 for SOS (2) and Figure 4.10 for SOS (3)); NO<sub>x</sub> measurements of NO (see Table 4.2); spectral radiometer measurement of  $j(O^1D)$  (see Figure 4.8 for SOS (1), Figure 4.9 for SOS (2) and Figure 4.10 for SOS (3)); FAGE measurements of [OH] and [HO<sub>2</sub>] (see Table 4.2); UV absorption detector (Thermo Environmental Instruments, Model 49i) measurement of ozone (see Table 4.2). See also Table 4.2 and section 3.1.3 in Chapter 3 for the data averaging process.

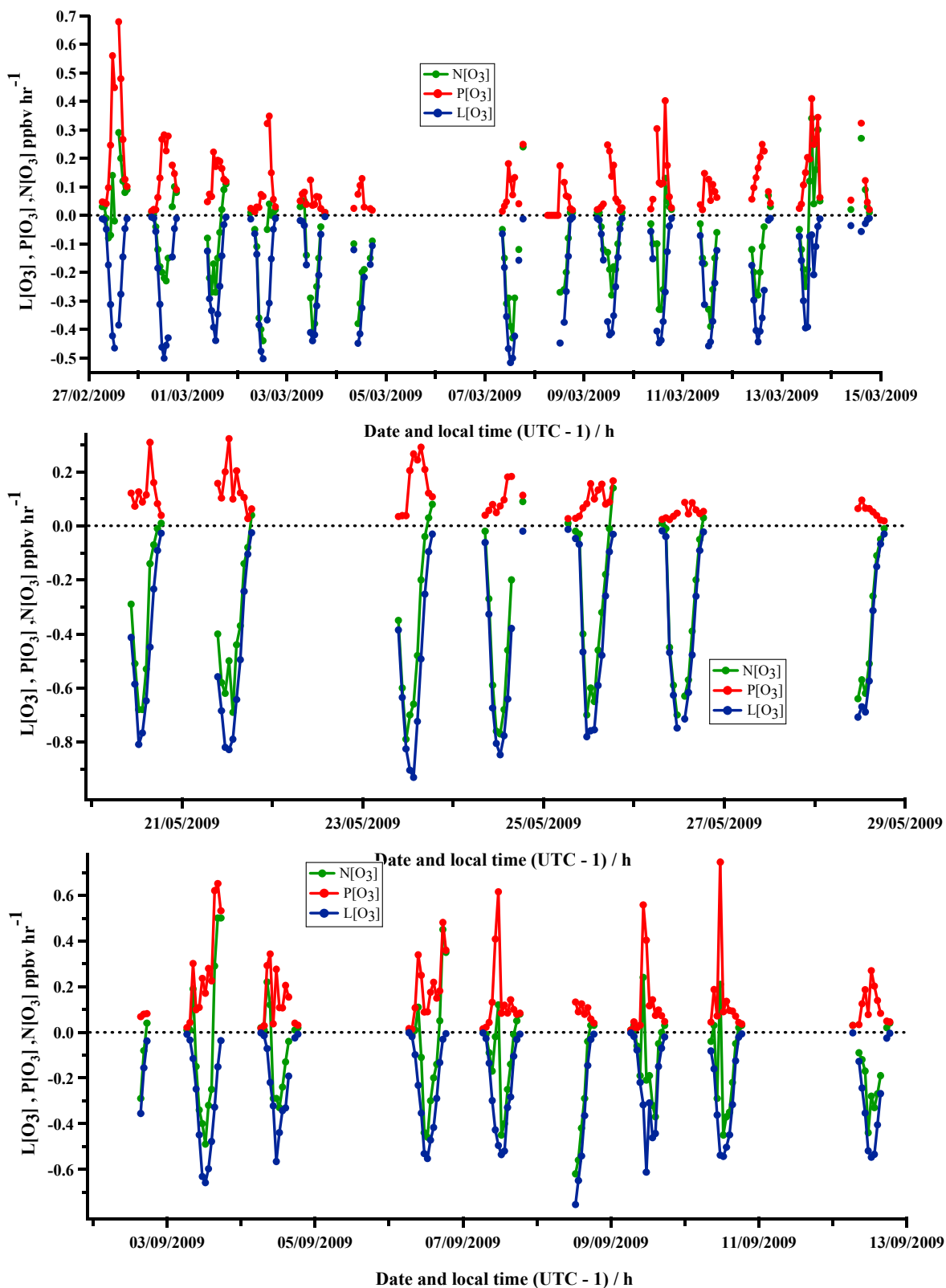


Figure 4.20 - Hourly averaged time series of ozone production rate,  $P(O_3)$  ozone loss rate,  $L(O_3)$  and net ozone rate,  $N(O_3)$  between 06:00-19:00 LT from the campaigns SOS (1) during February-March (top graph), SOS (2) during May-June (middle graph) and SOS (3) during September 2009 (bottom graph) at Cape Verde Atmospheric Observatory in the tropical marine boundary layer.

It can be noted that generally, the air-masses identified during SOS (1), SOS (2) and SOS (3) campaigns show obvious proof of ozone destruction. The median values of  $N(O_3)$  are -0.08, -0.39 and -0.08 ppb hr<sup>-1</sup> between 06:00-19:00 during SOS (1), SOS (2) and SOS (3) campaigns, respectively. The values for the mean of  $N(O_3)$  between 06:00-19:00 during SOS (1), SOS (2) and SOS (3) campaigns are -0.09, -0.28 and -0.11 ppb hr<sup>-1</sup>, respectively. There is a variation for the  $P(O_3)$  in SOS (1) campaign from 0.01 ppbv hr<sup>-1</sup> at 18:30 on 3<sup>rd</sup> March to 0.68 ppbv hr<sup>-1</sup> at 14:30 on 27<sup>th</sup> February, while, the  $L(O_3)$  values vary between -0.01 ppbv hr<sup>-1</sup> at 18:30 on 03<sup>rd</sup> March to -0.52 ppbv hr<sup>-1</sup> at 12:30 on 7<sup>th</sup> March (see top graph on Figure 3.9). The  $P(O_3)$  values in SOS (2) campaign vary between 0.02 ppbv hr<sup>-1</sup> at 18:30 on 28<sup>th</sup> May to 0.32 ppbv hr<sup>-1</sup> at 12:30 on 21<sup>st</sup> May, where as the  $L(O_3)$  values vary between -0.01 ppbv hr<sup>-1</sup> at 06:30 on 25<sup>th</sup> May to -0.93 ppbv hr<sup>-1</sup> at 13:30 on 23<sup>rd</sup> May (see middle graph on Figure 3.9). There is a fluctuation for the  $P(O_3)$  in SOS (3) campaign from 0.01 ppbv hr<sup>-1</sup> at 06:30 on 9<sup>th</sup> September to 0.75 ppbv hr<sup>-1</sup> at 11:30 on 10<sup>th</sup> September, while the  $L(O_3)$  values fluctuates between -0.01 ppbv hr<sup>-1</sup> at 06:30 on 6<sup>th</sup> September to -0.75 ppbv hr<sup>-1</sup> at 12:30 on 8<sup>th</sup> September (see bottom graph on Figure 4.20).

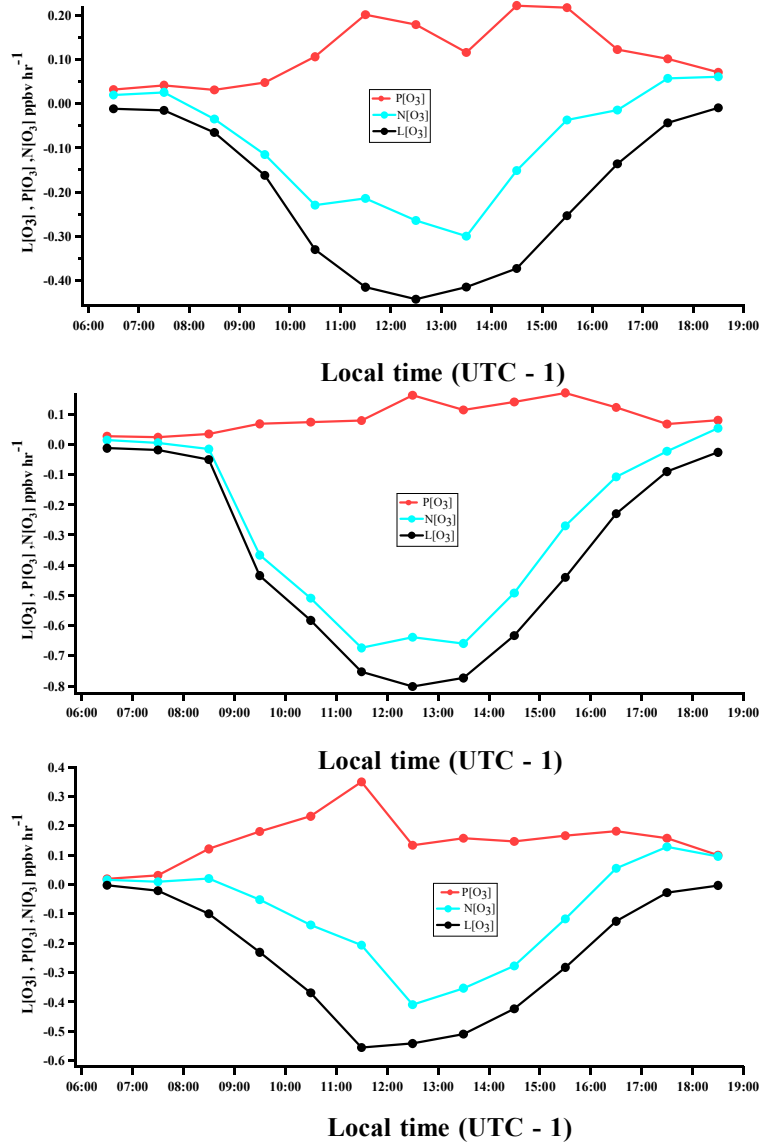


Figure 4.21 - Hourly averaged diurnal cycle data of  $N(O_3)$ ,  $P(O_3)$ , and  $L(O_3)$  between 06:00-19:00 LT from the campaigns SOS (1) during February-March (top graph), SOS (2) during May-June (middle graph) and SOS (3) during September 2009 (bottom graph) at Cape Verde Atmospheric Observatory in the tropical marine boundary layer. Figure 4.21 generated from the hourly averaged time series of ozone production rate,  $P(O_3)$  ozone loss rate,  $L(O_3)$  and net ozone rate,  $N(O_3)$  show previously in Figure 4.20.

The diurnal cycles for  $L(O_3)$  and  $N(O_3)$  tended to be variable throughout the day time with the maximum reached at 12:30 LT and 13:30 LT, whereas  $P(O_3)$  has two different peaks: one at 11:30 LT and the second one, during mid afternoon, during SOS (1) campaign (see top graph on Figure 4.21).  $P(O_3)$  tends to follow  $N(O_3)$  between 06:00-19:00 LT (this will be discussed in Section 4.5.2). The  $[NO]$  diurnal profile has two

different peaks (see middle graph on Figure 4.5), driving the double peaks of  $P(O_3)$  associated with  $[NO]$  during SOS (1) campaign. Maximum photolysis of  $NO_2$  is expected at midday (i.e. during peak solar photolysis). Therefore,  $NO$  is largely produced during midday from photolysis of  $NO_2$ . There was a sudden drop in the  $[NO]$  diurnal profile between 11:00-14:00 (see middle graph on Figure 4.5). It might be caused by the enhancement of  $[HO_2+RO_2]$  between 11:00-14:00 (see Figure 4.11 and bottom graph on Figure 4.15). A valley shape of diurnal cycle of the  $L(O_3)$  concentrations are obtained during day time (see Figure 4.21). The day time values for  $P(O_3)$  reach a peak value at 12:30 LT and 15:30 respectively during SOS (2) campaign (see middle graph on Figure 4.22).  $P(O_3)$  is very smallest in SOS (2) than in SOS (1) and SOS (3).  $[NO]$  is lower in SOS (2) than in SOS (1) and SOS (3) (see middle graph on Figure 4.5). Hence, SOS (2) has largest  $N(O_3)$  and smallest  $P(O_3)$ . There is little difference between the  $L(O_3)$  terms for the SOS (1), SOS(2) and SOS (3) campaigns as photolysis always dominates (see Tables 4.6).  $L(O_3)$  peaked at 12:30 LT while  $N(O_3)$  broadly increased between 11:00 LT and 14:00 LT, as similar rate during SOS (2) campaign (see middle graph on Figure 4.22). The diurnal value for  $L(O_3)$  are tend to be variable, with a peak value at 11:30 LT (see bottom graph on Figure 4.22) during the SOS (3) campaign.  $P(O_3)$  peaked at 11:30 LT and changes in an identical way after midday, where as  $N(O_3)$  reaches its peak value at 12:30 LT during SOS (3) campaign (see bottom graph on Figure 4.22). Top, middle and bottom graph on Figure 4.21 present the way in which mean diurnal cycles highlight the differences between the three seasons. It can be noted that  $L(O_3)$  values have a tendency to change much more than  $P(O_3)$  values, between the three seasons and this factor determines the increase and decrease in net ozone loss on summer days relative to spring days.

Hourly averaged diurnal cycle data of photolysis of ozone rates, the ozone with OH reaction and the reaction of ozone with HO<sub>2</sub> were obtained between 06:00-19:00 LT for SOS (1), SOS (2) and SOS (3) campaigns (see Sections 3.1.3 and 3.2.3.5 in Chapter 3 for data averaging process). The individual loss terms add up to give the total ozone loss term  $L(O_3)$ .

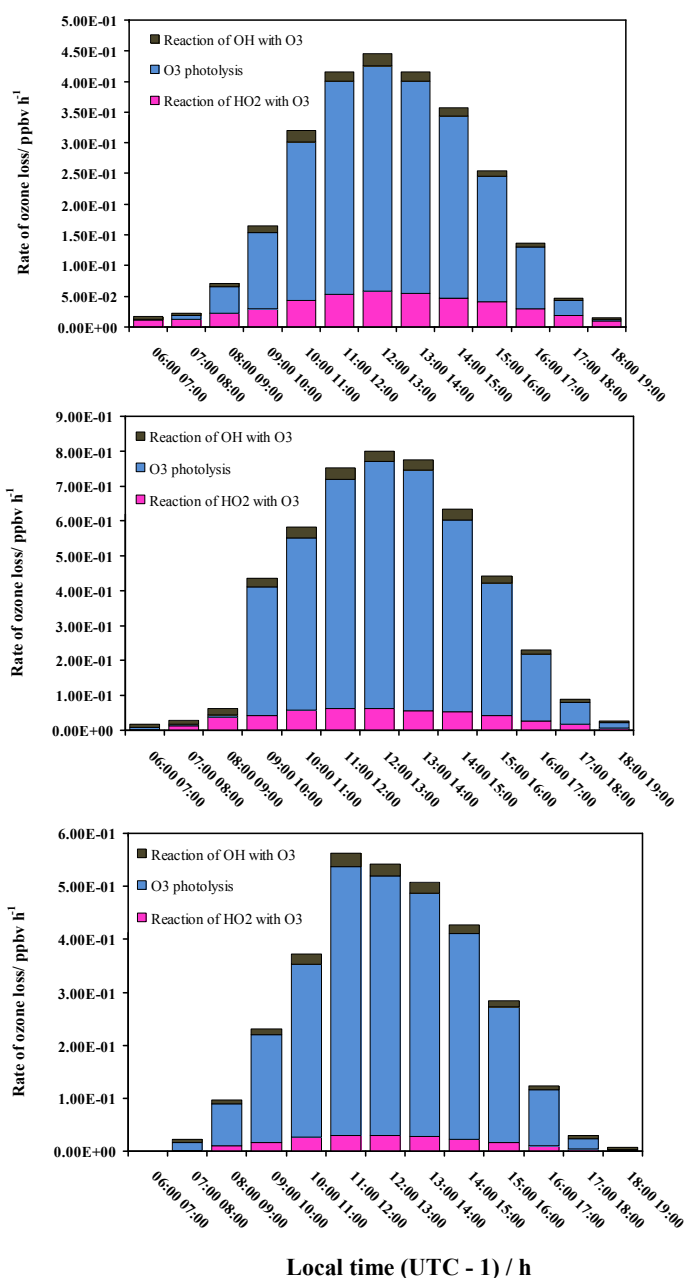


Figure 4.22 - Hourly averaged diurnal relative contributions of ozone loss terms to total  $L(O_3)$  between 06:00-19:00 LT from the campaigns SOS (1) during February-March (top graph), SOS (2) during May-June (middle graph) and SOS (3) during September 2009 (bottom graph) at Cape Verde Atmospheric Observatory in the tropical marine boundary layer.

Photolysis has a large contribution to the ozone loss compared with the reactions for  $\text{HO}_2+\text{O}_3$  and  $\text{O}_3+\text{OH}$ . It has been observed that the day time contribution of OH loss term contributes little. Figure 4.22 shows how little the  $\text{OH}+\text{O}_3$  reaction contributes to  $L(\text{O}_3)$ , which is therefore quite insensitive to  $[\text{OH}]$ . Top, middle and bottom graph on Figure 4.22 shows a contrast between SOS (1), SOS (2) and SOS (3) with respect to the photochemical ozone loss and the diurnal contribution of the individual components.  $L(\text{O}_3)$  having the lowest and highest contribution to OH concentration and photolysis in SOS (3), compared to SOS (2) and SOS (1), respectively.

<b>Ozone removal (<math>L(\text{O}_3)</math>) / ppbv day<sup>-1</sup></b>				
<b>Experiment</b>	<b>Photolysis</b>	<b><math>\text{HO}_2+\text{O}_3</math></b>	<b><math>\text{OH}+\text{O}_3</math></b>	<b>Total</b>
<b>SOS (1) (Feb-March)</b>	$2.12 \pm 0.15$ (79)	$0.43 \pm 0.08$ (16)	$0.13 \pm 0.01$ (5)	$2.68 \pm 0.24$
<b>SOS (2) (May-June)</b>	$4.14 \pm 0.28$ (85)	$0.48 \pm 0.02$ (10)	$0.26 \pm 0.01$ (5)	$4.88 \pm 0.31$
<b>SOS (3) (September)</b>	$2.85 \pm 0.19$ (89)	$0.20 \pm 0.01$ (6)	$0.16 \pm 0.01$ (5)	$3.21 \pm 0.21$

Table 4.6 – A comparison between the campaigns SOS (1) during February-March, SOS (2) during May-June and SOS (3) during September 2009 at Cape Verde Atmospheric Observatory in the tropical marine boundary layer in terms of the hourly averaged time series of photochemical total loss rates  $L(\text{O}_3)$  and their percentage contribution in brackets to the overall loss rates between 06:00-19:00 LT.

Table 4.6 shows the calculated photochemical loss rates and their percentage contribution to the overall loss rate. 79 %, 85 % and 89 % of ozone loss is driven by photolysis at Cape Verde during February-March, May-June and September respectively. Monks *et al.*, (2000b) observed that at Cape Grim, the values of 87% and 64% of ozone destruction are realized through photolysis during summer and winter, respectively. Within the remote marine boundary layer, even on a seasonal basis, photochemical ozone loss is mainly through photolysis. There is a decrease in the

photochemical loss rates,  $L(O_3)$  from 4.88 ppbv day<sup>-1</sup> in May-June to 3.21 ppbv day<sup>-1</sup> in September to 2.68 ppbv day<sup>-1</sup> during February-March. The photochemical loss rates,  $L(O_3)$  decreases in February-March being of 45% relative to in May-June. Clearly, photolysis is the major photochemical loss process for ozone in the remote marine subtropical Atlantic boundary layer throughout the year.

<b>Ozone tendencies <math>N(O_3)</math> / ppbv hr<sup>-1</sup></b>			
	<b>SOS (1)</b>	<b>SOS (2)</b>	<b>SOS (3)</b>
<b>Median</b>	-0.08	-0.39	-0.08
<b>Mean</b>	-0.09	-0.28	-0.11
<b>Standard deviation</b>	0.16	0.28	0.23
<b>10th percentile</b>	-0.31	-0.68	-0.40
<b>90th percentile</b>	0.09	0.01	0.12

Table 4.7 – Hourly averaged time series of  $N(O_3)$ , median, mean, standard deviation and 10<sup>th</sup> and 90<sup>th</sup> percentiles between 06:00-19:00 LT from the campaigns SOS (1) during February-March, SOS (2) during May-June and SOS (3) during September 2009 at Cape Verde Atmospheric Observatory in the tropical marine boundary layer.

$N(O_3)$  was calculated between 06:00-19:00 LT for SOS (1), SOS (2) and SOS (3) campaign. From Table 4.7, the net ozone destruction rate ( $N(O_3)$ ) drops from 0.28 ppbv hr<sup>-1</sup> in SOS (2) (May-June) to 0.11 ppbv hr<sup>-1</sup> in SOS (3) (September) to 0.09 ppbv hr<sup>-1</sup> in SOS (1) (February-March) between 06:00-19:00 LT. The calculations of the mean ozone tendencies presented in Table 4.7, prove that  $N(O_3)$  in spring period (SOS (1)) is less than in summer ((SOS (2)) and in autumn (SOS (3)). Therefore, there is less ozone destruction during spring than during summer and autumn seasons.

<b><math>P(O_3)</math>, <math>L(O_3)</math> and <math>N(O_3)</math> / ppbv hr<sup>-1</sup></b>			
	<b>SOS (1)</b>	<b>SOS (2)</b>	<b>SOS (3)</b>
<b><math>P(O_3)</math></b>	0.13	0.10	0.15
<b><math>L(O_3)</math></b>	0.22	0.38	0.26
<b><math>N(O_3)</math></b>	-0.09	-0.28	-0.11

Table 4.8 - Hourly averaged time series of  $N(O_3)$ ,  $P(O_3)$  and  $L(O_3)$  between 06:00-19:00 LT from the campaigns SOS (1) during February-March, SOS (2) during May-June and SOS (3) during September 2009 at Cape Verde Atmospheric Observatory in the tropical marine boundary layer.

It can be seen in Table 4.8 that higher ozone loss rate,  $L(O_3)$  is calculated in SOS (2), over that in SOS (1) and SOS (3), while  $L(O_3)$  in SOS (1) and SOS (3) were not significantly different. Lower ozone production rate,  $P(O_3)$  is calculated in SOS (2), over that in SOS (1) and SOS (3), while  $P(O_3)$  in SOS (1) and SOS (3) were not significantly different. It can be conclude that greater net ozone loss rate,  $N(O_3)$  calculated in SOS (2) than of SOS (1) and SOS (3) and that this is being driven differences in  $L(O_3)$  rather than in  $P(O_3)$ . From Table 4.6, the net ozone destruction rate ( $N(O_3)$ ) drops from 0.28 ppbv hr<sup>-1</sup> (~3.64 ppbv day<sup>-1</sup>) in SOS (2) to 0.11 ppbv hr<sup>-1</sup> (~1.43 ppbv day<sup>-1</sup>) in SOS (3) to 0.09 ppbv hr<sup>-1</sup> (~1.20 ppbv day<sup>-1</sup>) in SOS (1) (February-March) between 06:00-19:00 LT. Ozone loss rates were estimated from the observed ozone diurnal profile as shown in bottom graph on Figure 4.5 between 06:00-19:00 LT. The campaign averaged observed ozone loss rates were 5.58 ppbv day<sup>-1</sup> in SOS (2) (May-June), 3.76 ppbv day<sup>-1</sup> in SOS (1) ((February-March)) and 2.15 ppbv day<sup>-1</sup> in SOS (3) (September). From this observational test of ozone loss rate calculations it might be suggested that influences of halogen species can contribute to

the extra ozone loss in the marine boundary layer and it will be discussed in Section 4.5.1.

#### 4.5.1 Halogen compounds possible contribution to ozone loss

Halogen chemistry has been previously described in section 1.4.3 and section 1.5.2 in Chapter 1 and in section 4.2.1 in Chapter 4. This section investigates the role of IO and BrO from the previous marine field campaigns and their influences are considered for this work.

Davis *et al.*, (1996) noted that, iodine species can be significant in the marine boundary layer and have the potential to affect tropospheric ozone formation. The measurements of reactive halogen species (RHS) have been made in Marine boundary layer (MBL) coastal locations (in Ireland, at Mace Head coastal marine site and in Roscoff on the North West coast of France) and have identified both bromine (e.g. Saiz-Lopez *et al.*, 2004a; Peters *et al.*, 2005) and iodine (e.g. Alicke *et al.*, 1999; Allan *et al.*, 2000a; Saiz-Lopez and Plane, 2004; Peters *et al.*, 2005) species.

Andrés Hernández *et al.*, (2001) speculated in the AEROSOLS99 campaign that the proportion of halogen influence can reach up to 60% of the total ozone loss in remote areas across the Atlantic Ocean.

Bloss *et al.*, (2005b) noted during NAMBLEX (The North Atlantic Marine Boundary Layer Experiment) at Mace Head coastal marine site, during the summer of 2002 in Ireland, the reaction between IO and HO<sub>2</sub> to form HOI accounted for up to 40% of the total HO<sub>2</sub> radical sink. Saiz-Lopez *et al.*, (2006) observed IO between 18<sup>th</sup> and 20<sup>th</sup>

August in 2002 for three days from the NAMBLEX campaign, varying between the detection limit of 0.5 and the maximum concentrations of 7 pptv and maximising at low tide. Bloss *et al.*, (2005b) shows that the IO reaction dominated HO<sub>2</sub> loss where IO concentrations peaked on the 18<sup>th</sup> August during the NAMBLEX campaign.

McFiggans *et al.*, (2010) reported that two instruments measured BrO and four instruments measured IO during Reactive Halogens in the Marine Boundary Layer (RHAMBLE) coastal study throughout September 2006 in Roscoff on the North West coast of France. The LP-DOAS (University of Leeds) measurements of IO were made between 07<sup>th</sup> and 26<sup>th</sup> September. The peak LP-DOAS IO mixing ratios vary between 4.8 pptv to 10.1 pptv with a mean of 7.5 pptv. BrO was observed for 8 days, the maximum concentration of BrO detected as  $7.5 \pm 1.0$  pptv whilst minimum concentration measured was under the detection limit (2 pptv).

FAGE LIF (University of Leeds), detected IO above the instrument detection limit (0.4 - 4 pptv for a 150 s integration period) for 14 days during RHAMBLE campaign. A clear diurnal profile was observed for 11 days. The maximum IO concentration was observed  $30 \pm 7.1$  pptv (10s integration periods) (McFiggans *et al.*, 2010; Whalley *et al.*, 2007; Furneaux *et al.*, 2010).

The narrow-band CRDS (University of Bristol) deployed during RHAMBLE campaign to detect IO. CRDS measurements were broadly in agreement with the LIF measurements. Both measurements exhibited a clear tidal signal between 8<sup>th</sup> and 25<sup>th</sup> September at elevated mixing ratios. These two measurements are greater than those observed by the LP-DOAS (McFiggans *et al.*, 2010; Wada *et al.*, 2007).

CMAX-DOAS (University of Leicester), IO measured for 17 days between 5<sup>th</sup> and 26<sup>th</sup> September where as BrO measured for 4 days between 17<sup>th</sup> and 20<sup>th</sup> September during RHaMBLe campaign, respectively. IO was frequently detected above the average detection limit ( $3 \times 10^{13}$  molecule  $\text{cm}^{-2}$ ) where as BrO was detected for all 4 days above the detection limit ( $9 \times 10^{13}$  molecule  $\text{cm}^{-2}$ ) (McFiggans *et al.*, (2010)).

The instantaneous *in-situ* net ozone loss rate calculated considering non halogen analysis was described for Cape Verde in Section 4.5. There was obvious proof of more ozone destruction during May-June, 2009 compared with other seasons in 2009. The role of halogens in the marine boundary layer has been observed as discussed previously to consider the input of halogen as well as finding the differences between halogen and non-halogen analysis in terms of ozone loss rate. During a personal communication with Dr Z. Fleming (University of Leicester) and Dr A. Mahajan (The Laboratory for Atmospheric and Climate Science, Spain), IO and BrO data are still pending for SOS (1), SOS (2) and SOS (3) campaigns and not available to use at this moment.

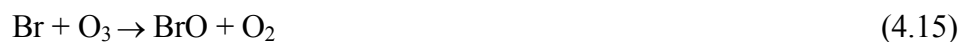
It must be note that IO and BrO data obtained from the non-SOS campaigns for this work. UOL (University Of Leeds) LP-DOAS IO data taken from Cape Verde archive on BADC website for May-June 2007 can be used for the SOS (2) campaign to give an hourly averaged IO data obtained (see Table 4.2 and see Section 3.13 in Chapter 3 for data averaging process). The hourly average diurnal profile of BrO measured by UOH (University Of Heidelberg) LP-DOAS instrument for layer 0-10 m height between the 12<sup>th</sup> and 20<sup>th</sup> June 2010 at Cape Verde has taken from Carpenter *et al.*, (2010) used for the SOS (2) campaign. The reactions of the halogen atom with ozone (i.e. reactions 4.8

and 4.15), the subsequent recycling of the halogen atom via the peroxy radical reactions (4.13 and 4.22) and also HOX photolysis (4.10 and 4.17) are the important chain steps for the ozone destruction. Reactions (4.13), (4.20) and (4.22), respectively, by employing the rate constants from Vogt *et al.*, (1999) and Arlanda *et al.*, (1997), illustrative calculations have been made to estimate how much the reaction of CH<sub>3</sub>O<sub>2</sub> with halogen oxides.

Considering the reactions between peroxy radical and IO,



Similarly, peroxy radical considered for BrO,

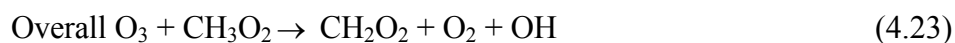




Focussing on the significant reactions, Arlanda *et al.*, (1997) explained that OBrO and CH<sub>3</sub>OBr were not detected in her study, ruling out a significant contribution from channels (4.19) and (4.21). BrOO would decompose rapidly to Br + O<sub>2</sub>; in the reaction (4.18), other product of CH<sub>3</sub>O reacted with O<sub>2</sub> and generating HCHO and HO<sub>2</sub> as shown in the reaction (4.22).



Considering reaction (4.20)



Or

Considering reaction (4.22)





Peroxy radicals are the rate limiting steps in ozone loss kinetics. An equation (B) has been employed for calculating the ozone loss rates, containing a further analysis for ozone reactions with I and Br. Ozone loss rate for BrO and IO together

$$= \left\{ \begin{aligned} & f(\text{O}^1\text{D})[\text{O}_3] + k_{3.1}[\text{OH}][\text{O}_3] + k_{3.2}[\text{HO}_2][\text{O}_3] + k_{4.16}[\text{BrO}][\text{HO}_2] \\ & + (k_{4.20} + k_{4.22})[\text{BrO}][\text{CH}_3\text{O}_2] + k_{4.9}[\text{IO}][\text{HO}_2] + k_{4.13}[\text{IO}][\text{CH}_3\text{O}_2] \end{aligned} \right\} \quad (\text{B})$$

Table 4.9 shows the halogen chemistry reaction scheme

Reaction	Rate coefficient/ $\text{cm}^3 \text{ molecule}^{-1} \text{ s}^{-1}$	Reference
$\text{IO} + \text{HO}_2 \rightarrow \text{HOI} + \text{O}_2$	$1.4 \times 10^{-11} \exp^{(540/T)}$ Temp range / K 270-380	Atkinson <i>et al.</i> , (2007)
$\text{BrO} + \text{HO}_2 \rightarrow \text{HOBr} + \text{O}_2$	$4.5 \times 10^{-12} \exp^{(460/T)}$ Temp range / K 210-360	Sander <i>et al.</i> , (2006)
$\text{IO} + \text{CH}_3\text{O}_2 \rightarrow \text{I} + \text{HO}_2 + \text{HCHO}$	$2.3 \times 10^{-11}$	Vogt <i>et al.</i> , (1999)
$\text{BrO} + \text{CH}_3\text{O}_2 \rightarrow \text{HOBr} + \text{CH}_2\text{O}_2$	$4.1 \times 10^{-12}$	Arlanda <i>et al.</i> , (1997)
$\text{BrO} + \text{CH}_3\text{O}_2 \rightarrow \text{Br} + \text{HO}_2 + \text{HCHO}$	$1.6 \times 10^{-12}$	Arlanda <i>et al.</i> , (1997)

Table 4.9- Halogen chemistry reaction scheme

Hourly averaged diurnal data obtained for photolysis of ozone rates, the ozone with OH reaction, the reaction of ozone with HO<sub>2</sub> between 06:00-19:00 LT for SOS (2) campaigns as described in previous section 4.5 (see Section for data averaging process 3.12 in Chapter 3). The hourly averaged diurnal data were estimated for the reactions of HO<sub>2</sub> + IO, CH<sub>3</sub>O<sub>2</sub> + IO between 06:00-19:00 LT using measured [IO] between May-

June 2007, as well as for the reactions of  $\text{HO}_2 + \text{BrO}$ ,  $\text{CH}_3\text{O}_2 + \text{BrO}$  between 06:00-19:00 LT using measured BrO in June 2010.

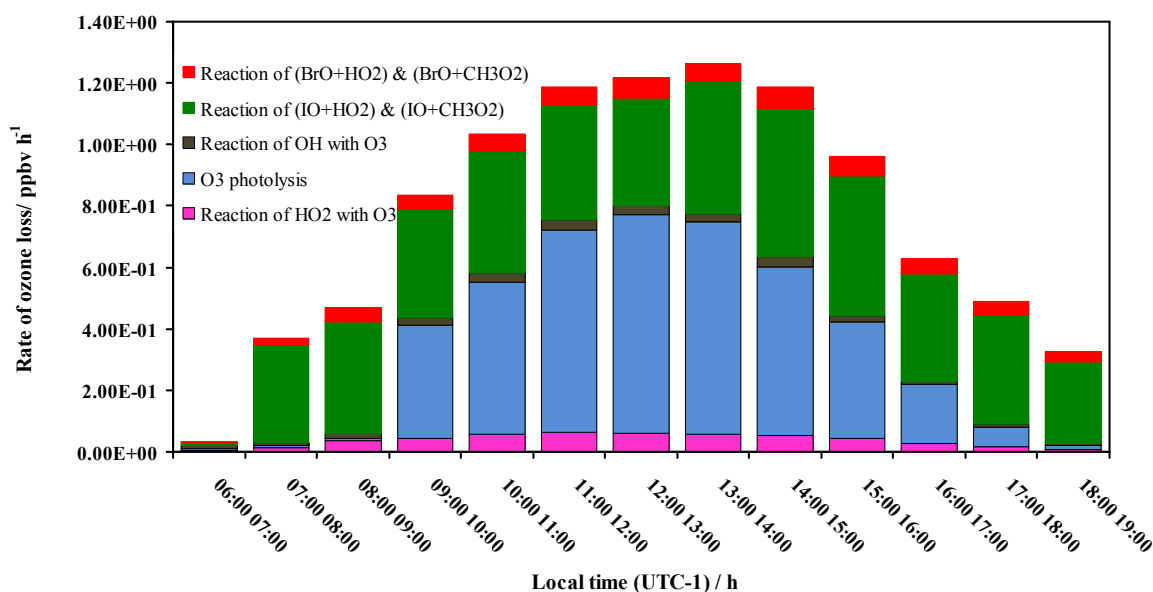


Figure 4.23 - Hourly averaged diurnal relative contributions of ozone loss terms including reactions of IO with  $\text{O}_3$  and BrO with  $\text{O}_3$  to total  $L(\text{O}_3)$  between 06:00-19:00 LT from the campaign SOS (2) during May-June 2009 at Cape Verde Atmospheric Observatory in the tropical marine boundary layer. The pink, blue and brown data points for the whole SOS (2) campaign are the same data as plotted previously in middle graph on Figure 4.22.

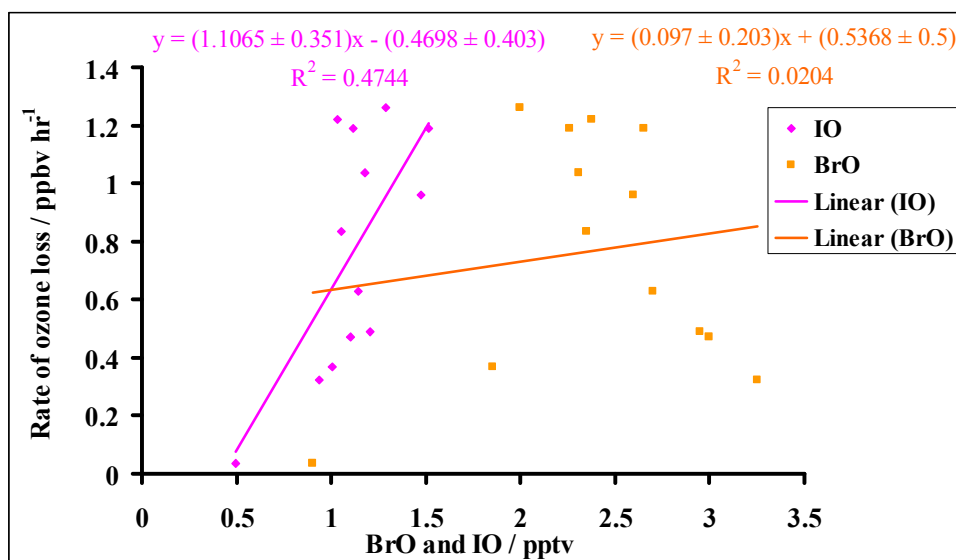


Figure 4.24 - Hourly averaged diurnal cycle data of ozone loss rate and  $[\text{BrO}+\text{IO}]$  between 06:00-19:00 LT from the campaign SOS (2) during May-June 2009 at Cape Verde Atmospheric Observatory in the tropical marine boundary layer.

There is a positive and fairly better correlation between [IO] and the rate of ozone loss as shown in Figure 4.24. In contrast, [BrO] was not correlated with rate of ozone loss as shown in Figure 4.24. It is worth noting that [IO] and [BrO] data obtained during the different field campaigns instead of SOS (2) campaign.

Photochemical ozone loss is mainly controlled through the ozone photolysis and reaction of IO with ozone (see Figure 4.23). The contribution of photolysis and reaction of ozone with IO to total ozone loss varies from time to time (see Figure 4.23). During morning and afternoon, the reaction of ozone with IO is always predominant. At midday, ozone photolysis tends to dominate over the reactions of ozone with IO as seen in Figure (4.23).

Ozone removal ( $L(O_3)$ ) / ppbv day <sup>-1</sup>						
Experiment	Photolysis	HO <sub>2</sub> +O <sub>3</sub>	OH+O <sub>3</sub>	IO+O <sub>3</sub>	BrO+O <sub>3</sub>	Total
<b>SOS (2) (May-June)</b>	4.14 ± 0.28 (41)	0.48 ± 0.02 (5)	0.26 ± 0.01 (3)	4.51 ± 0.12 (45)	0.62 ± 0.02 (6)	10.01 ± 0.45

Table 4.10 – The photochemical total loss rates  $L(O_3)$  and their percentage contribution in brackets to the overall loss rates including the reactions of IO with O<sub>3</sub> and BrO with O<sub>3</sub> between 06:00-19:00 LT from the campaign SOS (2) during May-June 2009 at Cape Verde Atmospheric Observatory in the tropical marine boundary layer.

Table 4.10 shows the calculated photochemical ozone loss rates including IO +O<sub>3</sub> and BrO+O<sub>3</sub> and their percentage contribution to the overall loss terms. The substantial contribution made to the total ozone loss is with the contribution of IO and BrO, in proportions of 45% and 6%, respectively (see Table 4.10). This greater contribution and this pathway was not considered when calculating  $L(O_3)$  as in the classic analysis explained in section 4.5 and in Table 4.6 in this Chapter. Read *et al.*, (2008) reported that, LP-DOAS (University of Leeds) deployed at the Cape Verde Observatory from

November 2006 until June 2007 measured mean day time of IO and BrO radicals of  $(1.4 \pm 0.8)$  ( $1\sigma$ ) pptv and  $(2.5 \pm 1.1)$  ( $1\sigma$ ) pptv, respectively. She postulated around 50% of daily photochemical ozone loss was from the presence of the 1.4 and 2.5 pptv concentrations of IO and BrO, respectively. In this work, averaged daytime mixing ratio of IO and BrO were measured  $(1.12 \pm 0.25)$  ( $1\sigma$ ) and  $(2.41 \pm 0.60)$  ( $1\sigma$ ), respectively. In this study, 51% of the daily ozone loss rate was calculated in the presence of the 1.12 and 2.41 pptv of IO and BrO, respectively.

Whalley *et al.*, (2010) mentioned that during the RHAMBLE project at the CVAO, a daily  $O_3$  loss was observed of the order of  $3.5 \text{ ppbv day}^{-1}$ . She further analysed that considering the daytime average concentrations for the period 21<sup>st</sup> May-2<sup>nd</sup> June 2007, the values of 22.5 % and 16.5% of total ozone destruction is realized through reaction with IO and BrO at this site, respectively. Whalley *et al.*, (2010) noted combination of IO and BrO together destroy  $1.5 \text{ ppbv day}^{-1}$  of ozone for the month of May in 2007 where as Read *et al.*, (2008) found similar observation from the box model calculation. The daytime average concentration for the period 20<sup>th</sup> May-2<sup>nd</sup> June 2009, the values of 45% and 6% of total ozone destruction is realized through reaction with IO and BrO for this work. Combination of IO and BrO together destroy  $5.13 \text{ ppbv day}^{-1}$  of ozone for the period 20<sup>th</sup> May-2<sup>nd</sup> June 2009 (see Table 4.10). Larger value of ozone destruction calculated in this work than in the Whalley *et al.*, (2010) analysis. It might be suggested that IO and BrO data obtained during the different field campaigns instead of SOS (2) campaign. Hence, it might be difficult to compare the ozone destruction values for SOS (2) campaign with the Whalley *et al.*, (2010) and Read *et al.*, (2008) results. These estimates are theoretical calculations for ranking the factors influencing the ozone loss. Peroxy radical reactions with IO and BrO would be

important to find out the exact ozone destruction in marine boundary layer using kinetic studies.

#### 4.5.2 The ozone production rate $P(O_3)$ , peroxy radicals and NO relationships

Past studies carried out in clean rural/marine environments concluded that ozone production is a part of natural cycle and it can be disturbed by pollution occurrences: at Mace Head (Salisbury *et al.*, 2001, 2002) during the EASE 96 and 97 (Eastern Atlantic Summer-Spring Experiment) and at Cape Grim in Tasmania (Monks *et al.*, 1998, 2005) at the SOAPEX 2 (Southern Ocean Atmospheric Photochemistry Experiment) campaign in 1998.

To understand how the rate of ozone production correlates with the changing concentration of  $HO_2+RO_2$  and NO between 10:00-16:00 LT. Similar analysis demonstrated between 10:00-16:00 LT for OP3 (1) and OP3 (3) campaigns (See Section 3.2.3.7 in Chapter 3). See Section 5.2.2.4 in Chapter 5 for ozone photochemistry variations between the OP3 and SOS campaigns. The following hourly averaged time series of data were taken: Calculated hourly averaged  $P(O_3)$  (Top, middle and bottom graphs on Figure 4.20 show for SOS (1), SOS (2) and SOS (3), respectively). Hourly averaged measured  $[HO_2+RO_2]$  (see Figure 3.8 for SOS (1), see Figure 3.9 for SOS (2) and see Figure 3.10 for SOS (3). Hourly averaged measured  $[NO]$  (see middle graph on Figure 4.5). See Section 3.1.3 in Chapter 3 for data averaging process. The natural logarithms of generated hourly averaged time series of  $P(O_3)$ ,  $HO_2+RO_2$ , NO were taken to plot  $\ln P(O_3)$  vs.  $\ln(HO_2+RO_2)$  and  $\ln P(O_3)$  vs.  $\ln(NO)$  for three of campaigns.

The  $P(O_3)$  is itself limited by NO between 10:00-16:00 LT throughout the three measurement campaigns, as evidenced in Figure 4.25 where a plot of natural log of  $P(O_3)$  with the natural log of NO concentration shows a good correlation ( $R^2 = 0.81$ ), ( $R^2 = 0.73$ ) and ( $R^2 = 0.70$ ) in SOS (1), SOS (2) and SOS (3) respectively. In contrast the correlation between natural log of  $P(O_3)$  and natural log of peroxy radical is poor, with  $R^2 = 0.27$ ,  $R^2 = 0.27$  and  $R^2 = 0.27$  in SOS (1), SOS (2) and SOS (3) respectively.

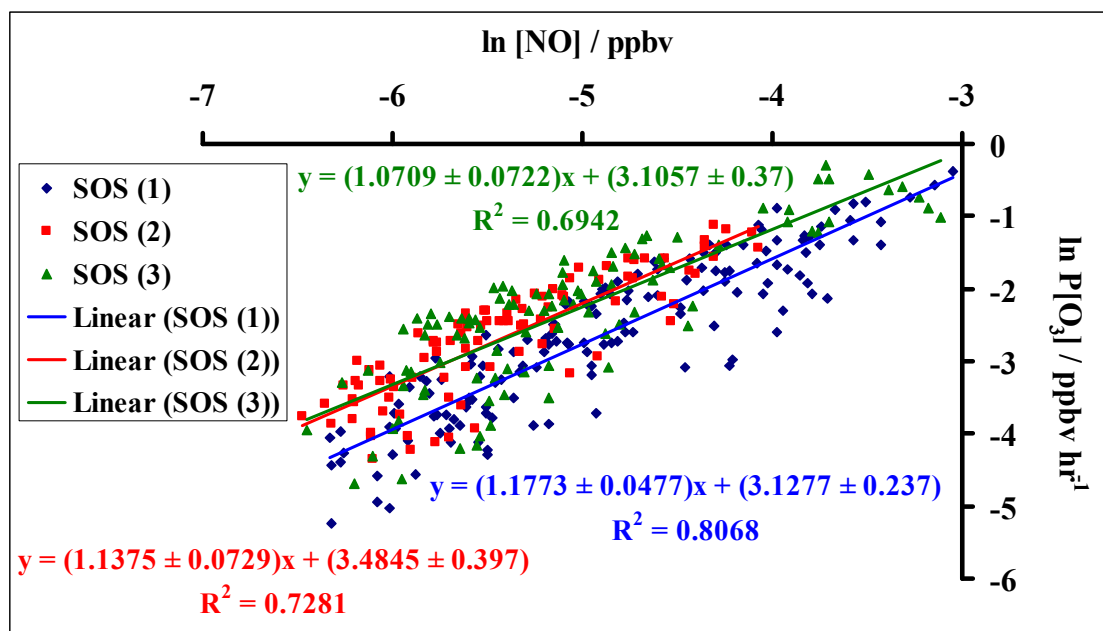


Figure 4.25 – Natural logarithms of hourly-averaged time series of  $P(O_3)$  and  $[NO]$  between 10:00-16:00 LT from the campaigns SOS (1) during February-March, SOS (2) during May-June and SOS (3) during September 2009 at Cape Verde Atmospheric Observatory in the tropical marine boundary layer.

The outcome can help determine that the reduction of NO on summer days mainly causes an increased net ozone loss observed on summer days relative to spring and autumn days. The variability in NO concentration has a much larger effect on  $N(O_3)$  than the peroxy radical concentrations. The results imply that the  $N(O_3)$  (the in-situ net photochemical rate of ozone production or destruction) will be strongly sensitive in the marine boundary layer to small changes in  $[NO]$ .

As compared to past campaigns, e.g. SOAPEX 1 in 1995 (Monks *et al.*, 1998, 2000b, and Carpenter *et al.*, 1997) and SOPEX 2 in 1998 (Monks *et al.*, 2005), the measurements carried out at Cape Verde during Seasonal Oxidant Study (SOS (1), SOS (2) and SOS (3)) 2009 campaigns helped reach the conclusion that the photochemical O<sub>3</sub> destruction predominates the production and there were more days with net O<sub>3</sub> destruction. The same aspect of O<sub>3</sub> destruction being predominant has been pointed out by Andres-Hernandez *et al.* (2002) during the Atlantic and Southern Indian Ocean Cruise of AEROSOL 99. On the other hand, more photochemical O<sub>3</sub> production than destruction has been encountered at Mace Head during the EASE 96 and 97 campaigns (Salisbury *et al.*, (2002) and Fleming *et al.* (2006) and during ATAPEX-95 (Atlantic Atmospheric Photochemistry Experiment) (Carpenter *et al.*, 1997).

By carrying out a comparison between  $\text{dln}P(\text{O}_3)/\text{dln}(\text{NO})$  and  $\text{dln}P(\text{O}_3)/\text{dln}(\text{RO}_x)$ , Stroud *et al.*, (2004) determined that  $P(\text{O}_3)$  presents a more increased sensitivity to  $[\text{NO}]$  than to  $[\text{HO}_2+\text{RO}_2]$ . Fleming *et al.*, (2006) demonstrated an identical sensitivity analysis from data at Mace Head, Weybourne and Cape Grim observing the NO dependence on  $P(\text{O}_3)$ . Applying the natural log to all the hourly-averaged  $P(\text{O}_3)$  and  $[\text{NO}]$  and plotting  $P(\text{O}_3)$  vs.  $[\text{NO}]$  yields linear correlations, with gradients of  $\text{dln}(P(\text{O}_3))/\text{dln}(\text{NO})$ , a measure of the sensitivity of  $P(\text{O}_3)$  to NO.

Locations	Campaigns	$\text{dln}(P(\text{O}_3))/\text{dln}(\text{NO})$
Cape Grim, Australia	SOAPEX 2	0.90
Mace Head, Ireland, UK	EASE 97	1.10
Weybourne, UK	Weybourne winter	0.92
Weybourne, UK	Weybourne summer	0.95
Mace Head, Ireland, UK	NAMBLEX	1.00

Table 4.11 - Sensitivity of derived  $P(\text{O}_3)$  to  $[\text{NO}]$  from a series of marine boundary layer campaigns from Fleming, (2005).

All the campaigns show a fairly similar trend of  $P(O_3)$  with  $[NO]$ , with a slightly greater dependence on  $[NO]$  for the Mace Head campaigns. The gradients of  $P(O_3)$  vs.  $[NO]$  are just over 1 in Mace Head campaigns than in Cape Grim and Weybourne campaigns that had a lower linear sensitivity of around 0.9. This suggests that ozone formation at Mace Head is marginally more sensitive to  $[NO]$  than at Weybourne and Cape Grim and explains why the arrival of  $NO_x$  - loaded air-masses can cause very high ozone production periods. Weybourne ozone production was more sensitive to  $[NO]$  in summer than in the winter.

The gradients of  $d\ln(P(O_3))/d\ln([NO])$ , a measure of the sensitivity of  $P(O_3)$  to  $[NO]$  and graphs for all the three campaigns in Cape Verde are shown in Figure 4.25 and the gradients are listed in Table 4.12.

	$d\ln(P(O_3))/d\ln([NO])$	Correlation ( $R^2$ )
SOS (1)	$1.18 \pm 0.048$	0.81
SOS (2)	$1.14 \pm 0.073$	0.73
SOS (3)	$1.07 \pm 0.072$	0.70

Table 4.12 - Sensitivity of derived  $P(O_3)$  to  $[NO]$  from a series of marine boundary layer campaigns SOS (1), SOS (2) and SOS (3).

The ozone production rate is strongly dependent on  $[NO]$  having a strong linear sensitivity averaging of  $d\ln(P(O_3))/d\ln([NO])$  from Cape Verde marine boundary layer is 1.13 (averaged from three different seasonal data sets) and the results imply that the  $N(O_3)$  will be strongly sensitive in the marine boundary layer to small changes in  $[NO]$ .

An overall analysis of the findings of all three SOS campaigns point to a similar identical trend of  $P(\text{O}_3)$  with  $[\text{NO}]$ . The most increased dependence on  $[\text{NO}]$  being observed for the Cape Verde campaigns SOS (1) and SOS (2), with gradients above 1.14; as compared to Mace Head that had a lower linear sensitivity, of around 1.10. This indicative that ozone formation at Cape Verde is more sensitive to  $[\text{NO}]$  than at Mace Head, Weybourne and Cape Grim (see Table 4.11 and 4.12).

#### 4.5.3 Ozone compensation point

The ozone compensation point (Lelieveld and Crutzen, (1990), Salisbury *et al.*, (2002) and Zanis *et al.*, (2000a)) is a measure of the NO concentration at which neither net ozone production nor destruction occurs. Zanis *et al.*, (2000a) defined that the ozone compensation point that corresponds to the NO concentration at which  $N(\text{O}_3)$  becomes zero and this is the same point at which *in-situ* ozone production matches *in-situ* loss. Zanis *et al.*, (2000a) method was followed to calculate the ozone compensation point in this work. To this end, hourly averaged time series of  $[\text{NO}]/[\text{O}_3]$  and  $N(\text{O}_3)$  data were generated between 08:00-16:00 LT for SOS (1), SOS (2) and SOS (3) campaigns. The times of 08:00 LT to 16:00 LT correspond to the period of the day because  $j(\text{O}^1\text{D})$  will be small number with large associated error around sun rise and sun set. Decreasing  $j(\text{O}^1\text{D})$  will raise the  $N(\text{O}_3)$  with large associated uncertainty (see equation (A) in Section 3.2.3.5 in Chapter 3). The following hourly averaged time series of data were taken: Calculated hourly averaged  $N(\text{O}_3)$  (Top, middle and bottom graphs on Figure 4.20 show for SOS (1), SOS (2) and SOS (3), respectively). Hourly averaged measured  $[\text{NO}]$  (see middle graph on Figure 4.5) and  $[\text{O}_3]$  (see bottom graph on Figure 4.5). See Table 4.2 and see Section 3.1.3 for data averaging process. Figure 4.26 shows hourly averaged diurnal  $[\text{NO}]/[\text{O}_3]$  data vs. hourly averaged diurnal  $N(\text{O}_3)$  data between

08:00-16:00 LT from the SOS (1) (top graph), SOS (2) (middle graph) and SOS (3) (bottom graph) campaigns.

The correlations are good ( $R^2 = 0.82$ ), ( $R^2 = 0.70$ ) and ( $R^2 = 0.80$ ) for SOS (1), SOS (2) and SOS (3) and from the linear fit a values of  $[\text{NO}]/[\text{O}_3] = 5.32 \times 10^{-04} \pm 2.33 \times 10^{-05}$ ,  $3.09 \times 10^{-04} \pm 3.26 \times 10^{-05}$  and  $5.41 \times 10^{-04} \pm 3.67 \times 10^{-05}$  have been obtained for when  $N(\text{O}_3) = 0$ . The mean concentrations of ozone are 37, 37 and 21 pptv between 08:00-16:00 during SOS (1), SOS (2) and SOS (3) campaigns (see bottom graphs on Figure 4.5). Using the mean ozone concentration for the period during which  $N(\text{O}_3)$  and  $[\text{NO}]/[\text{O}_3]$  data has been plotted, values of  $20 \pm 0.9$  pptv,  $11.5 \pm 1.2$  pptv and  $11.3 \pm 0.8$  pptv of  $[\text{NO}]$  are obtained as an estimate for the ozone compensation point in spring, summer and autumn respectively. Influences of halogen species can contribute to the extra ozone loss, i.e. additional negative values of  $N(\text{O}_3)$  (see Section 4.5.1). Hence, halogen monoxide may raise the ozone compensation point.

Compensation points vary depending upon various sets of conditions, particularly  $j(\text{O}^1\text{D})$ ,  $[\text{O}_3]$  and  $[\text{H}_2\text{O}]$ , which determine the value of  $[\text{NO}]$  needed to reach and exceed the balance point between net ozone loss and production (See Section 3.2.3.5 in Chapter 3).

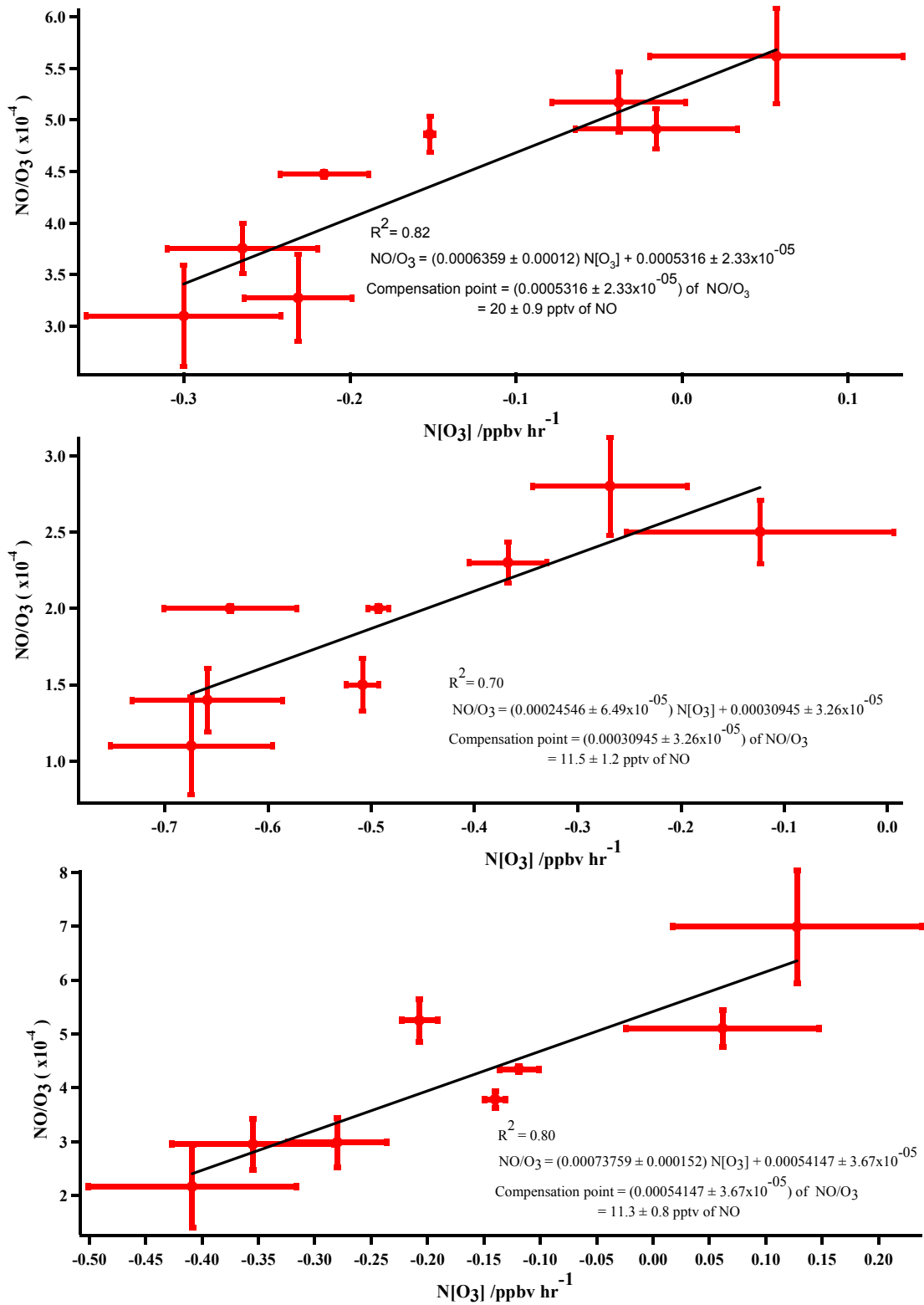


Figure 4.26 - Hourly averaged diurnal data of  $[\text{NO}]/[\text{O}_3]$  and  $N(\text{O}_3)$  between 08:00-16:00 LT from the campaigns SOS (1) during February-March (top graph), SOS (2) during May-June (middle graph) and SOS (3) during September 2009 (bottom graph) at Cape Verde Atmospheric Observatory in the tropical marine boundary layer. Error bars show  $\pm 1\sigma$  of hourly averaged diurnal values.

This suggest that in these conditions experienced on three different seasons at the Cape Verde, a [NO] of greater than approximately 20 pptv in February-March, 11 pptv in May-June and beginning of September are required in order for net *in-situ* ozone production to occur.

The compensation point can be calculated by drawing a trend line through all the data or distributing the data into three  $N(O_3)$  diurnal averages and drawing a line between the average of the first and last third (known as the thirds method or the organic correlation method). Thirds method does not include standard deviation due to calculation of linear regression from a straight line through two points. Three of SOS (1), SOS (2) and SOS (3) campaigns' compensation points were compared to those from data at previous campaigns are shown in Table 4.13.

<b>ozone compensation point</b>			
<b>Campaign</b>	<b>All data</b>	<b>Thirds method*</b>	<b>Reference</b>
<b>EASE 97</b>	63 ± 34	10.5 <sup>a</sup>	Fleming (2002)
<b>SOAPEX II</b>	25 ± 2	27	Fleming (2002)
<b>NAMBLEX</b>	27 ± 9	19	Fleming (2002)
<b>Weybourne summer</b>	-43 ± 61 <sup>b</sup>	17	Fleming (2002)
<b>Weybourne winter</b>	94 ± 171 <sup>c</sup>	-	Fleming (2002)
<b>Mace Head 1995</b>	55 ± 30 (Carpenter <i>et al.</i> , 1997)	30 (Cox <i>et al.</i> , 1999)	Fleming (2002)
<b>SOS (1)</b>	20.0 ± 0.9	-	This work
<b>SOS (2)</b>	11.5 ± 1.2	-	This work
<b>SOS (3)</b>	11.3 ± 0.8	-	This work

Table 4.13 - Ozone compensation points in pptv [NO] for all campaigns

<sup>a</sup>Thirds method not used due to scatter producing poor fit

<sup>b</sup> Negative compensation point does not make physical sense and is not included in analysis

<sup>c</sup>Calculated with insufficient data

\*Thirds method

Fleming (2005) found that the Weybourne summer data did not provide enough points for calculating the compensation point, this gives a negative intercept  $[\text{NO}] = -43$  pptv. This method should be ignored and this negative intercept could have been determined by the data point at the highest  $N(\text{O}_3)$ . The method of thirds determined a value of 17 pptv calculated for  $[\text{NO}]$  whereas averaged mixing ratio of NO was 200 pptv (Fleming, 2005). Owing to this reduced compensation point, it can be concluded that net ozone production can often happen at Weybourne. In contrast, much reduced NO mixing ratio (see middle graph on Figure 4.5) observed at Cape Verde and ozone destruction happened during SOS (1), SOS (2) and SOS (3) (see Sections 4.5, 4.5.1). It might be suggested that halogen influences contributed to the further ozone lost at Cape Verde (see Section 4.5.1). The value for the ozone compensation point, of 63 pptv  $[\text{NO}]$  has been calculated during EASE 97. Almost identical values, of 25 and 27 pptv, have been calculated during SOAPEX 2 and NAMBLEX, respectively, while the lowest value during the Weybourne summer campaign reached 17 pptv. The highest values for  $[\text{NO}_x]$  have been established during EASE 97 and Weybourne and the values were quite similar, but EASE 97 had a higher compensation point (Fleming, (2005)). Reduced  $[\text{NO}_x]$  values have been obtained at Cape Verde for SOS (2) and SOS (3) with low compensation points.

## 4.6 Peroxy radical production and loss

In order to do the further analysis for the peroxy radicals at Cape Verde Atmospheric Observatory in the tropical marine boundary layer air, a steady state analysis of the production and loss of peroxy radicals during three of SOS campaigns has been carried out using the method described by Mihele and Hastie (2003) and demonstrated in section 3.3 in Chapter 3.  $\beta$  and  $\gamma$  derived from equation (M) and (Q) respectively (see section 3.3, Chapter 3). The steady state analysis of production and loss of peroxy radicals can be shown as:  $\beta$  represents the pre-dominant loss process for peroxy radicals. If  $\beta$  has a value smaller than one, then the pre-dominant loss process is the radical self-reaction rather than loss through reaction of OH with NO<sub>2</sub>.  $\gamma$  is an amount of supplementary peroxy radical production from sources other than ozone photolysis. If  $\gamma$  has the value of zero, this shows no excess production, whilst a  $\gamma$  of less than zero proves that a higher concentration of peroxy radicals is obtained from ozone photolysis than the one observed.

$$\beta = \frac{k[\text{OH}][\text{NO}_2]}{2\alpha k_{SR}[\text{HO}_2 + \text{RO}_2]^2} \quad (\text{C})$$

$$\gamma = \frac{[\text{HO}_2 + \text{RO}_2]^2 \alpha (1 + \beta) k_{SR}}{fj(\text{O}^1\text{D})[\text{O}_3]} - 1 \quad (\text{D})$$

The hourly averaged time series of  $\beta$  and  $\gamma$  were calculated between 06:00-19:00 LT using the equation of (C) and (D), respectively for SOS (1), SOS (2) and SOS (3) campaigns. The following measurements were taken to calculate  $\beta$  and  $\gamma$ . PERCA measurements of [HO<sub>2</sub>+RO<sub>2</sub>] (see Figure 3.8 for SOS (1), see Figure 3.9 for SOS (2) and see Figure 3.10 for SOS (3)). University of Leeds FAGE measurements of [OH] and [HO<sub>2</sub>] (see Table 4.2). The University of York NO<sub>x</sub> measurements of NO<sub>2</sub> (see Table 4.2).  $\alpha$  obtained by the ratio of [HO<sub>2</sub>]: [HO<sub>2</sub>+CH<sub>3</sub>O<sub>2</sub>] on the basis of [HO<sub>2</sub>] and

[HO<sub>2</sub>+RO<sub>2</sub>] measurements (see Sections 4.4.3.7 and 4.4.3.9). University of Leicester spectral radiometer measurement of  $j(\text{O}^1\text{D})$  (see Figure 3.8 for SOS (1), see Figure 3.9 for SOS (2) and see Figure 3.10 for SOS (3)). University of York thermo Electron Instrument (TEI) Model 49i UV Analyser measurements of [ozone] (see Table 4.2). See section 3.13 for the data averaging process. Figures 4.27 and 4.28 show the hourly averaged time series of  $\beta$  and  $\gamma$  between 06:00-19:00 LT from the SOS (1) (top graph), SOS (2) (middle graph) and SOS (3) (bottom graph) campaigns.

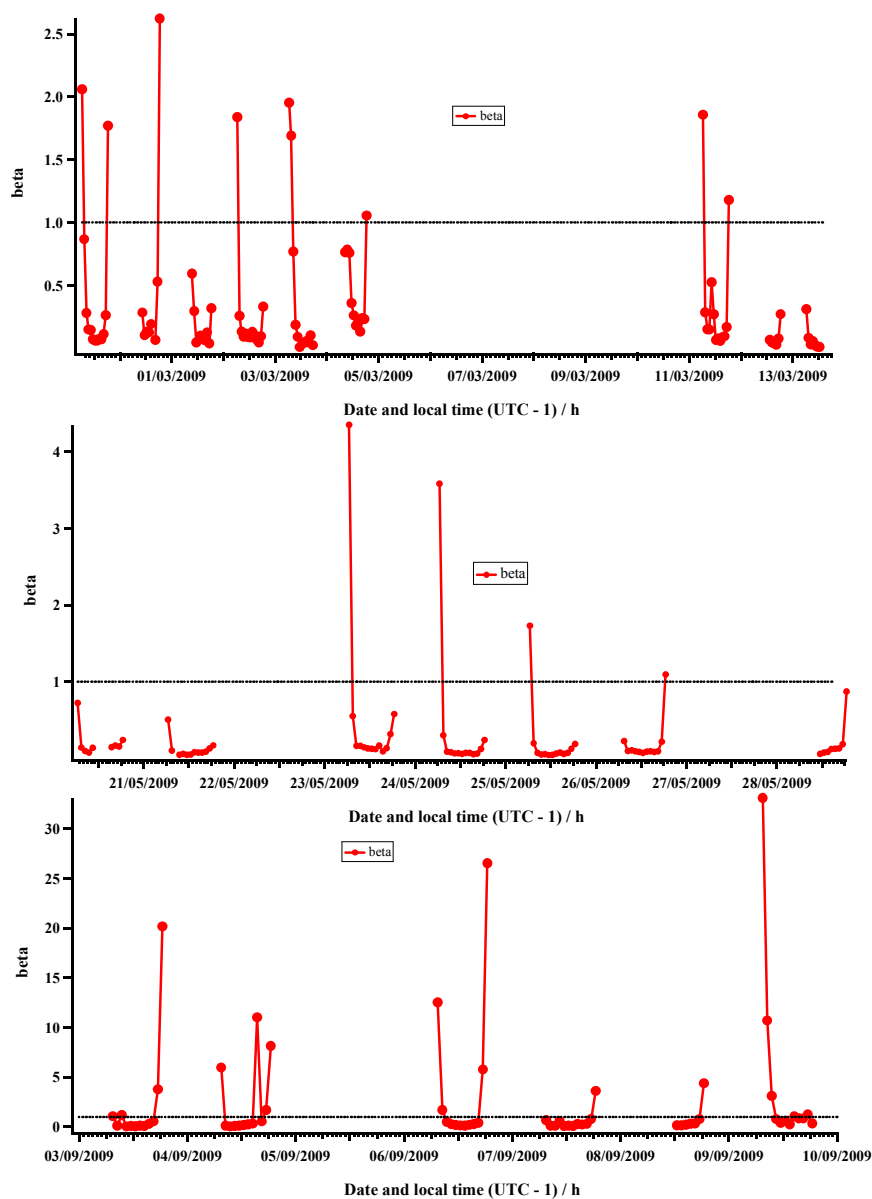


Figure 4.27 - Hourly averaged time series of  $\beta$  between 06:00-19:00 LT from the campaigns SOS (1) during February-March (top graph), SOS (2) during May-June (middle graph) and SOS (3) during September 2009 (bottom graph) at Cape Verde Atmospheric Observatory in the tropical marine boundary layer.

$\beta$  is mostly less than 1 for the three SOSs campaigns (see Figure 4.27). The median of  $\beta$  is 0.13 in SOS (1), 0.10 in SOS (2) and 0.34 in SOS (3) respectively between 06:00-19:00 LT. Considering the  $\beta$  values, this indicates that the loss of peroxy radical is controlled by the peroxy radical self-reaction, rather than the reaction of OH with NO<sub>2</sub> and the process of peroxy radical loss owing to reaction of OH with NO<sub>2</sub> appears to be less favourable.

During the SOS (1), SOS (2) and SOS (3) campaigns, the large values of  $\beta$  are calculated during early morning (07:00-08:00 LT) and late afternoon (18:00-19:00 LT) as shown in Figure 4.32. Higher values of  $\beta$  are calculated for SOS (3) against SOS (1) and SOS (2) it could be possible to owing to the lowest values of  $\alpha$  ( $=[\text{HO}_2]/[\text{HO}_2+\text{RO}_2]$ ) obtained in SOS (3) against SOS (1) and SOS (2) campaigns as shown in Figure 4.17. Equation (C) explains the reduction of  $\alpha$  in the conditions of a  $\beta$  increase. There is no significant difference in [OH] and [HO<sub>2</sub>+RO<sub>2</sub>] observed during early morning and late afternoon in SOS (1), SOS (2) and SOS (3) campaigns as shown in Figure 4.15 (top graph) and Figure 4.15 (bottom graph). It is important to note that no NO<sub>2</sub> measurements are available during SOS (3) campaign, unlike the case of SOS (1) and SOS (2) and therefore hourly averaged NO<sub>2</sub> data have been obtained from previous measurements made at Cape Verde Atmospheric Observatory site in September 2007 to calculate  $\beta$  and  $\gamma$  for the SOS (3) campaign. Hence, it might be difficult to compare the  $\beta$  and  $\gamma$  values for SOS (3) campaign with the SOS (1) and SOS (2) campaigns.

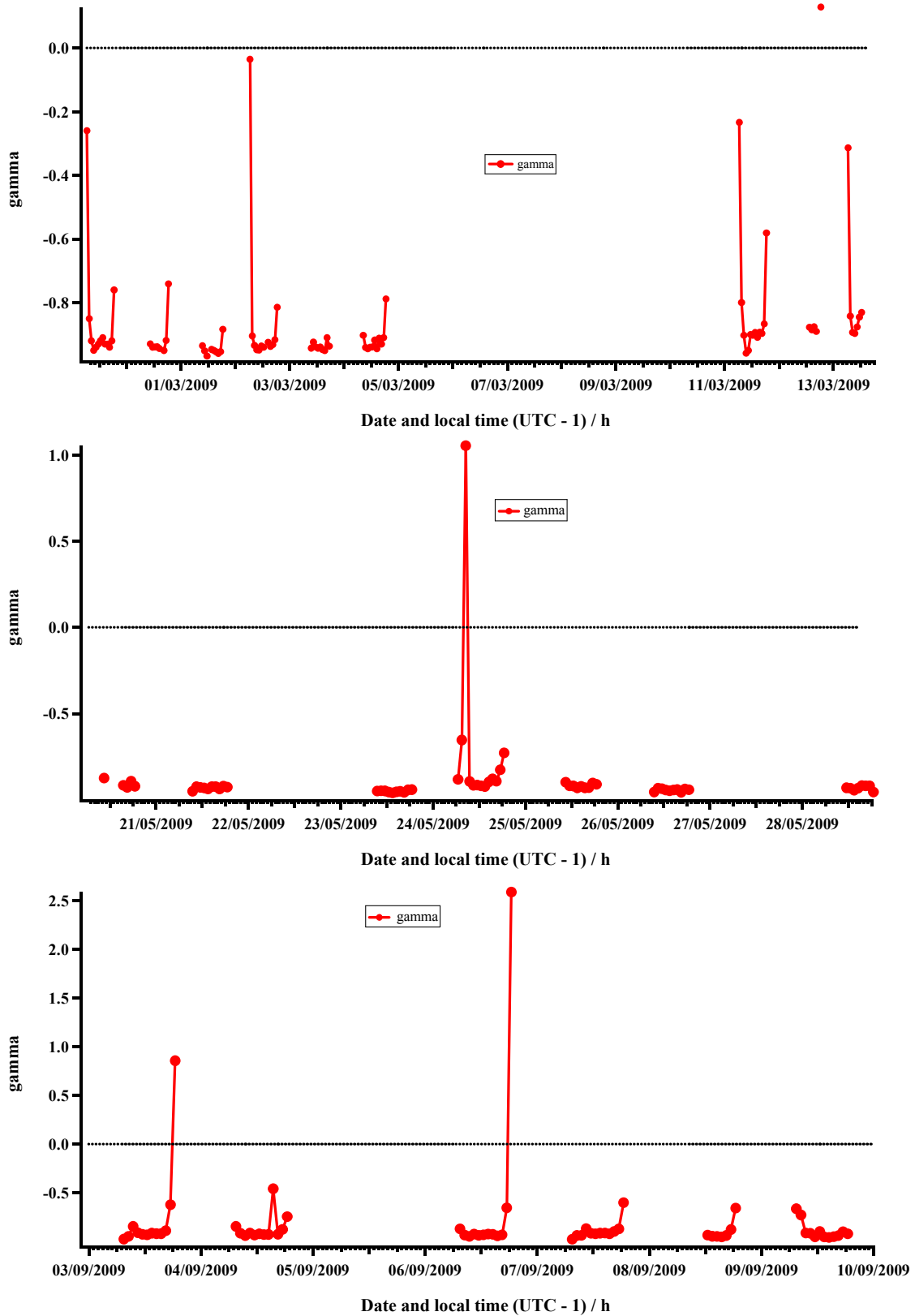


Figure 4.28 - Hourly averaged time series of  $\gamma$  between 06:00-19:00 LT from the campaigns SOS (1) during February-March (top graph), SOS (2) during May-June (middle graph) and SOS (3) during September 2009 (bottom graph) at Cape Verde Atmospheric Observatory in the tropical marine boundary layer.

Figure 4.28 indicates values smaller than 0 for  $\gamma$  for the three SOS campaigns in the hourly averaged time series 06:00-19:00 LT. The values for the median of  $\gamma$  during SOS (1), SOS (2) and SOS (3), respectively are -0.92, -0.93 and -0.92, between 06:00-19:00 LT. The negative values of  $\gamma$ , indicate that either there is an overestimation of peroxy radical production from ozone photochemistry or the peroxy radical losses have been underestimated, or a combination of both. It can be concluded that the peroxy radical losses have been underestimated owing to the fact that production *via* ozone photolysis has fairly well constrained conditions (with measurements of both  $j(\text{O}^1\text{D})$  and water vapour) and any additional production terms would lead to  $\gamma$  being even more negative. There is chance for an underestimation of peroxy radical losses from self-reactions supposing that all  $\text{RO}_2$  is present in the form of  $\text{CH}_3\text{O}_2$ . The underestimation of peroxy radical losses is possible in the current analysis. The current analysis has neglected the self reaction of  $\text{CH}_3\text{O}_2$ , i.e.  $k_{3.15} = 0$  (It was discussed in Section 3.3 in Chapter 3). The afternoon proportions of  $\text{CH}_3\text{O}_2:\text{HO}_2$  were observed 2.5:1, 3.3:1 and 5:1 during SOS (1), SOS (2) and SOS (3) campaigns, respectively (see Sections 4.4.3.2 and 4.4.3.7). Therefore,  $\text{CH}_3\text{O}_2$  is the main peroxy radicals during the late afternoon. The self reaction of  $\text{CH}_3\text{O}_2$  has been neglected from the calculation for  $\alpha$ ,  $\beta$  and  $\gamma$ . It might be suggested that the self reaction of  $\text{CH}_3\text{O}_2$  should be an important part of the  $\alpha$ ,  $\beta$  and  $\gamma$  analysis at the Cape Verde marine boundary layer. Furthermore, it could be implemented by considering the halogen chemistry at the Cape Verde in the tropical marine boundary layer (see section 4.6.1). Whalley *et al.*, (2010) concluded that halogen oxides do acted regenerate OH upon reaction with  $\text{HO}_2$  radicals as well as dominant sink for  $\text{HO}_2$  at the Cape Verde Atmospheric Observatory in the tropical marine boundary layer (section 4.6.1).

### 4.6.1 Sensitivity analysis of radical budget with halogen chemistry

A steady state analysis of the production and loss of peroxy radicals during the three SOS campaigns have been analyzed in section 4.5 without considering the influence of halogens.

Bloss *et al.*, (2005b) pointed out that during NAMBLEX, under low NO<sub>x</sub> conditions (NO~50 pptv), the calculations prove that 40% of the total HO<sub>2</sub> radical sink is caused by the reaction IO + HO<sub>2</sub> → HOI + O<sub>2</sub>, while the photolysis of HOI to form OH + I is responsible for 15% of the total midday OH production rate.

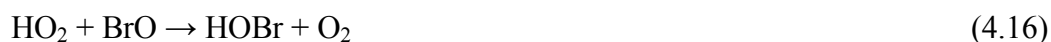
Sjostedt *et al.*, (2007) observed that during the campaign at Summit research station, Greenland, (at an altitude of 3200 m) in June-July 2003 for polar boundary layer, chemical ionisation mass-spectrometry has been employed for carrying out OH and HO<sub>2</sub>+RO<sub>2</sub> measurements and the observations showed a median OH and peroxy radical concentrations of  $6.4 \times 10^6$  molecule cm<sup>-3</sup> and  $2.2 \times 10^8$  molecules cm<sup>-3</sup>. Sjostedt *et al.*, (2007) and Chen *et al.*, (2007) concluded that the model calculations reproduced the observed peroxy radical concentrations, but OH concentrations have been much underestimated. Sjostedt *et al.*, (2007) suggested that (unmeasured) halogen chemistry may provide an additional RO<sub>2</sub>/HO<sub>2</sub> to OH conversion mechanism, accounting for the discrepancy - this suggestion is consistent with the results from Halley Research Station in coastal Antarctica during the austral summer 2004/2005 (Bloss *et al.*, (2010)); where IO and BrO have been shown to overwhelmingly dominate HO<sub>2</sub>-to-OH conversion.

Bloss *et al.*, (2010) showed that peroxy radical self and cross-reactions mainly account for the HOx sinks; more precisely, 40% of the total sinks are the result of all halogen mediated HOx loss processes. Photolysis of the hypohalous acids such as HOI and HOBr are the important sources for OH, has been modelled at Halley Research Station in coastal Antarctica during the austral summer 2004/2005 in the polar boundary layer.

The peroxy radical production obtained from ozone photochemistry has been shown to be overestimated, and/or peroxy radicals losses have been underestimated according to strongly negative  $\gamma$  values calculated during SOS (1), SOS (2) and SOS (3) campaigns as presented in section 4.6. The variation can be explained either by the missing peroxy radical sinks or missing OH sources rather than ozone photolysis and the lacking sources could be halogen chemistry.

In marine environments, IO and BrO will affect HOx concentrations through a number of processes, most significantly (from the perspective of performing steady-state OH calculations) by converting HO<sub>2</sub> to OH via formation of HOI and HOBr, which can then either be removed through heterogeneous reaction with aerosol or photolysis to produce OH and a halogen atom, X (where X = I, Br) via the reaction 4.10 and 4.17. This halogen atom can then regenerate XO (where X = I, Br) via the reaction 4.8 and 4.15 (Monks *et al.*, 2005; Bloss *et al.*, 2005b; Smith *et al.*, 2006; Sommariva *et al.*, 2006; Kanaya *et al.*, 2007; Saiz-Lopez *et al.*, 2007).





Where x is Br or I



IO data for May-June 2007 and BrO in June 2010 could be used for calculating the radical budget for May-June 2009. This section explains an analysis of the halogen functions within the marine boundary layer in order to detect the differences between halogen and non-halogen analysis in terms of radical budget.

Carrying out a further analysis of the peroxy radicals at Cape Verde Atmospheric Observatory in the tropical marine boundary layer air, a pre-supposed steady state analysis of the production and loss of peroxy radicals during the SOS (2) campaign introducing the contribution of halogens in the equation (B). The equation (B) was described by Mihele and Hastie (2003) and demonstrated and also used in section 3.3 in Chapter 3 and applied in section 4.6 in Chapter 4 with non halogen chemistry. Peroxy radicals are considered to be steady state during this analysis and moreover, the analysis includes repartitioned peroxy radical loss rate term,  $L_{XO}$  (see the equation T on page number 274). The repartitioned peroxy radical loss rate term,  $L_{XO}$  obtained from the reaction with XO (IO and BrO), which is introduced into the earlier equation (B) in

Chapter 3.  $L_{SR}$  and  $L_{NO_2}$  are explained in section 3.3 in Chapter 3; hence, the equation can be the following:

$$\text{In steady state } \frac{d[\text{HO}_2 + \text{RO}_2]}{dt} = P_{\text{HO}_2 + \text{RO}_2} - L_{SR} - L_{NO_2} - L_{XO} = 0 \quad (\text{E})$$

The radical production term becomes:

$$P_{\text{HO}_2 + \text{RO}_2} = 2f\hat{f}(\text{O}^1\text{D})[\text{O}_3](1 + \gamma) \quad (\text{F})$$

$$\gamma = \frac{[\text{HO}_2 + \text{RO}_2]^2 \alpha(1 + \beta)k_{SR}}{f\hat{f}(\text{O}^1\text{D})[\text{O}_3]} - 1 \quad (\text{G})$$

By considering halogen chemistry,  $\gamma$  would be replaced by  $\gamma_{\text{new}}$ , which acts to be a function of the repartitioned OH from halogen chemistry (excluding ozone photolysis) and not an additional fraction of radical production routes.

$$P_{\text{HO}_2 + \text{RO}_2} = 2f\hat{f}(\text{O}^1\text{D})[\text{O}_3](1 + \gamma_{\text{new}}) \quad (\text{H})$$

$$\beta = \frac{L_{NO_2}}{L_{SR}} \quad (\text{I})$$

When considering halogen chemistry,  $\beta_{\text{new}}$ , which takes the place of  $\beta$ . If  $\beta_{\text{new}}$  is less than one, radical self-reaction, ( $L_{SR}$ ) is the main loss process replacing the loss facilitated by reaction of OH with  $\text{NO}_2$  and halogen monoxide (IO and BrO). Hence,  $\beta_{\text{new}}$  becomes,

$$\beta_{\text{new}} = \frac{L_{NO_2} + L_{XO}}{L_{SR}} \quad (\text{J})$$

$$\beta_{\text{new}} = \frac{L_{NO_2}}{L_{SR}} + \frac{L_{XO}}{L_{SR}} \quad (\text{K})$$

$$\alpha = \frac{[\text{HO}_2]}{[\text{HO}_2 + \text{RO}_2]}, \quad (\text{L})$$

Assuming that all RO<sub>2</sub> is in the form of CH<sub>3</sub>O<sub>2</sub>,  $\alpha$  becomes

$$\alpha = \frac{[HO_2]}{[HO_2 + CH_3O_2]} \quad (M)$$

$$\alpha = \frac{1}{\left(1 + \frac{[CH_3O_2]}{[HO_2]}\right)} \quad (N)$$

gives the radical loss terms as:

$$L_{HO_2+RO_2} = L_{SR} + L_{NO_2} + L_{XO} \quad (O)$$

$$L_{HO_2+RO_2} = (1 + \beta_{new})L_{SR} \quad (P)$$

$$L_{SR} = 2k_{SR}\alpha[HO_2 + RO_2]^2 \quad (Q)$$

$$\text{But } L_{NO_2} = k[OH][NO_2] \quad (R)$$

Substituting  $L_{SR}$  and  $L_{NO_2}$  into equation (J)

$$\beta_{new} = \frac{k[OH][NO_2] + L_{XO}}{2\alpha k_{SR}[HO_2 + RO_2]^2} \quad (S)$$

where

$$L_{XO} = \left( \begin{array}{l} k_{4.9}[HO_2][IO] + k_{4.13}[CH_3O_2][IO] + k_{4.16}[HO_2][BrO] \\ + \\ k_{4.20+4.22}[CH_3O_2][BrO] \end{array} \right) \quad (T)$$

and  $k_{4.9}$ ,  $k_{4.13}$ ,  $k_{4.16}$  and  $k_{4.20+4.22}$  are the values obtained from Table 4.9.

The effect of halogen chemistry on the relationship between  $\beta_{new}$  and  $\beta$  will lead

to  $\beta_{new} > \beta$  while comparing equations (I) and (K)

Substituting  $L_{SR}$  into equation (P)

$$L_{HO_2+RO_2} = 2k_{SR}\alpha(1 + \beta_{new})[HO_2 + RO_2]^2 \quad (U)$$

The peroxy radical steady state can thus be re-written as

$$\frac{d[P_{HO_2+RO_2}]}{dt} = 2ff(O^1D)[O_3](1 + \gamma) - 2k_{SR}\alpha(1 + \beta_{new})[HO_2 + RO_2]^2 = 0 \quad (V)$$

Under the assumption that  $[HO_2 + RO_2]$  is in steady state, equation (V) can be rearranged to give the following expression for  $\gamma_{new}$

$$\gamma_{new} = \frac{[HO_2 + RO_2]^2 \alpha(1 + \beta_{new})k_{SR}}{ff(O^1D)[O_3]} - 1 \quad (W)$$

Where  $\gamma_{new} > \gamma$  where as  $\beta_{new} > \beta$  as shown in equation (W) and (G).

This analysis must absolutely take into consideration the ratio of  $[CH_3O_2]: [HO_2]$  in order to explore the role of  $\alpha$  within halogen chemistry. With increasing NO<sub>x</sub> (or XO), radical cycling from RO<sub>2</sub> to HO<sub>2</sub> and HO<sub>2</sub> to OH becomes more significant, e.g. Bloss *et al.*, (2007). Bloss *et al.*, (2010) noted reactions with the halogen monoxides dominated CH<sub>3</sub>O<sub>2</sub>-HO<sub>2</sub>-OH inter conversion and iodine chemistry accelerates production of formaldehyde through the CH<sub>3</sub>O<sub>2</sub>+IO reaction (4.13). The environment at Halley is thus one in which rapid radical cycling occurs, but driven by XO rather than NO, and with associated ozone destruction rather than ozone production.



To explore the fate of CH<sub>3</sub>O<sub>2</sub> at Cape Verde marine boundary layer, during the SOS (2) campaign, the time frame between 06:00-19:00 LT is employed for the calculations determining the hourly averaged diurnal data for: [IO] that was obtained by using measured [IO] between May-June 2007 (see Table 4.2). [BrO] by employing measured

[BrO] in June 2010 (see Table 4.2 and Carpenter *et al.*, (2010)). Measured [NO] (see middle graph on Figure 4.5) during SOS (2) campaign. Alpha is obtained from the ratio of [HO<sub>2</sub>]: [HO<sub>2</sub>+CH<sub>3</sub>O<sub>2</sub>] (see Section 4.4.3.7 and Figure 4.17). Figure 4.29 shows the hourly averaged diurnal data of alpha vs. [IO+BrO] (top graph) and the hourly averaged diurnal data of alpha vs. [NO] (bottom graph) between 06:00-19:00 LT from the SOS (2) campaign.

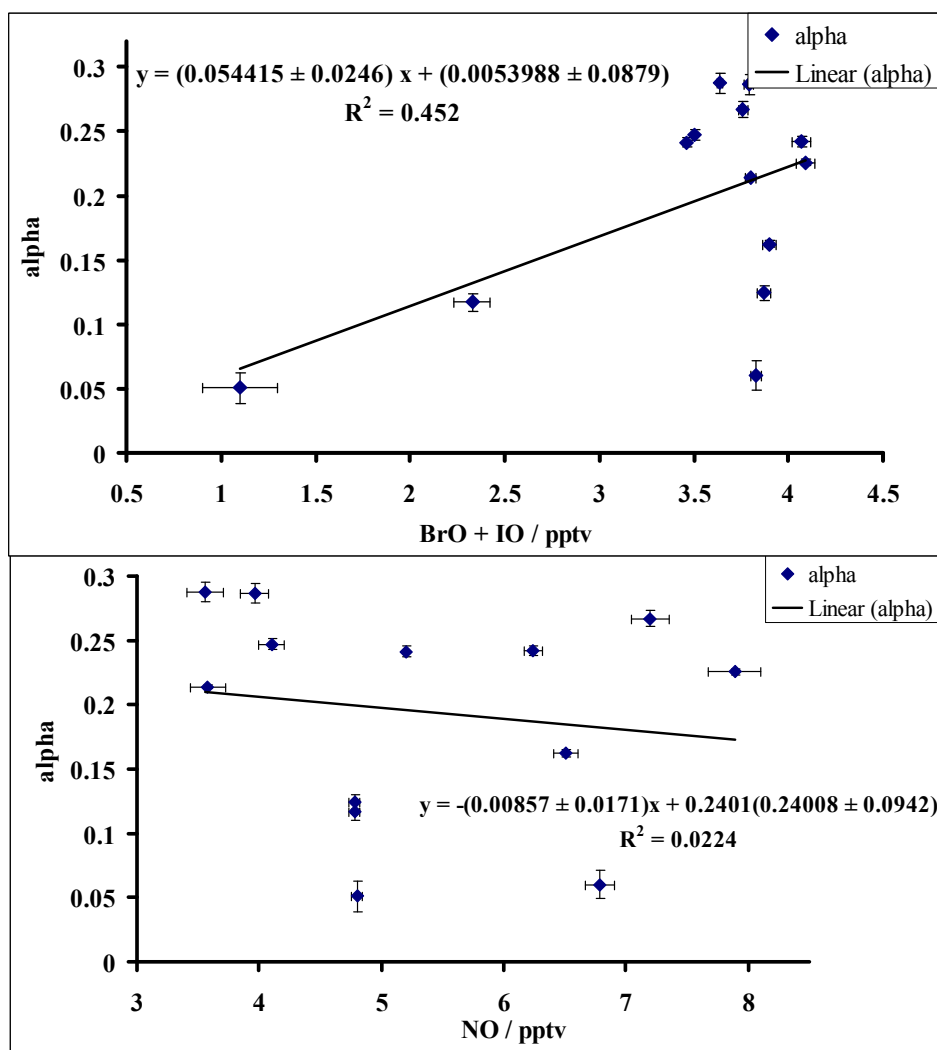


Figure 4.29 - The hourly averaged diurnal cycle data of alpha vs. [IO+BrO] (top graph) and the hourly averaged diurnal data of alpha vs. [NO] (bottom graph) between 06:00-19:00 LT from the campaign SOS (2) during May-June 2009 at Cape Verde Atmospheric Observatory in the tropical marine boundary layer. Error bars show  $\pm 1\sigma$  of hourly averaged diurnal values.

Increasing quantities of halogen monoxide correlate with a rise in the alpha values from the transformation of CH<sub>3</sub>O<sub>2</sub> into HO<sub>2</sub> radicals. The ratio of [CH<sub>3</sub>O<sub>2</sub>]: [HO<sub>2</sub>] is

decreasing and its decreasing rate determines an increase in the alpha values according to the equation (N). The alpha values increasing with XO (IO+BrO) (see top graph on Figure 4.34). It might be suggested that the radical cycling from CH<sub>3</sub>O<sub>2</sub> to HO<sub>2</sub> turns out to be important between 06:00-19:00 LT. The sink for CH<sub>3</sub>O<sub>2</sub> is overwhelmingly reaction with IO and BrO (by considering PERCA and FAGE measurements). Alpha values do not correlate with NO (see bottom graph on Figure 4.34). The information provided for the role of CH<sub>3</sub>O<sub>2</sub> shows that it is more likely to react with XO (IO or and BrO) rather than with NO and that CH<sub>3</sub>O<sub>2</sub> to HO<sub>2</sub> radicals are essential between 06:00-19:00 LT. Bloss *et al.*, (2010) showed that it is the halogen oxides dominating the radical cycling, compared with NO<sub>x</sub>. He further explained that the halogens' reaction is that of moving the radical cycling from organic peroxy radicals and HO<sub>2</sub> to OH, together with ozone destruction owing to reformation of halogen atoms. Halogen chemistry has an impact on the budgets of OH, HO<sub>2</sub> and O<sub>3</sub> at Cape Verde in the tropical marine boundary layer (Read *et al.*, (2008), Whalley *et al.*, (2010)). Similar observations were established at Cape Verde for this work. Ozone loss was greatly controlled by halogen chemistry (See section 4.5.1).

The time frame is used for the  $\beta_{\text{new}}$  and  $\gamma_{\text{new}}$  calculations during SOS (2) campaign is 10:00-16:00 LT. The basis for this is discussed follow. Equation (W) shows that  $\gamma_{\text{new}}$  is inversely proportional to  $j(\text{O}^1\text{D})$ ; but  $j(\text{O}^1\text{D})$  will be a small number with large associated error around sunset and sunrise, hence expect  $\gamma_{\text{new}}$  values to be highly uncertain. Additionally, the RO<sub>2</sub>+RO<sub>2</sub> reaction, which is the main peroxy radical sink in the evening. The RO<sub>2</sub>+RO<sub>2</sub> reaction is excluded from the derivation of  $\gamma_{\text{new}}$  (see equation (W)) and  $\beta_{\text{new}}$  (see equation (S)).

The hourly averaged diurnal data was obtained for IO with the help of measured IO between May-June 2007, as well as for measured BrO in June 2010, where as for beta and gamma the equation of (S) and (W) were applied respectively for carrying out the calculations (see Section 4.6 for details of supporting measurement).

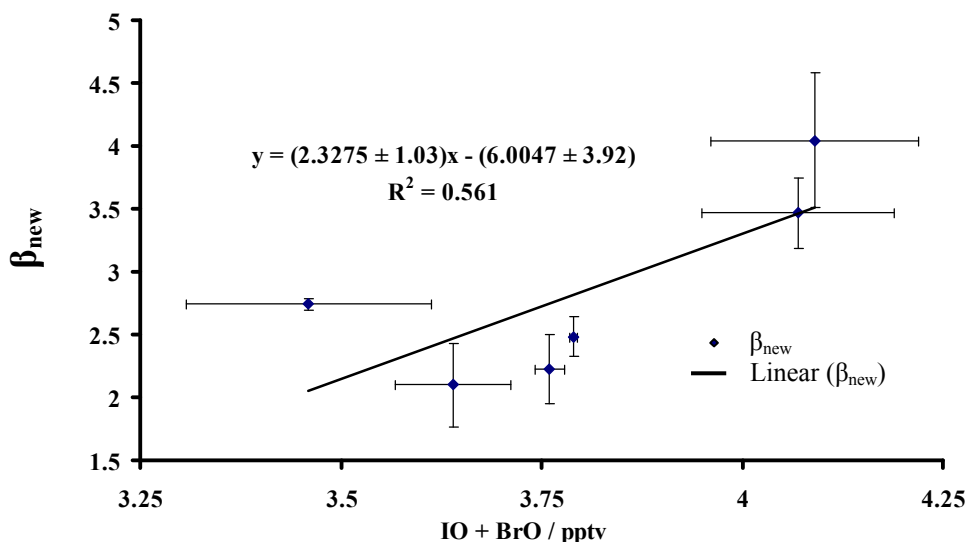


Figure 4.30 - The hourly averaged diurnal cycle data of  $\beta_{new}$  and [IO + BrO] between 10:00-16:00 LT from the campaign SOS (2) during May-June 2009 at Cape Verde Atmospheric Observatory in the tropical marine boundary layer. Error bars show  $\pm 1\sigma$  of hourly averaged diurnal values.

Peroxy radical loss was underestimated in the classical analysis owing to the exclusion of halogen chemistry (as explained in section 4.6). By considering halogen chemistry,  $\beta_{new}$  is increasing along with XO between 10:00-16:00 LT (see Figure 4.30). If halogen monoxide values increase, this determines  $\beta_{new}$  to rise its values alter to greater than 1 (from  $\beta$  which was lower than 1 obtained in section 4.6 during day time). Hence,  $\beta_{new}$  values implies that concentration of peroxy radical loss is dominated by reactions other than peroxy radical self reactions. In this case, the reactions of peroxy radicals with halogen monoxides are important. Halogen monoxide acts as a repartitioning loss term and determines the peroxy radical conversion into OH.

Whalley *et al.*, (2010) observed that at Cape Verde, IO and BrO, although having values of a few pptv, accounted for 19% of the instantaneous sinks for HO<sub>2</sub>, while a further 23% of the HO<sub>2</sub> loss at noon was constituted by aerosol uptake and surface deposition to the ocean. In the case of underestimated peroxy radical loss, halogen chemistry supplies an extra RO<sub>2</sub>/HO<sub>2</sub> to OH conversion mechanism to this work.

The steady state analysis substantially overestimated the peroxy radical concentrations and higher concentration of peroxy radical is obtained from ozone photolysis than actually observed where as without considered halogen chemistry in the section 4.6. OH sources are considered as ozone photolysis within this analysis identified by the  $\gamma$  values (negative values obtained during day time). When considering halogen chemistry,  $\gamma_{\text{new}}$  will increase with XO (IO + BrO) between 10:00-16:00 LT (see Figure 4.31).  $\gamma_{\text{new}}$  gets less negative at higher halogen oxide concentration as shown in Figure 4.31. This still seems to imply that the peroxy radical sinks are still too small in the presence of halogens.

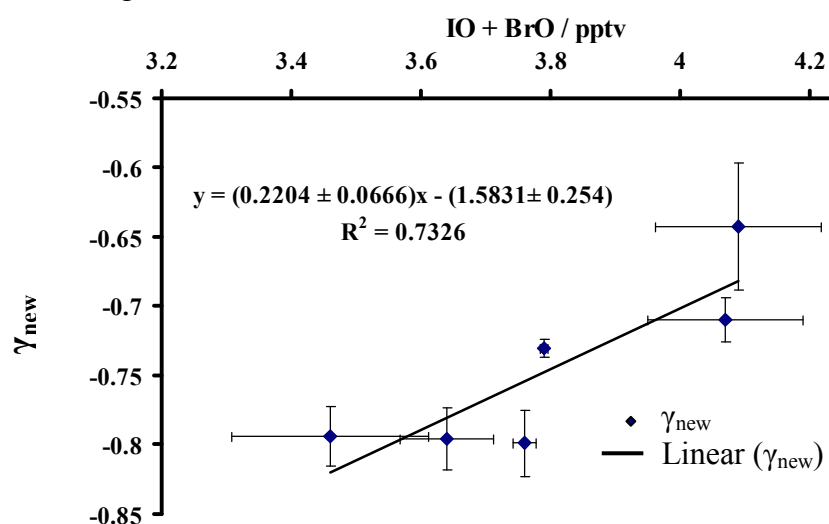


Figure 4.31 - The hourly averaged diurnal cycle data of  $\gamma_{\text{new}}$  and [IO+BrO] between 10:00-16:00 LT from the campaign SOS (2) during May-June 2009 at Cape Verde Atmospheric Observatory in the tropical marine boundary layer. Error bars show  $\pm 1\sigma$  of hourly averaged diurnal values.

Sjostedt *et al.*, (2007) observed that halogen perturbing the HOx cycling and enhancing OH concentration. Whalley *et al.*, (2010) noted that at Cape Verde, 13% of the instantaneous OH formation is produced through photolysis of HOI and HOBr. Halogen chemistry may contribute to the repartitioning of OH (i.e. photolysis of HOBr and HOI) with the total OH in this work.

#### 4.6.2. Effect of averaging period on data analysis for SOS (1), SOS (2) and SOS (3) campaigns

Averaging data to a 1 hour time step could introduce artefacts, e.g. photolysis rate of  $j(\text{O}^1\text{D})$  changes by a factor of 10 inside a 1 hour time step.  $j(\text{O}^1\text{D})$  will be a small number with large associated error around sunrise and sunset. Equation (D) shows that  $\gamma$  is inversely proportional to  $j(\text{O}^1\text{D})$ , hence gamma values to be highly uncertain around sunrise and sunset.

### 4.7 Conclusions from the SOS campaigns

Measurement of peroxy radicals were made with the peroxy radical chemical amplification (PERCA (V3.5)) technique during February-March 2009 (from 27<sup>th</sup> February to 14<sup>th</sup> March), May-June 2009 (from 20<sup>th</sup> May to 2<sup>nd</sup> June) and August-September 2009 (from 30<sup>th</sup> August to 13<sup>th</sup> September) with a range of other compounds and meteorological parameters.

The shape of  $j(\text{O}^1\text{D})$  diurnal cycles indicate that the photochemistry powering peroxy radical production can vary significantly from season to season even at the same site (see Figures 4.8-4.10). The midday average concentration of the peroxy radicals is 22.2

$\pm 2.3$  ( $1\sigma$ ) in SOS (1),  $32.3 \pm 3.2$  ( $1\sigma$ ) in SOS (2) and  $37.2 \pm 3.3$  ( $1\sigma$ ) in the SOS (3) (all in the units of pptv).

It would seem smaller ozone photolysis rates give smaller concentrations of peroxy radicals and the highest ozone concentrations during the day time indicative of the main source of day time radicals being ozone photolysis.

Peroxy radical diurnal cycle maxima were typically shifted towards the afternoon, with daily maximum values between 14 and 48 pptv. Night-time peroxy radical concentrations at Cape Verde were similar  $\sim 10$  pptv during SOS (2) and SOS (3), but slightly lower by 2 pptv during SOS (1).

SOS (2), NO concentration were 50% less than those of SOS (1) and SOS (3) and SOS (2) peroxy radical diurnal cycles were slightly broader than those of SOS (1) and SOS (3). Peroxy radicals were very closely correlated with  $\sqrt{j(O^1D)}$ , a feature noted to occur in the clean air at Cape Grim (Penkett *et al.*, 1997). The scatter plot of the averaged peroxy radical concentrations versus the photolysis rate constant  $j(O^1D)$  during all SOS (1), SOS (2) and SOS (3) revealed a better square root dependence (than first-order) of peroxy radicals on  $j(O^1D)$ , indicative of a relative clean atmosphere and net photochemical destruction of ozone at Cape Verde.

Net ozone loss without halogen rates have been calculated during this work at the tropical marine site where ozone destruction was observed during three different seasons. Also ozone loss rates were generated from the observational ozone diurnal profile (see Figure 4.5) for SOS (1), SOS (2) and SOS (3) campaigns. The

observational test of ozone loss rate calculations indicates that influences of halogen species can contribute to the extra ozone loss (see Section 4.5).

The ozone compensation point was calculated during the campaigns and suggests that under the conditions experienced NO concentrations of greater than approximately 20, 11 and 11 pptv are required in order for net *in-situ* ozone production to occur in SOS (1), SOS (2) and SOS (3) respectively. Daytime hourly averaged mixing ratio of NO are being 10, 5 and 9 pptv for SOS (1), SOS (2) and SOS (3) campaigns, respectively.

The ozone production rate were driven by NO for the campaigns as a whole (having a linear sensitivity  $(d\ln(P(O_3))/d\ln(NO)) = 1.13$  averaged from three different seasonal data sets) and thus ozone production at Cape Verde Atmospheric Observatory in the tropical marine boundary layer may be said to be NO<sub>x</sub> limited.

Role of IO and BrO would be important to find out the exact ozone destruction and radical budget in marine boundary layer. 51% of daily ozone loss was calculated at Cape Verde Atmospheric Observatory in the presence of the 1.12 and 2.41 pptv concentrations of IO and BrO, respectively. Halogen oxides act as dominant sink for HO<sub>2</sub> as well as sources of OH at the Cape Verde Atmospheric Observatory in the tropical marine boundary layer.

# Chapter 5

## A comparison of boundary layer photochemistry in both tropical rainforest and tropical marine air

### 5.1 Introduction

#### 5.1.1 Role of rainforest and marine in the atmosphere

It is essential to decide upon the main elements that control the ozone concentration within the tropical rainforest as well as marine boundary layer during day or night, seasonal cycles for underlying the global ozone budget.

Guenther *et al.*, (1995, 2006) and Hewitt *et al.*, (2010) noted that, overall, half of all biogenic reactive volatile organic compound (VOC) emissions into the atmosphere originate from the tropical and equatorial forests: out of the total 1150 Tg C/year (where Tg C-teragrams of carbon), the approximate contribution from tropical forests was calculated at 500 Tg C/y. Monks *et al.*, (1998) acknowledged that the remote marine boundary layer, constituting around 25% of the atmosphere, makes up the perfect environment for carrying out research regarding the fundamental processes that control ozone photochemistry and the relationships between free radical sources and sinks.

An examination of the function of *in-situ* photochemistry in determining the tropospheric ozone budget is considered fundamental for developing policies for

minimizing photochemical pollution. More accurate forecasting regarding pollution episodes and their avoidance demand a deeper knowledge of the ozone formation processes according to atmospheric composition and the role of different chemical species.

The annual cycle of the ozone mixing ratios appears to be distinct, with a noticeable maximum in the northern hemisphere mid-latitude (NH) during spring time and a minimum in the summer (Derwent *et al.*, 1998; Monks *et al.*, 2000a; Bronnimann, 1999). On a regional scale, there is noticeable variation of  $[O_3]$  and it is necessary to measure and map them through the extended worldwide network of monitoring sites.

The influence of air-mass composition on  $[O_3]$  has been intensively researched over the last twenty years. Simmonds *et al.*, (2004) and Monks *et al.*, (2003b) discovered that all over Europe, there are raising background ozone trends. On the other hand, Derwent *et al.*, (2003) established a reduction in peak ozone episodes at Mace Head, possibly due to the reduction of  $[CO]$ ,  $[NO_x]$  and VOC emissions over the last few years.

This chapter seeks to compare the peroxy radical and ozone photochemistry between the southeast Asian tropical rainforest and northeast mid tropical Atlantic boundary layer site. A variety of analyses were carried out in order to detect similarities and differences between the two sites and between seasons. VOC and  $NO_x$  concentrations at these sites show large variations and lead to different ozone photochemistry.

## 5.1.2 Characteristics of Borneo rainforest GAW station, and Cape Verde Atmospheric Observatory

The first peroxy radical measurements were carried out in 2008 at the Borneo rainforest boundary layer site while the ones at the marine boundary layer sites, only one year later, in 2009 at Cape Verde. The measurements provide the basis for a comparison of ozone-production/ destruction conditions between sites and seasons. The geographical locations of these observatories are described in Section 3.1.1 in Chapter 3 for the Borneo rainforest, Section 4.1 in Chapter 4 for Cape Verde atmospheric station.

Peroxy radical measurements and ozone production analysis in the rainforest are discussed in Chapter 3 for April-May and June-July 2008 (OP3-2008) and peroxy radical measurements and ozone destruction analysis in the northeast mid Atlantic are discussed in Chapter 4 for in February-March, May-June and September 2009 (SOS - 2009).

## 5.2 Results

### 5.2.1 A comparison of chemical species between rainforest and marine campaigns

#### 5.2.1.1 Peroxy radical diurnal cycles

Figure 5.1 illustrates the hourly averages diurnal cycles, for the  $[\text{HO}_2+\text{RO}_2]$  and for  $j(\text{O}^1\text{D})$ , during the Borneo rainforest (OP3 (1) and OP3 (3)) and the Cape Verde marine (SOS (1), SOS (2) and SOS (3)) campaigns, respectively.

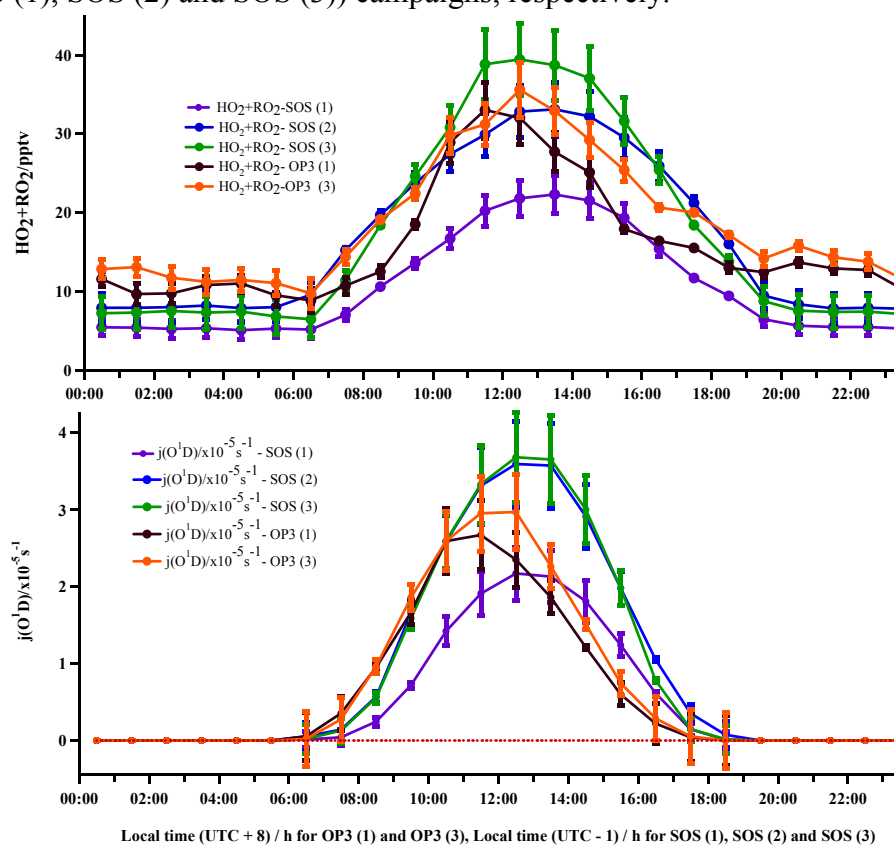


Figure 5.1 - Hourly-averaged  $[\text{HO}_2+\text{RO}_2]$  (top graph) and the photolysis rate coefficient for  $j(\text{O}^1\text{D})$  (bottom graph) from the OP3 (1) (maroon) and OP3 (3) (orange) campaigns at Bukit Atur in the tropical rainforest in Borneo during April-May and June-July 2008 and for SOS (1) (purple), SOS (2) (blue) and SOS (3) (green) campaigns at Cape Verde Atmospheric Observatory in the tropical marine boundary layer during February-March, May-June and September 2009. Figure 5.1 shows the maroon and orange data points for the OP3 (1) and OP3 (3) campaigns which has been plotted previously on Figure 3.10 in Chapter 3, as well as the purple, blue and green data points for the SOS (1), SOS (2) and SOS (3) campaigns plotted previously on Figure 4.11 in Chapter 4. Error bars show  $\pm 1\sigma$  of hourly averaged diurnal values.

Figure 5.1 shows how the  $[\text{HO}_2+\text{RO}_2]$  tracked ozone photolysis ( $j(\text{O}^1\text{D})$ ) during all the campaigns at both sites. The measurements during OP3 (1) and OP3 (3) show the maximum midday hourly average  $[\text{HO}_2+\text{RO}_2]$  are 33 pptv and 36 pptv, respectively, while during SOS (1), SOS (2) and SOS (3), the midday has a value of 22 pptv, 32 pptv and 37 pptv, respectively (see Figure 5.1 (top graph)). The peak hourly average of photolysis rate coefficient for  $j(\text{O}^1\text{D})$  observed at midday during OP3 (1) and OP3 (3) were recorded for  $2.7 \times 10^{-5}$  and  $3.0 \times 10^{-5}$  (all in the units of  $\text{s}^{-1}$ ) while the values during SOS (1), SOS (2) and SOS (3) point out an hourly average midday upper limit of  $2.2 \times 10^{-5}$ ,  $3.6 \times 10^{-5}$  and  $3.7 \times 10^{-5}$  (all in the units of  $\text{s}^{-1}$ ), respectively as shown in Figure 5.1(bottom graph).

However, higher  $[\text{HO}_2+\text{RO}_2]$  are recorded for the Borneo rainforest, as opposed to Cape Verde marine concentrations during the midday of some of the days for April-May and June-July (see Figure 3.9, Chapter 3 and Figures 4.8-4.10, Chapter 4). The lowest midday value, of 22 pptv, is recorded during SOS (1), compared to the values of 32, 33, 36 and 37 for SOS (2), OP3 (1), OP3 (3) and SOS (3).

The  $j(\text{O}^1\text{D})$  diurnal cycles indicate that the photochemistry powering peroxy radical production can vary significantly from season to season and from site to site. Both the Borneo rainforest campaigns had similar  $j(\text{O}^1\text{D})$  values during April-May and June-July, which is not the case at the Cape Verde marine site, where higher  $j(\text{O}^1\text{D})$  values were registered during May-June and September as shown in Figure 5.1 (bottom graph). Owing to the influence that latitude plays on the site, the late winter time (February) SOS (1) campaign had the lowest  $j(\text{O}^1\text{D})$  values as shown in Figure 5.1

(bottom graph), peroxy radical production being dominated by reduced photochemistry.

The night-time  $[\text{HO}_2+\text{RO}_2]$  at Cape Verde during SOS (2) and SOS (3) were very similar, while the ones during SOS (1) were slightly lower, but the concentrations from the Borneo rainforest campaigns (OP3 (1) and OP3 (3)) exceeded all the night-time radical concentrations of the Cape Verde marine campaigns (SOS (1), SOS (2) and SOS (3) (see Figure 5.1 (top graph)). This observation suggests the possibility of higher rate of night time oxidation taking place in the Borneo rainforest compared to the Cape Verde.

The OP3 (3), SOS (2) and SOS (3) peroxy radical diurnal cycles were slightly broader than those of OP3 (1) and SOS (1) (see Figure 5.1 (top graph)). Peroxy radicals were closely correlated with measured  $j(\text{O}^1\text{D})$ , on other hand and in the afternoon as photolysis of compounds other than ozone could cause peroxy radical formation. Particularly, during the OP3 (3) campaign, additional photolysis sources were more noticeable in the early morning and late afternoon, when ozone photolysis had a smaller contribution (see section 3.3.1.4, Chapter 3).

### 5.2.1.2 Peroxy radical correlation with other chemical species

Table 5.1 provides the details of campaign averaged  $\text{HO}_2+\text{RO}_2$ ,  $\text{NO}_x$ ,  $\text{O}_3$ , mixing ratios, temperature for during whole time (LT) and  $j(\text{O}^1\text{D})$  between 06:00-19:00 LT.

Experiment	$\text{HO}_2+\text{RO}_2$ /pptv	$\text{NO}_x$ /pptv	$\text{O}_3$ /ppbv	T/C	$j(\text{O}^1\text{D})$ /s <sup>-1</sup>
OP3 (1) (April-May) 2008	16(8)	225(134)	11(1)	24(2)	$1.12 \times 10^{-05}$ ( $1.24 \times 10^{-05}$ )
OP3 (3) (June-July) 2008	19(8)	351(257)	7(1)	26(3)	$1.27 \times 10^{-05}$ ( $1.14 \times 10^{-05}$ )
SOS (1) (Feb-March) 2009	15(6)	56(10)	37(1)	21(0.3)	$9.6 \times 10^{-06}$ ( $7.84 \times 10^{-06}$ )
SOS (2) (May-June) 2009	24(8)	47(11)	37(2)	22(0.3)	$1.7 \times 10^{-05}$ ( $1.30 \times 10^{-05}$ )
SOS (3) (September) 2009	26(11)	95(27)	20(1)	27(0.5)	$1.68 \times 10^{-05}$ ( $1.34 \times 10^{-05}$ )

Table 5.1 - Details of campaign averaged  $\text{HO}_2+\text{RO}_2$ ,  $\text{NO}_x$  ( $\text{NO}+\text{NO}_2$ ),  $\text{O}_3$  mixing ratios, for during whole time (LT) and  $j(\text{O}^1\text{D})$  for between 06:00-19:00 LT; LT (UTC+8) for OP3 (1) and OP3 (3) at Bukit Atur in the tropical rainforest in Borneo during April-May and June-July 2008, LT (UTC-1) for SOS (1), SOS (2) and SOS (3) at Cape Verde Atmospheric Observatory in the tropical marine boundary layer during February-March, May-June and September 2009 and  $1\sigma$  standard deviations are shown in brackets. Table 5.1 presents the campaign averaged of  $\text{HO}_2+\text{RO}_2$ ,  $\text{NO}_x$ ,  $\text{O}_3$ , mixing ratios for during whole time (LT) and  $j(\text{O}^1\text{D})$  for between 06:00-19:00 LT for the OP3 (1) and OP3 (3) campaigns which has been shown previously in Table 3.3 in Chapter 3.

The highest mean  $\text{NO}_x$  mixing ratio (225 and 351 pptv during April-May and June-July, respectively) were registered during the Borneo rainforest campaigns, as compared to the lowest mean  $\text{NO}_x$  mixing ratio (less than 100 pptv) experienced by the Cape Verde marine campaigns (see Table 5.1). The lowest ozone mixing ratios occurred in July for the rainforest and in September for Cape Verde marine boundary layer. The Borneo rainforest campaigns, as well the Cape Verde marine campaigns experienced the lowest ozone mixing ratios at a moment when the highest mean  $\text{NO}_x$  mixing ratios occur as shown in Table 5.1.

### 5.2.1.3 The effect of NO<sub>x</sub> on peroxy radicals

To understand how the effect of [NO<sub>x</sub>] on [HO<sub>2</sub>+RO<sub>2</sub>] during daytime from the OP3 (1), SOS (1) and SOS (2) campaigns, the following plots are considered in this section: Figure 3.11b (bottom) shown in Chapter 3 for OP3 (1) campaign; Figure 4.16 shown in Chapter 4 for SOS (1) and SOS (2) campaigns. The graphs presented in Figure 3.11b (bottom) in Chapter 3 and Figure 4.16 in Chapter 4 show that for low NO<sub>x</sub> conditions during the day light hours. When [NO<sub>x</sub>] increases, [HO<sub>2</sub>+RO<sub>2</sub>] increases but with poor correlation ( $R^2 = 0.22$ ) for OP3 (1) campaign and a better correlations ( $R^2 = 0.58$ ) and ( $R^2 = 0.77$ ) for SOS (1) and SOS (2) campaigns, respectively.

At higher NO<sub>x</sub> while the increases in [NO<sub>x</sub>] from ca. 175-570 pptv for OP3 (1) as shown in Figure 3.11b (bottom) shows no increase in the [HO<sub>2</sub>+RO<sub>2</sub>] (see Section 3.2.3.3). It needs to noted that, peroxy radical concentrations do not correlate with NO<sub>x</sub> concentrations between 10:00-16:00 LT during the OP3 (3) campaign (see Section 3.2.3.3 in Chapter 3). NO<sub>2</sub> data is not available for SOS (3) campaign (see Table 4.2 in Chapter 4).

During OP3 (1), SOS (1) and SOS (2) campaigns, the loss of peroxy radical seems to be controlled by the peroxy radical self-reaction rather than the reaction of OH with NO<sub>2</sub> (explained in section 3.3 in Chapter 3 and section 4.6 in Chapter 4 using parameters  $\alpha$ ,  $\beta$  and  $\gamma$ ). Figure 3.11b (bottom) in Chapter 3 and Figure 4.16 in Chapter 4 shows that the process of peroxy radical loss estimated to be caused by the reaction of OH with NO<sub>2</sub> appears to be less favourable (see section 3.3 in Chapter 3 for OP3 (1) and see section 4.6 in Chapter 4 for SOS (1) and SOS (2) campaigns).

#### 5.2.1.4 Night time radicals

During OP3 (1) and OP3 (3) campaigns, the reactions of alkenes and monoterpenes with O<sub>3</sub>, as well as the potential for NO<sub>3</sub> chemistry could account for the HO<sub>2</sub> radical source sustaining elevated [HO<sub>2</sub>+RO<sub>2</sub>] at night. Carslaw *et al.*, (1997) discovered a positive relation between NO<sub>3</sub> and HO<sub>2</sub>+RO<sub>2</sub> during spring and autumn at Weybourne, UK (52° N, 1° E) on the North Sea, pointing out that the reactions of the nitrate radical produce peroxy radicals. Salisbury *et al.*, (2001) reported [HO<sub>2</sub>] of up to 5.1 x 10<sup>7</sup> molecule cm<sup>-3</sup> on two nights during the EASE 97 campaign, Mace Head under comparatively clean conditions. Except when the air originates from west and south west, the EASE 97 research established that oxidation routes of alkenes and ozone are more noticeable than those initiated by NO<sub>3</sub>. Fleming *et al.*, (2006a) reported a value of 25 pptv for night-time [HO<sub>2</sub>+RO<sub>2</sub>] during the NAMBLEX campaign at Mace Head in 2002, when the approximate proportions to the night time peroxy radical production were 59% for the ozone-alkenes chemistry and 41% for the NO<sub>3</sub>-alkenes chemistry. Figure 5.1 shows the hourly averaged diurnal data of peroxy radicals during the Borneo rainforest (OP3 (1) and OP3 (3)) and the Cape Verde marine (SOS (1), SOS (2) and SOS (3)) campaigns together.

The Borneo rainforest (OP3 (1) and OP3 (3)) and Cape Verde marine (SOS (1), SOS (2) and SOS (3)) campaigns results show peroxy radical chemistry at night and that significant oxidant levels are sustained in both tropical Borneo rainforest and Cape Verde marine boundary layer. Maximum night time [HO<sub>2</sub>+RO<sub>2</sub>] were measured up to 29 pptv at 22:30 on 15<sup>th</sup> April during OP3 (1) and 13 pptv at 23:30 on 3<sup>rd</sup> September during SOS (3) campaigns, respectively (see Figure 3.9 (left) in Chapter 3 for OP3 (1) and Figure 4.10 in Chapter 4 for SOS (3)). Table 5.2 contains the concentration values

that have been obtained during both the Borneo rainforest and the Cape Verde marine campaigns by calculating the average  $[\text{HO}_2+\text{RO}_2]$  in daylight hours (06:00-19:00 LT; LT (UTC+8) for Borneo rainforest and LT (UTC-1) for Cape Verde marine)) vs. darkness hours (19:00-06:00LT; LT (UTC+8) for Borneo rainforest and LT (UTC-1) for Cape Verde marine)).

<b><math>\text{HO}_2+\text{RO}_2</math> / pptv</b>			
	<b>Day time</b>	<b>Night time</b>	<b>Day/Night Ratio</b>
<b>OP3 (1)</b>	20	11	1.8 : 1
<b>OP3 (3)</b>	24	13	1.9 : 1
<b>SOS (1)</b>	15	5	2.8 : 1
<b>SOS (2)</b>	24	8	3.0 : 1
<b>SOS (3)</b>	26	7	3.5 : 1

Table 5.2 - Hourly averaged  $[\text{HO}_2+\text{RO}_2]$  during day and night time and ratio between the day and night for campaigns OP3 (1) and OP3 (3) at Bukit Atur in the tropical rainforest in Borneo during April-May and June-July 2008 and for campaigns SOS (1), SOS (2) and SOS (3) at Cape Verde Atmospheric Observatory in the tropical marine boundary layer during February-March, May-June and September 2009.

The ratio between day time (06:00-19:00 LT) and night time (19:00-06:00 LT) for  $[\text{HO}_2+\text{RO}_2]$  was higher at the Cape Verde marine site compared to the Borneo rainforest site. It can be concluded that more active peroxy radical chemistry was observed in the Borneo rainforest site than the Cape Verde marine site during night time.

Figure 3.13 shown in Chapter 3 for OP3 (1) and OP3 (3) campaigns and Figure 4.18 shown in Chapter 4 for SOS (1) and SOS (2) campaigns show the main differences.

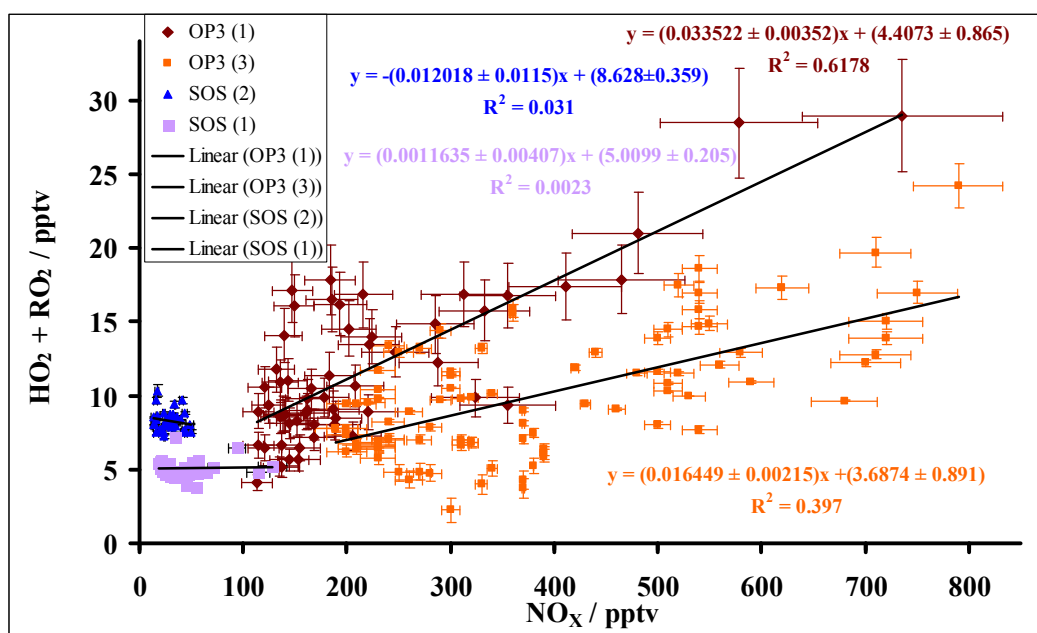


Figure 5.2 - Hourly averaged  $[HO_2+RO_2]$  vs. hourly averaged  $[NO_x]$  between 19:00-06:00 LT; LT (UTC+8) for OP3 (1) and OP3 (3) at Bukit Atur in the tropical rainforest in Borneo during April-May 2008, LT (UTC-1) for SOS (1) and SOS (2) at Cape Verde Atmospheric Observatory in the tropical marine boundary layer during May-June 2009. Maroon and orange data points for the OP3 (1) and OP3 (3) campaigns which has been plotted previously on Figure 3.13 in Chapter 3, as well as the purple and blue data points for the SOS (1) and SOS (2) campaigns plotted previously on Figure 4.18 in Chapter 4. Error bars show  $\pm 1\sigma$  of hourly averaged values.

At night, peroxy radical trends increase with  $NO_x$  during OP3 (1) and OP3 (3) campaigns, as compared to the relatively flat peroxy radical trends with increasing  $NO_x$  observed during the SOS (1) and SOS (2) campaigns.  $[NO_x]$  vary between 100 and 790 pptv in the Borneo rainforest boundary layer (see Figure 5.2, Figure 3.13 in Chapter 3). On the other hand,  $[NO_x]$  are very low and did not exceed 128 pptv at Cape Verde in the tropical marine boundary layer (see Figure 5.2, Figure 4.18 in Chapter 4). It might be suggested that in the case of the Borneo rainforest boundary level,  $NO_3$  chemistry is active (explained in section 3.2.3.4 in Chapter 3). For the night

time radicals at the Cape Verde in the tropical marine boundary layer, ozone-alkene reactions could be important (explained in section 4.4.3.8 in Chapter 4).

## 5.2.2 Photochemical ozone formation

### 5.2.2.1 Comparisons of daily ozone production between campaigns

Table 5.3 provides details of hourly averaged time series of  $P(O_3)$ , maximum, minimum, average and standard deviation between 06:00-19:00 LT.

$P(O_3) / \text{ppbv hr}^{-1}$				
Experiment	Maximum	Minimum	Average	Standard deviation
OP3 (1) (April-May) 2008	3.54	0.04	0.74	0.59
OP3 (3) (June-July) 2008	21.5	0.16	1.85	2.70
SOS (1) (Feb-March) 2009	0.68	0.01	0.13	0.19
SOS (2) (May-June) 2009	0.32	0.02	0.10	0.07
SOS (3) (September) 2009	0.75	0.01	0.15	0.16

Table 5.3 – Hourly averaged time series of  $P(O_3)$ , maximum, minimum, average and standard deviation for during day time between 06:00-19:00 LT; LT (UTC+8) for OP3 (1) and OP3 (3) campaigns at Bukit Atur in the tropical rainforest in Borneo during April-May and June-July 2008, LT (UTC-1) for SOS (1), SOS (2) and SOS (3) campaigns at Cape Verde Atmospheric Observatory in the tropical marine boundary layer during February-March, May-June and September 2009. Table 5.3 presents the hourly averaged time series of  $P(O_3)$  for the OP3 (1) and OP3 (3) campaigns which has been shown previously in Table 3.7 in Chapter 3, as well as the average of  $P(O_3)$  for the SOS (1), SOS (2) and SOS (3) campaigns contained previously in Table 4.8 in Chapter 4.

OP3 (3) showed a bigger range of ozone production values from day to day than during OP3 (1). The ozone production rate during OP3 (3) varied between the values of 0.16 and 21.5 ppbv hr<sup>-1</sup>, while an estimation of the standard deviation indicates a greater day

to day variation. Very high  $P(O_3)$  require co-existence of  $[NO]$  and  $[HO_2+RO_2]$ . The calculated large value for  $P(O_3)$  ( $21.5 \text{ ppbv hr}^{-1}$ ) might be caused by the result of hourly averaging calculations (as explained in Sections 3.2.3.5 and 3.3.2 in Chapter 3). Both tropical rainforest campaigns having much higher ozone production rates than the tropical marine campaigns.

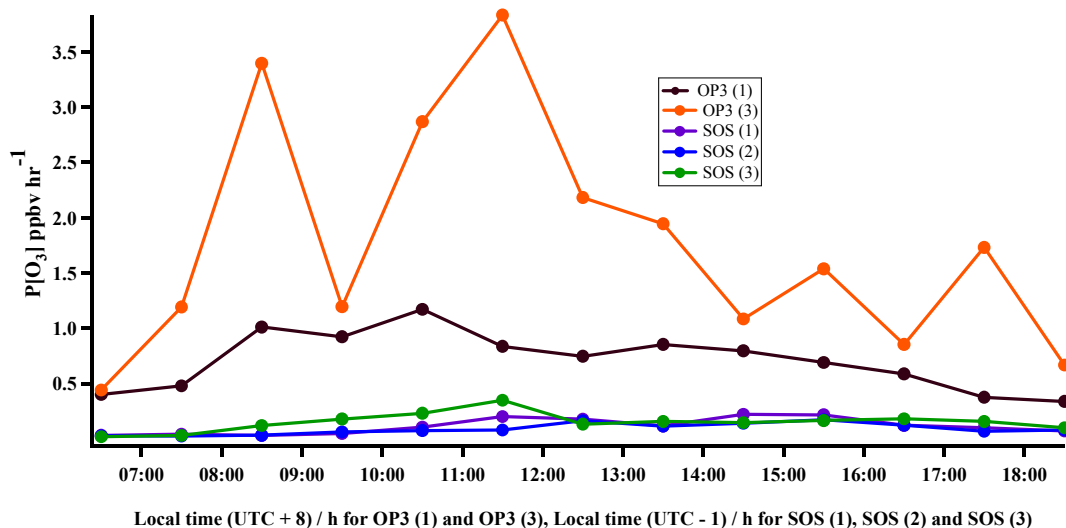


Figure 5.3 - Hourly averaged diurnal data of  $P(O_3)$  between 06:00-19:00 LT; LT (UTC+8) for OP3 (1) (maroon) and OP3 (3) (orange) campaigns at Bukit Atur in the tropical rainforest in Borneo during April-May and June-July 2008, LT (UTC-1) for SOS (1) (purple), SOS (2) (blue) and SOS (3) (green) campaigns at Cape Verde Atmospheric Observatory in the tropical marine boundary layer during February-March, May-June and September 2009. Figure 5.3 shows the maroon and orange data points for the OP3 (1) and OP3 (3) campaigns which has been plotted previously on Figures 3.16 and 3.19 in Chapter 3, respectively. Figure 5.3 shows the purple, blue and green data points for the SOS (1), SOS (2) and SOS (3) campaigns which have been plotted previously on Figure 4.21 (top), Figure 4.21 (middle) and Figure 4.21 (bottom) in Chapter 4, respectively.

During the OP3 (1) and OP3 (3) campaigns, there is a great fluctuation from one season to the other concerning the mean diurnal cycles of  $P(O_3)$ . The cause for this fluctuation in ozone production for the two periods, June-July and April-May, is considered to be the different  $[NO_x]$ .  $[NO_x]$  are at a high values in June-July, compared to the April-May period in the Borneo rainforest (see section 3.2.3.7 in Chapter 3 for the correlation between  $P(O_3)$  and NO). As opposed to the great

fluctuation of ozone production for the Borneo rainforest campaigns, there is a quite similar  $P(O_3)$  profile for the three SOS campaigns. The  $P(O_3)$  profiles displayed a typical diurnal cycle where  $P(O_3)$  is greatly correlated to the NO profile from each of the campaigns (see section 4.5.2 in Chapter 4 for the correlation  $P(O_3)$  with NO). The analysis carried out in Chapter 3 and Chapter 4, for the rainforest campaign and the marine campaign, respectively, points out that at both sites, by comparing  $d\ln P(O_3)/d\ln(HO_2+RO_2)$  and  $d\ln P(O_3)/d\ln(NO)$ , the  $P(O_3)$  sensitivity to NO was calculated to be greater than sensitivity to  $HO_2+RO_2$ .

#### 5.2.2.2 Comparisons of daily ozone losses between campaigns

Table 5.4 provides details of hourly averaged time series of  $L(O_3)$ , maximum, minimum, average and standard deviation for daytime between 06:00-19:00 LT.

$L(O_3) / \text{ppbv hr}^{-1}$				
Experiment	Maximum	Minimum	Average	Standard deviation
OP3 (1) (April-May) 2008	0.34	0.001	0.06	0.07
OP3 (3) (June-July) 2008	0.16	0.001	0.05	0.05
SOS (1) (Feb-March) 2009	0.52	0.01	0.22	0.17
SOS (2) (May-June) 2009	0.93	0.01	0.38	0.30
SOS (3) (September) 2009	0.75	0.01	0.26	0.21

Table 5.4 – Hourly averaged time series of  $L(O_3)$ , maximum, minimum, average and standard deviation for during day time between 06:00-19:00 LT; LT (UTC+8) for OP3 (1) and OP3 (3) campaigns at Bukit Atur in the tropical rainforest in Borneo during April-May and June-July 2008, LT (UTC-1) for SOS (1), SOS (2) and SOS (3) campaigns at Cape Verde Atmospheric Observatory in the tropical marine boundary layer during February-March, May and September 2009. Table 5.4 presents the hourly averaged time series of  $L(O_3)$  for the OP3 (1) and OP3 (3) campaigns which has been shown previously in Table 3.7 in Chapter 3, as well as the average of  $L(O_3)$  for the SOS (1), SOS (2) and SOS (3) campaigns contained previously in Table 4.8 in Chapter 4.

There are great variations from day to day concerning total ozone loss which is achieved by various processes, such as photolysis of ozone, the reaction of ozone with OH, and the reaction of ozone with HO<sub>2</sub>. However, Table 5.4 indicates that the total loss within the marine layer is far greater, with values ranging between 0.01 ppbv hr<sup>-1</sup> and 0.93 ppbv hr<sup>-1</sup>, than the one in the rainforest (it detailed in Section 4.5 in Chapter 4). Total ozone loss varies between 0.001 ppbv hr<sup>-1</sup> and 0.34 ppbv hr<sup>-1</sup> in the Borneo rainforest (see Table 5.4) (it detailed in Section 3.2.3.5 in Chapter 3).

A comparison of the photochemical  $L(O_3)$  between OP3 (1) , OP3 (3) and SOS (1), SOS (2) and SOS (3) campaigns. Figure 5.4 shows the hourly averaged diurnal data of  $L(O_3)$  between 06:00-19:00 LT.

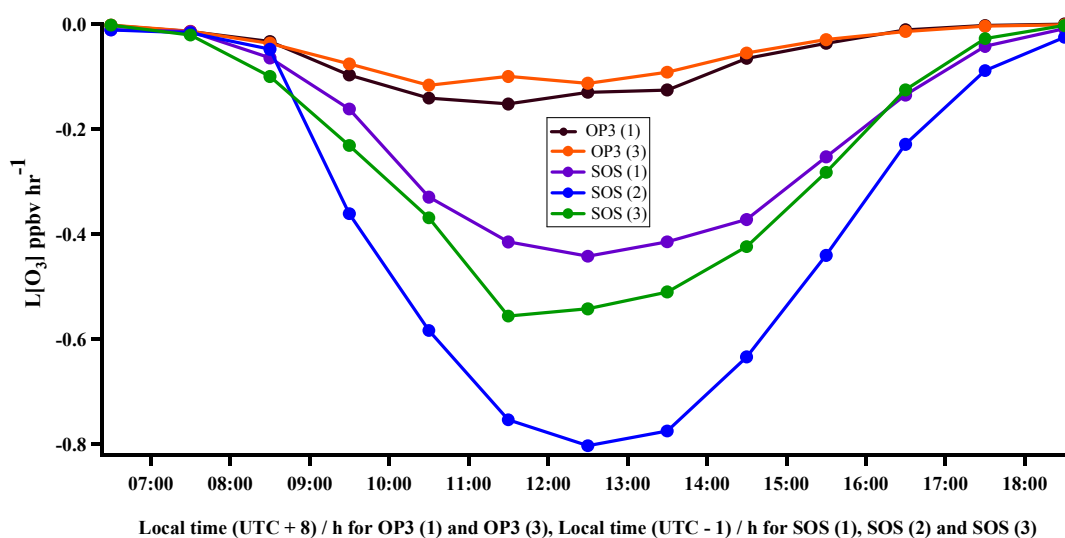


Figure 5.4 - Hourly averaged diurnal data of  $L(O_3)$  on hourly basis for daytime between 06:00-19:00 LT; LT (UTC+8) for OP3 (1) (maroon) and OP3 (3) (orange) campaigns at Bukit Atur in the tropical rainforest in Borneo during April-May and June-July 2008, LT (UTC-1) for SOS (1) (purple), SOS (2) (blue) and SOS (3) (green) campaigns at Cape Verde Atmospheric Observatory in the tropical marine boundary layer during February-March, May-June and September 2009. Figure 5.4 shows the maroon and orange data points for the OP3 (1) and OP3 (3) campaigns which has been plotted previously on Figures 3.16 and 3.19 in Chapter 3, respectively. Figure 5.4 shows the purple, blue and green data points for the SOS (1), SOS (2) and SOS (3) campaigns which have been plotted previously on Figure 4.21 (top), Figure 4.21 (middle) and Figure 4.21 (bottom) in Chapter 4, respectively.

Table 5.5 represents a comparison between the Borneo rainforest (OP3 (1) and OP3 (3)) and Cape Verde marine (SOS (1), SOS (2) and SOS (3)) campaigns in terms of the photochemical total loss rates  $L(O_3)$  and percentage contribution to the overall loss between 06:00-19:00 LT.

<b>Ozone removal (<math>L(O_3)</math>) / ppbv day<sup>-1</sup></b>				
<b>Experiment</b>	<b>Photolysis</b>	<b>HO<sub>2</sub> + O<sub>3</sub></b>	<b>OH + O<sub>3</sub></b>	<b>Sum</b>
OP3 (1) (April-May) 2008	0.73 ± 0.05 (87)	0.07 ± 0.01 (8)	0.04 ± 0.01 (5)	0.84 ± 0.06
OP3 (3) (June-July) 2008	0.57 ± 0.04 (86)	0.05 ± 0.01 (8)	0.04 ± 0.01 (6)	0.66 ± 0.04
SOS (1) (Feb-March) 2009	2.12 ± 0.15 (79)	0.43 ± 0.08 (16)	0.13 ± 0.01 (5)	2.68 ± 0.17
SOS (2) (May-June) 2009	4.14 ± 0.28 (85)	0.48 ± 0.02 (10)	0.26 ± 0.01 (5)	4.88 ± 0.31
SOS (3) (September) 2009	2.85 ± 0.19 (89)	0.20 ± 0.01 (6)	0.16 ± 0.01 (5)	3.21 ± 0.21

Table 5.5 – Hourly averaged time series of  $L(O_3)$ , the photochemical total loss rates  $L(O_3)$  and their percentage contribution in brackets to the overall loss rate during day time between 06:00-19:00 LT; LT (UTC+8) for OP3 (1) and OP3 (3) campaigns at Bukit Atur in the tropical rainforest in Borneo during April-May and June-July 2008, LT (UTC-1) for SOS (1), SOS (2) and SOS (3) campaigns at Cape Verde Atmospheric Observatory in the tropical marine boundary layer during February-March, May-June and September 2009. Table 5.5 also presents the hourly averaged time series of all data for the OP3 (1) and OP3 (3) campaigns which has been shown previously in Table 3.5 in Chapter 3, as well as the all data for the SOS (1), SOS (2) and SOS (3) campaigns contained previously in Table 4.6 in Chapter 4.

The proportions for the contributions to ozone loss chemistry were in the range 79 % to 89 % from ozone photolysis, the range of 5% to 6% from the OH+O<sub>3</sub> reaction and the range of 6% to 16 % from the HO<sub>2</sub>+O<sub>3</sub> reaction (see Table 5.5). At both tropical sites,

the greatest contribution to the loss is associated through ozone photolysis (see Table 5.5). Table 5.5 shows that at both rainforest and marine boundary layer, there is a reduced contribution of OH initiated loss, compared to [OH].

During the SOS (3) campaign, photochemistry was at a maximum and thus, ozone photolysis contributes more to ozone destruction, though [O<sub>3</sub>] is at its lowest values (mean ozone mixing ratio < 22 ppbv, as shown in Table 5.1. The contribution of HO<sub>2</sub>+O<sub>3</sub> is minimised in SOS (3) campaign than in SOS (1) and SOS (2) as shown in Table 5.1.

### 5.2.2.3 $N(O_3)$ variations through the campaigns

Experiment	$N(O_3) / \text{ppbv hr}^{-1}$			
	Maximum	Minimum	Average	Standard deviation
OP3 (1) (April-May) 2008	3.52	0.04	0.68	0.57
OP3 (3) (June-July) 2008	21	0.12	1.80	2.68
SOS (1) (Feb-March) 2009	0.34	-0.44	-0.09	0.16
SOS (2) (May-June) 2009	0.14	-0.79	-0.28	0.28
SOS (3) (September) 2009	0.50	-0.62	-0.11	0.23

Table 5.6 – Hourly averaged time series of  $N(O_3)$ , maximum, minimum, average and standard deviation between 06:00-19:00 LT; LT (UTC+8) for OP3 (1) and OP3 (3) campaigns at Bukit Atur in the tropical rainforest in Borneo during April-May and June-July 2008, LT (UTC-1) for SOS (1), SOS (2) and SOS (3) campaigns at Cape Verde Atmospheric Observatory in the tropical marine boundary layer during February-March, May-June and September 2009. Table 5.6 presents the hourly averaged time series of  $N(O_3)$ , average and standard deviation for the OP3 (1) and OP3 (3) campaigns which has been shown previously in Table 3.6 in Chapter 3, as well as the average and standard deviation of  $L(O_3)$  for the SOS (1), SOS (2) and SOS (3) campaigns contained previously in Table 4.7 in Chapter 4.

The highest net ozone production was observed during OP3 (3) campaign, with an average  $N(O_3)$  of 1.80 ppbv hr<sup>-1</sup>. In contrast, the highest net ozone destruction was obtained during SOS (2) campaign with an average  $N(O_3)$  of -0.28 ppbv hr<sup>-1</sup>. The greatest net ozone loss rate was registered during SOS (2) and the smallest net ozone loss rate was recorded during SOS (1) compared to SOS (2) and SOS (3). A comparison of the two seasons of the Borneo rainforest campaigns shows more ozone production than destruction during the measurement periods, which contrasts with the ozone destruction predominating over the ozone production during the measurements carried out for the three seasons of the Cape Verde marine campaigns. Figure 5.5 shows the hourly averaged diurnal data of  $N(O_3)$  between 06:00-19:00 LT

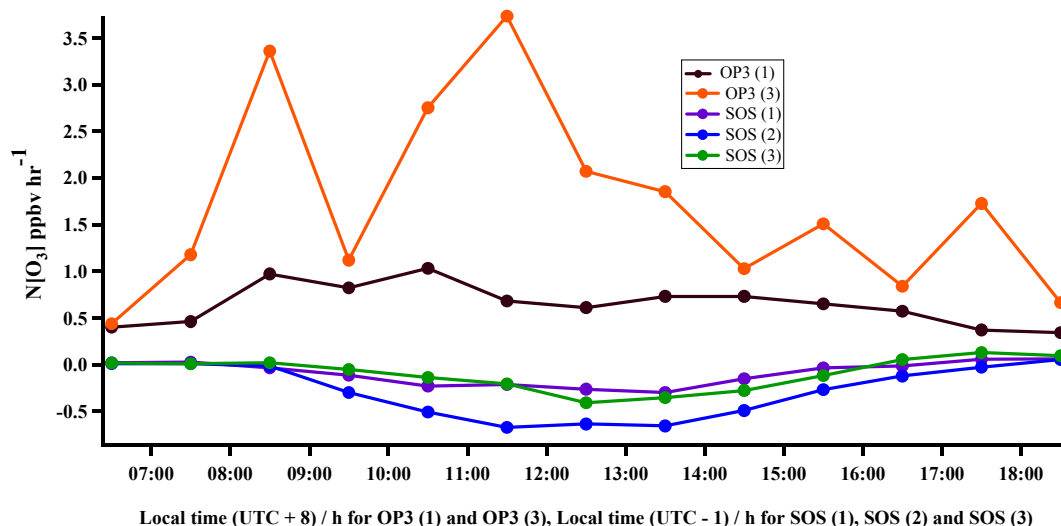


Figure 5.5 - Hourly averaged diurnal data of  $N(O_3)$  between 06:00-19:00 LT; LT (UTC+8) for OP3 (1) (maroon) and OP3 (3) (orange) campaigns at Bukit Atur in the tropical rainforest in Borneo during April-May and June-July 2008, LT (UTC-1) for SOS (1) (purple), SOS (2) (blue) and SOS (3) (green) campaigns at Cape Verde Atmospheric Observatory in the tropical marine boundary layer during February-March, May-June and September 2009. Figure 5.5 shows the maroon and orange data points for the OP3 (1) and OP3 (3) campaigns which has been plotted previously on Figures 3.16 and 3.19 in Chapter 3, respectively. Figure 5.5 shows the purple, blue and green data points for the SOS (1), SOS (2) and SOS (3) campaigns which have been plotted previously on Figure 4.21 (top), Figure 4.21 (middle) and Figure 4.21 (bottom) in Chapter 4, respectively.

During the Cape Verde marine campaigns (SOS (1), SOS (2) and SOS (3)), the  $N(\text{O}_3)$  profiles displayed diurnal cycles with negative values for  $N(\text{O}_3)$  and the net ozone destruction had its highest value at midday with the solar maximum. During the Borneo rainforest (OP3 (1) and OP3 (3)) campaigns, the  $N(\text{O}_3)$  profiles displayed diurnal cycles, but with positive values for  $N(\text{O}_3)$ .  $N(\text{O}_3)$  having a peak values during early morning and another one at midday. Within the Cape Verde marine campaigns, the balance between net ozone production and destruction is equilibrated in the conditions of the solar maximum, while  $N(\text{O}_3)$  values reach nearly zero before 08:30 and after 17:30 during the day time. This feature differs for the Borneo rainforest campaigns, where net ozone production during OP3 (1) and OP3 (3) campaigns was observed for the two different peaks. The nearly zero  $N(\text{O}_3)$  (but positive values) for Borneo rainforest campaigns are actually as large in magnitude as the negative values for Cape Verde marine campaigns (see Figure 5.5). The  $N(\text{O}_3)$  profiles displayed broad diurnal cycles as net ozone destruction during May-June in the northeast mid Atlantic tropical marine layer, as opposed to the net ozone production during June-July in southeast Asian tropical rainforest.

#### 5.2.2.4 Ozone photochemistry variations

What do the variations and similarities in  $[\text{HO}_2+\text{RO}_2]$  and ozone photochemistry between sites tell us? This section presents the measurements of peroxy radicals,  $j(\text{O}^1\text{D})$  and other related trace species with the purpose of establishing the interconnections between them and comparison of the role of photochemistry in the control of ozone for each season during the rainforest and marine boundary layer campaigns. The Borneo rainforest and the Cape Verde marine campaigns are opposed from the point of view of ozone mixing ratios. The lowest average ozone mixing ratios for the

Borneo rainforest campaigns, with an average of 11 ppbv and 7 ppbv and the lowest variations throughout OP3 (1) and OP3 (3), respectively. The Cape Verde marine campaigns displayed the highest ozone mixing ratios ( $> 30$  ppbv) during both February-March and May-June periods, whereas September had the lowest value ( $< 22$  ppbv), with the lowest variations from all the campaigns. OP3 experienced the highest ozone production during June-July, and a low production during April-May. The highest ozone production rate was calculated with the Borneo rainforest for the month of July. As opposed to these observations, SOS (1) experienced the lowest overall ozone destruction and SOS (2) experienced the highest overall ozone destruction, while the values of overall ozone destruction for SOS (3) are situated between SOS (1) and SOS (2). Cape Verde marine experienced reduced ozone production during February-March and in September, while the lowest ozone production period is between May-June.

Ozone deposition rates are partly controlled by stomatal uptake over a plant canopy. However, stomatal uptake only accounts for ca 40-60% of the total deposition on average, while the non stomatal contribution is not constant (Fowler *et al.*, 2001; Coyle *et al.*, 2009; Hogg *et al.*, 2007). Ozone deposition fluxes to a forest site, as well as other vegetated surfaces, are particularly controlled by the physiological activity and associated gas exchange of the vegetation, with solar radiation, air humidity, air temperature, and soil moisture as the primary controlling variables as shown in Figure 5.6. In addition, there are other significant processes to stomatal maintenance of gas exchange that control the magnitude and variation of the ozone deposition ability of forests (Altimir *et al.*, 2006; Cieslik, 2004; Dorsey *et al.*, 2004; Goldstein *et al.*, 2004; Hogg *et al.*, 2007; Lamaud *et al.*, 2002; Tuovinen, 2000; Tuovinen *et al.*, 2008; Zhang

*et al.*, 2002). Measured ozone is lower in the Borneo rainforest (OP3 (1) and OP3 (3)) campaigns whilst greater values of  $N(O_3)$  obtained; by considering above features of ozone deposition at Bukit Atur in the tropical rainforest in Borneo site, it might be concluded that ozone deposition fluxes are significant.

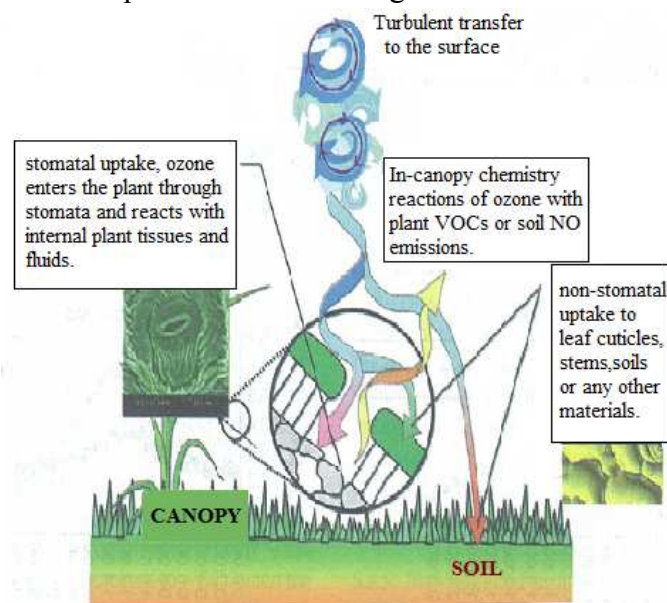


Figure 5.6 - The sinks for ozone at terrestrial surfaces and processes regulating the exchange from Fowler *et al.*, (2009).

The Cape Verde marine campaigns show a rapid increase in  $O_3$  production (average gradient of 1.13 for the three campaigns) with increasing  $NO$ , unlike the Borneo rainforest campaigns, where the increase in ozone production is slower (average gradient of 0.97 for the two campaigns) as  $NO$  increased. Not only is the increased gradient of ozone production to varying  $NO$  at Cape Verde marine larger than the one from the Borneo rainforest campaigns, but it is also larger when compared with other marine campaigns, as shown in Tables 4.11 and 4.12 in Chapter 4 in section 4.5.2

Ozone production is the net consequence of photochemistry within the tropical Borneo rainforest layer, as opposed to the ozone destruction as an action of photochemistry within the remote Cape Verde marine boundary layer. The above result of this thesis is

also supported by Hewitt *et al.*, (2009); Pike *et al.*, (2010); Pugh *et al.*, (2010) for the Borneo rainforest campaigns (OP3 (1) and OP3 (3)), who suggested that increasing [NO<sub>x</sub>] will lead to increased ozone. Read *et al.*, (2008); Lee *et al.*, (2009); Mahajan *et al.*, (2010) explained for the Cape Verde marine site, the net ozone destruction in the Cape Verde marine boundary layer is balanced by entrainment of ozone into the marine boundary layer from the lower free troposphere.

### 5.3 Conclusions

The sum of peroxy radicals was measured during April-May 2008 (from 14<sup>th</sup> April to 2<sup>nd</sup> May 2008) and June-July 2008 (from 23<sup>rd</sup> June to 22<sup>nd</sup> July 2008) for the tropical Borneo rainforest and February-March 2009 (from 27<sup>th</sup> February to 14<sup>th</sup> March), May-June 2009 (from 20<sup>th</sup> May to 2<sup>nd</sup> June) and August-September 2009 (From 30<sup>th</sup> August to 13<sup>th</sup> September 2009) for the Cape Verde marine boundary layer.

Net ozone production rates have been calculated that show that overall the conditions encountered during this work at the rainforest were ozone production and marine were ozone destruction, respectively. The ozone production rate in the southeast Asian rainforest boundary is strongly dependent on [NO] having a linear sensitivity ( $d\ln(P(O_3))/d\ln(NO) = 0.97$  averaged from two different seasonal data sets). The ozone production rate in the northeast Atlantic marine boundary is even more strongly dependent on [NO] having a linear sensitivity ( $d\ln(P(O_3))/d\ln(NO) = 1.13$  averaged from three different seasonal data sets). Hence, the results imply that the  $P(O_3)$  will be strongly sensitive in the Borneo rainforest and the Cape Verde marine boundary layer to changes in [NO].

# Chapter 6

## Conclusions and future work

The focus of this chapter is to bring together the important conclusions from the previous five chapters and to give an overall perspective on the results. Five field campaign results have been described within this thesis. Although detailed conclusions on the work may be found within the relevant chapters; some more general conclusions are brought together here.

Chapter 1 contains an introduction of tropospheric photochemistry, the function of peroxy radicals in ozone photochemistry, the chemical processes in the tropical rainforest and the marine boundary layer together with a summary of previous measurement campaigns.

Chapter 2 outlines the different techniques employed for peroxy radicals measurements in the atmosphere. The chemical amplification technology for the PERCA instrument (V3.5) has a detailed discussion within this chapter together with the function of each PERCA's sub-systems (V3.5) and deployment in the field sites. The calibration of chain length and NO<sub>2</sub> sensitivity undertaken in field sites, as well as the experimental and analytical work for calibrations are included here. Chapter 2 also shows the advantages of the dual-channel PERCA (V3.5) as opposed to the single-channel PERCA (V3.5) instrument. The analytical work for data analysis from the raw signals into [HO<sub>2</sub>+RO<sub>2</sub>], as well as the error analysis is demonstrated.

Chapter 3 provides an overview of the “Oxidant and particle photochemical processes above a south-east Asian tropical rain forest” campaigns OP3 (1) (during April-May 2008-ground based measurements only) and OP3 (3) (during June-July 2008-both ground and aircraft measurements) at Bukit Atur Global Atmospheric Watch station (4° 58' 59" N, 117° 50' 39" E). A single channel PERCA (V3.5) instrument was deployed in the tropical rainforest boundary layer in Borneo. There were higher mean concentrations of isoprene and methacrolein detected in OP3 (3) compared to OP3 (1) which could be due to the photochemical processing of isoprene causing its oxidation products to increase. Additional [NO], [NO<sub>2</sub>] were detected and this is considered to be related to soil emissions, while increasing [NO<sub>x</sub>] will determine an increase in the rate of ozone production, and increasing [isoprene] will hold back the rate of ozone production.

Peroxy radical production has other sources than ozone photolysis: the presence of the biogenic species isoprene influences [HO<sub>2</sub>+RO<sub>2</sub>]. The greatest sensitivity to isoprene has been observed for the tropical rainforest boundary layer in Borneo for peroxy radical production in the morning between April-May and in the afternoon between June-July. Another peroxy radical production source considered in Chapter 3 was the photolysis of species such as HCHO and HONO (see Section 3.3.1.4 in Chapter 3). In the rainforest, the loss of peroxy radical is dominated by the self-reaction in OP3 (1) and by the reaction of OH with NO<sub>2</sub> in OP3 (3) owing to the [NO<sub>x</sub>] in OP3 (3) exceeding that in OP3 (1).

Chapter 4 focuses on calculating the fast photochemical budget of the oxidative chemistry at the Cape Verde Atmospheric Observatory in the tropical marine boundary

layer during the three campaigns: the Seasonal Oxidant Study campaigns SOS (1) (February-March 2009), SOS (2) (May-June 2009) and SOS (3) (September 2009). The Cape Verde Atmospheric Observatory is situated at Calhau Sao Vicente (16° 51' 49" N, 24° 52' 02" W). The dual channel PERCA (V3.5) instrument took measurements in the marine boundary layer at Cape Verde, where the Atmospheric Observatory is not influenced by coastal factors, but receives air masses within the marine troposphere from NE and therefore only experiences rare pollution from local activities. Chapter 4 presents how the control of radical process by ozone photolysis and radical self-and cross- reactions through the linear interaction between  $\sqrt{j(O^1D)}$  and  $[HO_2+RO_2]$  under the very clean condition during day time (06:00-19:00 LT (UTC-1)) from SOS (1), SOS (2) and SOS (3) campaigns.

The photolysis loss of ozone at Cape Verde Atmospheric Observatory in the tropical marine boundary layer during February-March, May-June and September, respectively, were calculated at values of 79 %, 85 % and 89 %, respectively. This proves that photolysis dominates the ozone loss process in the remote marine sub-tropical Atlantic boundary layer for the three different seasons.

To assess the possible importance of halogen chemistry on ozone production or loss Chapter 4 describe a summary of IO and BrO measurements from the marine field campaigns carried out before. The exact ozone destruction in the marine boundary layer can be determined through kinetic studies and through photostationary steady state of *in-situ* net ozone loss rate with and without halogen oxide chemistry. In this study, 51% of the daily ozone loss rate was calculated in the presence of the 1.12 and 2.41 pptv of IO and BrO, respectively.

Data analysis in Chapter 4 demonstrates that not only ozone formation sensitivity to NO at Cape Verde exceeds the ones at Mace Head, Weybourne and Cape Grim, but also the lowest values of ozone compensation point were derived for Cape Verde site. This chapter also includes an analysis of the production and loss of peroxy radicals during three SOSs campaigns and it points out that either peroxy radical production from ozone photochemistry has been overestimated or the peroxy radical losses have been underestimated.

Chapter 5 summarizes the role of the rainforest and the marine in the atmosphere. This chapter provides a comparison between the peroxy radical and ozone photochemistry between the South eastern Asian tropical rainforest and the North eastern mid tropical Atlantic boundary layer site. Different analyses were undertaken for exploring the similarities and the differences between the two sites and seasons.

The peroxy radical values from both rainforest campaigns proved to be higher than the night-time  $[\text{HO}_2+\text{RO}_2]$  of the three marine campaigns. This indicates that the oxidation process rates are particularly higher in the tropical rainforest as opposed to the tropical marine boundary layer.

The lowest ozone mixing ratios are observed in the conditions of the highest mean NO<sub>x</sub> mixing ratios in both the rainforest and marine campaign. Ozone photolysis appears to contribute to ozone loss chemistry in proportions varying between 79 % to 89 %, while OH+O<sub>3</sub> reaction contribute in a proportion ranging from 5 % to 6 % and the HO<sub>2</sub>+O<sub>3</sub> reaction in proportions between 6 % to 16 %; ozone photolysis is the major factor influencing the loss as a result of the calculations carried out at both

tropical sites. Table 5.5 in Chapter 5 shows the reduced contribution of OH initiated loss as opposed to the existing [OH] from both the rainforest and the marine boundary layer.

## 6.1 Peroxy radical measurements

WHO, (2005) stated “Clean air is considered to be a basic requirement of human health and well-being. However, air pollution continues to pose a significant threat to health worldwide”.

Monks *et al.*, (2003a) explained that peroxy radicals are intermediates between the hydroxyl (OH) radical and ozone formation/destruction, and due to this status as intermediates, their measurement is essential for understanding the processes that establish the composition of the atmosphere. Peroxy radicals are perfect targets for the validation of models of atmospheric chemistry owing to their ability to be diagnostics of in-situ chemistry because they have a short lifetime. Well defined measurements are essential for calculating fast processes directly and this may be the key factor for past or future predictions of the effects of the changing composition of the atmosphere, as well as climate change.

A range of techniques available for measuring peroxy radicals within the atmosphere, are detailed in Chapter 2. These techniques depend on a range of techniques from chemical amplification to chemiluminescence, PerCIMS is based on a different chemical amplification scheme and mass spectrometry, and FAGE is based on (for HO<sub>2</sub> measurements) chemical conversion to OH and then laser induced fluorescence of the resultant OH radicals. This brings an advantage for the accuracy of peroxy radical

measurements (FAGE measures OH and HO<sub>2</sub>), by carrying out controlled inter-comparisons; the determination of biases can be undertaken.

Owing to the fact that the measurement of the peroxy radicals requires these radicals to be converted into other species that can be more easily measured, the above employed techniques present a disadvantage through their indirect character. However, there is a direct technique, MIESR, but Chapter 2 outlines the reasons for the difficulty of employing it during field applications. A potential area of research could be developed by direct techniques, especially due to their ability of removing the errors of the indirect techniques. (PERCA (V3.5) has a typical of uncertainty 36% for non-humidity corrected single channel instrument as calculated in section 2.6 in Chapter 2.

The methods for RO<sub>2</sub> and HO<sub>2</sub> measurements are established by the application of two channels to the LIF instrument: one for OH (Holland *et al.*, 2003; Geyer *et al.*, 2003) and the second called ROxLIF (Fuchs *et al.*, 2008). In ROxLIF Radical detection is achieved through its chemical conversion and the applied LIF is operated in to chemical modes: ROx and HOx. The laser-induced fluorescence (LIF) has high sensitivity for the detection of the conversion of ROx radicals (HO<sub>2</sub> and RO<sub>2</sub>) to OH. The photooxidation of methane in tropospheric conditions is responsible for the production of HO<sub>2</sub> and CH<sub>3</sub>O<sub>2</sub> radicals. The accuracy of ROxLIF measurements is reduced due to the calibration accuracy, which is limited to 20% (2σ), while HO<sub>2</sub> and RO<sub>2</sub> have a detection limit of 0.1 pptv with a 1 min time resolution (Fuchs *et al.*, (2008)).

Hofzumahaus *et al.*, (2009) noted that two different techniques of ROxLIF and MIESR have been deployed during the atmospheric simulation chamber SAPHIR campaign in Julich, Germany for measuring hydroperoxy radical ( $\text{HO}_2$ ) and organic peroxy radical ( $\text{RO}_2$ ) concentrations. The intercomparison employed radical concentration values of 16 to 100 pptv for  $\text{HO}_2$  and 12 to 45 pptv for  $\text{RO}_2$ . Making a contrast between ROxLIF and MIESR measurements leads to the conclusion that there is good agreement between these techniques within their experimental uncertainties. No significant offsets are noticed when there is a linear regression to the combined data set of  $1.02 \pm 0.13$  ( $1\sigma$ ) for  $\text{RO}_2$  and  $0.98 \pm 0.08$  ( $1\sigma$ ) for  $\text{HO}_2$ . This result validates the ROxLIF calibration and points out that it is reliable and good accuracy for measurements of atmospheric peroxy radical concentrations.

Both PERCA (V3.5) and FAGE instruments were deployed together for OP3 (1) and OP3 (3) campaigns at Bukit Atur in the tropical rainforest in Borneo during April-May and June-July 2008 and for SOS (1), SOS (2) and SOS (3) field campaigns at Cape Verde Atmospheric Observatory in the tropical marine boundary layer during February-March, May-June and September 2009. PERCA (V3.5) necessarily measures the  $\text{HO}_2 + \text{RO}_2$  whereas  $\text{HO}_2$  measurements taken by FAGE provide the  $\text{HO}_2$  mixing ratio directly. The FAGE  $\text{HO}_2$  data are compared with PERCA (V3.5)'s  $\text{HO}_2 + \text{RO}_2$  to get the organic peroxy radical concentration and work out the further analysis during these field campaigns for this thesis work. Underlying the fact that all measurement techniques have their advantages and disadvantages, none can yet obtain the speciation of organic peroxy radicals, except the limited speciation of MIESR; but the latter is an inconvenient technique through practical drawbacks.

## 6.2 Global picture of ozone photochemistry in both of rainforest and marine sites

Ozone photochemistry from site to site showed large variations, from the dominant net ozone-destroying conditions at Cape Verde as described in section 4.5 in Chapter 4, to high values of ozone production at rainforest, particularly in the July as described in section 3.2.3.5 in Chapter 3. There is a greater sensitivity of the ozone production to NO present at Cape Verde than at the rainforest sites. Therefore, a sharp increase in ozone production could be induced by an increase in NO<sub>x</sub>. Owing to the fact that the ozone production sensitivity to NO<sub>x</sub> or VOCs differs from one site to the other, implies that it is quite complicated to anticipate ozone production episodes as they depend on pollution levels, as well as sensitivity to NO<sub>x</sub>.

To explore the ozone photochemistry in the Borneo rainforest boundary layer, Hewitt *et al.*, (2009) considered day time (10:00-16:00 LT (UTC+8)) measurements of the VOC and NO<sub>x</sub> emissions from Borneo rainforest and oil palm plantation. The oil palm plants influence exclusively the rise in VOC emission rates. The rise in [NO<sub>x</sub>] is also determined by the increased fossil fuel consumption, accompanied by industrialization, throughout the region. Moreover, increased mechanization, together with fossil fuel emissions and applying fertilizer increases [NO<sub>x</sub>] in the plantation landscape. Industrialization and economic development not only bring an increase in NO<sub>x</sub> emissions, but an increase of ozone in the region too.

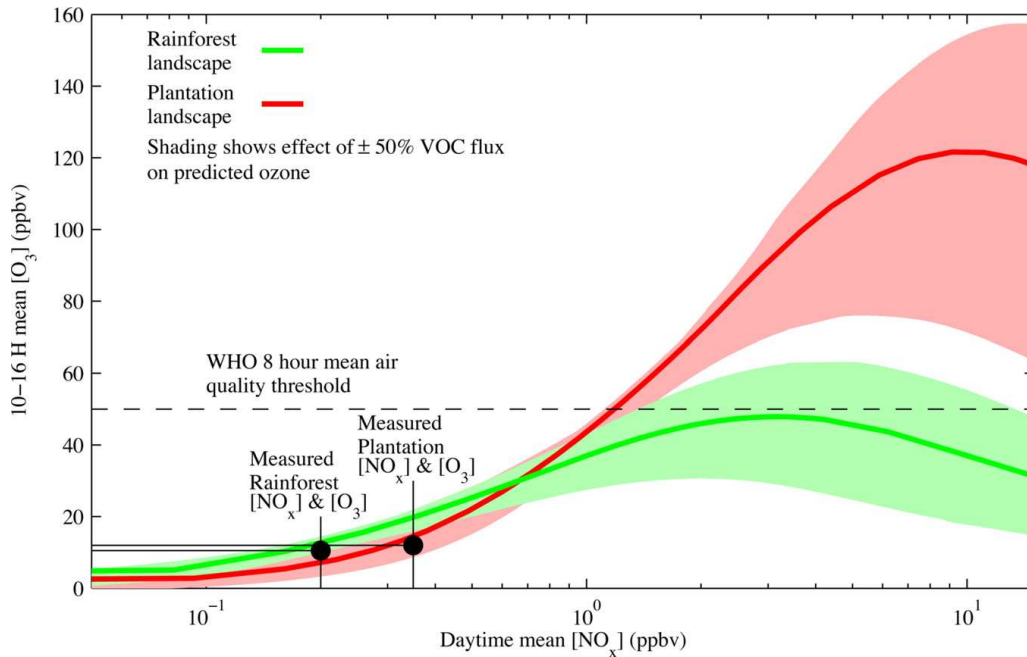


Figure 6.1 - Daytime (10.00–16.00 LT (UTC+8)), sensitivity of average  $[O_3]$  to  $[NO_x]$  in the boundary layer, for the rainforest and oil palm landscape measurements for isoprene and monoterpene emission rates, as computed by CiTTYCAT. The solid lines are not always in the shaded region due to the different point of infection of each model, though they have an identical shape. Measured concentrations of  $NO_x$  and  $O_3$  in the rainforest and plantation are noted by black circle, from Hewitt *et al.*, (2009).

The CiTTYCAT model, used at ground level at the Bukit Atur GAW location and oil palm landscapes, was run out in stationary box mode by Pugh *et al.*, (2010) as described in section 3.4 in Chapter 3. The model facilitates the nonlinearity in the chemistry to be apparent. The model predicts  $[O_3]$  in the rainforest not exceeding 50 ppbv (apart from advection of ozone and its precursors from outside the rainforest landscape), irrespective of  $[NO_x]$ . In contrast the  $[O_3]$  can exceed 100 ppbv in the oil palm landscape when  $[NO_x]$  reaches 3-5 ppbv. Hewitt *et al.*, (2009) noted that large-scale palm oil production can be reduce a from developing serious effects on the regional air quality by controlling nitrogen emissions at both the local (plantation) and regional scales.

To explore the ozone photochemistry in the Cape Verde marine boundary layer, Read *et al.*, (2008) undertook a comparison between the monthly averaged daytime (09:00–17:00 LT (UTC-1)) [O<sub>3</sub>] at Cape Verde from October 2006 and October 2007 and simulations through the global tropospheric chemistry transport model GEOS-CHEM. Monthly averaged data regarding BrO and IO, H<sub>2</sub>O, CO, CH<sub>4</sub>, CH<sub>3</sub>CHO, NO and temperature, calculated at Cape Verde Observatory were employed for the box model verification.

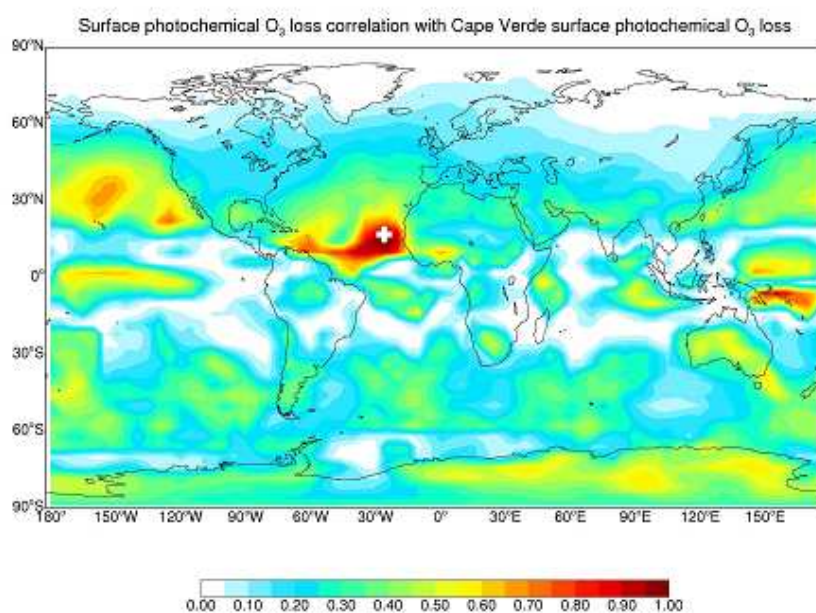


Figure 6.2 - Presents the correlation coefficient between the modelled yearly mean photochemical O<sub>3</sub> loss from Cape Verde and the grid box photochemical O<sub>3</sub> loss from other sites, from Read *et al.*, (2008).

Surface photochemical loss of ozone in neighbouring grids may well correspond to the tropical North Atlantic and parts of the Pacific as shown in Figure 6.2.

### 6.3 Summary of peroxy radical concentrations and trends in this thesis

This thesis presents results from peroxy-radical measurements at various campaigns, obtained by the author, the Leicester PERCA (V3.5) group and by many other peroxy-radical research groups around the world.

Peroxy radical data collected at Bukit Atur in the tropical rainforest boundary layer in Borneo in 2008 during OP3 campaigns and at Cape Verde Atmospheric Observatory in the tropical marine boundary layer in 2009 during SOS campaigns have been analysed and compared to other chemical and meteorological measurements.

At both the Borneo rainforest and the Cape Verde marine layer the calculated net ozone production rates indicate that the overall conditions dominating these sites were ozone production for the Borneo rainforest and ozone destruction for the Cape Verde marine layer. All summer campaigns were characterized by the classic, bell-shaped peroxy radical diurnal cycle with high midday values.

In conclusion, there is much more available to be discovered. Atmospheric science shall remain a limitless exciting research area and will be for a long time to come.

# Appendix A

## Postgraduate Record

### A.1 Induction/Training Sessions Attended

1) Applications of 'Endnote'	19 <sup>th</sup> October 2007
2) Information skills for chemists	8 <sup>th</sup> November 2006
3) NMR techniques (1D NMR Spectroscopy)	15 <sup>th</sup> November 2006
4) NMR techniques (2D NMR Spectroscopy)	14 <sup>th</sup> February 2007
5) NMR techniques (The nOe effect)	14 <sup>th</sup> February 2007
6) Reading and note making skills	28 <sup>th</sup> February 2007
7) Study skills (Project managing PhD)	21 <sup>st</sup> February 2007
8) Study skills (More efficient reading and note taking)	28 <sup>th</sup> February 2007
9) Writing skills (part 1)	17 <sup>th</sup> January 2007
10) Writing skills (part 2)	24 <sup>th</sup> January 2007
11) Starting your research	11 <sup>th</sup> October 2006
12) Advanced Safety and Departmental procedures	10 <sup>th</sup> October 2006
13) Introduction to techniques	9 <sup>th</sup> October 2006
14) Demonstrating/small group teaching (part 2)	25 <sup>th</sup> October 2006
15) Demonstrating/small group teaching (part 1)	18 <sup>th</sup> October 2006
16) Departmental procedures and fire safety	1 <sup>st</sup> November 2006
17) Faculty induction	5 <sup>th</sup> October 2006
18) Graduate school induction	4 <sup>th</sup> October 2006
19) Departmental induction	3 <sup>rd</sup> October 2006

## A.2. Academic Courses

### University of Leicester Lecture Courses

Atmospheric Chemistry – CH4008

Convenor: Prof. Paul Monks

Summary: Exploration of fundamental physical and chemical processes that control atmospheric composition

Assessment: Written examination

Advanced Molecular Spectroscopy – CH3035

Convenor: Dr. Jonny Woodward

Summary: The module aims to build on the concepts of spectroscopy and will deal in particular with advanced concepts and techniques in spectroscopy, including the use of lasers.

Assessment: Written examination

1<sup>st</sup> year research proposal presentation 26<sup>th</sup> March 2007

1<sup>st</sup> year research committee meeting 24<sup>th</sup> October 2007

## A.3. Departmental Seminars

1. The Atmospheric Chemistry Experiment (ACE) Prof Peter Bernath (University of York) 7<sup>th</sup> February 2007.
2. Chemistry and Giant Thunderstorms Prof Geraint Vaughan (University of Manchester) 7<sup>th</sup> March 2007.
3. Solar variability and climate change Prof Joanna Haigh (College of London) 28<sup>th</sup> March 2007

4. DOAS UV/vis Balloon studies of atmospheric radicals with a focus on halogen oxides and nitrogen oxides (Space research centre, University of Leicester)
5. On-line sensor systems to capture the chemical signature of brain injury Dr. Martyn G Boutelle (Imperial College, London) 18th February 2008.
6. Synchrotron Radiation Studies of Processes near Electrode Surfaces Prof. Trevor Rayment (University of Birmingham) 10<sup>th</sup> December 2007.
7. Laser Studies of Photo fragmentation Dynamics Dr. Grant Richie, University of Oxford 26<sup>th</sup> November 2007
8. Exploring the Dynamics of Single Aerosol Particles Dr. Jonathan Reid, University of Bristol 12<sup>th</sup> November 2007.

## A.4. Summer school attended

NCAS summer school-2007 - Isle of Arran - 11 day programme.

## A.5. Conferences and meetings

### A.5.1 Conferences

1. First European Science Foundation (ESF) conference 2007 - Sweden: poster  
*“Tropospheric Organic Chemistry Experiment”*
2. International Global Atmospheric Chemistry (IGAC) conference 2008- Annecy, France: Poster *“Ozone photochemistry in the tropical South East rainforest in April and July 2008.”*
3. National Centre for Atmospheric Science (NCAS) conferences 2008- Bristol  
Poster: *“Peroxy radical concentration in the tropical troposphere over the South East rainforest in April and July 2008”*

4. Surface Ozone Lower Atmosphere Study (SOLAS) conferences 2009 -  
Barcelona, Spain. Poster: “*Seasonal comparison of the peroxy radical in the eastern tropical Atlantic marine boundary layer at Cape Verde.*”

### A.5.2 Meetings

1. 14/12/2007- Notes on the OP3 team meeting at the University of Manchester
2. 23/04/2008 - OP3 Preliminary Results Meeting – Danum Valley, rainforest.  
Talk entitled “*PERCA measurement in rainforest*”
3. 03/05/2008 - OP3 Preliminary Results Meeting – Danum Valley, rainforest.  
Talk entitled “*PERCA measurement in rainforest*”
4. 03/07/2008 - OP3 Preliminary Results Meeting – Danum Valley, rainforest.  
Talk entitled “*PERCA measurement in rainforest*”
5. 13/07/2008 - OP3 Preliminary Results Meeting – Danum Valley, rainforest.  
Talk entitled “*PERCA measurement in rainforest*”
6. 23/07/2008 - OP3 Preliminary Results Meeting – Danum Valley, rainforest.  
Talk entitled “*PERCA measurement in rainforest*”
7. 20/08/2008 - Cape Verde SOLAS preparation meeting –University of Leeds
8. 27/11/2008 -28/11/2008-OP3 Science Meeting at the University of Leeds  
Talk entitled “*PERCA measurement in rainforest*”
9. 30/03/2009 - Photo-oxidants sub-group meeting at the University of York  
Talk entitled “*PERCA -  $\Sigma RO_2 + HO_2$* ”
10. 07/04/2009 - SOS 1 preliminary results and planning for SOS 2 meeting  
University of York: Talk entitled “peroxy radical measurement –SOS 1”
11. 05/05/2009 - planning for SOS 2 meeting  
University of York: Talk entitled “peroxy radical measurement –SOS 1”

12. 24/09/2008 - SOS 2 preliminary results and planning for SOS 3 meeting  
University of York: Talk entitled “peroxy radical measurement –SOS 2”
13. 05/10/2009 - SOS 3 preliminary results and planning for SOS 4 meeting  
University of Leeds: Talk entitled “peroxy radical measurement –SOS 3”

## A.6. Presentations

1. 26<sup>th</sup> January 2007- Molecular Properties group meeting –topic presentation- Is the Ozone layer recovery?
2. 5<sup>th</sup> June 2007 - Molecular Properties group meeting-topic presentation- Presentation about the PERCA measurement on LAMP campaign at the Space Research Centre, University of Leicester in Leicester.
4. 10<sup>th</sup> June 2007- First year research work presentation, Chemistry Department, University of Leicester in Leicester.

## A.7 Field campaigns

1. OP3-Danum-08 Phase 1 (Oxidant and Particle Photochemical Processes above a South-East Asian tropical rain forest. From the 7<sup>th</sup> April to 4<sup>th</sup> May 2008 at GAW station, Danum Valley Field Centre in Sabah, Malaysian Borneo.
2. OP3-Danum-08 Phase III (Oxidant and Particle Photochemical Processes above a South-East Asian tropical rain forest. From the 23<sup>rd</sup> June to 23<sup>rd</sup> July 2008 at GAW station, Danum Valley Field Centre in Sabah, Malaysian Borneo.
3. (SOS 1) Seasonal Oxidant Study-1. From 27<sup>th</sup> February to 14<sup>th</sup> March 2009 at Northeast Atlantic Marine boundary layer, Cape Verde Atmospheric Observatory

4. (SOS 2) Seasonal Oxidant Study-2. From 20<sup>th</sup> May to 02<sup>nd</sup> June 2009 Northeast Atlantic Marine boundary layer, at Cape Verde Atmospheric Observatory
5. (SOS 3) Seasonal Oxidant Study-3. From 30<sup>th</sup> August to 13<sup>th</sup> September 2009 Northeast Atlantic Marine boundary layer, at Cape Verde Atmospheric Observatory

## A.8 Publications

Archibald, A. T., Levine, J. G., Abraham, N. L., Cooke, M. C., Edwards, P. M., Heard, D. E., Jenkin, M. E., Karunaharan, A., Pike, R. C., Monks, P. S., Shallcross, D. E., Telford, P. J., Whalley, L. K., and Pyle, J. A.: Impacts of HO<sub>x</sub> regeneration and recycling in the oxidation of isoprene: Consequences for the composition of past, present and future atmospheres *Geophys. Res. Lett.*, 38, L05804, 2011.

Carpenter, L. J., Fleming, Z. L., Read, K. A., Lee, J. D., Moller, S. J., Hopkins, J. R., Purvis, R. M., Lewis, A. C., Müller, K., Heinold, B., Herrmann, H., Wadinga Fomba, K., Van Pinxteren, D., Müller, C., Tegen, I., Wiedensohler, A., Müller, T., Niedermeier, N., Achterberg, E. P., Patey, M. D., Kozlova, E. A., Heimann, M., Heard, D. E., Plane, J. M. C., Mahajan, A., Oetjen, H., Ingham, T., Stone, D., Whalley, L. K., Evans, M. J., Pilling, M. J., Leigh, R. J., Monks, P. S., Karunaharan, A., Vaughan, S., Arnold, S. R., Tschritter, J., Pöhler, D., Frieß, U., Holla, R., Mendes, L. M., Lopez, H., Faria, B., Manning, A. J., and Wallace, D.W.R.: Seasonal characteristics of tropical marine boundary layer air measured at the Cape Verde Atmospheric Observatory., *J. Atmos. Chem.*, 67, 87-140, 2010.

Hewitt, C. N., Lee, J. D., MacKenzie, A. R., Barkley, M. P., Carslaw, N., Carver, G. D., Chappell, N. A., Coe, H., Collier, C., Commane, R., Davies, F., Davison, B., DiCarlo, P., Di Marco, C. F., Dorsey, J. R., Edwards, P. M., Evans, M. J., Fowler, D., Furneaux, K. L., Gallagher, M., Guenther, A., Heard, D. E., Helfter, C., Hopkins, J., Ingham, T., Irwin, M., Jones, C., Karunaharan, A., Langford, B., Lewis, A. C., Lim, S. F., MacDonald, S. M., Mahajan, A. S., Malpass, S., McFiggans, G., Mills, G., Misztal, P., Moller, S., Monks, P. S., Nemitz, E., Nicolas-Perea, V., Oetjen, H., Oram, D. E., Palmer, P. I., Phillips, G. J., Pike, R., Plane, J. M. C., Pugh, T., Pyle, J. A., Reeves, C. E., Robinson, N. H., Stewart, D., Stone, D., Whalley, L. K., and Yin, X.: Overview: oxidant and particle photochemical processes above a south-east Asian tropical rainforest (the OP3 project): introduction, rationale, location characteristics and tools, *Atmos. Chem. Phys.*, 10, 169-199, 2010

MacKenzie, A. R., Langford, B., Pugh, T. A. M., Robinson, N., Misztal, P. K., Heard, D. E., Lee, J. D., Lewis, A. C., Jones, C. E., Hopkins, J. R., Philips, G., Monks, P. S., Karunaharan, A., Hornsby, K. E., Nicolas-Perea, V., Coe, H., Gabey, A. M., Gallagher, M. W., Whalley, L. K., Edwards, P. M., Evans, M. J., Stone, D., Ingham, T.,

Commane, R., Furneaux, K. L., McQuaid, J., Nemitz, E., Seng, Y.K., Fowler, D., Pyle, J. A., and Hewitt, C. N.: The atmospheric chemistry of trace gases and particulate matter emitted by different land uses in Borneo, Submitted to *Phil. Trans. R. Soc. B.*, 366, 2177-2195, 2011.

Pugh, T. A. M., MacKenzie, A. R., Hewitt, C. N., Langford, B., Edwards, P. M., Furneaux, K. L., Heard, D. E., Hopkins, J. R., Jones, C. E., Karunaharan, A., Lee, J., Mills, G., Misztal, P., Moller, S., Monks, P. S., and Whalley, L. K.: Simulating atmospheric composition over a South-East Asian tropical rainforest: performance of a chemistry box model, *Atmos. Chem. Phys.*, 10, 279-298, 2010.

Whalley, L. K., Edwards, P. M., Furneaux, K. L., Goddard, A., Ingham, T., Evans, M. J., Stone, D., Hopkins, J. R., Jones, C. E., Karunaharan, A., Lee, J. D., Lewis, A. C., Monks, P. S., Moller, S. J., Heard, D. E.: Quantifying the magnitude of a missing hydroxyl radical source in a tropical rainforest, *Atmos. Chem. Phys.*, 2011, 11, 7223-7233.

## A.9 References

Alicke, B., Hebestreit, K., Stutz, J., and Platt, U.: Iodine oxide in the marine boundary layer, *Nature.*, 397, 572-573, 1999.

Allan, B. J., Carslaw, N., Coe, H., Burgess, R. A., and Plane, J. M. C.: Observations of the nitrate radical in the marine boundary layer, *J. Atmos. Chem.*, 33, 129-154, 1999.

Allan, B. J., McFiggans, G., Plane, J. M. C., and Coe, H.: Observations of iodine monoxide in the remote marine boundary layer, *J. Geophys. Res.*, 105, 14361-14369, 2000a.

Allan, B. J., McFiggans, G., Plane, J. M. C., Coe, H., and McFadyen, G. G.: The nitrate radical in the marine boundary layer, *J. Geophys. Res.*, 105, 24191-24204, 2000b.

Altimir, N., Kolari, P., Tuovinen, J. P., Vesala, T., Back, J., Suni, T., Kulmala, M., and Hari, P.: Foliage surface ozone deposition: a role for surface moisture? *Biogeosciences.*, 3, 209-228, 2006.

Andreae, M. O., Artaxo, P., Fischer, H., Freitas, S. R., Gregoire, J. M., Hansel, A., Hoor, P., Kormann, R., Krejci, R., Lange, L., Lelieveld, J., Lindinger, W., Longo, K., Peters, W., de Reus, M., Scheeren, B., Dias, M., Strom, J., van Velthoven, P. F. J., and Williams, J.: Transport of biomass burning smoke to the upper troposphere by deep convection in the equatorial region, *Geophys. Res. Lett.*, 28, 951-954, 2001.

Andrés Hernández, M. D., Burkert, A. J., Reichert, L., Stöbener, D., Meyer-Arnek, J., Burrows, J. P., Dickerson, R. R., and Doddridge, B. G.: Marine boundary layer peroxy radical chemistry during the AEROSOLS99 campaign: Measurements and analysis, *J. Geophys. Res.*, 106, 20, 833-20, 846, 2001

Andrés-Hernández, M. D., Stone, D., Brookes, D. M., Commane, R., Reeves, C. E., Huntrieser, H., Heard, D. E., Monks, P. S., Burrows, J. P., Schlager, H., Kartal, D., Evans, M. J., Floquet, C. F. A., Ingham, T., Methven, J., and Parker, A. E.: Peroxy radical partitioning during the AMMA radical intercomparison exercise, *Atmos. Chem. Phys.*, 10, 10621-10638, 2010

Aranda, A., Le Bras, G., La Verdet, G., and Poulet, G.: The BrO + CH<sub>3</sub>O<sub>2</sub> reaction: Kinetics and role in the atmospheric ozone budget, *Geophys. Res. Lett.*, 24, (22), 2745-2748, 1997

Archibald, A. T., Levine, J. G., Abraham, N. L., Cooke, M. C., Edwards, P. M., Heard, D. E., Jenkin, M. E., Karunaharan, A., Pike, R. C., Monks, P. S., Shallcross, D. E., Telford, P. J., Whalley, L. K., and Pyle, J. A.: Impacts of HO<sub>x</sub> regeneration and recycling in the oxidation of isoprene: Consequences for the composition of past, present and future atmospheres *Geophys. Res. Lett.*, 38, L05804, 2011

Ashbourn, S. F. M., Jenkin, M. E., and Clemitshaw, K. C.: Laboratory studies of the response of a peroxy radical chemical amplifier to HO<sub>2</sub> and a series of organic peroxy radicals, *J. Atmos. Chem.*, 29, 233-266, 1998.

Atkinson, R.: Gas-phase tropospheric chemistry of volatile organic compounds: Alkanes and alkenes, *J. Phys. Chem. Ref. Data.*, 26, 215-290, 1997.

Atkinson, R., and Arey, J.: *Chemical Reviews*, 103, 4605-4638, 2003.

Atkinson, R., D. L. Baulch, R. A. Cox, J. N. Crowley, R. F. Hampson Jr, R. G. Hynes, M. E. Jenkin, J. A. Kerr, M. J. Rossi, and Troe, J.: Summary of Evaluated Kinetic and Photochemical Data for Atmospheric Chemistry, *Atmos. Chem. Phys.*, 6, 3625-4055, 2006.

Atkinson, R., Baulch, D. L., Cox, R. A., Crowley, J. N., Hampson, R. F., Hynes, R. G., Jenkin, M. E., Rossi, M. J., and Troe, J.: Evaluated kinetic and photochemical data for atmospheric chemistry: Volume III - gas phase reactions of inorganic halogens, *Atmos. Chem. Phys.*, 7, 981-1191, 2007.

Aubinet, M., Grelle, A., Ibrom, A., Rannik, U., Moncrieff, J., Foken, T., Kowalski, A. S., Martin, P. H., Berbigier, P., Bernhofer, C., Clement, R., Elbers, J., Granier, A., Grunwald, T., Morgenstern, K., Pilegaard, K., Rebmann, C., Snijders, W., Valentini, R., and Vesala, T.: Estimates of the annual net carbon and water exchange of forests: *The EUROFLUX methodology, in Advances in Ecological Research, Academic Press Inc, San Diego.*, 30, 113-175, 2000.

Ayers, G. P., Penkett, S. A., Gillett, R. W., Bandy, B. J., Galbally, I. E., Meyer, C. P., Elsworth, C. M., Bentley, S. T., and Forgan, B. W.: Evidence for photochemical control of ozone concentrations in unpolluted air, *Nature.*, 360, 446-448, 1992.

Ayers, G. P., Penkett, S. A., Gillett, R. W., Bandy, B., Galbally, I. E., Meyer, C. P., Elsworth, C. M., Bentley, S. T., and Forgan, B. W.: Annual cycle of peroxides and ozone in marine air at Cape Grim, Tasmania, *J. Atmos. Chem.*, 23, (3), 221-252, 1996

Baillie, I. C.: Soils of the humid tropics, the tropical rainforest (Second edition), *Cambridge University Press, Cambridge*, 256-286, 1996.

Barket, D. J.: Intercomparison of automated methodologies for determination of ambient isoprene during the PROPHET 1998 summer campaign, *J. Geophys. Res.*, 106, 24,301-24,314, 2001.

Barth, M., McFadden, J., Sun, J., Wiedinmyer, C., Chuang, P., Collins, D., Griffin, R., Hannigan, M., Karl, T., Kim, S.-W., Lasher-Trapp, S., Levis, S., Litvak, M., Mahowald, N., Moore, K., Nandi, S., Nemitz, E., Nenes, A., Potosnak, M., Raymond, T., Smith, J., Still, C., and Stroud, C.: Coupling between land ecosystems and the atmospheric hydrologic cycle through biogenic aerosol pathways, *B. Am. Meteor. Soc.*, 86, (12), 1738-1742, 2005.

Bidin, K. and Chappell, N. A.: TECHNICAL NOTE: First evidence of a structured and dynamic spatial pattern of rainfall within a small humid tropical catchment, *Hydrol. Earth Syst. Sci.*, 7, 245-253, 2003.

Bloss, W., Evans, M., Lee, J., Sommariva, R., Heard, D., and Pilling, M.: The oxidative capacity of the troposphere: Coupling of field measurements of OH and a global chemistry transport model, *Faraday Discuss.*, 130, 425-436, 2005a.

Bloss W. J., Lee, J. D., Johnson, G. P., Sommariva, R., Heard, D. E., Saiz-Lopez, A., Plane, J. M. C., McFiggans, G., Coe, H., Flynn, M., Rickard, A. R., and Fleming, Z. L.: Impact of halogen monoxide chemistry upon boundary layer OH and HO<sub>2</sub> concentrations at a coastal site, *Geophys. Res. Lett.*, 32, L06814, 2005b.

Bloss, W., Lee J. D., Heard, D. E., Salmon, R. A., Bauguitte, S. J. B., Roscoe, H. K., and Jones, A. E.: Observations of OH and HO<sub>2</sub> radicals in coastal Antarctica, *Atmos. Chem. Phys.*, 7, 4171-4185, 2007.

Bloss, W. J., Camredon, M., Lee, J. D., Heard, D. E., Plane, J. M. C., Saiz-Lopez, A., Bauguitte, S. J. B., Salmon, R. A., and Jones, A. E.: Coupling of HO<sub>x</sub>, NO<sub>x</sub> and halogen chemistry in the Antarctic boundary layer, *Atmos. Chem. Phys.*, 10, 10187-10209, 2010.

Bohn, B., Corlett, G. K., Gillmann, M., Sanghavi, S., Stange, G., Tensing, E., Vrekoussis, M., Bloss, W. J., Clapp, L. J., Kortner, M., Dorn, H.-P., Monks, P. S., Platt, U., Plass-Dulmer, C., Mihalopoulos, N., Heard, D. E., Clemmitshaw, K. C., Meixner, F. X., Prevot, A. S. H., and Schmitt, R.: Photolysis frequency measurement techniques: results of a comparison within the ACCENT project, *Atmos. Chem. Phys.*, 8, 5373-5391, 2008.

Bridgeman, C. H., Pyle, J. A., and Shallcross, D. E.: A three-dimensional model calculation of the ozone depletion potential of 1-bromopropane (1-C<sub>3</sub>H<sub>7</sub>Br), *J. Geophys. Res. Atmos.*, 105, 26493-26502, 2000.

Bronnimann, S.: Early spring ozone episodes: Occurrence and case study. *Physics and Chemistry of the Earth.*, 24, 531-536, 1999.

Brookes, D. M.: *Characterisation of a PERCA instrument and measurements of peroxy radicals during the West African Monsoon 2006*, Ph.D. thesis, University of Leicester, 2010.

Brune, W. H., Faloon, I., Tan, D., Weinheimer, A., Campos, T., Ridley, B. A., Vay, S., Collins, J. E., Sachse, G. W., Jaeglé, L., and Jacob, D. J.: Airborne in-situ OH and HO<sub>2</sub> observations in the cloud-free troposphere and lower stratosphere during SUCCESS, *Geophys. Res. Lett.*, 25, 1701-1704, 1998.

Brune, W. H., Tan, D., Faloon, I., Jaegle, L., Jacob, D. J., Heikes, B. G., Snow, J., Kondo, Y., Shetter, R., Sachse, G. W., Anderson, B. Gregory, G. L., Vay, S., Singh, H. B., Davis, D. D., Crawford, J. H., and Blake, D. R.: OH and HO<sub>2</sub> chemistry in the North Atlantic free troposphere, *Geophys. Res. Lett.*, 26, 3077-3080, 1999.

Burkert, J., Andrés-Hernández, M. D., Stöbener, D., Burrows, J. P., Weissenmayer, M., and Kraus, A.: Peroxy radical and related trace gas measurements in the boundary layer above the Atlantic Ocean, *J. Geophys. Res.*, 106, 5457-5478, 2001.

Burkert, J., Andrés-Hernández, M. D., Reichert, L., Meyer-Arne, J., Doddridge, B., Dickerson, R. R., Mühle, J., Zahn, A., Carsey, T., and Burrows, J. P.: Trace gas and radical diurnal behaviour in the marine boundary layer during INDOEX 1999, *J. Geophys. Res.*, 108, (D8), 8000, 2003.

Calvert, J. G., Atkinson, R., Kerr, J. A., Madronich, S., Moortgat, G. L., Wallington, T. J., and Yarwood, G.: *The mechanisms of atmospheric oxidation of the alkenes*. Oxford University Press, New York, USA, 2000.

Cantrell, C. A. and Stedman, D. H.: A Possible Technique for the Measurement of Atmospheric Peroxy-Radicals, *Geophys. Res. Lett.*, 9, 846-849, 1982.

Cantrell, C. A., Stedman, D. H., and Wendel, G. J.: Measurement of atmospheric peroxy radicals by chemical amplification, *Anal. Chem.*, 56, 1496-1502, 1984.

Cantrell, C. A., Lind, J. A., Shetter, R. E., Calvert, J. G., Goldan, P. D., Kuster, W., Fehsenfeld, F. C., Montzka, S. A., Parrish, D. D., Williams, E. J., Buhr, M. P., Westberg, H. H., Allwine, G., and Martin, R.: Peroxy radicals in the ROSE experiment - Measurement and theory, *J. Geophys. Res.*, 97, (D18), 20671-20686, 1992.

Cantrell, C. A., Shetter, R. E., Calvert, J. G., Parrish, D. D., Fehsenfeld, F. C., Goldan, P. D., Kuster, W., Williams, E. J., Westberg, H. H., Allwine, G., and Martin, R.: Peroxy-Radicals as Measured in Rose and Estimated from Photostationary State Deviations, *J. Geophys. Res. Atmos.*, 98, 18355-18366, 1993a.

Cantrell, C. A., Shetter, R. E., Lind, J. A., McDaniel, A. H., Calvert, J. G., Parrish, D. D., Fehsenfeld, F. C., Buhr, M. P., and Trainer, M.: An Improved Chemical Amplifier Technique for Peroxy Radical Measurements, *J. Geophys. Res. Atmos.*, 98, 2897-2909, 1993b.

Cantrell, C. A.: Comparison of Peroxy Radical Concentrations at Several Contrasting Sites, *J. Atmos. Sci.*, 52, 3408-3412, 1995.

Cantrell, C. A., Shetter, R. E., Gilpin, T. M., Calvert, J. G., Eisele, F. L., and Tanner, D. J.: Peroxy radical concentrations measured and calculated from trace-gas measurements in the Mauna Loa Observatory Photochemistry Experiment 2, *J. Geophys. Res.*, 101, 14653-14644, 1996a

Cantrell, C. A., Shetter, R. E., and Calvert, J. G.: Dual-inlet chemical amplifier for atmospheric peroxy radical measurements, *Anal. Chem.*, 68, 4194- 4199, 1996b

Cantrell, C. A., Shetter, R. E., Calvert, J.: Peroxy radical chemistry during FIELDVOC 1993 in Brittany, France, *Atmos. Environ.*, 30, (23), 3947-3957, 1996c

Cantrell, C. A., Shetter, R. E., Calvert, J. G., Eisele, F. L., and Tanner, D. J.: Some considerations of the origin of nighttime peroxy radicals observed in MLOPEX 2. *J. Geophys. Res.*, 102, (D13), 15899-15913, 1997a

Cantrell, C. A., Shetter, R. E., Calvert, J. G., Eisele, F. L., Williams, E., Baumann, K., Brune, W. H., Stevens P. S., and Mather, J. H.: Peroxy radicals from photostationary-state deviations and steady-state calculations during the Tropospheric OH Photochemistry Experiment at Idaho Hill, Colorado, 1993, *J. Geophys. Res.*, 102, 6369-6378, 1997b

Cantrell C. A., Edwards, G. D., Stephens, S., Mauldin, L., Kosciuch, E., Zondlo, M., and Eisele, F. L.: Peroxy radical observations using chemical ionisation mass spectrometry during TOPSE, *J. Geophys. Res.*, 108, (D6), 8371, 2003a

Cantrell, C. A., Mauldin, L., Zondlo, M., Eisele, F., Kosciuch, E., Shetter, R., Lefer, B., Hall, S., Campos, T., Ridley, B., Walega, J., Fried, A., Wert, B., Flocke, F., Weinheimer, A., Hannigan, J., Coffey, M., Atlas, E., Stephens, S., Heikes, B., Snow, J., Blake, D., Blake, N., Katzenstein, A., Lopez, J., Browell, E. V., Dibb, J., Scheuer, E., Seid, G., Talbot, R., Shetter, R. E., Gilpin, T. M., Calvert, J. G., Eisele F. L., and Tanner, D. J: Steady state free radical budgets and ozone photochemistry during TOPSE, *J. Geophys. Res.*, 108, (D4), 8361, 2003b.

Cantrell, C. A., Edwards, G. D., Stephens, S., Mauldin, R. L., Zondlo, M. A., Kosciuch, E., Eisele, F. L., Shetter, R. E., Lefer, B. L., Hall, S., Flocke, F., Weinheimer, A., Fried, A., Apel, E., Kondo, Y., Blake, D. R., Blake, N. J., Simpson, I. J., Bandy, A. R., Thornton, D. C., Heikes, B. G., Singh, H. B., Brune, W. H., Harder, H., Martinez, M., Jacob, D. J., Avery, M. A., Barrick, J. D., Sachse, G. W., Olson, J. R., Crawford, J. H., and Clarke, A. D.: Peroxy radical behaviour during the transport and Chemical Evolution over the Pacific (TRACE-P) campaign as measured aboard the NASA P-3B aircraft, *J. Geophys. Res.*, 108, (D20), 8797, 2003c.

Carpenter, L. J., *Measurements of peroxy radicals in clean and polluted atmospheres*, PhD thesis, University of East Anglia, Norwich, 1996

Carpenter, L. J., Monks, P. S., Bandy, B. J., and Penkett, S. A.: A study of peroxy radicals and ozone photochemistry at coastal sites in the northern and southern hemispheres, *J. Geophys. Res.*, 102, 25,417-25,427, 1997.

Carpenter, L. J., Clemitshaw K. C., Burgess R. A., Penkett S. A., Cape J. N., and McFadyen G. C.: Investigation and evaluation of the NO<sub>x</sub>/O<sub>3</sub> photochemical steady state, *Atmos. Environ.*, 32, 3353-3365, 1998.

Carpenter, L. J., Green, T. J., Mills, G., Penkett, S. A., Zanis, P., Schuepbach, E., and Monks, P. S.: Oxidised nitrogen and ozone production efficiencies in the springtime free troposphere of the Alps, *J. Geophys. Res.*, 105, 14,547-14,559, 2000

Carpenter, L. J., Lewis, A. C., Hopkins, J. R., Read, K. A., Longley, I. D., and Gallagher, M. W.: Uptake of methanol to the North Atlantic Ocean surface, *Global Biogeochem. Cycles*, 18, GB4027, 2004.

Carpenter, L. J., Fleming, Z. L., Read, K. A., Lee, J. D., Moller, S. J., Hopkins, J. R., Purvis, R. M., Lewis, A. C., Müller, K., Heinold, B., Herrmann, H., Wadinga Fomba, K., Van Pinxteren, D., Müller, C., Tegen, I., Wiedensohler, A., Müller, T., Niedermeier, N., Achterberg, E. P., Patey, M. D., Kozlova, E. A., Heimann, M., Heard, D. E., Plane, J. M. C., Mahajan, A., Oetjen, H., Ingham, T., Stone, D., Whalley, L. K., Evans, M. J., Pilling, M. J., Leigh, R. J., Monks, P. S., Karunaharan, A., Vaughan, S., Arnold, S. R., Tschritter, J., Pöhler, D., Frieß, U., Holla, R., Mendes, L. M., Lopez, H., Faria, B., Manning, A. J., and Wallace, D.W.R.: Seasonal characteristics of tropical marine boundary layer air measured at the Cape Verde Atmospheric Observatory., *J. Atmos. Chem.*, 67, 87-140, 2010.

Carslaw, N., Carpenter, L. J., Plane, J. M. C., Allan, B. J., Burgess, R. A., Clemitshaw, K. C., Coe, H., and Penkett, S. A.: Simultaneous observations of nitrate and peroxy radicals in the marine boundary layer, 1. Model construction and comparison with field measurements, *J. Geophys. Res.*, 102, 18,917-18,933, 1997.

Carslaw, N., Creasey, D. J., Heard, D. E., Lewis, A. C., McQuaid, J. B., Pilling, M. J., Monks, P. S., Bandy, B. J., and Penkett, S. A.: Modelling OH, HO<sub>2</sub> and RO<sub>2</sub> radicals in the marine boundary layer. 1. Model construction and comparison with field measurements, *J. Geophys. Res.*, 104, 30, 241-30,255, 1999

Carter, W. P. L., Winer, A. M., and Pitts, J. N.: Effect of Peroxyacetyl Nitrate on the Initiation of Photochemical Smog, *Environ. Sci. Technol.*, 15, 831-834, 1981

Chappell, N. A., Sherlock, M., Bidin, K., Macdonald, R., Najman, Y., and Davies, G.: Runoff processes in Southeast Asia: role of soil, regolith and rock type: *Forest Environments in the Mekong River Basin*, Springer Verlag, Tokyo, 3-23, 2007.

Chen, G., Huey, L. G., Crawford, J. H., Olson, J. R., Hutterli, M. A., Sjostedt, S., Tanner, D., Dibb, J., Lefer, B., Blake, N., Davis, D., and Stohl, A.: An assessment of the polar HO<sub>x</sub> photochemical budget based on 2003 Summit Greenland field observations, *Atmos. Environ.*, 41, (36), 7806-7820, 2007.

Cieslik, S. A.: Ozone uptake by various surface types: a comparison between dose and exposure. *Atmos. Environ.*, 38, 2409-2420, 2004.

Clemitshaw, K. C., Carpenter, L. J., Penkett, S. A., and Jenkin, M. E.: A calibrated peroxy radical chemical amplifier (PERCA) for ground-based measurements in the troposphere, *J. Geophys. Res.*, 102, 25405-25416, 1997

- Clemmitshaw, K. C.: A review of instrumentation and measurement techniques for ground-based and airborne field studies of gas-phase tropospheric chemistry, *Critical Reviews in Environmental Science and Technology*, 34, 1-108, 2004.
- Coe, H., Gallagher, M. W., Choularton, T. W., and Dore, C.: Canopy Scale Measurements of Stomatal and Cuticular O<sub>3</sub> Uptake by Sitka Spruce, *Atmos. Environ.*, 29, 1413-1423, 1995.
- Cox, R. A.: Ozone and peroxy radical budgets in the marine boundary layer: Modeling the effect of NO<sub>x</sub>, *J. Geophys. Res.*, 104, 8047-8056, 1999.
- Coyle, M., Nemitz, E., Storeton-West, R., Fowler, D., and Cape, J. N.: Measurements of ozone deposition to a potato canopy, *Agricultural and Forest Meteorology*, 149, 656-666, 2009.
- Creasey, D. J., Heard, D. E., Halford-Maw, P. A., Pilling M. J., and Whitaker, B. J.: Implementation and initial deployment of a field instrument for measurement of OH and HO<sub>2</sub> in the troposphere by laser-induced fluorescence. *J. Chem. Soc., Faraday Trans.*, 93, 2907, 1997.
- Creasey, D. J., Evans, G. E., Heard, D. E., and Lee, J. D.: Measurements of OH and HO<sub>2</sub> concentrations in the Southern Ocean marine boundary layer, *J. Geophys. Res.*, 108, (D15), 4475, 2003.
- Dari-Salisburgo, C., Di Carlo, P., Giammaria, F., Kajii, Y., and D'Altorio, A.: Laser induced fluorescence instrument for NO<sub>2</sub> measurements: observations at a central Italy background site, *Atmos. Environ.*, 43, 970-977, 2009.
- Davis D., Crawford J., Liu S., McKeen S., Bandy A., Thornton D., Rowland F., and Blake, D.: Potential impact of iodine on tropospheric levels of ozone and other critical oxidants, *J. Geophys. Res.*, 101, (1), 2135-2147, 1996.
- Derwent, R. G., Simmonds, P. G., Seuring, S., and Dimmer, C.: Observation and interpretation of the seasonal cycles in the surface concentrations of ozone and carbon monoxide at Mace Head, Ireland from 1990 to 1994, *Atmos. Environ.*, 32, 145-157, 1998.
- Derwent, R. G., Jenkin, M. E., Saunders, S. M., Pilling, M. J., Simmonds, P. G., Passant, N. R., Dollard, G. J., Dumitrescu, P., and Kent, A.: Photochemical ozone formation in north west Europe and its control, *Atmos. Environ.*, 37, (14), 1983-1991, 2003
- Dillon, T. J., and Crowley, J. N.: Direct detection of OH formation in the reactions of HO<sub>2</sub> with CH<sub>3</sub>C(O)O<sub>2</sub> and other substituted peroxy radicals, *Atmos. Chem. Phys.*, 8, 4877-4889, 2008
- Donovan, R., Hope, E., Owen, S., Mackenzie, A., and Hewitt, C.: Development and Application of an Urban Tree Air Quality Score for Photochemical Pollution Episodes Using the Birmingham, United Kingdom, Area as a Case Study, *Environ. Sci. Technol.*, 39, 6730-6738, 2005.

Dorsey, J. R., Duyzer, J. H., Gallagher, M. W., Coe, H., Pilegaard, K., Weststrate, J. H., Jensen, N. O., and Walton, S.: Oxidised nitrogen and ozone interaction with forest. 1: experimental observations and analysis of exchange with Daouglas fir. *Quarterly Journal of the Royal Meteorological Society.*, 130, 1941-1955, 2004.

Edwards, G. D., and Monks, P. S.: Performance of a single monochromator diode array spectroradiometer for the determination of actinic flux and atmospheric frequencies, *J. Geophys. Res.*, 108, 8546-8558, 2003.

Eisele, F. L., and Tanner, D. J.: Measurement of the Gas-Phase Concentration of H<sub>2</sub>SO<sub>4</sub> and Methane Sulfonic-Acid and Estimates of H<sub>2</sub>SO<sub>4</sub> Production and Loss in the Atmosphere, *J. Geophys. Res. Atmos.*, 98, 9001-9010, 1993.

Emmerson, K. M., MacKenzie, A. R., Owen, S. M., Evans, M. J., and Shallcross, D. E.: A Lagrangian model with simple primary and secondary aerosol scheme 1: comparison with UK PM10 data, *Atmos. Chem. Phys.*, 4, 2161-2170, 2004.

Emmerson, K. M., N. Carslaw, D. C. Carslaw, J. D. Lee, G. McFiggans, W. J. Bloss, T. Gravestock, D. E. Heard, J. R. Hopkins, T. Ingham, M. J. Pilling, S. C. Smith, M. J. Jacob, and P. S. Monks, Free radical modelling studies during the UK TORCH Campaign in Summer 2003, *Atmos. Chem. Phys.*, 7, 161-181, 2007.

Emmerson, K. M. and Evans, M. J.: Comparison of tropospheric gas-phase chemistry schemes for use within global models, *Atmos. Chem. Phys.*, 9, 1831-1845, 2009.

Evans, M., Shallcross, D., Law, K., Wild, J., Simmonds, P., Spain, T., Berrisford, P., Methven, J., Lewis, A., McQuaid, J., Pilling, M., Bandy, B., Penkett, S., and Pyle, J.: Evaluation of a Lagrangian box model using field measurements from EASE (Eastern Atlantic Summer Experiment) 1996, *Atmos. Environ.*, 34, 3843-3863, 2000.

Fallowski, P. G.: Evolution of the nitrogen cycle and its influence on the biological sequestration of CO<sub>2</sub> in the ocean, *Nature.*, 387, 272-275, 1997.

Faloona, I., D. Tan, W. H. Brune, L. Jaeglé, D. J. Jacob, Y. Kondo, M. Koike, R. Chatfield, R. Pueschel, G. Ferry, G. Sachse, S. Vay, B. Anderson, J. Hannon, and H. Fuelberg.: Observations of HO<sub>x</sub> and its relationship with NO<sub>x</sub> in the upper troposphere during SONEX, *J. Geophys. Res.*, 105, 3771-3783, 2000.

Farman, J. C., Gardiner, B. G. & Shanklin, J. D.: Large losses of total ozone in Antarctica reveal seasonal ClO<sub>x</sub>/NO<sub>x</sub> interaction *Nature.*, 315, 207-210, 1985.

Farmer, D. K., Wooldridge, P. J., and Cohen, R. C.: Application of thermal-dissociation laser induced fluorescence (TD-LIF) to measurement of HNO<sub>3</sub>, Σalkyl nitrates, Σperoxy nitrates, and NO<sub>2</sub> fluxes using eddy covariance, *Atmos. Chem. Phys.*, 6, 3471-3486, 2006.

Finlayson-Pitts, B. J., and Pitts, J. N.Jr.: Atmospheric chemistry of tropospheric ozone formation: scientific and regulatory implications, *Air & Waste*, 43, 1091-1100, 1993.

Finlayson-Pitts, B. J. and Pitts, J. N.: Chemistry of the upper and lower atmosphere: theory, experiments, and applications, *Academic Press*, San Diego, 2000.

Fiore, A. M., Jacob, D. J., Logan, J. A., and Yin, J. H.: Long-term trends in ground level ozone over the contiguous United States, 1980-1995, *J. Geophys. Res.*, 103, 1471- 1480, 1998.

Fleming, Z. L.: *The measurement of peroxy radicals in the marine boundary layer using the PERCA technique*, Ph.D. thesis, University of Leicester, Leicester, 2005

Fleming, Z. L., Monks, P. S., Rickard, A. R., Bandy, B. J., Brough, N., Green, T. J., Reeves, C. E., and Penkett, S. A.: Seasonal dependence of peroxy radical concentrations at a Northern hemisphere marine boundary layer site during summer and winter: evidence for radical activity in winter, *Atmos. Chem. Phys.*, 6, 5415-5433, 2006a.

Fleming, Z. L., Monks, P. S., Rickard, A. R., Heard, D. E., Bloss, W. J., Seakins, P. W., Still, T. J., Sommariva, R., Pilling, M. J., Morgan, R., Green, T. J., Brough, N., Mills, G. P., Penkett, S. A., Lewis, A. C., Lee, J. D., Saiz-Lopez, A., and Plane, J. M. C.: Peroxy radical chemistry and the control of ozone photochemistry at Mace Head, Ireland during the summer of 2002, *Atmos. Chem. Phys.*, 6, 2193-2214, 2006b.

Fowler, D., Flechard, C., Cape, J. N., Storeton-West, R. L., and Coyle, M.: Measurements of ozone deposition to vegetation quantifying the flux, the stomatal and non-stomatal components, *Water, Air and Soil Pollution.*, 130, 63-74, 2001.

Fowler, D., Pilegaard, K., Sutton, M. A., Ambus, P., Raivonen, M., Duyzer, J., Simpson, D., Fagerli, H., Schjoerring, J. K., Neftel, A., Burkhardt, J., Daemmgen, U., Neiryink, J., Personne, E., Wichink-Kruit, R., Butterbach-Bahl, K., Flechard, C., Tuovinen, J. P., Coyle, M., Gerosa, G., Loubet, B., Altimir, N., Gruenhage, L., Ammann, C., Cieslik, S., Paoletti, E., Mikkelsen, T. N., Ro-Poulsen, H., Cellier, P., Cape, J. N., Horvath, L., Loreto, F., Niinemets, U., Palmer, P.I., Rinne, J., Misztal, P., Nemitz, E., Nilsson, D., Pryor, S., Gallagher, M. W., Vesala, T., Skiba, U., Brüeggemann, N., Zechmeister-Boltenstern, S., Williams, J., O'Dowd, C., Facchini, M. C., de Leeuw, G., Flossman, A., Chaumerliac, N., Erisman, J.W.: Atmospheric composition change: Ecosystems and atmosphere exchange, *Atmos. Environ.*, 43, 5192-5263, 2009.

Fried, A.: Photochemistry of formaldehyde during the 1993 Tropospheric OH photochemistry experiment. *J. Geophys. Res.*, 102, 6283-6296, 1997.

Frost, G. J., Trainer, M., Allwine, G., Buhr, M. P., Calvert, J. G., Cantrell, C. A., Fehsenfeld, F. C., Goldan, P. D., Herwehe, J., Hübler, G., Kuster, W. C., Martin, R., McMillen, R. T., Montzka, S. A., Norton, R. B., Parrish, D. D., Ridley, B. A., Shetter, R. E., Walega, J. G., Watkins, B. A., Westberg, H. H., and Williams, E. J.: Photochemical ozone production in the rural southeastern United States during the 1990 Rural Oxidants in the Southern Environment (ROSE) program, *J. Geophys. Res.*, 103, (D17), 22491-22508, 1998.

Fuchs, H.: Measurement of peroxy radicals using laser-induced fluorescence, *Schriften des Forschungszentrums Juelich, Reihe Umwelt/Environment*, 72, 2006.

Fuchs, H., Holland, F., and Hofzumahaus, A.: Measurement of tropospheric RO<sub>2</sub> and HO<sub>2</sub> radicals by a laser-induced fluorescence instrument, *Rev. Sci. Instrum.*, 79 (8), 084104-12, 2008.

Fuchs, H., Bohn, B., Hofzumahaus, A., Holland, F., Lu, K. D., Nehr, S., Rohrer, F., and Wahner, A.: Detection of HO<sub>2</sub> by laser-induced fluorescence: calibration and interferences from RO<sub>2</sub> radicals., *Atmos. Meas. Tech.*, 4, 1209-1225, 2011

Fuentes, J., Lerdau, M., Atkinson, R., Baldocchi, D., Bottenheim, J., Ciccioli, P., Lamb, B., Geron, C., Gu, L., Guenther, A., Sharkey, T., and Stockwell, W.: Biogenic hydrocarbons in the atmospheric boundary layer: A review, *B. Am. Meteor. Soc.*, 81, 1537-1575, 2000.

Furueux, K. L., Whalley, L. K., Heard, D. E., Atkinson, H. M., Bloss, W. J., Flynn, M. J., Gallagher, M. W., Ingham, T., Kramer, L., Lee, J. D., Leigh, R., McFiggans, G. B., Mahajan, A. S., Monks, P. S., Oetjen, H., Plane, J. M. C., Whitehead, J. D.: Measurements of iodine monoxide at a semi polluted coastal location, *Atmos. Chem. Phys.*, 2010, 10, 3645-3663

Gerbig, C., Schmitgen, S., Kley, D., Volz-Thomas, A., Dewey, K., and Haaks, D.: An improved fast-response vacuum-UV resonance fluorescence CO instrument, *J. Geophys. Res.*, 104, 1699-1704, 1999.

Geyer, A., Bächmann, K., Hofzumahaus, A., Holland, F., Konrad, S., Klüpfel, T., Pätz, H.-W., Perner, D., Mihelcic, D., Schäfer, H.-J., Volz-Thomas, A., and Platt, U.: Nighttime formation of peroxy and hydroxyl radicals during the BERLIOZ campaign: Observations and modelling studies, *J. Geophys. Res.*, 108, (D4), 8249, 2003.

Geyer, A., and Stutz, J.: The vertical structure of OH-HO<sub>2</sub>-RO<sub>2</sub> chemistry in the nocturnal boundary layer: a one-dimensional model study, *J. Geophys. Res.*, 109, D16301, 2004

Gilman, J. B., Kuster, W. C., Goldan, P. D., Herndon, S. C., Zahniser, M. S., Tucker, S. C., Brewer, W. A., Lerner, B. M., Williams, E. J., Harley, R. A., Fehsenfeld, F. C., Warneke, C., and de Gouw, J. A.: Measurements of volatile organic compounds during the 2006 TexAQS/GoMACCS campaign: industrial influences, regional characteristics, and diurnal dependencies of the OH reactivity, *J. Geophys. Res.*, 114, D00F06, 2009.

Goldstein, A. H., McKay, M., Kurpius, M. R., Schade, G. W., Lee, A., Holzinger, R., and Rasmussen, R. A.: Forest thinning experiment confirms ozone deposition to forest canopy is dominated by reaction with biogenic VOCs, *Geophys. Res. Lett.*, 31, L22106, 2004.

Green, T. J., Brough, N., Reeves, C. E., Edwards, G. D., Monks, P. S., and Penkett, S. A.: Airborne measurements of peroxy radicals using the PERCA technique, *J. Environ. Monit.*, 5, 75-83, 2002.

- Green, T. J., Brough, N., Reeves, C. E., Edwards, G. D., Monks, P. S., and Penkett, S. A.: Airborne measurements of peroxy radicals using the PERCA technique, *J. Environ. Monit.*, 5, 75-83, 2003
- Green, T. J., Reeves, C. E., Flemming, Z. L., Brough, N., Rickard, A. R., Bandy, B. J., Monks, P. S., and Penkett, S. A.: An improved dual channel PERCA instrument for atmospheric measurements of peroxy radicals, *J. Environ. Monit.*, 8, 530-536, 2006.
- Guenther, A., Hewitt, C. N., Erickson, D., Fall, R., Geron, C., Graedel, T., Harley, P., Klinger, L., Lerdau, M., McKay, W. A., Pierce, T., Scholes, B., Steinbrecher, R., Tallamraju, R., Taylor, J., and Zimmerman, P.: A global-model of natural volatile organic-compound emissions, *J. Geophys. Res. Atmos.*, 100, 8873-8892, 1995.
- Guenther, A., Karl, T., Harley, P., Wiedinmyer, C., Palmer, P. I., and Geron, C.: Estimates of global terrestrial isoprene emissions using MEGAN (Model of Emissions of Gases and Aerosols from Nature), *Atmos. Chem. Phys.*, 6, 3181-3210, 2006.
- Gusten, H., Heinrich, G., Schmidt, R. W. H., and Schurath, U.: A Novel Ozone Sensor for Direct Eddy Flux Measurements, paper presented at 7th International Symp of the Commission for Atmospheric Chemistry and Global Pollution: *The Chemistry of the Global Atmosphere, Kluwer Academic Publ, Chamrousse, France, 5-11 September, 1990.*
- Gusten, H., and Heinrich, G.: On-line measurements of ozone surface fluxes .1. methodology and instrumentation, *Atmos. Environ.*, 30, 897-909, 1996.
- Handisides, G. M., Plass-Dulmer, C., Gilge, S., Bingemer, H., and Berresheim, H.: Hohenpeissenberg Photochemical Experiment (HOPE 2000): Measurements and photostationary state calculations of OH and peroxy radicals, *Atmos. Chem. Phys.*, 3, 1565-1588, 2003
- Hanke, M., Ueker, J., Reiner, T., and Arnold, F.: Atmospheric peroxy radicals: ROXMAS, a new mass-spectrometric methodology for speciated measurements of HO<sub>2</sub> and ΣRO<sub>2</sub> and first results, *Int. J. Mass. Spec.*, 213, 91-99, 2002.
- Hansen, J., Sato, M., Ruedy, R., Lacis, A., and Oinas, V: Global warming in the twenty first century: An alternative scenario, *Proc. Nat. Acad. Sci. USA.*, 97, 9875-9880, 2000.
- Hard, T. M., O'Brien, R.J., C. Y. Chan., C.Y., and Mehrabzadeh., A.A.: Tropospheric Free-Radical Determination by Fage, *Environmental Science & Technology*, 18, 768-777, 1984.
- Harrison, R. M., Yin, J., Tilling, R. M., Cai, X., Seakins, P. W., Hopkins, J. R., Lansley, D. L., Lewis, A. C., Hunter, M. C., Heard, D. E., Carpenter, L. J., Creasy, D. J., Lee, J. D., Pilling, M. J., Carslaw, N., Emmerson, K. M., Redington, A., Derwent, R. G., Ryall, D., Mills, G., and Penkett, S. A.: Measurement and modelling of air pollution and atmospheric chemistry in the UK West Midlands conurbation: Overview of the PUMA Consortium project, *Sci. Total Environ.*, 360, 5-25, 2006.

Hasson, A. S., Tyndall, G. S., and Orlando, J. J.: A product yield study of the reaction of HO<sub>2</sub> radicals with ethyl peroxy (C<sub>2</sub>H<sub>5</sub>O<sub>2</sub>), Acetyl Peroxy (CH<sub>3</sub>C(O)O<sub>2</sub>) and acetyl peroxy (CH<sub>3</sub>C(O)CH<sub>2</sub>O<sub>2</sub>) radicals, *J. Phys. Chem.*, 108, 5979-5989, 2004.

Heard, D. E., and Pilling, M.J.: Measurement of OH and HO<sub>2</sub> in the Troposphere, *Chemical Reviews*, 103, 5163-5198, 2003.

Heard, D. E., Carpenter, L. J., Creasey D. J., Hopkins, J. R., Lee, J. D., Lewis, A. C., Pilling, M. J., Seakins, P. W., Carslaw, N., and Emmerson, K. M.: High levels of the hydroxyl radical in the winter urban troposphere, *Geophys. Res. Lett.*, 31, L18112, 2004.

Heard, D. E., Read, K. A., Methven, J., Al-Haider, S., Bloss, W. J., Johnson, G. P., Pilling, M. J., Seakins, P. W., Smith, S. C., Sommariva, R., Stanton, J. C., Still, T. J., Ingham, T., Brooks, B., De Leeuw, G., Jackson, A. V., McQuaid, J. B., Morgan, R., Smith, M. H., Carpenter, L. J., Carslaw, N., Hamilton, J., Hopkins, J. R., Lee, J. D., Lewis, A. C., Purvis, R. M., Wevill, D. J., Brough, N., Green, T., Mills, G., Penkett, S. A., Plane, J. M. C., Saiz-Lopez, A., Worton, D., Monks, P. S., Fleming, Z., Rickard, A. R., Alfarra, M. R., Allan, J. D., Bower, K., Coe, H., Cubison, M., Flynn, M., McFiggans, G., Gallagher, M., Norton, E. G., O'Dowd, C. D., Shillito, J., Topping, D., Vaughan, G., Williams, P., Bitter, M., Ball, S. M., Jones, R. L., Povey, I. M., O'Doherty, S., Simmonds, P. G., Allen, A., Kinnersley, R. P., Beddows, D. C. S., Dall'Osto, M., Harrison, R. M., Donovan, R. J., Heal, M. R., Jennings, S. G., Noone, C., and Spain, G.: The North Atlantic Boundary Layer Experiment (NABBLEX). Overview of the campaign held at Mace Head, Ireland, in summer 2002, *Atmos. Chem. Phys.*, 6, 2241-2272, 2006.

Hewitt, C. N., MacKenzie, A. R., Di Carlo, P., Di Marco, C. F., Dorsey, J. R., Evans, M., Fowler, D., Gallagher, M.W., Hopkins, J. R., Jones, C. E., Langford, B., Lee, J. D., Lewis, A. C., Lim, S. F., McQuaid, J., Misztal, P., Moller, S. J., Monks, P. S., Nemitz, E., Oram, D. E., Owen, S. M., Phillips, G. J., Pugh, T. A. M., Pyle, J. A., Reeves, C. E., Ryder, J., Siong, J., Skiba, U., and Stewart, D. J.: Nitrogen management is essential to prevent tropical oil palm plantations from causing ground-level ozone pollution, *Proc. Natl. Acad. Sci. USA.*, 106, 18447-18451, 2009.

Hewitt, C. N., Lee, J. D., MacKenzie, A. R., Barkley, M. P., Carslaw, N., Carver, G. D., Chappell, N. A., Coe, H., Collier, C., Commane, R., Davies, F., Davison, B., DiCarlo, P., Di Marco, C. F., Dorsey, J. R., Edwards, P. M., Evans, M. J., Fowler, D., Furneaux, K. L., Gallagher, M., Guenther, A., Heard, D. E., Helfter, C., Hopkins, J., Ingham, T., Irwin, M., Jones, C., Karunaharan, A., Langford, B., Lewis, A. C., Lim, S. F., MacDonald, S. M., Mahajan, A. S., Malpass, S., McFiggans, G., Mills, G., Misztal, P., Moller, S., Monks, P. S., Nemitz, E., Nicolas-Perea, V., Oetjen, H., Oram, D. E., Palmer, P. I., Phillips, G. J., Pike, R., Plane, J. M. C., Pugh, T., Pyle, J. A., Reeves, C. E., Robinson, N. H., Stewart, D., Stone, D., Whalley, L. K., and Yin, X.: Overview: oxidant and particle photochemical processes above a south-east Asian tropical rainforest (the OP3 project): introduction, rationale, location characteristics and tools, *Atmos. Chem. Phys.*, 10, 169-199, 2010.

Hoffmann, T., Odum, J. R., Bowman, F., Collins, D., Klockow, D., Flagan, R. C., and Seinfeld, H. J.: Formation of organic aerosols from the oxidation of biogenic hydrocarbons, *J. Atmos. Chem.*, 26, 189-222, 1997.

Hogg, A., Uddling, J., Ellsworth, D., Carroll, M. A., Pressley, S., Lamb, B., and Vogel, C.: Stomatal and non-stomatal fluxes of ozone to a northern mixed hardwood forest, *Tellus B.*, 59, 514-525, 2007.

Holland, F., Hofzumahaus, A., Schäfer, J., Kraus, A., and Pätz, H. W.: Measurements of OH and HO<sub>2</sub> radical concentrations and photolysis frequencies during BERLIOZ, *J. Geophys. Res.*, 108, (D4), 8246, 2003

Horowitz, L. W., Walters, S., Mauzerall, D. L., Emmons, L. K., Rasch, P. J., Granier, C., Tie, X. X., Lamarque, J. F., Schultz, M. G., Tyndall, G. S., Orlando, J. J., Brasseur, G., P.: A global simulation of tropospheric ozone and related tracers: Description and evaluation of MOZART, version 2. *J. Geophys. Res. Atmos.*, 108, 2003.

Hosaynali Beygi, Z., Fischer, H., Harder, H. D., Martinez, M., Sander, R., Williams, J., Brookes, D. M., Monks, P. S., Lelieveld, J.: Oxidation photochemistry in the Southern Atlantic boundary layer: unexpected deviations of photochemical steady state. *Atmos. Chem. Phys.*, 11, 8497-8513, 2011.

Hu, J., and Stedman, D. H.: Atmospheric ROx radicals at an urban site; Comparison to a simple theoretical model, *Environ. Sci. Technol.*, 29, 1655-1659, 1995

Hurst, J. M.: Investigation of the nighttime decay of isoprene, *J. Geophys. Res.*, 106, 24, 335-24, 346, 2001.

Ingham, T., Goddard, A., Whalley, L. K., Furneaux, K. L., Edwards, P. M., Seal, C. P., Self, D. E., Johnson, G. P., Read, K. A., Lee, J. D., and Heard, D. E.: A flow-tube based laser-induced fluorescence instrument to measure OH reactivity in the troposphere, *Atmos. Meas. Tech.*, 2, 465-477, 2009.

IUPAC: <http://www.iupac-kinetic.ch.cam.ac.uk/>, 2006.

Jacob, M. J.: *Measurement of Peroxy Radicals in the Regional Boundary Layer using the PERCA Technique*. PhD Thesis, University of Leicester, 2006

Jacobi, H. W., Weller, R., Bluszczyk, T., Schrems, O.: Latitudinal distribution of peroxyacetyl nitrate (PAN) over the Atlantic Ocean, *J. Geophys. Res.*, 104, 26901-26912, 1999.

Jenkin, M. E., Saunders, S. M. and Pilling, M. J.: The tropospheric degradation of volatile organic compounds: A protocol for mechanism development, *Atmos. Environ.*, 31, 81-104, 1997

Jenkin, M. E., Saunders, S. M., Wagner, V., and Pilling, M. J.: Protocol for the development of the Master Chemical Mechanism, MCM v3 (Part A): Tropospheric degradation of non-aromatic volatile organic compounds (Part B): tropospheric

degradation of aromatic volatile organic compounds, *Atmos. Chem. Phys.*, 3, 161- 193, 2003

Jenkin, M. E., Hurley, M. D., Wallington, T. J.: Investigation of the radical product channel of the  $\text{CH}_3\text{C}(\text{O})\text{O}_2 + \text{HO}_2$  reaction in the gas phase, *Phys. Chem. Chem. Phys.*, 9, 3149-3162, 2007.

Johnson, D., and Marston, G.: The gas-phase ozonolysis of unsaturated volatile organic compounds in the troposphere, *Chem. Soc. Rev.*, 2008, 37, 699-716.

Kanaya, Y.: Nighttime observation of the  $\text{HO}_2$  radical by an LIF instrument at Oki island, Japan, and its possible origins, *Geophys. Res. Lett.*, 26, 2179-2182, 1999.

Kanaya, Y.: Daytime  $\text{HO}_2$  concentrations at Oki Island, Japan, in summer 1998: Comparison between measurement and theory, *J. Geophys. Res. Atmos.*, 105, 24205-24222, 2000.

Kanaya, Y., Matsumoto, J., and Akimoto, H.: Photochemical ozone production at a subtropical island of Okinawa, Japan: Implications from simultaneous observations of  $\text{HO}_2$  radical and  $\text{NO}_x$ , *J. Geophys. Res.*, 107, 4368, 2002.

Kanaya, Y., Cao, R., Kato, S., Miyakawa, Y., Kajii, Y., Tanimoto, H., Yokouchi, Y., Mochida, M., Kawamura, K., and Akimoto, H.: Chemistry of OH and  $\text{HO}_2$  radicals observed at Rishiri Island, Japan, in September 2003: Missing daytime sink of  $\text{HO}_2$  and positive nighttime correlations with monoterpenes, *J. Geophys. Res. Atmos.*, 112, D11308, 2007.

Kelly, T. J., Spicer, C. W., and Ward, G. F.: An assessment of the luminal Chemiluminescence technique for measurement of  $\text{NO}_2$  in ambient air, *Atmos. Environ.*, 24, (9), 2397-2403, 1990.

Kleinman, L. I., Lee, Y. N., Stephen, S. R., Springston, R., Lee, J. H., Nunnermacker, L., Weinstein- Loyd, J., and Zhou, X.: Peroxy radical concentration and ozone formation rate at a rural site in the southeastern, United States, *J. Geophys. Res.*, 100 (D4), 7263-7273, 1995.

Kleissl, J., Honrath, R. E., Owen, R. C., Val Martin, M., and Dziobak, M. P.: The occurrence of upslope flows at the Pico mountain observatory: a case study of orographic flows on small, volcanic islands, *J. Geophys. Res.*, 112, D10S35, 2007.

Kramer, L. J., Leigh, R. J., Remedios, J. J., and Monks, P. S.: Comparison of OMI and ground based in situ and MAX-DOAS measurements of tropospheric nitrogen dioxide in an urban area, *J. Geophys. Res.*, 113, D16S39, 2008.

Kraus, A., and Hofzumahaus, A.: Field measurements of atmospheric photolysis frequencies for  $\text{O}_3$ ,  $\text{NO}_2$ , HCHO,  $\text{CH}_3\text{CHO}$ ,  $\text{H}_2\text{O}_2$  and HONO by UV, *J. Atmos. Chem.*, 31, 161-180, 1998.

Kroll, J. H., Nga, N. L., Murphy, S. M., Flagan, R. C., and Seinfeld, J. H.: Secondary organic aerosol formation from isoprene photooxidation under high-NO<sub>x</sub> conditions, *Geophys. Res. Lett.*, 32, L18808, 2005.

Lamaud, E., Carrara, A., Brunet, Y., Lopez, A., and Druilhet, A.: Ozone fluxes above and within a pine forest canopy in dry and wet conditions. *Atmos. Environ.*, 36, 77-88, 2002.

Langford, B., Davison, B., Nemitz, E., and Hewitt, C. N.: Mixing ratios and eddy covariance flux measurements of volatile organic compounds from an urban canopy (Manchester, UK), *Atmos. Chem. Phys.*, 9, 1971-1987, 2009.

Lawrence, M. G., Jockel, P., and von Kuhlmann, R.: What does the global mean OH concentration tell us? *Atmos. Chem. Phys.*, 1, 37-49, 2001.

Lee, J. D., Lewis, A. C., Monks, P. S., Jacob, M., Hamilton, J. F., Hopkins, J. R., Watson, N. M., Saxton, J. E., Ennis, C., Carpenter, L. J., Carslaw, N., Fleming, Z., Bandy, B. J., Oram, D. E., Penkett, S. A., Slemr, J., Norton, E., Rickard, A. R., Whalley, L. K., Heard, D. E., Bloss, W. J., Gravesstock, T., Smith, S. C., Stanton, J., Pilling, M. J., and Jenkin, M.E.: Ozone photochemistry and elevated isoprene during the UK heatwave of August 2003, *Atmos. Environ.*, 40, 7598-7613, 2006.

Lee, J. D., Moller, S. J., Read, K. A., Lewis, A. C., Mendes, L., Carpenter, L. J.: Year round measurements of nitrogen oxides and ozone in the tropical North Atlantic marine boundary layer. *J. Geophys. Res. Atmos.*, 114, 2009.

Lee, J. D., McFiggans, G., Allan, J. D., Baker, A. R., Ball, S. M., Benton, A. K., Carpenter, L. J., Commane, R., Finley, B. D., Evans, M., Fuentes, E., Furneaux, K., Goddard, A., Good N., Hamilton, J. F., Heard, D. E., Herrmann, H., Hollingsworth, A., Hopkins, J. R., Ingham, T., Irwin, M., Jones, C. E., Jones, R. L., Keene, W. C., Lawler, M. J., Lehmann, S., Lewis, A. C., Long, M. S., Mahajan, A., Methven, J., Moller, S. J., Muller, K., Muller, T., Niedermeier, N., O'Doherty, S., Oetjen, H., Plane, J. M. C., Pszenny, A. A. P., Read, K. A., Saiz-Lopez, A., Saltzman, E. S., Sander, R., von Glasow, R., Whalley, L., Wiedensohler, A., Young, D.: Reactive Halogens in the Marine Boundary Layer (RHAMBLE): The tropical North Atlantic experiments, *Atmos. Chem. Phys.*, 10, 1031-1055, 2010

Leigh, R. J., Corlett, G. K., Friess, U., and Monks, P. S.: Concurrent multi-axis differential absorption spectroscopy system for the measurement of tropospheric nitrogen dioxide, *Appl. Optics*, 45, (28), 7504-7518, 2006.

Lelieveld, J., and Crutzen, P.J.: Influences of cloud photochemical processes on tropospheric ozone, *Nature*, 343, 227-233, 1990.

Lelieveld, J., Butler, T. M., Crowley, J. N., Dillon, T. J., Fischer, H., Ganzeveld, L., Harder, H., Lawrence, M. G., Martinez, M., Taraborrelli, D., and Williams, J.: Atmospheric oxidation capacity sustained by a tropical forest, *Nature.*, 452, 737-740, 2008.

Levy, H.: Normal Atmosphere - Large Radical and Formaldehyde Concentrations Predicted, *Science.*, 173, 141-143, 1971.

Lewis, A. C., Hopkins, J. R., Carpenter, L. J., Stanton, J., Read, K. A., and Pilling, M. J.: Sources and sinks of acetone, methanol, and acetaldehyde in North Atlantic marine air, *Atmos. Chem. Phys.*, 5, 1963-1974, 2005.

Lewis, A. C., Evans, M. J., Methven, J., Watson, N., Lee, J. D., Hopkins, J. R., Purvis, R. M., Arnold, S. R., McQuaid, J. B., Whalley, L. K., Pilling, M. J., Heard, D. E., Monks, P. S., Parker, A. E., Reeves, C. E., Oram, D. E., Mills, G., Bandy, B. J., Stewart, D., Coe, H., Williams, P., and Crosier J.: Chemical composition observed over the mid-Atlantic and the detection of pollution signatures far from source regions, *J. Geophys. Res. Atmos.*, 112, D10S39, 2007.

Limbeck, A., Kulmala, M. and Puxbaum, H.: Secondary organic aerosol formation in the atmosphere via heterogeneous reaction of gaseous isoprene on acidic particles, *Geophys. Res. Lett.*, 30, GL017738, 2003.

Lippman, M.: Health effects of tropospheric ozone: review of current research findings and their implications to ambient air quality standards, *J.Exposure Anal. Environ. Epidemiol.*, 3, 103-128, 1993

Liu, S. C., Kley, D., McFarland, M., Mahlman, M. D., and Levy, H.: On the origin of tropospheric ozone, *J. Geophys. Res.*, 85, 7546-7552, 1980.

Liu, S. C., Trainer, M., Fehsenfeld, F. C., Parrish, D. D., Williams, E. J., Fahey, D. W., Hubler, G., and Murphy, P. C.: Ozone Production in the Rural Troposphere and the Implications for Regional and Global Ozone Distributions, *J. Geophys. Res.*, 92, 4191-4207, 1987.

Liu, Z., Wang, Y., Gu, D., Zhao, C., Huey, L. G., Stickel, R., Liao, J., Shao, M., Zhu, T., Zeng, L., Liu, S. C., Chang, C. C., Amoroso, A., and Costabile, F.: Evidence of Reactive Aromatics As a Major Source of Peroxy Acetyl Nitrate over China, *Environ. Sci. Technol.*, 44, 7017-7022, 2010

Logan, J. A., Prather, M. J., Wofsy, S. C., and McElroy, M.B.: Tropospheric chemistry: A global perspective, *J. Geophys. Res.*, 86, 7210-7254, 1981.

Ludwig, J., Meixner, F. X., Vogel, B. and Forstner, J.: Soil-air exchange of nitric oxide: An overview of processes, environmental factors, and modelling studies. *Biogeochemistry*, 52, 225-257, 2001.

Mahajan, A. S., Plane, J. M. C., Oetjen, H., Mendes, L., Saunders, R. W., Saiz-Lopez, A., Jones, C. E., Carpenter, L. J., McFiggans, G. B.: Measurement and modelling of tropospheric reactive halogen species over the tropical Atlantic Ocean. *Atmos. Chem. Phys.*, 10, 4611-4624, 2010.

Martin, M. V., Honrath, R. E., Owen, R. C., and Li, Q. B.: Seasonal variation of nitrogen oxides in the central North Atlantic lower free troposphere, *J. Geophys. Res.*, 113, D17307, 2008

Mather, J. H., Stevens, P. S., and Brune, W. H.: OH and HO<sub>2</sub> measurements using laserinduced fluorescence, *J. Geophys. Res.*, 102, (D5), 6427-6436, 1997

Mauldin, R. L., Frost, G. J., Chen, G., Tanner, D. J., Prevot, A. S. H., Davies, D. D., Eisele, F. L.: OH measurements during the first aerosol characterization experiment (ACE-1): observations and model comparisons, *J. Geophys. Res.*, 103, 16713-16729, 1998.

McFiggans, G., Bale, C. S. E., Ball, S. M., Beames, J. M., Bloss, W. J., Carpenter, L. J., Dorsey, J., Dunk, R., Flynn, M. J., Furneaux, K. L., Gallagher, M. W., Heard, D. E., Hollingsworth, A. M., Hornsby, K., Ingham, T., Jones, C. E., Jones, R. L., Kramer, L. J., Langridge, J. M., Leblanc, C., LeCrane, J.-P., Lee, J. D., Leigh, R. J., Longley, I., Mahajan, A. S., Monks, P. S., Oetjen, H., Orr-Ewing, A. J., Plane, J. M. C., Potin, P., Shillings, A. J. L., Thomas, F., von Glasow, R., Wada, R., Whalley, L. K., and Whitehead, J. D.: Iodine-mediated coastal particle formation: an overview of the Reactive Halogens in the Marine Boundary Layer (RHAMBLE) Roscoff coastal study, *Atmos. Chem. Phys.*, 10, 2975-2999, 2010.

Merten, A., Tschritter, J., and Platt, U.: Design of differential optical absorption spectroscopy long-path telescopes based on fiber optics, *Applied Optics.*, 50, 738-754, 2011.

Mickley, L. J., Jacob, D. J., Field, B. D., and Rind, D. H.: Climate response to the increase in tropospheric ozone since preindustrial times: A comparison between ozone and equivalent CO<sub>2</sub> forcings, *J. Geophys. Res.*, 109, D05106, 2004

Mihelcic, D., Ehhalt, D. H., Kulesa, G. F., Klomfass, J., Trainer, M., Schmidt, U., and, Roers, H.: Measurements of free radicals in the atmosphere by matrix isolation and electron paramagnetic resonance, *Pure Applied Geophysics.*, 116, 530, 1978

Mihelcic, D., Musgen, P., and Ehhalt, D. H.: An improved method of measuring tropospheric NO<sub>2</sub> and RO<sub>2</sub> by matrix isolation and electron-spin-resonance, *J. Atmos. Chem.*, 3, (3), 341-361, 1985

Mihelcic, D., Klemp, D., Müsgen, P., Pätz, H. W., Kley, D., and Volz-Thomas, A.: Simultaneous measurements of peroxy and nitrate radicals at Schauinsland, *J. Atmos. Chem.*, 16, 313-335, 1993

Mihelcic, D., Holland, F., Hofzumahaus, A., Hoppe, L., Konrad, S., Müsgen, P., Pätz, H.-W., Schäfer, H.-J., Schmitz, T., Volz-Thomas, A., Bächmann, K., Schlonski, S., Platt, U., Geyer, A., Alicke, B., and Moorgat, G.K.: Peroxy radicals during BERLIOZ at Pabstthum: Measurements, radical budgets and ozone production, *J. Geophys. Res.*, 108, (D4), 8254, 2003

Mihele, C. M., and Hastie, D. R.: The sensitivity of the radical amplifier to ambient water vapour, *Geophys. Res. Lett.*, 25, 1911-1913, 1998

Mihele, C. M., Mozurkewich, M., and Hastie, D. R.: Radical loss in a chain reaction of CO and NO in the presence of water: Implications for the radical amplifier and atmospheric chemistry, *Int. J. Chem. Kin.*, 31, 145-152, 1999

- Mihele, C. M., and Hastie, D. R.: Radical chemistry at a forested site: Results from the PROPHET 1997 campaign, *J. Geophys. Res.*, 108, (D15), 4450, 2003.
- Molina, M. J., and Rowland, F. S.: Stratospheric sink for chlorofluoromethanes. Chlorine atom-catalyzed destruction of ozone, *Nature (London, United Kingdom)*, 249, 810-812, 1974.
- Monks, P. S., Carpenter, L. J., and Penkett, S. A.: Night-time peroxy radical chemistry in the remote marine boundary layer over the Southern ocean, *Geophys. Res. Lett.*, 23, 535-538, 1996
- Monks, P. S., Carpenter, L. J., Penkett, S. A., Ayers, G. P., Gillett, R. W., Galbally, I. E., and Meyer, C. P.: Fundamental ozone photochemistry in the remote boundary layer: The SOAPEX experiment, measurement and theory, *Atmos. Environ.*, 32, 3647- 3664, 1998.
- Monks, P. S.: A review of the observations and origins of the spring ozone maximum, *Atmos. Environ.*, 34, 3545-3561, 2000a
- Monks, P. S., Holland, G., Salisbury, G., Penkett, S. A., and Ayers, G. P.: A seasonal comparison of ozone photochemistry in the remote marine boundary layer, *Atmos. Environ.*, 34, 2547-2561, 2000b.
- Monks, P. S.: Handbook of Atmospheric science: Principle and Application, *Blackwell Publishing, Oxford*, 2003a.
- Monks, P. S.: TROTREP Synthesis and Integration Report, Report to the EU FPV Energy, Environment and Sustainable Development Program, *European Union*, 2003b.
- Monks, P. S.: Gas-phase radical chemistry in the troposphere, *Chemical Society, Reviews*, 34, 376-395, 2005.
- Moore, R., Oram, D., and Penkett, S. A.: Production of isoprene by marine phytoplankton cultures, *Geophys. Res. Lett.*, 21, 2507-2510, 1994.
- Parker, A. E. *Measurement of Peroxy Radicals, Chemistry and Transport in the Atmosphere*, PhD. thesis, University of Leicester, 2007
- Parker, A. E., Monks, P. S., Wyche, K. P., Balzani-Lv, J. M., Staehelin, J., Reimann, S., Legreid, G., Vollmer, M. K., and Steinbacher, M.: Peroxy radicals in the summer free troposphere: seasonality and potential for heterogeneous loss, *Atmos. Chem. Phys.*, 9, 1989-2006, 2009.
- Paulson, S. E., and Seinfeld, J. H.: Development and Evaluation of a Photooxidation Mechanism for Isoprene. *J. Geophys. Res.*, 97, 20703-20717, 1992a
- Paulson, S. E., Flagan, R. C., and Seinfeld, J. H.: Atmospheric photooxidation of Isoprene, Part1, The hydroxyl radical and ground state oxygen reactions, *Int. J. Chem. Kinet.*, 24, 79-101, 1992b.

- Paulson, S. E., Flagan, R. C., and Seinfeld, J. H.: Atmospheric photooxidation of isoprene, Part 2, The hydroxyl radical and ground state oxygen reactions, *Int. J. Chem. Kinet.*, 24, 103-125, 1992c.
- Pearson, G., Davies, F., and Collier, C. G.: An analysis of the performance of the UFAM pulsed Doppler LIDAR for observing the boundary layer, *J. Atmos. Ocean. Tech.*, 26, 240-250, 2009.
- Pearson, G., Davies, F., and Collier, C.G.: Remote sensing of the tropical rain forest boundary layer using pulsed Doppler lidar, *Atmos. Chem. Phys.*, 10, 5891-5901, 2010.
- Peeters, J., Nguyen, T. L., and Vereecken, L.: HOx radical regeneration in the oxidation of isoprene, *Phys. Chem. Chem. Phys.*, 28, 5935-5939, 2009.
- Penkett, S. A., Monks, P. S., Carpenter, L. J., and Clemitshaw, K. C.: Relationships between ozone photolysis rates and peroxy radical concentrations in clean air over the Southern Ocean, *J. Geophys. Res.*, 102, (D11), 12, 805-12,817, 1997
- Penkett, S. A., Clemitshaw, K. C., Savage, N. H., Burgess, R. A., Cardenas, L. M., Carpenter, L. J., McFadyden, G. G., and Cape, J. N.: Studies of oxidant production at the Weybourne Atmospheric observatory in summer and winter conditions, *J. Atmos. Chem.*, 33, 111-128, 1999
- Peters, C., Pechtl, S., Stutz, J., Hebestreit, K., Hönninger, G., Heumann, K. G., Schwarz, A., Winterlik, J., and Platt, U.: Reactive and organic halogen species in three different European coastal environments, *Atmos. Chem. Phys.*, 5, 3357-3375, 2005.
- Pieterse, G., Krol, M. C., and Rockmann, T.: A consistent molecular hydrogen isotope chemistry scheme based on an independent bond approximation, *Atmos. Chem. Phys.*, 9, 8503-8529, 2009.
- Pike, R. C., Lee, J. D., Young, P. J., Carver, G. D., Yang, X., Warwick, N., Moller, S., Misztal, P., Langford, B., Stewart, D., Reeves, C. E., Hewitt, C. N., and Pyle, J. A.: NO<sub>x</sub> and O<sub>3</sub> above a tropical rainforest: an analysis with a global and box model, *Atmos. Chem. Phys.*, 10, 10607-10620, 2010.
- Plane, J. M. C. and Saiz-Lopez, A.: UV-Visible differential optical absorption spectroscopy (DOAS), in: Analytical techniques for atmospheric measurement, edited by: Heard, D. E., *Blackwell Publishing*, Oxford, 2006.
- Platt, U., Alicke, B., Dubois, R., Geyer, A., Hofzumahaus, A., Holland, F., Martinez, M., Mihelcic, D., Klüpfel, T., Lohrmann, B., Pätz, W., Perner, D., Rohrer, D., Scäfer, J., and Stutz, J.: Free radicals and fast photochemistry during BERLIOZ, *J. Atmos. Chem.*, 42, 359-394, 2002
- Poisson, N., Kanakidou, M., and Crutzen, P.: Impact of nonmethane hydrocarbons on tropospheric chemistry and the oxidizing power of the global troposphere: 3-dimensional modelling results, *J. Atmos. Chem.*, 36, 157-230, 2000.
- Pugh, T. A. M., MacKenzie, A. R., Hewitt, C. N., Langford, B., Edwards, P. M., Furneaux, K. L., Heard, D. E., Hopkins, J. R., Jones, C. E., Karunaharan, A., Lee, J.,

Mills, G., Misztal, P., Moller, S., Monks, P. S., and Whalley, L. K.: Simulating atmospheric composition over a South-East Asian tropical rainforest: performance of a chemistry box model, *Atmos. Chem. Phys.*, 10, 279-298, 2010.

Ravetta, F., Jacob, D. J., Brune, W. H., Heikes, B. G., Anderson, B. E., Blake, D. R., Gregory, G. L., Sachse, G. W., Sandholm, S. T., Shetter, R. E., Singh, H. B., and Talbot, R. W.: Experimental evidence for the importance of convected methylhydroperoxide as a source of hydrogen oxide (HOx) radicals in the tropical upper troposphere, *J. Geophys. Res.*, 106, 32,709-732,716, 2001.

Read, K. A., Mahajan, A. S., Carpenter, L. J., Evans, M. J., Faria, B. V. E., Heard, D. E., Hopkins, J. R., Lee, J. D., Moller, S. J., Lewis, A. C., Mendes, L., McQuaid, J. B., Oetjen, H., Saiz Lopez, A., Pilling, M. J., and Plane, J. M. C.: Extensive halogen mediated ozone destruction over the tropical Atlantic Ocean. *Nature.*, 453, 1232-1235, 2008

Reeves, C. E., Formenti, P., Afif, C., Ancellet, G., Atti, J.-L., Bechara, J., Borbon, A., Cairo, F., Coe, H., Crumeyrolle, S., Fierli, F., Flamant, C., Gomes, L., Hamburger, T., Jambert, C., Law, K. S., Mari, C., Jones, R. L., Matsuki, A., Mead, M. I., Methven, J., Mills, G. P., Minikin, A., Murphy, J. G., Nielsen, J. K., Oram, D. E., Parker, D. J., Richter, A., Schlager, H., Schwarzenboeck, A., and Thouret, V.: Chemical and aerosol characterisation of the troposphere over West Africa during the monsoon period as part of AMMA, *Atmos. Chem. Phys.*, 10, 7575-7601, 2010.

Reichert, L., Hernandez, M. D. A., Stobener, D., Burkert, J., and Burrows, J. P.: Investigation of the effect of water complexes in the determination of peroxy radical ambient concentrations: Implications for the atmosphere, *J. Geophys. Res.*, 108, 4017, 2003

Reiner, T., Hanke, M., and Arnold, F.: Atmospheric peroxy radical measurements by ion-molecule reaction-mass spectrometry: a novel analytical method using amplifying chemical conversion to sulphuric acid, *J. Geophys. Res.*, 102, 1311-1326, 1997

Ren, X., Edwards, G. D., Cantrell, C. A., Leshner, R. L., Metcalf, A. R., Shirley, T., and Brune, W. H.: Intercomparison of peroxy radical measurements at a rural site using laser-induced fluorescence and Peroxy Radical Chemical Ionization Mass Spectrometer (PerCIMS) techniques, *J. Geophys. Res.*, 108, (D19), 4605, 2003

Rickard, A. R., Johnson, D., McGill, C. D., and Marston, G.: OH yields in the gas-phase reactions of ozone with alkenes, *J. Phys. Chem.*, 103, 7656-7664, 1999

Roehl, C. M., Bauer, D., and Moortgat, G. K.: Absorption Spectrum and Kinetics of the Acetylperoxy Radical, *J. Phys. Chem.* 1996, 100, 4038-4047, 1995.

Ryall, D. B., Derwent, R. G., Manning, A. J., Simmonds, P. G., and O'Doherty, S.: Estimating source regions of European emissions of trace gases from observations at Mace Head, *Atmos. Environ.*, 35, 2507-2523, 2001.

Sadanaga, Y., J. Matsumoto, K. Sakurai, R. Isozaki, S. Kato, T. Nomaguchi, H. Bandow, and Kajii, Y.: Development of a measurement system of peroxy radicals

using a chemical amplification/laser-induced fluorescence technique, *Rev. Sci. Instrum.*, 75, 864-872, 2004.

Saiz-Lopez, A. and Plane, J. M. C.: Novel iodine chemistry in the marine boundary layer, *Geophys. Res. Lett.*, 31, 19215-19218, 2004.

Saiz-Lopez, A., Plane, J. M. C., and Shillito, J. A.: Bromine oxide in the mid-latitude marine boundary layer, *Geophys. Res. Lett.*, 31, L03111, 2004a.

Saiz-Lopez, A., Shillito, J. A., Coe, H., and Plane, J. M. C.: Measurements and modelling of I<sub>2</sub>, IO, OIO, BrO and NO<sub>3</sub> in the mid-latitude marine boundary layer, *Atmos. Chem. Phys.*, 6, 1513-1528, 2006

Saiz-Lopez, A., Chance, K., Liu, X., Kurosu, T. P., and Sander, S. P.: First observations of iodine oxide from space, *Geophys. Res. Lett.*, 34, L12812, 2007

Salisbury, G.: *Measurement of peroxy radicals in the marine boundary layer*, Ph.D. thesis, University of Leicester, 2001

Salisbury, G., Rickard, A. R., Monks, P. S., Allan, B. J., Bauguitte, S., Penkett, S. A., Carslaw, N., Lewis, A. C., Creasy, D. J., Heard, D. E., Jacobs, P. J., and Lee, J. D.: Production of peroxy radicals at night via reactions of ozone and the nitrate radical in the marine boundary layer, *J. Geophys. Res.*, 106, 12669-12687, 2001

Salisbury, G., Monks, P. S., Bauguitte, S., Bandy, B. J., and Penkett, S. A.: A seasonal comparison of the ozone photochemistry in clean and polluted air masses at Mace Head, Ireland, *J. Atmos. Chem.*, 41, 163-187, 2002

Sander, S. P., Friedl, R. R., Golden, D. M., Kurylo, M. J., Moortgat, C. K., Keller Rudek, H., Wine, P. H., Ravishankara, A. R., Kolb, C. E., Molina, M. J., Finlayson Pitts, B. J., Huie, R. E., and Orkin, V. L.: Chemical kinetics and photochemical data for use in atmospheric Studies, Evaluation number 15, *NASA Jet Propulsion Laboratory, Publication.*, 062, 2006.

Saunders, S. M., Jenkin, M. E., Derwen, R. G., and Pilling, M. J.: Protocol for the development of the Master Chemical Mechanism, MCM v3 (Part A): tropospheric degradation of non-aromatic volatile organic compounds, *Atmos. Chem. Phys.*, 3, 161-180, 2003.

Schrimpf, W., Muller, K. P., Johnen, F. J., Lienaerts, K., and Rudolph, J.: An Optimized Method for Airborne Peroxyacetyl Nitrate (PAN) Measurements, *J. Atmos. Chem.*, 22, 303-317, 1995.

Shaw, S. L., Chisholm, S.W., and Prinn, R. G.: Isoprene production by Prochlorococcus, a marine cyanobacterium and other phytoplankton, *Marine. Chem.*, 80, 227-245, 2003.

Simmonds, P. G., Derwent, R. G., Manning, A. L., and Spain, G.: Significant growth in surface ozone at Mace Head, Ireland, 1987-2003, *Atmos. Environ.*, 38, (28), 4769-4778, 2004.

Silva, G. D., Graham, C., and Wang, Z.-F.: Unimolecular betahydroxyperoxy radical decomposition with OH recycling in the photochemical oxidation of isoprene, *Environ. Sci. Tech.*, 44, 250–256, 2010.

Singh, H. B., Tabazadeh, A., Evans, M. J., Field, B. D., Jacob, D. J., Sachse, G., Crawford, J. H., Shetter, R., and Brune, W. H.: Oxygenated volatile organic chemicals in the oceans: Inferences and implications based on atmospheric observations and air-sea exchange models, *Geophys. Res. Lett.*, 30, (16), 1862, 2003.

Sjostedt, S. J., Huey, L. G., Tanner, D. J., Peischl, J., Chen, G., Dibb, J. E., Lefer, B., Hutterli, M. A., Beyersdorf, A. J., Blake, N. J., Blake, D. R., Sueper, D., Ryerson, T., Burkhardt, J., and Stohl, A.: Observations of hydroxyl and the sum of peroxy radicals at Summit, Greenland during summer 2003, *Atmos. Environ.*, 41, (24), 5122-5137, 2007.

Smith, S. C., Lee, J. D., Bloss, W. J., Johnson, G. P., Ingham, T., and Heard, D. E.: Concentrations of OH and HO<sub>2</sub> radicals during NAMBLEX: measurements and steady state analysis, *Atmos. Chem. Phys.*, 6, 1435-1453, 2006

Solberg, S., Dye, C., Walker, S.-M., and Simpson, D.: Long-term measurements and model calculations of formaldehyde at rural European monitoring sites, *Atmos. Environ.*, 35, 195-207, 2001.

Sommariva, R., Bloss, W. J., Brough, N., Carslaw, N., Flynn, M., Haggerstone, A.-L., Heard, D. E., Hopkins, J. R., Lee, J. D., Lewis, A. C., McFiggans, G., Monks, P. S., Penkett, S. A., Pilling, M. J., Plane, J. M. C., Read, K. A., Saiz-Lopez, A., Rickard, A. R., and Williams, P. I.: OH and HO<sub>2</sub> chemistry during NAMBLEX: roles of oxygenates, halogen oxides and heterogeneous uptake, *Atmos. Chem. Phys.*, 6, 1135-1153, 2006.

Sommariva, R., Brown, S. S., Roberts, J. M., Brookes, D. M., Parker, A. E., Monks, P. S., Bates, T. S., Bon, D., de Gouw, J. A., Frost, G. J., Gilman, J. B., Goldan, P. D., Herndon, S. C., Kuster, W. C., Lerner, B. M., Osthoff, H. D., Tucker, S. C., Warneke, C., Williams, E. J., and Zahniser, M.S.: Ozone production in remote oceanic and industrial areas derived from ship based measurements of peroxy radicals during TexAQS 2006, *Atmos. Chem. Phys.*, 11, 2471-2485, 2011.

Stedman, J. R.: The predicted number of air pollution related deaths in the UK during the August 2003 heatwave, *Atmos. Environ.*, 38, 1087-1090, 2004.

Stevens, P. S., Mather, J. H., Brune, W. H., Eisele, F., Tanner, D., Jefferson, A., Cantrell, C., Shetter, R., Sewall, S., Fried, A., Henry, B., Williams, E., Baumann, K., Goldan, P., and Kuster, W.: HO<sub>2</sub>/OH and RO<sub>2</sub>/HO<sub>2</sub> ratios during the Tropospheric Photochemistry Experiment: Measurements and theory *J. Geophys. Res.*, 102, (D5), 6379-6392, 1997.

Still, T. J., Al-Haider, S., Seakins, P. W., Sommariva, R., Stanton, J. C., Mills, G., and Penkett, S. A.: Ambient formaldehyde measurements made at a remote marine boundary layer site during the NAMBLEX campaign – a comparison of data from chromatographic and modified Hantzsch techniques, *Atmos. Chem. Phys.*, 6, 2711-2726, 2006.

Stone, D., Evans, M. J., Commane, R., Ingham, T., Floquet, C. F. A., McQuaid, J. B., Brookes, D. M., Monks, P. S., Purvis, R., Hamilton, J. F., Hopkins, J., Lee, J., Lewis, A. C., Stewart, D., Murphy, J. G., Mills, G., Oram, D., Reeves, C. E., and Heard, D. E.: HO<sub>x</sub> observations over West Africa during AMMA: impact of isoprene and NO<sub>x</sub>, *Atmos. Chem. Phys.*, 10, 9415-9429, 2010.

Stroud, C., Madronich, S., Atlas, E., Cantrell, C., Fried, A., Wert, B., Ridley, B., Eisele, F., Mauldin, L., Shetter, R., Lefer, B., Flocke, F., Weinheimer, A., Coffey, M., Heikes, B., Talbot, R., and Bealer, D.: Photochemistry in the Arctic Free Troposphere: Ozone Budget and Its Dependence on Nitrogen Oxides and the Production Rate of Free Radical, *J. Atmos. Chem.*, 47, (2), 107-138, 2004

Sumner, A. L., Shepson, P. B., Couch, T. L., Thornberry, T., Carroll, M. A., Sillman, S., Pippin, M., Bertman, S., Tan, D., Faloon, I., Brune, W., Young, V., Cooper, O., Moody, J., and Stockwell, W., 2001: A study of formaldehyde chemistry above a forest canopy, *J. Geophys. Res.*, 106, 24387-24427, 2001.

Tan, D., I. Faloon, J. B. Simpas, W. Brune, J. Olson, J. Crawford, M. Avery, G. Sachse, S. Vay, S. Sandholm, H.-W. Guan, T. Vaughn, J. Mastromarino, B. Heikes, J. Snow, J. Podolske, and Singh, H.: OH and HO<sub>2</sub> in the tropical Pacific: Results from PEM-Tropics B, *J. Geophys. Res.*, 106, 32,667- 32,681, 2001a.

Tan, D., Faloon, I., Simpas, J. B., Brune, W., Shepson, P. B., Couch, T. L., Sumner, A. L., Carroll, M. A., Thornberry, T., Apel, E., Riemer, D., and Stockwell, W.: HO<sub>x</sub> budgets in a deciduous forest: Results from the PROPHET summer 1998 campaign, *J. Geophys. Res.*, 106, (D20), 24407-24427, 2001b

Taraborrelli, D., Lawrence, M. G., Butler, T. M., Sander, R., and Lelieveld, J.: Mainz Isoprene Mechanism 2 (MIM2): an isoprene oxidation mechanism for regional and global atmospheric modelling, *Atmos. Chem. Phys.*, 9, 2751-2777, 2009

Thornton J. A., Wooldridge, P. J., Cohen, R. C., Martinez, M., Harder, H., Brune, W. H., Williams, E. J., Roberts, J. M., Fehsenfeld, F. C., Hall, S. R., Shetter, R. E., Wert, B. P., and Fried, A.: Ozone production rates as a function of NO<sub>x</sub> abundances and HO<sub>x</sub> production rates in Nashville urban plume, *J. Geophys. Res.* 107, (D12), 4146, 2002

Tuazon, E. C., Carter, W. P. L., and Atkinson, R.: Thermal decomposition of peroxyacetyl nitrate and reactions of acetyl peroxy radicals with nitric oxide and nitrogen dioxide over the temperature range 283-313 K, *J. Phys. Chem.*, 95, 2434-2437, 1991.

Tucker, A. C., Brewer, W. A., Banta, R. M., Senff, C. J., Sandberg, S. P., Law, D. C., Weickmann, A. M. and Hardesty, R. M.: Doppler Lidar Estimation of Mixing Height Using Turbulence, Shear, and Aerosol Profiles, *J. Atmos. Ocean Tech.*, 26, 673-688, 2009.

Tuovinen, J. P.: Assessing vegetation exposure to ozone: properties of the AOT40 index and modifications by deposition modelling, *Environmental Pollution.*, 109, 361-372, 2000.

Tuovinen, J. P., Simpson, D., and Altimir, N.: Modelling the Stomatal and Non-stomatal Ozone fluxes to Coniferous Forests in Northern Europe, presented at EGU General Assembly, *Geophysical Research Abstracts.*, vol. 10. EGU 2008a-A-08272, Vienna, Austria, 14-18, April 2008

Vaughan, S., Canosa-Mas, C. E., Pfrang, C., Shallcross, D. E., Watson, L., and Wayne, R. P.: Kinetic studies of reactions of the nitrate radical ( $\text{NO}_3$ ) with peroxy radicals ( $\text{RO}_2$ ): an indirect source of OH at night?, *Physical Chemistry Chemical Physics*, 8, 3749-3760, 2006.

Vogt, R., Sander, R., von Glasow, R., and Crutzen, P. J.: Iodine chemistry and its role in halogen activation and ozone loss in the marine boundary layer: A model study, *J. Atmos. Chem.*, 32, 375-395, 1999

Volz-Thomas, A., Lerner, A., Patz, H. S., Schultz, M., McKenna, D., Schmitt, R., Madronich, S., and Roth, E.: Airborne Measurements of the Photolysis of  $\text{NO}_2$ , *J. Geophys. Res. Atmos.*, 101, 18613-18627, 1996.

Volz-Thomas, A., Pätz, H.-W., Houben, N., Konrad, S., Mihelcic, D., Klüpfel, T., and Perner, D.: Inorganic trace gases and peroxy radicals during BERLIOZ at Pabstuum: An investigation of the photostationary state of  $\text{NO}_x$  and  $\text{O}_3$ , *J. Geophys. Res.*, 108, (D4), 8248, 2003

Von Glasow, R., von Kuhlmann, R., Lawrence, M. G., Platt, U., and Crutzen, P. J.: Impact of reactive bromine chemistry in the troposphere, *Atmos. Chem. Phys.*, 4, 2481-2497, 2004.

Wada, R., Beames, J. M., and Orr-Ewing, A. J.: Measurement of IO radical concentrations in the marine boundary layer using a cavity ring-down spectrometer, *J. Atmos. Chem.*, 58, 69-87, 2007.

Wayne, R. P., Barnes, I., Biggs, P., Burrows, J. P., Canos-Mas, C. E., Hjorth, J., LeBras, G., Moortgat, G. K., Perner, D., Poulet, G., Restelli, G., and Sidebottom, H.: The nitrate radical: Physics, chemistry and the environment, *Atmos. Environ.*, 25, 1-206, 1991

Wayne, R. P.: Chemistry of Atmospheres. *Oxford University Press, Third Edition*, 2000.

Westberg, H., Lamb, B., Hafer, R., Hills, A., Shepson, P. B., and Vogel, C.: Measurement of isoprene fluxes at the PROPHET site, *J. Geophys. Res.*, 106, 24,347-24,358, 2001.

Whalley, L. K., Furneaux, K. L., Gravestock, T., Atkinson, H. M., Bale, C. S. E., Ingham, T., Bloss, W. J., and Heard, D. E.: Detection of Iodine Monoxide Radicals in the Marine Boundary Layer using Laser Induced Fluorescence Spectroscopy, *J. Atmos. Chem.*, 58, 19-39, 2007.

Whalley, L. K., Furneaux, K. L., Goddard, A., Lee, J. D., Mahajan, A., Oetjen, H., Read, K. A., Kaaden, N., Carpenter, L. J., Lewis, A. C., Plane, J. M. C., Saltzman, E. S., Wiedensohler, A., Heard, D. E.: The chemistry of OH and HO<sub>2</sub> radicals in the boundary layer over the tropical Atlantic Ocean. *Atmos. Chem. Phys.*, 10, 1555-1576, 2010.

Whalley, L. K., Edwards, P. M., Furneaux, K. L., Goddard, A., Ingham, T., Evans, M. J., Stone, D., Hopkins, J. R., Jones, C. E., Karunaharan, A., Lee, J. D., Lewis, A. C., Monks, P. S., Moller, S. J., Heard, D. E.: Quantifying the magnitude of a missing hydroxyl radical source in a tropical rainforest, *Atmos. Chem. Phys.*, 11, 7223-7233, 2011.

WHO: Air Quality Guidelines for Particulates Matter, Ozone, Nitrogen Dioxide and Sulphur Dioxide. *World Health Organization*, Geneva, Switzerland., 2005.

Wild, O., Law, K., McKenna, D., Bandy, B., Penkett, S., and Pyle, J.: Photochemical trajectory modeling studies of the North Atlantic region during August 1993, *J. Geophys. Res.*, 101, 29269-29288, 1996.

Yang, J., Honrath, R. E., Peterson, M. C., Dibb, J. E., Sumner, A. L., Shepson, P. B., Frey, M., Jacobi, H.-W., Swanson, A., and Blake, N.: Impacts of snow pack emissions on deduced levels of OH and peroxy radicals at Summit, Greenland, *Atmos. Environ.*, 36, 2523-2534, 2002

Zanis, P., Monks, P. S., Schuepbach, E., Penkett, S. A.: On the relationship of HO<sub>2</sub>+RO<sub>2</sub> with  $j(\text{O}^1\text{D})$  during the FREE Tropospheric Experiment (FREETEX '96) at the Jungfraujoch Observatory (3850 m above sea level) in the Swiss alps, *J. Geophys. Res.*, 104, (D21), 26913-26926, 1999.

Zanis, P., Monks, P. S., Schuepbach, E., Carpenter, L. J., Green, T. J., Mills, G. P., Bauguitte, S., and Penkett, S. A.: In situ ozone production under free tropospheric conditions during FREETEX '98 in the Swiss Alps *J. Geophys. Res.*, 105, (D19), 24223-24234, 2000a

Zanis, P., Monks, P. S., Schuepbach, E., and Penkett, S. A.: The role of *In Situ* Photochemistry in the Control of Ozone during Spring at the Jungfraujoch (3,580 m asl) - Comparison of Model Results with Measurements, *J. Atmos. Chem.*, 37, 1-27, 2000b.

Zanis, P. Monks, P. S., Schuepbach, E., Carpenter, L. J., Green, T. J., Mills, G. P., Bauguitte, S., Rickard, A. R., Brough, N., and Penkett, S. A.: Seasonal variation of peroxy radicals in the lower free troposphere based on observations from the FREE Tropospheric Experiments, *Geophys. Res. Lett.*, 30, (10), 1497, 2003

Zechmeister-Boltenstern, S., Hahn, M., Meger, S., and Jandl, R.: Nitrous oxide emissions and nitrate leaching in relation to microbial biomass dynamics in a Beech forest soil. *Soil Biology and Biochemistry*, 34, 823-832, 2002.

Zhang, L., Brook, J. R., and Vet, R.: On ozone dry deposition-with emphasis on non-stomatal uptake and wet canopies, *Atmos. Environ.*, 36, 4787-4799, 2002.

Zhou, X., and Mopper, K.: Photochemical production of low molecular weight carbonyl compounds in seawater and surface microlayer and their air-sea exchange, *Mar. Chem.*, 56, 201-213, 1997.